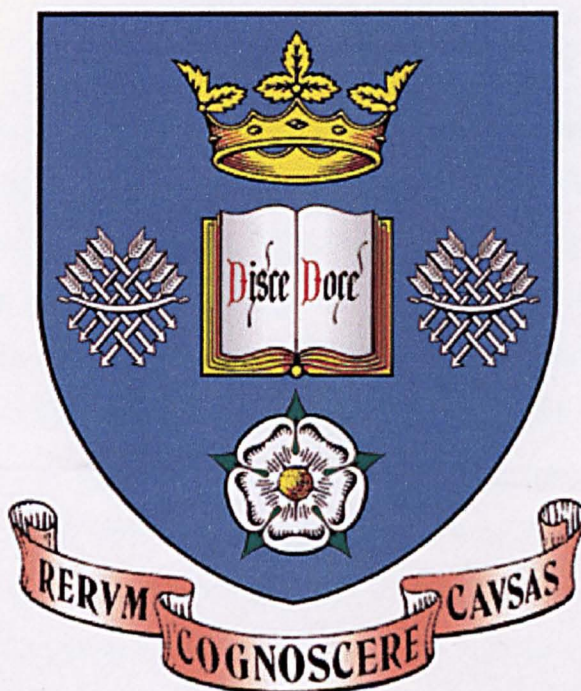


**The University of Sheffield**



**HIGH-SPEED PERMANENT MAGNET  
BRUSHLESS DC MOTORS**

by

**Jason David Ede**

A thesis submitted for the degree of  
Doctor of Philosophy in the Department  
of Electronic and Electrical Engineering,  
University of Sheffield

June 2003

## Summary

This thesis describes an investigation into some of the key design issues for high-speed permanent magnet brushless DC motors. The investigation encompasses the optimal design of motors for operation using a simple sensorless commutation strategy based on the detection of the zero-crossing of the back-emf waveforms, the optimal split ratio of the rotor diameter to the stator outer diameter, with due account of iron loss, and a systematic investigation into rotor resonances and the influence of key design parameters on the rotor resonant frequencies.

The investigation was initiated by a design study on a high-speed, exterior rotor permanent magnet brushless DC motor which was undertaken on behalf of Urenco (Capenhurst) Ltd. Comprehensive electromagnetic design and analysis was performed using proprietary CAD software developed by the Electrical Machine and Drives Research Group at the University of Sheffield. However, due to fairly rigid constraints on the prototype motor, as specified by Urenco, the design options were limited, and, consequently, the resultant motor performance was not optimal. Nevertheless, despite the occurrence of resonance modes which prevented operation of the motor above ~16krpm, useful results were obtained from a prototype motor and good agreement was obtained with dynamic simulations. This motor also served to highlight several key design issues pertaining to high-speed permanent magnet brushless DC motors, which are investigated in subsequent chapters.

Previous work on high-speed permanent magnet brushless DC drives has focussed primarily on the motor with little attention being given to the commutation strategy at the design stage. For operation using a simple sensorless commutation scheme based on the detection of the zero-crossing of the back-emf waveforms a low freewheel diode conduction angle is required if the zero-crossings are not to be obscured due to the current which flows through the freewheel diodes. It is shown that by employing a stator core design which differs somewhat from conventional designs, in terms of the width of the teeth and the back-iron radial thickness, high-speed motors which result in a low diode conduction angle are realisable without any significant degradation in machine performance. The design process has been validated by measurements on small prototype motors, and sensorless operation has been achieved at speeds in excess of 120krpm.

It had been reported previously for low speed motors, that the optimal ratio of the rotor diameter to the stator outer diameter, or split ratio, is important in determining the optimal motor design for minimum copper loss and a simple expression had been derived for

determining this optimal ratio for a motor equipped with distributed windings. This work has been extended to cater for motors with concentrated windings, and comparisons have been made with results deduced from a comprehensive CAD package and, neglecting the effects of the end-windings, good agreement has been obtained. It has also been shown that as the motor speed is increased the optimal ratio of rotor diameter to stator diameter is determined increasingly by the iron loss, which significantly reduces the optimal split ratio. The influence of key design parameters on this optimal ratio has been investigated, and it has been shown that the optimal ratio of rotor to stator diameter is highly dependent on the torque density, the stator flux density and the pole number.

Finally a systematic investigation into the resonant modes of a prototype high-speed rotor has been undertaken. Finite element predicted and measured natural frequencies have been compared at each step of the rotor assembly process, to enable an accurate model of the complete rotor to be constructed. This model has then been validated on another prototype high-speed rotor, and good agreement has been obtained. The bearings have also been incorporated into the finite element model, and, again, good agreement has been obtained with measured resonant frequencies. Utilising this model, the influence of design parameters such as the rotor active length, the bearing spacing, the shaft extension and the shaft diameter were then investigated. It was found that the shaft extension can significantly affect the rotor resonant modes, and this is illustrated by the damage caused by a resonant mode on the shaft extension. Thus, careful attention needs to be paid to rotor resonance modes during the design of high-speed motors to ensure that resonant frequencies occur outside the operating speed range.

## Acknowledgements

I should like to express my sincere thanks to everyone who contributed to making this thesis possible, in particular:

- Professor Z.Q. Zhu and Professor D. Howe for their continuous encouragement, advice, guidance and invaluable discussions throughout the duration of the investigation.
- Members of the Electrical Machines & Drives Research Group for all their advice, and the technical support staff for all their help with the construction of the various test motors.
- My family and friends for their continuous encouragement and support during the course of this Ph.D.

# Contents

Summary .....	i
Acknowledgements.....	iii
Nomenclature.....	vii
<b>Chapter 1 General Introduction .....</b>	<b>1</b>
1.1 Introduction .....	1
1.2 Motor technologies .....	2
1.2.1 Induction machines .....	2
1.2.2 Reluctance machines .....	7
1.2.3 Permanent magnet machines.....	11
1.3 General issues applicable to high-speed motors .....	20
1.4 Sensorless motor control.....	22
1.5 Scope and contribution of thesis .....	31
<b>Chapter 2 Design study of an external rotor, slotless, brushless DC motor with Halbach magnetised magnetically loaded composite rotor.....</b>	<b>33</b>
2.1 Introduction .....	33
2.1.1 Uranium enrichment.....	33
2.1.2 Magnetically loaded composite (MLC).....	35
2.1.3 Motor specification .....	36
2.2 Brushless dc motor design .....	37
2.2.1 CAD design software.....	37
2.2.2 Design methodology.....	38
2.2.3 Pole number and winding thickness .....	39
2.2.4 Magnet radial thickness .....	41
2.3 Finite element validation.....	43
2.3.1 Back-emf calculation .....	43
2.3.2 Inductance calculations.....	44
2.3.3 Comparison of results .....	46
2.4 Dynamic Simulations.....	46
2.5 Comparison of predicted and measured stator parameters.....	49
2.5.1 Self-inductance and mutual inductance .....	49
2.5.2 Phase resistance .....	52
2.5.3 Verification of NdFeB powder loading.....	52
2.5.4 Back-emf.....	54
2.6 Hall sensors .....	55
2.7 Motor tests.....	59
2.7.1 Test rig.....	59
2.7.2 Test methodology.....	60
2.7.3 ‘Run-down’ method for determination of motor torque .....	61
2.7.4 Motor performance with steel (SKF 708CC) bearing.....	63
2.7.5 Motor performance with ceramic (C38HDL C22 OJ-201) bearing.....	66
2.7.6 Voltage and current waveforms .....	69
2.7.7 Natural frequency measurements of MLC rotor.....	70
2.8 Research issues to be investigated further .....	72

<b>Chapter 3</b>	<b>Electromagnetic design of high-speed, permanent magnet, brushless DC motor for sensorless operation.....</b>	<b>74</b>
3.1	Introduction .....	74
3.2	Analysis of current waveform .....	76
3.3	Basic principles of back-emf sensorless operation .....	78
3.4	Proposed design criteria.....	78
3.5	Design for sensorless commutation .....	79
3.5.1	Design considerations and constraints.....	80
3.5.2	100mNm motors.....	81
3.5.3	15mNm motors.....	88
3.6	Finite element analysis .....	92
3.6.1	Airgap field distributions.....	92
3.6.2	Back-emf waveforms .....	93
3.6.3	Winding inductances .....	97
3.6.4	No-load stator iron loss .....	99
3.7	Manufacture of prototype motors.....	101
3.7.1	Rotors.....	101
3.7.2	Stators .....	102
3.8	Experimental validation.....	104
3.8.1	Winding resistance .....	104
3.8.2	Winding inductances .....	105
3.8.3	Back-emf waveforms .....	107
3.8.4	Experimental method for performance measurement.....	110
3.8.5	100mNm motor ( $A_1$ & $B_1$ ) phase current waveforms.....	110
3.8.6	15mNm motor ( $A_2$ & $B_2$ ) phase current waveforms.....	112
3.9	Summary .....	113
<b>Chapter 4</b>	<b>Optimal split ratio.....</b>	<b>115</b>
4.1	Introduction .....	115
4.2	Simplified analytical technique for derivation of the optimal split ratio ....	116
4.2.1	Distributed (overlapping) winding.....	118
4.2.2	Concentrated (non-overlapping) winding .....	122
4.2.3	Optimum split ratio for minimum copper loss .....	125
4.2.4	Comparison between optimal split ratio derived from CAD package and analytical expression .....	127
4.3	Optimal split ratio accounting for both iron and copper loss .....	129
4.4	Summary .....	141
<b>Chapter 5</b>	<b>Rotor mechanical resonances .....</b>	<b>143</b>
5.1	Mechanical resonant frequencies.....	143
5.1.1	Introduction .....	143
5.1.2	Finite element modelling of rotor resonances .....	145
5.1.3	Impulse response tests.....	147
5.2	Finite element analysis of resonant frequencies.....	149
5.2.1	Rotor shaft with one end-cap.....	149
5.2.2	Shaft with and without both end-caps .....	154
5.2.3	Shaft with laminations .....	155
5.2.4	Shaft with laminations and permanent magnets .....	159
5.2.5	Complete rotor .....	162
5.2.6	Summary .....	163
5.3	Derivation of bearing stiffness.....	165

5.3.1	Rotor from motor A <sub>1</sub> .....	168
5.3.2	Rotor from motor B <sub>1</sub> .....	179
5.4	Influence of leading design parameters .....	183
5.4.1	Shaft extension .....	183
5.4.2	Bearing spacing.....	190
5.4.3	Active length.....	193
5.4.4	Shaft diameter.....	194
5.5	Summary .....	197
<b>Chapter 6 General conclusions .....</b>		<b>200</b>
6.1	Design of high-speed permanent magnet brushless DC motors for sensorless operation.....	200
6.2	Mechanical resonance frequencies of high-speed brushless permanent magnet motor rotors.....	203
6.3	Overall conclusion .....	204
<b>References .....</b>		<b>206</b>
<b>List of publications.....</b>		<b>211</b>
Appendix A	MLC motor designs .....	212
Appendix B	MLC motor construction .....	215
Appendix C	Design equations for proprietary CAD software .....	224
Appendix D	Data Acquisition .....	236
Appendix E	AutoCAD motor drawings for all motors .....	240
Appendix F	Further experimental investigations to determine load torque on 100mNm motors (A <sub>1</sub> & B <sub>1</sub> ) .....	247
Appendix G	Winding design methodology .....	254
Appendix H	Validation of finite element analysis on rotor B <sub>1</sub> .....	261

## Nomenclature

		Units
$A_a$	Magnetic vector potential due to phase 'a' winding current source	Wb/m
$a_n$	Numerical constant calculated from Rayleigh method	
$A_s$	Slot area	$m^2$
$b$	Stator slot width	m
$b_0$	Stator slot opening width	m
$B_0$	Magnitude of slot ripple	T
$\hat{B}$	Peak flux density	T
$B_g$	Average airgap flux density	T
$B_m$	Peak flux density in stator core	T
$B_{max}$	Peak airgap flux density	T
$B_r$	Magnet remanence	T
$d$	Lamination thickness	m
$d_b$	Stator back-iron radial thickness	m
$D_o$	Stator outer diameter	m
$D_r$	Rotor outer diameter	m
$D_s$	Stator inner diameter	m
$e$	Phase-emf	V
$E$	Young's modulus	Pa
$E_c$	Young's modulus of composite	Pa
$E_f$	Young's modulus of carbon fibres	Pa
$E_I$	Stored energy for self-inductance calculation	J
$E_{II}$	Stored energy for mutual-inductance calculation	J
$f$	Frequency	Hz
$g$	Airgap length	m
$g'$	Effective airgap length	m
$h$	Tooth body height	m
$h_0$	Tooth tip height	m
$H_a$	Field strength due to phase 'a' winding current source	A/m
$h_i$	Heat transfer coefficient	$W/m^2/^\circ C$
$h_m$	Magnet height	m
$I$	Current	A

$I_a$	Current in phase A	A
$I_p$	Polar moment of inertia	kg m <sup>2</sup>
$I_T$	Transverse moment of inertia	kg m <sup>2</sup>
$J$	Current density	A/m <sup>2</sup>
$K$	Spring constant	N/m
$K_c$	Carter coefficient	
$K_{dn}$	Winding pitch factor	
$K_{dp}$	Winding factor	
$k_e$	Eddy current loss constant	N <sup>2</sup> sΩ/m <sup>3</sup> T <sup>3</sup>
$k_h$	Hysteresis loss constant	
$k_p$	Slot packing factor	
$K_{pn}$	Winding distribution factor	
$K_{son}$	Slot opening factor	
$K_w$	Winding coefficient	
$l$	Active core length	m
$L$	Self-inductance	mH
$l$	Length	m
$L_\delta$	Airgap component of self-inductance	mH
$l_a$	Active length	m
$L_e$	End-winding self-inductance	mH
$l_e$	Total length of end-windings	m
$l_{eff}$	Effective axial length	m
$L_{sa}$	Slot component of self-inductance	mH
$M$	Mutual inductance	mH
$m$	Mass	kg
$m_{ph}$	Phase number	
$M_\delta$	Airgap component of mutual-inductance	mH
$M_e$	End-winding mutual-inductance	mH
$n$	Critical speed	Hz
$N_c$	Number of turns per coil	
$N_p$	Number of series turns per phase	
$N_s$	Number of turns on search coil	
$p$	Number of pole pairs	
$P_c$	Classical eddy current loss	W
$P_{cu}$	Copper loss	W

$P_d$	Eddy current or dynamic loss	W
$P_{exc}$	Excess eddy current loss	W
$P_h$	Hysteresis loss component	W
$P_t$	Total iron loss	W
$Q$	Electric loading	A/m
$Q_s$	Number of stator slots	
$R$	Resistance	$\Omega$
$R_\alpha$	Temperature coefficient of resistance	
$R'$	Resistance at motor operating temperature	$\Omega$
$R_m$	Rotor magnet outer radius	m
$R_o$	Stator outer radius	m
$R_{phase}$	Phase resistance	$\Omega$
$R_r$	Rotor lamination outer radius	m
$R_s$	Stator bore radius	m
$T$	Time	s
$T_e$	Electromagnetic torque	Nm
$\nu$	Angular velocity	rads <sup>-1</sup>
$V_f$	Volume fraction of fibre in composite	
$W$	Energy	J
$w_d$	Coil winding width	m
$W_p$	Turns per pole times number of poles	
$w_t$	Tooth body width	m
$\tilde{\lambda}$	Relative permeance	
$\alpha$	Hysteresis loss constant	
$\alpha_p$	Pole-arc to pole-pitch ratio	
$\delta$	Density	kg m <sup>-3</sup>
$\rho$	Resistivity of copper	$\Omega\text{m}^{-1}$
$\Phi_n$	Flux in a tooth	Wb
$\Phi_p$	Flux per pole	Wb
$\sigma$	Electrical conductivity	S
$\Lambda_{ref}$	Reference permeance	H
$\lambda_{sa}$	Permeance coefficient	
$\Delta T$	Temperature rise	$^{\circ}\text{C}$
$\tau_i$	Stator tooth pitch	

$\tau$	Pole pitch	
$\mu_0$	Permeability of free space	H/m
$\mu_l$	Mass per unit length	kg m <sup>-1</sup>
$\mu_r$	Relative permeability	
$\omega$	Angular speed	rad s <sup>-1</sup>
$\omega_b$	Burst speed	Hz

# Chapter 1 General Introduction

## 1.1 Introduction

Up until the mid-1980's the only viable drive option for high-speed motors of any significant power was the thyristor commutated synchronous inverter [Ram95]. Recent advances in inverter technology [Rei95], in particular developments in power switching devices, have meant that brushless motor speeds have been able to be increased accordingly. There are numerous applications for high-speed motors, for example, drilling spindles [Pic96], compressors [Mek99][Soo00], centrifuges, energy storage systems such as flywheels, gyroscopes, turbo-generators [Cal99], etc. For such applications, operation at high-speed is highly desirable as it enables the motor to be considerably smaller for a given output power and eliminates the need for gearing, which can be noisy, is an extra source of loss and requires maintenance [Rei95].

A high-speed motor is generally defined as one whose design must be altered mechanically or electrically from that of standard motors in order to achieve the desired speed [Jok96]. This might range from machines running at, say, 10-20krpm developing a few 10's of kW to machines running at over 100krpm and developing a few watts. The types of problem, which are likely to be encountered in the design of such machines, are the choice of bearing technology, resonances of the rotor, containment of the rotor, rotor loss, iron/copper loss in the stator and cooling of the machine.

As regards permanent magnet brushless DC motors, there are several significant issues relating to their high-speed operation, and this thesis considers some of these in relation to a motor which is required to run at 120krpm. Some of the more pertinent issues are listed below, the highlighted ones being investigated in this thesis.

- **Mechanical resonances of the rotor.**
- Losses in rotor due to the stator slot openings, winding spatial mmf harmonics and current temporal harmonics.[Ng98]
- **Electromagnetic design of motor to minimise the iron and copper losses.**
- **Sensorless control, since few sensorless commutation schemes have been proposed for high-speed motors, but no work has been reported on the design of high-speed motors to utilise existing sensorless drives.**
- Windage loss of rotor, which can be considerable for large high-speed rotors [Cal00].

The possible types of motor, which are generally considered for high-speed operation are induction machines, brushless permanent magnet machines and both switched and

synchronous reluctance machines. The relative advantages and disadvantages of each of these technologies are discussed briefly in the following sections.

## **1.2 Motor technologies**

### **1.2.1 Induction machines**

[Soo00] assessed various motor technologies for a high-speed compressor system. From this comparison, it was clear that a permanent magnet brushless machine had a higher efficiency and could operate at a significantly higher speed. However, the motor investigated cost approximately twice as much as an induction machine. Switched reluctance motors had nearly the same efficiency, but, again, the motor cost more than the induction machine. Consequently, the induction machine was preferred.

Generally, although induction machines are not as energy efficient as permanent magnet brushless machines, they remain significantly cheaper. This, combined with their relatively simple construction, means that they are likely to remain a popular choice for many applications.

#### **a) Stator design**

The stator design of induction motors has received considerable attention over the years. Comparisons have been made between solid (ferrite) and laminated (silicon steel) stators and the influence of parameters such as the width of the slot openings [Hes83a][Hes83b][Pyr94] has also been investigated although this is discussed later in section 1.3 as it also applies to permanent magnet brushless machines. For example, [Hes83a] constructed 2 small high-speed induction motors with conducting sheet rotors with an outer diameter of 1cm. One of the motors was constructed with a laminated stator and one with a solid ferrite stator. Understandably the laminated stator design had a significantly better performance capability, as it was able to support a much higher flux density. Consequently, it had a significantly higher specific torque capability, even allowing for the forced cooling of the laminated stator. Lamination of the stator in another paper [Jok99] also provided the largest decrease in stator iron loss observed. However, it was also observed [Soo00] that heat treatment of stator laminations also helps to minimise the iron loss. Figure 1.1 shows the reduction in iron loss density at 60Hz and 800Hz when compared with untreated laminations and laminations treated with conventional heat treatment.

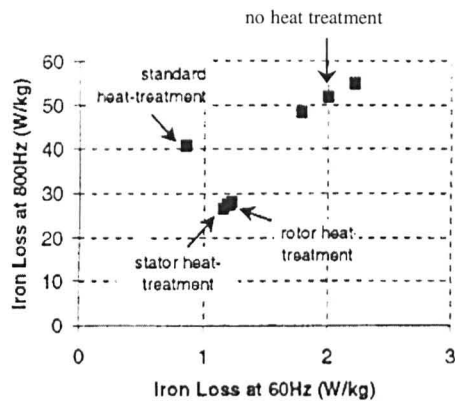


**Figure 1.1 - Comparison of iron loss densities in non-orientated silicon steel [Soo00]**

**b) Rotor design**

There are several possible rotor designs for an induction motor, some of the possible permutations being shown in Figure 1.2.

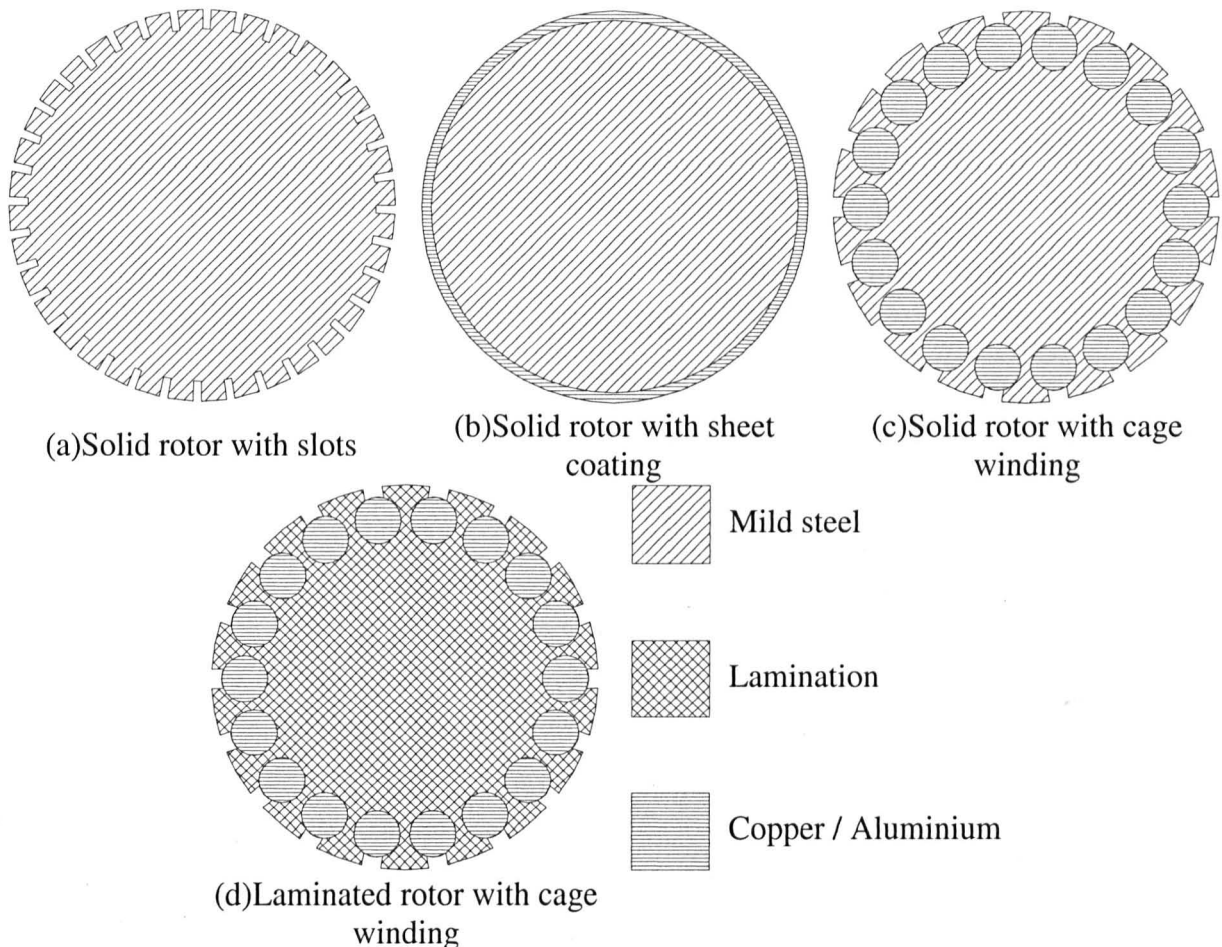


**Figure 1.2 - Alternative induction motor rotor designs**

In terms of construction and structural integrity, the solid rotor induction machine is probably the simplest and most robust. There are two main types of solid rotor, viz. the unwound rotor, Figure 1.2(a) and (b) and the wound rotor, Figure 1.2(c). However, a solid

rotor with a smooth surface has very poor efficiency, a poor power factor and a relatively high slip [Jok99], and is, therefore, rarely used. One improvement is the slotted rotor shown in Figure 1.2(a), which is normally made from solid mild steel into which the slots are, machined a short-circuited end-ring being soldered onto the ends of the teeth. The slots serve to reduce skin effect and decrease the rotor resistance. However, they also have the undesirable effect of increasing the windage loss, which may be unacceptable at high speed.

The solid rotor with a sheet coating, as shown in Figure 1.2(b), consists of a solid steel rotor with a low resistance, low permeability sheet on its surface, which is normally either copper or aluminium. [Pyr94] investigates the effect of both the rotor body and surface material on the performance, and shows that the choice of materials can have a significant effect on the rotor loss at high speed. With sheet rotors either a thicker section of the sheet material or short-circuited end-rings are used to provide a low resistance path for the induced currents. [Pyr94] also makes the observation that whilst aluminium end-rings are better for high-speed rotors, they can cause problems in relation to soldering reliably to the rotor sheet. Hence, copper end-rings are often used. Such rotors have the advantage that the rotor surface is smooth, which reduces windage losses. Thus, the efficiency is higher than that of slotted rotor motors. One example of a sheet rotor is described in [Hes83a] where comparisons are made between a sheet rotor motor and a motor equipped with a cage winding. A cage winding of the type shown in Figure 1.2(c) was shown in [Hes83a] to be more efficient than a sheet rotor, but not sufficiently superior to justify the more complex manufacture associated with the cage winding. The sheet rotor motors in [Hes83a] were successfully tested at high speed, although they had a poor power factor and a high slip. Numerous precautions were taken to ensure the integrity of the soldering of the end-rings to the conducting sheet on the rotor. However, despite the precautions, one of the solder joints failed at 185krpm.

The solid cage induction machine consists of a solid mild steel rotor with machined slots filled with a low resistance material either copper or aluminium or an alloy of the two and low resistance end-rings. There appears to be some debate about the best material to use in the cage winding since whilst copper has a better conductivity it is quite a soft metal compared with aluminium which is lighter and stronger, and at high speed, where precise balance is required, aluminium can have the advantage. The rotor slots depicted in Figure 1.2 are of the open slot type, but many rotors exist which employ the closed slot designs. [Lah00] compares a solid mild steel rotor with open slots filled with copper with a rotor having a sheet winding in the form of a copper sheet. The construction employed permitted a maximum rotor surface speed of  $\sim 500\text{m/s}$ . However, in [Lah00] poor utilisation of the rotor slots was achieved due to

construction problems. The comparison showed that there was little performance difference between the two machines.

The laminated cage rotor shown in Figure 1.2(d) is essentially the same as the solid cage rotor except that the rotor is laminated. By careful design of the cage winding the electromagnetic performance of a solid rotor motor [Jok99] can be nearly as good as that of a laminated rotor machine. [Ike90] compares solid and laminated cage rotors, and shows that the laminated core rotor is superior in terms of electromagnetic performance, although the motors were only tested up to speeds of 200Hz (12,000 rpm) driven by a thyristor inverter. However, as the speed is increased it was predicted that the performance of the laminated rotor motors would be even better when compared to that of the solid rotor motor. From mechanical considerations, however, and despite inferior electromagnetic performance, solid rotors may be the only possibility for use at high speeds [Rei95].

Another high-speed motor of 21kW at 57krpm employing a laminated cage rotor is described in [Soo00]. The rotor had a cage winding made of a copper and aluminium alloy called glidcop<sup>2</sup>, which was required to withstand the high stress that would result at high speed. However, fixing the cage bars both to the rotor and to the end-rings required careful brazing. Again, as in the previous papers, load testing at high speed proved problematical, and the motor was only tested at high speed under no-load. An extrapolation to the rated load from a load-test performed at 2/3 of rated speed and ½ rated power showed the motor to be behaving as predicted, but testing would be required to validate this extrapolation to rated speed and power to ensure its validity.

### c) Mechanical Considerations

[Rei95] identifies some mechanical considerations, which limit the rotor dimensions and speed. The maximum critical speed of a solid rotor under ideal conditions, i.e. a solid homogenous rotor, is given by (1.1), where  $n$ ,  $D$ ,  $l$  are the upper limit of the critical speed, the rotor diameter and the length of the rotor between the bearings, respectively. However, this is significantly reduced for a laminated rotor, as the stiffness tends to be much lower. Nevertheless, it will be seen that since the critical speed is inversely proportional to  $l^2$  even a small increase in shaft length can dramatically reduce the critical speed.

$$n \leq 2 \times 10^3 \frac{D}{l^2} \quad (1.1)$$

The rotor diameter is also constrained by the maximum mechanical stress that can be tolerated as defined by [Rei95] for both solid (1.2) and laminated rotors (1.3), viz.

$$D \leq \sqrt{\frac{8\sigma_{\max}}{\gamma\pi^2 n^2 (3+\mu)}} \tag{1.2}$$

$$D \leq \sqrt{\frac{4\sigma_{\max}}{\gamma\pi^2 n^2 (3+\mu)} - \frac{1-\mu}{3+\mu} d^2} \tag{1.3}$$

where  $\gamma$ ,  $\sigma_{\max}$ ,  $\mu$ ,  $D$  and  $n$  are the density of the rotor material, the material critical stress (50% of the ultimate tensile stress), the Poisson ratio, the rotor shaft diameter and the rotor speed, respectively. Obviously, as the power and the speed are increased more restrictions will be placed on the rotor by the various mechanical limits, such as resonance modes, which the rotor may have to pass through.

[Jok99] and [Rei95] also investigated the maximum permissible rotor speed and how it varies for both solid and laminated rotors. Although laminating the rotor improves the electromagnetic performance, as discussed previously, the rotor stiffness is reduced as shown in Figures 1.3 & 1.4 in which the resultant mechanical speed with a laminated rotor is significantly lower than with a solid rotor. In Figure 1.4, the shaded area indicates the usable rotor diameter and speed envelope with the upper bounds being limited by the strength of the laminated rotor. The lower bounds of this area are defined by achievable output power, with a length-to-diameter ratio  $l/D$  of 3, and the need for dissipation of heat from the rotor surface.

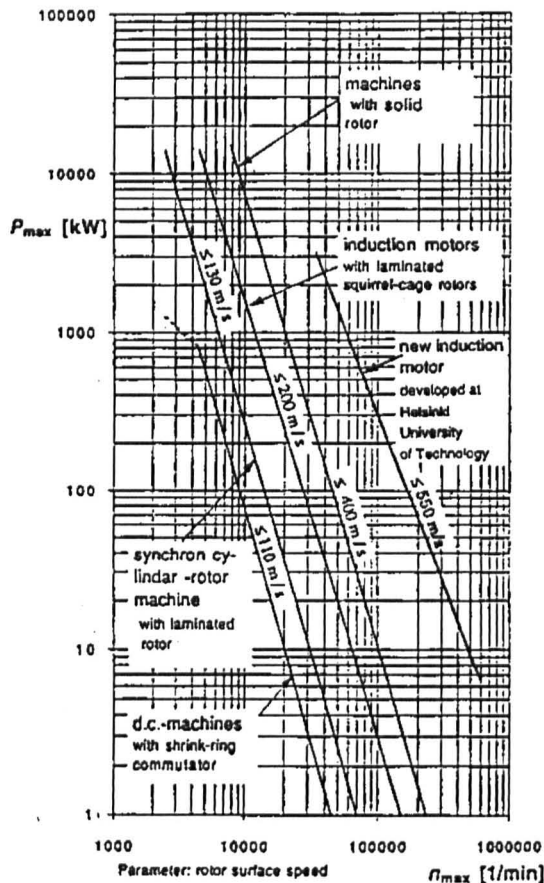


Figure 1.3 – Maximum power vs speed of air cored machine [Jok99]

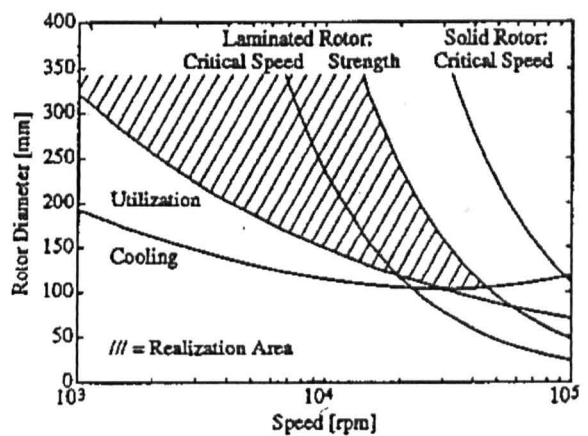


Figure 1.4 – Speed limiting curves for 100kW machine [Rei95]

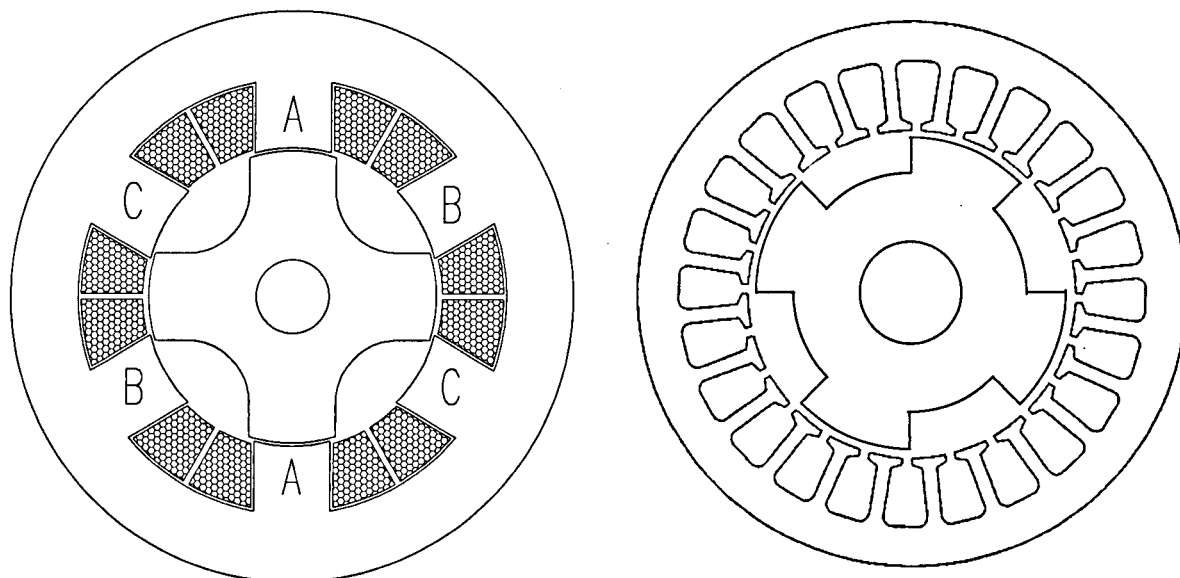
In general, although some induction motors, e.g. [Hes83a], have been designed to operate at speeds in excess of 100krpm, their output power was ~10W. The efficiencies, typically 70%-80%, which have been reported for induction machines, are significantly lower than those normally expected from permanent magnet excited machines [Soo00]. In its favour, however, the induction machine is very simple and relatively cheap to manufacture, a factor which may be significant in deciding whether to use this technology for high-speed applications.

### 1.2.2 Reluctance machines

There has been some interest in both switched reluctance and synchronous reluctance machines for high-speed operation, despite the lack of published literature for these machine technologies at high speeds. There are a number of advantages in using reluctance machines at high-speeds: viz. [Hof00]

- Irreversible demagnetisation is not a problem, as there are no permanent magnets in the motor.
- They can be relatively cheap to manufacture, as permanent magnet material is not employed.
- They are suitable for use in relatively harsh environments, again due to the absence of magnets.

Again, however, there are several issues related to the high-speed operation of reluctance motors, the nature of which is both electrical and mechanical. Figure 1.5 shows examples of switched reluctance and synchronous reluctance motors. Synchronous reluctance machines generally have distributed windings spread over several teeth and the current waveform approximates to a sinusoid. In contrast, switched reluctance motors generally have a concentrated winding round each tooth and there are fewer teeth with the 6-tooth, 4-pole machine shown in Figure 1.5 being typical, whilst the teeth tend to be parallel-sided. Both switched and synchronous reluctance machines have salient rotors, the same design of rotor being suitable for both machine technologies.



(a) Switched reluctance machine      (b) Synchronous reluctance machine  
**Figure 1.5 - Schematics of switched reluctance and synchronous reluctance machines**

### a) Synchronous reluctance machines

In synchronous reluctance machines the maximum achievable power factor is directly related to  $L_d$  (Direct-axis inductance) and  $L_q$  (Quadrature-axis inductance) by equation (1.4) [Hof00]. A high  $L_d/L_q$  ratio is best for both synchronous reluctance and switched reluctance machines, since it results in a higher power factor and it reduces the inverter rating.

$$PF_{\max} = \frac{\frac{L_d}{L_q} - 1}{\frac{L_d}{L_q} + 1} \quad (1.4)$$

The  $L_d/L_q$  ratio is highly dependent on the airgap length, a large airgap offsetting the benefit of a rotor designed for a high  $L_d/L_q$  ratio. [Cal00] recommends the normal airgap length for small electrical machines to be in the range of 0.1 to 0.3mm, which is considerably smaller than that which is normally used in permanent magnet excited machines. Figure 1.6 illustrates the effect of the airgap length on the  $L_d/L_q$  ratio for the motor described in [Hof00]. It can be seen that even a relatively small change in the airgap length has a large effect on the achievable  $L_d/L_q$  ratio. However, although a small airgap is desirable, there are limitations on the minimum airgap length. Firstly, from purely manufacturing considerations there is a limit to the tolerances to which the stator and rotor can be produced, whilst there will always be some radial movement in the bearings. Further, at high-speeds there will be some expansion of the rotor due to the centrifugal stress and the stator will be slightly deformed due to the electromagnetic forces which are exerted on it, as described in [Lon98]. This deformation

although small in itself could with very small nominal airgap lengths significantly change the  $L_d/L_q$  ratio, and thereby cause problems for the drive system.

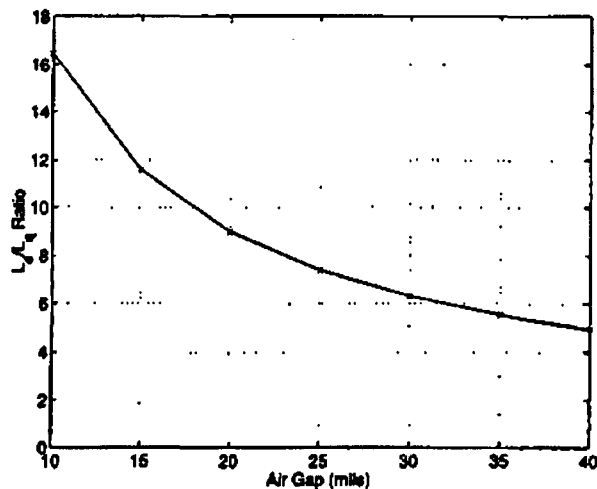


Figure 1.6 - Influence of airgap length on  $L_d/L_q$  [Hof00]

Another effect of a small airgap is to increase the rotor loss, due to increased field in the rotor iron. Consequently, there is a trade-off between reducing the rotor loss and increasing the  $L_d/L_q$  ratio.

[Hof00] employed a laminated rotor as shown in Figure 1.7 to reduce the rotor loss whilst maximising the  $L_d/L_q$  ratio. However, this rotor construction requires extremely careful brazing of the materials to ensure the integrity of the rotor.

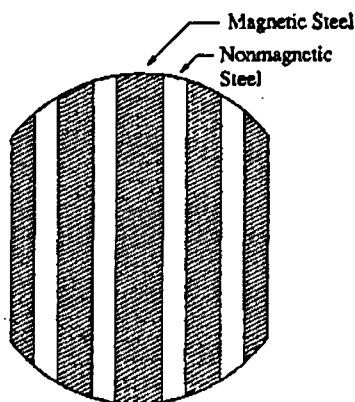


Figure 1.7 - Rotor design utilised in [Hof00]

Due to the distributed (overlapping) nature of the windings of synchronous reluctance machines, the end-windings are longer than for switched reluctance machines. Thus, for a

given space envelope, the active volume is less, and the extra distance between the bearings may create problems with resonance modes on the rotor.

As regards the stator design, careful design of the windings and slots can help reduce the rotor losses, which are speed dependent. Consequently, their minimisation becomes more important as the motor speed is increased. [Hof00] investigated the influence of the winding distribution and the slot number, and found that for a synchronous reluctance machine an ideal sinusoidal winding distribution results in the lowest rotor loss. Increasing the number of slots enables the windings to be more sinusoidally distributed and reduces the rotor loss, and it was established that 60 slots resulted in a significant reduction in the rotor loss and that a further increase in the slot number only resulted in a marginal improvement. Further, it was also found that closed slots reduced the loss even further, and a stator design with a very small slot opening was adopted. With this and the rotor design described earlier in [Hof00], the power factor and efficiency were 0.76 and 91%, respectively, albeit at half rated speed. The measured rotor loss was only ~45W at an output power of ~10kW although finite element analysis could not determine the loss distribution.

## **b) Switched reluctance machines**

Unfortunately, very few papers have been published on high-speed switched reluctance machines. Again, however, as for synchronous reluctance motors, their performance is very dependent on the airgap length, which is normally in the range 0.1-0.3mm.

However, as seen in Figure 1.5 the salient rotor can result in a very windage loss at high speed. Reduction of the windage loss by careful aerodynamic design of the rotor was discussed in [Cal00] & [Cal99], which considered the ratio of the fillet radius to the rotor diameter in a 6-4 SR motor. A large fillet radius to rotor diameter ratio reduces the rotor saturation but also reduces the  $L_d/L_q$  ratio, and, therefore, the torque capability. However, a small fillet radius to rotor diameter ratio compromises the mechanical strength of the rotor, which is a prime consideration at high speed. [Cal99] found that for a 6-4 SR machine topology a fillet radius to rotor diameter ratio of 0.1 was the optimum for that particular motor. Even then, it was observed that the windage loss was still significant and it was also found that the iron losses at rated speed were 1kW compared with a rated output power of 5kW[Cal01].

### 1.2.3 Permanent magnet machines

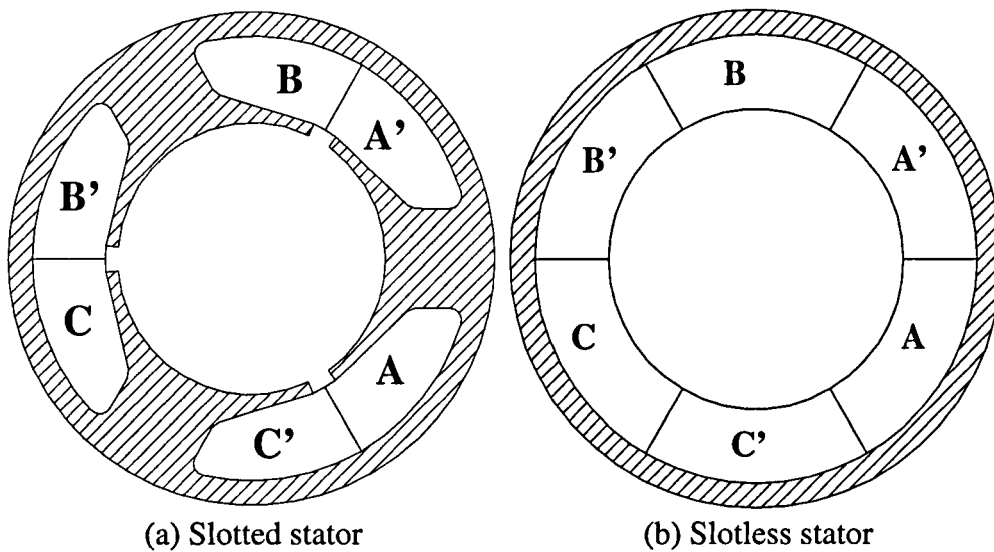
Over recent years permanent magnet brushless machines have become the favoured choice for high-speed applications. This has due primarily to the emergence of NdFeB magnets, the cost of which has been falling gradually in recent years and looks set to fall even further with the expiry of relevant patents. Some of the applications for high-speed permanent magnet brushless machines, which have been reported in the literature, are:

- A rotary atomiser [Coc99] (30W @ 30krpm)
- Alternator for small CHP plant [Jam95] (1kW @ 150krpm)
- Small diameter PCB drill [Pic96] (~60W @ 250krpm), Dentists drill [Hes85a][Hes87] (10W @ 150krpm)
- Compressors [Pri99](3.5kW @ 140krpm), [Mek99] (21 kW @ 54krpm).

There are various design issues related to high-speed brushless permanent magnet machines, in relation to the design of the stator and rotor, mechanical issues and losses, which are all significant and are discussed in the following section.

#### a) Stator design

One of the early debates in high-speed motor design concerned the relative advantages of slotted and slotless machine topologies of which typical examples are shown in Figure 1.8. [Hes82] investigated a slotless topology for a motor operating at speeds in excess of 100krpm. It was shown that similar torque density to that of a slotted motor could be developed, but at the expense of an increase in the magnet volume. Slotted motors have a significantly lower copper packing factor due to the presence of the teeth, whilst slotless motors can have pre-formed coils which make it easier to achieve a high packing factor (53% in this case) and can be significantly easier to manufacture. A more recent publication by the same author [Hes84], however, concluded that high-speed applications favoured a slotted design due to the large eddy current loss which results in windings by the magnetic field in slotless designs, but this eddy current loss can be reduced with use of Litz wire. An even more recent study [Che99] investigated the influence of design parameters on the performance of slotless motors, and although the winding eddy current loss was not considered it was shown that slotless machines, when properly designed, have great potential in terms of performance and efficiency.



(a) Slotted stator (b) Slotless stator  
**Figure 1.8 – Schematic of slotted and slotless stators**

From the investigations carried out in [Hes82][Hes84][Jac88b][Ark92][Che99] there is broadly similar agreement about the suitability of slotless machines for high-speed applications, viz.:

- Slotless machines require a higher magnet volume for the same torque capability as slotted machines and consequently are likely to be more expensive.
- Slotted machines can have a higher torque density due to their smaller airgaps.
- The eddy current loss in the stator conductors is lower in slotted machine designs. [Ark92] reported nearly a thirty-fold reduction in eddy current loss by changing from a slotless to a slotted design.
- Slotless machines have a significantly lower iron loss since the volume of iron is reduced together with the flux density in the back-iron [Ark92][Jac88b].
- The cogging torque is eliminated in slotless machines, and whilst it can be minimised in slotted designs the design features for achieving this reduction compromised the performance [Jac88b].

Another important issue that has been investigated is the ratio of the rotor diameter to the stator diameter, often called the split ratio. [Hes82] briefly investigates this for both slotted and slotless motors. Whilst no definite conclusions were drawn, it paved the way for later work undertaken by [Cha93] and extended in [Cha00]. All these works investigate the optimal split ratio for a particular magnetisation distribution, but neglect the iron loss. However, whilst the iron loss can be safely neglected at low speeds, as will be shown in Chapter 4, at high speeds the iron loss is the dominant loss component. [Cha93], despite containing errors and ambiguities, still manages to derive an expression for the optimal split ratio for a given

stator outer diameter and magnetic loading. Later work by the same author [Cha00] investigated the optimal split ratio in terms of the magnet cost. However, whilst in large machines the magnet cost may be many times the cost of the other motor components and its reduction may be highly beneficial, small high-speed motors do not require large volumes of magnet material and the manufacturing cost may be the dominant cost. In addition, recent reductions in the cost of high energy rare-earth magnets are making this less of a consideration.

The stator winding design can also influence the motor performance. There are two main types of winding, viz. the concentrated or non-overlapping winding, in which there is only one coil per pole-pair per phase, and the distributed or overlapping winding, in which there is at least one coil per pole-pair per phase and some slots may contain coils of more than one phase, as illustrated in Figure 1.9. Non-overlapping windings have shorter end-windings, which, in turn, generally leads to a lower copper loss. Overlapping windings have longer end-windings, so that for a given space envelope the active volume is reduced. If the active volume of the machine is fixed then an overlapping winding will increase the distance between the bearings, which as will be shown in Chapter 5, causes increased resonance problems.

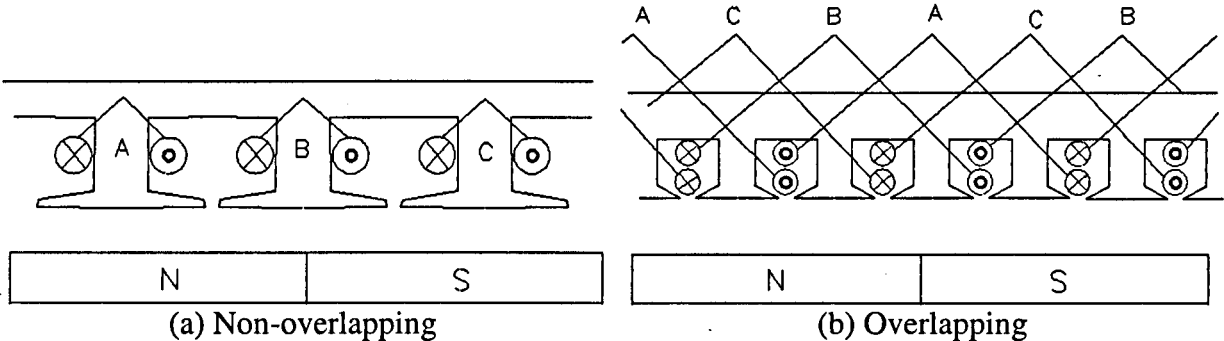


Figure 1.9 - Schematics of winding dispositions

The influence of the stator slot openings on the rotor loss, especially if a stainless steel can is used for magnet containment, may be significant, and this is discussed briefly in section 1.3.

**b) Rotor design**

A lot of the attention has been given to the design of the rotors for high-speed machines, and various magnet arrangements, including both internal-mounted and surface-mounted have been studied extensively over the years. Figure 1.10 shows a selection of 2-pole rotor designs that have been employed, whilst Figure 1.11 shows examples of 4-pole rotor designs. In all of

these designs, the rotor tends to be constructed from laminations in order to reduce the loss due to spatial and temporal mmf harmonics.

In 1980 [Miy80] developed a hybrid motor called a line-start motor having a rotor similar to that shown in Figure 1.10(a), which combined a squirrel cage and permanent magnets. Power MOSFETs and IGBTs were not then generally available and inverters typically employed thyristors. Hence, the machine was started direct-on-line as an induction machine and the rotor was pulled into synchronisation by the permanent magnets. The synchronous speed was 12krpm, which at the time was considered high speed for a line-start PM synchronous motor, the output power being ~1kW and the efficiency being ~89%, which was still significantly higher than that of a conventional induction machine.

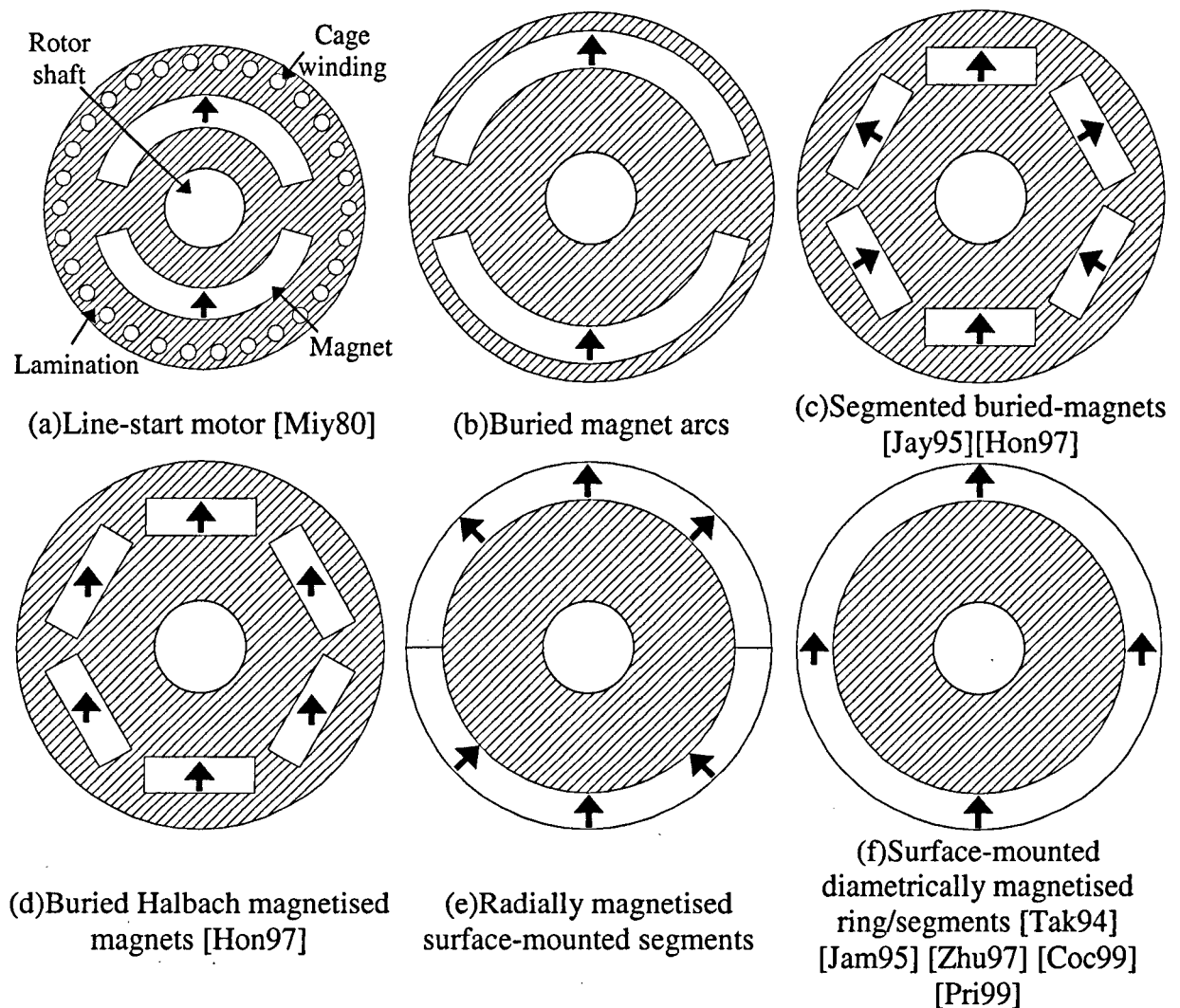
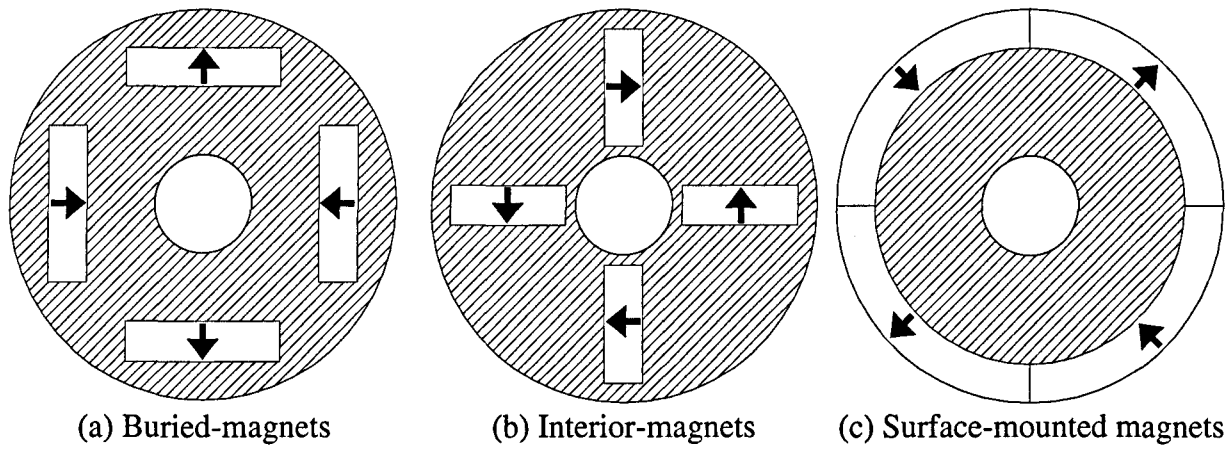
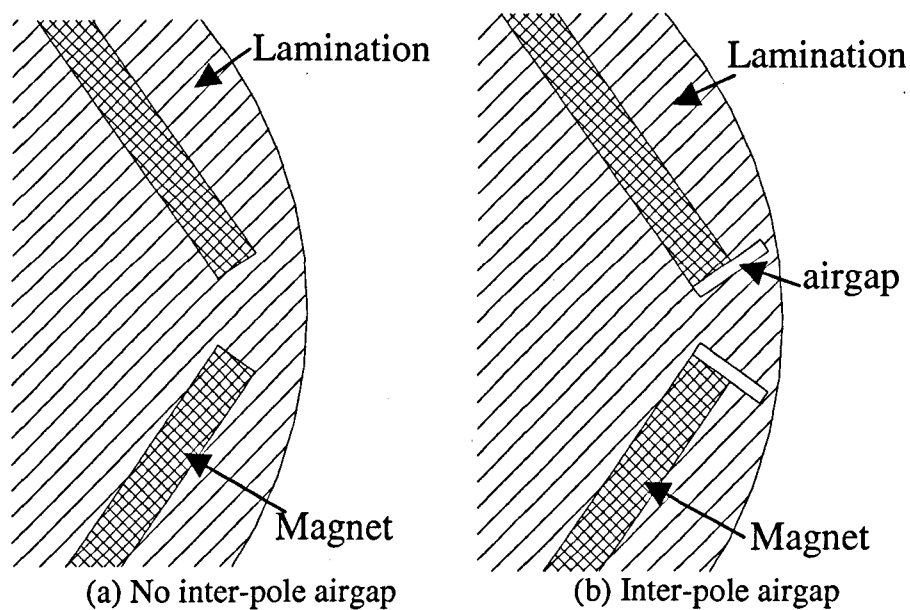


Figure 1.10 – Examples of 2-pole rotors



**Figure 1.11 – Examples of 4-pole rotors**

Once MOSFETs became readily available such hybrid motors became more or less redundant. Considerable attention was then given to the rotor design, in terms of both mechanical and electromagnetic considerations. By way of an example, [Jay95] investigated a buried-magnet rotor structure similar to that shown in Figure 1.10(c). This simplified construction as the magnets were simply flat segments, which are considerably easier to manufacture and magnetise than the arcs shown in Figure 1.10(b). In addition the rotor laminations provided containment for the magnets, thus avoiding the need for a stainless steel ‘can’ or carbon fibre banding for the retention of the magnets. [Miy80] and [Jay95] introduced an airgap, as illustrated in Figure 1.12, between the magnets pole segments, and increase the airgap flux density, albeit, significantly reducing the mechanical strength of the rotor and thus limiting its speed.



**Figure 1.12 – Inter-pole airgap as used in [Miy80]**

Subsequent work on buried-magnet machines, such as [Hon97], investigated the effect of the magnetisation pattern, viz. radial, parallel and Halbach. From finite element modelling, it was observed that for a radial magnetisation (Figure 1.10(c)) both the torque and the torque pulsation were high, whilst for a parallel magnetisation (Figure 1.10(d)) the output torque and the torque pulsation were reduced, and for a Halbach magnetisation the output torque was similar to that for a radial magnetised rotor, but the torque pulsation was significantly reduced. However, for a surface-mounted magnet rotor, the airgap field distribution and the electromagnetic performance for 2-pole Halbach and 2-pole parallel magnetised rotor is identical. However, close inspection of the field plots in the paper [Hon97] shows that the Halbach magnetised machine and the radially magnetised machine are almost identical, which suggests an error in the finite element calculation. Thus, the conclusions must be treated with some caution.

The simplest, and consequently preferred, form of rotor construction tends to employ surface-mounted permanent magnets, as for example in [Tak94][Jam95][Zhu97][Coc99] & [Pri99] and in Figure 1.10(e) & (f). For high-speed applications, a 2-pole diametric magnetisation is preferred due to simple manufacture and high torque density. For a 2-pole rotor the airgap field distribution for diametric and Halbach magnetisations is sinusoidal in nature. The sinusoidal nature of the airgap field results in an essentially sinusoidal flux density distribution in the stator, which then results in a low iron loss [Zhu97]. Whilst NdFeB magnets are usually the preferred choice for high-speed applications, [Jam95] uses SmCo magnets ( $\sim 300^{\circ}\text{C}$ ) as they have a significantly higher operating temperature range than NdFeB magnets ( $<100\text{-}150^{\circ}\text{C}$ ) before being vulnerable to partial irreversible demagnetisation.

### c) Mechanical issues

For all high-speed surface-mounted permanent magnet rotors there is a need to provide suitable containment on the rotor to retain the magnets. Although sintered NdFeB is a brittle material, often the method of attachment to the rotor, which is normally by an adhesive, is mechanically the weakest point. [Con92] [Tak94] [Jam95] [Zhu97] & [Pri99] consider containment of the rotor magnets using either a non-magnetic stainless steel can or a fibre impregnated resin, such as carbon fibre or glass fibre.

[Con92] develops an equation for the burst speed ( $\omega_b$ ) of the rotor containment assuming that the magnet is not a stressed component of the rotor. Equation 1.6, however, is an alternative equation given in [Jam95], which is somewhat easier to understand.

$$\omega_b = \frac{15}{\pi R_s} \times \left\{ \frac{\frac{(R_s - R_m)}{R_s}}{1 - \left(1 - \frac{(R_s - R_m)}{R_s}\right)^3 \left(1 - \frac{\delta_m}{\delta_s}\right)} \cdot \frac{12\lambda\sigma_s}{\delta_s} \right\}^{0.5} \quad (1.6)$$

where  $R_s$ ,  $R_m$ ,  $\delta_m$ ,  $\delta_s$ ,  $\lambda$  and  $\sigma_s$  are the magnet outer radius (m), magnet inner radius (m), density of the magnet material ( $\text{kg/m}^3$ ), density of the containment material ( $\text{kg/m}^3$ ), safety factor (normally 0.9) and the tensile strength of the outer shell ( $\text{N/m}^2$ ), respectively. As will be seen, the radial thickness of the containment is not included in this calculation. Above this bursting speed, the centrifugal force on the magnets and the containment due to its own mass will exceed the tensile strength of the material. Figure 1.13 shows the maximum rotor dimensions which can be tolerated at 250krpm for both stainless steel and carbon fibre containment. As can be seen, carbon fibre containment is necessary for large magnets, where the centrifugal force due to its mass is far less than that for steel containment as the carbon fibre is considerably less dense ( $\sim 1613 \text{ kg/m}^3$  for carbon fibre c.f.  $\sim 8000 \text{ kg/m}^3$  for mild steel), whilst having a high tensile strength. [Pri99] also prefers carbon fibre to stainless due to its high strength to weight ratio, zero-conductivity, zero eddy-current loss and the fact that it enables larger diameter rotors to be accommodated. In general, the higher the speed the more important the method of containment as a higher centrifugal force is exerted by the rotor magnets. Generally, therefore, carbon fibre is preferred.

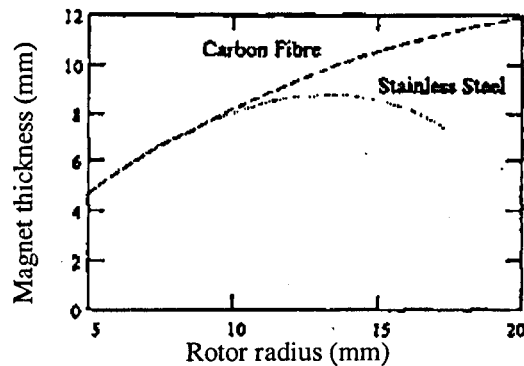


**Figure 1.13 - Influence of containment on maximum rotor diameter at 250krpm [Jam95]**

However, for some high-speed applications requiring a very small shaft diameter, a solid magnet 'slug' enclosed in a non-magnetic shaft may be the optimum arrangement, since it facilitates a very small rotor as the rotor shaft itself acts as the magnet containment shaft [Hes85a][Hes87][Pic96]. However, the bearing bore at one end must be at least the diameter

of the magnet plus the shaft radial thickness, which encloses it, Figure 1.14. Measurements on such motors have been encouraging, although all the losses have not been accounted for.

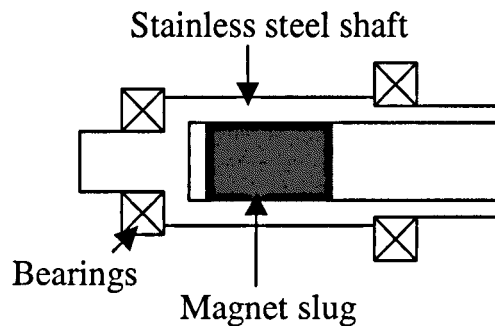


**Figure 1.14 – Integrated magnet and shaft arrangement as used in [Hes87]**

#### **d) Motor losses**

The effects of stator slotting, which can be significant if stainless steel rotor containment is used, are considered in section 1.3, as the same loss mechanism also applies to other motor types, viz. induction motors.

In large permanent magnet brushless DC machines with a high electrical loading, such as traction machines, the magnet eddy current losses can be significant. On a smaller machine, [Zhu97], it was shown that the eddy current loss in the rotor magnets of brushless DC permanent magnet machines with a steel containment are generally minimal, with the main loss occurring in the stainless steel magnet containment. [Ng98][Zhu01a][Zhu01b] also investigated the eddy current loss in the rotor magnets, and it was shown that due to eddy current redistribution in the magnets the rotor loss is significantly lower than that predicted from a magnetostatic model, and that the ratio of the magnet loss to the containment loss is highly dependent on the containment material. However, since [Zhu01a][Zhu01b] only considered the magnet eddy current loss in a 3000rpm 12-pole brushless DC motor further work is needed to establish how well this relates to high-speed permanent magnet motors. Clearly, however, as the conductivity of the containment sleeve is increased the eddy current loss in the magnets decreases and the loss in the sleeve increases. It was concluded that there was an optimum value of conductivity for a containment sleeve, which happened to correspond to that for brass. It was also shown in [Zhu01] & [Tak94] that increasing the airgap length significantly reduces the rotor loss.

In permanent magnet brushless AC motors, the rotor loss is due to mmf harmonics that result from stator slotting [Pyr94]. However, as conventional AC machines operate on the fundamental mmf then the magnet eddy current losses are minimal. However, in modular

machines, viz. fault-tolerant machines, where the motor is operating on a higher harmonic than the magnet eddy current loss is quite significant due to the presence of lower order harmonics of a high magnitude. [Ata00] developed a method for predicting magnet eddy current loss in brushless AC machines in which the interaction of space and time harmonics in the mmf can generate significant loss, and lead to the need to segment the magnet pole arcs in order to reduce loss to a sensible level [Ata00][Ede02a].

Whilst the rotor loss poses problems in terms of dissipating the heat, the stator loss is often significantly larger than the rotor loss. The open-circuit stator iron loss, in the form of eddy current, excess eddy current and hysteresis loss components in the stator can be significant at high speeds. [Zhu97][Jac99] compares the loss in laminated stator core with that in a soft magnetic composite stator. Further work in [Zhu01c] accounted for the iron loss under a specified load condition. [Jac99] describes several experimental motors that use a soft magnetic composite stator and it was shown that by careful design the performance can be nearly as good as that for a laminated stator.

#### **(e) Summary**

The principle advantages of permanent magnet machines are:

- The excitation field is developed by magnets not by stator coils, the airgap field is significantly higher than for induction or reluctance machines, and the airgap length is not such a critical dimension.
- The efficiency is higher, permanent magnet machines frequently having efficiencies >95%.
- They are quieter acoustically.
- They have a higher torque density, and consequently a smaller overall motor size.
- Potentially, they have a lower rotor windage loss, as the rotor can be cylindrical.
- They have a better power factor than either reluctance or induction machines, and therefore require smaller inverter VA rating.

However, permanent magnet machines do have some potential disadvantages. Hence, they may not be suitable for all high-speed applications. Some potential problems are:

- High temperature applications since rare-earth magnets degrade with temperature, although Samarium Cobalt magnets are capable of operating at temperatures of ~350°C.

- Containment of magnets in motors equipped with surface-mounted magnets [Con90] [Tak94][Pri99] & [Jam95].
- Stator iron loss due to the high fundamental frequency, and rotor eddy current loss due to spatial and temporal mmf harmonics [Hof00].

Despite these potential drawbacks permanent magnet machines are likely to emerge as the favoured choice for high-speed applications.

### 1.3 General issues applicable to high-speed motors

#### (a) Electromagnetic

The dominant losses in a high-speed machine are shown in [Jok96] to be determined mainly by the iron eddy current component of the stator iron loss and the windage loss, although this paper only considered the classical eddy current loss and not the excess eddy current loss component. The efficiency depends on the quotient shown in equation 1.7 and is proportional to the eddy current loss times the speed and the windage loss multiplied by speed squared whilst the copper loss is inversely proportional to speed, viz.

$$\frac{P_H}{P_{out}} = \frac{P_{Cu} + P_h n + P_e n^2 + p_\rho n^3}{cn} = \frac{P_{Cu}}{c} \frac{1}{n} + \frac{P_h}{c} + \frac{P_e}{c} n + \frac{P_\rho}{c} n^2 \quad (1.7)$$

where  $P_H$ ,  $P_{out}$ ,  $P_{Cu}$ ,  $P_h$ ,  $P_e$ ,  $P_\rho$ ,  $n$  &  $c$  are the total loss, the output power, the stator copper loss, the hysteresis loss, the eddy current loss, the windage loss, the rotor speed and a constant which represents the utilisation factor and the rotor volume. Obviously, this is a very simplified view and neglects the effects of winding inductance, which become pronounced at high-speed and other forms of inefficiency in the system, viz. winding eddy current loss, magnet eddy current loss etc, but is still useful in showing the way in which losses such as the iron loss can dominate the machine performance at high speed.

Mechanical issues that can cause problems include resonances of the rotor due to critical speeds and the increased loading on the shaft and bearings due to rotor imbalance and airgap eccentricity. The bearings also require careful consideration as ball race bearings require special ceramic balls and lubrication at high-speed. Magnetic bearings, which can actively damp rotor resonant modes, are becoming more popular [Jok96][Rei95] but can be difficult to accurately control at high-speeds. Air journal and other forms of gas bearings have been

successfully employed at high speed [Pic96][Lar95]. However, these are susceptible to half speed whirl, which can cause bearings to seize.

Specialised ball race bearings have been used at high speed [Hes83], but these are sensitive to shock loads and requires careful lubrication if the lifetime is not to rapidly diminish. Also if air-cooling is to be provided then it requires filtering to prevent contamination of the bearing lubricant [Hes83]. One recent development has been the bearingless motor [Fuk00] in which the stator winding also act as active magnetic bearings, thereby eliminating the need for physical bearings. Essentially a motor is composed of two stator sections and two rotor sections with either the stator or the rotor rotated by  $90^\circ$  electrical between the two sections with the currents in the stator windings controlled to produce both torque and levitation. However, the complexity of the motor control system is greatly increased, and for high-speed applications this would require fast, and relatively expensive, digital control.

## **(b) Mechanical**

For any rotor rotating at a very high speed its resonant frequencies become of increasing importance since they may ultimately limit the rotor speed. [Har56] and [Van88] examine the natural frequencies of simple rotating systems, and [Har56] provides some useful analytical expressions for predicting the natural frequencies of simple rotor structures, some of which are used later in this thesis to compare with predictions from more complex finite element analyses. However, the models proposed in both these publications are for relatively simple systems, and whilst these might be readily applied to a solid rotor induction motor, for example, they become much harder to reliably apply to a permanent magnet rotor or indeed a squirrel cage laminated induction rotor motor. Given their relative complexity, the only reliable method of predicting their resonant frequencies and modes of vibration is by finite element analysis. However, even this method has its difficulties, as will be evident later. Whilst some attempts have been made to calculate and take account of the resonant modes [Con92] it appears that no systematic work has been performed to investigate this important aspect of design.

For induction machines and permanent magnet brushless machines the stator slot openings affect the variation of the field at the rotor surface, and consequently the rotor loss [Hes83b][Con92][Tak94][Pyr94][Zhu97][Soo00][Zhu01a]. For a permanent magnet machine [Tak94] investigated the effect of stator slot ripple on a metallic containment sleeve. The loss mechanism is similar to that for sheet rotors in induction machines. The magnitude of the slot ripple field is given by (1.8), and is shown graphically in [Tak94].

$$B_o = \frac{1+u^2 - 2u}{2(1+u^2)} k_c B_g \quad (1.8)$$

$$\text{where } u = \frac{b_o}{2g} + \sqrt{1 + \left(\frac{b_o}{2g}\right)^2} \quad (1.9)$$

in which  $B_g$ ,  $b_o$ ,  $g$  and  $k_c$  represent the airgap flux density, the width of the stator slot openings, the airgap length and Carter's coefficient, respectively. For the motor described in [Tak94] the slot ripple had a magnitude of up to 1 Tesla for a large slot opening .

From equations 1.8 and 1.9 it can be seen that either reducing the width of the slot openings or increasing the airgap length reduces the magnitude of the slot ripple. Normally the slot openings are quite small, and so the potential for reductions are somewhat limited. Consequently, the technique favoured in [Tak94] was to increase the airgap length. However, the use of a non-metallic containment for the rotor, such as a carbon fibre or glass fibre sleeve, eliminates the problem of eddy current loss in the containment. The efficiency of three prototype motors were compared, two employing a stainless steel (SUS) containment sleeve and one employing a fibre reinforced plastic (FRP) sleeve.

#### 1.4 Sensorless motor control

In permanent magnet brushless motors, both DC and AC, accurate rotor position information is needed in order to control the commutation of the three phases, and in the case of AC operation the current waveforms. This position feedback is usually provided by sensors mounted on the motor, the general layout of a brushless drive system being shown in Figure 1.15.

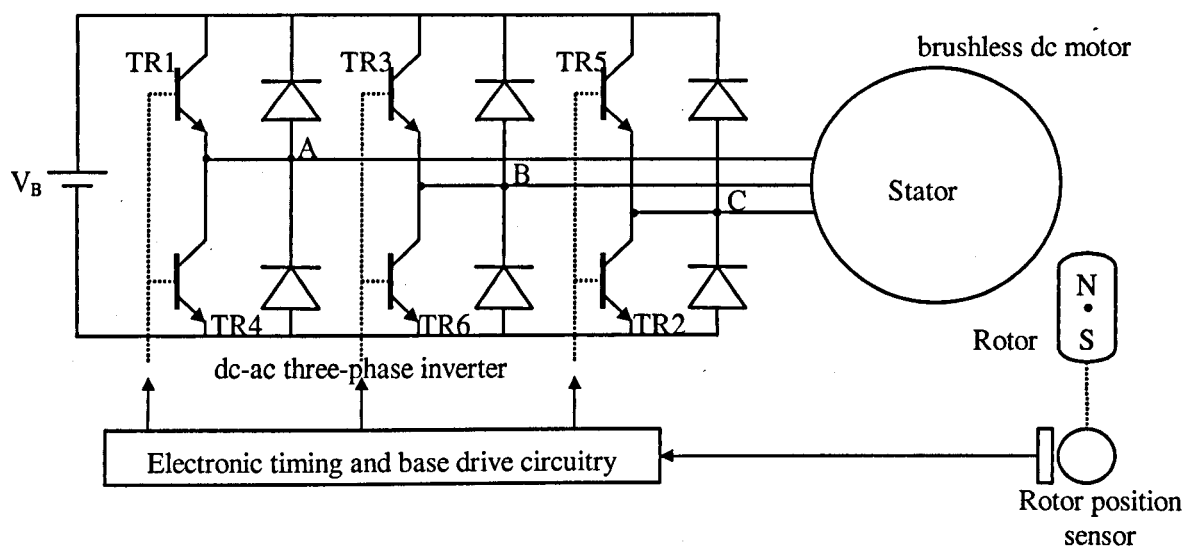
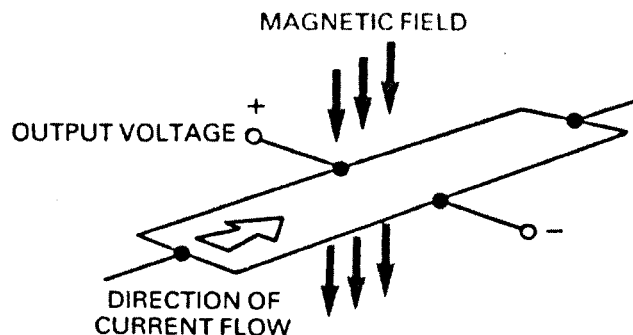


Figure 1.15 - Typical permanent magnet brushless drive system

The rotor position sensor may take several forms, viz. Hall effect sensors, optical encoder, incremental or absolute encoders and resolver. However, they all have drawbacks in terms of cost, alignment accuracy, robustness, volume, etc. Regardless of the type of sensor which is employed precise positioning is required, the normal required tolerance [Orc90] being  $\pm 2^\circ$  electrical or less, which leads to:

$$\text{Mechanical degrees} = \frac{\text{Electrical degrees}}{\text{No. of pole pairs}} \quad (1.10)$$

Whilst this may readily be achievable for a 2-pole motor as the pole number is increased, for example to 8-pole the required tolerance reduces to  $\frac{1}{2}^\circ$  mechanical, which is difficult to achieve. Hall effect sensors, Figure 1.16, are widely used in brushless DC motors partly because they are relatively cheap and of a relatively small size. Normally, the output is passed through a Schmitt trigger to provide a digital output. For normal brushless dc operation, 3 Hall effect sensors, spaced  $120^\circ$  electrical apart, are required to provide a 'switching event' every  $60^\circ$  electrical.



**Figure 1.16 - Operation of Hall effect sensor**

Hall sensors must be sited either close to the rotor magnets or adjacent to a special commutation magnet. However, if the airgap is relatively large, the magnetic field is low and the Hall sensors are subject to hysteresis. Also there is the risk that the armature reaction field can trigger can cause spurious triggering of the Hall sensors if they are located close to the stator winding. By way of example, Figure 1.17 shows the Hall signals and phase current and phase voltage (to neutral) waveforms in one phase of a 2-pole 3-phase brushless motor ( $A_1$ ) which is described in chapter 3, in which a 5mm airgap is employed. As can be seen, the phase angle between consecutive commutation events is not  $60^\circ$  and the phase current and voltage waveforms are retarded by about  $30^\circ$ . By advancing the sensors by  $30^\circ$  mechanical, as shown in Figure 1.18, the phase current and voltage waveforms are improved, Figure 1.19,

but the spacing of the commutation events is still not even. Further, advancing the Hall sensors by  $30^\circ$  in this manner limits the motor to one direction of rotation only, which in many applications would not be acceptable.

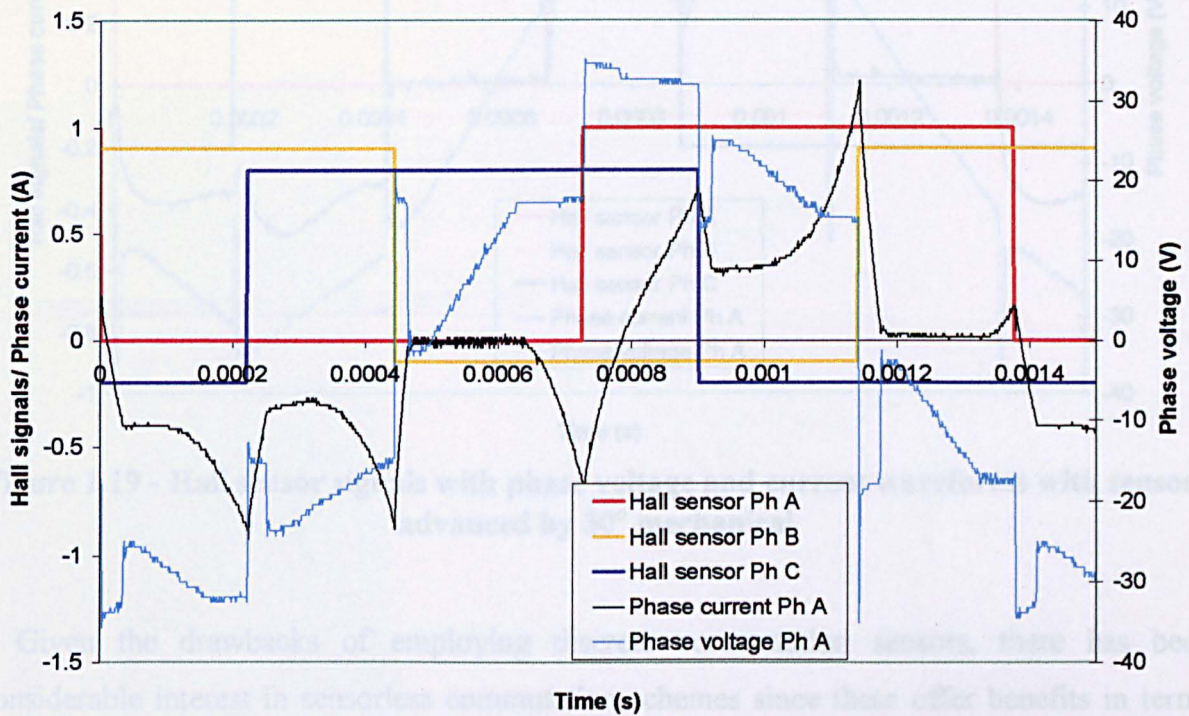


**Figure 1.17 - Hall sensor signals with phase current and voltage waveforms with  $0^\circ$  advance**

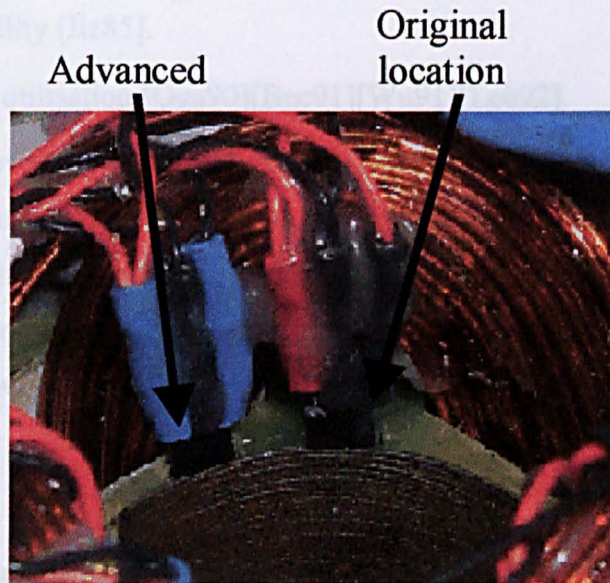


**Figure 1.18 - Hall sensor for one phase showing original and advanced location**

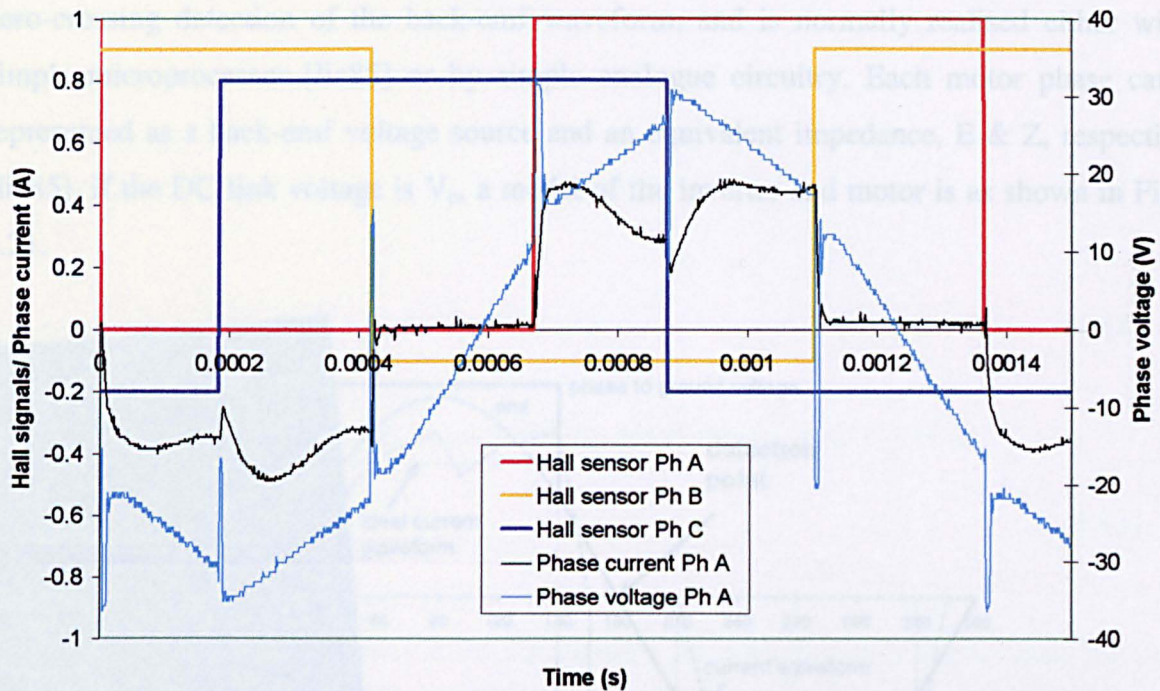


**Figure 1.19 - Hall sensor signals with phase voltage and current waveforms with sensors advanced by 30° mechanical**

Given the drawbacks of employing discrete commutation sensors, there has been considerable interest in sensorless commutation schemes since these offer benefits in terms of:

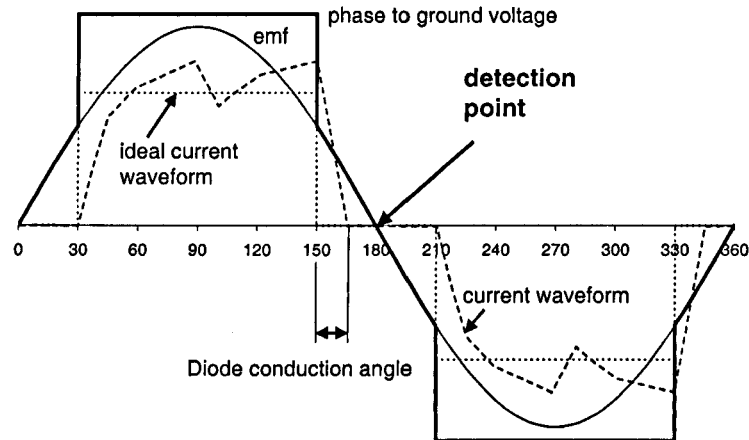
- Reduced component count.
- Improved reliability [Iiz85].
- Improved space utilisation [Oga90][Bec91][Wu91][Lee92].

Whilst there are several methods of realising sensorless commutation, their suitability depends on the operating speed range of the motor, high-speed motors demanding very fast response times from any commutation strategy. The influence of the design of a permanent magnet brushless DC motor specifically for sensorless commutation, using a well established scheme based on the detection of the zero-crossing of the back-emf waveforms, is investigated in Chapter 3, the principle of the method being as follows:

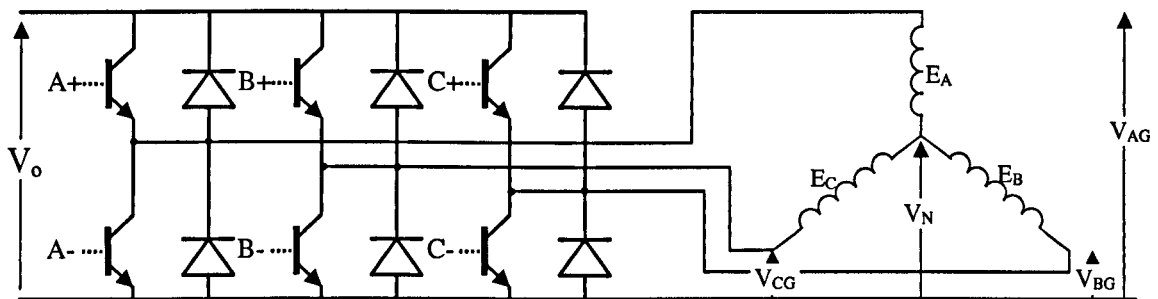
**(a) Simple zero-crossing of back-emf method**

Figure 1.20 illustrates the principle of the sensorless commutation of a brushless DC motor based on the detection of the zero-crossing of the phase back-emf waveforms [Zhu92]. Figure 1.20 shows ideal phase voltage, current and back-emf waveforms, together with a typical current waveform in order to highlight the diode conduction angle. The simplest method is the

zero-crossing detection of the back-emf waveform, and is normally realised either with a simple microprocessor [Iiz85] or by simple analogue circuitry. Each motor phase can be represented as a back-emf voltage source and an equivalent impedance,  $E$  &  $Z$ , respectively [Iiz85]. If the DC link voltage is  $V_o$ , a model of the inverter and motor is as shown in Figure 1.21.



**Figure 1.20 - Principle of sensorless back-emf detection**



**Figure 1.21 - Motor & Inverter showing applied and back-emf voltages**

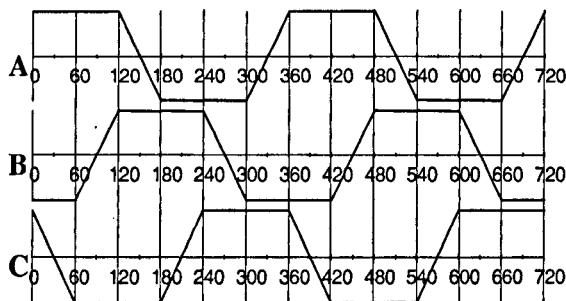


**Figure 1.22 – Idealised motor phase back emf**

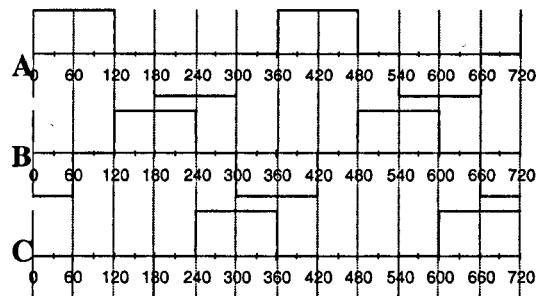


**Figure 1.23 – Idealised motor phase current**

From the idealised phase voltage and current waveforms, shown in Figures 1.23 & 1.24, it can be seen that the current flows in phase A from  $0^\circ$  to  $120^\circ$  electrical in the positive direction and from  $180^\circ$  to  $300^\circ$  electrical in the negative direction. During the period from

120° to 180° electrical, the terminal voltages, motor currents and star-point voltage are as follows:

$$\left. \begin{aligned} V_{AG} &= V_N + E_A, \\ V_{BG} &= V_O, \\ V_{CG} &= 0 \end{aligned} \right\} \quad (1.11)$$

$$I = V_O - \frac{(E_B - E_C)}{Z_B + Z_C}, \quad V_N = V_O - E_B - I * Z_B \quad (1.12)$$

In general,  $Z_A = Z_B = Z_C$ , as the phase windings are identical, and, therefore,:

$$V_{AG} = V_N + E_A = \frac{V_O - E_B - E_C}{2} + E_A \quad (1.13)$$

This has been implemented as shown in Figure 1.24, with Figure 1.25 providing the timing chart. When  $E_A = 0$ , i.e. the back-emf in phase A is zero (point P), then  $E_B = -E_C$  &  $V_{AG} = V_N = V_O/2$ , and this instant is the zero crossing point, which can be easily detected by using a simple comparator. After the zero crossing point for phase A, a delay of 90° electrical, needs to be introduced in order to use the signals to directly control the inverter switching devices ( $S_a, S_b, S_c$ ). The simplest method of introducing such a delay is to use a low pass filter to provide the switching signals directly [Iiz85]. However, this method of introducing delays of 90° electrical means that during transient conditions, such as when a load is suddenly applied, the calculated rotor position signals differ from the actual motor position. Hence, under these conditions optimal torque operation cannot be achieved, resulting in poor performance.

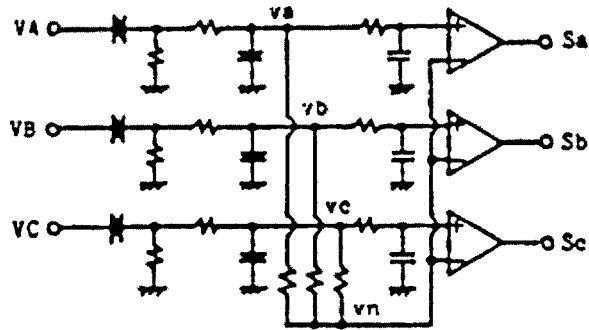


Figure 1.24 - Back-emf detection circuit [Iiz85]

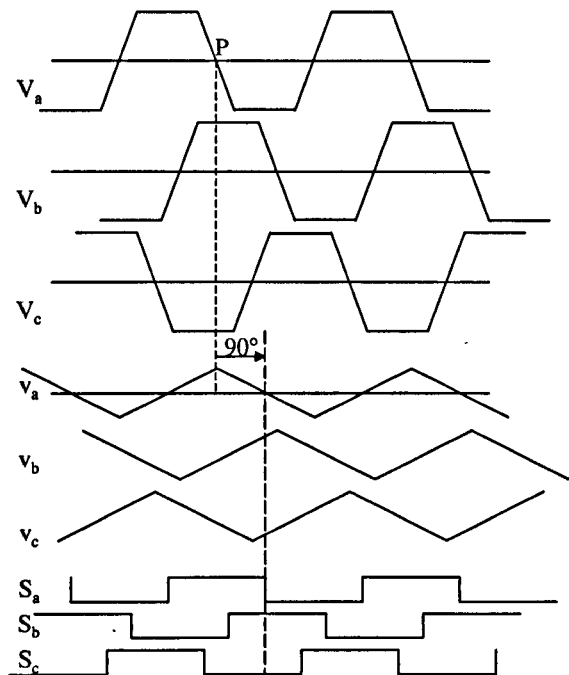


Figure 1.25 - Back-emf detection timing chart

The motor speed is controlled by modulating the gate drive signals in one of the conducting switches, and it is normally arranged so that the gate is chopped for  $\frac{1}{2}$  of its on-time so that the switching losses are distributed between all of the switching devices, as illustrated in Figure 1.26.

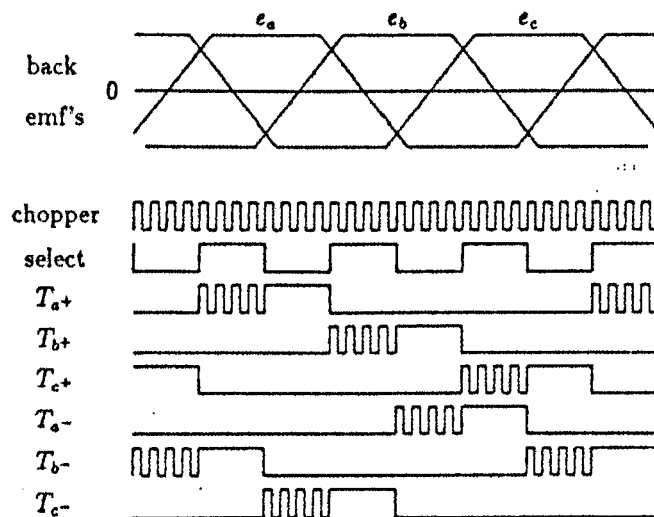


Figure 1.26 - Chopper control showing sharing of PWM [Oga90]

However, this type of drive is normally limited to operating at low speeds and over a relatively small speed range, as the low pass filter has to be designed to operate over the entire speed range of the motor. The introduction of digital filters has made drives more efficient over a wider speed range, but maximum speeds are still generally limited to below 10krpm. This method also has problems at low speeds when the back-emf is very small, and, hence,

cannot be reliably detected, limiting the lower speed of this technique in closed-loop operation. Further, the PWM strategy used to control the motor speed can introduce noise onto the back-emf signals and thus make the detection of the 'true' zero crossing more difficult and unreliable.

### (b) Integrated back-emf method

In order to address some of the shortcomings of the method described in the previous section the technique was enhanced as follows. Rather than commutating at a fixed instant after the zero-crossing of the back-emf has been detected, which has inherent drawbacks [Juf87][Tak94][Pic96] in relation to the dynamic performance, this method starts integrating the back-emf until a pre-set threshold is reached whereupon commutation takes place.

The integration method works as follows:

$$\int e_j dt = \int u_j dt - R_j \int i_j dt - L_j i_j \quad (1.14)$$

The unexcited phase is automatically selected using a signal selector, and the neutral voltage, required to give the back-emf voltages, can be artificially generated [Juf87]. During the unexcited period of each phase the zero-crossing of the back-emf voltage is sensed, and the integrated voltage ( $V_{int}$ ) can be shown to have the following form [Juf87]:

$$e_{(t)} = e_o t \quad (1.15)$$

$$V_{int} = \int_0^t \frac{e_{(t)}}{k} dt \quad (1.16)$$

$$V_{int} = \frac{e_o t^2}{2k} \quad (1.17)$$

where  $k$  is a constant of integration,  $t$  is the time since the zero crossing, and  $e$  is the amplitude of the back-emf.

Commutation then occurs at the instant  $V_{int}$  reaches a pre-set threshold, and, as the amplitude of the back-emf is proportional to the speed, then as the speed increases the time for  $V_{int}$  to reach its threshold decreases accordingly. Another technique uses a comparator to produce commutation pulses similar to that produced using Hall sensors [Tak94]. This removes the need for a low pass filter associated with the previous method, which requires the filter components to be selected for operation at rated speed and results in a reduced performance during run up and at lower speeds. Figure 1.27 shows the output waveform from, the integrator, and it can be seen that this is relatively free of switching noise.

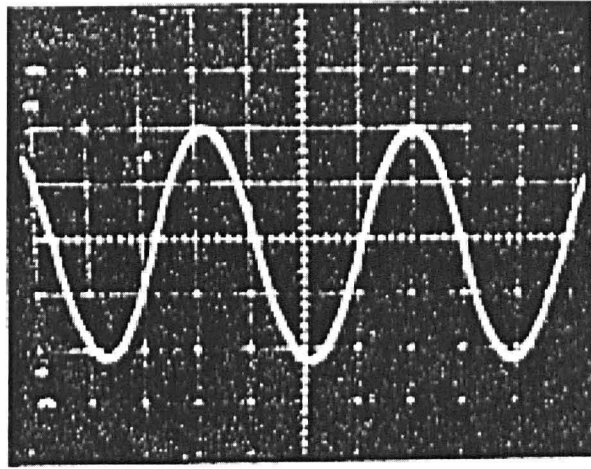


**Figure 1.27 - Integrated back-emf waveform. [Juf87]**

The threshold voltage and the integrator constant ( $k$ ) can be changed to optimise the motor performance, i.e. to facilitate phase advance or to force a faster current build up (more torque at high speeds). Obviously, the commutation advance is limited to  $< 30^\circ$  electrical, and it has been suggested [Bec91] that an angle of about  $10^\circ$  electrical would be useful, but this was for relatively low speeds, and is highly dependent on the phase inductance of the motor. The need for commutation advance increases at high speeds due to the effects of winding inductance as mentioned previously. With this scheme, if commutation advance is to be used effectively at high speeds, then to ensure the phase current and back-emf are brought into phase careful attention needs to be paid to the design of the windings in order to ensure that they have a low inductance.

This scheme has been successfully used at speeds up to 150krpm [Tak94] and provides several advantages over the previous back-emf based method, viz.:

- Greater immunity to switching noise, as the integrator naturally absorbs the switching spikes, Figure 1.27.
- As an integrator is used, the algorithm automatically adjusts, within certain limitations, for changes in rotor speed.
- Operates over a larger speed range.
- It is the favoured choice for high-speed brushless DC motors [Tak94][Pic96].

Consequently a commercial IC employing this scheme (ML4425) and using a Phase Locked Loop to help maintain synchronisation was used as the sensorless motor controller in Chapter 3.

## 1.5 Scope and contribution of thesis

This thesis examines several issues related to the design, construction and operation of high-speed permanent magnet brushless DC motors.

In Chapter 2, an external rotor, brushless DC motor with a slotless winding is designed and built as part of an external contract for Urenco (Capenhurst) Ltd. This motor has a magnetically loaded composite (MLC) rotor with a Halbach magnetisation, and is designed to operate at 120krpm and produce a peak torque of 50mNm. The design and construction of this prototype motor reveals several issues, some of which are addressed in later chapters of the thesis.

Chapter 3 investigates simple brushless DC sensorless commutation schemes and the design of a high-speed brushless DC motor, which is suitable for reliably utilising such sensorless schemes in high-speed applications. It is shown that in order to use a simple sensorless scheme a low freewheel diode conduction angle is required so that the zero-crossing of the back emf waveform in an unexcited phase can be detected. To date, there have been no similar investigations into the design of high-speed motors specifically for use with simple sensorless zero-crossing commutation strategies. It will be shown that the stator design which is most suitable for sensorless operation differs significantly from that of conventional low speed brushless DC machines.

In Chapter 4, the optimum ratio of the rotor diameter to the stator outer diameter, or the split ratio, is investigated. Previous work on this has focussed solely on the influence of the stator winding copper loss and relatively low speed operation. The resulting expression for the optimal split ratio derived previously in [Cha93] is compared to results derived from a comprehensive CAD software package. The influence of the iron loss is then investigated, and it is shown that as the motor speed increases the iron loss is an increasingly dominant component of the motor loss, and the mechanism for this is discussed. The effect of design parameters, such as the electric loading, the active length, the airgap length, the pole-number and the motor speed, on the iron loss and the optimum split ratio is investigated.

Rotor resonances, which as mentioned previously, are one of the main considerations for high-speed motors, have received some attention. However, this has generally only been in relation to the burst speed of a rotor. As shown in Chapter 2, a resonant mode can prevent a motor from accelerating up to its rated speed. Generally, this is a problem only applicable for low torque, high inertia motors, for which the acceleration is low, and it is not possible to accelerate quickly through resonant modes. However, resonant modes can still be destructive, as will be shown in Chapter 5. Consequently, they need to be predicted if a high-speed motor

is to operate satisfactorily. In Chapter 5, two high-speed rotors are modelled at different stages during their manufacture, and predicted resonant modes are compared to those derived from finite element analysis. A model of a complete rotor is then used to investigate the influence of design parameters such as the shaft extension, the axial spacing between bearings, the active length and the shaft diameter on the resonant modes.

The major contributions of this thesis include:

- (a) Integrated design of high-speed permanent magnet brushless DC motor for sensorless operation based on the back-emf zero-crossing detection technique.
- (b) Optimal ratio of rotor diameter to stator outer diameter for high-speed permanent magnet brushless DC motors, accounting for both the winding copper loss and the stator iron loss.
- (c) Systematic investigation of rotor mechanical resonances of high-speed permanent magnet brushless DC motors, and quantification of the influence of key design parameters.

To date, the research has resulted in 2 conference papers [Ede00][Ede01] and 2 journal papers [Ede02b][Zhu01d].

## Chapter 2 Design study of an external rotor, slotless, brushless DC motor with Halbach magnetised magnetically loaded composite rotor.

### 2.1 Introduction

This chapter describes a design study which was initially undertaken on behalf of Urenco Capenhurst Ltd, on a high-speed, slotless, external rotor, permanent magnet brushless dc motor with a maximum speed capability of 120krpm. The intended application was to drive the centrifuges in Urenco's uranium enrichment plant, described in the following section, which currently employ hysteresis motors. The motor design was based around a magnetically loaded composite (MLC) tube, with an interior diameter of 124mm. In order to maintain mechanical integrity only the inner 1mm was impregnated with isotropic NdFeB powder, the maximum powder loading being limited to ~14%, which equates to a remanence of ~0.11T. The design and testing of this motor raised several issues, which are highlighted in this chapter, and are investigated further in subsequent chapters.

#### 2.1.1 Uranium enrichment

When uranium is mined two isotopes are present in the ore, viz.  $U^{235}$  and  $U^{238}$ .  $U^{235}$  is the fissile component, which is required for use in the fuel for light water nuclear reactors, but it is normally only present in quantities of about 0.7% by weight, with larger amounts of the  $U^{238}$  isotope being present. For fabrication into uranium oxide ( $UO_2$ ) for the nuclear reactors the concentration of  $U^{235}$  needs to be about 3-5% by weight [Ure02]. In order to achieve this the fuel needs to be processed or enriched. The process of enriching the uranium requires gaseous components. Consequently, the uranium is firstly chemically combined with fluorine to form the compound  $UF_6$ . This compound whilst being a gas at 70° C is a solid at room temperature and it is in this state that the uranium is delivered to Urenco for further processing.

Figure 2.1 illustrates the uranium enrichment process. Once the solid  $UF_6$  has been heated up to 70° C and become gaseous the pressure is reduced and the gas is passed into the centrifuges, as shown in Figure 2.2(a). A rotational motion is conveyed to the  $UF_6$  from the centrifuge, which is spinning at 120krpm, and this causes the heavier  $U^{238}$  isotope to migrate towards the outside of the centrifuge whilst the slightly enriched  $U^{235}$  remains towards the centre of the centrifuge. The slightly enriched  $U^{235}$  is drawn off the centre of the centrifuge as the product stream, whilst the slightly higher concentration of  $U^{238}$  is drawn off from the outside of the centrifuge as the tail stream. As the enrichment provided by one centrifuge is

insufficient to increase the concentration of  $U^{235}$  to the required 3-5% by weight, a series of centrifuges, also known as a cascade, is used to gradually refine the  $U^{235}$  to the required concentration. At this point the depleted  $U^{238}$  has been reduced to about 0.7% by weight. These cascades can be seen in Figure 2.2(b). Once the required concentration of  $U^{235}$  has been reached, the  $UF_6$  gas is then cooled, re-solidified and then shipped for conversion to  $UO_2$  for use in fuel pellets.

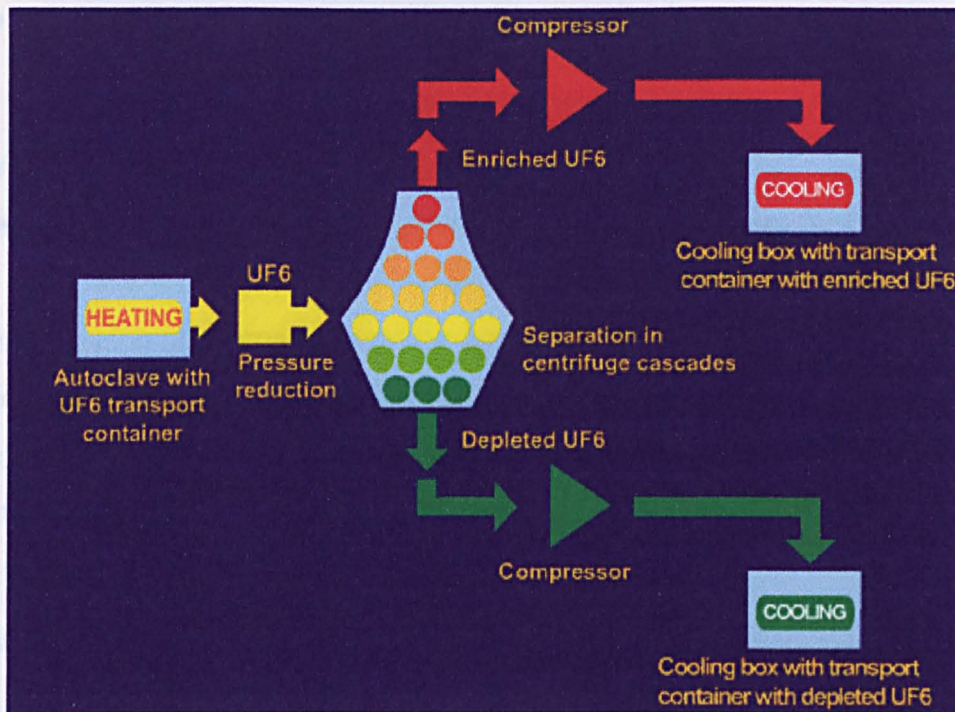
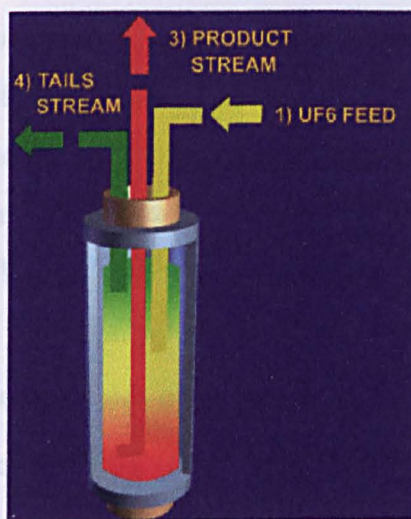
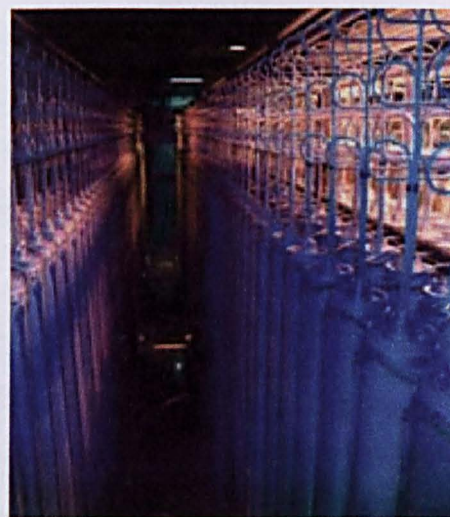


Figure 2.1 - The uranium enrichment process as performed by Urenco [Ure02]



(a) Schematic of a centrifuge



(b) Cascade or series of centrifuges

Figure 2.2 - Centrifuges for separation of  $U^{235}$  and  $U^{238}$  [Ure02]

The centrifuges are a thin walled tube made from ultra-light materials. This is coupled to a motor at the bottom of the centrifuge (currently a hysteresis motor), which provides the rotation and the heat generated by the motor forms a temperature gradient in the centrifuge,

which helps in the separation process. Whilst the hysteresis motors which are currently in use are satisfactory for driving the centrifuge they operate on an open-loop control strategy. Hence, their speed is not easily adjustable, and they have a comparatively poor efficiency. Urenco would like to employ a motor with a higher efficiency and one whose speed can be easily controlled. Permanent magnet brushless machines are the obvious alternative to the hysteresis motor as they have a high efficiency and, due to the closed loop control strategy for commutation, their speed is easily detectable and controllable.

### 2.1.2 Magnetically loaded composite (MLC)

Advanced carbon fibre composite technology has been developed by Urenco over the past 25 years or so, and recently this been extended by impregnating a magnetic powder such as NdFeB into a region of the composite. This has facilitated the realisation of technologies such as low inertia self-powered rollers for handling sheet materials [Buc96]. This loading of magnetic powder into a carbon fibre composite is commonly known as Magnetically Loaded Composite or MLC. Neglecting the stiffness from the epoxy, it can be shown that the Young's modulus ( $E_c$ ) of the composite is:

$$E_c = E_f \times V_f \quad (2.1)$$

The carbon fibre has a modulus of  $\approx 400\text{GPa}$ . Thus, with a readily achievable volume fraction of 60%-70%, a composite modulus of 240GPa - 280GPa is achievable [Buc96]. This is comparable with steel, for which the Young's modulus is of the order of 200GPa. The density of the composite is  $\approx 1600\text{kg/m}^3$ , which compares with  $\approx 8000\text{kg/m}^3$  for steel. Thus, the composite structure makes a very attractive alternative to steel. By varying the winding angle ( $\phi$  relative to the rotor axis) of the carbon fibre filaments, the properties of the carbon fibre can be adjusted. There are 2 winding types, which are generally used:

- Hoop winding. ( $\phi \sim 90^\circ$ ) - All the strength is circumferential and the full strength of the composite ( $E_c$ ) is obtained.
- Helical winding ( $\phi < 90^\circ$ ) - This consists of winding in 2 directions ( $\pm\phi$ ) and imparts strength in both the radial and axial directions. Radially the strength and stiffness are proportional to  $\sin^4(\phi)$  and axially they are proportional to  $\cos^4(\phi)$ .

Urenco required the rotor of the motor be an integral part of the carbon fibre composite centrifuges and be an integral part of them, and specified that the rotor should be made from a magnetically loaded composite tube which consists of a number of layers, as can be seen in Figure 2.3. The innermost layer consists of 0.4mm of 'helical' winding, in which the fibres

are overlaid at 45° angles to provide a high degree of axial rigidity. The second layer consists of carbon fibre impregnated with NdFeB powder. Finally, a 2.1mm ‘hoop’ wound layer of fibre is applied to provide circumferential containment for the other two layers. However, the magnetic powder loading is limited to ~14% so as to ensure the mechanical integrity of the rotor.

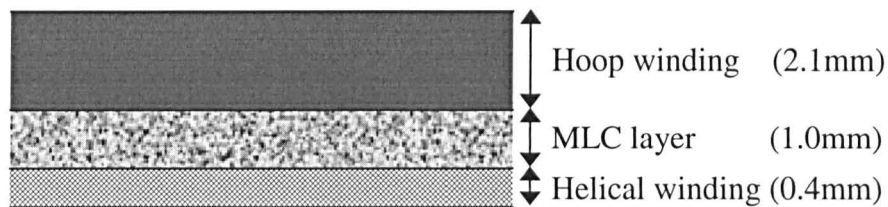


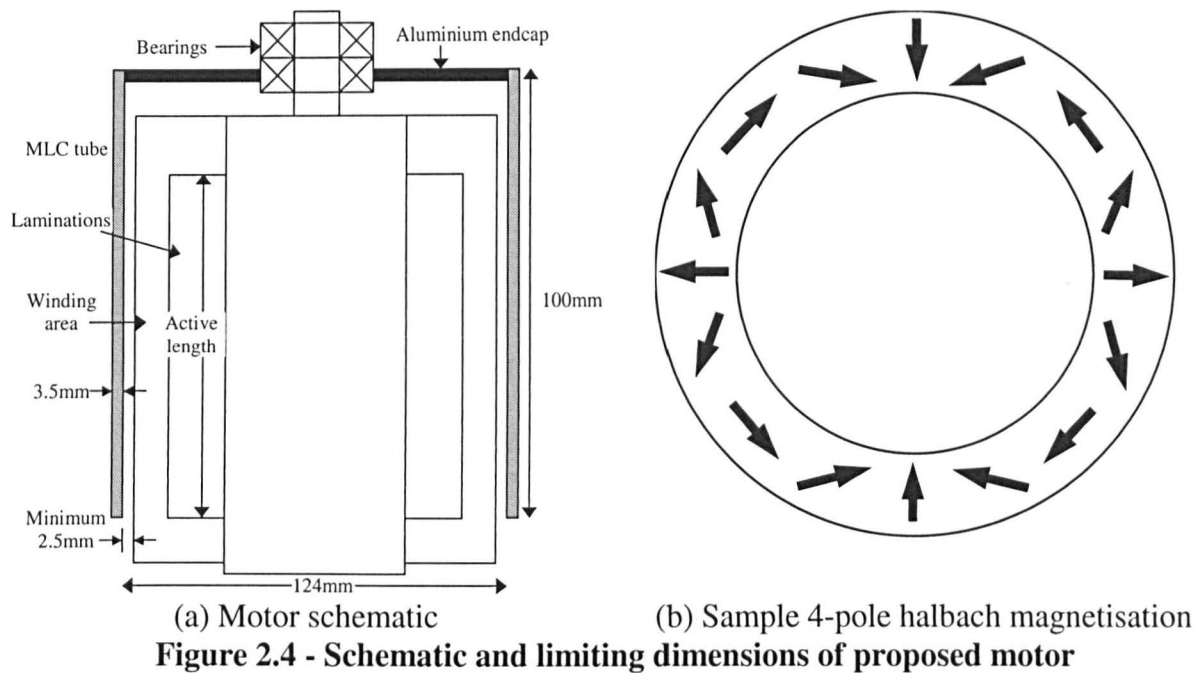
**Figure 2.3 - Structure of MLC tube**

### 2.1.3 Motor specification

The motor specification, as supplied originally by Urenco, was as follows:

- Maximum rotational speed : 120,000rpm
- Rated torque : 50mNm
- Inner diameter of MLC external rotor : 124mm
- Radial thickness of magnet : 1mm
- Minimum air-gap length : 2.5mm (increases by 0.4mm at 120,000rpm)
- Effective remanence of magnet : 0.11 T
- Maximum axial length : 100mm (inclusive of active length, one end-winding and ferrite screen, and clearance to rotor)
- Stator bore diameter : 70mm
- DC link voltage : 500 V
- Maximum operating speed : 120,00 rpm
- Motor efficiency : >90%
- Target overall efficiency (motor + drive) : >80%
- Maximum rotor temperature : 70°C (limited by resin)

In addition, the rotor had to be supported at one end only, by a double bearing. A schematic of the proposed motor, showing the limiting dimensions, is shown in Figure 2.4. Despite considerable reservations about the mechanical stability of the motor, Urenco insisted that it be designed in this way and that their mechanical analyses showed that the design was feasible. It was also requested that the design be slotless to eliminate cogging torque.



## 2.2 Brushless dc motor design

### 2.2.1 CAD design software

Design optimisation was undertaken using proprietary CAD software developed in ‘The Electrical Machines and Drives Group, University of Sheffield’, which employs analytical techniques [Hal85][Zhu93][Ata97][Zhu02] to derive the airgap flux distribution, and a non-linear lumped reluctance model [Zhu92] to derive the flux density in the stator and the resulting iron loss [Ata92]. The winding copper loss is calculated as described in [Ark92][Eng97]. The winding inductances are also predicted analytically [Zhu95], as is the motor performance [Ack92][Zhu92]. The various elements of the design process have all been validated extensively using finite element analysis. The CAD software incorporates the following features:

- Synthesis of motor designs according to specified dimensions.
- Variation of design parameters (viz. leading dimensions ) over prescribed ranges.
- Alternative magnetisation distributions, including radial, parallel and Halbach.
- Graphically-based design optimisation, which enables the design and performance of feasible designs to be compared.

A detailed description of the more important analytical equations will be presented in Appendix C, with comparisons of predicted results with finite element and measured results being shown in Chapter 3.

### 2.2.2 Design methodology

The brushless dc motor was designed to have a multi-pole Halbach magnetised external rotor, with no back-iron, and a slotless stator winding. The Halbach magnetisation has the advantage of being self-shielding, and therefore, has negligible leakage flux external to the rotor. Consequently, no rotor back-iron is required to provide a return flux path. Alternative winding dispositions, viz. overlapping and non-overlapping were considered, the winding thickness being optimised for each design so as to maximise the specific torque. Since the winding inductances have a significant effect on the motor dynamic performance at the high fundamental operating frequency, these were taken into account.

In order to ensure that the motor could be accommodated within the specified space envelope, the core length was limited to 60mm to allow adequate space for the end-windings and to allow for any unforeseen losses the motor was designed to have a torque of 55mNm, 10% higher than rated. A commutation advance of 30° electrical was employed in order to help increase the developed torque, reduce the motor current and, consequently, ensure the efficiency met the specified requirement. As an example of the effect of the commutation advance, Figure 2.5 shows the efficiency of a 6-pole motor both with and without commutation advance for an over-lapping winding topology. At this point it should be noted that in the CAD packages the winding is always designed to have an integer number of turns, and this explains the 'zigzag' nature of some of the curves. In Figure 2.5, when there is no commutation advance it can be seen that changing the winding thickness from 10mm to 11mm increases the efficiency. This is caused by a change of one turn per coil. A more detailed explanation of this is given in Appendix G.

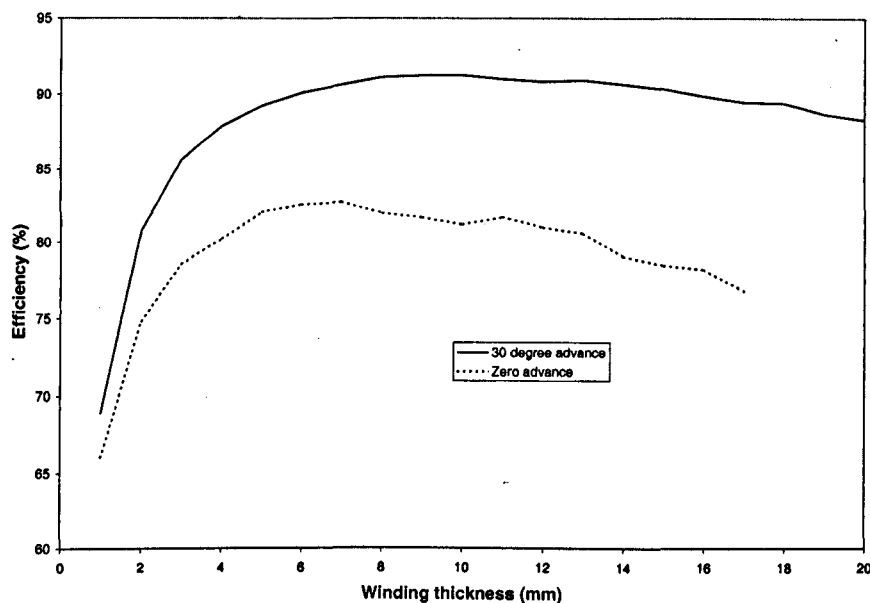


Figure 2.5 – Influence of commutation advance on efficiency of 6-pole motor at 120krpm

A value of  $100 \text{ W/m}^2\text{K}$  was used for the heat transfer coefficient, and whilst initially this seems large it results from the motor geometry and the particular application. As the motor is to operate in a vacuum, the only significant path for heat to flow from the stator, other than by radiation, is through the aluminium hub to one end of the motor. Consequently, the thermal model assumes that the motor heat is dissipated over the end surface area of the aluminium core. In reality, the motor will be attached to a much larger structure, as can be seen from the photograph of the centrifuges shown in Figure 2.2(b), and the heat will be dissipated from a significantly larger surface than the comparatively small surface of the aluminium core.

The nominal minimum airgap specified by Urenco was 2.5mm at low speed, but allowing for a 0.4mm expansion of the rotor at high-speed, results in a minimum airgap of 2.9mm. As the dominant loss component is the copper loss then increasing the airgap length further would only serve to further increase the copper loss. Therefore, the airgap length was maintained at the 2.9mm minimum.

### 2.2.3 Pole number and winding thickness

An investigation was undertaken into the influence of the pole number and the winding thickness on the efficiency at the rated torque and operating speed. The findings are summarised in Figure 2.6, which shows that the efficiency increases with pole number. However, the fundamental electrical frequency also increases with pole number, and ultimately this limits the switching devices that can be used in the drive. Table 2.1 shows the capabilities of commonly available switching devices. Whilst Bipolar junction transistors (BJT), MOS controlled thyristors (MCT) and Gate turnoff thyristors (GTO) are limited to switching speeds of  $<10\text{kHz}$  for any significant power [Moh95], IGBT's can be used above  $10\text{kHz}$ . However, as the switching frequency increases the device needs to be derated as the switching loss becomes significant and the efficiency of the device drops significantly. At switching frequencies of around  $100\text{kHz}$ , MOSFET's have a significant advantage as their switching time on average tend to be  $\sim 10$  times lower than IGBT's, with a corresponding lower switching loss, which makes MOSFET's attractive for high-speed drives. It can also be seen that for each pole number there is an optimal winding thickness.

**Table 2.1 - Switching speeds and power capability of commonly available semiconductor devices [Moh95]**

Device	Power capability	Switching speed
BJT	Medium	Medium
MOSFET	Low	Fast
GTO	High	Slow
IGBT	Medium	Medium
MCT	Medium	Medium

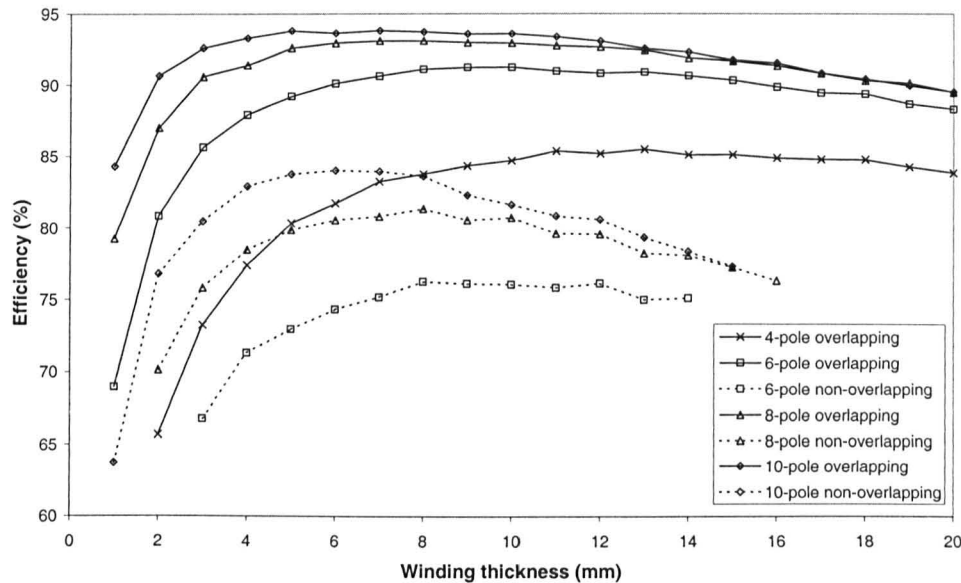
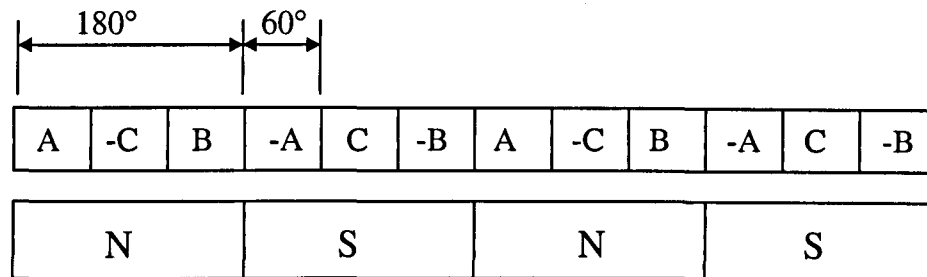


**Figure 2.6 - Influence of winding thickness and pole number on efficiency, (60mm active core length)**

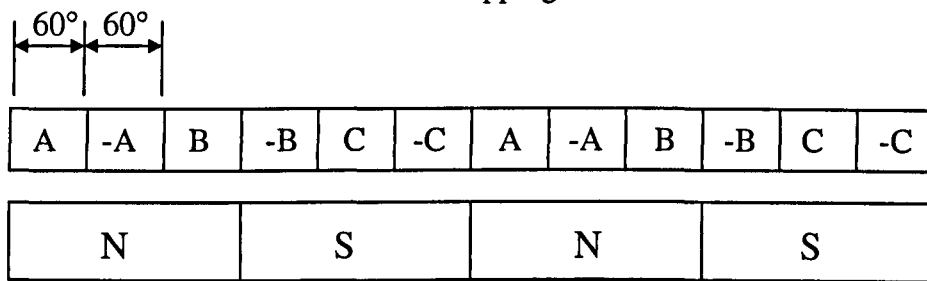
This initial design study showed that the only feasible winding configuration within the available space envelope that meets the efficiency requirement of 90% is the overlapping winding shown in Figure 2.7(a), with 180° elec. pitched coils having 60° elec. widths. Although the non-overlapping winding configurations shown in Figure 2.7(b) & (c) would have shorter end-windings, they result in a significantly lower power density due to having winding factors, which is defined as the percentage of the pole spanned by one coil, of only 50% and 75% respectively, compared to 100% for the overlapping winding shown in Figure 2.7(a), and the copper loss would have been excessive.

It can be seen from the results of the design study displayed in Figure 2.6 that the efficiency of the 4-pole designs is well below the minimum efficiency requirement of 90% and that the efficiency of the 6-pole designs are at the lower end of the specified efficiency range. However, it was decided to adopt an overlapping 6-pole design, viz. Figure 2.7(a), the 8-and 10-pole motor designs being disregarded since their fundamental frequency at 120krpm is 8kHz and 10kHz, respectively, which could present problems in controlling the motor phase currents as the PWM frequency would need to be excessively high. For the 6-pole

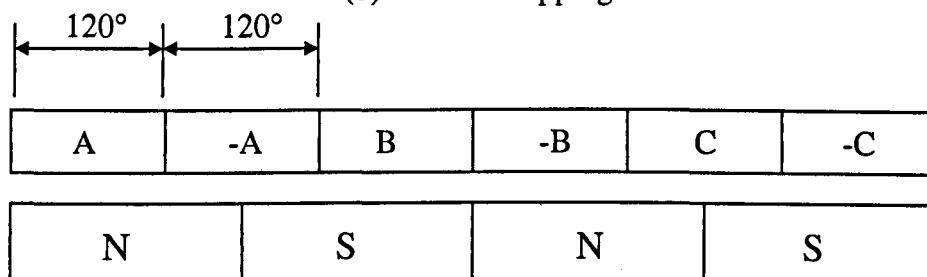
motor topology which was selected, it can be seen from Figure 2.6 that the optimal winding thickness is 10mm. Subsequent investigations were undertaken to examine how the 6-pole design, equipped with both overlapping and non-overlapping windings, could be further improved.



180- 60 winding: 180° pitch, 60° width  
Power Density 100%  
Overlapping



60- 60 winding: 60° pitch, 60° width  
Power Density 50 %  
(b) Non-overlapping



120- 120 winding: 120° pitch, 120° width  
Power Density 75%  
(c) Non-overlapping

**Figure 2.7 – Stator winding configurations**

## 2.2.4 Magnet radial thickness

The effect of increasing the magnet thickness on the loss, (ie. copper loss plus iron loss) of a 6-pole slotless motor, with the winding thickness optimised for the maximum efficiency, is shown in Figure 2.8. Throughout, the magnet remanence was assumed to be 0.11T, and a commutation advance of 30° electrical was maintained.

As can be seen, a relatively small increase in magnet thickness has a dramatic effect on the motor performance, an increase from 1mm to 2 mm increasing the efficiency to ~96% for an overlapping winding and to ~93% for a non-overlapping winding.

However, after consultation with Urenco and despite the benefits of employing a thicker magnet, it was decided to employ a 1 mm thick magnet in order to comply with Urenco’s application requirements. As stated earlier, a 6-pole motor design with an active core length of 60 mm was selected for prototyping. The main design parameters are given in Table 2.2, whilst the design details are given in Figure A.1 of Appendix A. A schematic of the motor is shown in Figure 2.9.

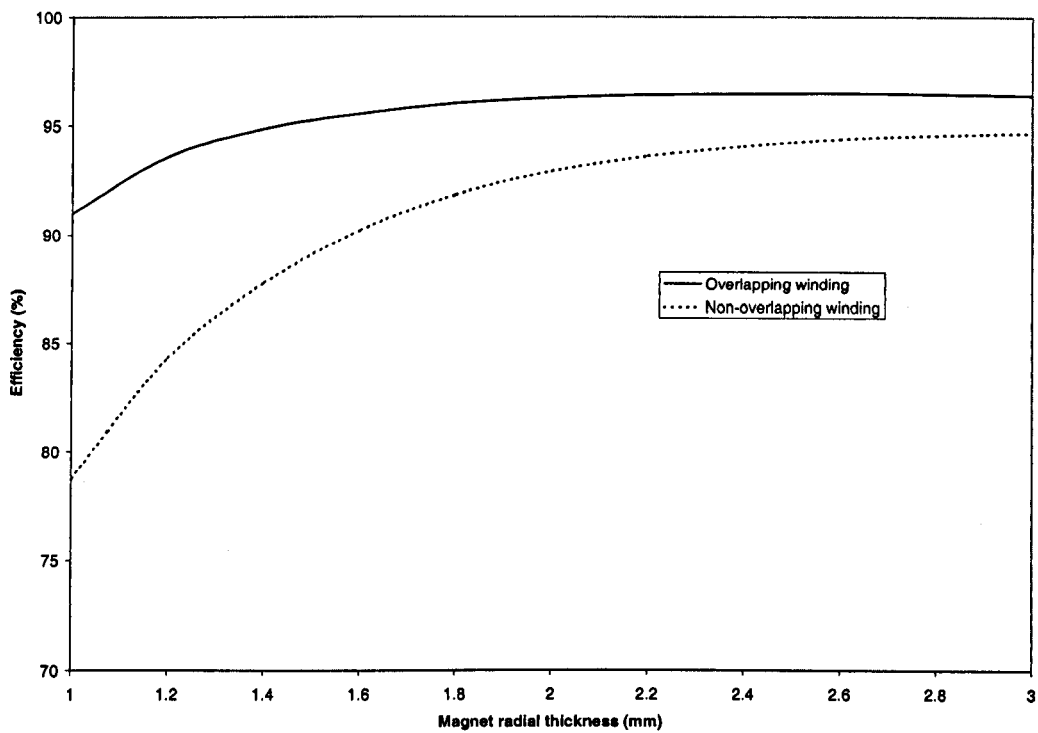


Figure 2.8 - Influence of magnet thickness on efficiency of 6-pole motor

Table 2.2 - Original 6-pole design with overlapping winding as shown in Figure 2.7(a)

Turns per coil	80
Phase self inductance	1.297 mH
Phase mutual inductance	-0.49 mH
Phase resistance	2.70 $\Omega$
Strands per coil	2
Torque	56.12 mNm
Peak Phase emf	115 V
rms phase current	2.93 A
Copper loss	70 W
Winding eddy loss	1.7 W
Iron loss	0.6 W
Efficiency	90.7

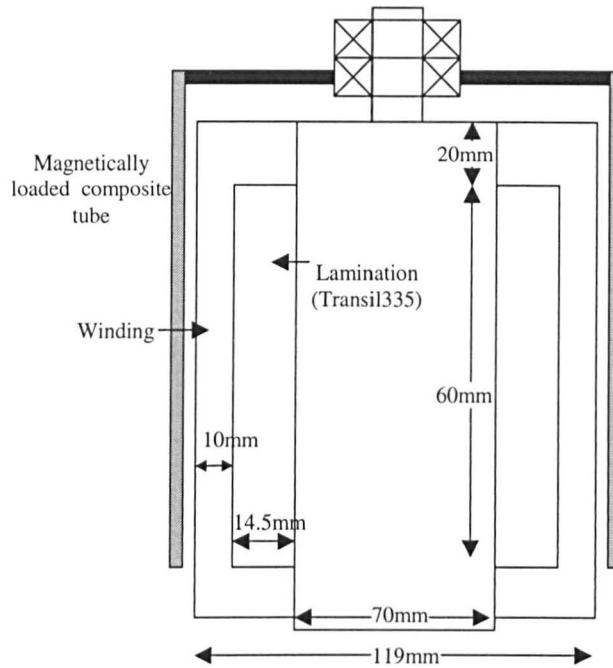


Figure 2.9 - Schematic of 6 –pole design

## 2.3 Finite element validation

### 2.3.1 Back-emf calculation

An ideal Halbach magnetisation distribution was assumed, and a finite element model of the motor was analysed for 20 discrete rotor positions, spanning a rotation of 120° mechanical, at each of which the instantaneous back-emf/phase was calculated using equation 2.2 with  $\Phi$  being the result of an integration over the coil width.

$$e = \omega N_c l \frac{d\Phi}{d\theta} p \quad (2.2)$$

The instantaneous open-circuit field distribution, from the finite element analysis, is shown in Figure 2.10, whilst the resulting back-emf waveforms are shown in Figure 2.11.

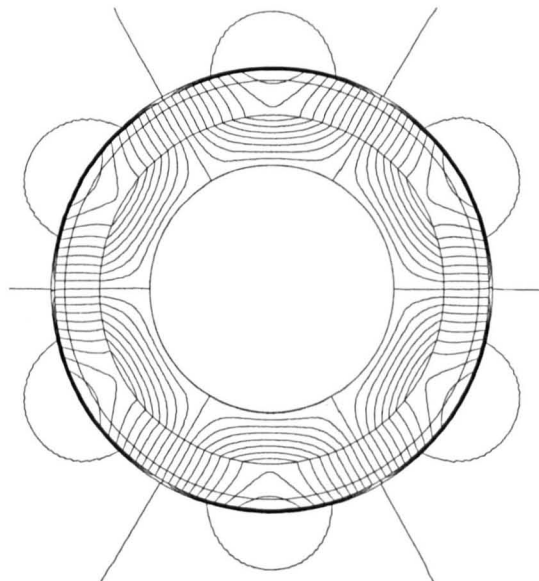
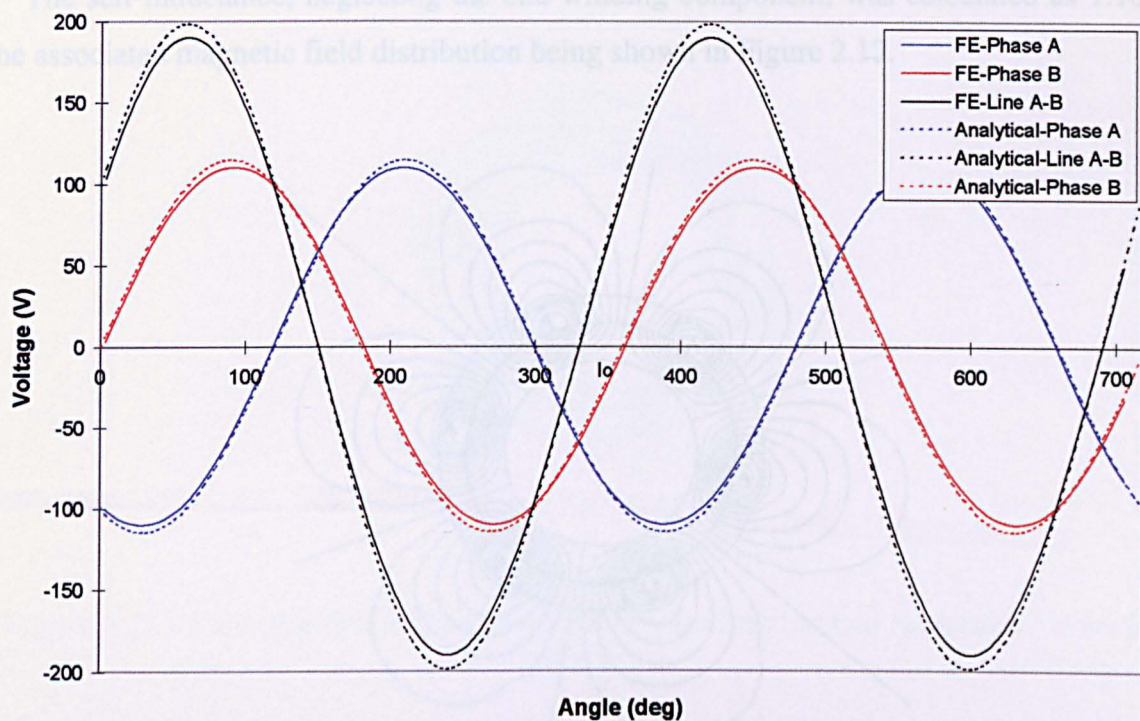


Figure 2.10 – Open-circuit field distribution, 6-pole, 80-turn/coil motor



**Figure 2.11 - Comparison between analytical and finite element calculated back-emf waveforms at 120krpm.**

### 2.3.2 Inductance calculations

For the calculation of the self and mutual inductances, the permanent magnet was simply assumed to have the same permeability as that of air i.e.  $\mu_r=1.0$ . As the rotor is made of carbon fibre and the powder loading is only 11% then  $\mu_r$  will only be fractionally larger than 1 and significantly below the value of  $\sim 1.05$  normally used for NdFeB magnets. Appropriate phase windings were then assumed to have a current density of  $0.1 \text{ A/mm}^2$ , a small value  $<2\%$  of rated current density of  $5.4 \text{ A/mm}^2$ , and the self- and mutual-inductances were calculated as follows:

#### a) Self-inductance

In order to determine the self-inductance, one phase was energised and the magnetic field distribution was calculated. The inductance was then determined using equations 2.3 to 2.5.

$$\frac{1}{2}LI^2 = E_l \left( = \frac{1}{2}I \int JA ds \right) \quad (2.3)$$

$$L = \frac{2E_l}{I^2} \quad (2.4)$$

$$\text{where } I = \left( \frac{JA}{N_p} \right) \quad (2.5)$$

The self-inductance, neglecting the end-winding component, was calculated as 1.186mH, the associated magnetic field distribution being shown in Figure 2.12.

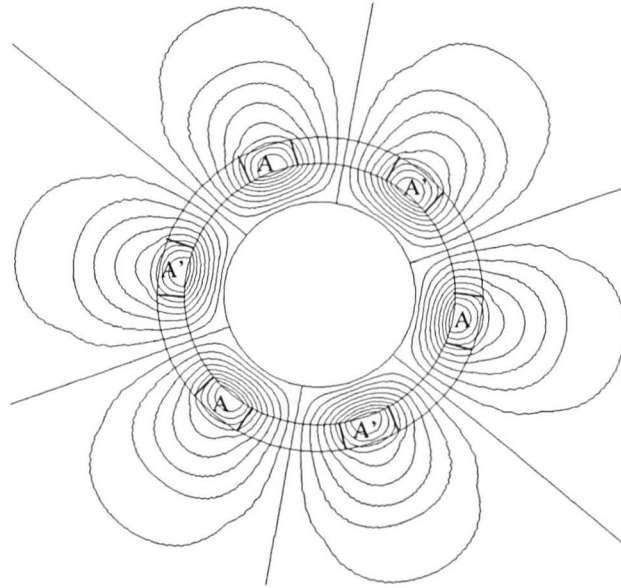


**Figure 2.12 - Flux distribution with one phase excited for self-inductance calculation.**

#### **b) Mutual inductance**

For the calculation of the mutual inductance, two phases were excited and the magnetic field distribution was calculated. The mutual inductance was then determined using equation 2.6.

$$M = \frac{l}{I^2} \frac{E_{II}}{2} - L = \frac{l}{I^2} \left( \frac{E_{II}}{2} - E_I \right) \quad (2.6)$$

The mutual inductance, again neglecting the effect of the end-windings, was calculated as -0.444mH, the associated magnetic field distribution being shown in Figure 2.13.

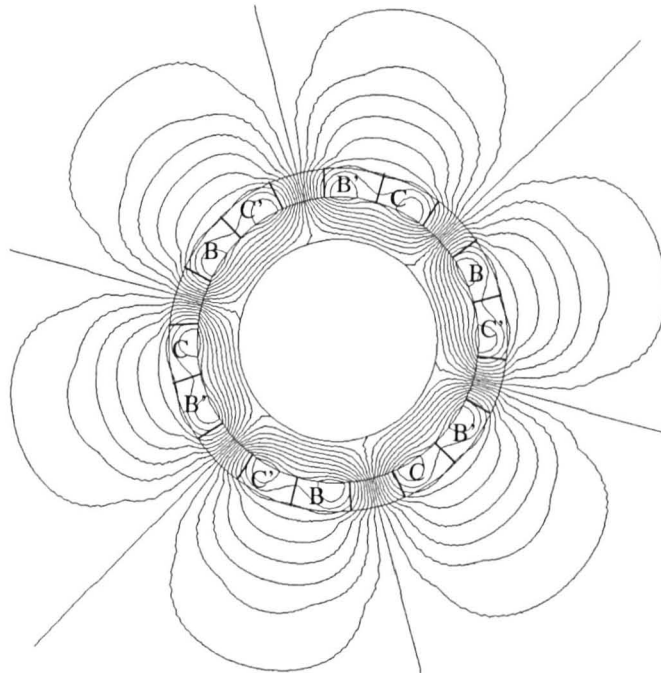


**Figure 2.13 - Flux distribution with two phase windings excited for mutual inductance calculation.**

### 2.3.3 Comparison of results

As can be seen in Table 2.3, the back-emfs deduced from finite element analysis compare well with those obtained analytically from the CAD software.

**Table 2.3 - Comparison of back-emfs at 120krpm**

	Analytical	Finite element
Peak line voltage	198.58 V	190.10 V
Peak phase voltage	114.65 V	109.98 V

The inductance values also agree well, as can be seen in Table 2.4, although it should be noted that neither of the predicted values include the end-winding inductance components.

**Table 2.4 - Comparison of inductances**

	Analytical	Finite element
Self-inductance	1.297 mH	1.186 mH
Mutual inductance	-0.489 mH	-0.444 mH

## 2.4 Dynamic Simulations

Prior to construction of the prototype motor, a dynamic simulation was performed using the parameters obtained from finite element analysis to ensure that the motor was capable of developing the required torque at 120krpm.

### a) Dynamic simulation model

The steady-state dynamic simulation model of a 3-phase permanent magnet, brushless dc drive is implemented in a single functional block, designated 'BLDC3' in Figure 2.14, which is one of a number of dynamic models for use in a system simulation package called SIMNET which has been developed by members of the Electrical Machines and Drives Group, University of Sheffield. It utilises a frequency domain analysis, full details of the simulation model being given in [Zhu92][Ack92]. The 'con' blocks in Figure 2.14 represent specified constants, the 'av-rms' blocks display the average and rms values of various input and output quantities, whilst the 'm-gra' block is a graphical display routine, which outputs specified waveforms.

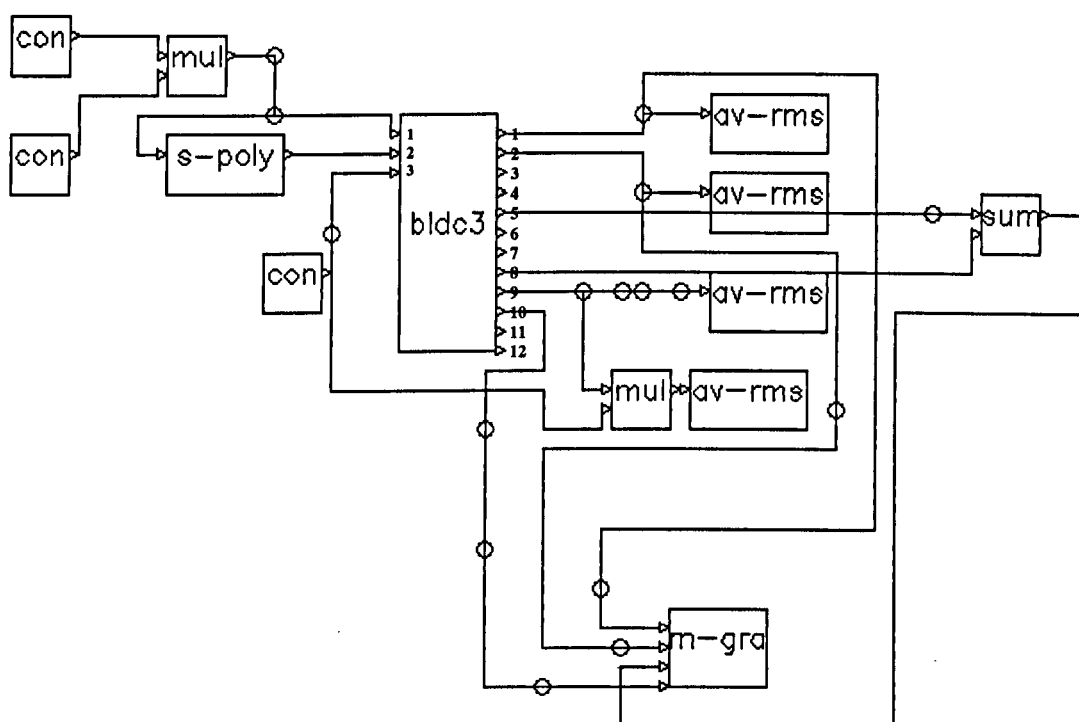


**Figure 2.14 - Block diagram of steady state dynamic simulation model of brushless dc drive.**

The inputs to the 'BLDC3' block are:

- 1 rotor mechanical speed (mech rad/s)
- 2 rotor mechanical position (mech rad)
- 3 DC link voltage (V)

The constants, which are user-specified, are the self- and mutual-inductances, the back-emf constant, the phase winding resistance, and parameters related to the drive, viz switch voltage drop, diode voltage drop and switch and diode resistances.

The outputs of the 'BLDC3' block are:

1	electromagnetic torque
2-4	motor phase current waveforms
5-7	inverter terminal voltages
8	motor star point voltage
9	DC Link current
10-12	motor phase emf waveforms

The motor phase voltages are obtained by subtracting the star-point voltage from the terminal voltages, whilst the DC link current is multiplied by the DC link voltage to obtain the total input power.

### b) Simulation results

Dynamic simulations were performed using parameters derived from the CAD software and those obtained from the finite element analysis. Figure 2.15 shows the torque and current waveforms from these simulations. As can be seen, when the finite element parameters are used the average torque is higher (60mNm) than that when the simulation is based on the CAD design parameters (54mNm). However, as both are greater than the 50mNm required, construction of the prototype motor proceeded.

Details of the prototype motor construction and of the dimensioning of soft ferrite cores, which are employed to contain the magnetic field produced by any high frequency components due to switching harmonics in the windings, are given in Appendix B and can be seen in Figure 2.16, where the internal diameter was reduced from 70mm to 68mm to accommodate the ferrite components, which could only be manufactured in limited sizes.

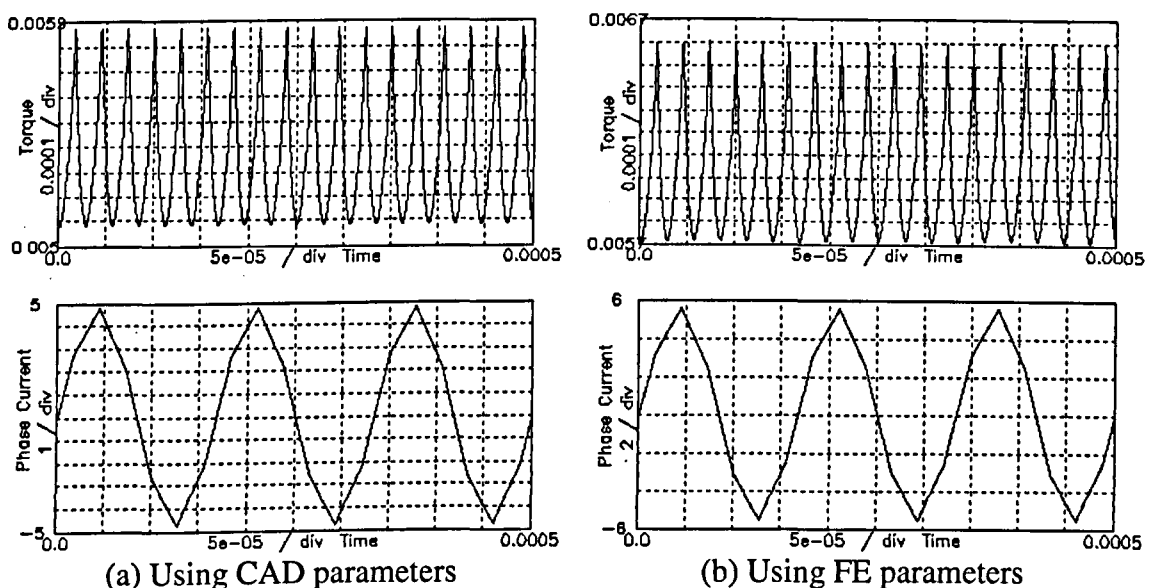


**Figure 2.15 - Comparison of dynamic simulations for 6-pole motor with 30° commutation advance**

## 2.5 Comparison of predicted and measured stator parameters

It should be noted that, at this stage, Urenco decided to reduce the active length of the motor from 60mm to 40mm in order to overcome a predicted resonance problem that would have prevented the motor from running up to its rated speed of 120krpm. Accordingly, the rotor was shifted as shown in Figure 2.16 an attempt to avoid the resonance problem, and consequently the active magnet length was reduced to 40mm. However, the stator, which had already been constructed, remained unchanged.

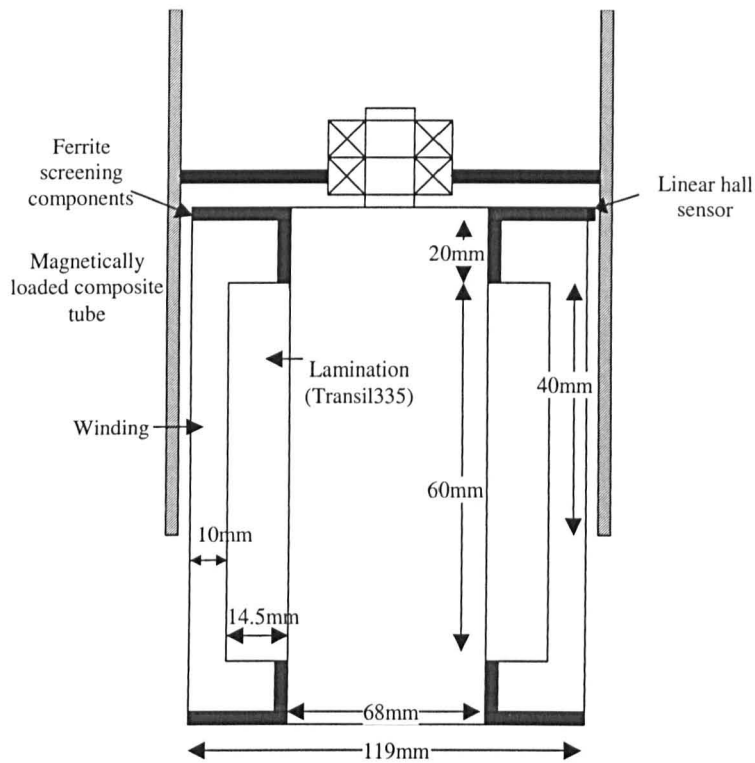


Figure 2.16 - Schematic showing shortened rotor magnet length

### 2.5.1 Self-inductance and mutual inductance

#### a) End-winding inductance

Initially the end-winding inductance was not accounted for at the design stage. However, once the coils were wound it quickly became apparent, as will be seen later, that the end-winding inductances were significant and needed to be considered. Thus, a method for calculating the end-winding inductances was incorporated in the CAD package. For the 3 cases (a, b, c) illustrated previously in Figure 2.7, the end-winding self-inductance ( $L_e$ ) was calculated by a method similar to that given in [Liw61]; viz:

$$L_e = 2\mu_0 l_e \frac{W_p^2}{p} 1.2K_{dp}^2 \quad (2.7)$$

where  $l_e = \frac{l_{e1}}{2} + l_{e2}$

$$K_{dp} = \begin{cases} \frac{3}{\pi} & (a) \\ \frac{3}{2\pi} & (b) \text{ winding factor} \\ \frac{9}{4\pi} & (c) \end{cases}$$

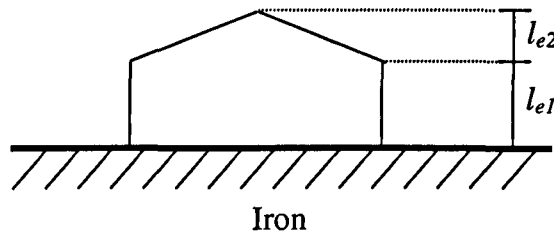


**Figure 2.17 - Dimensions for end-winding calculation**

Whilst for the end-winding component of the mutual inductance:

$$M_e = \begin{cases} L_e \cos\left(\frac{2\pi}{3}\right) & (a) \\ 0 & (b) \\ 0 & (c) \end{cases}$$

### b) Measured inductances

Due to their relatively complex geometry, of the end-winding components of the self and mutual inductances are difficult to predict accurately. However, analytical values were calculated using the foregoing equations.

The winding inductances were measured using an inductance bridge, at a frequency of 1kHz. The predicted and measured results are shown in Tables 2.5 & 2.6. As can be seen, there is a reasonable agreement between the predicted and measured values.

**Table 2.5 - Comparison of measured and predicted self-inductances**

Phase self-inductance		
Phase	Predicted (mH)	Measured (mH)
Red	2.39	2.59
Yellow	2.39	2.60
Blue	2.39	2.57

**Table 2.6 - Comparison of measured and predicted mutual inductances**

Phase mutual-inductance		
Phase	Predicted (mH)	Measured (mH)
Red	-1.04	-1.33
Yellow	-1.04	-1.33
Blue	-1.04	-1.33

However, the measurements are for the stator winding alone, without the connecting leads and the soft ferrite screening. The cables are routed from the top of the motor down the aluminium core next to the laminations, and it is thought that this routing partly contributes to the increases in the measured inductances, when the average measured values become:

Phase self-inductance	3.47mH	(3.46mH without leads)
Phase mutual-inductance	-0.104mH	(-0.076mH without leads)

Thus, whilst the connecting leads have a relatively small influence on the inductances, the addition of the soft ferrite shielding when assembling the complete stator accounts for most of the difference observed here. The mutual inductance on this finished assembly is measured across 2 phases and then calculated from  $2L-M$  and this methodology accounts for the potential significant reduction in the mutual inductance. As can be seen the difference is dramatic and this will adversely affect the motor performance, by limiting the maximum achievable speed, as will be shown in Section 2.7.

### **c) Revised calculation of winding inductances based on prototype stator**

Using end-winding inductance calculations previously described, the effect of the increased winding inductances on the motor performance was investigated. As can be seen from Table 2.7, the inclusion of the end-winding inductance has a dramatic effect on the developed torque. Consequently, the motor design needed to be further modified in order to generate the desired torque at the rated speed of 120krpm. Utilising the CAD software with the end-winding inductance incorporated then the winding was modified as shown in Table 2.7. However, since the predictions showed that a 6-pole motor design having 80 turns/coil would still be able to run at the rated speed of 120krpm albeit with a reduced torque, it was decided to investigate its performance further.

**Table 2.7 - Effect of end-winding inductance on motor performance**

	Neglecting end-winding inductance	Including end-winding inductance	Modified design for rated torque
Turns per coil	80	80	49
Phase self inductance	1.30 mH	2.39 mH	0.79 mH
inc. end-winding of	-	1.09 mH	0.31 mH
Phase mutual inductance	-0.49 mH	-1.04 mH	-0.34 mH
inc. end-winding of	-	-0.55 mH	-0.15 mH
Phase resistance	2.70 $\Omega$	2.88 $\Omega$	0.93 $\Omega$
Strands per coil	2	2	2
Torque	56.1 mNm	29.13 mNm	54.3 mNm
Speed	120,000 rpm	120,000 rpm	120,000 rpm
Peak Phase emf	115 V	115 V	70 V
rms phase current	2.93 A	1.53 A	4.82 A
Copper loss	69.8 W	20.3 W	64.9 W
Winding eddy loss	1.74 W	1.74 W	3.35 W
Iron loss	0.56 W	0.56 W	0.56 W
Efficiency	90.7 %	94.2 %	90.8 %

### 2.5.2 Phase resistance

The CAD software predicts the winding resistance at the operating temperature of the motor (114° C), as can be seen in Appendix A. The measured resistance is compared with the calculated value taking into account the temperature rise and length of the end-windings, from:

$$R' = R(1 + [R_{\alpha}\Delta T]) \quad (2.8)$$

where  $R_{\alpha}$  is the temperature coefficient of resistivity.

**Table 2.8 - Comparison of measured and predicted phase resistances**

Phase resistance			
Phase	Predicted ( $\Omega$ ) @ 114°C	Measured ( $\Omega$ ) @ 20°C	Measured ( $\Omega$ ) @ 114°C
Red	2.88	2.01	2.75
Yellow	2.88	2.01	2.75
Blue	2.88	2.01	2.75

At this point, however, it should also be noted that the supply leads to the motor also serve to increase the effective resistance to 2.125 $\Omega$  @20° C per phase.

### 2.5.3 Verification of NdFeB powder loading

In order to assess the magnetisation of the magnetically loaded fibre composite rotor, a 5-turn search coil in which each turn spanned 1 pole-pitch, and had an axial length ( $l$ ) of 60mm was manufactured. The search coil was mounted on a non-magnetic former inside the

magnetically loaded composite rotor, the airgap being 2mm. Measurements were made on two nominally identical Halbach magnetised MLC rotors (designated Rotor 1 and Rotor 2) which were impulse magnetised by Urenco, using a 6-pole impulse magnetising fixture designed and manufactured at the University of Sheffield, described briefly in Appendix B, and the voltage induced in the search coil was measured at 2 different rotational speeds. The measured values were then compared with values calculated from the peak airgap flux density from CAD and finite element analyses, using equations 2.9 and 2.10, as shown in Tables 2.9 & 2.10. The field distribution from which the finite element value of  $B_{max}$  was obtained is shown in Figure 2.18

$$E_{peak} = 2N_s \times B_{max}lv \quad (2.9)$$

$$E_{pk-pk} = 2E_{peak} \quad (2.10)$$

where  $r = 60$  mm

$B_{max} = 4.52$  mT (Finite element); 4.65 mT (CAD)

**Table 2.9 - Comparison of predicted and measured peak to peak emf for Rotor 1**

Speed (rpm)	CAD	Finite element	Measured
676	23.23 mV	23.03 mV	23.8 mV
879	30.21 mV	29.9 mV	29.2 mV

**Table 2.10 - Comparison of predicted and measured peak to peak emf for Rotor 2**

Speed (rpm)	CAD	Finite element	Measured
656	22.65 mV	22.46 mV	23.0 mV
865	29.74 mV	29.49 mV	29.8 mV

The measurements confirm that the MLC rotors have the NdFeB powder loading which was assumed in the motor design synthesis, viz  $B_{rem}=0.11$ T, and that the rotors have been successfully impulse magnetised with the 6-pole Halbach magnetisation distribution.

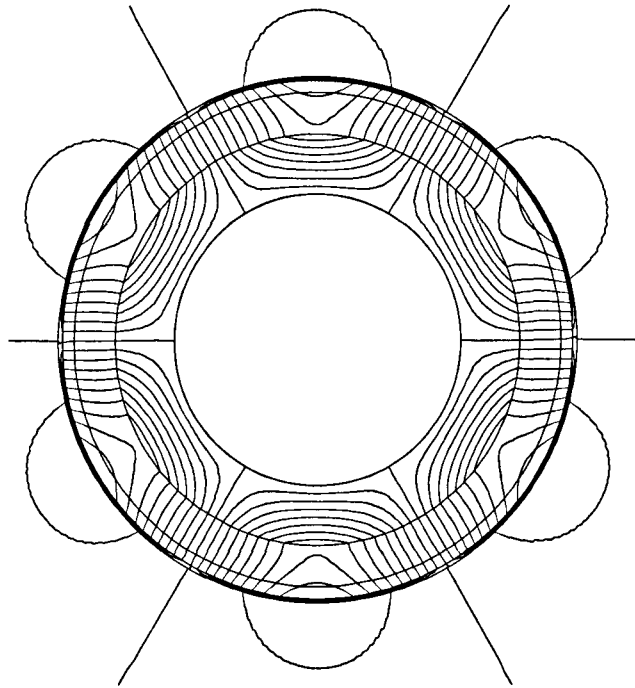


**Figure 2.18 – 6-pole open-circuit field distribution.**

#### 2.5.4 Back-emf

The back-emf was measured during a run-down test of the motor, the rotational speed being deduced from the frequency. The predicted and measured phase back-emf waveforms are essentially sinusoidal, as shown in Figure 2.19. Table 2.11 compares the peak phase back-emf values and emf constants, as predicted by finite element analysis and the CAD software assuming an active axial length of 40mm for both the stator winding and the permanent magnet rotor.

**Table 2.11 - Comparison of predicted and measured phase emfs (@ 5714rpm)**

	CAD	Finite element	Measured
Peak phase emf (V)	3.639	3.491	3.223
Peak emf constant (V/rads <sup>-1</sup> )	0.006077	0.00583	0.00539

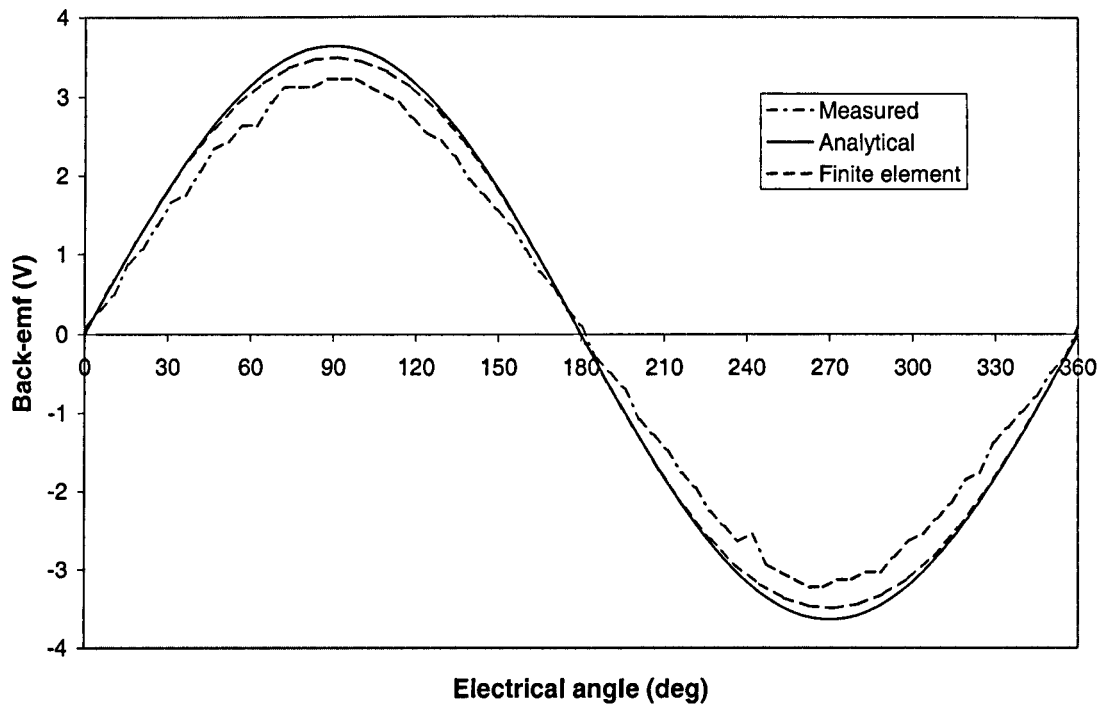


**Figure 2.19 - Measured and predicted back-emf waveform at 5714rpm**

It can be seen that the measured back-emf is slightly lower than expected, which contrasts with the slightly higher measurement obtained previously in 2.5.3. However, both the CAD and finite element models assume that the stator coils are distributed evenly over the 10mm of radial winding thickness of the stator coils. In reality, however, the coils needed to be retained on the stator prior to potting in stycast, which meant that the outer layer of conductors of each coil is further away from the rotor surface than calculated, which leads to a slight reduction in the flux-linkage, and a smaller back-emf.

## 2.6 Hall sensors

Since the flux density produced by the MLC rotor at the end of the stator is only  $\pm 9.54\text{mT}$ , it is too low to operate commercially available Schmitt triggered Hall sensors. Hence, linear Hall sensors were employed together with external electronic circuitry to generate the required commutation pulses. The Hall sensors were located as shown in Figure 2.16

UGN3503 linear Hall sensors were used in conjunction with an AC coupled amplifier, shown in Figure 2.20, to remove the DC offset voltage and amplify the output signal – which is  $\pm 10\text{mV}$  per mT.

A test was performed by rotating the MLC rotor in order to capture the raw Hall sensor output signal and the output of the conditioning circuit. These waveforms are shown in Figures 2.20 – 2.23.

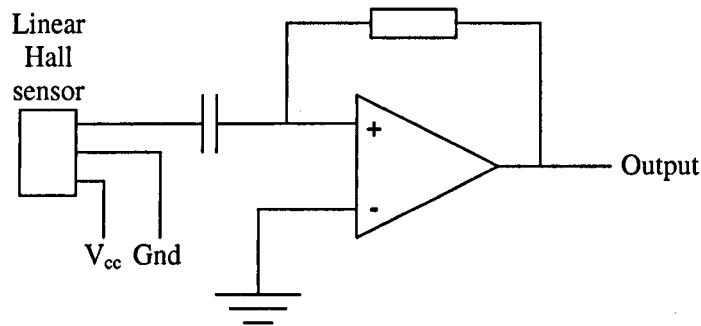


**Figure 2.20 - Schematic of circuit used for linear hall sensors**

Unfortunately, however, due to mechanical limitations at this stage, it was not possible to rotate the rotor at high speed. Hence, an input signal was generated by using a signal generator at frequencies up to 6kHz in order to simulate the motor running at speeds up to 120krpm. As the signal generator was operating at very low voltages the noise on the signal is significant as can be seen, however, the circuit still produces the correct output. At the simulated rated speed of 120krpm (i.e. 6kHz electrical) there is a phase lag of  $\pm 20^\circ$  between the input and output signals of the Hall sensor conditioning circuit, which has to be accounted for when implementing the  $30^\circ$  electrical commutation advance, which was discussed in Section 2.2.

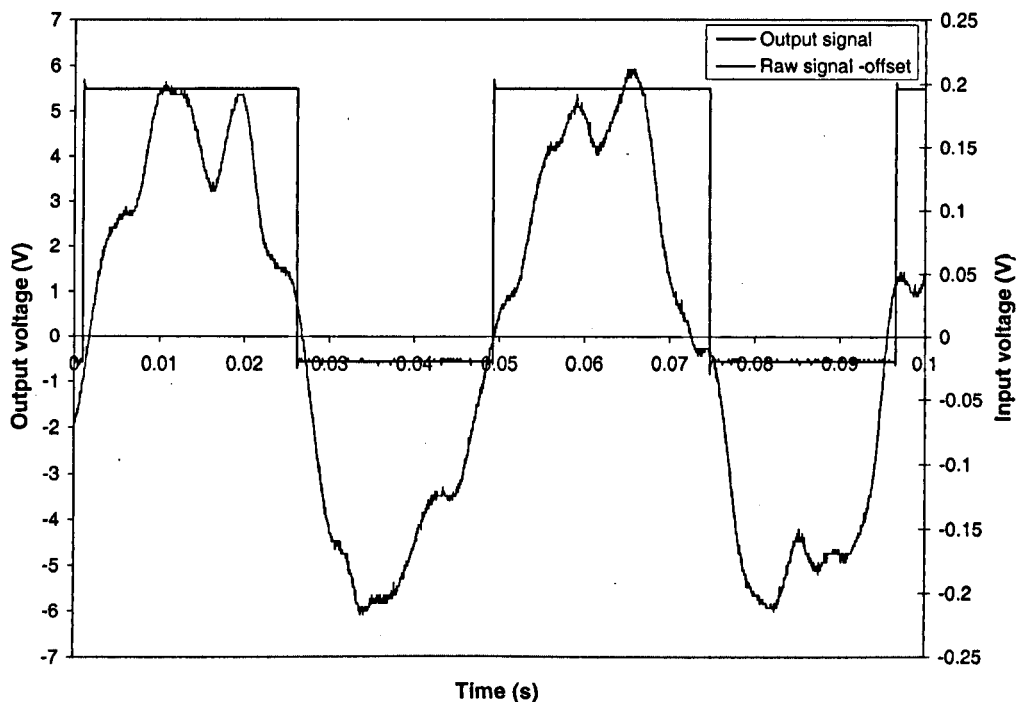


**Figure 2.21 – Input and output signals of Hall sensor - 409rpm**

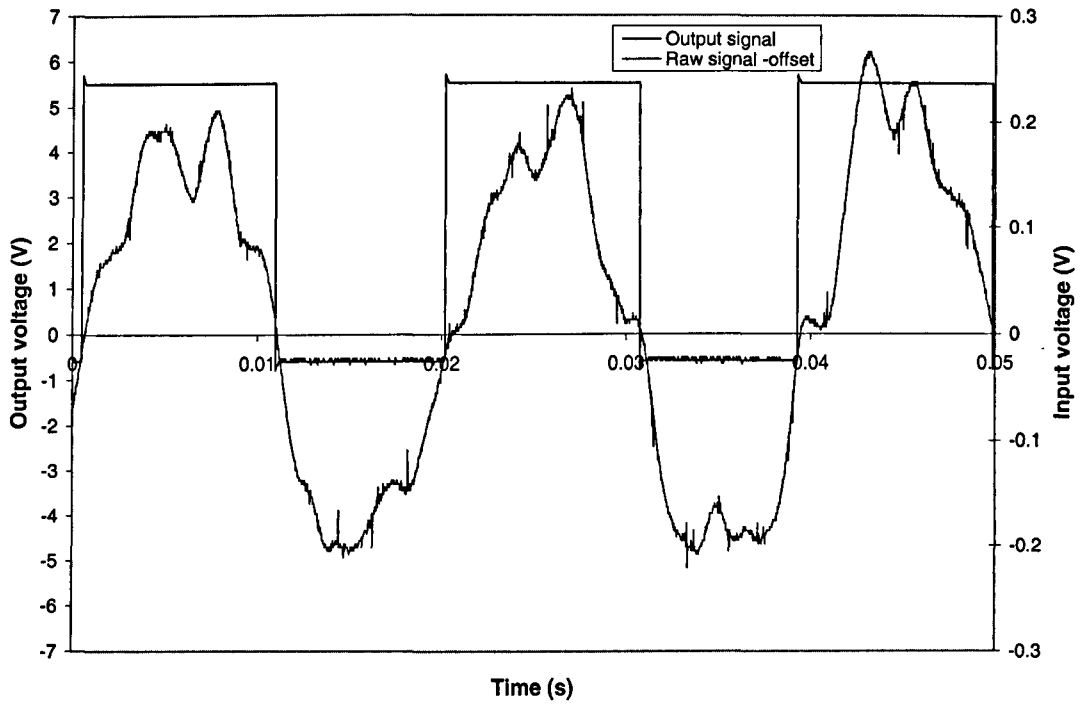


**Figure 2.22 – Input and output signals of Hall sensor - 1000rpm**

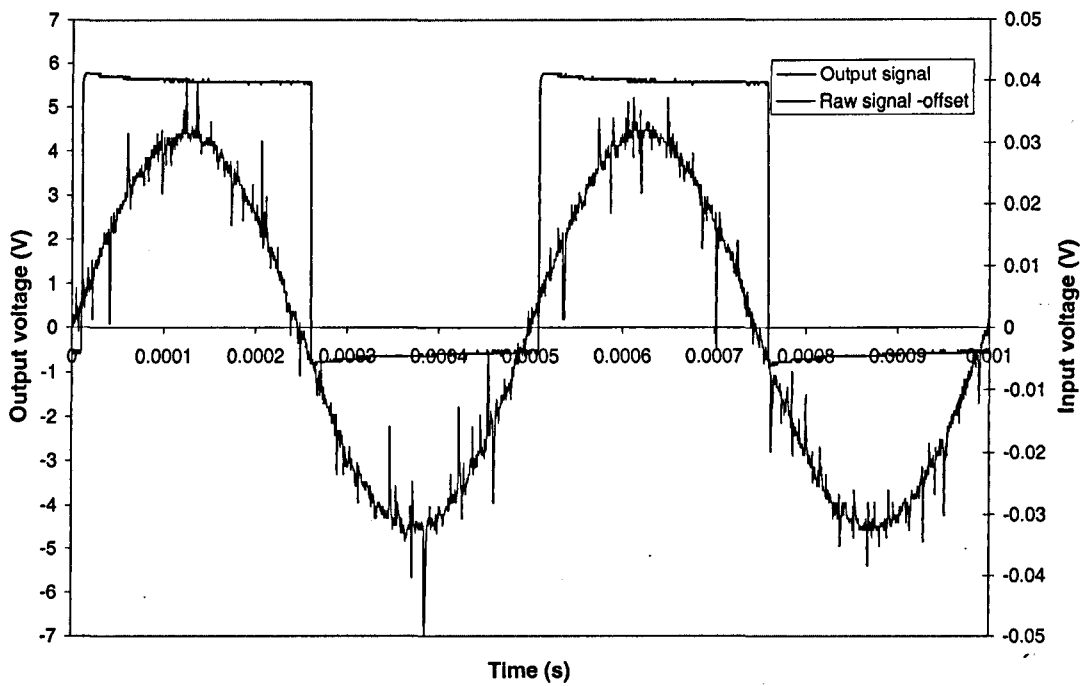


**Figure 2.23 - Input and output signals of Hall sensor - 2kHz sine wave applied**

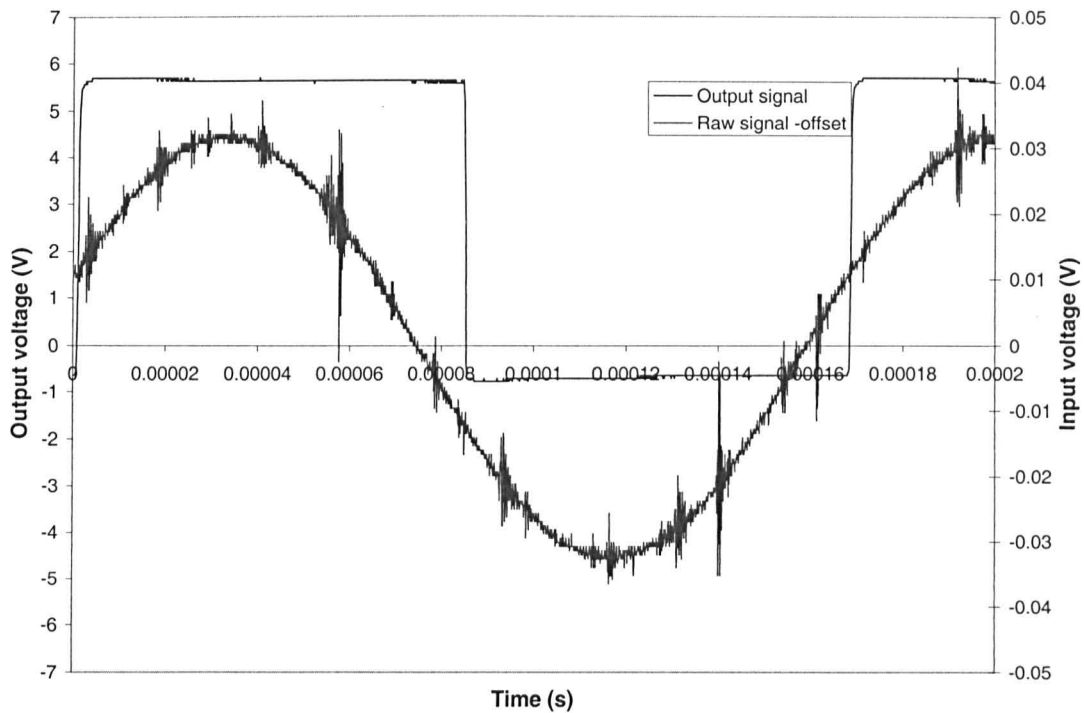


**Figure 2.24 - Input and output signals of Hall sensor -6kHz sine wave applied**

Due to the need to remove the DC offset from the Hall sensor the signal needs to be AC coupled, however, this means a reliable signal is unavailable on start-up. Removing the DC offset to produce a signal at start-up requires a hysteresis band to take account of the drift in the DC offset due to temperature, but due to the low field available from the rotor magnet this hysteresis band is comparable to the output signal and consequently Hall sensors are unsuitable for use with this motor. Thus, optical sensors with a 30° electrical commutation advance had to be employed in the prototype motor, as shown in Figure 2.25. Despite the need to position the optical sensors close to the rotating disc and the sensitivity of the orientation of both the sensors and the disc within the MLC rotor this arrangement successfully generated the commutation signals for the motor, as will be seen in section 2.7.

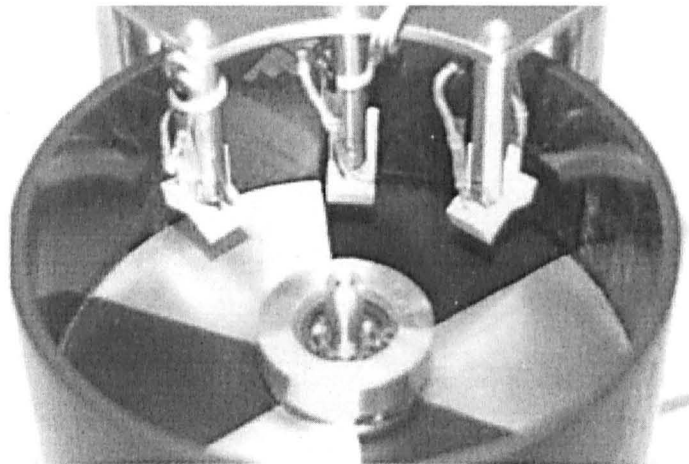


**Figure 2.25 - Optical sensor arrangement**

## 2.7 Motor tests

### 2.7.1 Test rig

For obvious safety reasons, the prototype motor needed to be tested in a secure enclosure. There was a need to provide containment if the rotor accidentally burst during operation or collided with the stator during a resonance mode. A high-speed, evacuated test rig was commissioned as shown in Figure 2.26. The motor is located in a spin pot, shown in Figure 2.27, which has a 2 inch thick steel wall to contain any possible fragments from the motor. As can be seen, the motor is also surrounded by steel rings which would serve to absorb energy from any fragments from the rotor, and is bolted down to the base of the spin pot. The buffer vessel is a large container designed to absorb small fluctuations in pressure caused by the motor operation. In the event of failure of the rotor or sudden heating in the spin-pot, caused by an electrical fault, for example, which would cause a sudden expansion in gas volume, the buffer vessel protects the vacuum pumps from a sudden increase in pressure since this could damage the diffusion pump. The spin pot has 2 ports to provide access for the motor electrical power connections and connections to the optical sensors, through special vacuum glands.

There are 2 vacuum pumps on the test rig. One is a standard Edwards rotary pump, which reduces the air pressure from atmospheric down to about 1millibar, which takes about 10 minutes. A diffusion pump is then used to reduce the pressure down to around  $0.002\tau$  ( $1\tau=1.2\text{mb}$ ), a process that takes approximately 2 hours. At this pressure, aerodynamic friction torque on the rotor is negligible, which enables the 'run-down' test described in section 2.7.3 to be used to determine the motor torque.

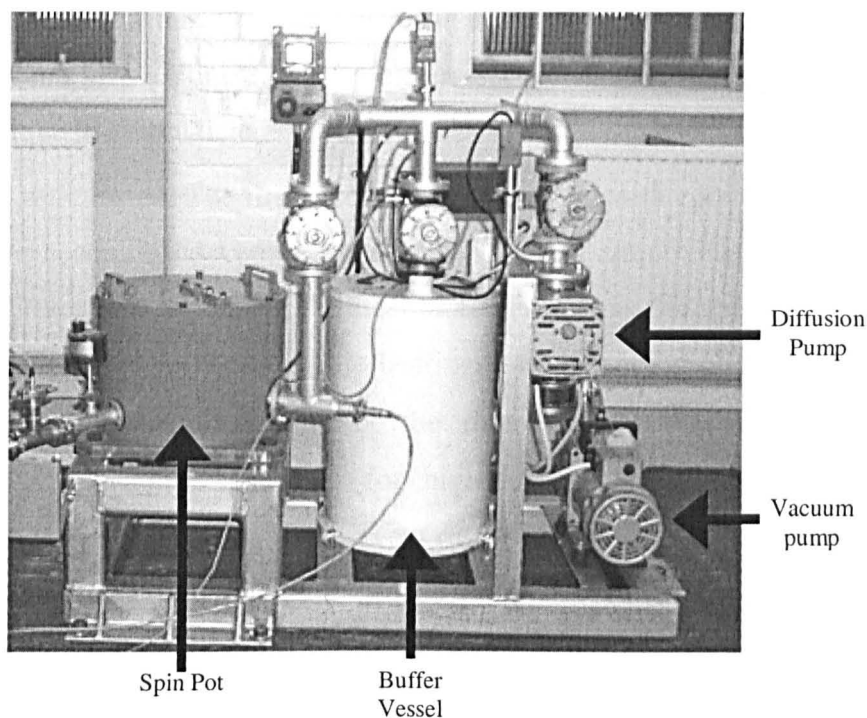


**Figure 2.26 - High-speed test rig**

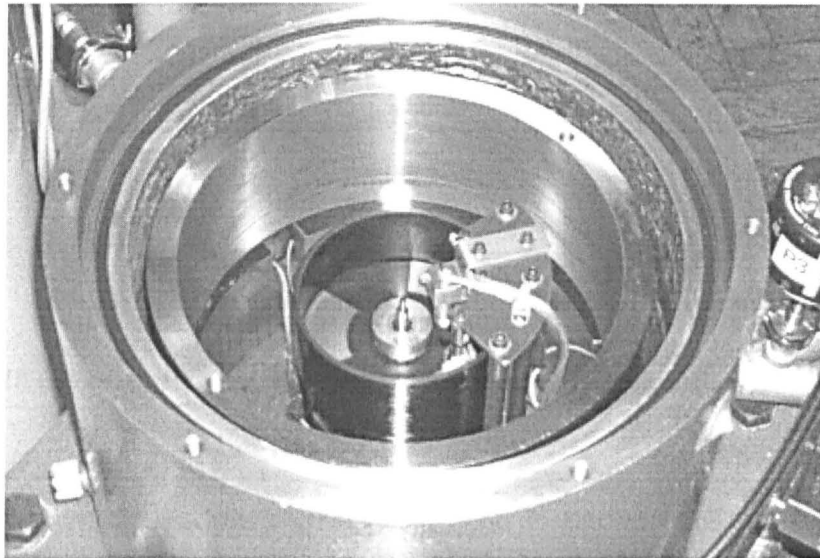


**Figure 2.27 - Spin pot with prototype motor installed**

### 2.7.2 Test methodology

The MOSFET drive, shown schematically in Figure B.13 & B.14 of Appendix B, was supplied from a variable DC power source, and the prototype motor was run up to a steady-state speed for a given dc link voltage, and the speed, DC link current and input power were measured. After the maximum speed was reached, the motor was disconnected from the drive, and allowed to run-down to stand-still, the torque being calculated using the method described in section 2.7.3. The efficiency was calculated from the measured input power and the output power, which is deduced from the calculated torque and the maximum rotor speed.

The maximum rotor speed which was attained for each value of DC link voltage was subsequently specified as an input parameter in a dynamic simulation model, as described in section 2.4, which also assumed the parameters shown in Table 2.12, to enable the DC link current and torque to be predicted.

Two rotors were tested. The first incorporated a bearing with conventional steel balls (SKF 708CC) and the second used a special high-speed bearing employing ceramic balls (C38HDL C22 OJ-201). The rotor employing the steel ball bearing was limited to a maximum speed of ~10,000rpm due to the limitation of the bearings and balancing of the rotor. However, this rotor enabled low speed evaluation of the motor whilst the second rotor was being manufactured and balanced specially for high-speed operation. Both bearings required lubrication to ensure free running and prevent over-heating. This was accomplished by a wick above the bearing that slowly released oil over a period of time. However, failure to lubricate correctly at high-speed can result in damage to the bearings, as will be evident in Figure 2.28.



**Figure 2.28 - Damaged bearings caused by lack of lubricant oil at high-speed**

Parameter	Value	Comments
Phase resistance	2.125 $\Omega$	(including supply leads) 2.01 $\Omega$ (no leads)
Phase self-inductance	3.47 mH	(including supply leads) 2.6mH(no leads)
Phase mutual-inductance	-0.104 mH	(including supply leads) -1.3mH(no leads)
Back-emf constant	5.83 mV/rad.s <sup>-1</sup>	
Commutation advance	30° electrical	
MOSFET voltage drop	0.284 V	
Diode voltage drop	1.527 V	
Switch resistance	0.577 $\Omega$	for both MOSFET and diode

**Table 2.12 - Simulation data**

### Inverter components

MOSFET : IXTH13N  
 Diode : 131646  
 Schottky Diode: RHR15120

### 2.7.3 'Run-down' method for determination of motor torque

The motor torque was estimated using a 'run-down' method. Since the motor runs in a vacuum, the major decelerating torque on the rotor is due to friction in the mechanical bearings. As the flux density in the back-iron is very small and the open-circuit iron loss is low (<0.1% at rated power) then the effect is neglected for this calculation. It has been shown that the deceleration of the rotor is a function of the bearing torque and the inertia torque [Tak91][Bor94][Kas94].

In [Tim91][Pal59] it is shown that the friction torque of a bearing is proportional to speed to the power 0.66. However, with the unbalance present in the rotor, which creates additional radial loading on the bearings, and from their considerable experience, Urenco have found that a linear relationship between speed and bearing torque provides a good approximation for the motor torque. This also takes into account the slight windage loss on the rotor, which is present in the levels of vacuum obtained here. Therefore if the torque is assumed to vary linearly with speed then:

$$\text{Instantaneous torque } T = I_p \cdot \frac{d\omega}{dt} + \frac{P_{loss}(\omega)}{\omega}$$

where  $P_{loss}(\omega)$  comprises of  $P_{bearing}(\omega) + P_{drag}(\omega)$ , which are effectively equal to  $Q \cdot \omega^2$

The constant  $Q$  is derived by running the motor up to the steady-state speed for a given DC link voltage, then disconnecting the supply and allowing the motor to run-down to standstill whilst recording the variation of  $\omega$  against time. From the initial slope of the resulting curve, the constant  $Q$  is estimated from:

$$Q \approx - \frac{\left( I_p \cdot \frac{d\omega}{dt} \Big|_{\omega} \right)}{\omega}$$

Once the function  $Q$  has been established, the torque can be measured over the whole operating range.

The polar moment of inertia ( $I_p$ ) for the rotor, endcap and bearing assembly was calculated by Urenco, to be  $1.41 \times 10^{-3} \text{ kg m}^2$

Although from published bearing characteristics [Tim91] and from advice received from Urenco it was expected that the rundown curves would have a quadratic nature, since it was anticipated that the bearing torque would be speed dependent, it can be seen in Figure 2.29 that the  $x^2$  term is negligible compared with the  $x$  term. It is expected that this dominant speed invariant friction could be due to a number of factors in the curve fit of the rundown curve including incorrect preload on the bearings, slight misalignment of the bearings, unbalance in the rotor, slipping of bearing in the housing etc. The increase in torque observed during the tests at different speeds could then be explained by the bearing and bearing lubricant warming up and thus affecting the torque.

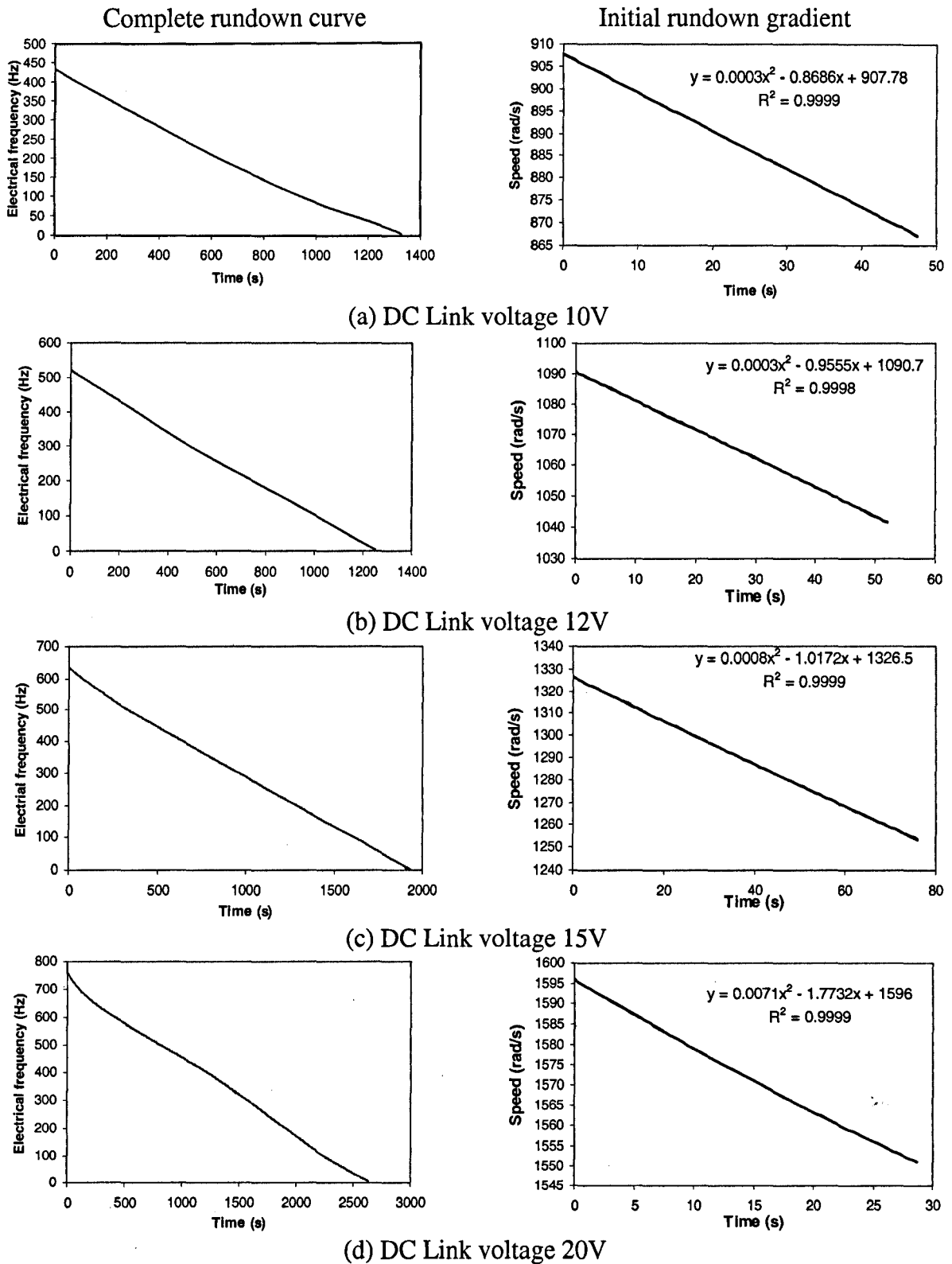
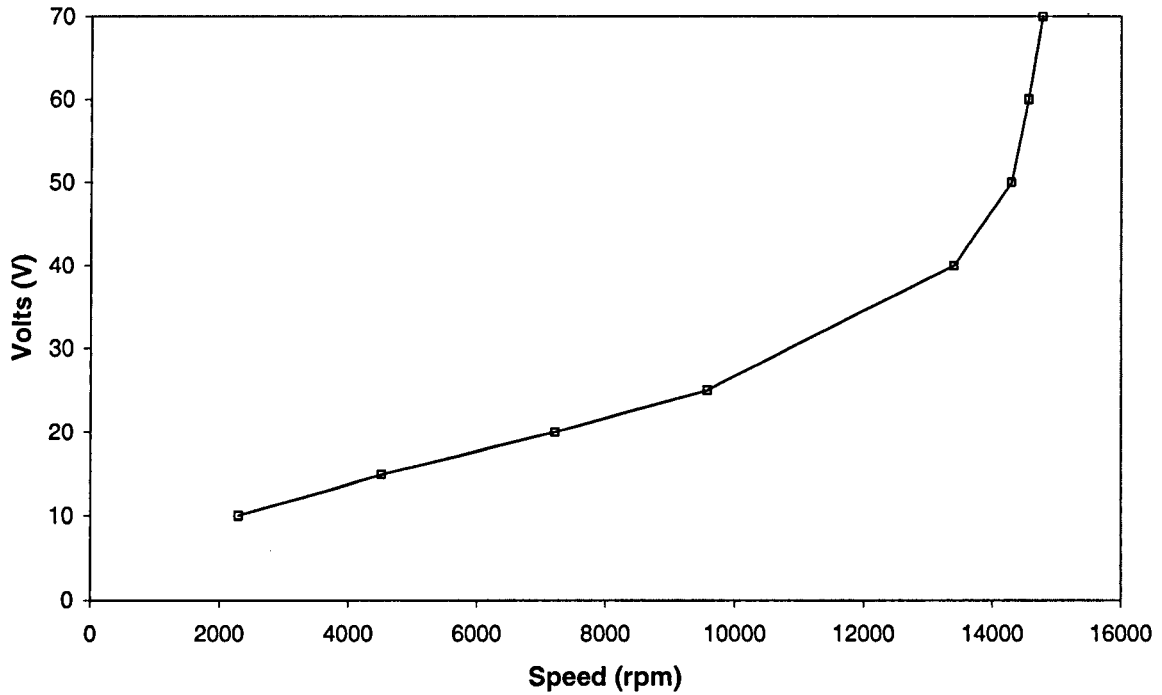


**Figure 2.29 - Motor run-down tests showing full curve and initial gradients**

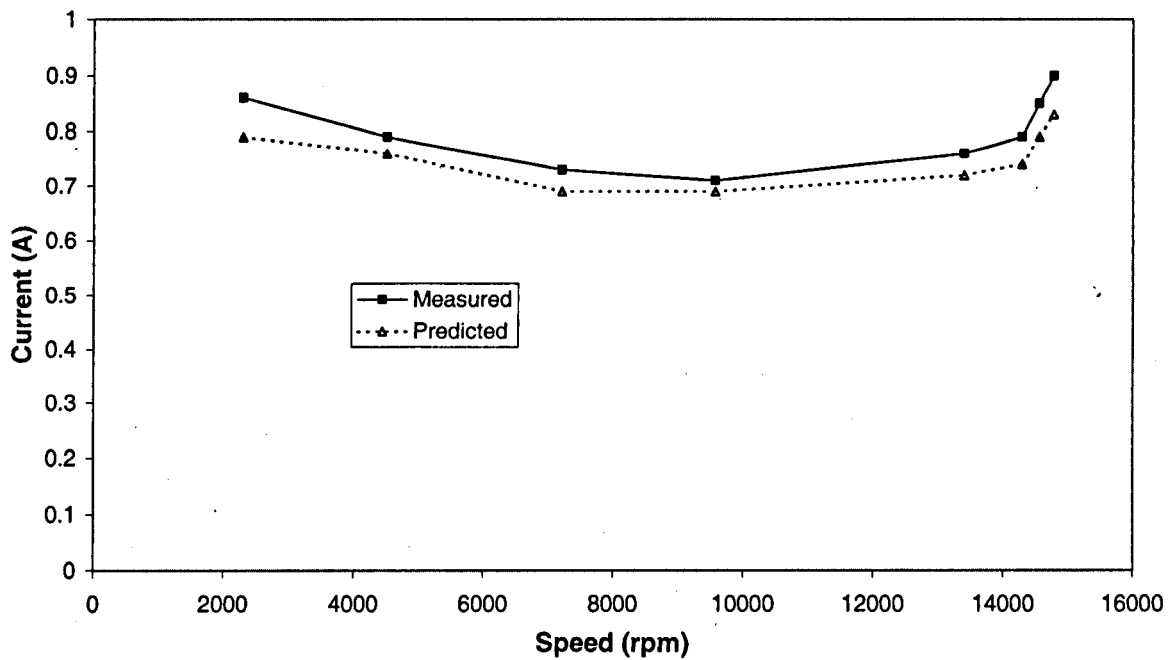
### 2.7.4 Motor performance with steel (SKF 708CC) bearing

Figure 2.30 shows the measured variation of the rotor speed with the dc link voltage, whilst a comparison between the predicted and measured performance is shown in Figures

2.30 – 2.33. As can be seen, there is good correlation. However, it will be noted that a marked increase in the torque occurs above ~10,000 rpm, due to the bearings effectively being used beyond their recommended operating speed, which leads to an increase in the measured motor current. Subsequent to these tests, the bearing performance deteriorated markedly, due to suspected damage of the ball race.



**Figure 2.30 - Variation of measured speed with DC link voltage**



**Figure 2.31 – Variation of DC link current with speed**

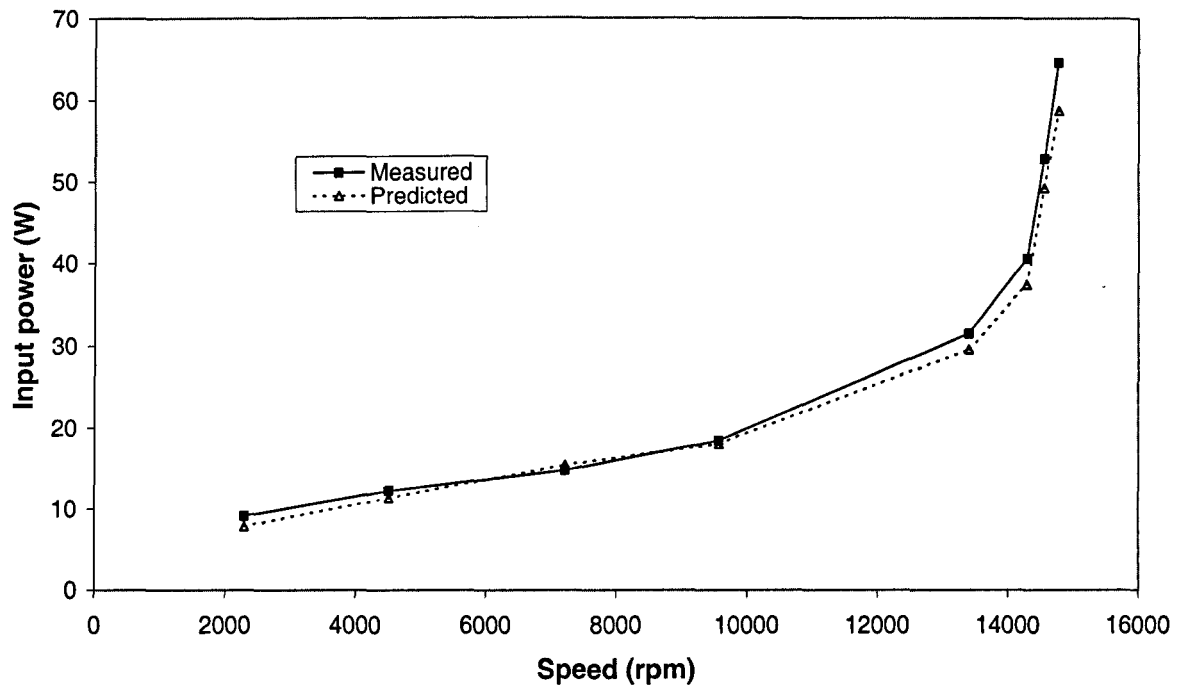


Figure 2.32 – Variation of input power with speed

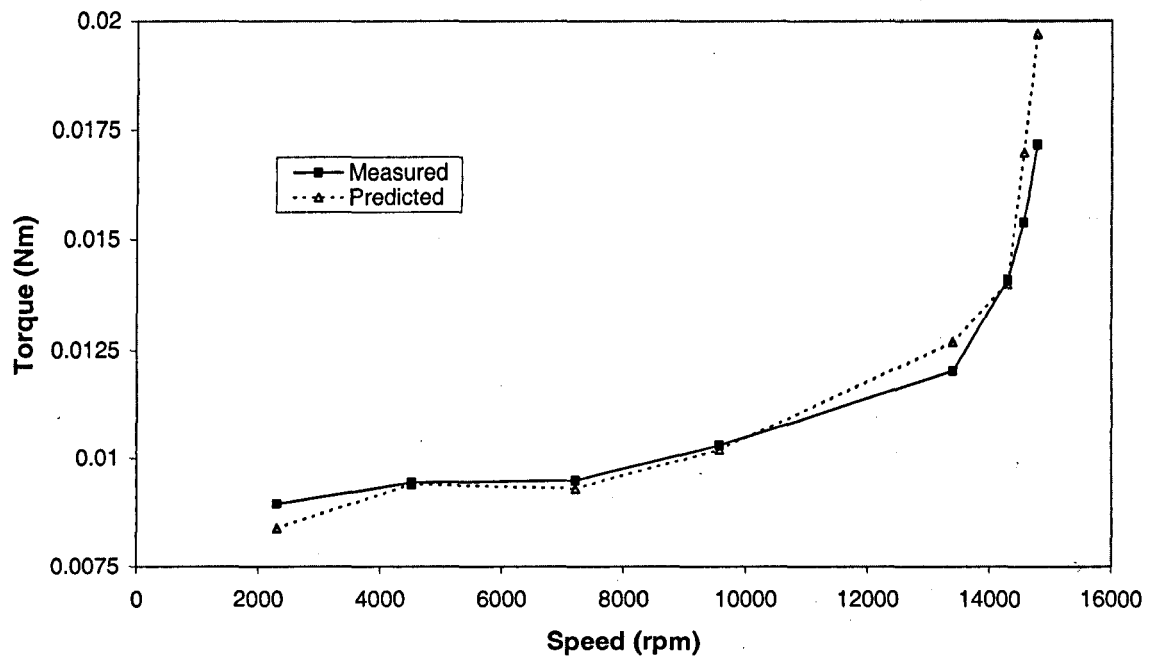
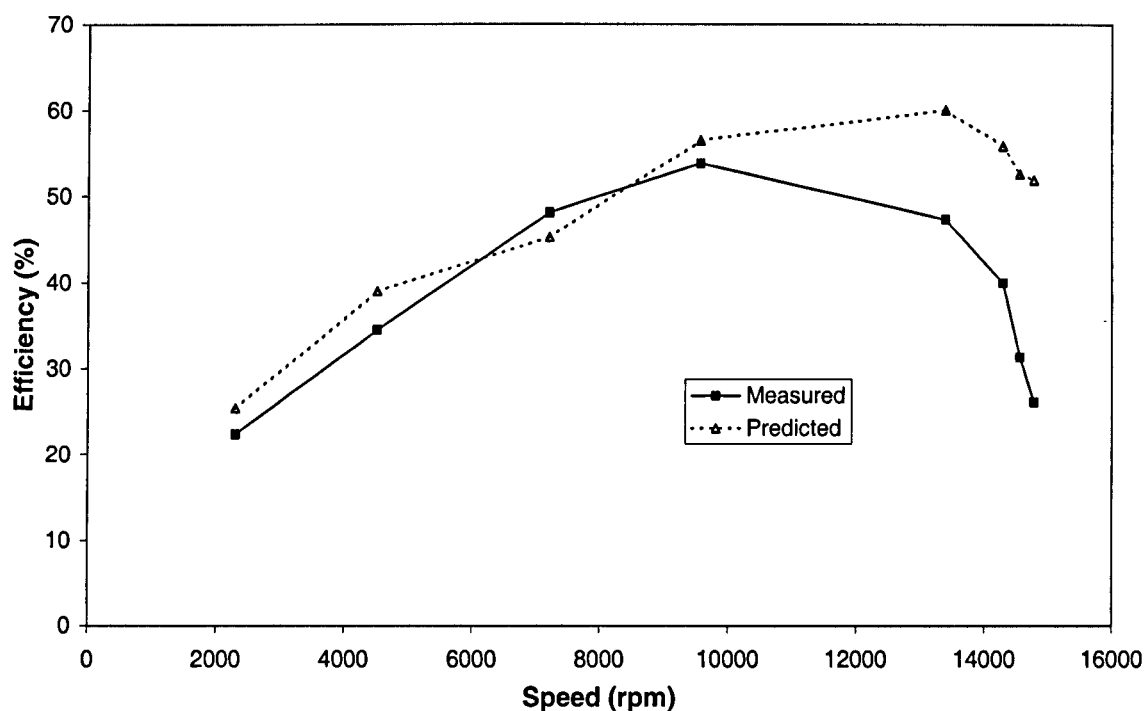


Figure 2.33 – Variation of torque with speed



**Figure 2.34 – Variation of efficiency with speed**

In Figure 2.34, it can be seen that the efficiency falls off dramatically as the motor speed exceeds 10krpm, and a marked increase in the acoustic noise emanating from the spin-pot was noted as the motor approached 14krpm. It was thought that this was due to the bearings being damaged by use above their recommended speed compounded by a possible imbalance in the rotor, which was not balanced for high-speed operation, causing vibration and further damage to the bearings, thereby accounting for the increased acoustic noise. This is also observable as a marked and sudden increase in the motor torque at  $\geq 14$ krpm in Figure 2.33.

### 2.7.5 Motor performance with ceramic (C38HDL C22 OJ-201) bearing

This bearing has a speed capability up to the required rated speed of 120krpm. However, due to a resonance problem, which is briefly considered in section 2.7.7, the maximum speed was intentionally limited to 16krpm, on the recommendation of Urenco personnel who predicted that the first resonant frequency would occur at around 17krpm.

From the test results shown in Figures 2.34 – 2.38, it can be seen that the bearing torque is reduced significantly, and, hence, the efficiency is much higher. The iron loss is negligible and the copper loss dominates. However, on approaching the resonant frequency the torque increases rapidly, and the efficiency drops off accordingly. It should be noted, however, that the input current, the input power and the torque are all relatively low, and susceptible to measurement error. Further, due to the sampling rate, there is a measurement error on the

motor speed of  $\pm 2\%$  @ 16krpm. There are also measurement errors in the DC link voltage and DC link current of  $\pm 0.1V$  &  $\pm 1\%$ , respectively.

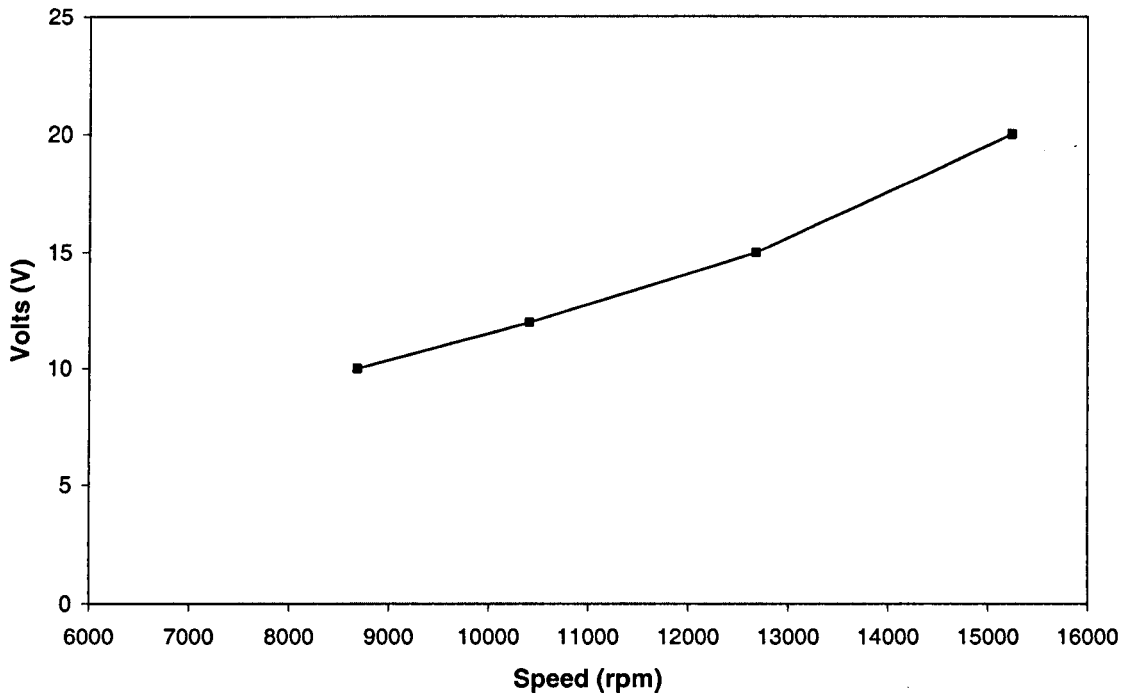


Figure 2.35 – Variation of measured speed with DC link voltage

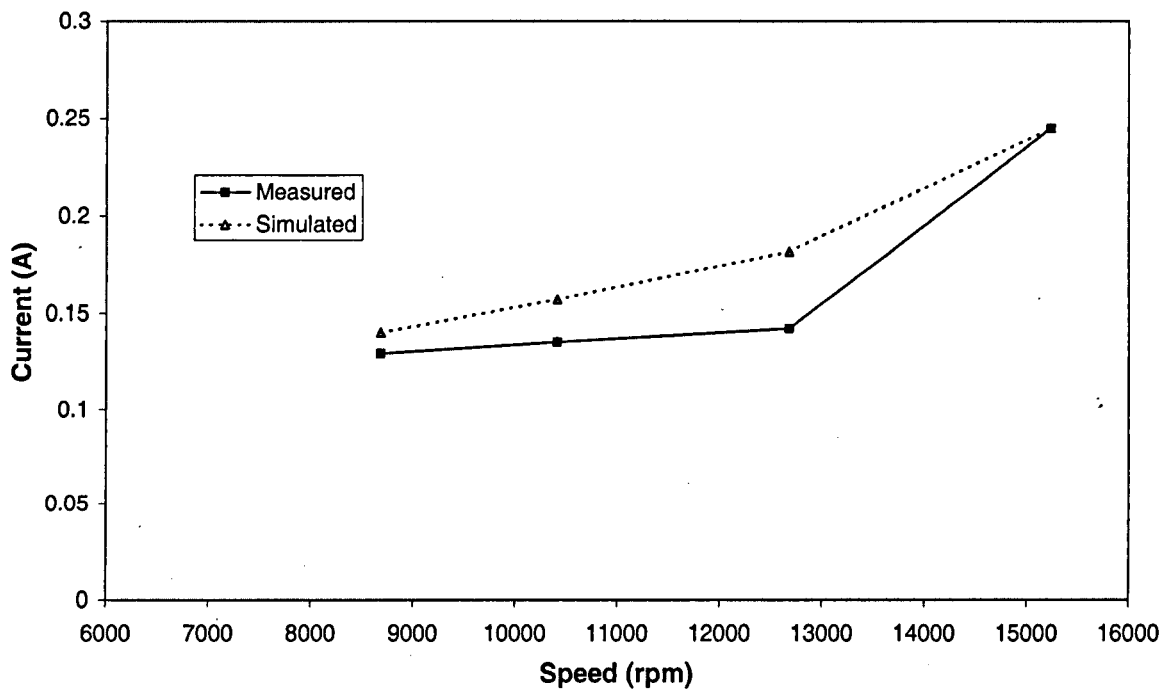


Figure 2.36 – Variation of DC link with current with speed

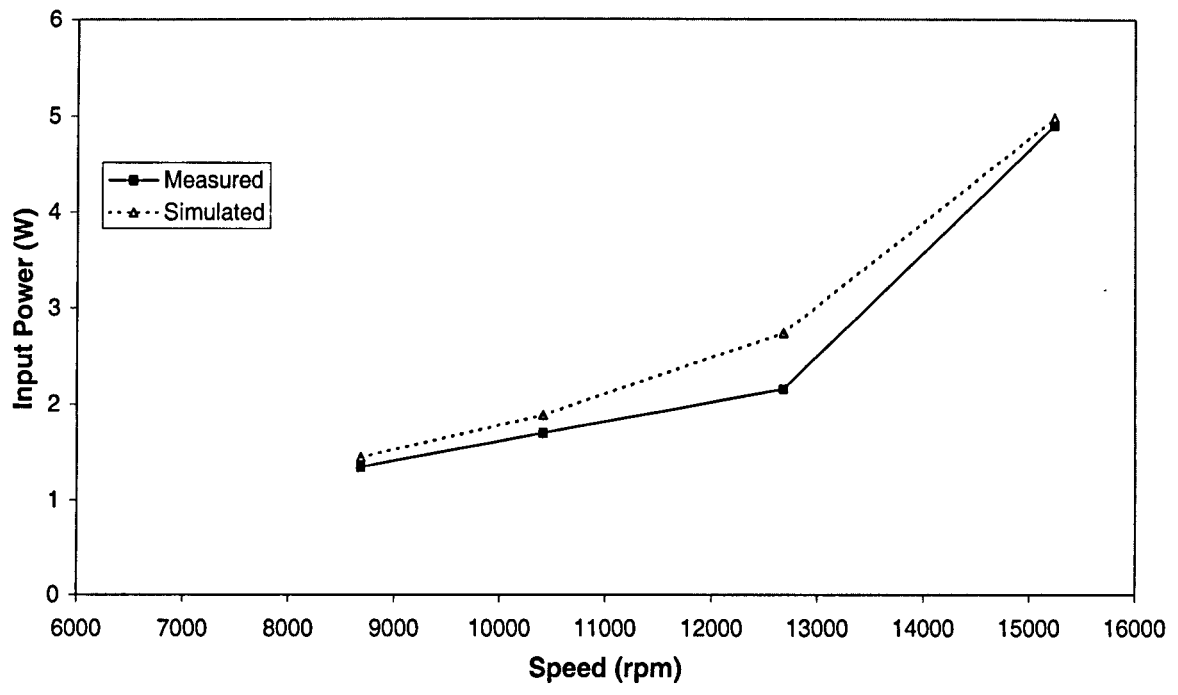


Figure 2.37 - Variation of input power with speed

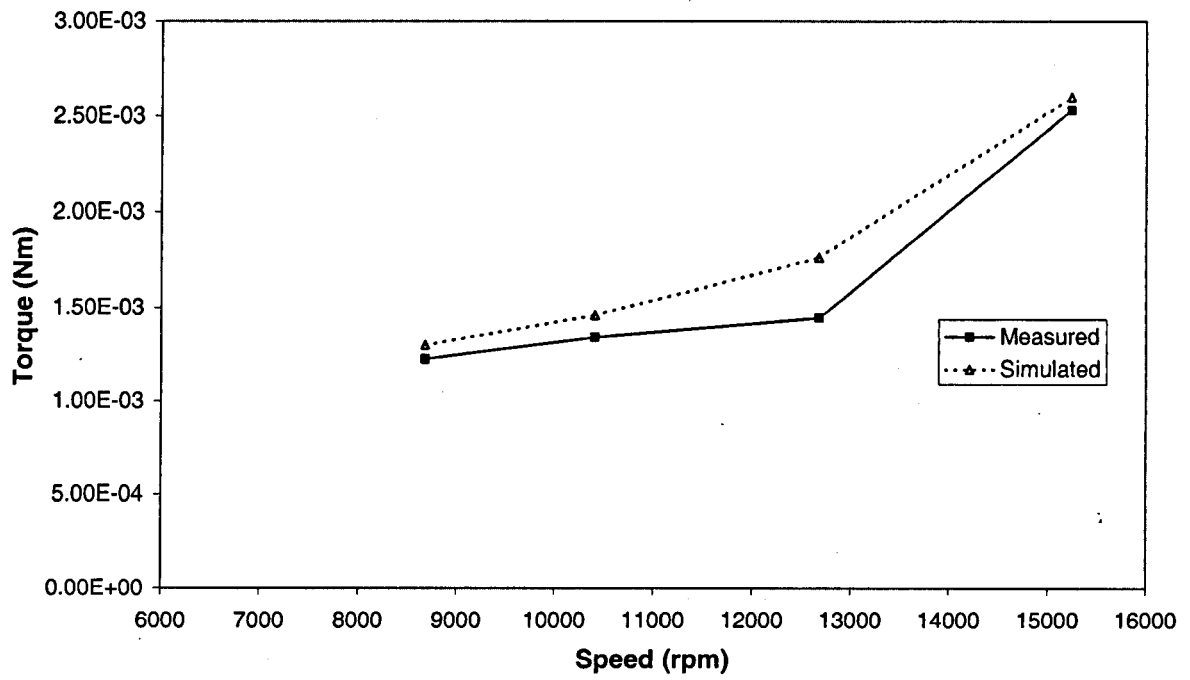
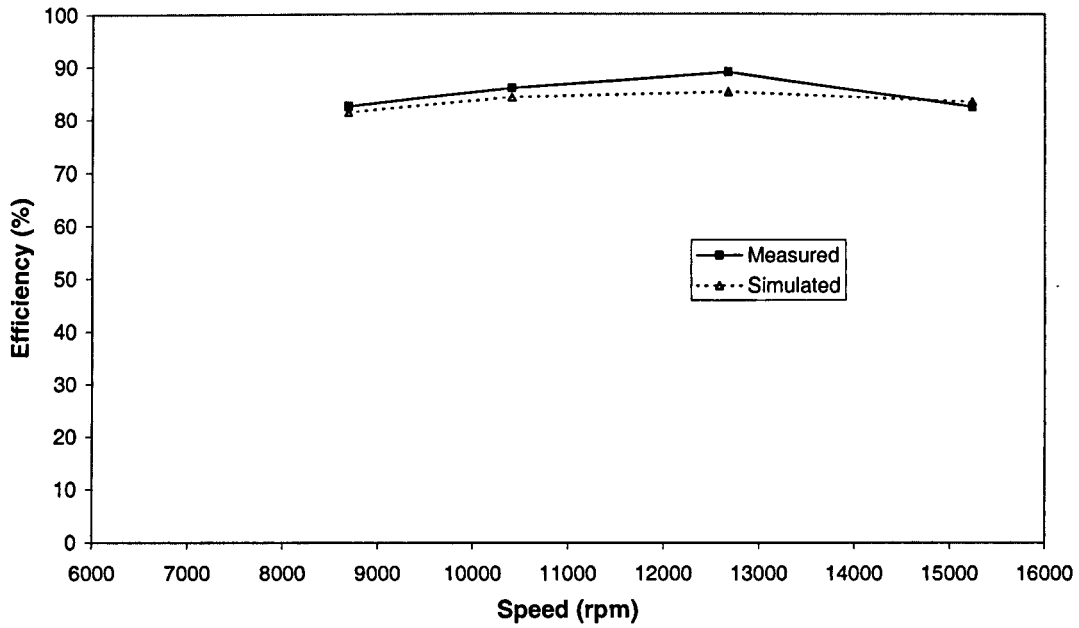


Figure 2.38 - Variation of torque with speed



**Figure 2.39 – Variation of efficiency with speed**

### 2.7.6 Voltage and current waveforms

The voltage and current waveforms were measured for a DC link voltage of 21V and a speed of ~6krpm, when the motor was equipped with the steel (SKF 708CC) bearing, and compared with predicted waveforms, Figures 2.39 & 2.40. It can be seen that good agreement is obtained, and that the phase current waveform are continuous.

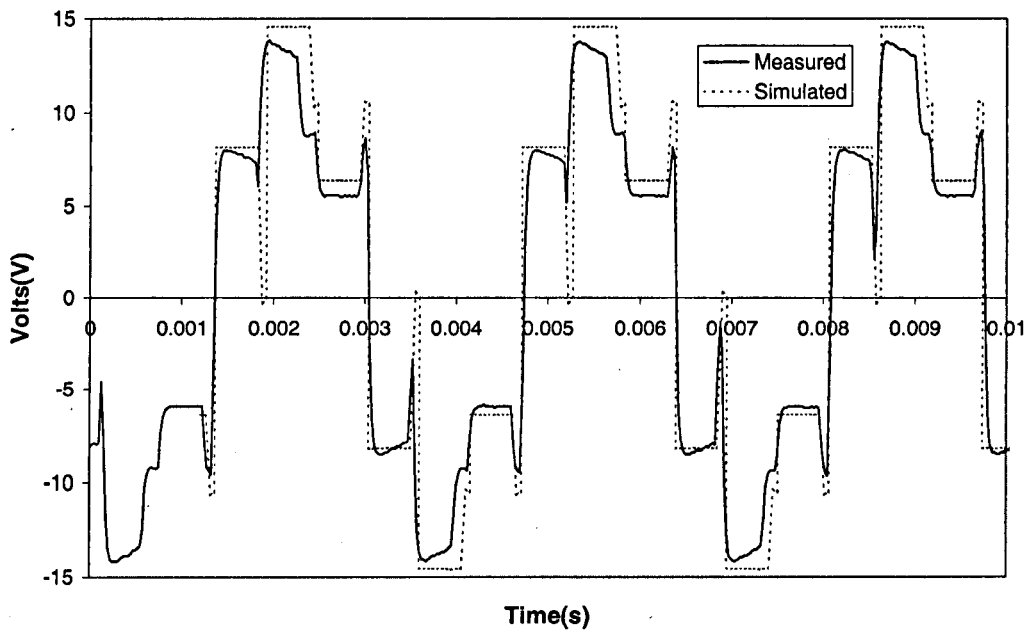


**Figure 2.40 – Predicted (red) and measured (blue) phase-neutral voltage waveforms (~6krpm, 21V DC, 30° electrical commutation advance)**

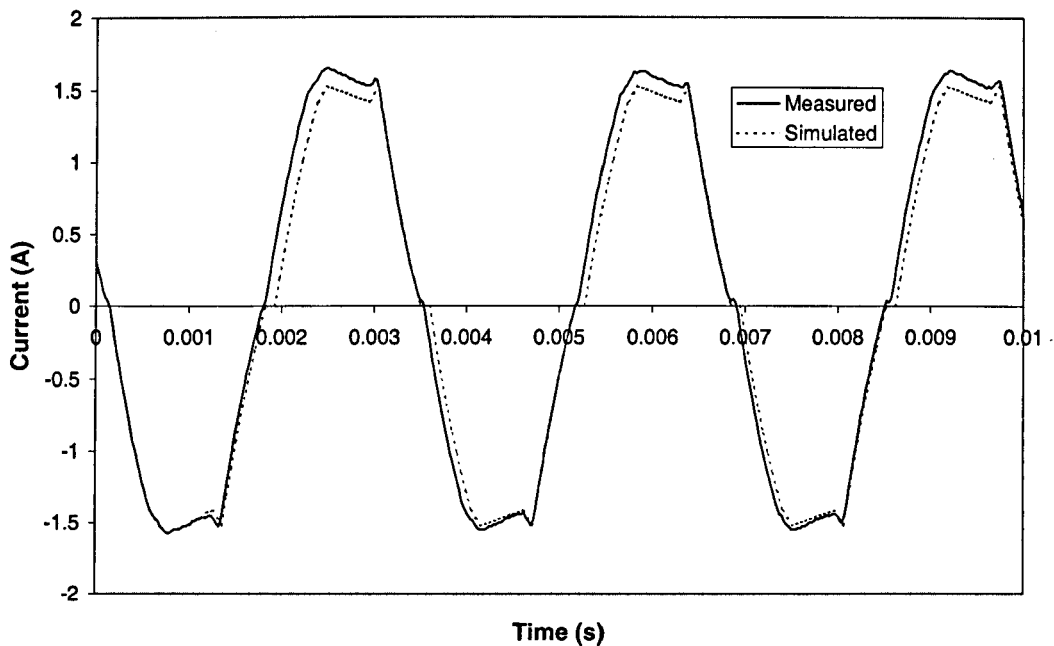


**Figure 2.41 – Predicted (red) and measured (blue) phase current waveforms (~6krpm, 21V DC, 30° electrical commutation advance)**

### 2.7.7 Natural frequency measurements of MLC rotor

The measurements, performed with the rotor mounted on the stator with the ceramic bearings, involved performing an impulse test with a modal hammer, an accelerometer and a dynamic signal analyser, the HP35660A. The accelerometer was attached to the rotor, and the rotor was struck from diametrically opposite with the modal hammer with sensor and impact being measured in 3 locations at the top, middle and bottom of the rotor. The resulting frequency spectrum was saved as a voltage, which was then converted in Excel to the same scale as the HP signal analyser, dBVrms, by multiplying the voltage by  $20\log(V/\sqrt{2})$ , and then plotted as frequency against dBVrms. Typical frequency responses are shown in Figures 2.42 – 2.44. The resonance at 120Hz (7,200rpm) was observed as a slight increase in acoustic noise emanating from the spin pot during the run-down test. The resonance at 280Hz (16,800rpm) is apparent only when the rotor is impacted at the bottom, the dominant resonance when the rotor is impacted at the middle or the top being 384Hz ( $\pm 23,000$ rpm).

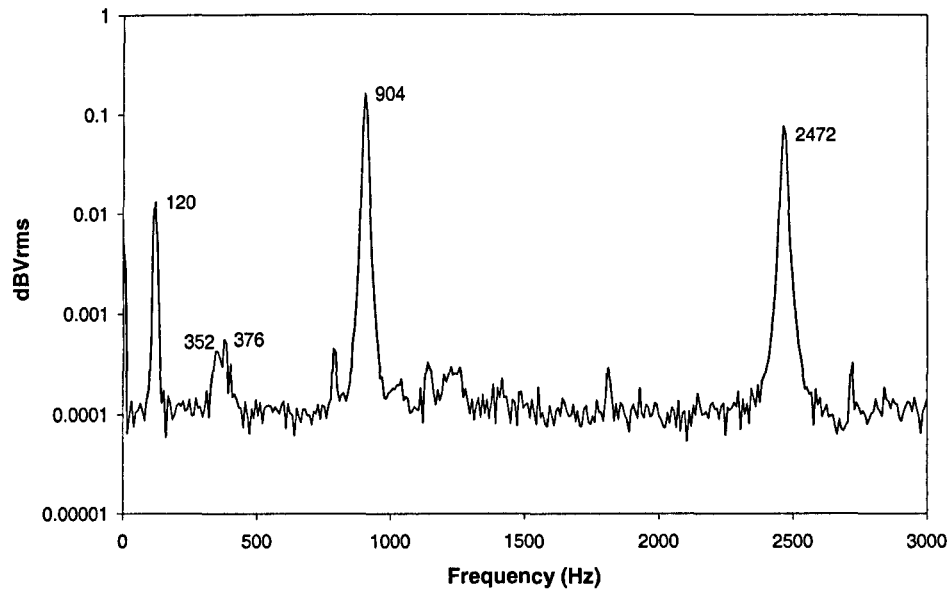


**Figure 2.42 - Frequency response measured at top of rotor**

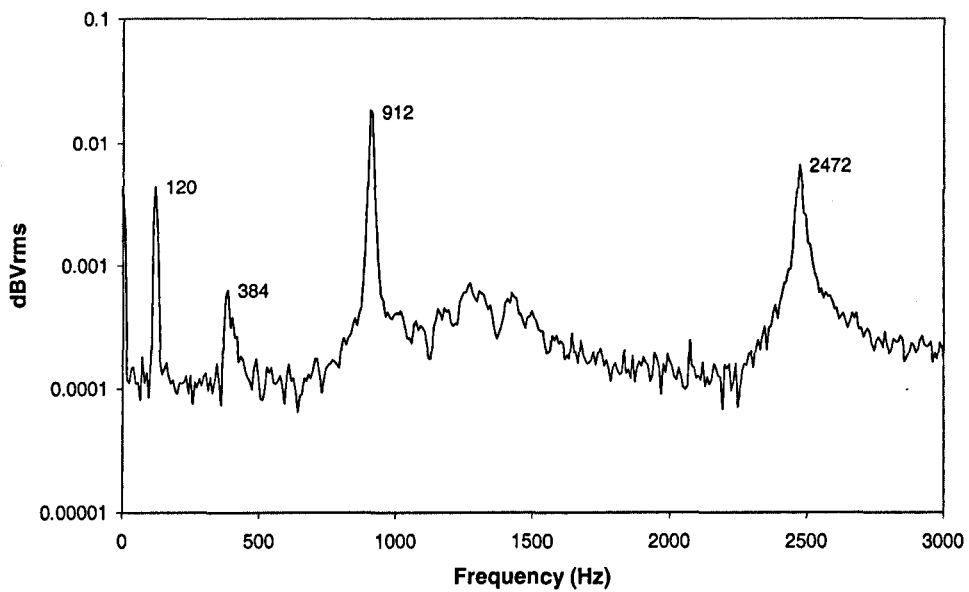


**Figure 2.43 - Frequency response measured at middle of rotor**

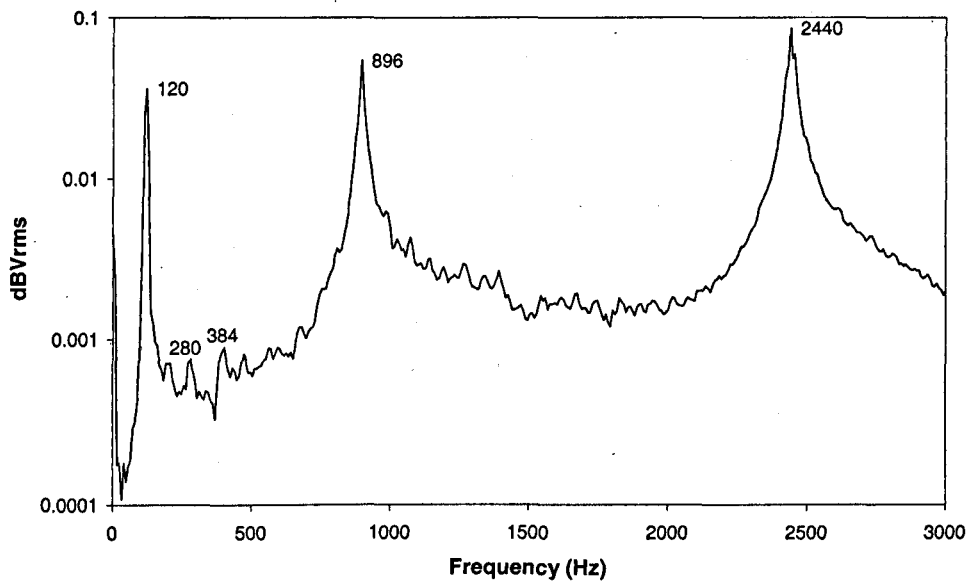


**Figure 2.44 - Frequency response measured at bottom of rotor**

## 2.8 Research issues to be investigated further

Since the research was being undertaken on behalf of a company, viz. Urenco (Capenhurst) Ltd, there were significant constraints on the motor design, in particular the motor topology, the bearing arrangement, the 1mm effective magnet thickness and a subsequent reduction in the motor active length, from 60mm to 40mm, which had a very significant impact on the resultant motor performance. Despite this, the measured motor parameters agreed well with the predicted parameters for the limited speed range over which the motor could be tested, and there was a very high level of agreement between predicted and measured current waveforms. Most importantly, however, this initial work revealed several important research issues which needed to be addressed. e.g.:

- **Optimal design of high-speed, brushless DC motors for sensorless operation.**

As can be seen in the voltage and current waveforms of Figures 2.39 & 2.40, this initial prototype motor could never be operated using commercially available sensorless commutation schemes based on the detection of the zero-crossing of the back-emf waveforms. However, it was deemed desirable to employ a commercially available sensorless commutation IC, since this would result in numerous advantages including:

- A reduction in the component count, thus reducing the cost of the motor/drive system.
- An improvement in reliability, since commutation sensors tend to be a weak link, and in a sealed motor failure of a sensor would involve an expensive motor replacement. A reduction in the number of connecting cables between the motor and drive would also simplify the system.
- Easier manufacture, since as the number of pole-pairs is increased, discrete commutation sensors need to be located with increasing accuracy. Sensorless commutation eliminates this problem.
- Smaller motor size, since position sensors can be relatively bulky. Their elimination reduces the required motor volume.

The issue of high-speed brushless dc motor design for sensorless operation will be addressed in Chapter 3, in which a motor will be designed which is capable of operating from a sensorless IC based on the detection of the zero-crossing of its back-emf waveforms at 120krpm, and a design synthesis strategy will be proposed. However, this motor will employ an internal rotor for ease of fabrication and to improve the mechanical integrity, and to overcome many of the problems, which were encountered during this initial design study.

- **Iron loss and optimal ratio of rotor to stator diameter**

This motor had almost all of its leading dimensions pre-specified in advance by Urenco (Capenhurst) Ltd in order to comply with their particular application. However, it is clearly advantageous to establish an optimal motor design in order to maximise the specific torque capability and to minimise the losses. In the external rotor MLC motor the iron loss has been minimal due to the slotless nature of the machine. However, in practice most machines have stator teeth to help focus the flux and improve the specific torque capability. Whilst this gives significant advantages in terms of electromagnetic performance, however it may also create a significant iron loss. The iron loss and the optimal rotor to stator diameter ratio (or split ratio) are investigated in Chapter 4.

- **Rotor resonances**

The initial prototype motor was prevented from running at high-speed by a rotor resonance, which was investigated briefly in Section 2.7.7. Further it was appreciated that the external rotor motor topology with a bearing support at one end only is unusual, and that research into the natural frequencies of this type of rotor would be of limited value. However, little published work could be found covering the design of rotors to minimise the resonant modes that occur within the operating speed range of the motor. Chapter 5, therefore, investigates the influence of key design choices on the resonant modes of the rotor in an internal rotor permanent magnet brushless dc machine. The construction of the rotor is studied in detail, and a finite element model is used to predict the observed resonant modes, and then to investigate the influence of rotor design parameters.

# Chapter 3 Electromagnetic design of high-speed, permanent magnet, brushless DC motor for sensorless operation

## 3.1 Introduction

In chapter 2, a 120krpm external rotor, slotless, brushless DC motor with a Halbach magnetised magnetically loaded composite rotor was designed and built. However, as discussed in chapter 2, it was not possible to attain rated speed due to potential mechanical resonances of the rotor at relatively low speeds, viz. 120Hz (7.2krpm) and 896Hz (53.8krpm), as shown Figure 3.1. This was essentially due to the rotor being supported only at one end, as specified by the Urenco (Capenhurst) Ltd. After many discussions with the company, it was deemed necessary to make some major design changes, including employing an internal rotor, which would be supported by bearings at both ends. With an internal rotor motor, the shaft is supported by bearings at both ends and the rotors have a much smaller diameter than for an external rotor topology. This leads to a rotor that is mechanically more robust and likely to have significantly higher natural frequencies, as will be shown in Chapter 5. By way of example, Figure 3.2 shows the measured natural frequencies of the 100mNm rated motor which will be discussed in this chapter. As can be seen, its natural frequencies are considerably higher than those for the MLC motor, the lowest natural frequency being 1234Hz (74krpm) due to the frame and 2002Hz (120krpm) due to the rotor, as will be identified in Chapter 5.

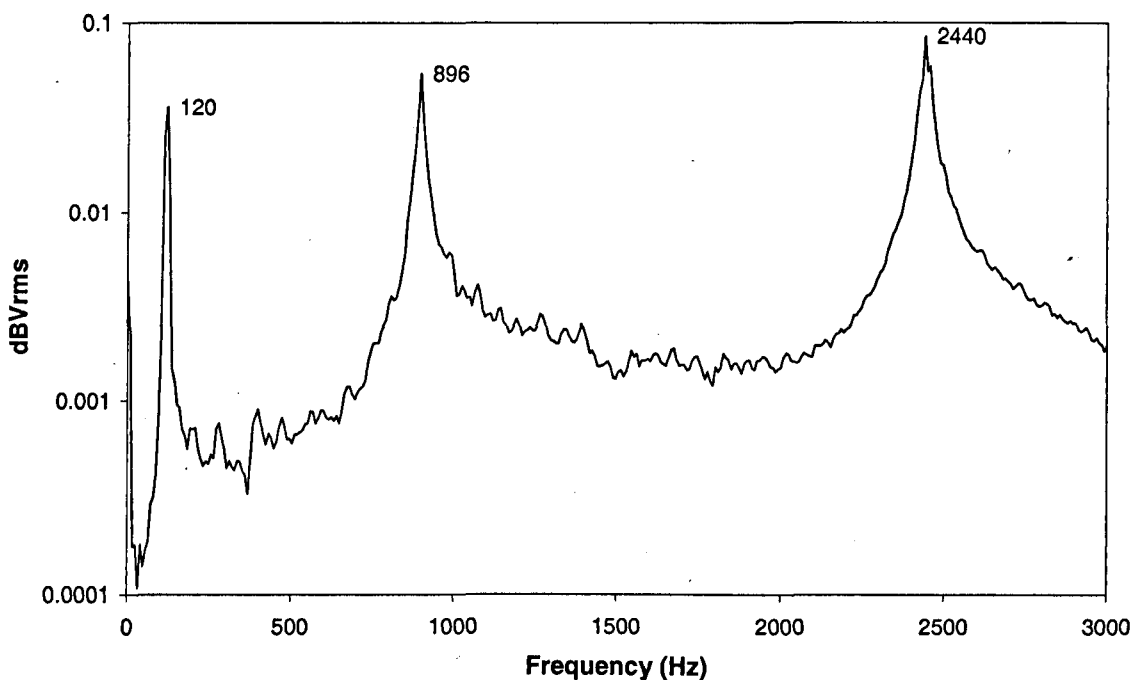
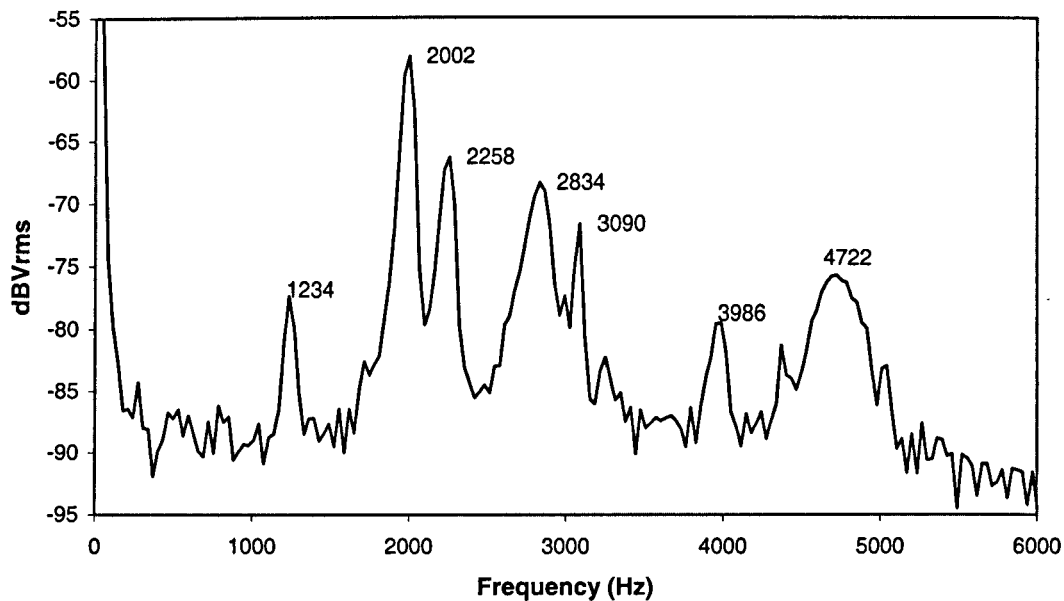


Figure 3.1 - Natural frequencies of MLC motor rotor.



**Figure 3.2 - Natural frequencies of internal rotor motor, which results in a low diode conduction angle, designated  $A_1$ .**

In addition, the MLC motor, which was described in Chapter 2, had a very low magnet remanence, and consequently a low magnetic loading and a high electrical loading. This resulted in an almost continuous current waveform and a low back-emf, both of which make the motor unsuitable for sensorless operation using a simple scheme based on the detection of the zero crossing of the back-emf waveforms.

The design considerations for a 2-pole diametrically magnetised interior rotor permanent magnet brushless dc motor to be operated from a sensorless drive at 120krpm are discussed in this chapter. A design methodology is presented that considers not only the primary consideration of a low diode conduction angle, but also a high efficiency. Two motors, which were designed to develop a torque of 100mNm at 120krpm are then described, one which results in a low diode conduction angle and being capable of being operated from a sensorless drive based on detection of the back-emf waveform and one with a high diode conduction angle which, in theory, should not be capable of being operated from a sensorless drive. The relative merits of each motor design are discussed, prototypes are built and tested, and their performance is compared with predictions from dynamic simulations. A commercially available IC, the ML4425, is selected for use in the drive for the prototype motors.

However, due to less torque being required to overcome the bearing friction than was previously anticipated, both the foregoing motors were capable of being operated by the sensorless drive at 120krpm. Thus, two smaller motors each capable of developing a torque of 15mNm at 120krpm, which was the revised value of bearing torque for the previous motors,

were prototyped. Then only the motor with the low diode conduction angle could be operated at 120krpm using the sensorless drive, the other motor requiring discrete commutation sensors, which led to a less than ideal performance, as will be shown.

At high rotational speeds, direct measurement of the torque is difficult due partly to coupling the motor shaft safely to the load. To date the only coupling found is the Rexnord Thomas Metal Disc Coupling model 965 size 25 obtainable from Lenze and is only suitable at speeds <80krpm with light loads and not for sustained use. Consequently, when torque data was required, the 'run-down' method, which has been used to measure the torque of magnetic bearings [Tak91][Bor94][Kas94], was employed. Although the method had been validated previously on the slotless motor with negligible iron loss in chapter 2, it was adapted to account for the presence of iron loss in the slotted motors which are under consideration.

In total, 4 motors were built, and these were designated A<sub>1</sub> & B<sub>1</sub> and A<sub>2</sub> & B<sub>2</sub>, their performance being summarised in Table 3.1.

**Table 3.1 - Summary of motor designs**

Designation	A <sub>1</sub>	B <sub>1</sub>	A <sub>2</sub>	B <sub>2</sub>
Torque (mNm)	100	100	15	15
Diode conduction angle	Low	High	Low	High
Sensorless operation	Yes	Yes*	Yes	No

\*Operated at reduced torque (15mNm), sensorless operation not possible at rated torque.

## 3.2 Analysis of current waveform

The sensorless commutation scheme, which will be considered in this chapter, is based on the detection of the zero-crossing of the back-emf waveforms. As will be shown later, the success of the technique depends highly on the nature of the phase current waveforms, which will be briefly discussed here.

Figure 3.3 shows the 2-pole machine topology under consideration, whilst Figure 3.4 shows typical phase winding current, voltage and back-emf waveforms [Zhu92].

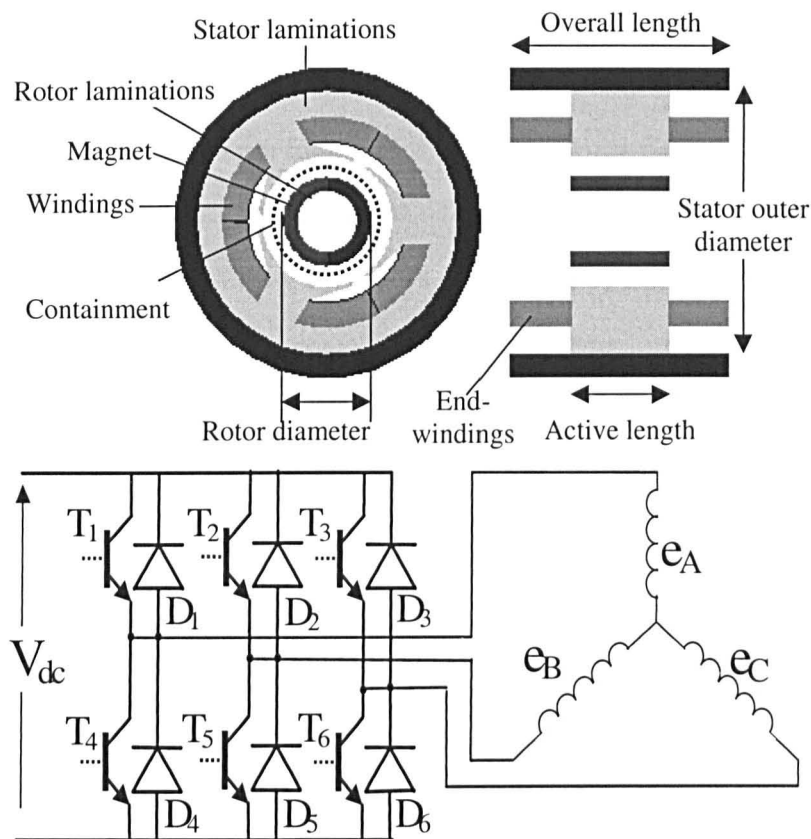


**Figure 3.3 - Typical internal rotor brushless DC motor and drive**

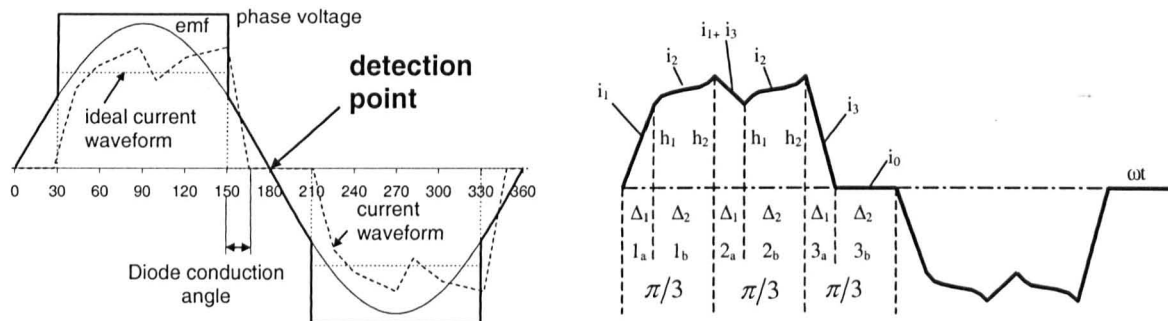


**Figure 3.4 - Basis of back-emf sensorless commutation, and typical phase current waveforms**

If the commutation timing on all three phases is correctly phased by  $60^\circ$  electrical, the phase current waveform is symmetrical and consists of three  $60^\circ$  electrical intervals per half-cycle, each interval being sub-divided into two periods whose relative length is determined by the conduction time of the associated free-wheeling diodes. For example, during Period 1 when  $T_1$  and  $T_5$  are on, free-wheeling diode  $D_6$  conducts in Period 1a (i.e. time interval  $\Delta_1$ ). All three phases then carry current, since there are two distinct current paths, the main one being from the supply through phase windings, A and B, via  $T_1$  and  $T_5$ , and the other being through one of these windings and phase winding C, via  $T_5$  and  $D_6$ . At the end of Period 1a the current through  $D_6$  has reduced to zero, and diode  $D_6$  does not conduct during Period 1b.

Because of the periodicity of the current waveforms and the symmetry of the switching events,

- (a) The Periods 1a, 2a, and 3a are identical, and similarly for Periods 1b, 2b, and 3b;
- (b) The current waveform during Period 1b is the same as that during Period 2b;
- (c) The value of the current during Period 2a is the sum of the currents which flow during Periods 1a and 3a.

The diode conduction time,  $\Delta_1$ , is influenced by the winding resistance, the back-emf, the winding inductance, the load, and, in particular, by the ratio  $\omega(L-M)/R$ , where  $\omega$  is the angular speed of rotation, and  $R$ ,  $L$  and  $M$  are the winding resistance and self- and mutual-inductances per phase, respectively.

### 3.3 Basic principles of back-emf sensorless operation

As mentioned in Chapter 1, the most common technique for the sensorless operation of brushless DC motors is based on the detection of the zero-crossing of the back-emf waveforms, in which a three-stage starting technique is generally employed, viz.

- (1) Initial rotor alignment - by exciting one or two phase windings so that the initial rotor position is known
- (2) Synchronous open-loop run-up – during which the phase windings are excited using the appropriate switching logic, until the back-emf is sufficiently high to enable the motor to be operated in step 3.
- (3) Sensorless closed-loop mode - when the zero-crossing of the back-emf waveforms of the three phases is detected during periods when they do not carry current.

The principle of back-emf sensorless operation was illustrated in Figure 3.4, assuming ideal current and voltage waveforms. As can be seen, the appropriate switching devices are commutated  $30^\circ$  electrical after detection of the zero-crossing of the associated back-emf. In high-speed machines, however, the phase currents can flow more or less continuously due to the effect of the winding inductances and the finite conduction time of the free-wheeling diodes, thereby preventing the detection of the zero-crossing of the back-emf.

### 3.4 Proposed design criteria

From the above, sensorless commutation based on detection of the zero-crossing of the back-emf waveforms is only possible if the phase current waveforms are discontinuous, with no current flowing for a sufficiently long interval near the zero-crossing of the back-emf. This

demands an appropriately designed motor. Thus, a design methodology has been followed in which the efficiency and the conduction angle of the free-wheeling diodes are key operational considerations, and the flux density in the laminated stator core is an important design parameter.

The design optimisation was undertaken using proprietary CAD software [How94], developed in the Electrical Machines and Drives Group at the University of Sheffield, which has been described briefly in chapter 2, with a more detailed description of the design software, including some of the design equations, being contained in Appendix C.

### 3.5 Design for sensorless commutation

As mentioned in the introductory chapter, in order to employ a simple sensorless commutation scheme based on the detection of the zero-crossing of the back-emf waveforms, the diode conduction angle needs to be  $<30^\circ$  electrical. By way of example, Figure 3.5 shows the phase current and voltage waveforms from the two prototype motors  $A_1$  &  $B_1$  whose design is described later in section 3.5.2. Figure 3.5(a) shows waveforms for motor  $A_1$  which results in a small diode conduction angle, and whose zero-crossing of its back-emfs can clearly be seen, whereas Figure 3.5(b) shows the waveforms for motor  $B_1$  in which the diode conduction angle is significantly larger than  $30^\circ$  electrical and whose zero-crossing of the back-emfs is not discernable. It will also be noted that as the diode conduction angle increases the current waveforms tends towards a continuously on state, which results when the diode conduction angle reaches  $60^\circ$  electrical.

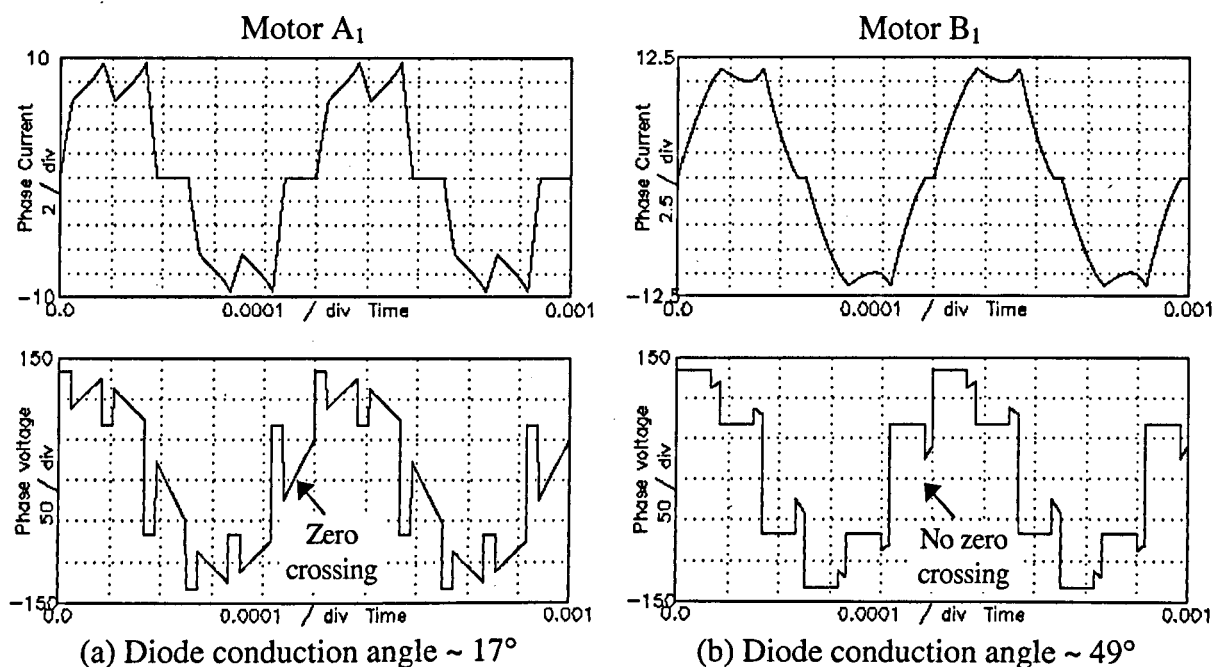


Figure 3.5 - Phase current and voltage waveforms

Once the diode conduction angle exceeds  $30^\circ$  electrical then none of the sensorless commutation methods described in chapter 1 can be used. However, all the back-emf based rotor position sensing schemes mentioned previously are relatively cheap to implement, and the ML4425 sensorless IC was employed for the prototype motors. Whilst some of the back-emf based detection schemes are unsuitable for operation over a wide speed range and for high-speed operation, there are some, namely integrated back-emf detection, which will function over a large speed range and at high-speed.

### 3.5.1 Design considerations and constraints

As mentioned earlier, when designing a high-speed permanent magnet brushless dc motor, there are a number of considerations that have to be taken into account, in terms of its electrical, magnetic and mechanical design. Further, the testing of prototype motors poses significant problems at high speeds. Consequently, the motors that were prototyped were tested using the 'run-down' method described previously in Chapter 2 and further in Appendix F.

The motors were designed to operate at a fundamental mechanical frequency of 2kHz or 120krpm. Two motors were originally prototyped to validate the design methodology, one which resulted in a low diode conduction angle that could be operated from a sensorless drive up to its rated speed, and one which resulted in a high diode conduction angle that, in theory, should not have been able to be operated from the sensorless drive. Both motors were designed to have the same space envelope and the same performance. The prototype motors were designed to have a rated torque of 0.1Nm, giving a rated power of 1.25kW at 120krpm. The motor design was also subject to the following constraints:

- DC link voltage of 200V
- Thermal dissipation factor of  $20\text{W}/\text{m}^2$
- Lamination material 0.35mm silicon steel, Transil335, (Loss constants  $k_e=1\times 10^4$ ,  $k_h=1.55\times 10^{-2}$ ,  $\alpha=2.45$ )
- Rotor shaft to accommodate bearing inner diameter of 8mm
- Packing factor 0.3
- 2-pole parallel magnetisation
- Magnet remanence 1.2 T (Sintered NdFeB magnets)

From these constraints, it will be obvious that there are some distinct differences from the motor that was designed in chapter 2. The DC link voltage was reduced from 570V to 200V to allow operation using a readily available power supply. Sintered NdFeB magnets were used as these had a high remanence, were relatively easy to cut to shape at the University of Sheffield using a wire eroding machine and were simple to magnetise using a solenoid impulse magnetising fixture. However, the magnet material is quite brittle. Consequently, for mechanical reasons, the minimum magnet thickness was set at 3mm. A minimum airgap length of 3mm was assumed to allow for containment of the rotor magnets. This allowed for 2mm of carbon fibre containment, which as shown later in section 3.7, is more than sufficient to retain the rotor magnets.

### 3.5.2 100mNm motors

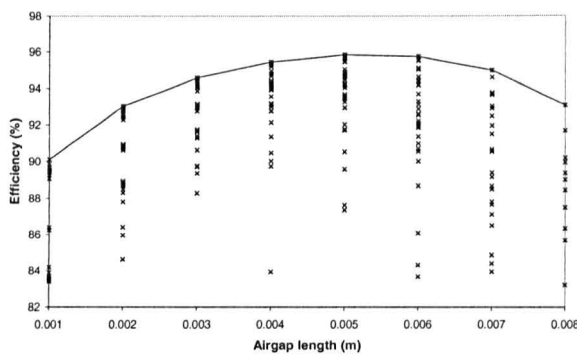
The CAD software was again employed to design 120,000rpm motors equipped with 2-pole parallel magnetised sintered NdFeB magnets on the rotor, and a 3-slot stator with non-overlapping coils. The motors were constrained to the same overall space envelope, viz. 70mm diameter  $\times$  50mm axial length. Within this space envelope the motors were designed to meet the optimum efficiency requirements as well as to have a low diode conduction angle. The minimum rotor diameter for these motors was 20mm, due to the bearing shaft bore diameter and the requirements of the rotor laminations to carry the magnet flux.

#### (a) Efficiency

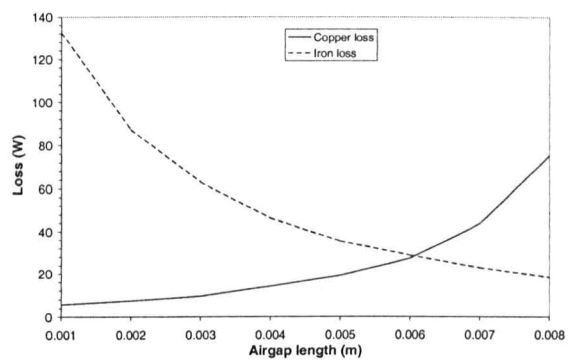
For a fixed motor volume, as mentioned previously, the airgap length, the rotor diameter and the stator flux density were all varied over prescribed ranges, and the result of this study is shown in Figure 3.6(a). The maximum efficiency locus is indicated on the graph by a solid line, and as can be seen this occurs at an airgap length of 5mm. At this point it was noted that all the designs on the maximum efficiency locus had a rotor diameter of 20mm, the variation of the iron and copper loss along this contour also being shown in Figure 3.6(b).

With the airgap length fixed at 5mm, the outer rotor diameter and the stator flux density were varied. As can be seen in Figure 3.7(a), the rotor diameter has a significant effect on the motor efficiency. Whilst it can be seen that a reduction of the rotor diameter below 20mm would improve the motor efficiency this is limited by mechanical constraints, as stated previously. Consequently, the rotor outer diameter was fixed at 20mm. Again, the solid line indicates the maximum efficiency locus and the copper and iron loss along this contour being shown in Figure 3.7(b).

Once both the optimal airgap length and the optimal rotor diameter were selected, the influence of the stator flux density on the efficiency was investigated. As seen in Figure 3.8(a), the efficiency is relatively insensitive to changes in the stator flux density. However, as shown later, the stator flux density has a large effect on the diode conduction angle. The ‘jagged’ nature of the copper loss in Figure 3.8(b) and the efficiency (dashed line) in Figure 3.8(a) is again due to the winding being designed to have an integer number of turns, as discussed in Appendix G. If the number of turns is not constrained to be an integer value the efficiency locus has the shape indicated in Figure 3.8(a) by the solid line. It can also be seen, in Figure 3.8(b), that the iron loss remains relatively constant.

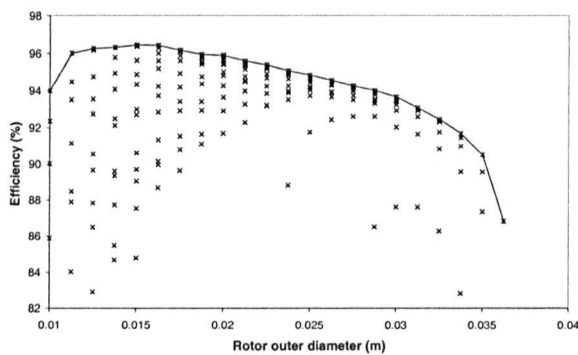


(a) Efficiency against airgap length

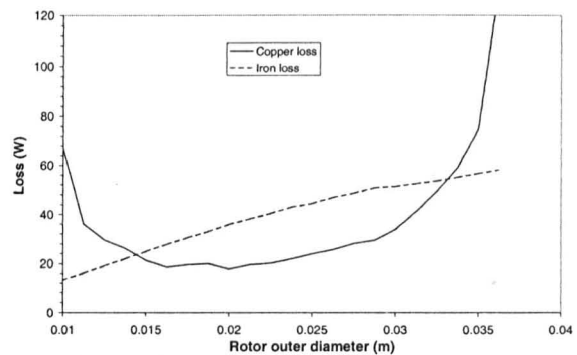


(b) Variation of iron and copper loss along maximum efficiency locus

**Figure 3.6 - Influence of airgap length on optimal efficiency and loss**

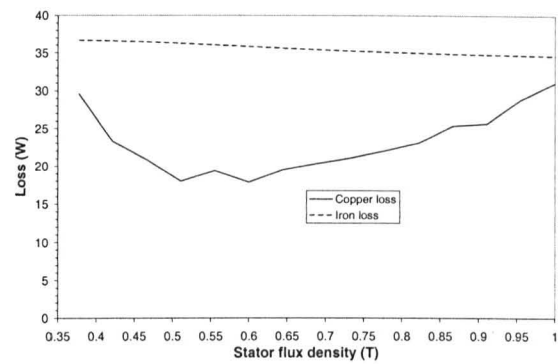
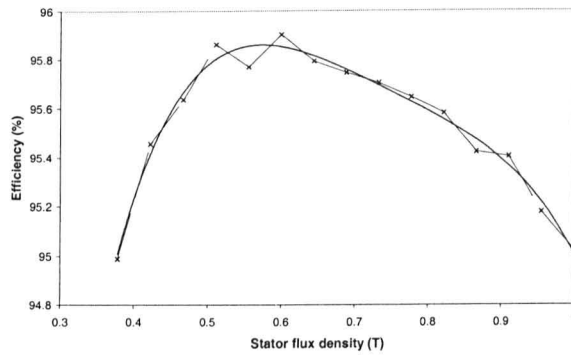


(a) Efficiency against rotor outer diameter



(b) Variation of iron and copper loss along maximum efficiency locus

**Figure 3.7 - Influence of rotor diameter on efficiency and loss**



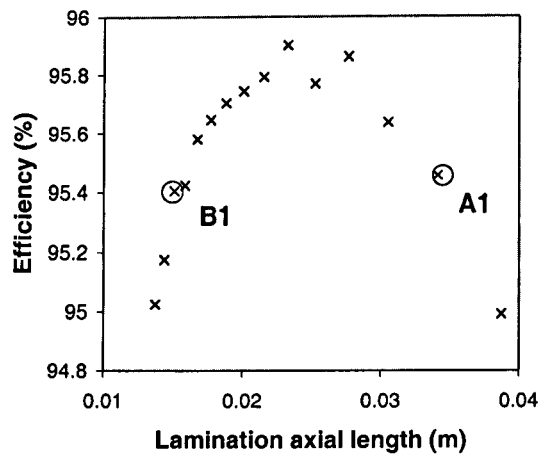
(a) Efficiency against stator flux density

(b) Variation of iron and copper loss

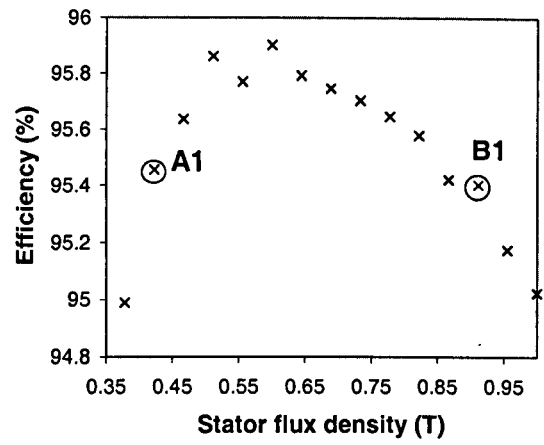
**Figure 3.8 - Influence of stator flux density on efficiency**

### (b) Diode conduction angle

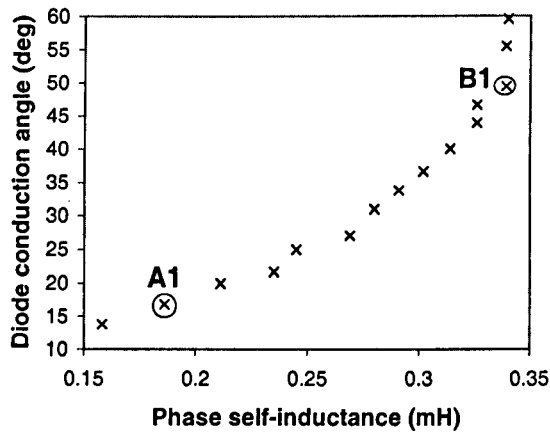
Whilst the efficiency of the motor has been optimised, as shown previously, one of the motors was also designed to have a low diode conduction angle. Two motors, one with a low diode conduction angle, designated  $A_1$ , and one with a high diode conduction angle, designated  $B_1$ , were selected for prototyping. Motor  $A_1$  has an active length of 34mm and a stator flux density of 0.42 T – which results in a diode conduction angle of  $\sim 17^\circ$ , whilst Motor  $B_1$  has an active length of 15mm and a stator flux density of 0.91T – which results in a diode conduction angle of  $\sim 50^\circ$ elec. Figures 3.9(a) & (b) show the variation of the motor efficiency when the stator core flux density, and therefore the required active length, is varied, with the overall space envelope maintained constant, as specified earlier. As was seen previously in Figure 3.8, the efficiency is relatively insensitive to quite a wide variation of these parameters mentioned previously in this section. However, the associated self- and mutual-inductances of the motor windings vary significantly, Figure 3.9(c), and this has a profound influence on the diode conduction angle. In other words, whilst the motors have widely varying design parameters and exhibit more or less the same performance, the diode conduction angle can vary by a factor of 2 or more, Figure 3.9(d).



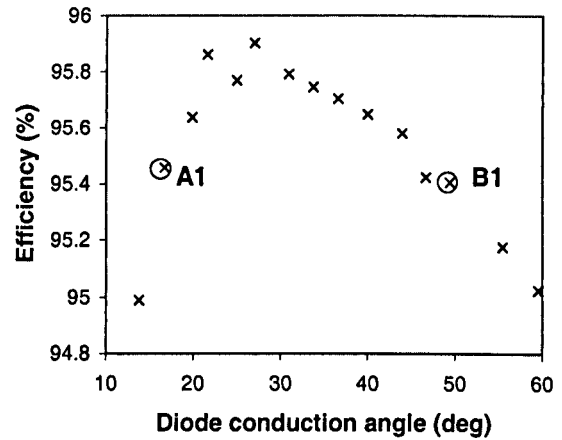
(a)



(b)



(c)



(d)

**Figure 3.9 - Influence of design parameters on motor efficiency, self-inductance and diode conduction angle**

Figures 3.10 & 3.11 show the influence of the stator flux density, the rotor magnet diameter, and the motor aspect ratio on the diode conduction angle. It can be seen that the stator flux density and the motor aspect ratio both have a very significant effect on the diode conduction angle. Figure 3.12 shows the relationship between the stator flux density and the weight of the lamination and the copper winding. It can be seen that the level of the stator flux density can significantly change the ratio of these materials.

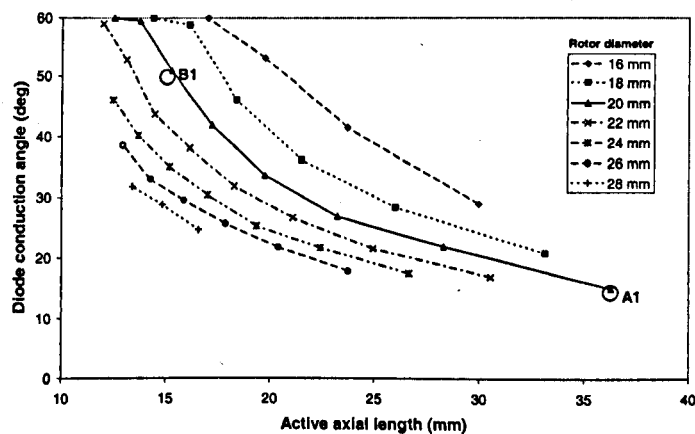


**Figure 3.10 – Influence of active length and motor diameter on diode conduction angle**

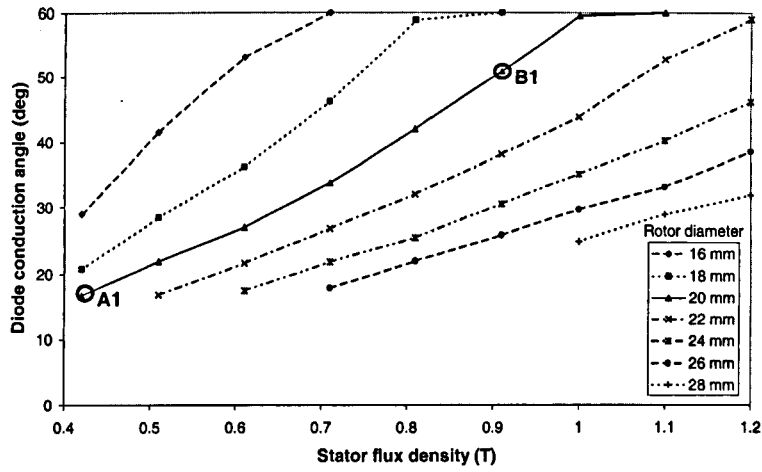


**Figure 3.11 - Influence of stator flux density and rotor diameter on diode conduction angle**

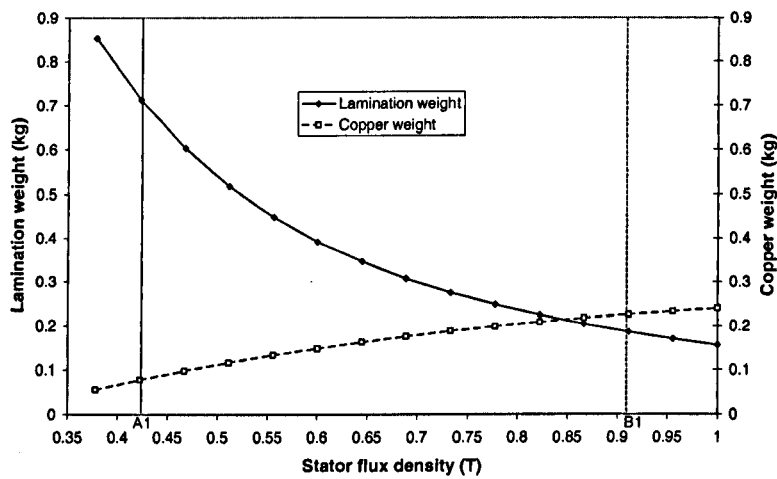


**Figure 3.12 - Influence of stator flux density on component weights**

Cross-sections of both prototype motors, together with their phase back-emf, current, terminal phase and line voltage waveforms at the rated speed of 120krpm and the rated torque of 100mNm, are shown in Figure 3.13, the main features being summarised in Table 3.2. The back-emf waveforms of both motors are essentially sinusoidal. Motor designs with a relatively low stator flux density and a high stator core length to diameter ratio generally use more iron and less copper, which results in fewer turns per phase, and consequently low winding inductances and a low diode conduction angle. The motor with the lower stator iron flux density has a longer axial length and a lower number of turns. Inductance is proportional to the square of the number of turns per phase and the emf is proportional to the number of turns per phase, whilst both are proportional to the axial length. Therefore, the motor with the longer active length has a lower inductance. Therefore, although both motors exhibit a similar efficiency, only Motor A<sub>1</sub> appears to be suitable for sensorless operation based on the detection of the zero-crossing of the back-emf waveforms and this can be seen in Figure 3.13 where for motor A<sub>1</sub> the zero-crossing point is clearly visible. In contrast, for motor B<sub>1</sub> the

zero-crossing of the back-emf is not discernable due to current flowing in the free-wheeling diodes.

**Table 3.2 - Summary of differences between motors A<sub>1</sub> & B<sub>1</sub>**

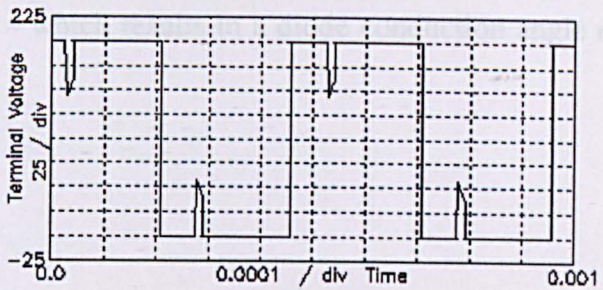
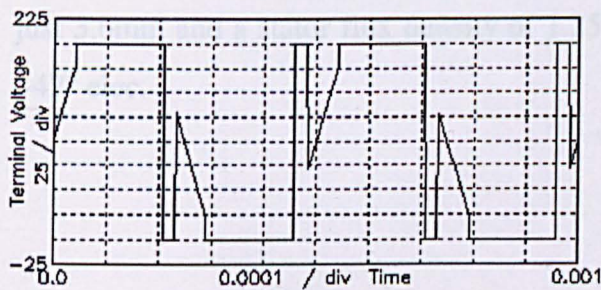
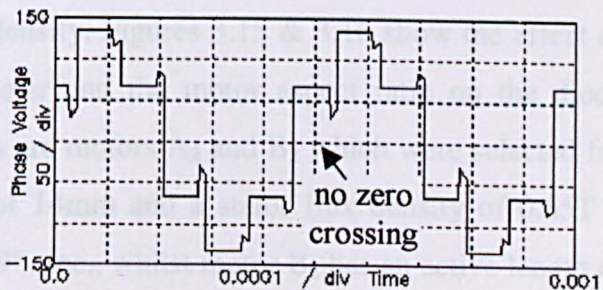
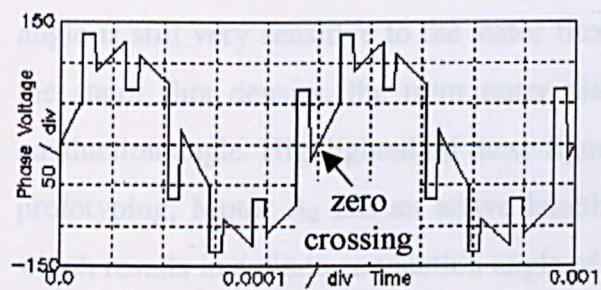
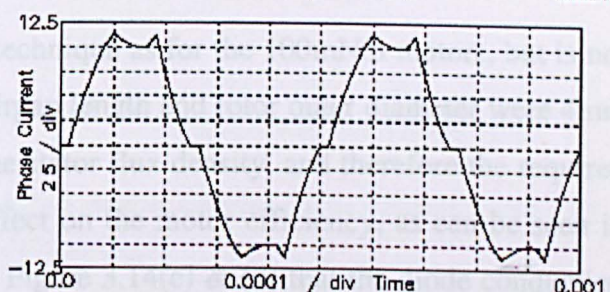
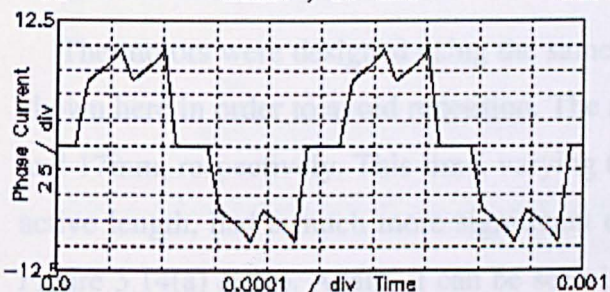
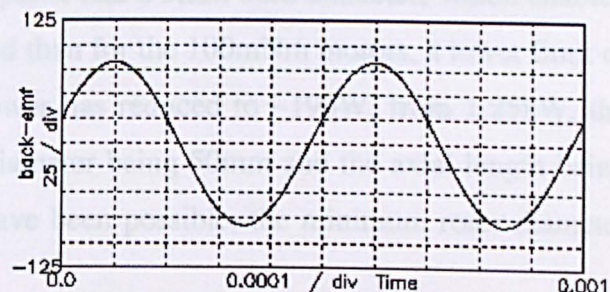
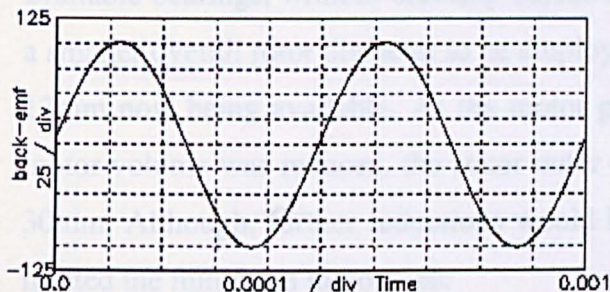
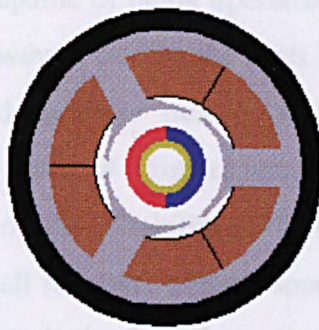
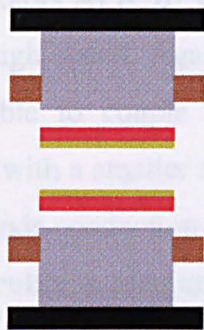
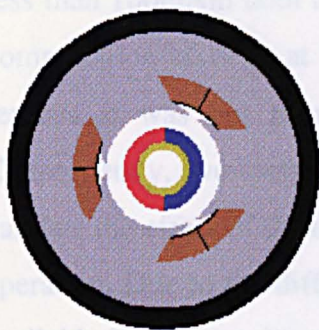
	Motor A <sub>1</sub>	Motor B <sub>1</sub>
DC link voltage, V	200	200
DC link current, A	6.5	6.5
Outer diameter, mm	70	70
Axial length, mm	50	50
Airgap length, mm	5	5
Rotor magnet outer diameter, mm	20	20
NdFeB magnet thickness, mm	3	3
Flux density in stator iron, T	0.42	0.91
Active axial length, mm	34	15
Diode conduction angle, °elec.	16.8	49.6
No of turns per phase	29	54
Winding self-inductance, mH	0.254	0.467
Copper weight, g	77.7	225
Stator iron weight, g	713	186
Overall weight, g	791	411
Phase resistance, mΩ	195	133
Peak phase emf, V	101.5	82.4
Magnet weight, g	40.5	17.9
Copper loss, W	23	24
Iron loss, W	36	35
Efficiency, %	95.5	95.5

■ Lamination  
■ Magnet

■ Rotor Iron  
■ Winding

■ Lamination  
■ Magnet

■ Rotor Iron  
■ Winding



(a) Motor A<sub>1</sub>

(b) Motor B<sub>1</sub>

**Figure 3.13 – Schematic of motors A<sub>1</sub> & B<sub>1</sub> and associated voltage and current waveforms**

### 3.5.3 15mNm motors

As will be shown, in section 3.8, due to the bearing torque at 120krpm being significantly less than 100mNm both motors  $A_1$  &  $B_1$  were capable of being operated using the sensorless commutation strategy at high speed. Again, however, due to the high speed and for safety reasons it was not possible to couple a load to these motors to increase the torque. Consequently, two motors with a smaller torque rating of 15mNm were designed and built to validate the effect of the diode conduction angle on the suitability of the motors for sensorless operation. Due to the difficulty in obtaining small numbers of high-speed bearings, the only available bearings, without ordering 10,000+ pairs, had a 5mm bore diameter, which enabled a smaller overall rotor diameter to be employed than for the 100mNm motors, a lower limit of 17mm now being available. As the motor power has reduced to ~190W, from 1.25kW, the motor volume was reduced, the stator outer diameter being 50mm and the axial length being 30mm. Although, further reductions would have been possible, the minimum rotor diameter limited the minimum motor size.

The motors were designed using the same technique as for the 100mNm motors, but is not shown here in order to avoid repetition. The airgap length and rotor outer diameter were 4mm and 17mm, respectively. This time, varying the stator flux density, and therefore the required active length, had a much more significant effect on the motor efficiency, as can be seen in Figure 3.14(a) & (b). Again, it can be seen in Figure 3.14(c) & (d) that the diode conduction angle is still very sensitive to the stator flux density. Figures 3.15 & 3.16 show the effect of the stator flux density, the rotor outer diameter and the motor aspect ratio on the diode conduction angle. Highlighted on these figures are motors  $A_2$  and  $B_2$  which were selected for prototyping. Motor  $A_2$  has an active length of 14mm and a stator flux density of 0.65T – which results in a diode conduction angle of  $\sim 9^\circ$  elec., whilst motor  $B_2$  has an active length of just 3.6mm and a stator flux density of 1.25T – which results in a diode conduction angle of  $\sim 42^\circ$  elec.

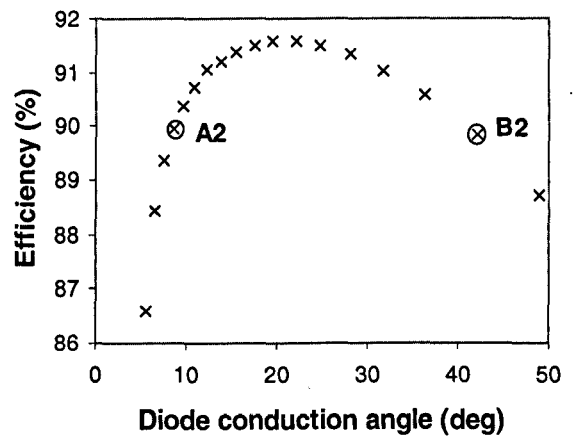
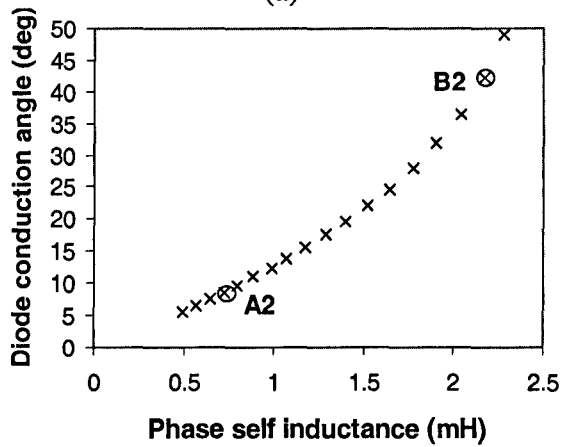
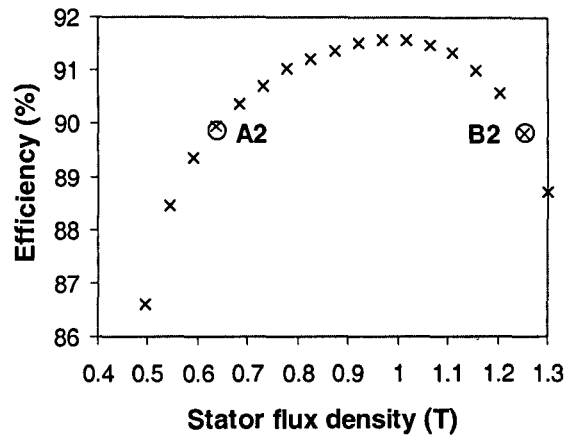
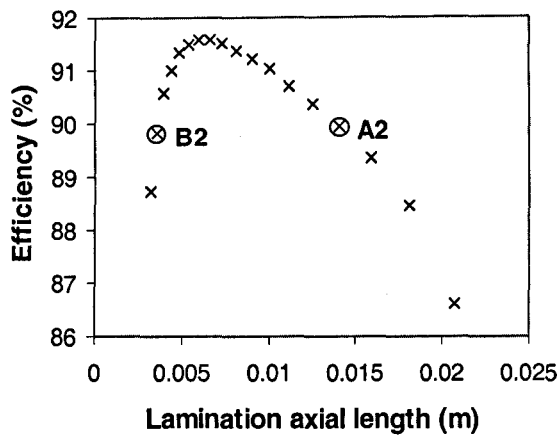


Figure 3.14 - Influence of design parameters on motor efficiency, self-inductance and diode conduction angle

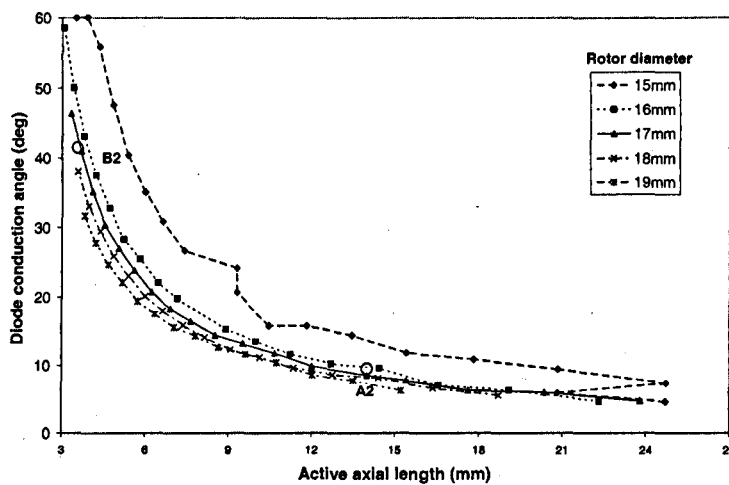
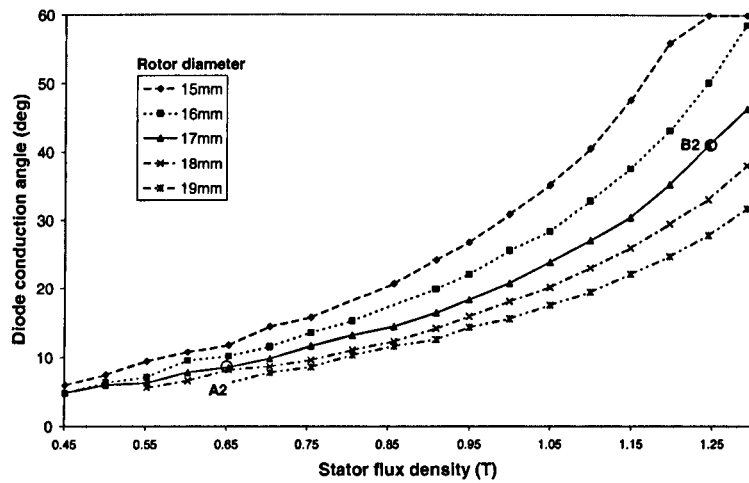


Figure 3.15 - Influence of active length and rotor diameter on diode conduction angle

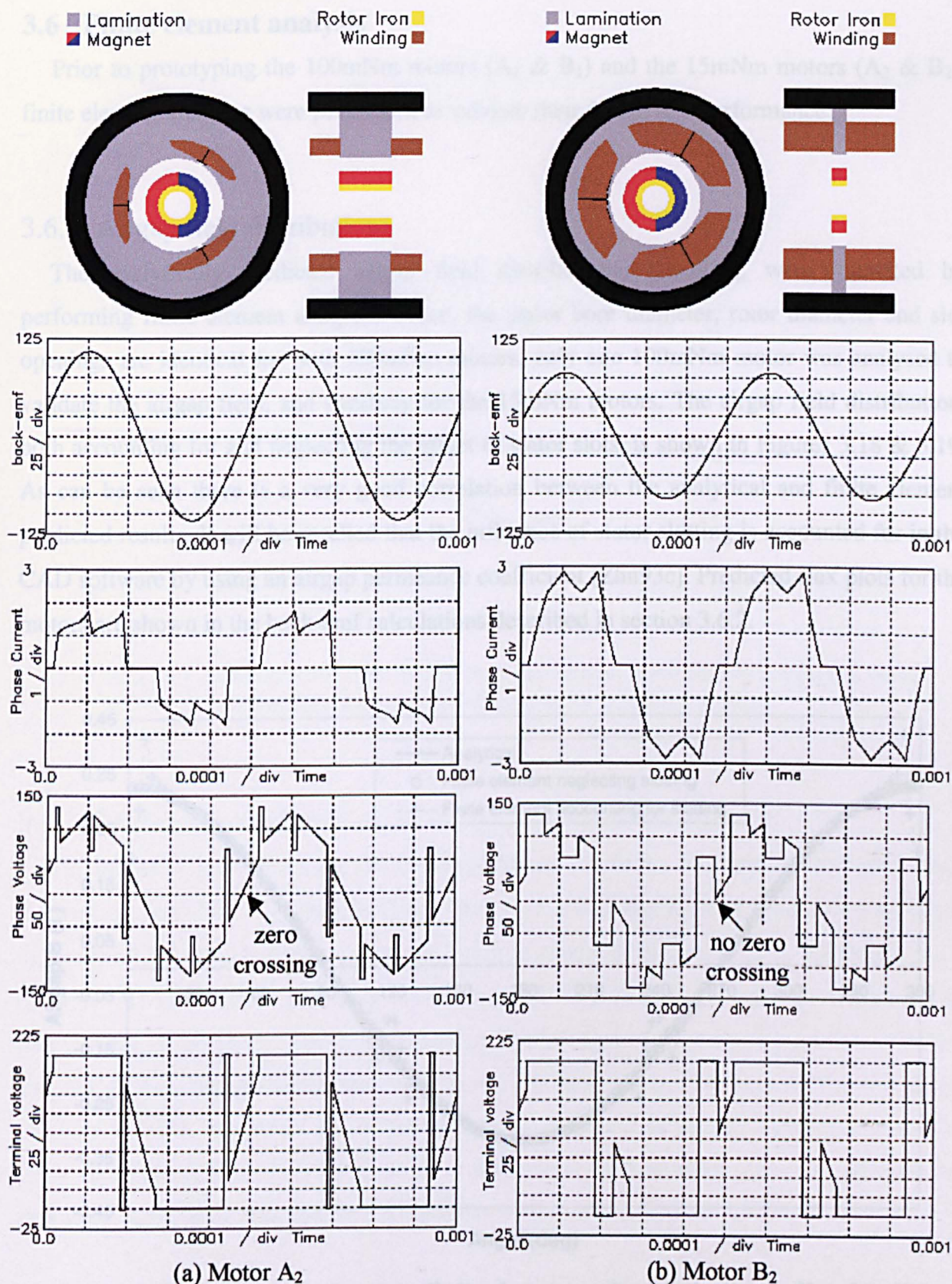


**Figure 3.16 - Influence of stator flux density and rotor diameter on diode conduction angle**

Cross-sections of both motors, together with their phase back-emf, current, terminal phase and line voltage waveforms at the rated speed of 120krpm and rated torque, are shown in Figure 3.17, the main features being summarised in Table 3.3.

**Table 3.3 - Summary of differences between motors A<sub>2</sub> & B<sub>2</sub>**

	Motor A <sub>2</sub>	Motor B <sub>2</sub>
DC link voltage, V	200	200
DC link current, A	1.1	1.1
Outer diameter, mm	50	50
Axial length, mm	30	30
Airgap length, mm	4	4
Rotor magnet outer diameter, mm	17	17
NdFeB magnet thickness, mm	3	3
Flux density in stator iron, T	0.65	1.25
Active axial length, mm	14	3.6
Diode conduction angle, °elec.	8.6	42.1
No of turns per phase	74	220
Winding self-inductance, mH	0.72	2.172
Copper weight, g	18.4	59.5
Stator iron weight, g	134	21.3
Phase resistance, Ω	1.76	2.92
Peak phase emf, V	108	82
Magnet weight, g	14	3.5
Copper loss, W	4.6	13
Iron loss, W	16.5	8.3
Efficiency, %	89.9	89.8



(a) Motor A<sub>2</sub> (b) Motor B<sub>2</sub>  
**Figure 3.17 - Schematic of motors A<sub>2</sub> & B<sub>2</sub> and associated voltage and current waveforms**

### 3.6 Finite element analysis

Prior to prototyping the 100mNm motors ( $A_1$  &  $B_1$ ) and the 15mNm motors ( $A_2$  &  $B_2$ ), finite element analyses were performed to validate their design and performance.

#### 3.6.1 Airgap field distributions

The analytically predicted airgap field distributions, [Zhu93a], were validated by performing finite element analyses. Since, the stator bore diameter, rotor diameter and slot openings are identical for both 100mNm motors, only one 100mNm motor was analysed to validate the airgap field, and similarly for the 15mNm motors. The airgap field distribution, both accounting for and neglecting the effect of stator slots, is shown in Figures 3.18 & 3.19. As can be seen there is a very good correlation between the analytical and finite element predicted results. It will be recalled that the influence of stator slotting is accounted for in the CAD software by using an airgap permeance coefficient [Zhu93c]. Predicted flux plots for the motors are shown in the back-emf calculations described in section 3.6.2.

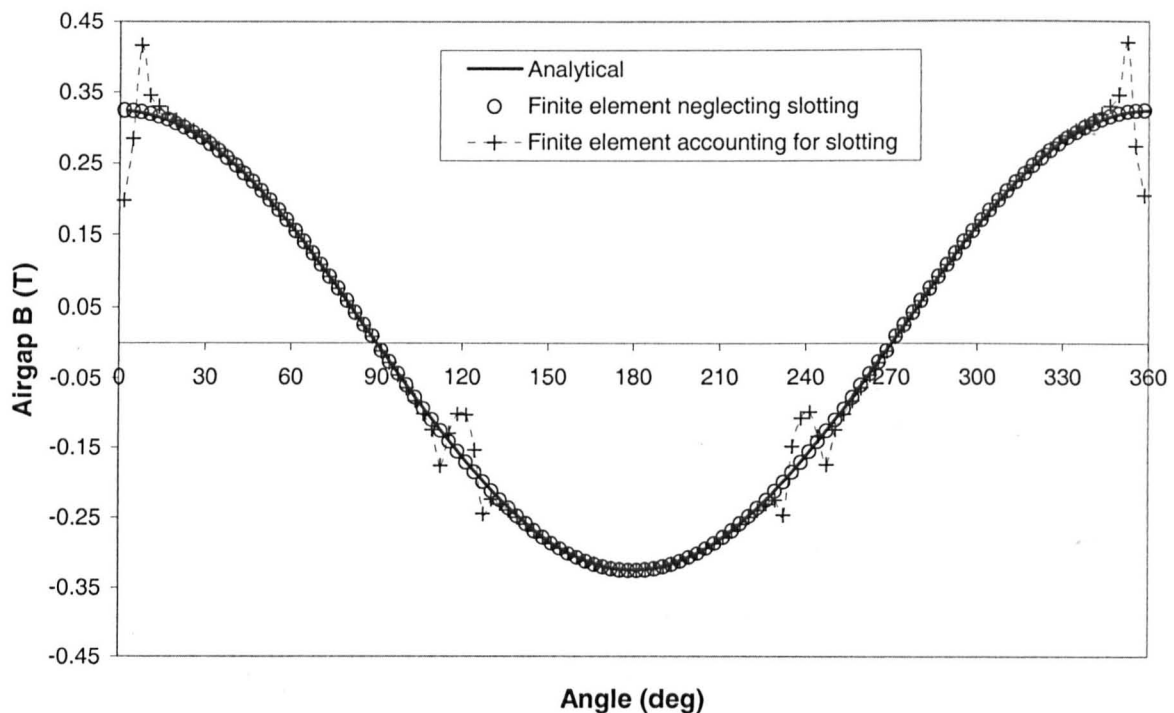


**Figure 3.18 - Comparison between finite element and analytically predicted radial airgap flux density distributions for 100mNm motors**

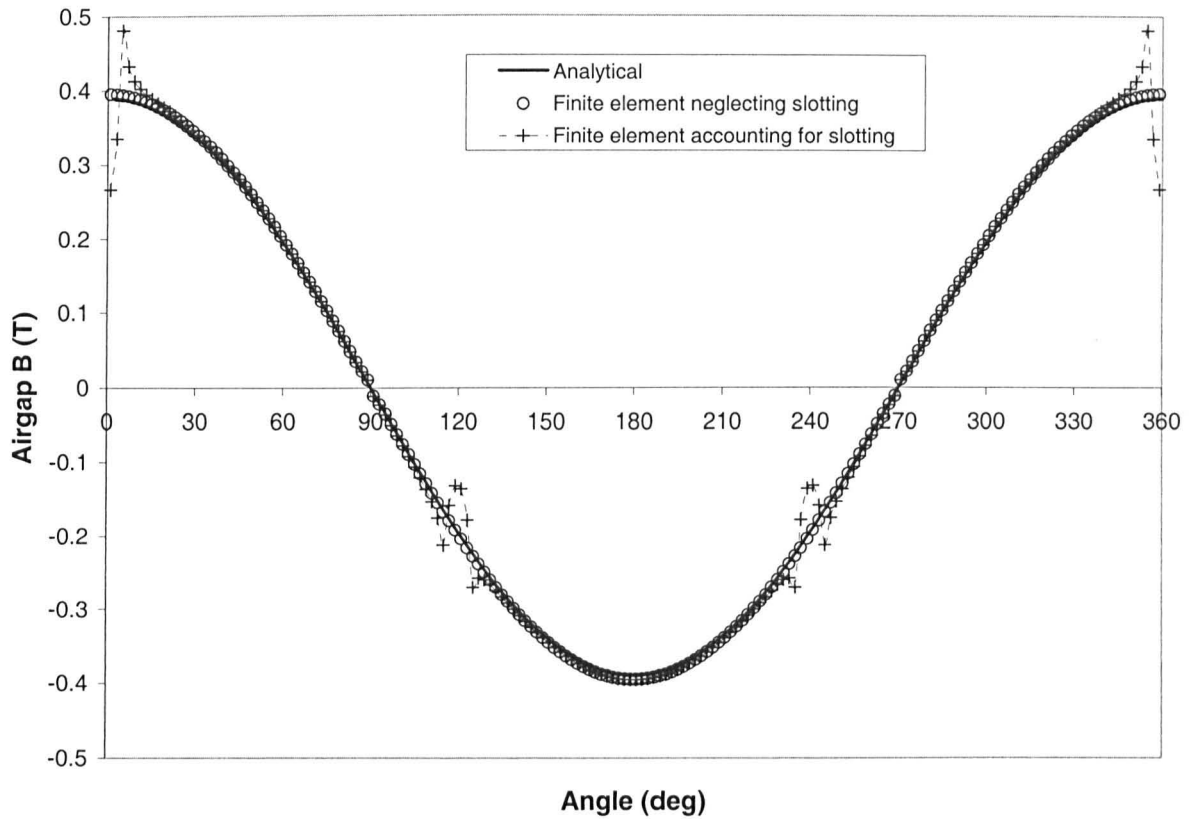


**Figure 3.19 - Comparison between finite element and analytically predicted radial airgap flux density distributions for 15mNm motors**

### 3.6.2 Back-emf waveforms

The back-emf waveforms for the 100mNm motors  $A_1$  &  $B_1$ , calculated analytically using the method described in Appendix C, are compared with finite element predicted waveforms in Figures 3.20 & 3.21. Again, good agreement is obtained. Figures 3.22 & 3.23 show finite element flux plots at the instant of maximum tooth flux density and maximum stator yoke flux density, respectively. There was a similar level of agreement between the finite element and the analytically predicted emf waveforms for the 15mNm motor with the low diode conduction angle, viz. motor  $A_2$ , as can be seen in Figures 3.24 & 3.25. Figures 3.26 & 3.27 show finite element predicted flux plots at the instant of maximum tooth flux density and maximum stator yoke flux density for motor  $A_2$ .

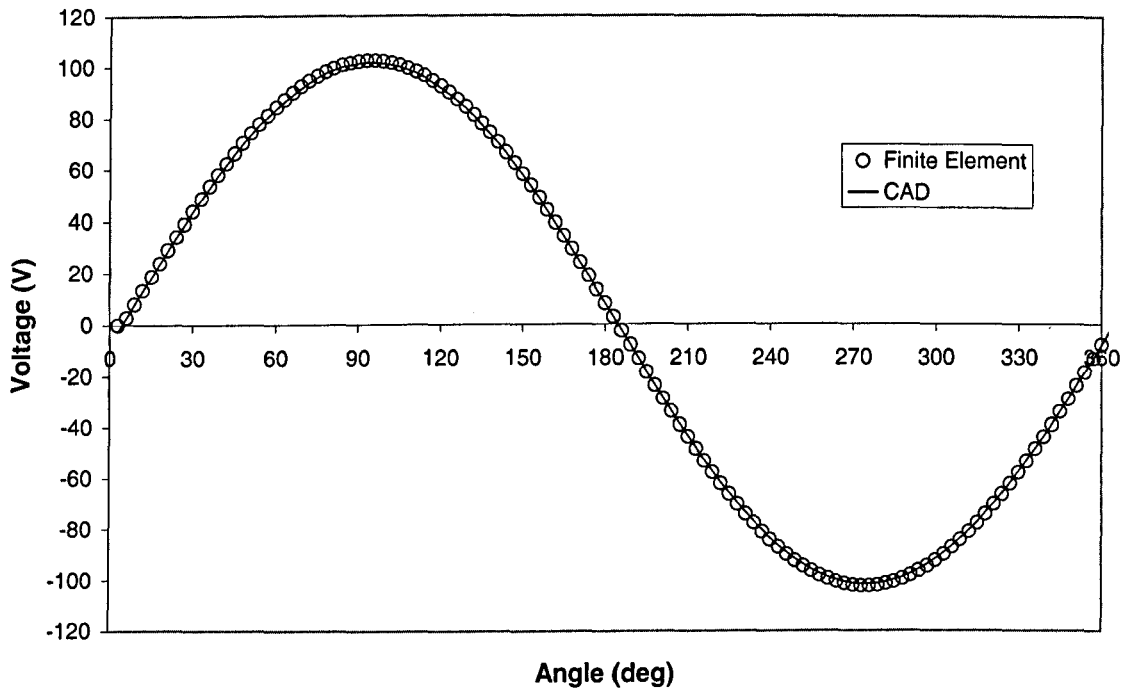


**Figure 3.20 - Comparison between finite element and analytically predicted emf waveforms for 100mNm motor with low diode conduction angle ( $A_1$ )**

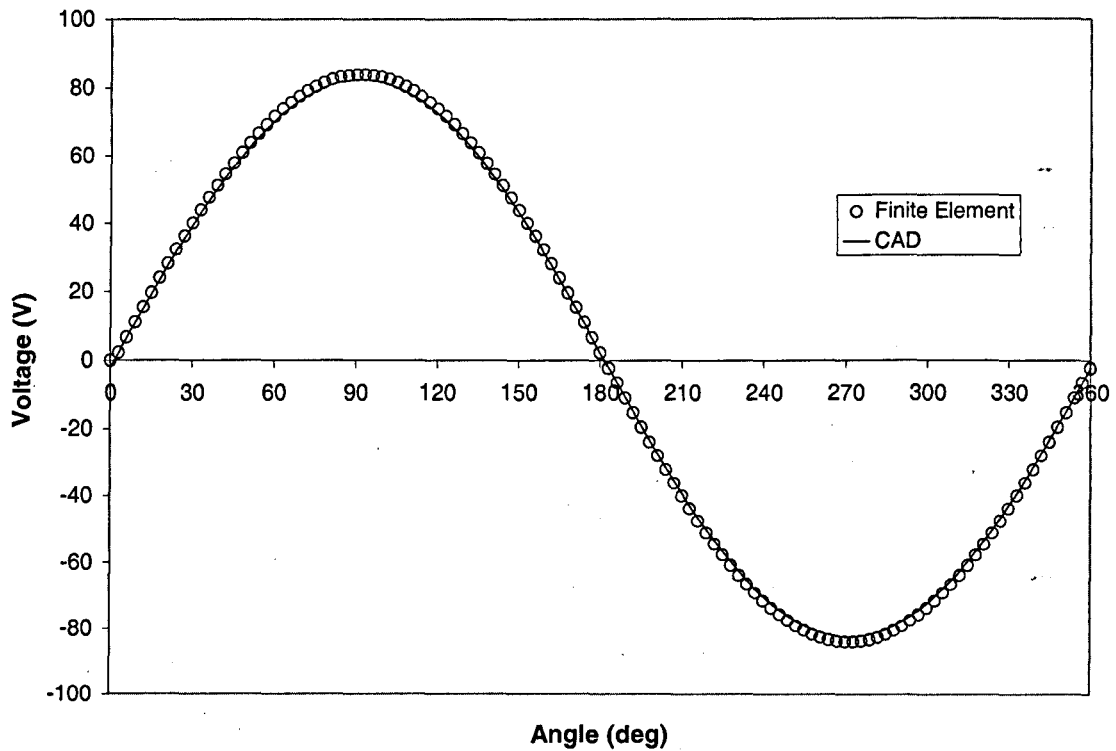
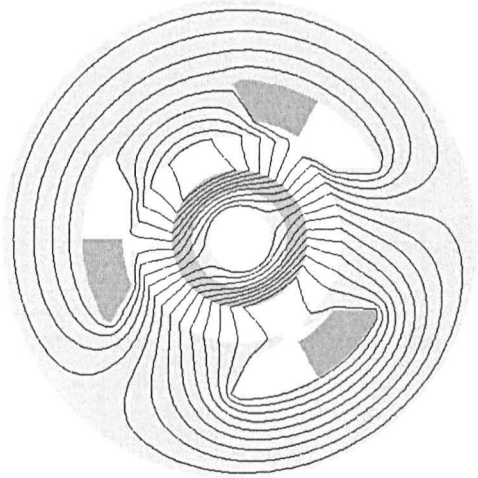
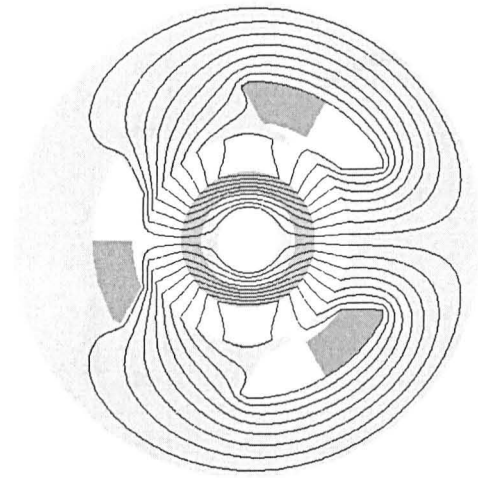
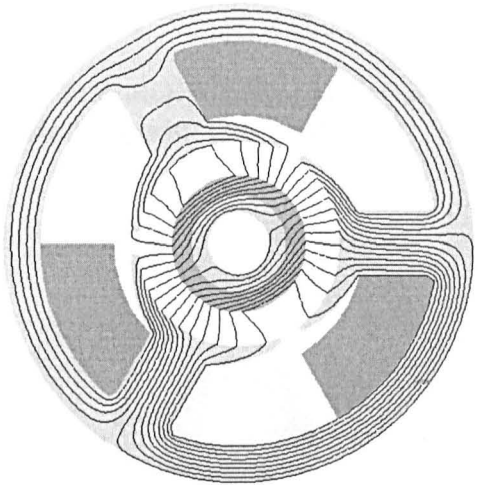
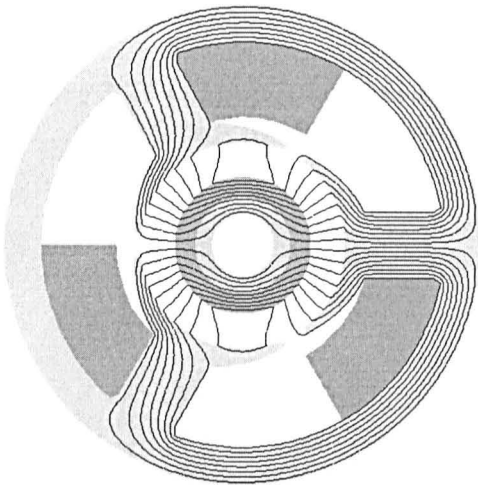


**Figure 3.21 - Comparison between finite element and analytically predicted emf waveforms for 100mNm motor with high diode conduction angle ( $B_1$ )**



(a) magnetisation aligned with tooth      (b) magnetisation offset 30° elec. from tooth  
**Figure 3.22 - Flux plots for 100mNm motor with low diode conduction angle (A<sub>1</sub>)**



(a) magnetisation aligned with tooth      (b) magnetisation offset 30° elec. from tooth  
**Figure 3.23 - Flux plots for 100mNm motor with high diode conduction angle (B<sub>1</sub>)**

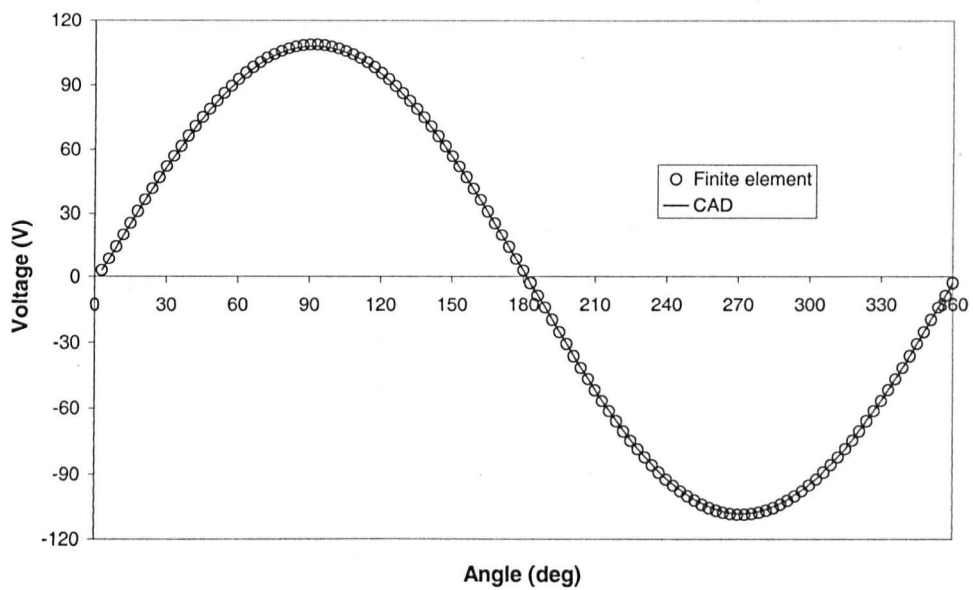


**Figure 3.24 - Comparison between finite element and analytically predicted emf waveforms for 15mNm motor with low diode conduction angle (A<sub>2</sub>)**

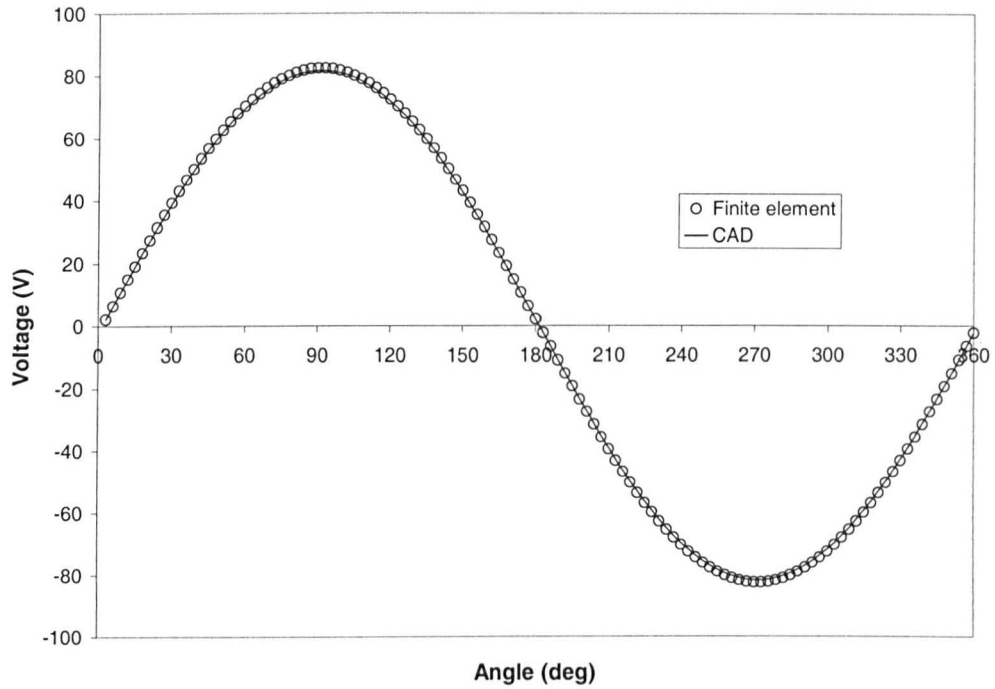
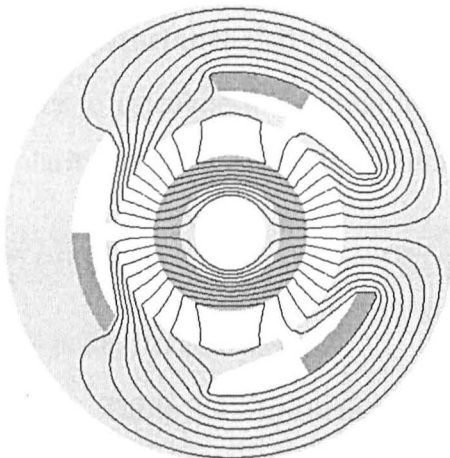
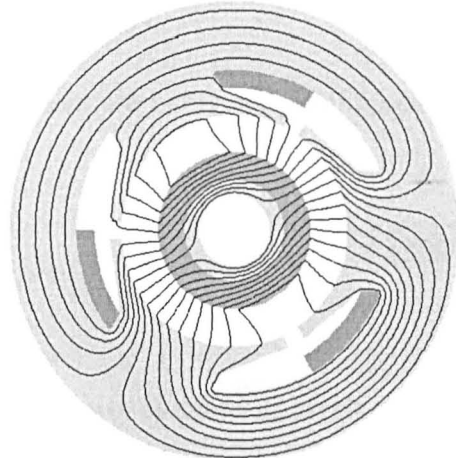


**Figure 3.25 - Comparison between finite element and analytically predicted emf waveforms for 15mNm motor with high diode conduction angle ( $B_2$ )**

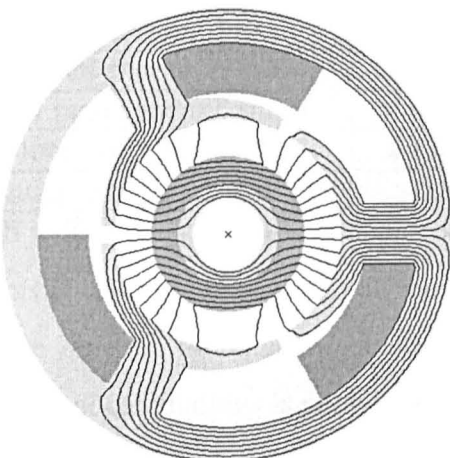


(a) magnetisation aligned with tooth

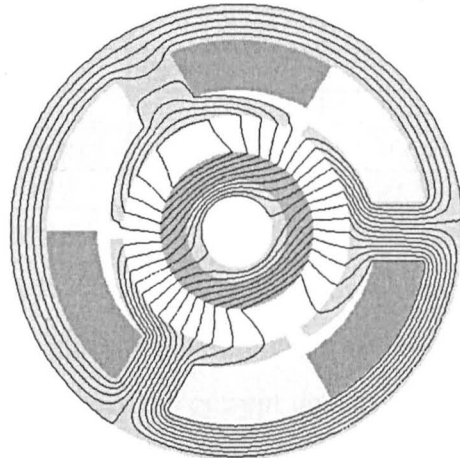


(b) magnetisation offset 30° elec. from tooth

**Figure 3.26 – Flux plots for 15mNm motor with low diode conduction angle ( $A_2$ )**



(a) magnetisation aligned with tooth



(b) magnetisation offset 30° elec. from tooth

**Figure 3.27 - Flux plots for 15mNm motor with high diode conduction angle ( $B_2$ )**

### 3.6.3 Winding inductances

The self- and mutual inductances were calculated from the stored magnetic energy when a specified current was applied to the appropriate windings. From the stored magnetic energy, which was determined per metre of active length, the inductances were calculated as follows:

#### (a) Self-inductance (L)

When one phase is energised with a specified current,  $I$ , the stored energy is:

$$E_l = \frac{1}{2} LI^2 \quad (3.1)$$

$$\therefore L = 2 \frac{E_l l}{I^2} \quad (3.2)$$

where  $E_l l$  is the stored energy for an active length,  $l$ , and  $I = \frac{JA}{N_p}$ , where  $J$  is the current density,  $A$  is the winding area (with due account of the packing factor) and  $N_p$  is the number of series turns per phase.

#### (b) Mutual inductance (M)

In order to calculate the mutual inductance, two phases are energised, with current of the same polarity and  $M$  is determined from:

$$M = L - \frac{E_{ll}}{I^2} \quad (3.3)$$

where  $E_{ll}$  is the stored energy.

**Table 3.4 - Inductance calculations from finite element analysis**

	Motor A <sub>1</sub>	Motor B <sub>1</sub>	Motor A <sub>2</sub>	Motor B <sub>2</sub>
Current density, $J$ (A/m <sup>2</sup> )	$3 \times 10^6$	$1.6 \times 10^6$	$5 \times 10^6$	$3 \times 10^6$
Winding area, $A$ (m <sup>2</sup> )	$0.598 \times 10^{-4}$	$0.223 \times 10^{-3}$	$0.2116 \times 10^{-4}$	$0.886162 \times 10^{-4}$
Number of turns, $N_p$	29	54	74	220
Phase current, $I$ (A)	6.191	6.604	1.43	1.2
Stored energy, $E_l l$ (J)	$3.51 \times 10^{-3}$	$6.563 \times 10^{-3}$	$6.952 \times 10^{-4}$	$1.126 \times 10^{-3}$
Self inductance, $L$ (mH)	0.183	0.301	0.68	1.542
Stored energy, $E_{ll} L$ (J)	$4.17 \times 10^{-3}$	$7.766 \times 10^{-3}$	$8.846 \times 10^{-4}$	$1.366 \times 10^{-3}$
Mutual inductance, $L$ (mH)	-0.074	-0.122	-0.247	-0.594

Both inductance calculations neglect the end-winding component of inductance. However, since this is calculated separately in the CAD software it is possible to compare the analytical and finite element inductance calculations neglecting the end-windings. The data for the finite element calculations is shown below in Table 3.4, where the current density was chosen such that  $I$  is close to the rated current of each motor. Table 3.5 compares the finite element and analytically predicted inductances for all four motors neglecting the end-windings, and as

can be seen there is good agreement. Figure 3.28 shows the flux plots associated with the inductance calculations.

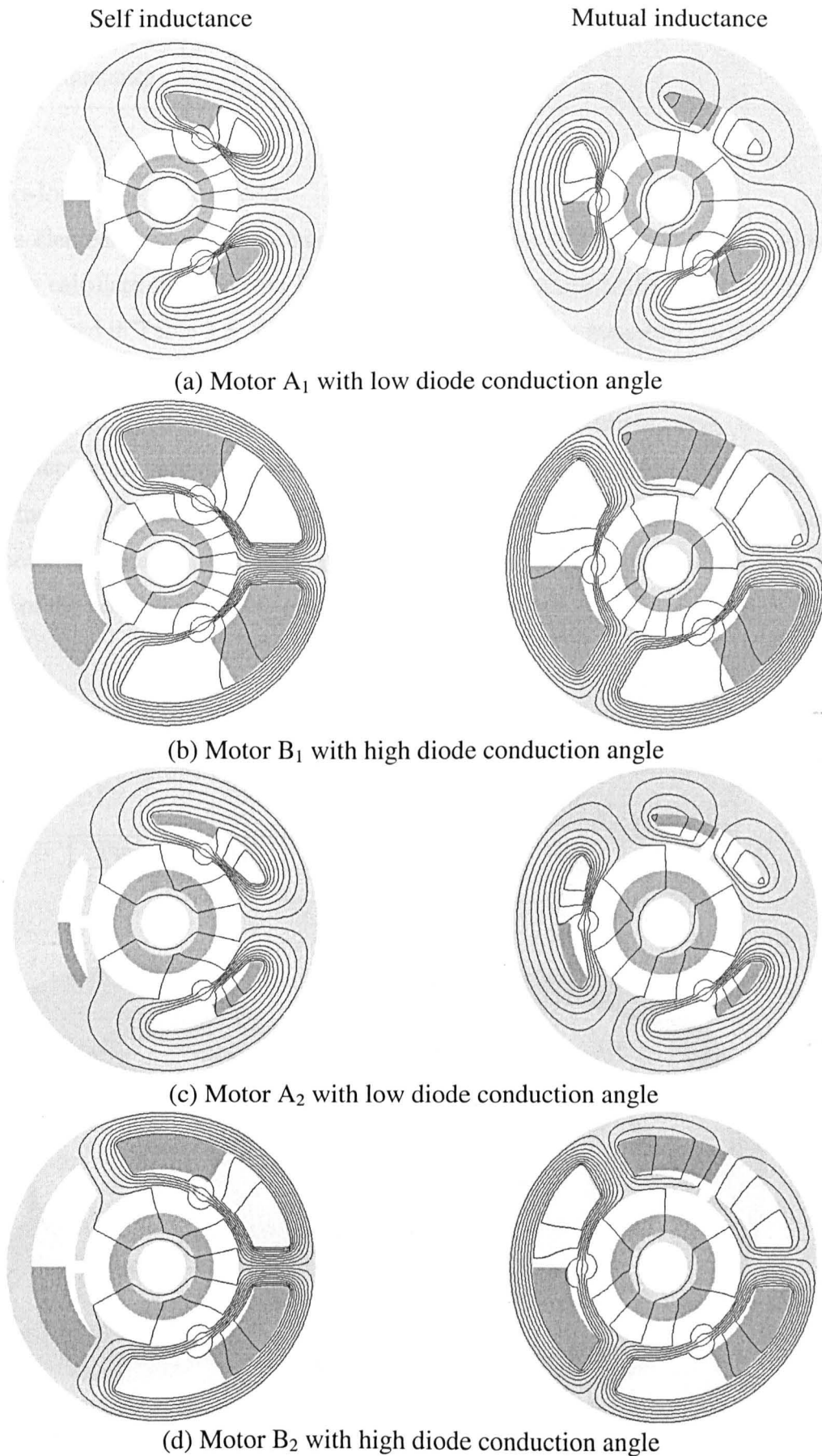


**Figure 3.28 - Flux plots associated with inductance calculations**

**Table 3.5 - Comparison of analytical and finite element predicted inductances neglecting end-windings**

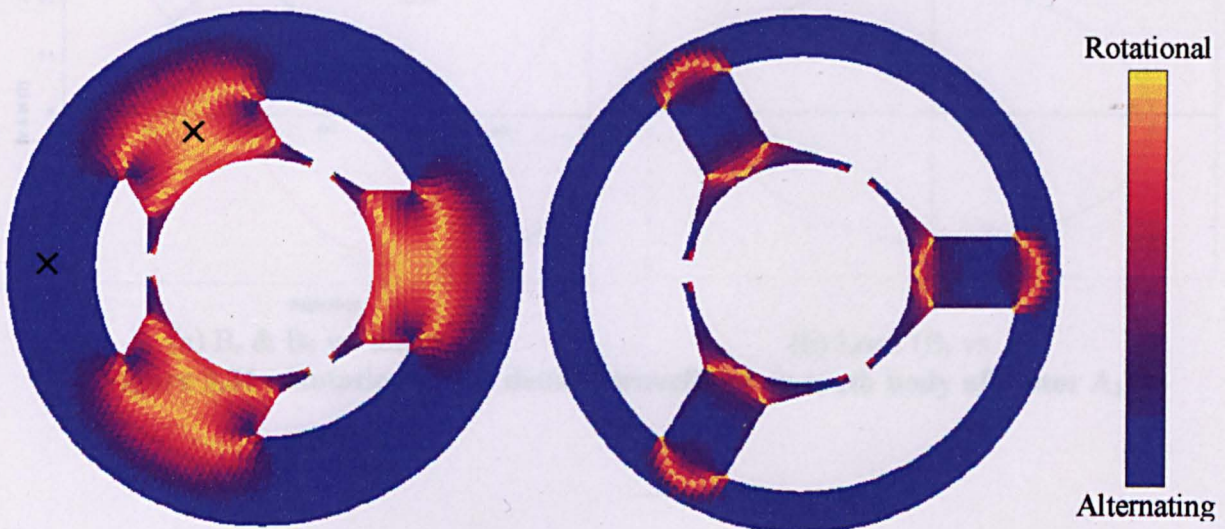
		Motor A <sub>1</sub>	Motor B <sub>1</sub>	Motor A <sub>2</sub>	Motor B <sub>2</sub>
Self-inductance	Analytical (mH)	0.178	0.284	0.671	1.45
	Finite element (mH)	0.183	0.301	0.68	1.54
Mutual inductance	Analytical (mH)	-0.068	-0.111	-0.224	-0.55
	Finite element (mH)	-0.074	-0.122	-0.247	-0.60

### 3.6.4 No-load stator iron loss

A finite element post-processor based on the equations which were cited in Appendix C was used to calculate the iron loss for all four prototype motors, the results of the analysis being summarised in Table 3.6. Where the flux is rotational, as mentioned in Appendix C, the iron loss is computed from the radial and tangential flux density components and then summed to give the total loss density in that part of the finite element mesh. Whilst this does not always accurately reflect the situation it is adequate for most applications [Ata93]. After designing the two 100mNm motors, the CAD software was refined slightly to more accurately size the motor to achieve specified flux densities. This refinement resulted in a more accurate prediction of the no-load iron loss, as can be seen in Table 3.6.

**Table 3.6 - Comparison of iron loss deduced from finite element analysis and CAD program**

	Iron loss (W)			
	Motor A <sub>1</sub>	Motor B <sub>1</sub>	Motor A <sub>2</sub>	Motor B <sub>2</sub>
Finite Element	34.1	38.7	16.0	8.5
CAD	36.6	35.0	16.5	8.3



(a) Motor A<sub>1</sub> with low diode conduction angle (b) Motor B<sub>1</sub> with high diode conduction angle

**Figure 3.29 – Alternating and rotational flux density distributions for 100mNm motors**

Figures 3.29 & 3.30 show the resultant flux density distributions, the yellow areas representing a rotational flux whilst the blue areas represent an alternating flux, with typical flux density loci being shown in Figures 3.31 & 3.32 for the areas marked on Figure 3.29(a) with an 'x'. As mentioned, in Appendix C, when calculating the iron loss the analytical program assumes that the rotational fluxes exist only in the two regions at the top and bottom of the stator teeth. In the case of motors B<sub>1</sub> & B<sub>2</sub> with the high diode conduction angle it can be seen that this essentially is the case. However, for motors A<sub>1</sub> & A<sub>2</sub> with the low diode conduction angle it can be seen that most of the tooth body has a rotational flux due to the relatively short tooth body length.

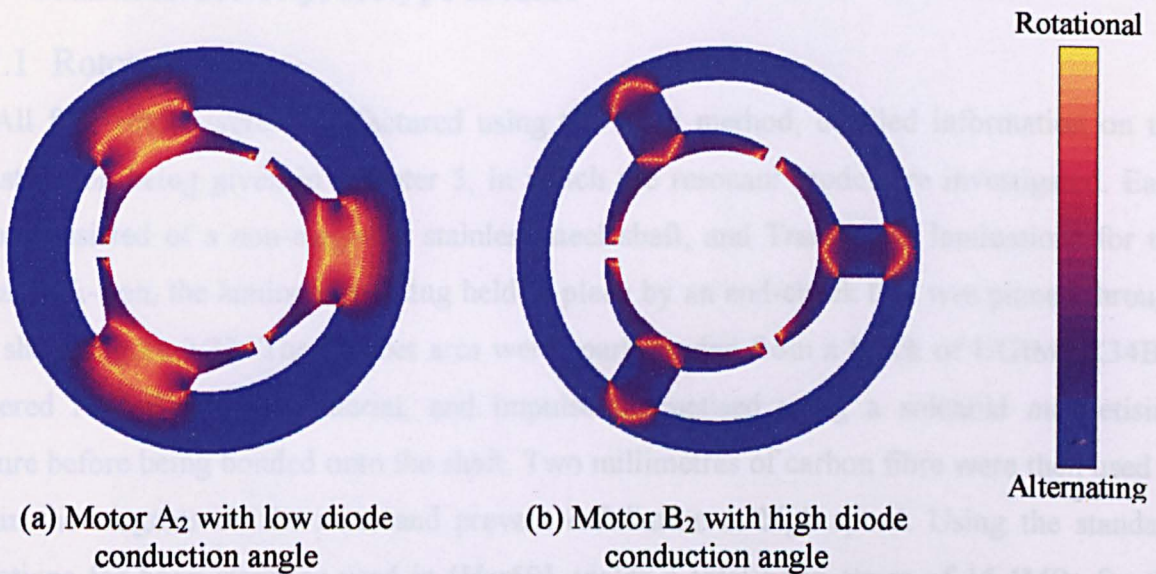


**Figure 3.30 - Alternating and rotational flux density distributions for 15mNm motors**

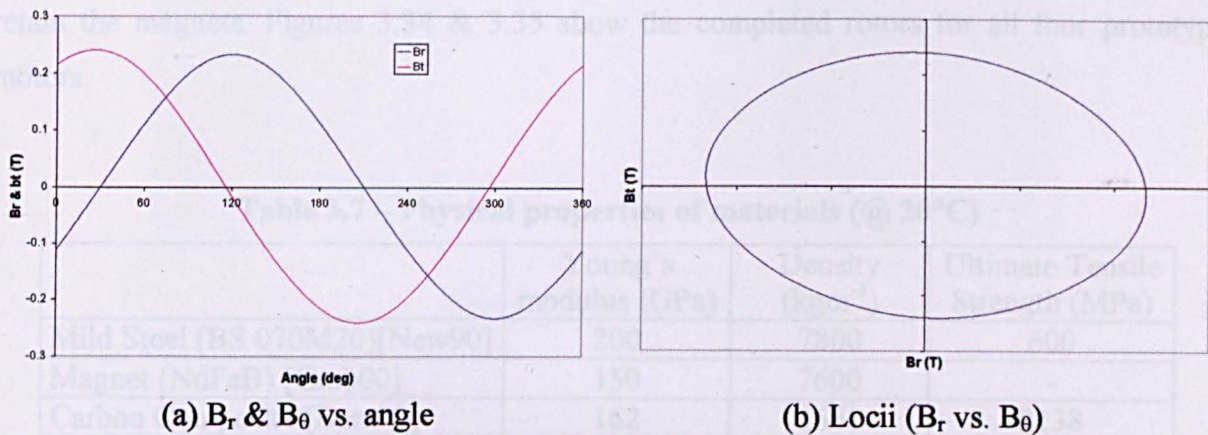
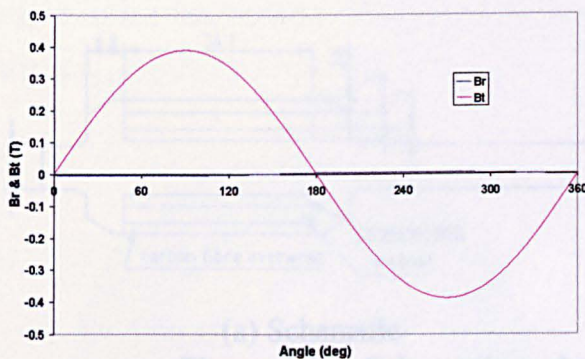
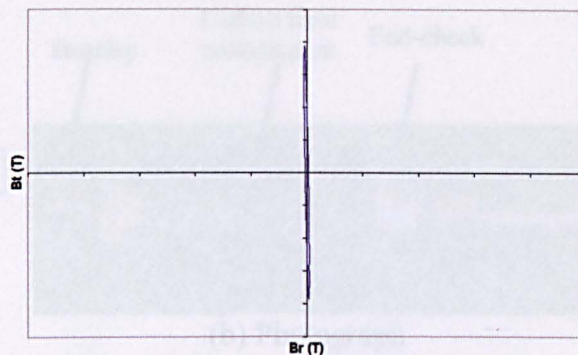


**Figure 3.31 - Rotational flux density waveform on tooth body of motor A<sub>1</sub>**



(a)  $B_r$  &  $B_\theta$  vs. angle



(b) Locii ( $B_r$  vs.  $B_\theta$ )

**Figure 3.32 - Alternating flux density waveform in back iron of motor  $A_1$**

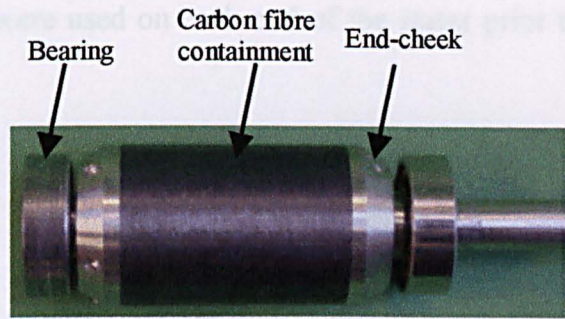
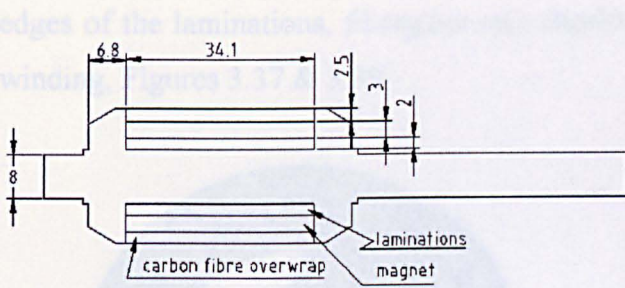
### 3.7 Manufacture of prototype motors

#### 3.7.1 Rotors

All four rotors were manufactured using the same method, detailed information on the construction being given in Chapter 5, in which the resonant modes are investigated. Each rotor consisted of a non-magnetic stainless steel shaft, and Transil 335 laminations for the rotor back-iron, the laminations being held in place by an end-cheek that was pinned through the shaft, Figure 3.33. The magnet arcs were spark eroded from a block of UGIMAX34B1, sintered NdFeB magnet material, and impulse magnetised using a solenoid magnetising fixture before being bonded onto the shaft. Two millimetres of carbon fibre were then used to retain the magnets on the rotor and prevent exfoliation at high speed. Using the standard equations for hoop stress as used in [Har59], yields a total hoop stress of 16.4MPa for the 100mNm motors. Table 3.7 shows that the carbon fibre containment is more than adequate to retain the magnets. Figures 3.34 & 3.35 show the completed rotors for all four prototype motors.

**Table 3.7 – Physical properties of materials (@ 20°C)**

	Young's modulus (GPa)	Density ( $\text{kgm}^{-3}$ )	Ultimate Tensile Strength (MPa)
Mild Steel (BS 070M20)[New90]	200	7800	600
Magnet (NdFeB) [Gmb00]	150	7600	-
Carbon Composite [Bam99]	162	1661	2138



(a) Schematic  
 (b) Photograph  
**Figure 3.33 - Schematic and photograph of prototype rotor A<sub>1</sub>**



(a) Rotor A<sub>1</sub>  
 (b) Rotor B<sub>1</sub>  
**Figure 3.34 - Completed rotors for 100mNm motor**



(a) Rotor A<sub>1</sub>  
 (b) Rotor B<sub>1</sub>  
**Figure 3.35 - Completed rotors for 15mNm motors**

### 3.7.2 Stators

The stator laminations were spark eroded from Transil 335, Figures 3.36 & 3.38, and then welded at three points around the outside circumference. The lamination stacks were then bonded into the motor frames and wound. In order to protect the windings from the sharp

edges of the laminations, fibreglass end-cheeks were used on each end of the stator prior to winding, Figures 3.37 & 3.39.

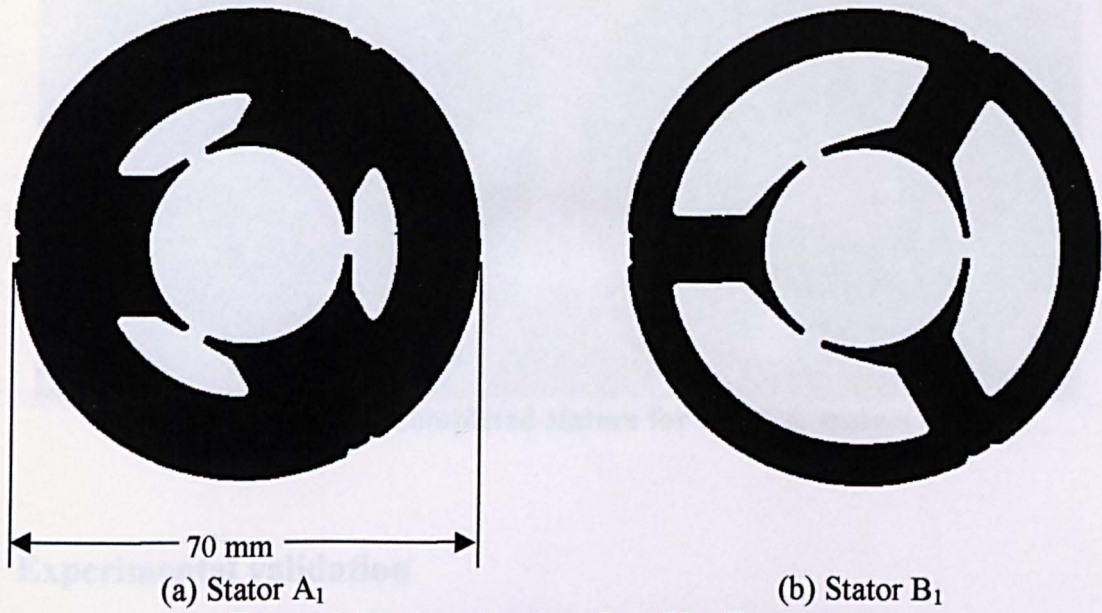


Figure 3.36 - Laminations for 100mNm motors

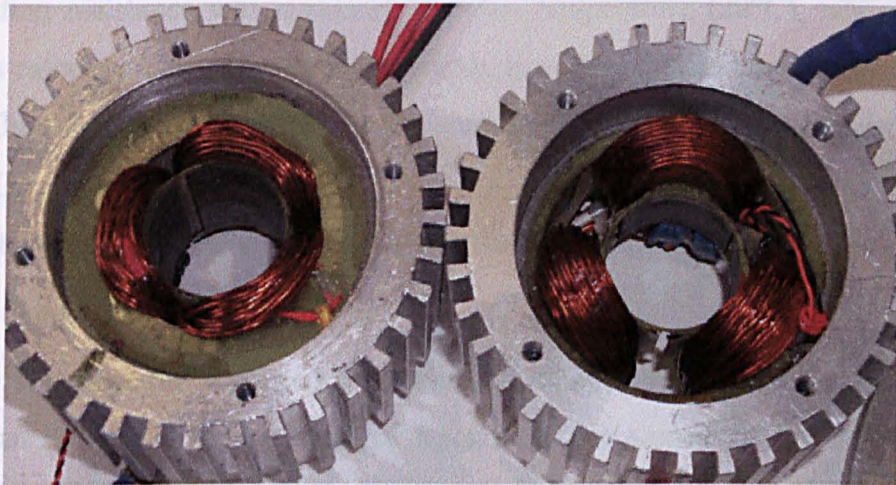


Figure 3.37 - Completed stators for 100mNm motors

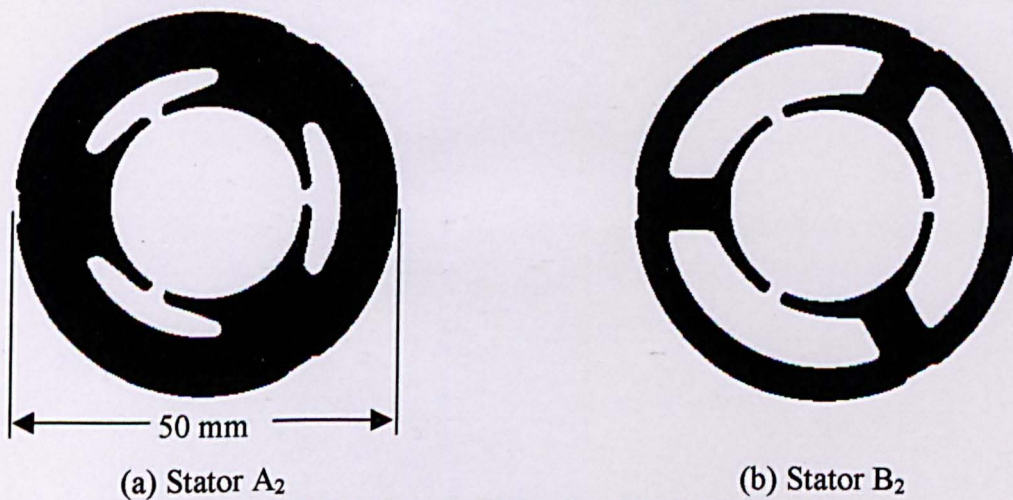
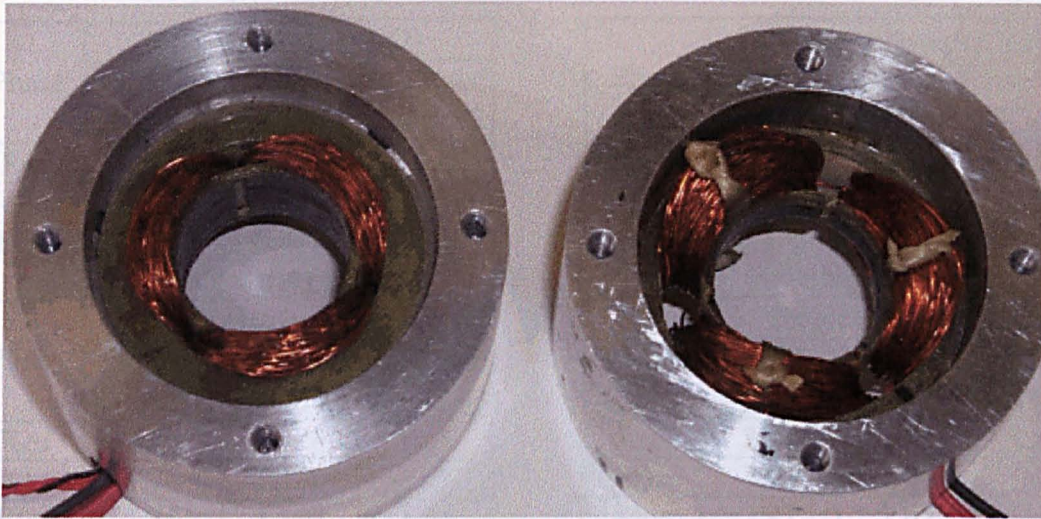


Figure 3.38 - Laminations for 15mNm motors



**Figure 3.39 - Completed stators for 15mNm motors**

### 3.8 Experimental validation

#### 3.8.1 Winding resistance

The winding resistance was measured at room temperature (20°C), whilst the winding resistance as calculated by the analytical software is at the predicted operating temperature of the motor. Thus, the measured resistance was extrapolated to this temperature from:

$$R' = R(1 + [R_{\alpha}\Delta T]) \quad (3.4)$$

where  $R_{\alpha}$  = temperature coefficient of resistance for copper ( $3.9 \times 10^{-3}$ )

$\Delta T$  = temperature rise (°C)

Table 3.8 compares the predicted and measured winding resistances for all the prototype motors. It can be seen that the measured resistances are somewhat lower than the values predicted by the CAD program. However, as seen from the photographs in section 3.7.2, the packing factor differs significantly from the 0.3 which was assumed in the CAD program.

Red	0.238	
Yellow	0.2115	0.1348
Blue	0.2148	

Table 3.10 - Measured inductances for motor B<sub>1</sub> with high diode conduction angle

Phase	Self-inductance (mH)	Mutual inductance (mH)
Red	0.4281	
Yellow	0.4296	-0.203
Blue	0.4472	

**Table 3.8 - Comparison of predicted and measured phase winding resistances**

Phase	Phase resistance ( $\Omega$ )		
	CAD @ 152°C	Measured @ 20°C	Predicted @ 152°C
Red	0.195	0.113	0.171
Yellow	0.195	0.119	0.180
Blue	0.195	0.122	0.185

(a) 100mNm motor A<sub>1</sub>

Phase	Phase resistance ( $\Omega$ )		
	CAD @ 113°C	Measured @ 20°C	Predicted @ 113°C
Red	1.76	1.126	1.53
Yellow	1.76	1.136	1.55
Blue	1.76	1.127	1.54

(c) 15mNm motor A<sub>2</sub>

Phase	Phase resistance ( $\Omega$ )		
	CAD @ 154°C	Measured @ 20°C	Predicted @ 154°C
Red	0.133	0.081	0.122
Yellow	0.133	0.079	0.120
Blue	0.133	0.081	0.122

(b) 100mNm motor B<sub>1</sub>

Phase	Phase resistance ( $\Omega$ )		
	CAD @ 114 °C	Measured @ 20°C	Predicted @ 114 °C
Red	2.92	1.81	2.47
Yellow	2.92	1.84	2.51
Blue	2.92	1.83	2.49

(d) 15mNm motor B<sub>2</sub>

### 3.8.2 Winding inductances

#### (a) 100mNm motors (A<sub>1</sub> & B<sub>1</sub>)

Tables 3.9 & 3.10 show the measured winding inductances, using the inductance bridge at 1kHz, for the two 100mNm motors, whilst Tables 3.11 & 3.12 compare the average measured and predicted inductances. It will be seen that the measured inductances are slightly larger than the predicted values. This is because the motors are comparatively small, and relatively small differences in the disposition of the coils and end-windings can have a comparatively large effect.

**Table 3.9 - Measured inductances for motor A<sub>1</sub> with low diode conduction angle**

Phase	Self-inductance (mH)	Mutual inductance (mH)
Red	0.2238	-0.1348
Yellow	0.2115	
Blue	0.2148	

**Table 3.10 - Measured inductances for motor B<sub>1</sub> with high diode conduction angle**

Phase	Self-inductance (mH)	Mutual inductance (mH)
Red	0.4281	-0.203
Yellow	0.4298	
Blue	0.4472	

**Table 3.11 - Comparison of predicted and measured inductances for motor with low diode conduction angle (Motor A<sub>1</sub>)**

	Self-inductance (mH)			Mutual inductance (mH)		
	Finite element	CAD	Measured	Finite element	CAD	Measured
Active length inductance (mH)	0.183	0.178	-	-0.074	-0.068	-
End-winding inductance (mH)	-	0.008	-	-	0	-
Total inductance (mH)	0.183	0.186	0.2167	-0.074	-0.068	-0.1348

**Table 3.12 - Comparison of predicted and measured inductances for motor with high diode conduction angle (Motor B<sub>1</sub>)**

	Self-inductance			Mutual inductance		
	Finite element	CAD	Measured	Finite element	CAD	Measured
Active length inductance (mH)	0.301	0.284		-0.122	-0.111	
End-winding inductance (mH)	-	0.055		-	0	
Total inductance (mH)	0.301	0.339	0.435	-0.122	-0.111	-0.203

**(b) 15mNm motors (A<sub>2</sub> & B<sub>2</sub>)**

Tables 3.13 & 3.14 show the measured inductance values, whilst Tables 3.15 & 3.16 compare the measured inductances with the predicted values. For motor A<sub>2</sub> with the low diode conduction angle it can be seen that the level of agreement is similar to that for the 100mNm motors. However, a relatively large discrepancy can be observed for motor B<sub>2</sub> with the high diode conduction angle. This probably arises for 2 reasons. Firstly, in order to ensure that the rotor was aligned axially with the stator the stator core was extended slightly. Secondly, because of the very small active length (3.6mm) compared with the comparatively thick laminations (0.35mm) the addition of a single lamination represents a relatively large change in the active length, and this is difficult to accurately control since although the lamination stack was welded around the periphery, the laminations had a tendency to spring open when they were released from the clamping fixture. Although this was minimised to some extent since the windings subsequently exerted axial pressure on the laminations. Nevertheless, the overall axial length was still difficult to control accurately.

**Table 3.13 - Measured inductances for motor A<sub>2</sub> with low diode conduction angle**

Phase	Self-inductance (mH)	Mutual inductance (mH)
Red	0.89	-0.54
Yellow	0.88	
Blue	0.90	

**Table 3.14 - Measured inductances for motor B<sub>2</sub> with high diode conduction angle**

Phase	Self-inductance (mH)	Mutual inductance (mH)
Red	3.33	-1.5
Yellow	3.35	
Blue	3.37	

**Table 3.15 - Comparison of predicted and measured inductances for motor with low diode conduction angle (Motor A<sub>2</sub>)**

	Self-inductance (mH)			Mutual inductance (mH)		
	Finite element	CAD	Measured	Finite element	CAD	Measured
Active length inductance (mH)	0.68	0.671	-	-0.247	-0.224	-
End-winding inductance (mH)	-	0.049	-	-	0	-
Total inductance (mH)	0.68	0.720	0.88	-0.247	-0.224	-0.54

**Table 3.16 - Comparison of predicted and measured inductances for motor with high diode conduction angle (Motor B<sub>2</sub>)**

	Self-inductance (mH)			Mutual inductance (mH)		
	Finite element	CAD	Measured	Finite element	CAD	Measured
Active length inductance (mH)	1.542	1.448	-	-0.594	-0.552	-
End-winding inductance (mH)	-	0.724	-	-	0	-
Total inductance (mH)	1.542	2.172	3.35	-0.594	-0.552	-1.53

### 3.8.3 Back-emf waveforms

#### (a) 100 mNm motors (A<sub>1</sub> & B<sub>1</sub>)

Figures 3.40 & 3.41 compare the predicted and measured back-emf waveform for each of the 100mNm motors. As can be seen, there is a good agreement. The noise evident on Figure 3.41 is due to the digitisation on the 8-bit scope used to record the waveform.

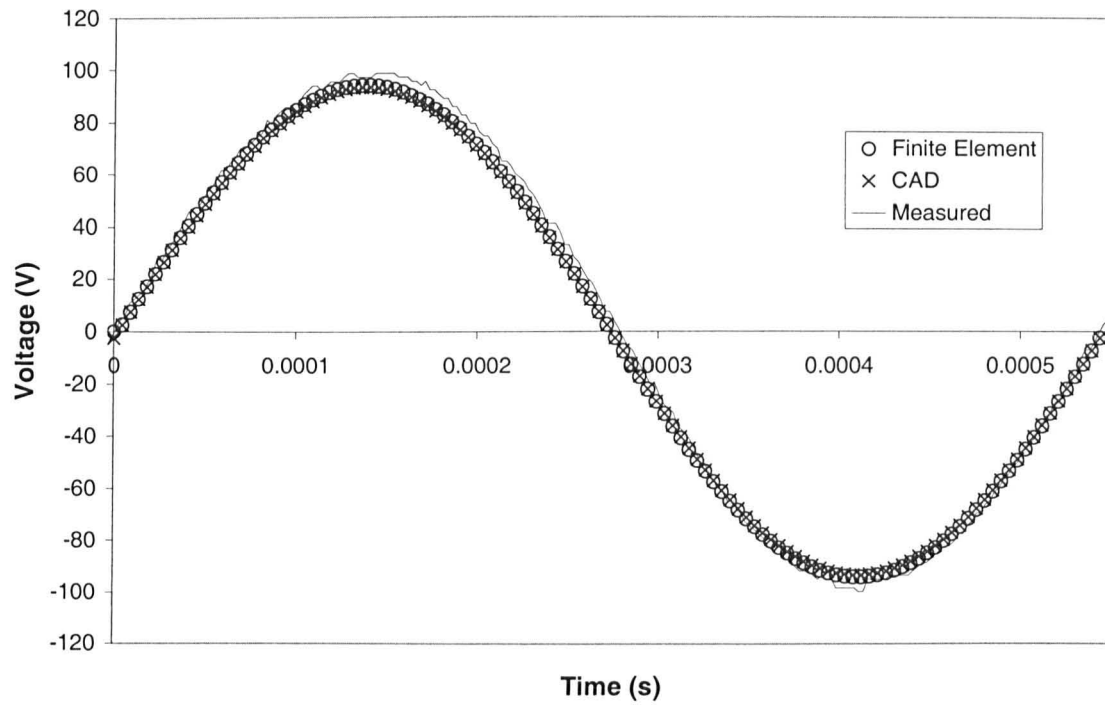


**Figure 3.40 - Comparison of predicted and measured back-emf waveforms for motor A<sub>1</sub> with low diode conduction angle at ~110krpm**

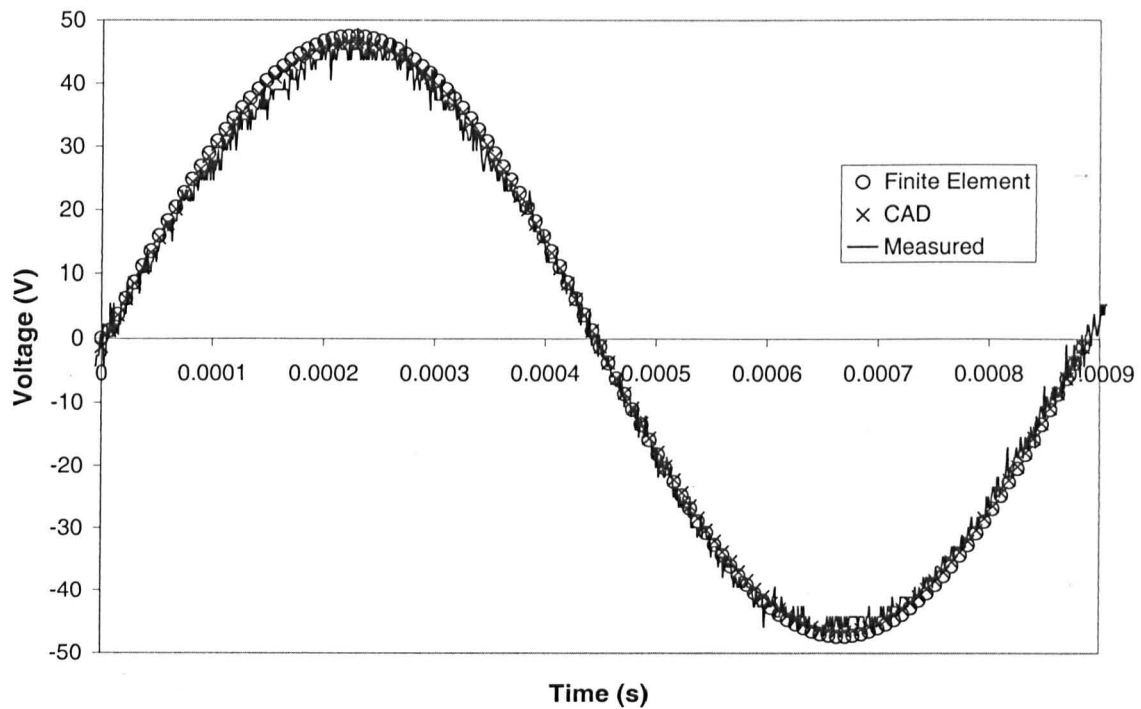


**Figure 3.41 - Comparison of predicted and measured back-emf waveforms for motor B<sub>1</sub> with high diode conduction angle at ~68krpm**

**(b) 15mNm motors (A<sub>2</sub> & B<sub>2</sub>)**

Figures 3.42 & 3.43 compare the predicted and measured back-emf waveforms for each of the 15mNm motors.

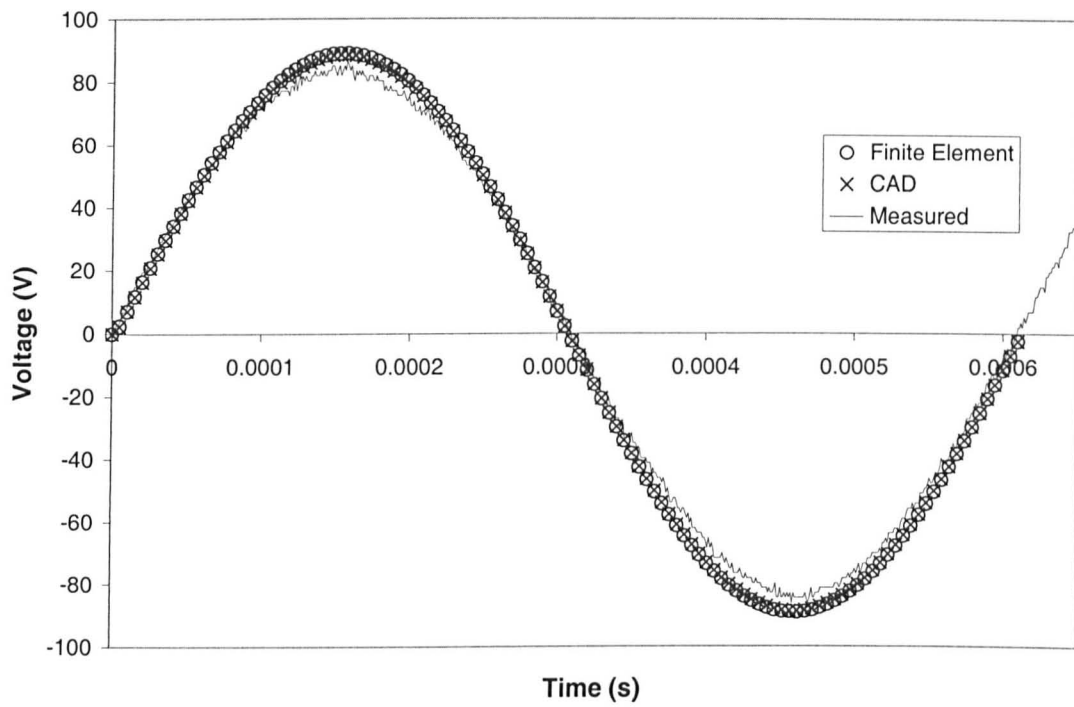


**Figure 3.42 - Comparison of predicted and measured back-emf waveforms for motor  $A_2$  with low diode conduction angle at  $\sim 99$ krpm**

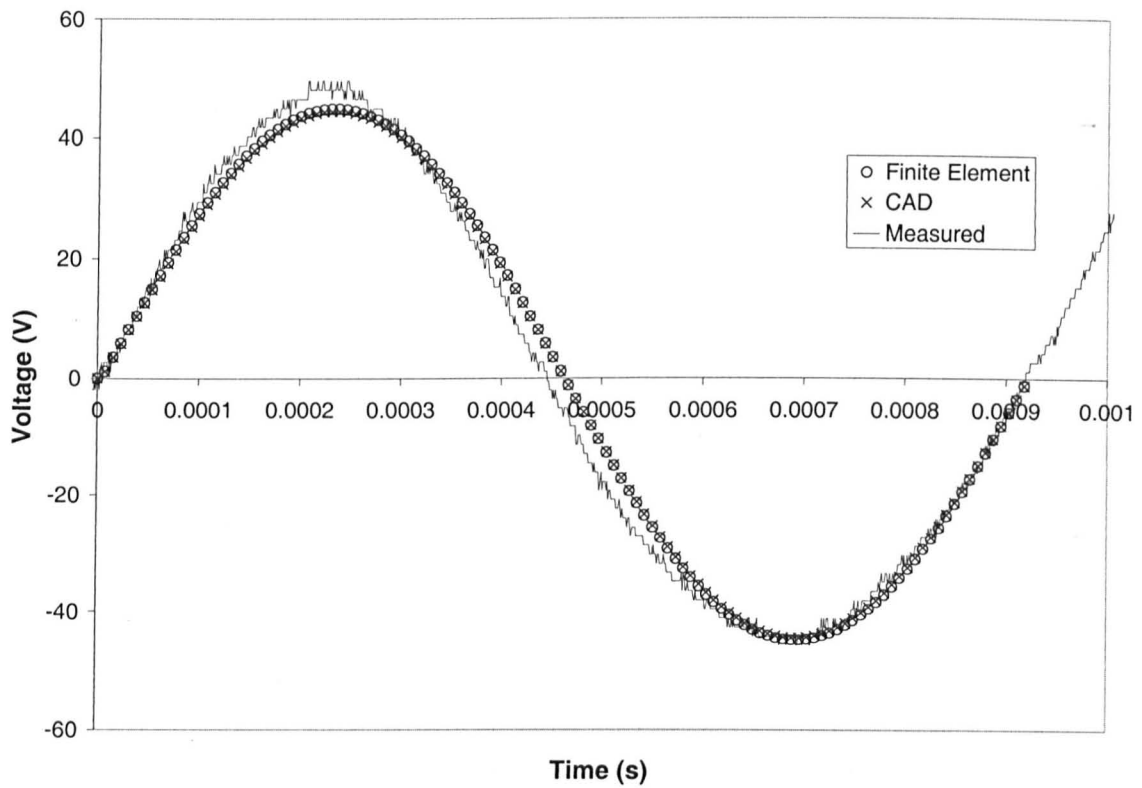


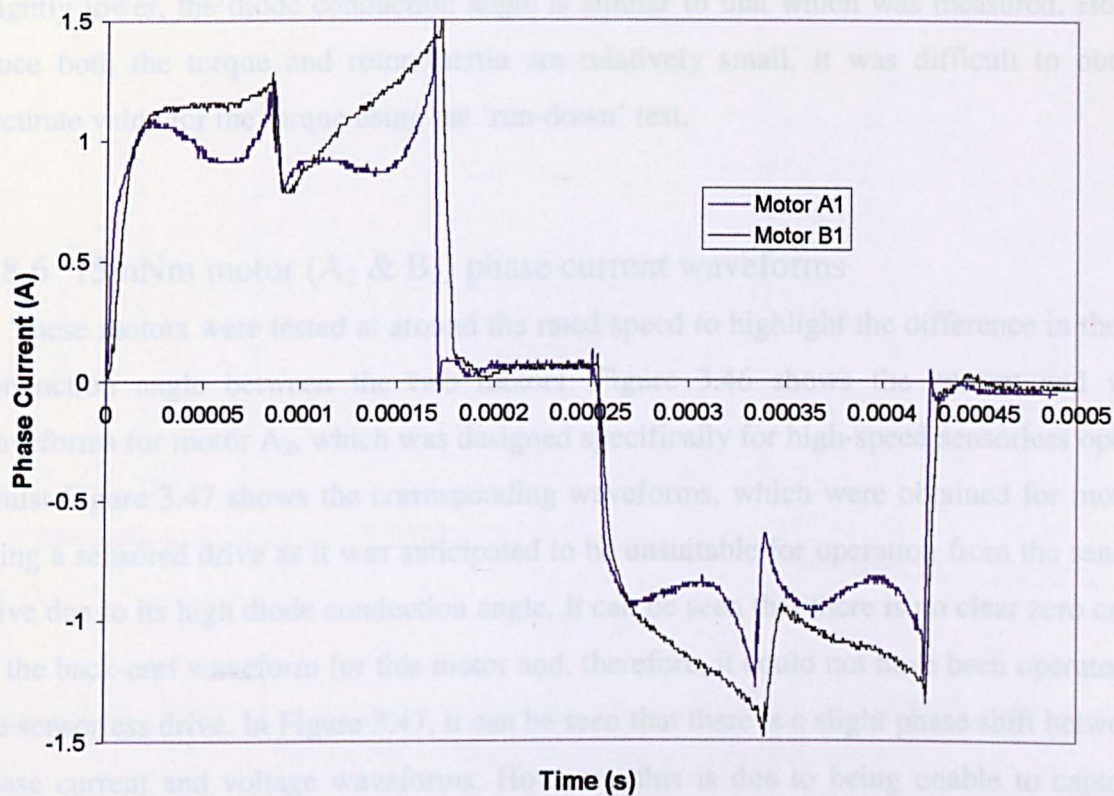
**Figure 3.43 - Comparison of predicted and measured back-emf waveforms for motor  $B_2$  with high diode conduction angle at  $\sim 65$ krpm**

### 3.8.4 Experimental method for performance measurement

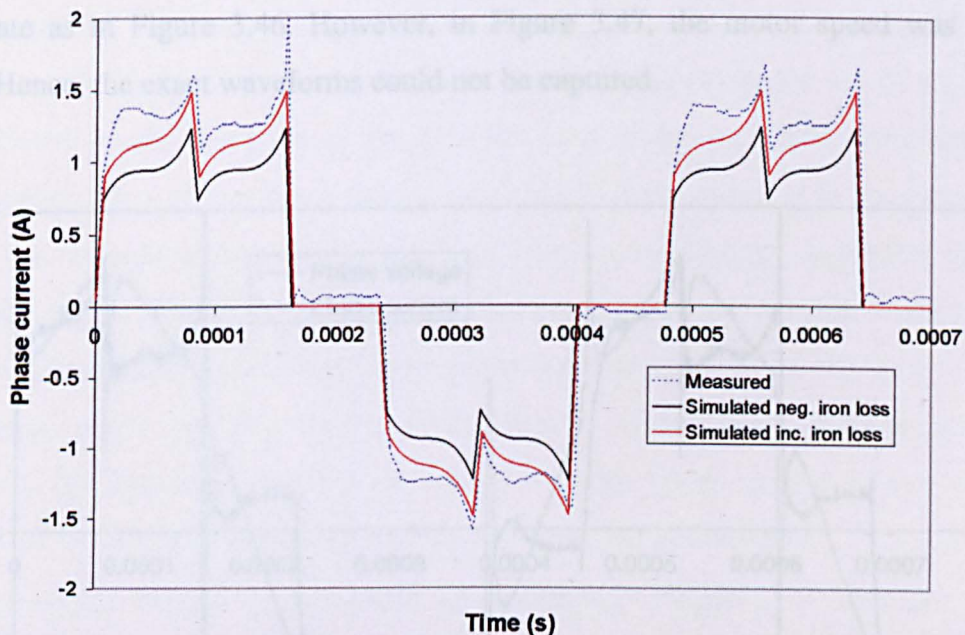
The experimental method employed is essentially identical to that which was employed in chapter 2. A specified DC link voltage was applied to the drive, and the motor was allowed to accelerate up to a steady-state speed. The DC link voltage, motor current, input power and speed were all captured by the data logging system described in Appendix D. Once steady-state had been achieved, the drive was disconnected and the motor was allowed to decelerate, whilst the speed against time curve was captured as accurately as the data logging would permit. Then, using the method which was first described in Chapter 2 and modified slightly in Appendix F, it was possible to calculate the torque. It should be noted that these tests were not conducted in a vacuum in order to allow the heat generated in the windings to be more easily dissipated. It is appreciated that this will increase the windage loss. However, as the rotors are relatively small with a smooth surface, it was anticipated that the windage loss would be minimal.

### 3.8.5 100mNm motor ( $A_1$ & $B_1$ ) phase current waveforms

When the two 100mNm motors were tested it was found that both were capable of being operated from the sensorless IC based drive at 120krpm. Investigations, described in Appendix F, confirmed that this was due to the torque measured by the 'run-down' test being significantly less than the rated torque. However a comparison of the motor phase currents shown in Figure 3.44 enables some significant observations to be made, viz., that the inductance of motor  $B_1$  is significantly higher than that of motor  $A_1$ . Consequently, the current waveform is significantly smoothed out during the on-period of the phase current, viz. periods  $1_b$  and  $2_a$  &  $2_b$  in Figure 3.4. Secondly, since the torque and the diode conduction angle are both low the current rise and decay times are comparable for both motors.



**Figure 3.44 - Comparison of phase current waveforms at ~119krpm**



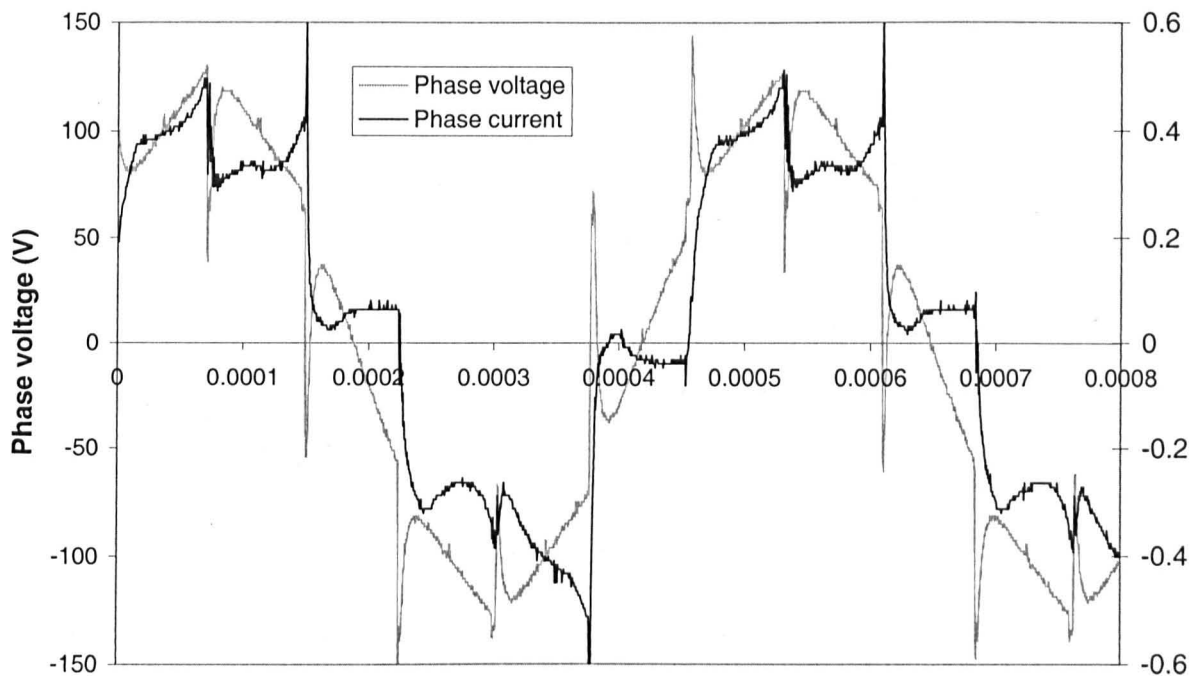
**Figure 3.45 - Comparison of measured and predicted current waveforms for 100mNm motor (A<sub>1</sub>) with low diode conduction angle at ~126krpm and 190Vdc**

Figure 3.45 compares measured and simulated phase current waveforms, for motor A<sub>1</sub>, with the motor speed and output torque being input parameters to the simulation together with the measured motor parameters. Simulations were undertaken both with and without the iron-loss torque being included. As can be seen, the predicted current waveform when the iron loss is accounted for compares favourably with the measured current waveform, and, despite being

slightly lower, the diode conduction angle is similar to that which was measured. However, since both the torque and rotor inertia are relatively small, it was difficult to obtain an accurate value for the torque using the ‘run-down’ test.

### 3.8.6 15mNm motor ( $A_2$ & $B_2$ ) phase current waveforms

These motors were tested at around the rated speed to highlight the difference in the diode conduction angle between the two motors. Figure 3.46 shows the current and voltage waveforms for motor  $A_2$ , which was designed specifically for high-speed sensorless operation whilst Figure 3.47 shows the corresponding waveforms, which were obtained for motor  $B_2$ , using a sensed drive as it was anticipated to be unsuitable for operation from the sensorless drive due to its high diode conduction angle. It can be seen that there is no clear zero crossing of the back-emf waveform for this motor and, therefore, it could not have been operated from the sensorless drive. In Figure 3.47, it can be seen that there is a slight phase shift between the phase current and voltage waveforms. However, this is due to being unable to capture the waveforms simultaneously on a digital oscilloscope. The scope captures channels in groups of 2 using the same trigger signal to start both captures, and works when the system is in a steady-state as in Figure 3.46. However, in Figure 3.47, the motor speed was fluctuating slightly. Hence, the exact waveforms could not be captured.



**Figure 3.46 - Phase current and phase voltage (to neutral) waveforms for motor  $A_2$  (Low diode conduction angle) at  $\sim 132$ krpm using a sensorless drive**

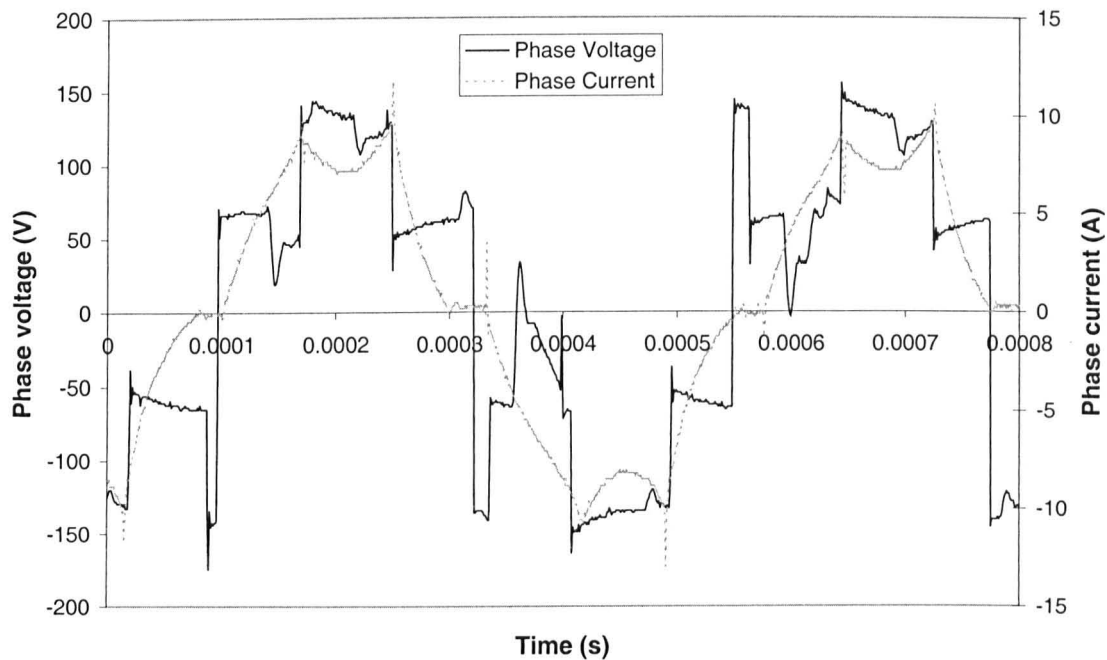


**Figure 3.47 - Phase current and voltage waveforms for motor B<sub>2</sub> (High diode conduction angle) at ~127k rpm using a sensed drive**

### 3.9 Summary

The benefits of a sensorless commutation strategy compared with employing discrete Hall or optical sensors for commutation have been discussed. However, the use of a commutation strategy based on the detection of the zero-crossing of the back-emf waveforms requires careful consideration of the motor design, particularly if the motor is to be operated at high speed. It has been demonstrated that the diode conduction is highly dependent on the stator flux density and to a lesser extent the rotor diameter. In general, a lower stator flux density leads to a lower diode conduction angle. However, this tends to be contrary to low-speed motor design where the flux density in the iron is usually high so as to achieve good utilisation of the lamination material and a large slot area, which leads to a lower copper loss. The effect of the iron loss on the motor design is discussed in Chapter 4.

Two prototype motors each capable of developing 100mNm at 120krpm have been designed to the same space envelope in order to show the importance of the motor design parameters. However, due to a smaller than anticipated bearing friction torque the actual load torque was considerably less than the expected 100mNm (as seen in Appendix F). Consequently, the diode conduction angle was less than expected. Therefore, two further prototype motors each capable of developing 15mNm at 120krpm were also designed and tested. It was shown that whilst the motor with the low diode conduction angle was capable of being operated from a sensorless drive at speeds in excess of 120krpm, the motor with the

high diode conduction angle could not be operated from a sensorless drive, and discrete commutation sensors were required.

However, it is recognised that this additional design criteria may result in non-optimal machine designs in terms of other performance factors. The extent to which this additional criteria impacts on the designs are very specific to the particular design specification. In the particular case studied in this chapter, the performance specification could be met whilst maintaining a low conduction angle. However, this will not be the case for all designs, particularly for machines with a very high power density, where the scope to trade-off axial length and number of series turns is more limited.

Clearly, a key consideration for emf-based sensorless operation is the diode conduction angle, and it was shown that this is highly dependent on the motor design and the load torque.

## Chapter 4 Optimal split ratio

### 4.1 Introduction

The ratio of the rotor outer diameter to the stator outer diameter, i.e. the split ratio, is one of the most important design parameters for permanent magnet machines, as it affects the efficiency and the maximum torque which can be achieved within a given volume envelope. Clearly, it is desirable to establish factors, which influence the optimal split ratio, and this will aid the initial choice of other dimensions. Even with the advent of fast computers and user-friendly finite element packages, which are capable of analysing a large number of motor designs in a short period of time, it is still necessary to initiate the design process by utilising appropriate analytical techniques.

[Hes87] investigated the optimum split ratio in a permanent magnet brushless DC motor whilst accounting for the copper loss and the influence of the winding design. Subsequent work [Cha93] yielded a simple expression for the optimum split ratio whilst again accounting for the copper loss in a distributed (overlapping) winding brushless motor topology, shown schematically in Figure 4.1a, but neglected the end-windings and the stator iron loss. It also assumed, for the slot area calculation, that the stator teeth had parallel sides, as illustrated in Figure 4.2(a), which also specifies the design parameters that were used in the derivation. However, most motors tend to have a stator geometry similar to that shown in Figure 4.2(b), in which tooth tips help focus the airgap flux. The work was subsequently extended [Cha00] to encompass the overall cost of a motor and the influence of the optimal split ratio assuming that the cost of the permanent magnets predominates. However, all the foregoing methods are appropriate only for brushless permanent magnet motors with distributed windings. Consequently, the expression for the optimal split ratio was extended in [Zhu97] for motors with a 2-pole diametrically magnetised rotor and a concentrated (non-overlapping) winding. The optimal split ratio as derived in previous work is appropriate only when the speed and/or pole number are low, since as these are increased the iron loss becomes significant, and will change the optimal split ratio.

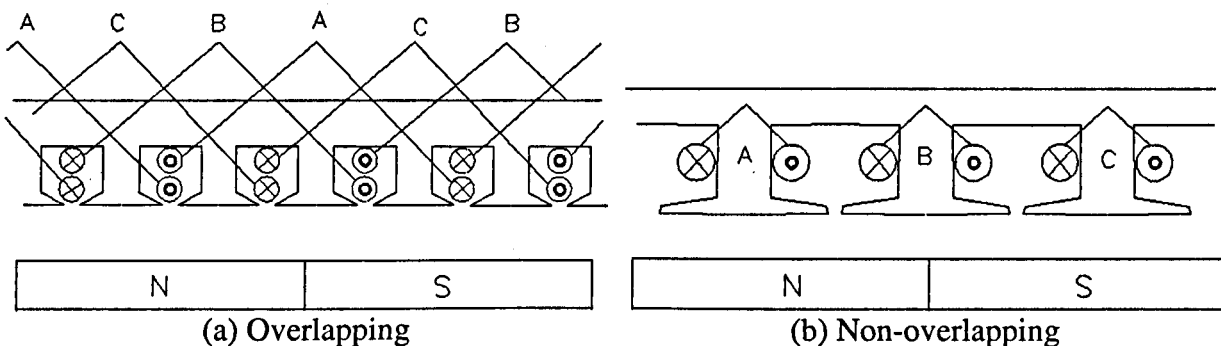
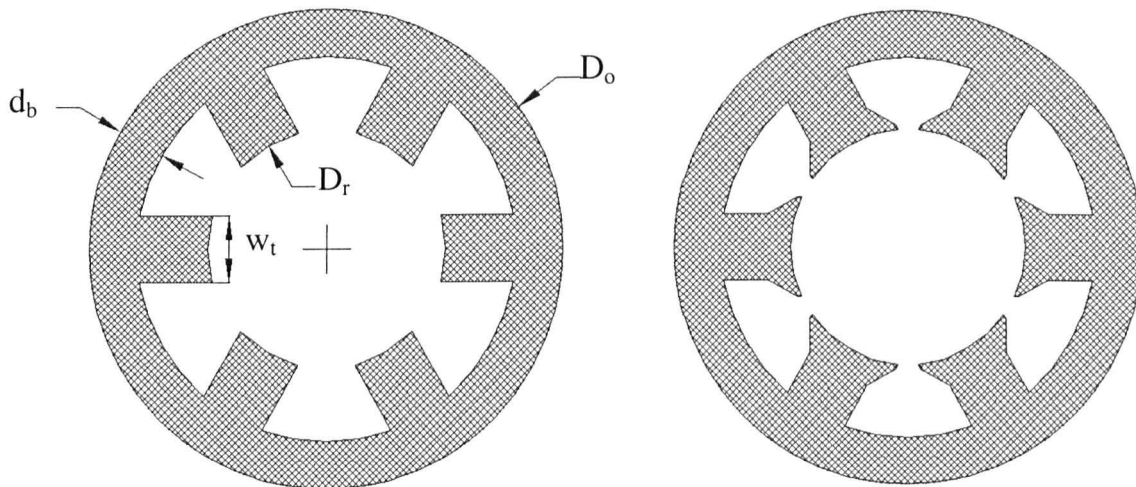


Figure 4.1 - Stator winding configurations



(a) Geometry assumed by [Cha93]

(b) Usual geometry

**Figure 4.2 – Stator lamination geometries**

In this chapter, the method for determining the optimal split ratio which was presented in [Cha93] will be extended to cater for machines with concentrated (non-overlapping) windings, shown schematically in Figure 4.1(b). In addition, rather than optimise the split ratio for maximum torque per volume, it will be optimised for minimum copper loss, and it will be shown that it results in the same optimal split ratio as that derived in [Cha93]. This will then be compared with the minimum copper loss motor design which was deduced by the CAD program described in detail in Chapter 3, which is capable of comprehensive design, analysis and synthesis, taking account of factors such as the presence of tooth tips, the end-windings, the winding inductances, the magnetisation distribution i.e. Halbach, radial or parallel, the airgap length, as well as magnetic circuit saturation. The model is then further developed to incorporate the influence of iron loss on the optimal split ratio, with the aid of CAD package. The influence of leading design/ performance parameters, such as the motor torque, stator flux density, active length, airgap length, speed and pole number is then investigated.

## 4.2 Simplified analytical technique for derivation of the optimal split ratio

Previous work [Cha93] yielded a simple expression for the optimal split ratio accounting only for the copper loss. Whilst this method has been extremely useful, the derivation only accounts for motors with the distributed overlapping windings. In this section the method is extended to cater for non-overlapping windings. Figure 4.3 shows the idealised flux paths for motors having overlapping and non-overlapping windings. As will be seen, for overlapping windings, the peak flux in the stator back-iron occurs when a magnet pole is aligned with the teeth as shown and is half of the total flux per pole. For non-overlapping windings, the flux divides evenly in the stator back-iron when a magnet pole is aligned with a stator tooth.

However, the peak flux occurs when a magnet pole is displaced by  $30^\circ$  electrical from a tooth, as shown in Figure 4.3(c), and  $2/3$  of the tooth flux passes circumferentially in one direction to an adjacent pole. However, this assumes that the permeability of the iron is not infinite, interpole flux leakage is negligible and a radial magnetisation distribution although similar principles apply to other magnetisation distributions.

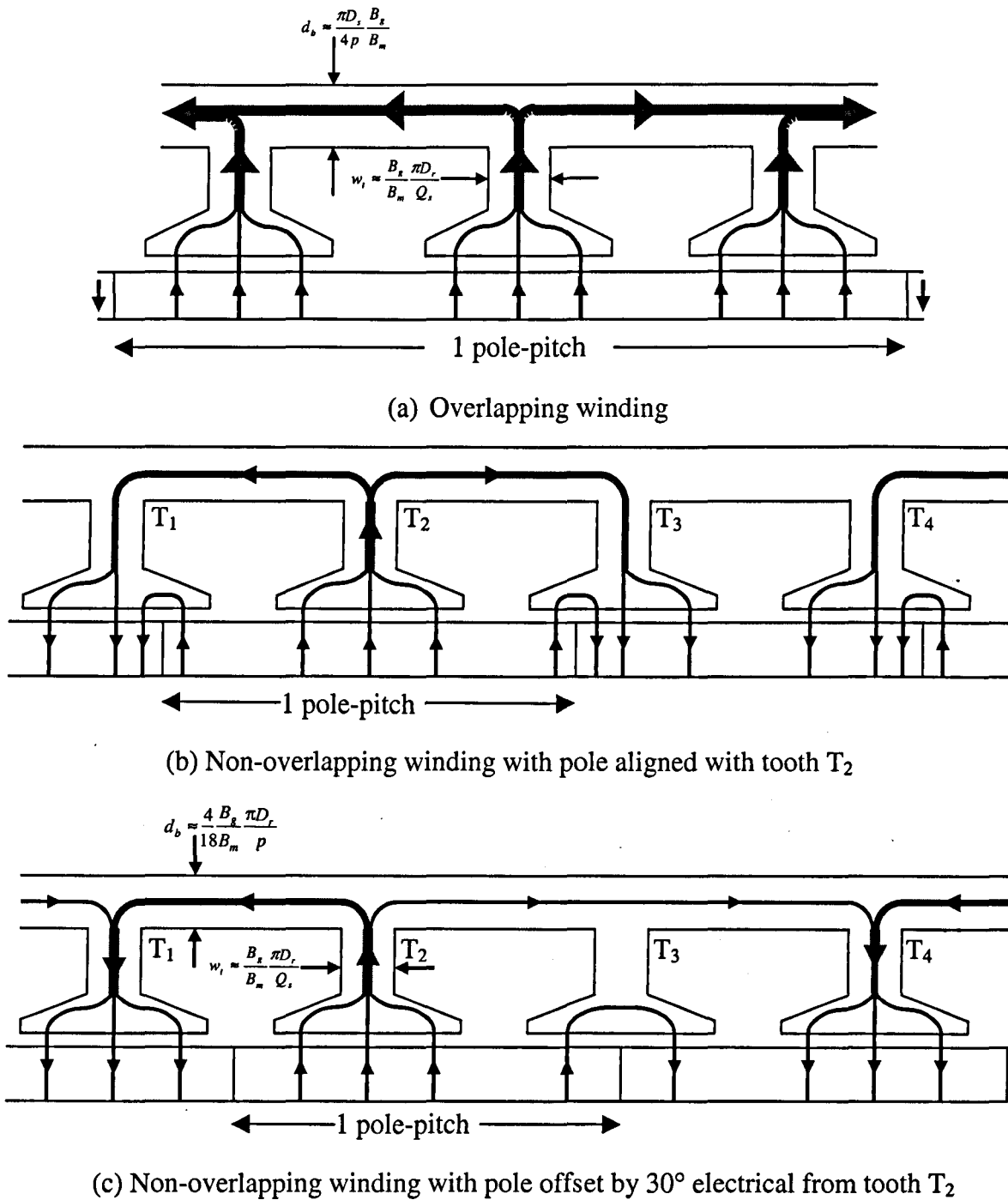


Figure 4.3 - Idealised flux paths for overlapping and non-overlapping windings

### 4.2.1 Distributed (overlapping) winding

The standard torque equation for permanent magnet DC motors is:

$$T = \frac{1}{2} \pi D_r^2 l_a B_g Q \quad (4.1)$$

where  $Q = \frac{J A_s k_p Q_s K_w}{\pi D_r} \quad (4.2)$

$$P = I^2 R = (J A_s k_p)^2 \rho \frac{Q_s l_a}{A_s k_p} = J^2 A_s k_p \rho Q_s l_a \quad (4.3)$$

Assuming all the generated heat is dissipated evenly from the outer surface of a motor, then the temperature for a given power dissipation and a constant copper loss can be shown to be approximately equal to:

$$P \approx h_i \pi D_o l_a \quad (4.4)$$

Equations 4.3 and 4.4, again assuming a given loss, can be combined to give the current density  $J$ :

$$J = \sqrt{\frac{h_i \pi D_o}{A_s k_p \rho Q_s}} \quad (4.5)$$

where:  $h_i$  = heat transfer coefficient

$k_p$  = slot packing factor

$l_a$  = active length

$Q_s$  = number of slots

$D_r$  = rotor outer diameter

$D_o$  = motor outside diameter

$B_g$  = average airgap flux density

$K_w$  = winding coefficient

$A_s$  = slot area

$\rho$  = resistivity of copper  $1.7 \times 10^{-8} \Omega \text{m}^{-1}$  at  $20^\circ \text{C}$

Neglecting the tooth tips and assuming a constant flux density throughout the stator core and assuming that the teeth capture all the flux available from the rotor magnets, then the slot area ( $A_s$ ) available for the winding is given by:

$$A_s = \frac{1}{Q_s} \left\{ \pi \frac{(D_o - 2d_b)^2}{4} - \pi \frac{D_r^2}{4} \right\} - w_t \left\{ \frac{D_o - D_r}{2} - d_b \right\} \quad (4.6)$$

where  $w_t \approx \frac{B_g \pi D_r}{B_m Q_s} \quad (4.7)$

If the airgap flux density is  $B_g$ , then the flux per pole at the stator surface is:

$$\Phi_p = \frac{\pi D_s l_a}{2p} B_g \quad (4.8)$$

It can be shown that for motors in which  $Q_s=6$  times the number of pole-pairs, i.e. having overlapping windings, then the stator back-iron carries a maximum flux of  $\frac{1}{2}$  the total flux per pole.

$$\therefore B_m \approx \frac{\Phi_p / 2}{d_b l_a} \quad (4.8)$$

$$\text{then, } d_b \approx \frac{\pi D_s B_g}{4p B_m} \quad (4.10)$$

Assuming that the airgap is sufficiently small that  $D_s \approx D_r$ , and substituting 4.10 & 4.7 into 4.6 gives:

$$A_s = \frac{1}{Q_s} \left[ \frac{\pi}{4} \left( D_o - \frac{B_g \pi D_r}{B_m 2p} \right)^2 - \pi \frac{D_r^2}{4} \right] - \frac{B_g \pi D_r}{B_m Q_s} \left( \frac{D_o}{2} - \frac{D_r}{2} - \frac{B_g \pi D_r}{B_m 4p} \right) \quad (4.11)$$

which can be rearranged to give:

$$A_s = \frac{\pi D_o^2}{4 Q_s} \left\{ 1 - \left[ 2 \left( \frac{B_g}{B_m} \right) \left( \frac{\pi}{2p} + 1 \right) \right] \left( \frac{D_r}{D_o} \right) + \left[ \left( \frac{B_g}{B_m} \right)^2 \frac{\pi}{2p} \left( \frac{\pi}{2p} + 2 \right) + 2 \left( \frac{B_g}{B_m} \right) - 1 \right] \left( \frac{D_r}{D_o} \right)^2 \right\} \quad (4.12)$$

Substituting 4.2 & 4.5 into 4.1 gives:

$$T = \frac{1}{3} B_g l_a \sqrt{\frac{h_i \pi Q_s k_p}{\rho}} D_r \sqrt{D_o A_s} \quad (4.13)$$

Using equation 4.13, a series of graphs can be drawn to show how the maximum torque varies as a function of the split ratio, as can be seen in Figure 4.4 & [Cha93] for a motor having an outer diameter of 100mm and an active length of 100mm, the thermal coefficient  $h_i$  being  $10 \text{ W/m}^2$ . As shown, there is an optimum torque for a specified stator flux density ( $B_m$ ) and pole number, although the actual torque will depend on the motor size and the value of the thermal dissipation coefficient. From this figure it can be seen that the optimum torque is related to both the split ratio ( $D_r/D_o$ ) and the pole number.

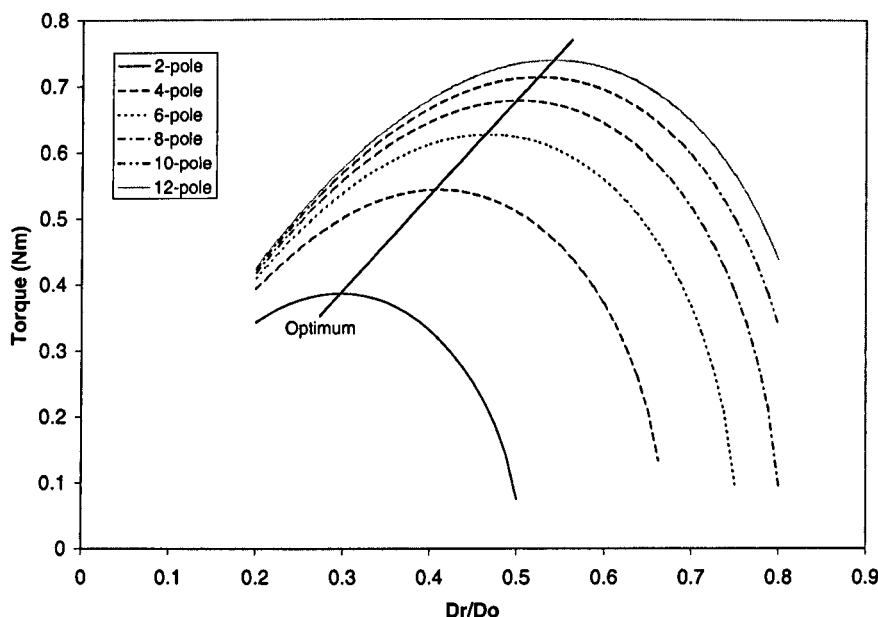


Figure 4.4 - Output torque against split ratio ( $B_m=1.6T$ ,  $B_g=1.0T$ )

The active volume of a motor is:

$$V = \pi \left( \frac{D_o}{2} \right)^2 l_a, \text{ and the torque per volume is given as:}$$

$$\frac{T}{V} = \frac{4}{\pi 3} B_g \sqrt{\frac{h_i \pi Q_s k_p}{\rho}} \sqrt{\frac{D_r^2}{D_o^3} A_s}$$

$$\frac{T}{V} = B_g \frac{2}{3} \sqrt{\frac{h_i k_p}{p}} \sqrt{D_o}$$

$$\cdot \left[ \sqrt{\left( \frac{D_r}{D_o} \right)^2 \left\{ 1 - \left[ 2 \left( \frac{B_g}{B_m} \right) \left( \frac{\pi}{2p} + 1 \right) \right] \left( \frac{D_r}{D_o} \right) + \left[ \left( \frac{B_g}{B_m} \right)^2 \frac{\pi}{2p} \left( \frac{\pi}{2p} + 2 \right) + 2 \left( \frac{B_g}{B_m} \right) - 1 \right] \left( \frac{D_r}{D_o} \right)^2 \right\}} \right] \quad (4.14)$$

If the outer diameter is fixed, then differentiating with respect to  $\left( \frac{D_r}{D_o} \right)$  gives:

$$\begin{aligned} & \frac{d \left( \frac{T}{V} \right)}{d \left( \frac{D_r}{D_o} \right)}_{D_o=\text{const}} \\ &= \frac{d}{d \left( \frac{D_r}{D_o} \right)} \left\{ \left( \frac{D_r}{D_o} \right)^2 - \left[ 2 \left( \frac{B_g}{B_m} \right) \left( \frac{\pi}{2p} + 1 \right) \right] \left( \frac{D_r}{D_o} \right)^3 + \left[ \left( \frac{B_g}{B_m} \right)^2 \frac{\pi}{2p} \left( \frac{\pi}{2p} + 2 \right) + 2 \left( \frac{B_g}{B_m} \right) - 1 \right] \left( \frac{D_r}{D_o} \right)^4 \right\} \\ &= 0 \\ &= 2 \left( \frac{D_r}{D_o} \right) - 6 \left[ \left( \frac{B_g}{B_m} \right) \left( \frac{\pi}{2p} + 1 \right) \right] \left( \frac{D_r}{D_o} \right)^2 + 4 \left[ \left( \frac{B_g}{B_m} \right)^2 \frac{\pi}{2p} \left( \frac{\pi}{2p} + 2 \right) + 2 \left( \frac{B_g}{B_m} \right) - 1 \right] \left( \frac{D_r}{D_o} \right)^3 = 0 \quad (4.15) \end{aligned}$$

By analogy with  $ax^2+bx+c=0$ ,

$$2\left[\left(\frac{B_g}{B_m}\right)^2 \frac{\pi}{2p}\left(\frac{\pi}{2p}+2\right)+2\left(\frac{B_g}{B_m}\right)-1\right]\left(\frac{D_r}{D_o}\right)^2 - 3\left[\left(\frac{B_g}{B_m}\right)\left(\frac{\pi}{2p}+1\right)\right]\left(\frac{D_r}{D_o}\right)+1=0 \quad (4.16)$$

$$\text{Optimal } \left(\frac{D_r}{D_o}\right) = \frac{b - \sqrt{b^2 - 4a}}{2a} \quad (4.17)$$

$$\text{where } a = 2\left[\left(\frac{B_g}{B_m}\right)^2 \frac{c\pi}{2p}\left(\frac{c\pi}{2p}+2\right)+2\left(\frac{B_g}{B_m}\right)-1\right] \quad (4.18)$$

$$b = 3\left[\left(\frac{B_g}{B_m}\right)\left(\frac{c\pi}{2p}+1\right)\right] \quad (4.19)$$

$$c=1 \quad (4.20)$$

Although in this case  $c=1$ , it is included here to facilitate a comparison with the analysis of non-overlapping winding motors, which is covered in the next section. From the above expression, it is possible to generate curves showing how the maximum torque per volume for different  $D_r/D_o$  ratios varies with the airgap flux density, the pole number and the stator flux density, as shown in Figure 4.5. It can be seen that a higher stator flux density leads to a higher split ratio, which becomes less sensitive to the airgap flux density. It can be seen that the optimum split ratio increases with the pole number and  $B_m$  but decreases with  $B_g$ . However, a higher pole number results in a higher fundamental operating frequency, which, in turn, can have an adverse affect on the motor efficiency, as will be seen later.

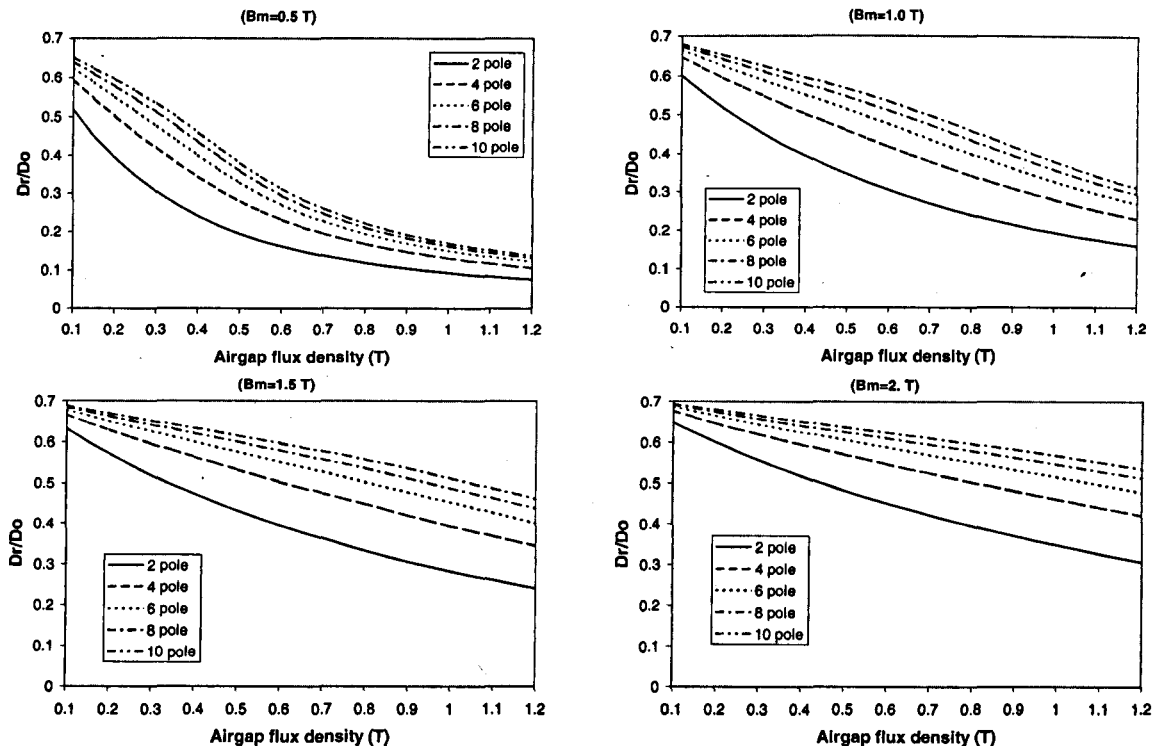


Figure 4.5 - Optimal split ratio for varying airgap length, stator flux density and different pole number

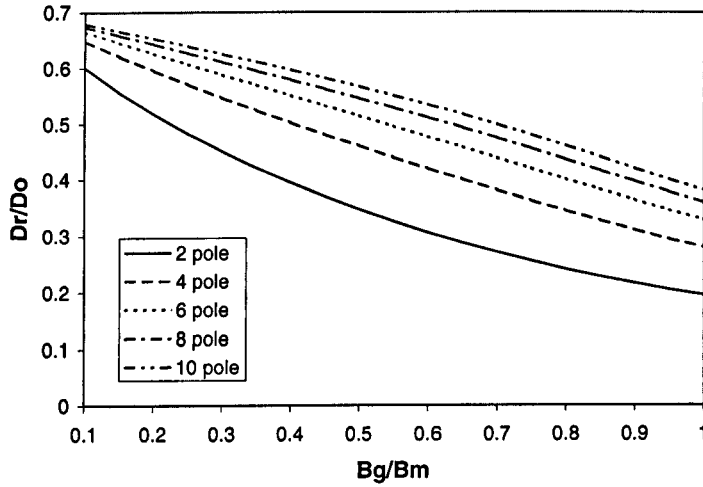


Figure 4.6- Variation of optimal split ratio with  $B_g/B_m$

Whilst Figure 4.5 shows the effect of  $B_g$  and  $B_m$  individually on the optimal split ratio, it is the ratio of  $B_g/B_m$  in equations 4.7 to 4.19 which affects the optimal split ratio, as shown in Figure 4.6.

#### 4.2.2 Concentrated (non-overlapping) winding

A non-overlapping winding is favoured for many permanent magnet brushless machines due to its simplicity. It is shown earlier that for motors in which  $Q_s=3$  times the number of pole-pairs then the peak flux in the stator-back iron occurs when a pole is  $30^\circ$  electrical offset from a stator tooth. The flux path through the back-iron does not divide equally, and the peak flux in the back iron is  $\sim 2/3$  of the maximum flux through a tooth. When the tooth body flux density is the same as the flux density in the stator back-iron then, as  $Q_s=3p/2$ , the required radial thickness of the back-iron is given by:

$$d_b \approx \frac{2}{3} w_t \approx \frac{4 B_g \pi D_r}{18 B_m p} \quad (4.21)$$

$$A_s = \frac{1}{Q_s} \left\{ \pi \frac{(D_o - 2d_b)^2}{4} - \pi \frac{D_r^2}{4} \right\} - w_t \left\{ \frac{D_o - D_r}{2} - d_b \right\} \quad (4.22)$$

Using the equation for  $A_s$  which was specified previously, which is restated in 4.22, it can be rearranged to incorporate the new radial thickness of the back-iron and the tooth body width:

$$A_s = \frac{1}{Q_s} \left[ \pi \left( D_o - \frac{8 B_g \pi D_r}{18 B_m p} \right)^2 - \pi \frac{D_r^2}{4} \right] - \frac{B_g \pi D_r}{B_m Q_s} \left( \frac{D_o}{2} - \frac{D_r}{2} - \frac{4 B_g \pi D_r}{18 B_m p} \right) \quad (4.23)$$

which can then be rearranged to give:

$$A_s = \frac{\pi D_o^2}{4 Q_s} \left\{ 1 - \left[ 2 \left( \frac{B_g}{B_m} \right) \left( \frac{8\pi}{18p} + 1 \right) \right] \left( \frac{D_r}{D_o} \right) + \left[ \left( \frac{B_g}{B_m} \right)^2 \frac{8\pi}{18p} \left( \frac{8\pi}{18p} + 2 \right) + 2 \left( \frac{B_g}{B_m} \right) - 1 \right] \left( \frac{D_r}{D_o} \right)^2 \right\} \quad (4.24)$$

The torque per volume is then given as:

$$\frac{T}{V} = B_g \frac{2}{3} \sqrt{\frac{h_i k_p}{p}} \sqrt{D_o} \cdot \left[ \sqrt{\left( \frac{D_r}{D_o} \right)^2 \left\{ 1 - \left[ 2 \left( \frac{B_g}{B_m} \right) \left( \frac{8\pi}{18p} + 1 \right) \right] \left( \frac{D_r}{D_o} \right) + \left[ \left( \frac{B_g}{B_m} \right)^2 \frac{8\pi}{18p} \left( \frac{8\pi}{18p} + 2 \right) + 2 \left( \frac{B_g}{B_m} \right) - 1 \right] \left( \frac{D_r}{D_o} \right)^2 \right\}} \right] \quad (4.25)$$

Then, as before, differentiating with respect to  $\left( \frac{D_r}{D_o} \right)$  gives:

$$\begin{aligned} & \frac{d\left(\frac{T}{V}\right)}{d\left(\frac{D_r}{D_o}\right)}_{D_o=const} \\ &= \frac{\partial}{\partial\left(\frac{D_r}{D_o}\right)} \left\{ \left( \frac{D_r}{D_o} \right)^2 - \left[ 2 \left( \frac{B_g}{B_m} \right) \left( \frac{8\pi}{18p} + 1 \right) \right] \left( \frac{D_r}{D_o} \right)^3 + \left[ \left( \frac{B_g}{B_m} \right)^2 \frac{8\pi}{18p} \left( \frac{8\pi}{18p} + 2 \right) + 2 \left( \frac{B_g}{B_m} \right) - 1 \right] \left( \frac{D_r}{D_o} \right)^4 \right\} \\ &= 0 \\ & 2 \left( \frac{D_r}{D_o} \right) - 6 \left[ \left( \frac{B_g}{B_m} \right) \left( \frac{8\pi}{18p} + 1 \right) \right] \left( \frac{D_r}{D_o} \right)^2 + 4 \left[ \left( \frac{B_g}{B_m} \right)^2 \frac{8\pi}{18p} \left( \frac{8\pi}{18p} + 2 \right) + 2 \left( \frac{B_g}{B_m} \right) - 1 \right] \left( \frac{D_r}{D_o} \right)^3 = 0 \quad (4.26) \end{aligned}$$

$$\text{Optimal } \left( \frac{D_r}{D_o} \right) = \frac{b - \sqrt{b^2 - 4a}}{2a} \quad (4.27)$$

$$\text{where } a = 2 \left[ \left( \frac{B_g}{B_m} \right)^2 \frac{c\pi}{2p} \left( \frac{c\pi}{2p} + 2 \right) + 2 \left( \frac{B_g}{B_m} \right) - 1 \right] \quad (4.28)$$

$$b = 3 \left[ \left( \frac{B_g}{B_m} \right) \left( \frac{c\pi}{2p} + 1 \right) \right] \quad (4.29)$$

$$c = \frac{8}{9} \quad (4.30)$$

The only difference between the two winding configurations is the value of the constant 'c' in equations 4.20 & 4.30. As was the case for the overlapping winding, the optimal split ratio depends on the ratio of  $B_g/B_m$ , as can be seen from equation 4.27 to 4.29 and Figure 4.7. By way of example, the optimal split ratio for both winding configurations and for various pole

numbers are compared in Figure 4.8. It can be seen that for low values of  $B_g$  the optimal split ratios are almost identical, whilst a significant difference exists for higher values of  $B_g$  due to the slight change in the radial thickness of the stator back-iron.

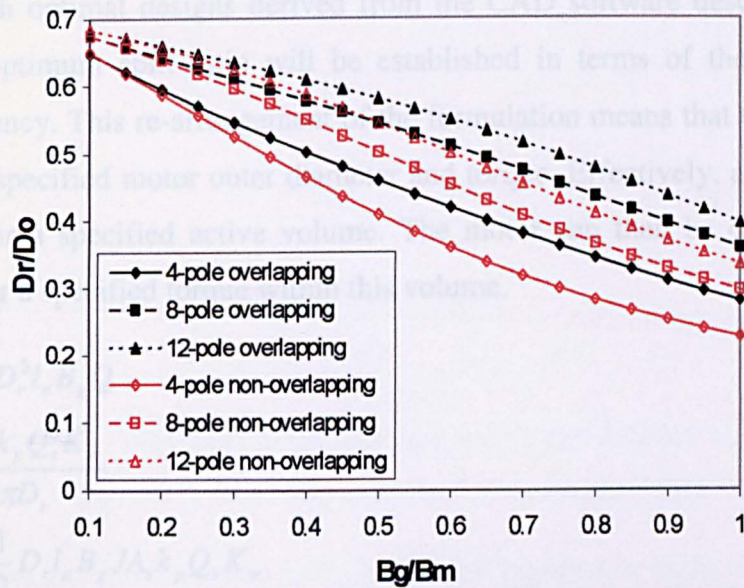


Figure 4.7 – Variation of optimal split ratio with  $B_g/B_m$

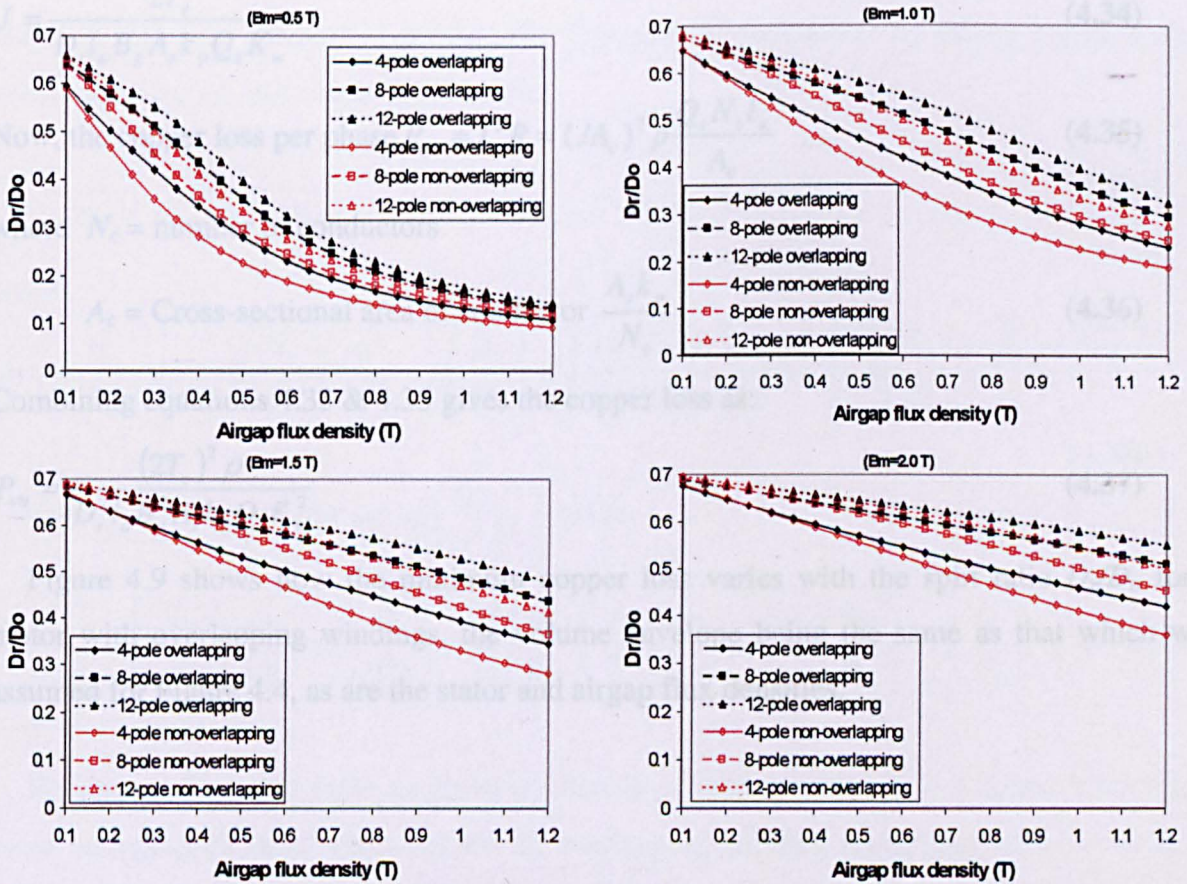


Figure 4.8 - Comparison of optimum split ratio for motors with overlapping and non-overlapping windings

### 4.2.3 Optimum split ratio for minimum copper loss

Whilst the expressions for the optimal split ratio that has been derived so far are useful, when the model is extended to cater for iron loss the complexity is such that a simple expression for the optimal split ratio cannot be derived. Consequently, to enable meaningful comparisons with optimal designs derived from the CAD software described previously in chapter 3, the optimum split ratio will be established in terms of the minimum loss, or maximum efficiency. This re-arrangement of the formulation means that the minimum loss is calculated for a specified motor outer diameter and torque. Effectively, an optimal split ratio will be found for a specified active volume. The motor can then be designed to give the minimum loss for a specified torque within this volume.

$$\text{Since } T_e = \frac{1}{2} \pi D_r^2 l_a B_g Q \quad (4.31)$$

$$\text{and } Q = \frac{J A_s k_p Q_s K_w}{\pi D_r} \quad (4.32)$$

$$\text{Therefore, } T_e = \frac{1}{2} D_r l_a B_g J A_s k_p Q_s K_w \quad (4.33)$$

which can be re-arranged to give the current density  $J$

$$J = \frac{2T_e}{D_r l_a B_g A_s k_p Q_s K_w} \quad (4.34)$$

$$\text{Now, the copper loss per phase } P_{cu} = I^2 R = (J A_c)^2 \rho \frac{Q_s N_c l_a}{A_c} \quad (4.35)$$

where  $N_c$  = number of conductors

$$A_c = \text{Cross-sectional area of conductor } \frac{A_s k_p}{N_c} \quad (4.36)$$

Combining equations 4.33 & 4.35 gives the copper loss as:

$$P_{cu} = \frac{(2T_e)^2 \rho}{D_r^2 l_a B_g^2 A_s k_p Q_s K_w^2} \quad (4.37)$$

Figure 4.9 shows how the minimum copper loss varies with the split ratio  $D_r/D_o$  for a motor with overlapping windings, the volume envelope being the same as that which was assumed for Figure 4.4, as are the stator and airgap flux densities.

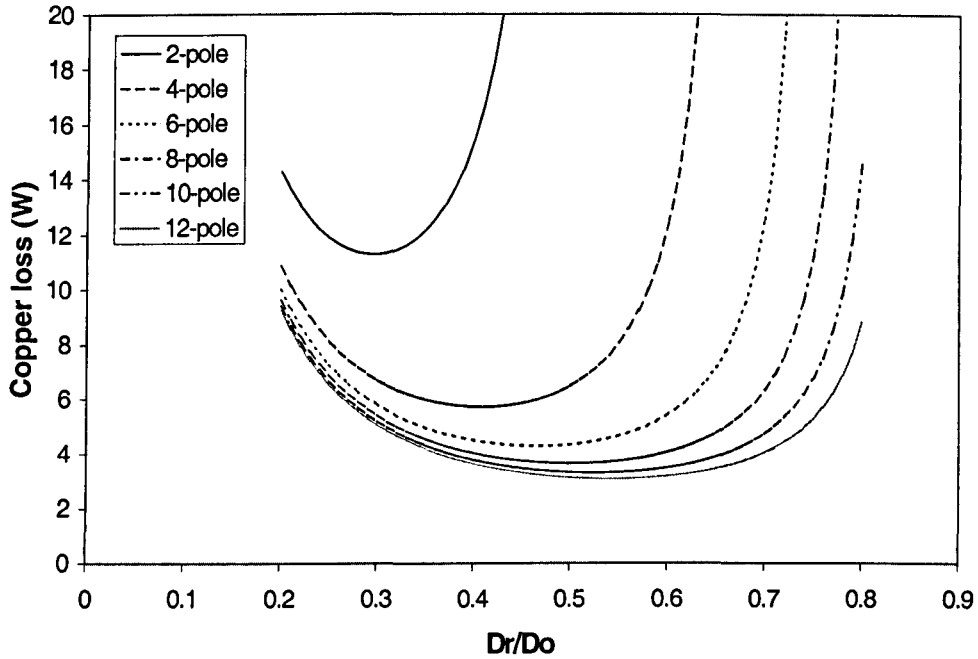


**Figure 4.9 - Variation of copper loss with pole number and  $D_r/D_o$**   
 ( $B_g=1.0T$ ,  $B_m=1.6T$ ,  $l_a=0.1m$ ,  $D_o=0.1m$ ,  $T_e=2Nm$ )

From inspection of Figure 4.9 and comparing with Figure 4.4, as in Figure 4.10, it can be seen that the minimum copper loss and the maximum torque both occur at the same split ratio. This is because the equation for minimum copper loss derived here is essentially the same equation that was established previously. This can be understood by taking equation 4.37, substituting for  $A_s$ , and rearranging to give:

$$P_{cu} = \frac{16T_e^2 \rho}{\pi D_o^4 l_a B_g^2 k_p K_w^2} \cdot \frac{1}{A_s} \quad (4.38a)$$

where

$$A_s = \left(\frac{D_r}{D_o}\right)^2 \left\{ 1 - \left[ 2\left(\frac{B_g}{B_m}\right)\left(\frac{c\pi}{2p} + 1\right) \right] \left(\frac{D_r}{D_o}\right) + \left[ \left(\frac{B_g}{B_m}\right)^2 \frac{c\pi}{2p} \left(\frac{c\pi}{2p} + 2\right) + 2\left(\frac{B_g}{B_m}\right) - 1 \right] \left(\frac{D_r}{D_o}\right)^2 \right\} \quad (4.38b)$$

Differentiating  $A_s$  with respect to  $\left(\frac{D_r}{D_o}\right)$  gives:

$$2\left(\frac{D_r}{D_o}\right) - 6\left[\left(\frac{B_g}{B_m}\right)\left(\frac{c\pi}{2p} + 1\right)\right]\left(\frac{D_r}{D_o}\right)^2 + 4\left[\left(\frac{B_g}{B_m}\right)^2 \frac{c\pi}{2p} \left(\frac{c\pi}{2p} + 2\right) + 2\left(\frac{B_g}{B_m}\right) - 1\right]\left(\frac{D_r}{D_o}\right)^3 = 0 \quad (4.39)$$

Equation 4.39 is the same as given previously in sections 4.2.1 & 4.2.2, and leads to the same optimal split ratio when  $c=1$  for an overlapping winding motor and when  $c=8/9$  for a non-overlapping winding motor.

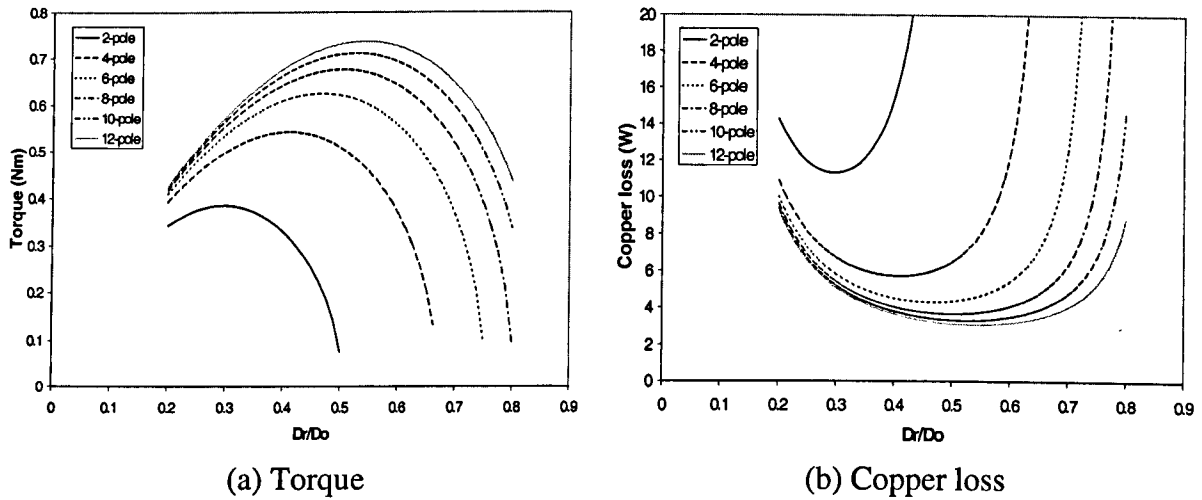


**Figure 4.10 – Influence of split ratio and pole number on torque and copper loss**

From the foregoing it is possible to compare the optimal split ratio as defined by [Cha93] with that derived from the CAD software, in order to investigate the influence of end-winding length, airgap length and the stator tooth tips on the motor copper loss, and, hence, optimal split ratio.

#### 4.2.4 Comparison between optimal split ratio derived from CAD package and analytical expression

Using the CAD software described in Chapter 3, it is possible to calculate the copper loss for a constant volume envelope as the rotor diameter is varied. In the example shown in Figure 4.11 the outer diameter and active length are constrained to be 100mm and 25mm, respectively, the design torque is 0.7 Nm at a speed of 120krpm, the airgap length and the magnet thickness are both 3mm, and the maximum stator flux density is fixed at 1.6 T.

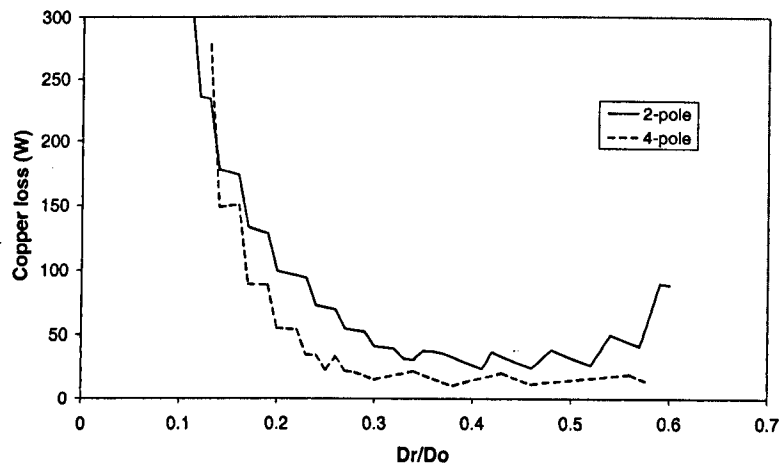


**Figure 4.11 - Copper loss from CAD software**

From Figure 4.11, it can be seen that for a 2-pole motor there is minimum copper loss for a split ratio of between 0.4 and 0.5. However, for a 4-pole motor the optimum split ratio is less obvious, but appears to be nearly at a ratio of 0.6 as will be seen later. It is hard to determine the optimal split ratio exactly due to jagged nature of the curves in Figure 4.11, which is due to the fact that the windings are designed to have an integer number of conductors, as covered in Appendix G.

As the CAD software takes into account the changing magnet volume as the rotor diameter is increased then, as can be seen from Figure 4.12, the airgap flux density ( $B_g$ ) also increases with the split ratio for a 2-pole motor design and a constant airgap length.

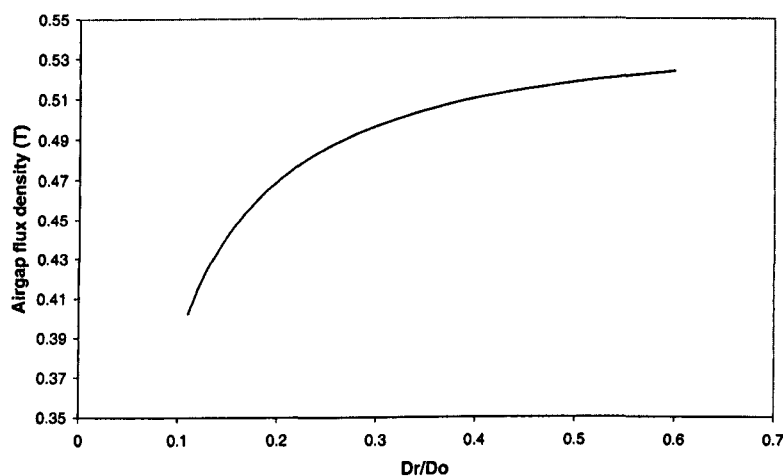


**Figure 4.12 - Variation of airgap flux density with  $D_r/D_o$**

However, the simple analytical expression derived in sections 4.2.1 & 4.2.2 assumes a constant ratio of airgap flux density to stator flux density, which, therefore, equates to a fixed airgap flux density for a given stator flux density. Thus, the average airgap flux density value of 0.49T is assumed in the analytical calculation of copper loss using the same parameters as specified for the CAD software. The resulting copper loss is shown in Figure 4.13 where it can be seen that the minimum copper loss for the 4-pole motor occurs around a split ratio of 0.6.

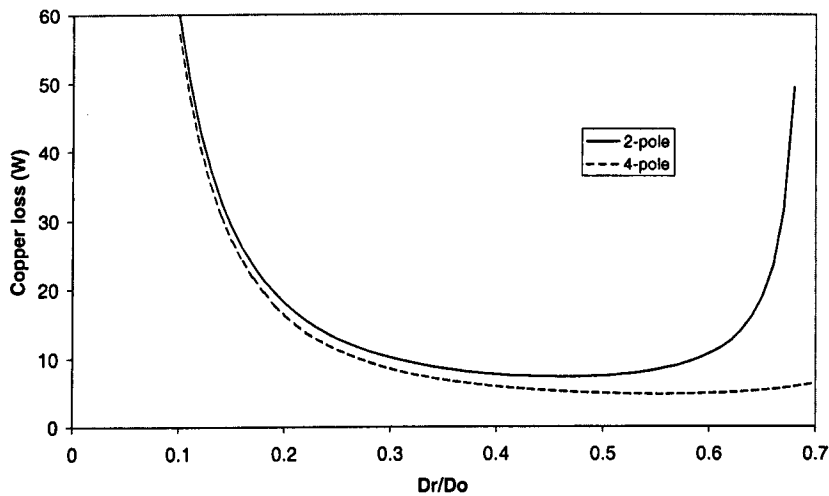
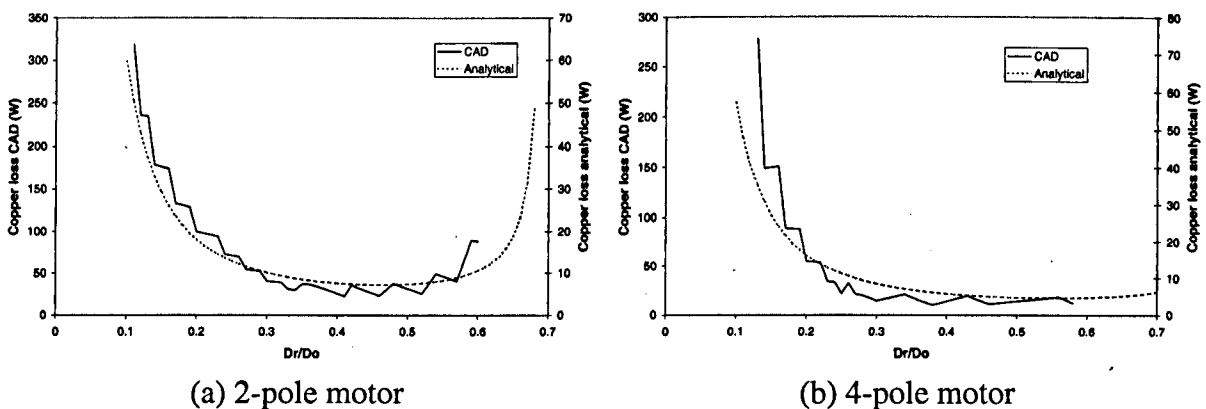


**Figure 4.13 - Copper loss predicted by analytical expression**

As can be seen by comparing Figures 4.11 & 4.13, as is done in Figure 4.14, although the magnitude of the copper loss predicted from the two different methods is significantly different, the general shape of the curves is similar, as are the optimal  $D_r/D_o$  ratios. The difference in magnitude is due mainly to the fact that the analytical method neglects the copper loss in the end-windings, the volume of the end-windings being considerably larger than the volume of the active section of the windings.



(a) 2-pole motor

(b) 4-pole motor

**Figure 4.14 - Comparison between CAD and simple expression for 2 & 4-pole motor winding**

### 4.3 Optimal split ratio accounting for both iron and copper loss

So far, the optimal split ratio has only considered the stator winding copper loss. For high-speed motors or motors with high pole numbers the fundamental electrical frequency can be very high (typically  $\geq 2\text{kHz}$ ) and consequently the no-load iron loss becomes significant and, indeed, tends to be the dominant loss component. The iron loss is dependent on the volume of the laminated stator core and the stator flux density. The influence of various design

parameters on the iron loss and optimal split ratio were investigated, and it will be shown that for a high-speed application the optimal split ratio when iron loss is accounted for is significantly different from that deduced from the analytical method covered in section 4.2, which only accounted for the copper loss. For high-speed motors the torque is correspondingly lower than for an equivalent low speed motor of the same power rating and, consequently, the iron loss tends to be the dominant loss component [Hes87][Pic96]. In the investigations which follow, the active volume is kept constant, unless otherwise stated, to allow the influence of various design parameters on the optimal split ratio to be more easily observed. However, it is appreciated that for some designs covered here, a smaller active volume would lead to a higher efficiency motor, and for other designs a larger active volume would result in a more efficient motor, but the volume is kept constant to facilitate comparisons to be made.

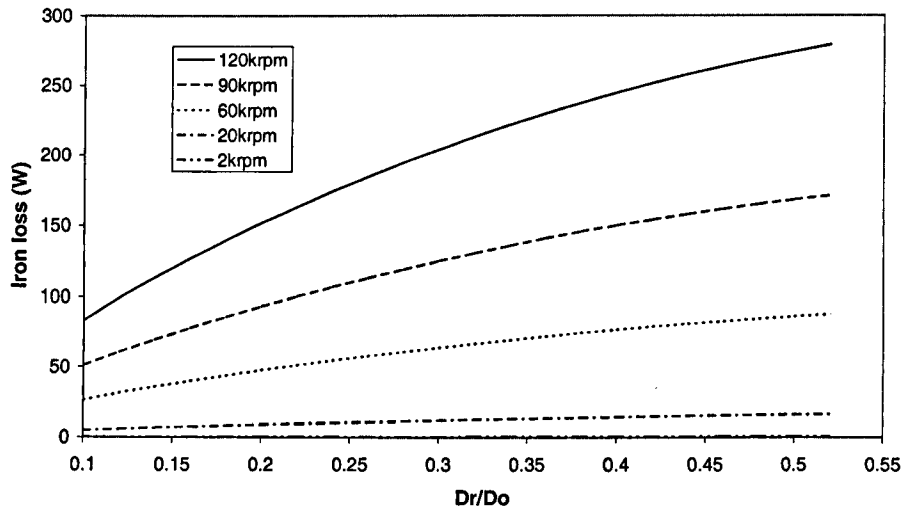
As the iron loss is highly dependent on the stator flux density and the volume of lamination material, then some additional constraints have to be defined at this stage. Unless otherwise stated in the sections which follow, the motor dimensions / properties are as defined below. For simplicity and as an example only one magnetisation distribution, diametric, is considered. Only the no-load iron loss is considered, details on the iron-loss calculation being given in Appendix C

- Lamination outer diameter, ( $D_o$ ), 100mm
- DC link voltage, 200V
- Speed, 120krpm
- Torque, ( $T_e$ ), 0.1,0.3,0.5,0.7 Nm
- Airgap length, ( $g$ ), 3mm
- Stator flux density, ( $B_m$ ), 0.7,1.1,1.5 T
- Lamination axial length, ( $l_a$ ) 25mm
- Copper space factor, ( $k_p$ ), 0.3
- Magnet remanence, ( $B_r$ ), 1.2 T (sintered NdFeB magnets) 3mm thick
- 2-pole parallel magnetisation
- Thermal effects neglected
- Lamination material, Transil 335

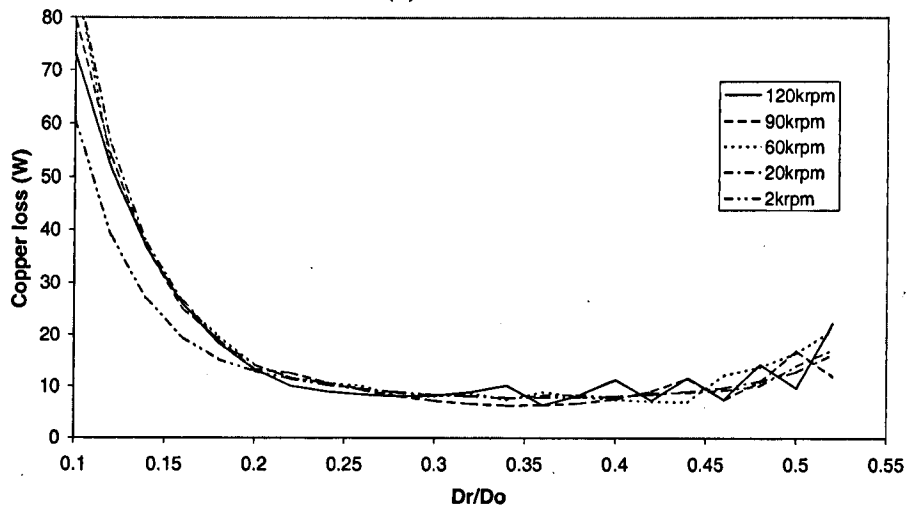
#### **(a) Combination of iron and copper loss**

As mentioned previously in section 4.1, the iron loss is usually minimal at low speeds, as can be seen in Figure 4.15(a) where, for a stator flux density of 1.1T and a speed of 2krpm,

the iron loss is  $<10$  W irrespective of the split ratio. However, the iron loss increases rapidly as the motor speed increases. Conversely, it can be seen in Figure 4.15(b) that apart from at very low split ratios, the magnitude of the copper loss is independent of the motor speed, the curves being for a constant torque of 0.3Nm and a constant stator flux density of 1.1 T, which results in an output power of 62W at 2krpm, and 3.8kW at 120krpm.. Again, it should be noted that the ‘zigzag’ nature of the copper loss curves result from the requirement that the winding design must have an integer number of turns, as discussed in detail in Appendix G.



(a) Iron loss



(b) Copper loss

**Figure 4.15 – Influence of motor speed on copper loss and iron loss ( $T_e=0.3\text{Nm}$ ,  $B_m=1.1\text{T}$ )**

From Figure 4.15, it can be seen that as the motor speed is increased to about 60krpm the iron loss exceeds the copper loss, and consequently is the dominant factor in determining the optimum split ratio for maximum efficiency. Between 20krpm & 60krpm the iron loss is comparable to the copper loss, as can be seen in the efficiency curves of Figure 4.17, in which

the split ratio becomes dominated by the iron loss. As can also be seen, the iron loss significantly reduces the optimal split ratio at high-speed.

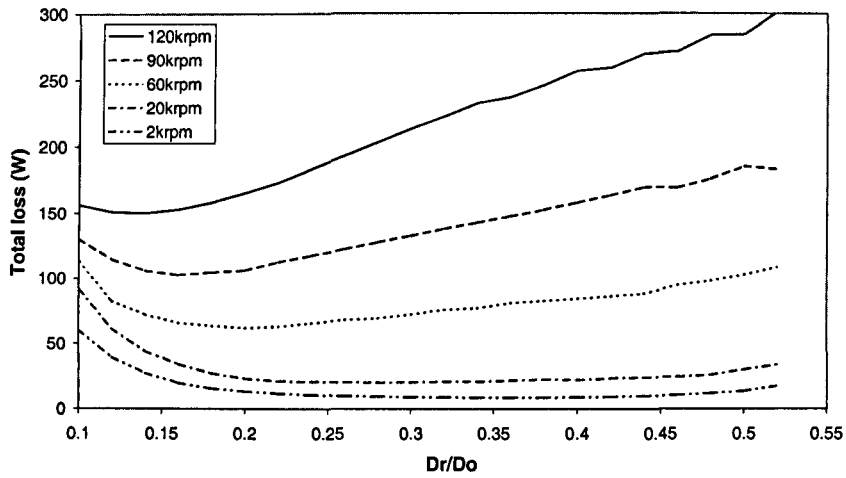
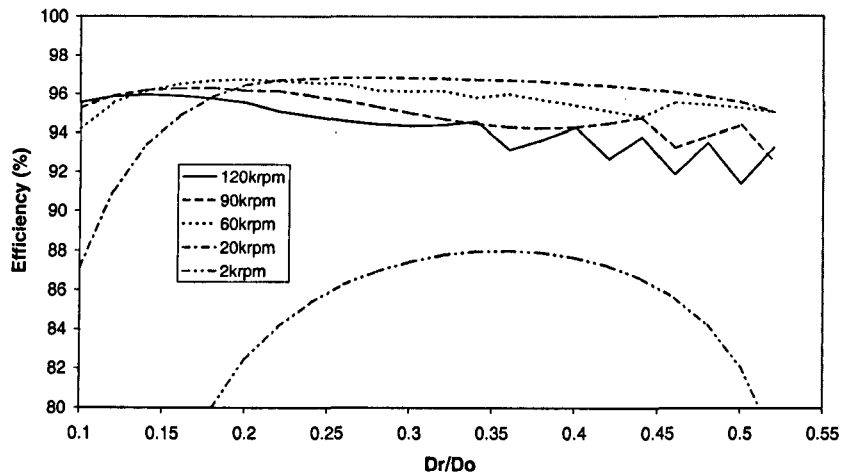
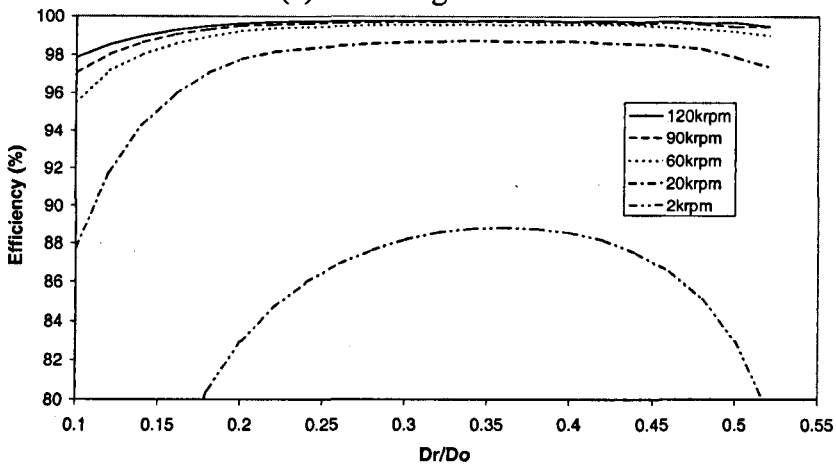


Figure 4.16 - Variation of total loss with frequency



(a) Including iron loss



(b) Neglecting iron loss

Figure 4.17 - Variation in efficiency with motor speed

### (b) Variation of iron loss with split ratio

From the previous section, it can be seen that the iron loss increases significantly with the split ratio, as shown in Figure 4.18 in which the stator flux density is fixed at 1.1T, and the rated torque and speed are 0.3Nm & 120krpm, respectively.

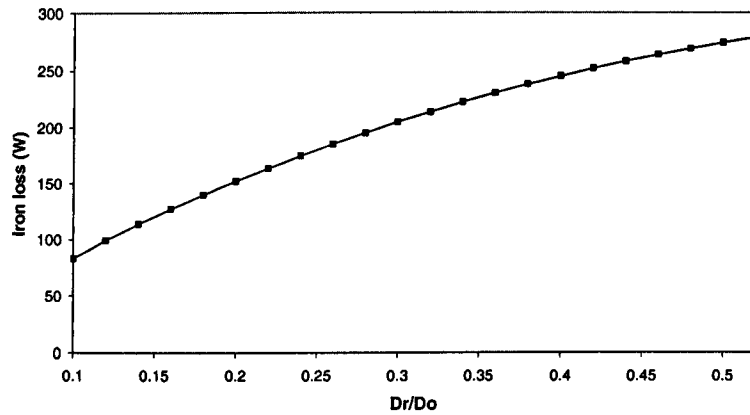


**Figure 4.18 - Variation of iron loss with split ratio for constant stator flux density ( $B_m=1.1T$ )**

If the magnet radial thickness is constant the volume of magnet material increases with the rotor diameter, and consequently the flux per pole increases as shown in Figure 4.19. The tooth width and the radial thickness of the back-iron need to increase in order to maintain a constant flux density in the stator, as can be seen in Figure 4.20. As a result, when  $D_r/D_o < 0.5$  the lamination volume increases, as shown in Figure 4.21.

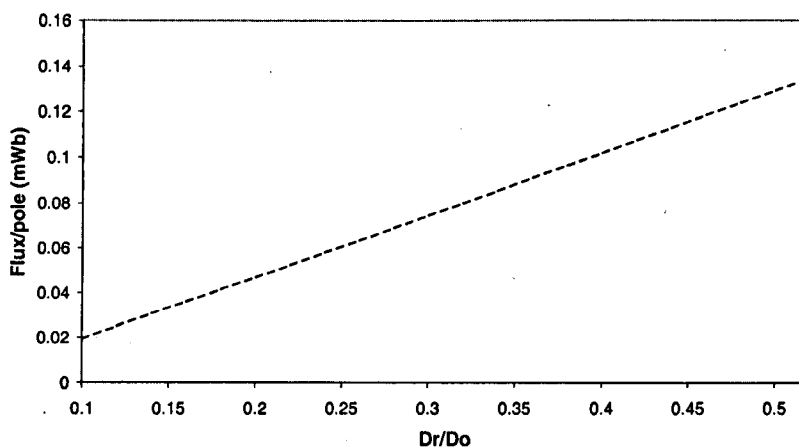


**Figure 4.19 - Variation of airgap flux**

The increase in lamination volume, observed in Figure 4.21, closely matches the increase in iron loss observed in Figure 4.18. There are, however, slight differences between the two graphs, as can be seen in Figure 4.22, due primarily to the change in shape of the stator tooth

tips. The increase in stator iron volume with split ratio can be observed in the representative motor schematics shown in Figure 4.23.

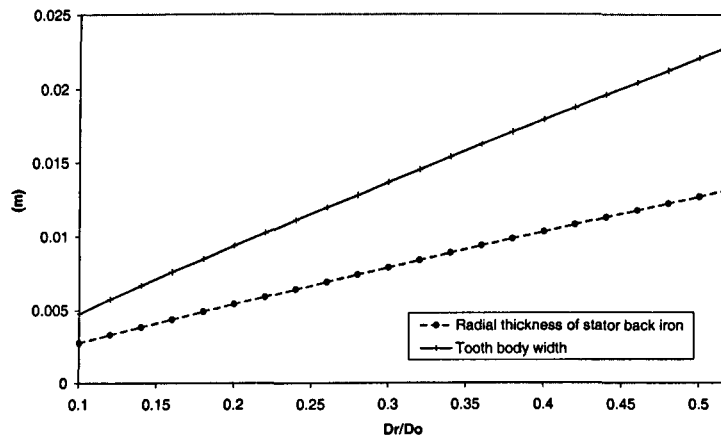


Figure 4.20 – Variation of lamination dimensions with  $D_r/D_o$   
 $(B_m=1.1T, T_e=0.3Nm)$

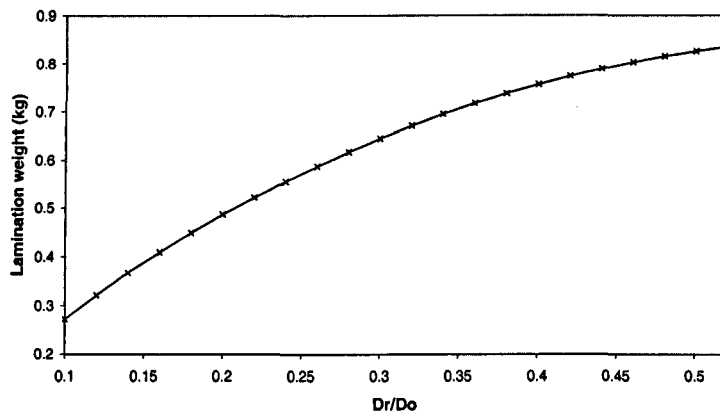


Figure 4.21 – Variation of lamination weight with  $D_r/D_o$   
 $(B_m=1.1T, T_e=0.3Nm)$

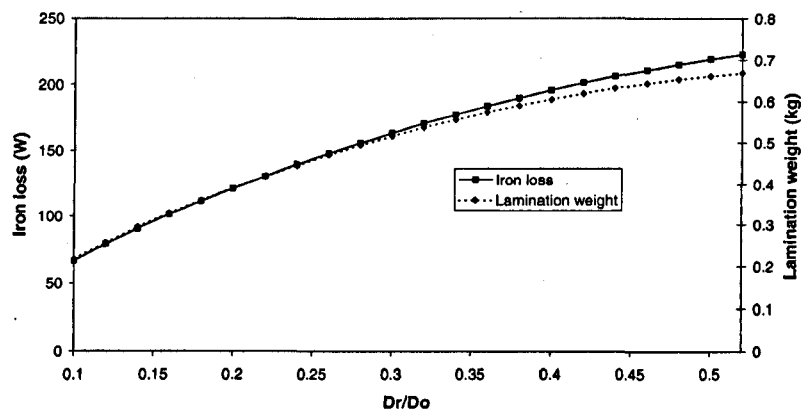
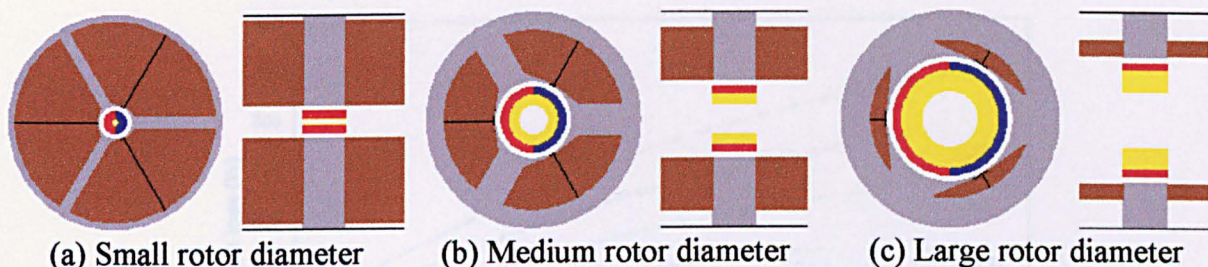


Figure 4.22 - Comparison of iron loss and lamination weight



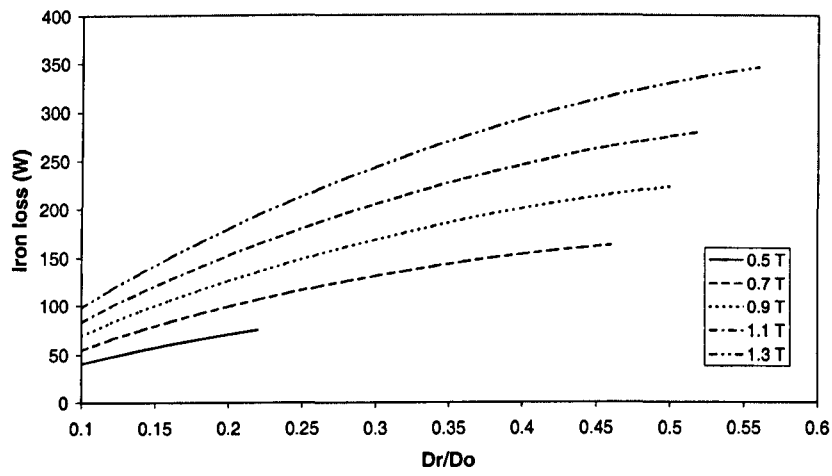
**Figure 4.23 - Motor plots showing increase in iron volume with split ratio**

Although it can be seen in Figure 4.23(a) that a small  $D_r/D_o$  is possible it is also clearly obvious that from a practical point of view this is a poor motor design as this is a very poor utilisation of the motor volume, and the copper loss will be excessive. However, it should be noted that this poor design is a result of the motor axial length being fixed. Figure 4.23(b) with a medium sized rotor diameter is practically a far better design of motor, despite the efficiency being less than for a smaller rotor diameter and when considering the optimal motor design this needs to be taken into account.

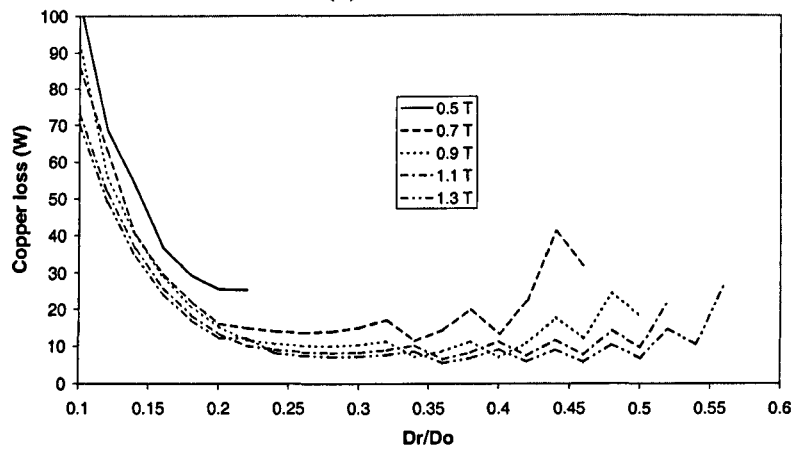
In order to maximise the efficiency, an investigation was carried out into the influence of leading design parameters on the iron loss and optimal split ratio

### **(c) Influence of stator flux density**

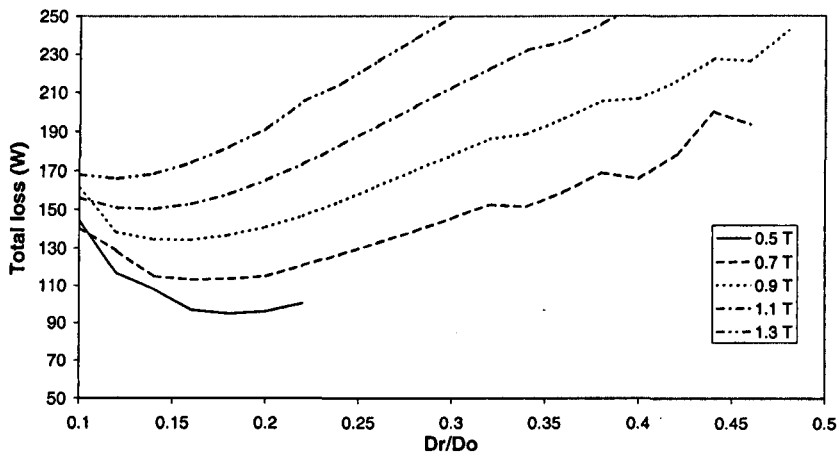
The stator flux density is a major factor in determining the iron loss and consequently the optimal split ratio. Thus, a range of stator flux densities from  $0.5T - 1.3T$  was considered. Whilst an increase in flux density can significantly increase the iron loss density, it also results in a reduction in the radial thickness of the back-iron and the tooth width, which leads to a larger slot area and a lower copper loss as a result of reduced current density, for a constant torque, as seen in Figure 4.24(b). However, the resultant stator iron loss still increases with the split ratio, Figure 4.24(a), and is significantly higher than the copper loss above a split ratio of  $\sim 0.15$  and it dominates the total loss curve, as seen in Figure 4.24(c). Consequently, a relatively low stator flux density is desirable for high-speed motors in order to maximise their efficiency, Figure 4.25. As mentioned previously, the graphs are jagged in nature, particularly at high split ratios, due to constraints on the winding design. However, it can still be seen in Figure 4.25 that when the iron loss is neglected the optimal split ratio does not change significantly with the stator flux density and the efficiency and is relatively insensitive to the split ratio. However, when the iron loss is taken into account, the optimal split is significantly reduced and the efficiency becomes noticeably more sensitive to the split ratio.



(a) Iron loss

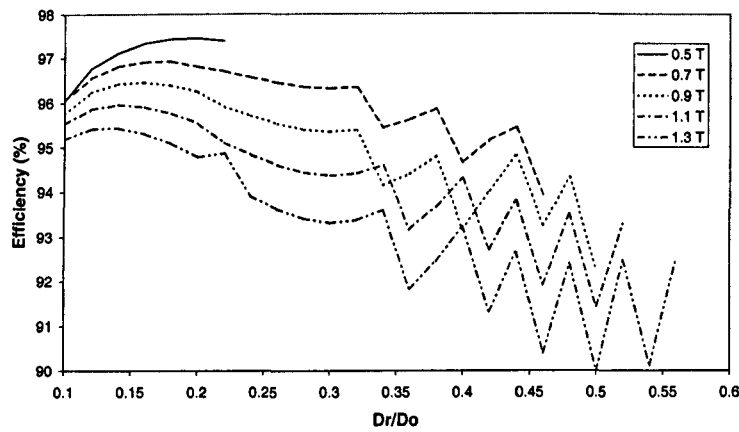


(b) Copper loss

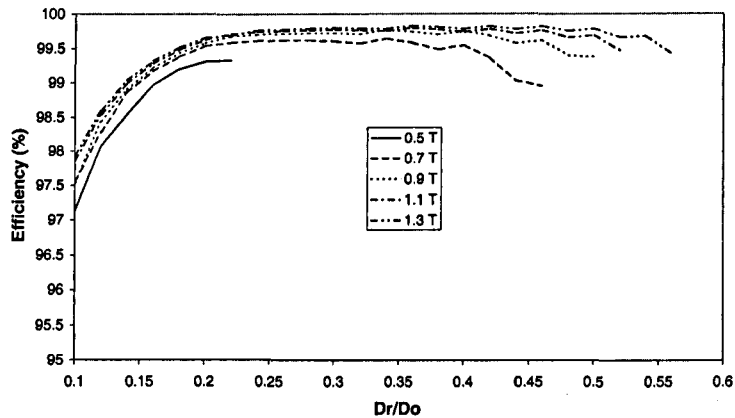


(c) Total loss

Figure 4.24 – Iron, copper and total loss variation with stator flux density, ( $T_e=0.3Nm$ )



(a) Including iron loss



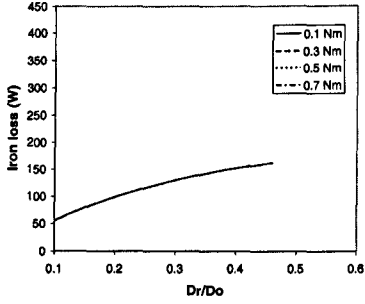
(b) Neglecting iron loss

Figure 4.25 - Variation in efficiency with stator flux density, ( $T_e=0.3Nm$ )

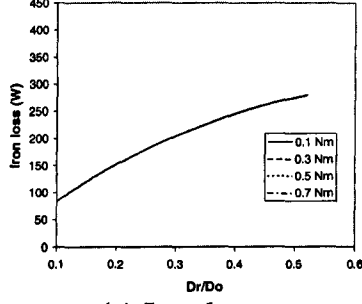
#### (d) Influence of torque density/electric loading

An investigation was performed to examine the influence of the motor torque density on the optimal split ratio. When the torque per volume is increased the copper loss also increases as a higher torque draws more current and thereby necessitates a higher electrical loading. When the iron loss is neglected, the optimal split ratio is independent of the torque density as it corresponds to the maximum efficiency i.e. the minimum loss for a given torque. However, when the iron loss is taken into account the situation changes since, at low torque densities, the iron loss can be significantly higher than the copper loss. Conversely at high torque densities the copper loss can dominate. Figure 4.26(a) shows the variation of no-load iron loss for three stator flux densities, viz. 0.7T, 1.1T & 1.5T. It can be seen that, as shown in the previous section, the iron loss increases significantly with the stator flux density. By way of an example, Figure 4.26(b) shows the effect of increasing the torque on the copper loss. At a low torque of 0.1Nm the copper loss is very small and the optimal split ratio is determined almost exclusively by the iron loss. When the torque is increased, however, the situation changes and at a high torque of 0.7Nm the optimal split ratio is determined primarily by the copper loss, Figure 4.26(e), and this is more evident at low stator flux densities.

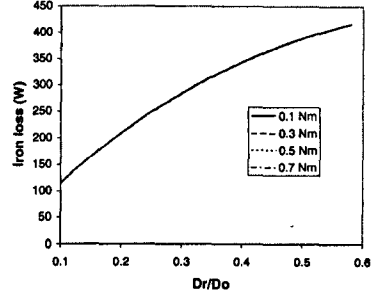
Stator flux density = 0.7 T



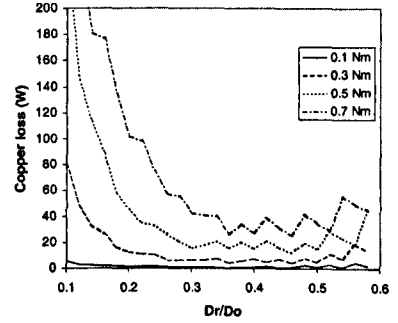
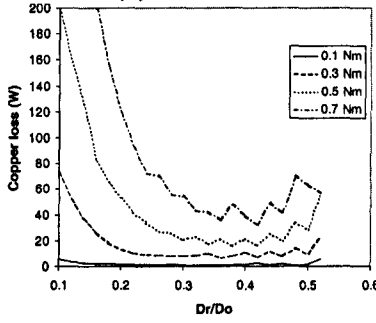
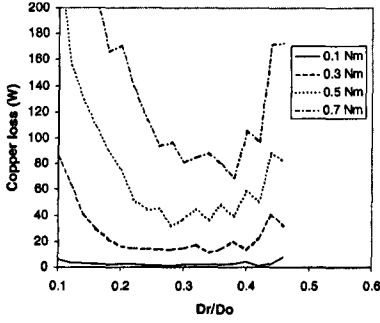
Stator flux density = 1.1 T



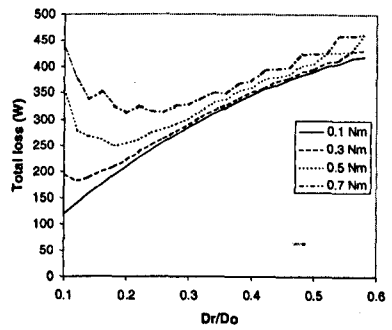
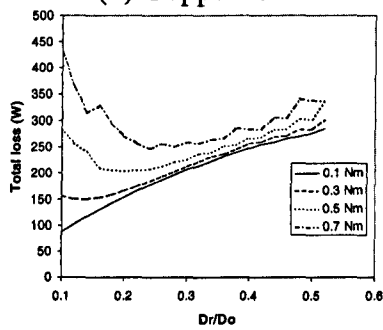
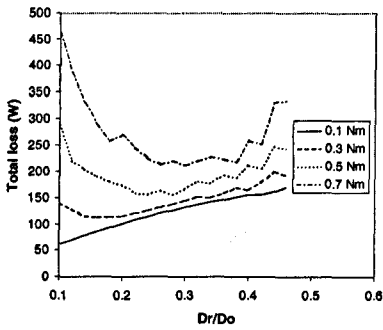
Stator flux density = 1.5 T



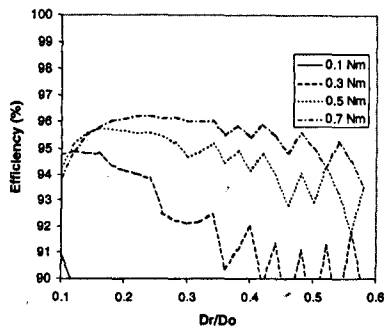
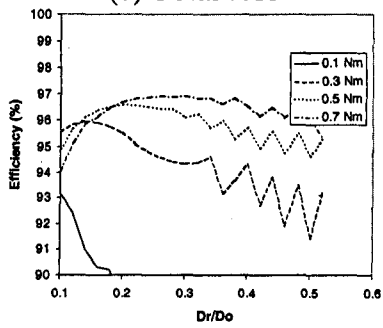
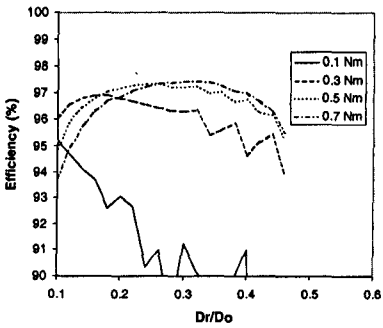
(a) Iron loss



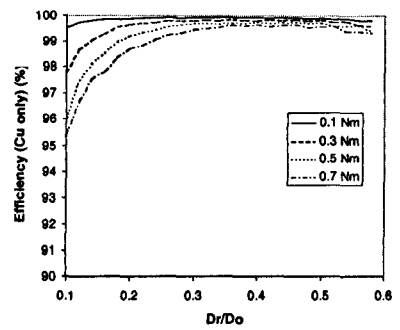
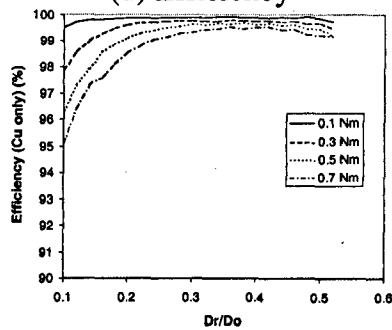
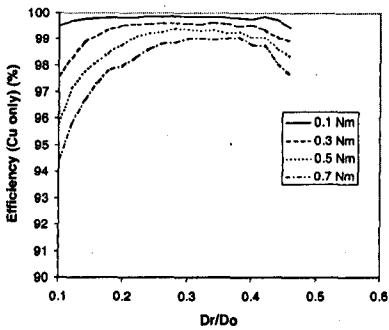
(b) Copper loss



(c) Total loss



(d) Efficiency



(e) Efficiency neglecting iron loss

Figure 4.26 - Influence of torque on losses and efficiency

### (e) Influence of pole number

So far only a 2-pole motor has been considered. However, whilst this is generally the preferred pole number for high-speed applications, higher pole number designs may be preferred since they offer benefits in terms of shorter end-windings and low unbalanced magnetic pull due to armature reaction. However, as the fundamental electrical frequency is then increased, the iron loss will be significantly higher than for a 2-pole motor. Thus, the influence of pole number on the optimal split ratio is investigated. Figure 4.27 shows the effect of increasing the pole number from 2 to 4 on the no-load iron loss for a range of stator flux densities. As expected, there is a significant increase in the iron loss since, from Appendix C:

$$P_t = P_h + P_d \quad (4.40)$$

where  $P_t$  = Total iron loss

$P_h$  = Hysteresis loss

$P_d$  = Eddy current or dynamic loss

$$\text{and } P_h = k_h \cdot f \cdot B_m^\alpha \cdot K(B_m) \quad (4.41)$$

$$P_d = \frac{\sigma d^2 \pi^2}{6\delta} f^2 B_m^2 + 8.67 k_e f^{1.5} B_m^{1.5} \quad (4.42)$$

Therefore, the respective loss components can be shown to be proportional to :  $f + f^2 + f^{1.5}$

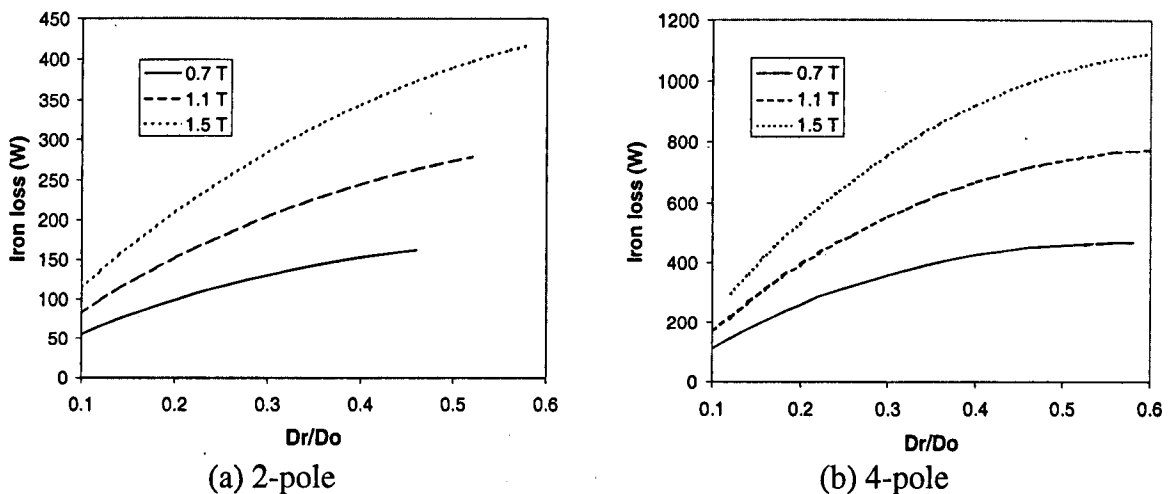
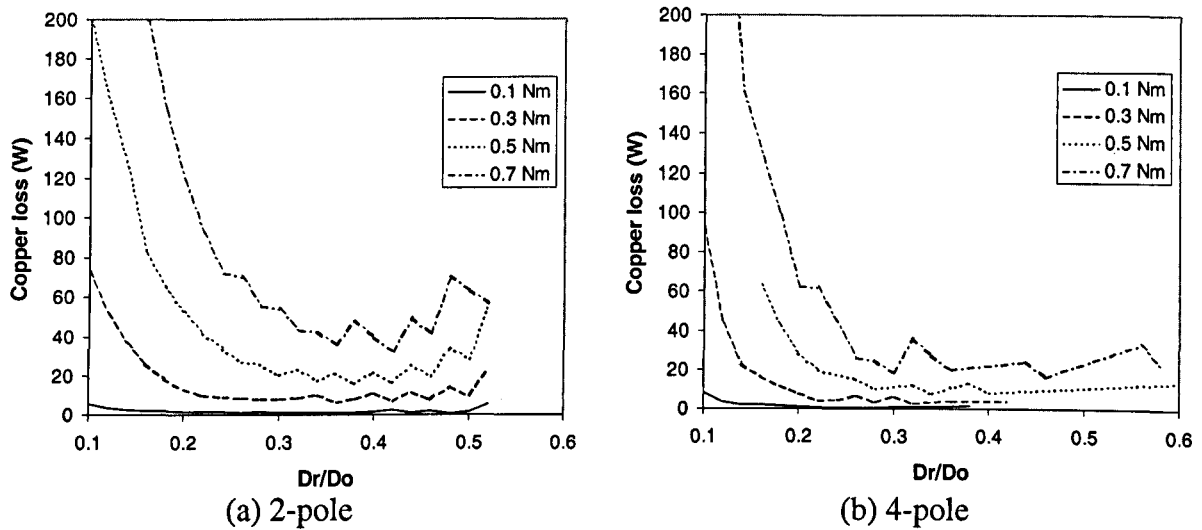


Figure 4.27 – Influence of pole number and stator flux density on iron loss

( $B_m=1.1\text{T}$ ,  $l_a=25\text{mm}$ )

However, whilst an increase in the pole number increases the iron loss, the copper loss decreases, as can be seen in Figure 4.28 for a range of output torques and a constant stator flux density of 1.1T. This reduction arises partly due to the stator teeth and stator back-iron

becoming thinner, leading to more area available for copper which results in a lower current density.



**Figure 4.28 - Influence of pole number and torque on copper loss**

$$(B_m=1.1T, l_a=25mm, T_e=0.3 Nm)$$

As a consequence of the increased iron loss, and the reduced copper loss, the efficiency of a 4-pole motor is dominated by the iron loss, as can be seen in Figure 4.29 in which the efficiency of 2 and 4-pole motors are compared. The optimum split ratio for the 4-pole motor is not only much lower than for a 2-pole motor, but the efficiency is more sensitive to the split ratio. However, as for the 2-pole motors, good judgement needs to be employed to make sure the motor volume is properly utilised.

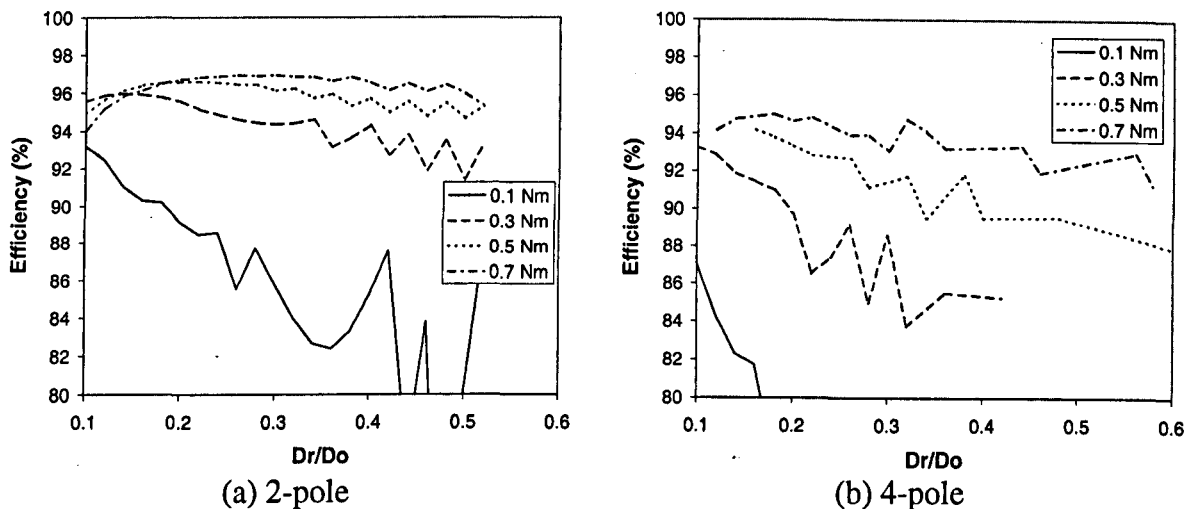


**Figure 4.29 - Influence of pole number and motor torque on motor efficiency**

$$(B_m=1.1T, l_a=25mm, T_e=0.3 Nm)$$

## 4.4 Summary

The ratio of the rotor diameter to the stator outer diameter, otherwise known as the split ratio, is an important parameter in motor design. Previous work [Cha93] to derive an optimal split ratio focussed on a distributed, or overlapping, winding configuration and only accounted for the copper loss. This work has been extended to cater for concentrated, or non-overlapping, windings, and a comparison with results derived from an extensive CAD analysis has been made. Neglecting iron loss, the following observations were made:

- As the ratio of  $B_g/B_m$  is increased, the optimal split ratio decreases. An increase in  $B_g/B_m$  results in wider teeth and thicker stator back-iron leading to a smaller slot area. Consequently, a smaller split ratio results in a larger slot area and a lower copper loss.
- As the pole number is increased, the optimal split ratio also increases. A higher pole number results in thinner teeth and thinner stator back iron, and leads to a larger slot area.
- Overlapping (distributed) windings tend to have a higher optimal split ratio than non-overlapping (concentrated) windings. This is due to the slight difference in thickness of the stator back-iron, as discussed in section 4.2.
- Incorporation of end-winding effects and comparisons with an extensive CAD system indicates that the end-windings do not affect the optimal split ratio. However, they do affect the total loss in the motor, which can be significantly higher.

The influence of the iron loss on the optimal split ratio has been investigated, and it has been shown that the iron loss causes a significant change in the optimal split ratio, which is proportional to the motor speed. Whereas a simple formula can be derived for the optimal split ratio when only the copper loss is accounted for, it is not possible to derive an equivalent expression when iron loss is introduced. The influence of the iron loss is as follows:

- As the speed increases the iron loss becomes dominant and serves to significantly reduce the optimal split ratio.
- An increase in the stator flux density causes an increase in the iron loss as a result of the optimal split ratio decreasing. A higher stator flux density results in a lower iron volume, a larger slot area and, consequently, a lower copper loss.
- An increase in the torque density/ electric loading serves to increase the optimal split ratio as an increase in the torque density causes a corresponding increase in the copper loss which then becomes dominant resulting in an increase in the optimal split ratio.

- An increase in pole number increases the frequency of the flux waveform in the stator iron and consequently causes an increase in the iron loss and a further reduction in the optimal split ratio.

Whilst it is appreciated that using thinner and more exotic lamination materials can reduce the iron loss, it is likely that the iron loss will be the dominant loss in high-speed motors. When cost is an issue, thinner lamination material may well be beyond the price range of a motor. Irrespective of the lamination material, the findings described in this chapter are useful in minimising the iron loss, and obtaining the optimal split ratio for a motor for maximum efficiency.

## Chapter 5 Rotor mechanical resonances

### 5.1 Mechanical resonant frequencies

#### 5.1.1 Introduction

As motor speeds become higher and higher, mechanical considerations related to the rotor, such as resonances and stresses, which are less important for small, low speed motors, become critical. Design choices in terms of the geometry of the rotor and the bearing arrangement increasingly affect dynamic behaviour since vibrational modes may occur near or in the operating speed range and design considerations, such as the length of the shaft, the diameter and the distance between bearings, and the choice of bearing technology becomes critical. An inappropriate choice can lead to problems such as excessive acoustic noise due to resonances, excessive bearing loss that may lead to drastically reduced bearing life and even failure of the bearings and distortion of the shaft. Consequently this chapter investigates the resonant frequencies of a high-speed rotor and the factors influencing the resonant frequencies.

Two 100mNm, 120krpm brushless, DC motors ( $A_1$  &  $B_1$ ) were prototyped as described in Chapter 3. One having a low diode conduction angle and a rotor with a relatively long active rotor length, as shown in Figure 5.1, and the other having a high diode conduction angle with a relatively short active rotor length, as shown in Figure 5.2. For each rotor a model was generated that could accurately predict the resonant modes, and support an investigation into a method of moving the modes, if necessary, above the rated operational speed. Each rotor had a stainless steel shaft with the laminations held in place by an end-cap that was pinned at one end, sintered NdFeB permanent magnets and a carbon fibre over-wrap to retain the magnets.

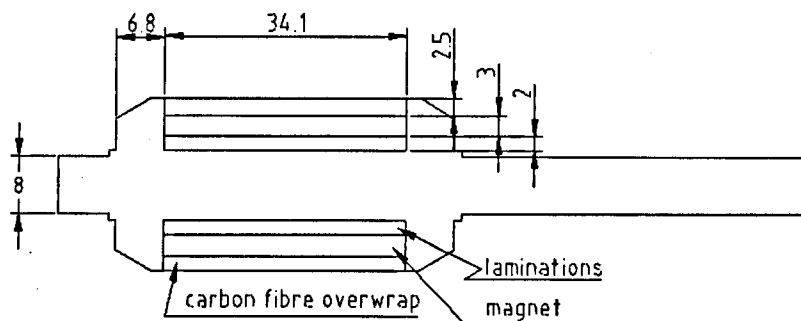
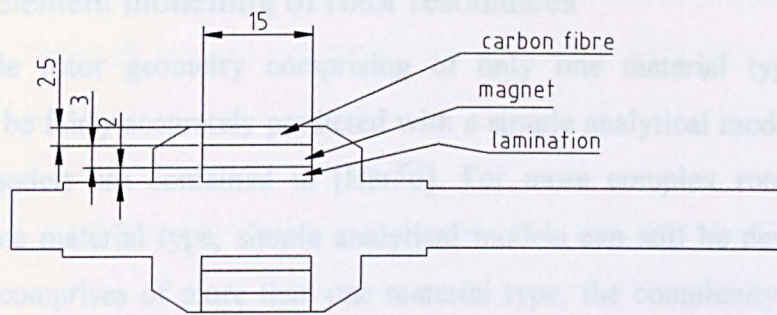


Figure 5.1 - Schematic of rotor with low diode conduction angle (Motor  $A_1$ )



**Figure 5.2 - Schematic of rotor with high diode conduction angle (Motor B<sub>1</sub>)**

In this chapter an accurate finite element model for predicting the rotor resonances, is employed to support an investigation into the influence of the shaft extension length, the shaft diameter and the distance between the bearings. Natural frequencies measured from impulse response tests will be compared with predicted values and, where possible, with values deduced from analytical models at the various stages of rotor construction. The finite element model will be extended to include the bearing arrangement, and the predicted natural frequencies will be compared with natural frequencies measured on the complete motor. Since the bearing stiffness was unknown, an investigation was also undertaken in order to determine its value.

During high-speed operation of the prototype motor, the rotor suffered a failure as evidenced by the photographs in Figure 5.3. It happened whilst the rotor was accelerating, and the last recorded speed was 106,000 rpm, or 1766 Hz, and it is probable that this was excited by the cylindrical resonance mode at 1248 Hz, which as will be shown in section 5.4 causes significant shaft flexing. Since the rotor would inevitably have some imbalance, despite being balanced to better than 0.1g mm, then once the shaft started to bend the centrifugal force would have caused the shaft to bend progressively, as can be seen.



**Figure 5.3 - Damage caused by suspected resonant mode**

### 5.1.2 Finite element modelling of rotor resonances

For a simple rotor geometry comprising of only one material type, e.g. steel, the resonances can be fairly accurately predicted with a simple analytical model. Some examples of the basic models are contained in [Har56]. For more complex rotor geometries still consisting of one material type, simple analytical models can still be developed. However, once the rotor comprises of more than one material type, the complexity increases rapidly, and finite element analysis becomes the only practical method of predicting the resonant modes. It will be shown in section 5.3 that for models which incorporate the bearing stiffness, finite element analysis is required to accurately predict the resonant modes.

The rotors were modelled using the finite element package ANSYS, and were discretised using a 3D structural solid element designated SOLID45. This element type is normally brick shaped, each element consisting of 8 nodes, one at each corner. Each node has three degrees of freedom, unless otherwise constrained, in the x, y and z coordinate directions. Figure 5.4, shows a quarter section of the complete finite element mesh for the rotor shown previously in Figure 5.1.

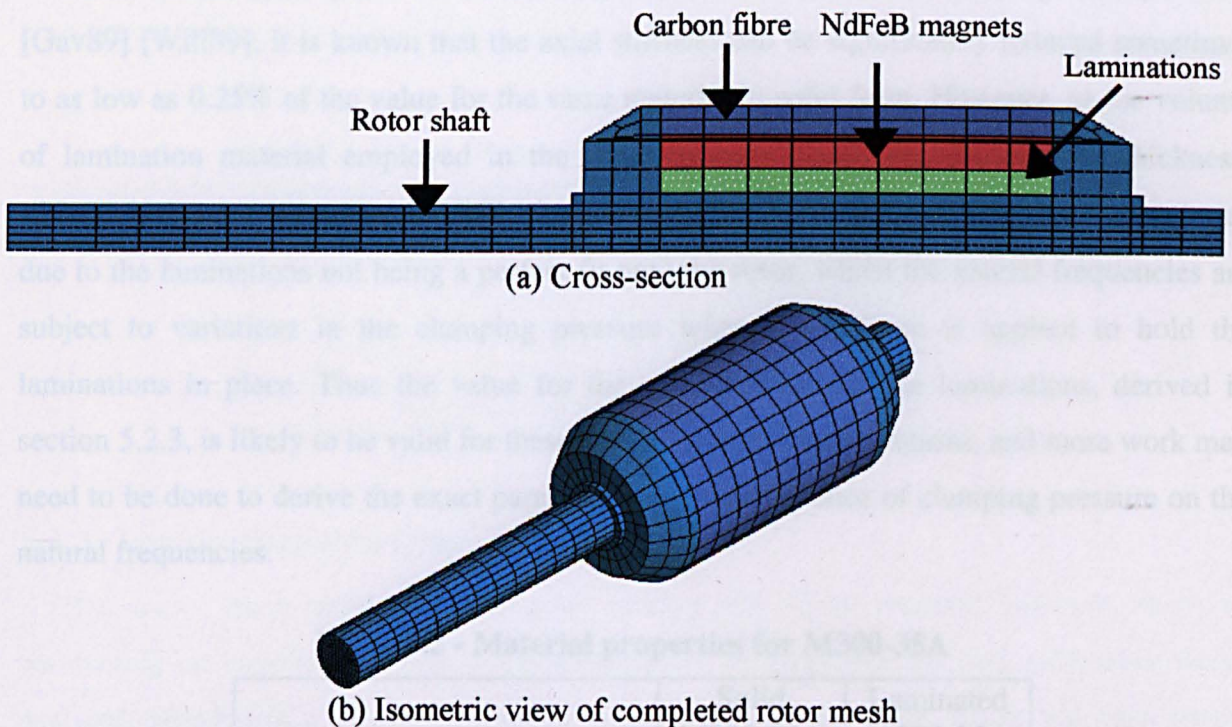


**Figure 5.4 - Section of complete finite element mesh for the rotor shown in Figure 5.1.**

Apart from the rotational modes, which are hard to detect from the impulse response test described in section 5.1.3, the vibration modes are represented by 2 planes, XZ and YZ due to the shaft being cylindrical and symmetrical about the x-y axis.

The properties for the various materials that are used in the rotor need to be specified for the modelling. The shaft is made out of stainless steel Type AISI 303, whose properties are shown in Table 5.1.

**Table 5.1 – Material properties for stainless steel**

Density ( $\rho$ )	8000 kg/m <sup>3</sup>
Young's Modulus ( $E_x, E_y, E_z$ )	193 GPa
Shear modulus ( $G_{xy}, G_{xz}, G_{yz}$ )	77.2 GPa
Poisson's ratio	0.3

The laminations are M300-35A, a material that has already been characterised [Lon98] as shown in Table 5.2. However, these properties are specified for a laminated stack that was welded at 6 points around its circumference, thus giving a relatively high axial stiffness. In this investigation the rotor lamination stack was simply compressed and not welded. Thus the parameters of the lamination material have to be determined for this particular application. As the laminations have relatively little axial stiffness, it was suspected that the effect of their addition to the rotor shaft would be to reduce the natural frequencies of the measured vibration modes from those, which are measured for the shaft alone. From previous studies [Gav89] [Will89], it is known that the axial stiffness can be significantly reduced sometimes to as low as 0.25% of the value for the same material in solid form. However, as the volume of lamination material employed in the rotors is very small, viz. 2mm radial thickness, accurate measurements may be difficult. It is also possible that there could be uncertainties due to the laminations not being a perfect fit onto the rotor, whilst the natural frequencies are subject to variations in the clamping pressure when the end-cap is applied to hold the laminations in place. Thus the value for the axial stiffness of the laminations, derived in section 5.2.3, is likely to be valid for these particular rotor configurations, and more work may need to be done to derive the exact parameters and the influence of clamping pressure on the natural frequencies.

**Table 5.2 - Material properties for M300-35A**

	Solid M300-35A	Laminated M300-35A
Density ( $\rho$ )	7650 kg/m <sup>3</sup>	7305 kg/m <sup>3</sup>
Young's Modulus ( $E_x, E_y, E_z$ )	215 GPa	215 GPa
Shear modulus ( $G_{xy}$ )	82.7 GPa	55 GPa
Shear modulus ( $G_{xz}, G_{yz}$ )	82.7 GPa	8 GPa
Poisson's ratio ( $\nu_{xy}, \nu_{yz}, \nu_{xz}$ )	0.3	0.3

The sintered NdFeB magnet (UGIMAX 34B1) has the properties given in Table 5.3. Since the shear modulus was unknown, it was deduced later from experimental measurements. As the magnets have a relatively high Young's modulus, it was anticipated that their addition to the rotor would stiffen the shaft and therefore increase the natural frequencies from those for the shaft with the laminations alone.

**Table 5.3 - Material properties of UGIMAX 34B1**

Density ( $\rho$ )	7500 kg/m <sup>3</sup>
Young's Modulus ( $E_x, E_y, E_z$ )	160 GPa
Poisson's ratio	0.3

The properties for the carbon fibre containment were difficult to ascertain since the material is a mixture of an epoxy resin and carbon fibre filaments. Normally it is assumed that the composition of the mixture will be 65% carbon fibre and 35% resin. Therefore properties were deduced from experimental data supplied by Urenco (Capenhurst). It was not possible to accurately measure the resonant modes for a carbon fibre tube as used on the rotors, as it is much lighter in weight compared to the accelerometer. The properties for a carbon-fibre and epoxy resin tube are given in Table 5.4.

**Table 5.4 - Material properties for carbon-fibre over-wrap**

Density ( $\rho$ )	1612.3 kg/m <sup>3</sup>
Young's Modulus ( $E_x, E_z$ )	7.9 GPa
Young's Modulus ( $E_y$ )	197 GPa
Shear modulus ( $G_{xy}, G_{xz}, G_{yz}$ )	6 GPa
Poisson's ratio ( $\nu_{xy}, \nu_{xz}$ )	0.3
Poisson's ratio ( $\nu_{yz}$ )	0.0155

### 5.1.3 Impulse response tests

The tests, which were undertaken to validate the finite element analyses, involved performing an impulse test with a modal hammer, an accelerometer and a dynamic signal analyser (HP35660A). The accelerometer was attached to the rotor, which was then struck from the opposite side with the modal hammer. The resulting frequency spectrum was then saved as a voltage, which was then converted in Excel to the same scale as on the HP signal analyser, dBVrms, by multiplying the voltage by  $20\log(V/\sqrt{2})$  and plotted as frequency against dBVrms.

In the frequency spectra as recorded by the accelerometer the amplitude of each peak is dependent on the force that is used to excite the rotor. A better representation of the natural frequencies is to use the frequency response known as the transfer function, in which the amplitude of all the resonances have the correct relationship to each other, since it is a function of both the modal hammer and the spectrum recorded from the accelerometer. However, whilst being more accurate, and arguably a better representation of the natural frequencies the transfer function is not as clear or easy to interpret as the frequency spectrum, as can be seen by comparing Figures 5.5 & 5.6. It can be seen that the transfer function is noisier and, although the peaks are easily distinguishable it should be noted that this particular transfer function is relatively free from extraneous noise. Previous work [Lon01] showed that the numerical digitisation error in the transfer function is unacceptable at frequencies > 2-3kHz. Thus in the spectra which are included in the remainder of this chapter are an average of 10 measurements so as to reduce the noise and prevent the likelihood of spurious readings.

At this stage, it should be noted that the discretisation of the frequency spectrum acquired from the signal analyser is dependent on the frequency range that was selected. With a frequency sweep of 3 kHz the frequency resolution is 8Hz, whilst for 6, 12 and 25 kHz it was 16,34 and 64 Hz, respectively. Consequently, the same test performed with different frequency ranges can give rise to slightly different results.

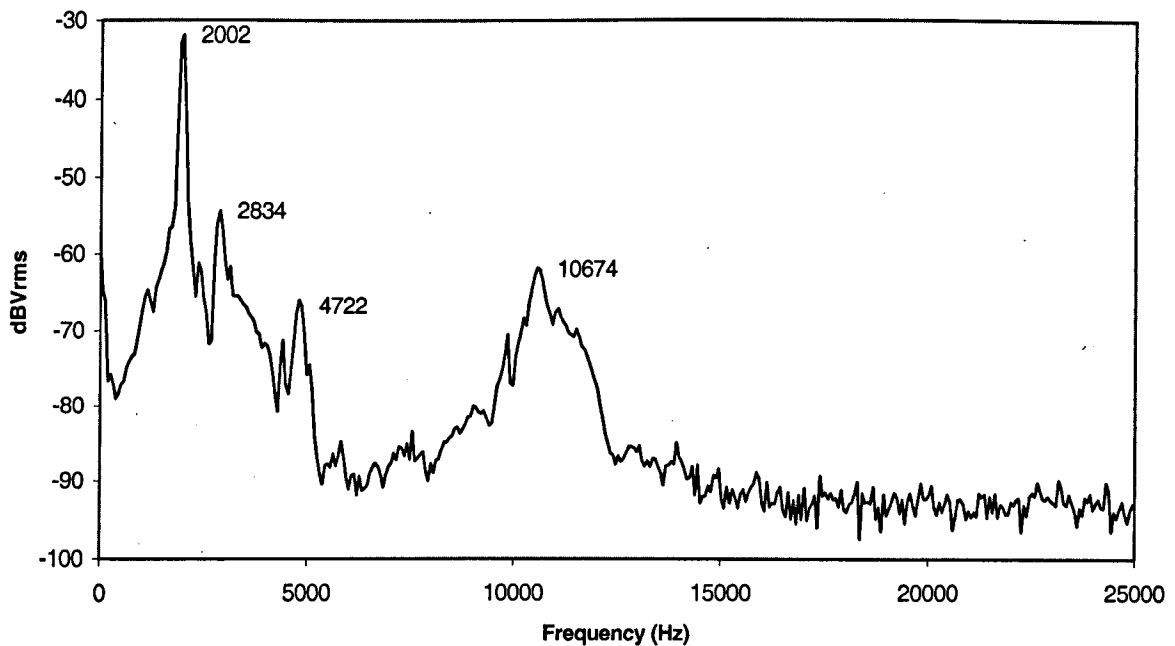


**Figure 5.5 - Frequency spectrum from accelerometer**

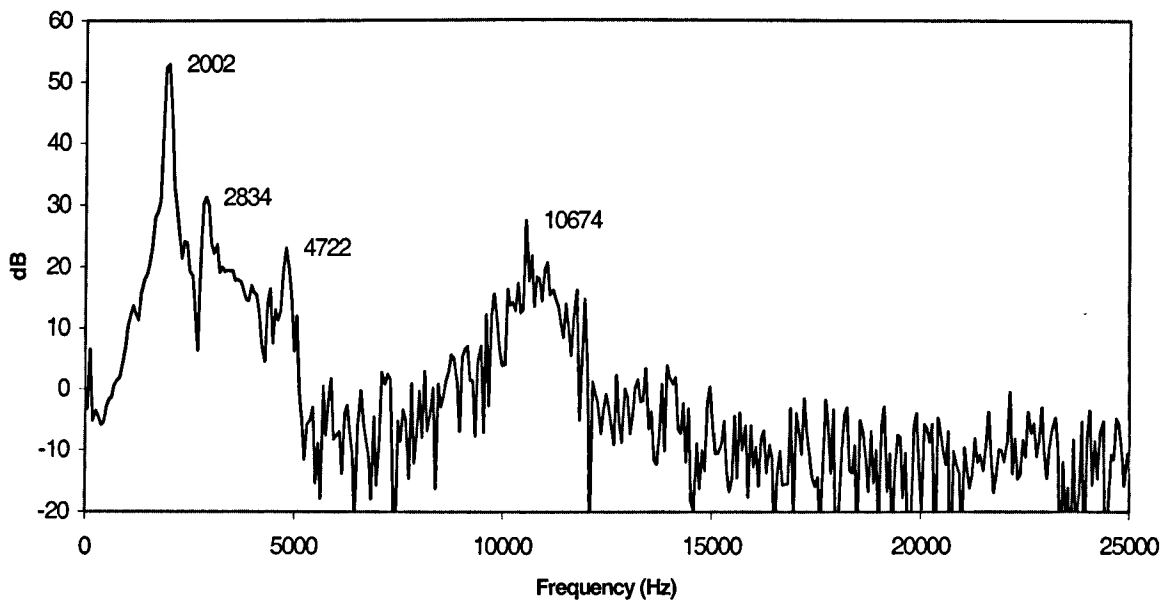


**Figure 5.6 - Transfer function incorporating signals from both modal hammer and accelerometer**

## 5.2 Finite element analysis of resonant frequencies

### 5.2.1 Rotor shaft with one end-cap

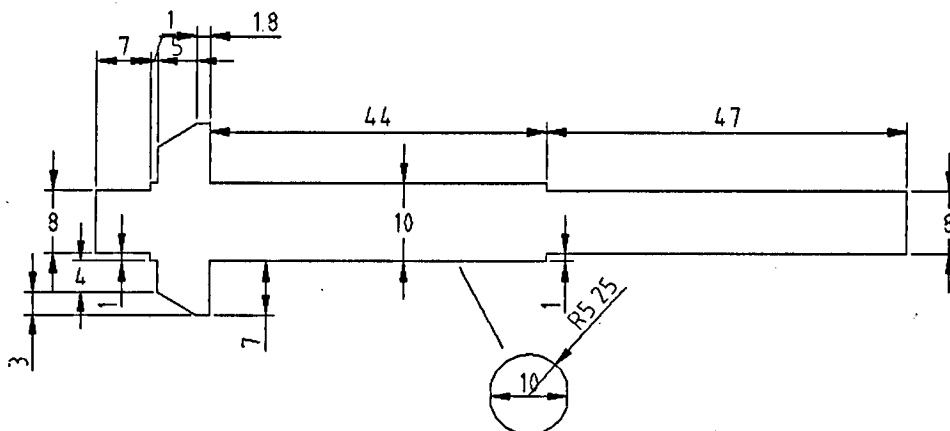


**Figure 5.7 - Rotor shaft showing flats on main section**

The stainless steel rotor shaft is shown in Figure 5.7, and has a significant extension at one end, of around 40mm beyond the end of the bearing, which was originally intended to allow the motor to be coupled to a dynamometer. Also at this stage the resonant problems associated with the shaft extension were not known. However, as will be seen in section 5.4.1 this extension caused resonance problems. Thus, new shorter rotors were later employed which alleviated some of the problems observed.

The finite element model is shown in Figure 5.8 together with a photograph of the shaft. For simplicity the flats on the central part of the shaft, which prevent the laminations from

rotating, were not modelled. However, as will be shown later in section 5.2.3 this had negligible effect on the predicted rotor resonances.

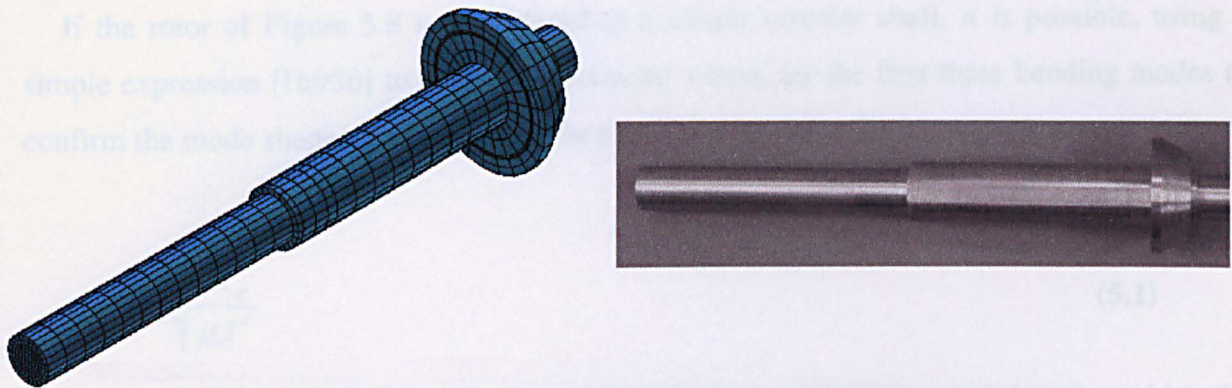


**Figure 5.8 - Finite element mesh and photograph of rotor shaft**

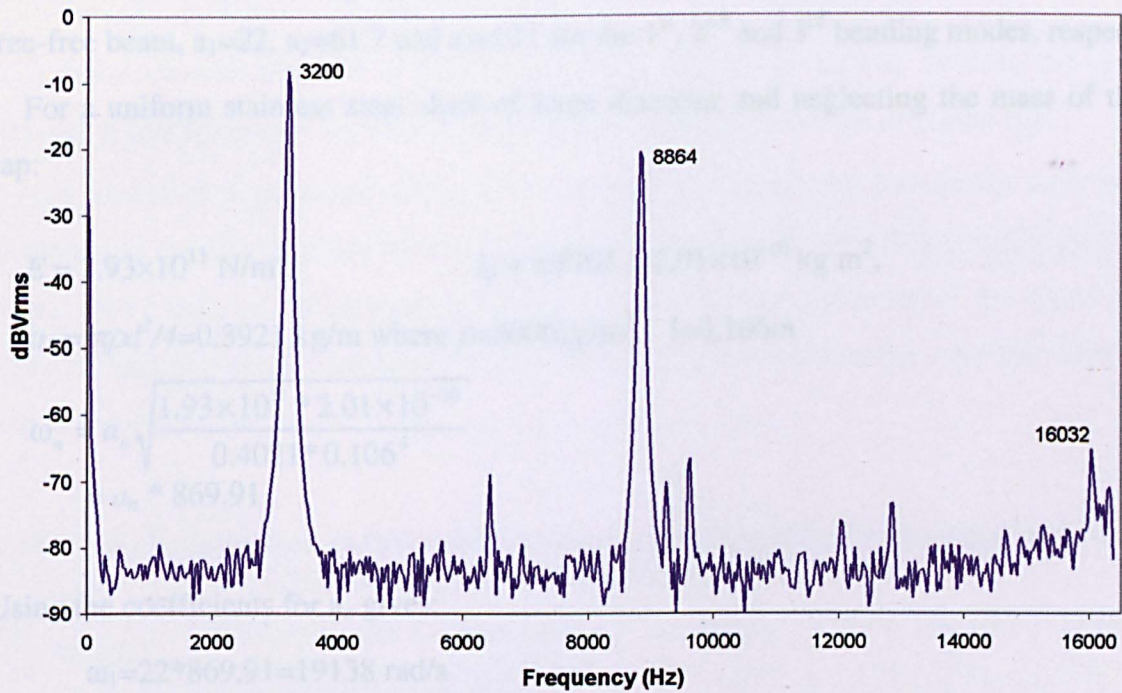


**Figure 5.9 - Measured frequency spectrum for shaft**

**Table 5.5 - Comparison of measured and predicted natural frequencies for shaft**

Mode	Finite element (Hz)	Measured (Hz)
1 <sup>st</sup> bending	3138	3200
2 <sup>nd</sup> bending	8751	8864
Rotational	11710	-
3 <sup>rd</sup> bending	15906	16032

The finite element results are in close agreement with the measured results, as can be seen in Table 5.5, and the measured results of Figure 5.9 with the resonant mode shapes shown in

Figure 5.11. It can also be seen that the predicted rotational vibration mode at 11.7kHz could not be detected. Although this mode is unlikely to be excited by the impulse response test, it may still occur during operation of a motor.

If the rotor of Figure 5.8 is considered as a simple circular shaft, it is possible, using a simple expression [Har56] to obtain approximate values for the first three bending modes to confirm the mode shapes. For a free-free beam:

$$\omega_n = a_n \sqrt{\frac{EI_p}{\mu_1 l^4}} \quad (5.1)$$

where E is the Young's modulus, I is the inertia,  $\mu_1$  is the mass per unit length, and l is the length of the shaft. EI equates to the bending stiffness of the section, and  $a_n$  is a constant calculated from the Rayleigh method, which is dependent on the problem boundaries. For a free-free beam,  $a_1=22$ ,  $a_2=61.7$  and  $a_3=121$  for the 1<sup>st</sup>, 2<sup>nd</sup> and 3<sup>rd</sup> bending modes, respectively.

For a uniform stainless steel shaft of 8mm diameter and neglecting the mass of the end-cap:

$$E = 1.93 \times 10^{11} \text{ N/m}^2, \quad I_p = \pi d^4 / 64 = 2.01 \times 10^{-10} \text{ kg m}^2,$$

$$\mu_1 = \pi \rho d^2 / 4 = 0.3921 \text{ kg/m where } \rho = 8000 \text{ kg/m}^3, \quad l = 0.106 \text{ m}$$

$$\begin{aligned} \omega_n &= a_n \sqrt{\frac{1.93 \times 10^{11} * 2.01 \times 10^{-10}}{0.4021 * 0.106^4}} \\ &= a_n * 869.91 \end{aligned}$$

Using the coefficients for  $a_n$  gives:

$$\omega_1 = 22 * 869.91 = 19138 \text{ rad/s}$$

$$f_1 = 19138 / 2\pi = 3046 \text{ Hz}$$

Repeating for  $\omega_2$  and  $\omega_3$  gives:

$$f_2 = 8542 \text{ Hz}$$

$$f_3 = 16752 \text{ Hz}$$

The foregoing analytically predicted natural frequencies were confirmed by measuring the natural frequencies of a 8.0mm steel bar 106mm long. The resulting frequency is shown in Figure 5.10.

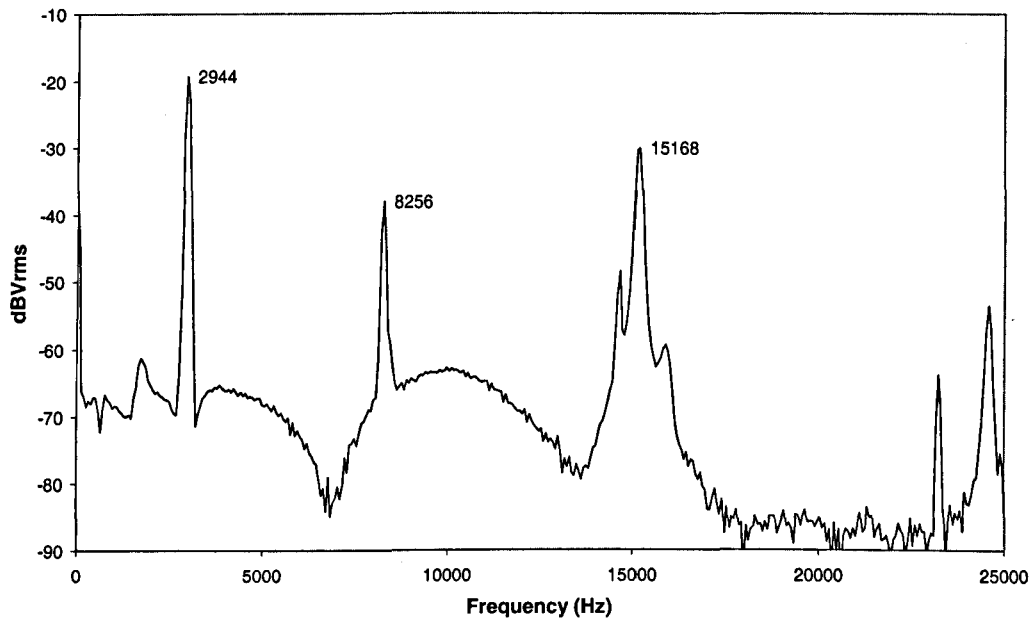


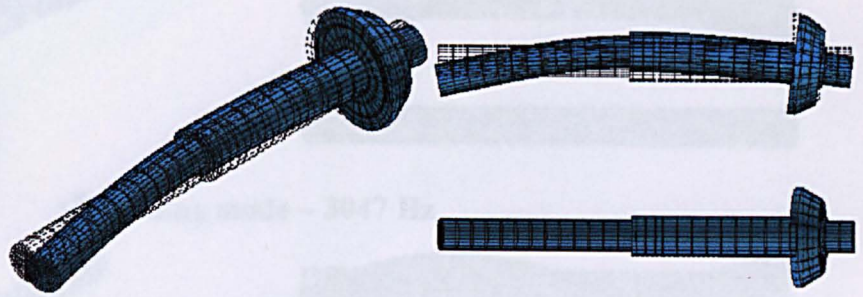
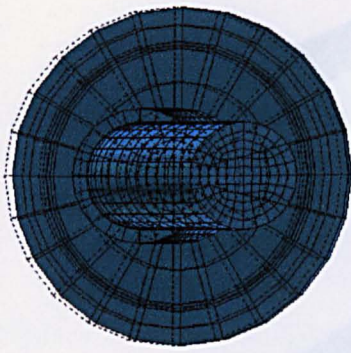
**Figure 5.10 - Natural frequencies for 8mm steel bar**

A finite element analysis of the steel bar was also undertaken to confirm the analytical prediction and to deduce the various mode shapes, which are shown in Figure 5.12.

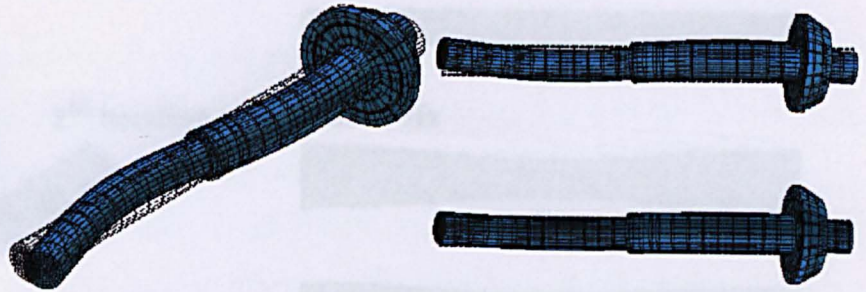
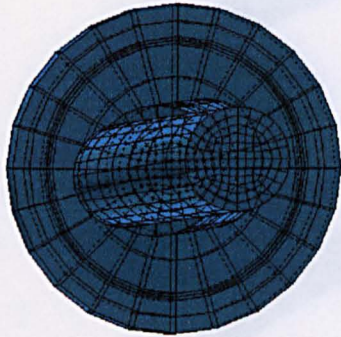
The analytically predicted vibration frequencies compare very favourably with the finite element and measured values for the 1<sup>st</sup>, 2<sup>nd</sup> and 3<sup>rd</sup> bending modes even with the assumptions which were made, as can be seen in Table 5.6. However, the resolution of the signal analyser on the frequency range, which was used, is 64 Hz, as mentioned earlier, and also accounts for part of the discrepancy.

**Table 5.6 - Comparison between finite element and analytically predicted and measured frequencies for rotor shaft and steel bar**

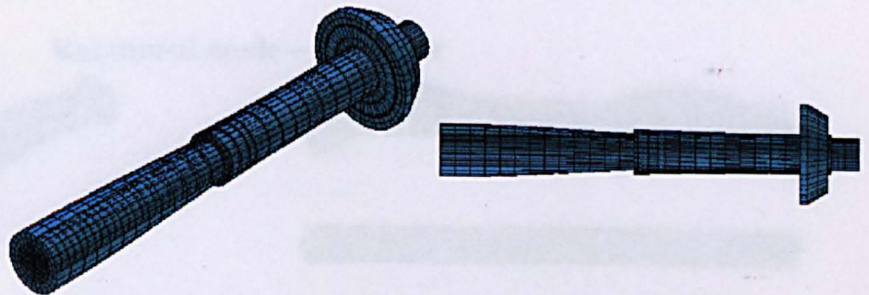
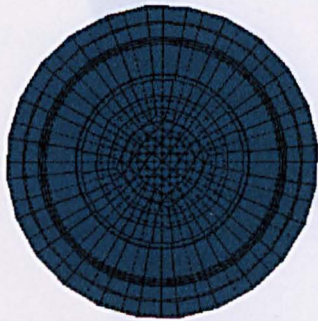
Mode	Finite element (rotor) (Hz)	Measured (rotor) (Hz)	Analytical (bar) (Hz)	Finite element (bar) (Hz)	Measured (bar) (Hz)
1 <sup>st</sup> bending	3138	3200	3046	3047	2944
2 <sup>nd</sup> bending	8751	8864	8542	8226	8256
Rotational	11710	-	-	14727	-
4 <sup>th</sup> bending	15906	16320	16752	15683	15168



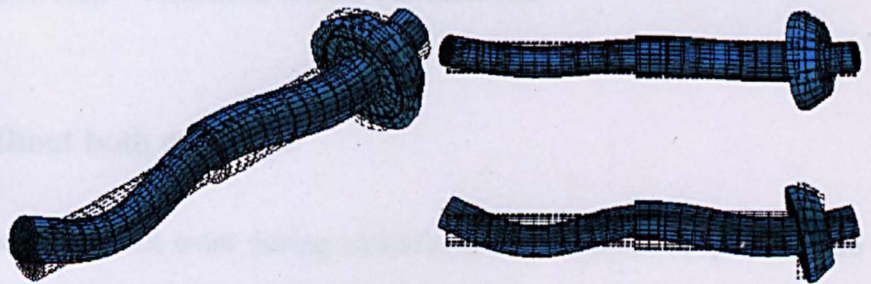
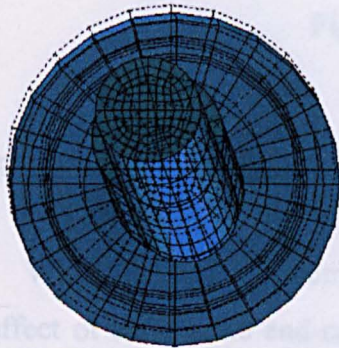
**1<sup>st</sup> bending mode – 3138 Hz**



**2<sup>nd</sup> bending mode – 8751 Hz**

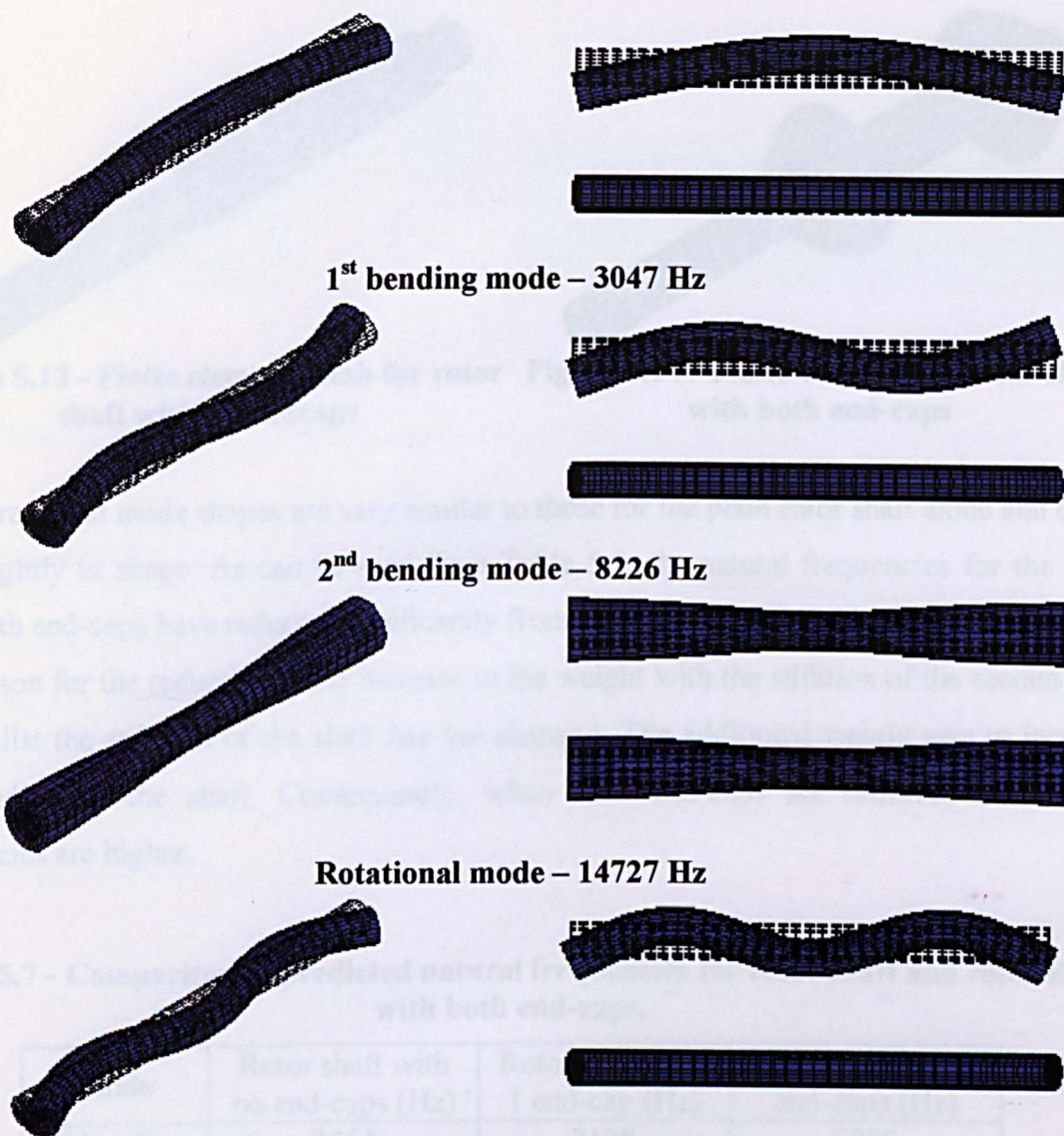


**Rotational mode – 11710 Hz**



**3<sup>rd</sup> bending mode – 15906 Hz**

**Figure 5.11 - Vibration modes for shaft**



**3<sup>rd</sup> bending mode – 15683 Hz**  
**Figure 5.12 - Vibration modes for steel bar**

### 5.2.2 Shaft with and without both end-caps

Whilst these shaft geometries did not exist during manufacture it is useful to quantify the effect of adding the end-caps on the natural frequencies. Therefore, the shaft was modelled both with and without end-caps, and the predictions are compared with those from the preceding section. Figure 5.13 shows the shaft with no end-caps, whilst Figure 5.14 shows the rotor with both end-caps.

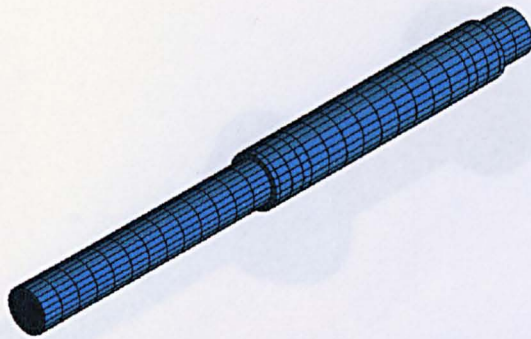


**Figure 5.13 - Finite element mesh for rotor shaft with no end-caps**

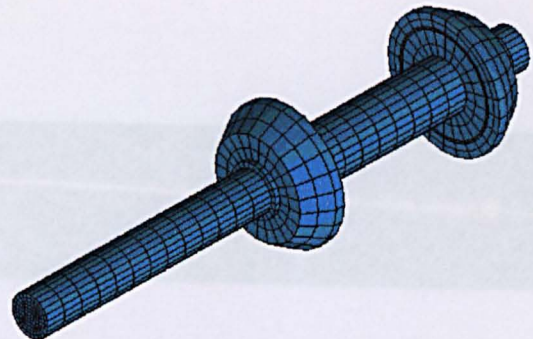


**Figure 5.14 - Finite element mesh for shaft with both end-caps**

The resonant mode shapes are very similar to those for the plain rotor shaft alone and differ only slightly in shape. As can be seen from Table 5.7, the natural frequencies for the shaft with both end-caps have reduced significantly from those for the rotor shaft with one end-cap. The reason for the reduction is the increase in the weight with the addition of the second end-cap, whilst the stiffness of the shaft has not changed. The additional weight acts to increase the bending of the shaft. Consequently, when both end-caps are removed the natural frequencies are higher.

**Table 5.7 - Comparison of predicted natural frequencies for rotor shaft and rotor shaft with both end-caps.**

Mode	Rotor shaft with no end-caps (Hz)	Rotor shaft with 1 end-cap (Hz)	Rotor shaft with 2 end-caps (Hz)
1 <sup>st</sup> bending	3464	3138	2795
2 <sup>nd</sup> bending	9649	8751	7943
Rotational	15465	11710	8293
3 <sup>rd</sup> bending	17721	15906	14370

### 5.2.3 Shaft with laminations

The next stage was to model the rotor shaft together with the laminations and both end-caps in place. Initial values for the Young's modulus and shear modulus for the lamination material were specified in section 5.1.2. As the laminations were not welded the axial stiffness is provided by the shaft itself and was unknown. Consequently,  $E_z$  (Young's modulus in  $z$  plane) was varied until the predicted resonant frequencies converged with those, which were measured by the impulse response test. The finite element mesh and a photograph of the shaft assembly are shown in Figure 5.15.

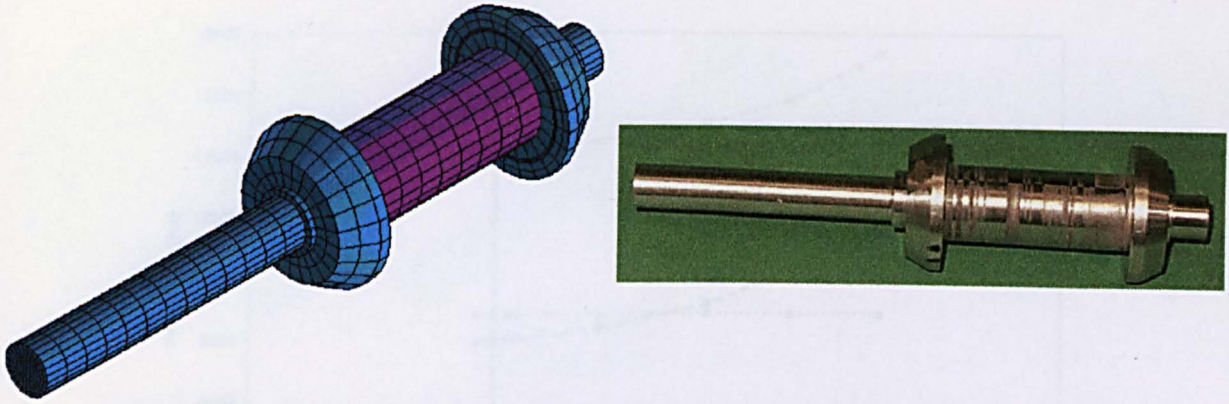


**Figure 5.15 – Finite element mesh and photograph of shaft with laminations**

In order for the finite element program to solve the generated equations, the Poisson's ratio in the xz and yz plane needed to be reduced from 0.3 to 0.1, so that the material had positive definite elastic properties. Physically this accounts for the fact that the laminations will tend to slide over one another rather than deform. The variation of the natural frequencies with a value of  $E_z$  is shown in Table 5.8 and Figure 5.16. From these it can be seen that a value of  $E_z = 8$  GPa results in the closest correlation to the measured resonant frequencies shown in the frequency spectrum of Figure 5.17.

**Table 5.8 - Variation of natural frequency with change in  $E_z$**

$E_z$ (Gpa)	Natural Frequency (Hz)			
	Mode 1	Mode 2	Mode 3	Mode 4
215	3095	11510	8805	17337
100	3008	10149	8806	15797
50	2920	9125	8806	15046
20	2823	8314	8806	14427
10	2777	8004	8806	14144
9	2771	7973	8806	14113
<b>8</b>	<b>2766</b>	<b>7941</b>	<b>8806</b>	<b>14082</b>
7	2761	7909	8806	14082

Again, the third resonant mode was not detected due to its rotational nature, as can be seen from the mode shapes in Figure 5.18. However, from Table 5.9 it can be seen that there is a very good correlation between the predicted and measured results after compensating for the change in  $E_z$  of the laminations. The 4<sup>th</sup> mode, however, has a dual peak due to the flats, which were machined onto the shaft. As reported in [Toy40], this creates resonant modes that have 2 peaks due to the fact that the horizontal and vertical vibration frequencies of the shaft differ slightly.

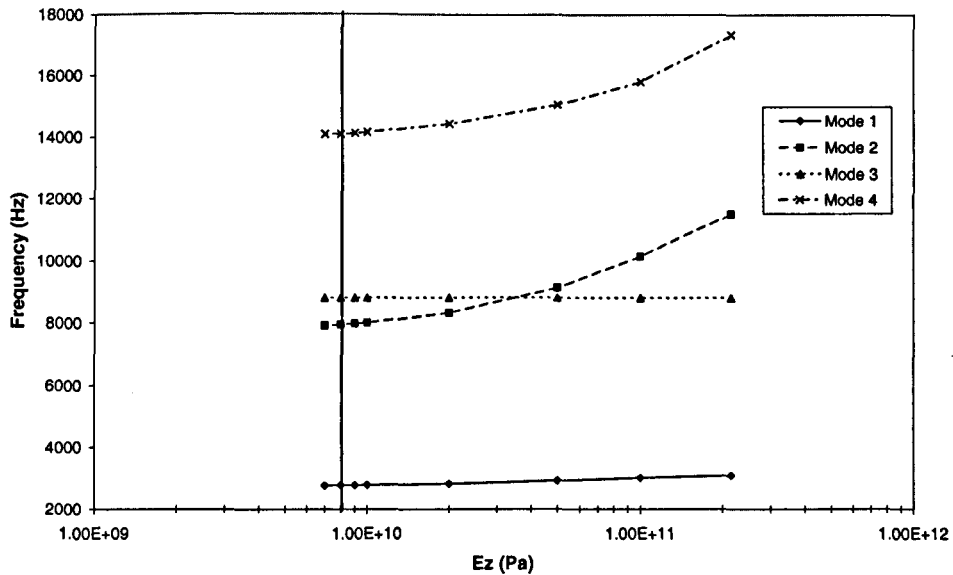


**Figure 5.16 - Variation of natural frequencies with change in  $E_z$**

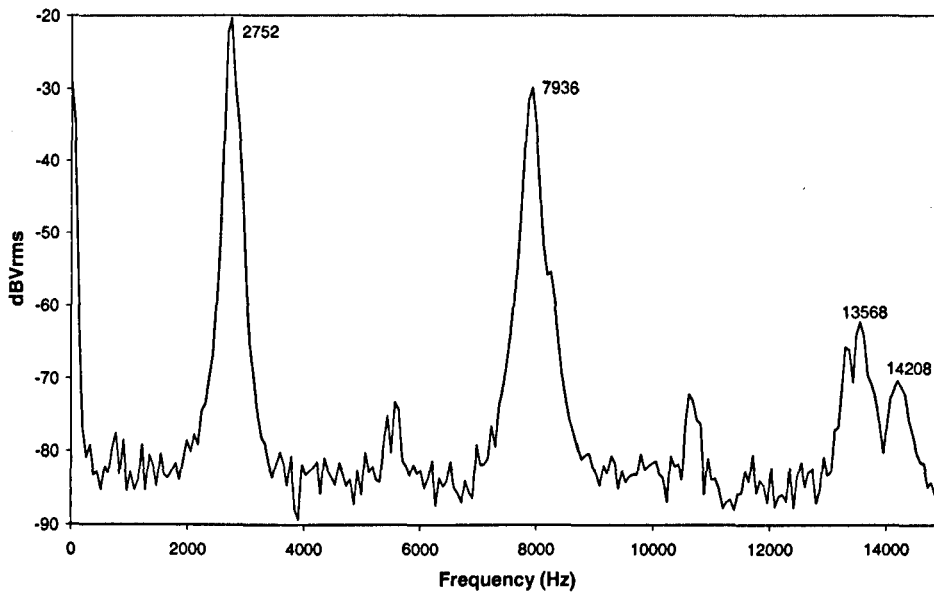


**Figure 5.17 - Measured frequency spectrum for rotor shaft with laminations**

Again, the third resonant mode was not detected due to its rotational nature, as can be seen from the mode shapes in Figure 5.18. However, from Table 5.9 it can be seen that there is a very good correlation between the predicted and measured results after compensating for the change in  $E_z$  of the laminations. The 4<sup>th</sup> mode, however, has a dual peak due to the flats, which were machined onto the shaft. As reported in [Tay40], this creates resonant modes that have 2 peaks due to the fact that the horizontal and vertical vibration frequencies of the shaft differ slightly.

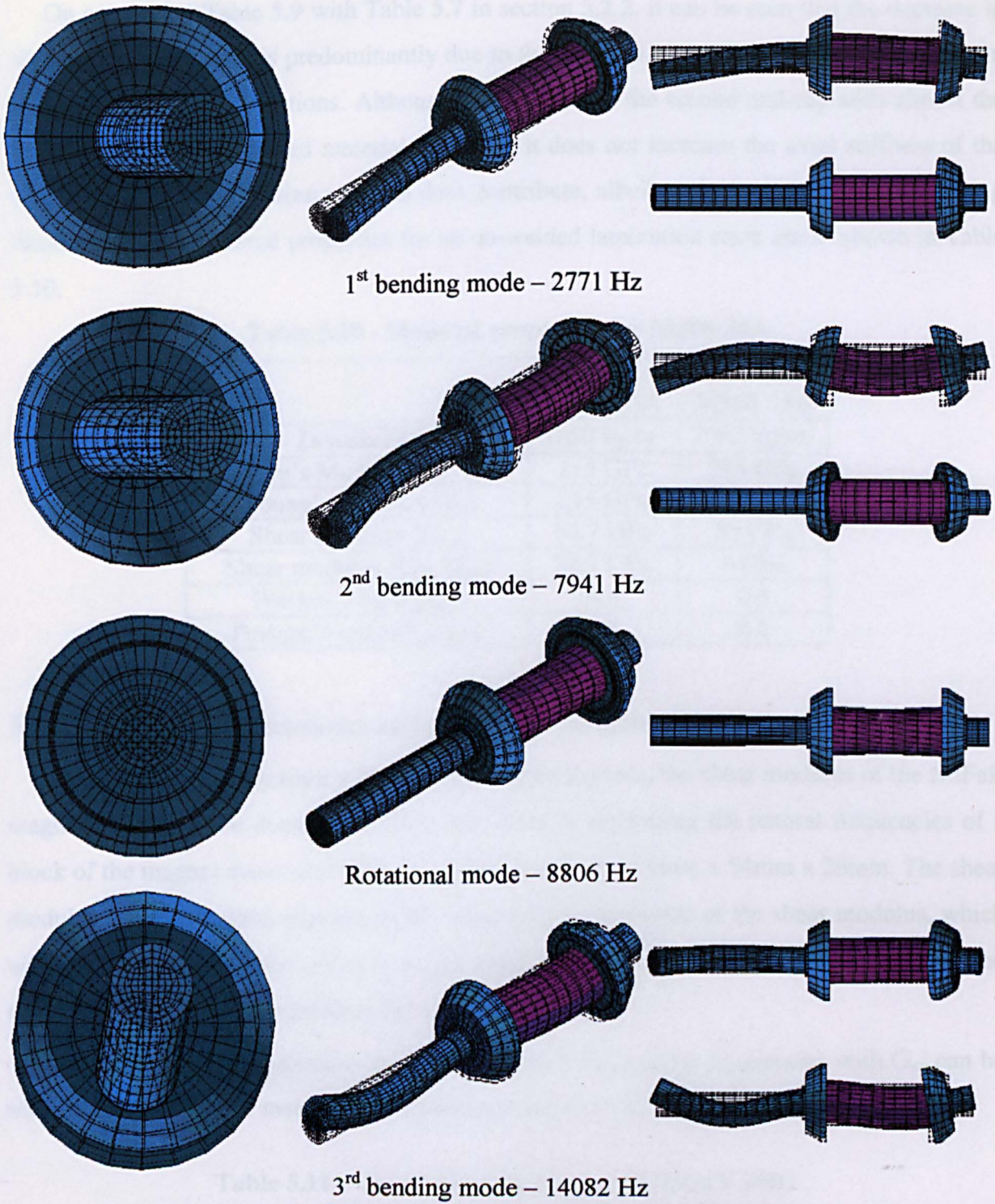


**Figure 5.18 - Vibration modes for shaft with laminations**

**Table 5.9 - Comparison of predicted and measured natural frequencies**

Mode	Finite element (Hz)	Measured (Hz)
1 <sup>st</sup> bending	2766	2752
2 <sup>nd</sup> bending	7941	7936
Rotational	8806	-
3 <sup>rd</sup> bending	14082	13568

On comparing Table 5.9 with Table 5.7 in section 5.2.2, it can be seen that the decrease in the natural frequencies is predominantly due to the addition of the second end-cap rather than the addition of the laminations. Although the addition of the second end-cap adds almost the same mass as the laminated material, viz. 18g, it does not increase the axial stiffness of the shaft whereas the lamination material does contribute, albeit in a relatively small way. Using these values, the material properties for an un-welded lamination stack are as shown in Table 5.10.

**Table 5.10 - Material properties for M300-35A**

	Solid M300-35A	Laminated M300-35A
Density ( $\rho$ )	7650 kg/m <sup>3</sup>	7305 kg/m <sup>3</sup>
Young's Modulus ( $E_x, E_y$ )	215 GPa	215 GPa
Young's modulus ( $E_z$ )	215 GPa	8 GPa
Shear modulus ( $G_{xy}$ )	82.7 GPa	55 GPa
Shear modulus ( $G_{xz}, G_{yz}$ )	82.7 GPa	8 GPa
Poisson's ratio ( $\nu_{xy}$ )	0.3	0.3
Poisson's ratio ( $\nu_{yz}, \nu_{xz}$ )	0.3	0.1

#### 5.2.4 Shaft with laminations and permanent magnets

Prior to modelling the rotor with the magnet arcs in place, the shear modulus of the NdFeB magnets needed to be determined. This was done by measuring the natural frequencies of a block of the magnet material (UGIMAX 34B1) measuring 54mm x 54mm x 26mm. The shear modulus was determined experimentally by modifying the value of the shear modulus, which was specified in the finite element model until the predicted frequencies converged to the natural frequencies measured from the impulse test.

The finite element predictions and the variation in the natural frequencies with  $G_{xy}$  can be seen in Table 5.11. The measured frequency spectrum is shown in Figure 5.19.

**Table 5.11 - Convergence of  $G_{xy}$  for UGIMAX 34B1**

$G_{xy}$ (GPa)	Natural frequency (Hz)			
	Mode1	Mode 2	Mode3	Mode 4
10	7393	17889	13751	18872
20	10403	21823	19284	24056
30	12729	23716	23517	27026
40	14690	24771	27049	28879
50	16416	25432	30121	30129
60	17976	25882	32884	31002
<b>61</b>	<b>18125</b>	<b>25919</b>	<b>33144</b>	<b>31075</b>
65	18707	26057	34163	31350
70	19411	26207	35387	31653
90	21998	26644	37621	32548

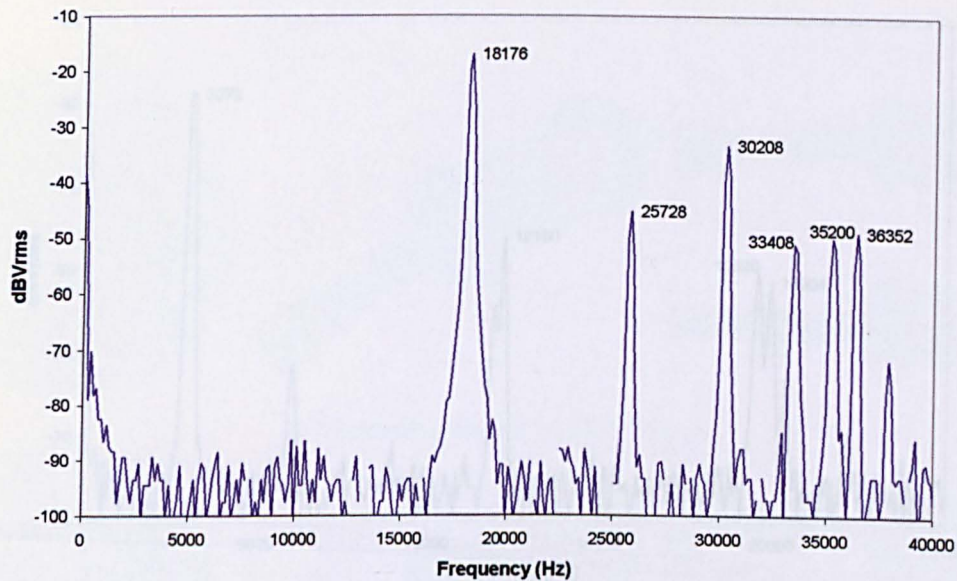


**Figure 5.19 - Measured frequency spectrum for block of UGIMAX34B1**

As can be seen by comparing Table 5.11 and Figure 5.19 the most appropriate value of  $G_{xy}$  is 61 GPa. Predicted natural frequencies based on this value are compared with measured values in Table 5.12, and very good correlation is achieved. This value was then assumed in the finite element model for the rotor shaft with laminations and magnets.

**Table 5.12 - Comparison of predicted and measured natural frequencies**

Mode	Finite element (Hz)	Measured (Hz)
1	18125	18176
2	25919	25728
3	33144	33408
4	31075	30208

The finite element model is shown in Figure 5.20, which also shows the component parts of the rotor, whilst the predicted natural frequencies are compared with the measured values in the frequency spectrum of Figure 5.21 and in Table 5.13.

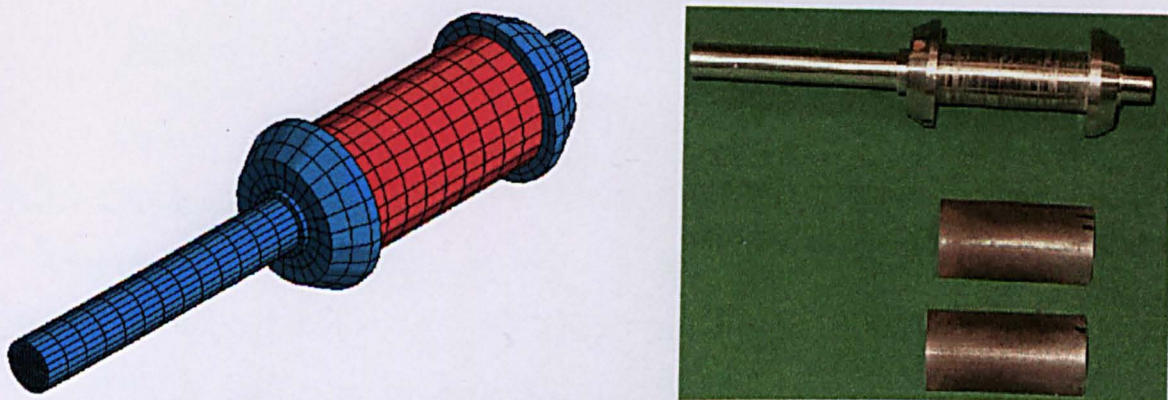


**Figure 5.20 - Finite element mesh and photograph of shaft and permanent magnets**

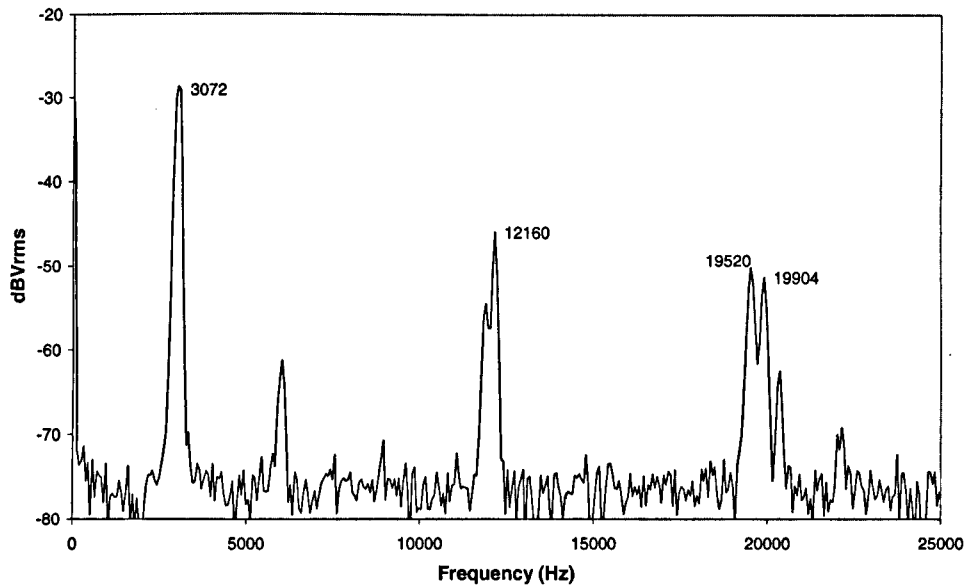
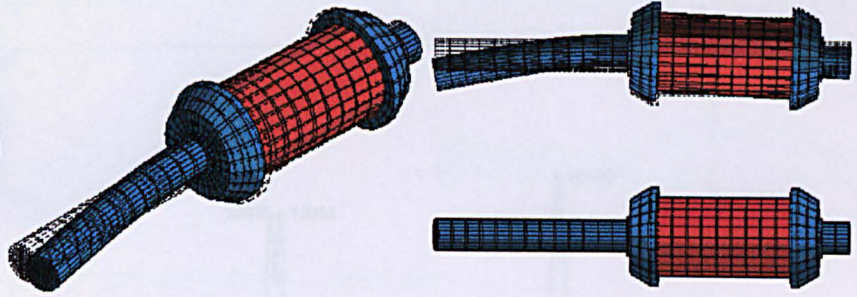
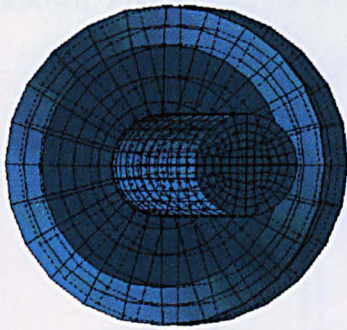


**Figure 5.21 - Measured frequency spectrum for shaft with laminations and permanent magnets**

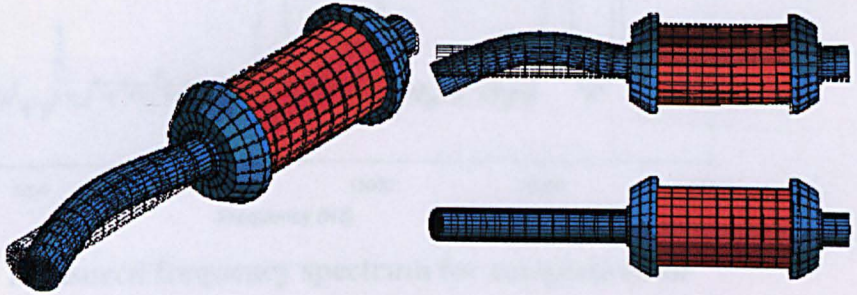
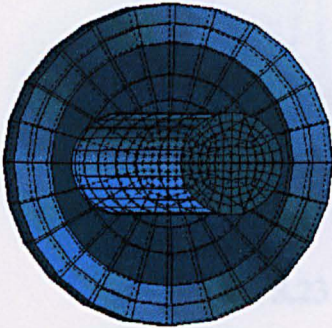
It can be seen that there is a fairly good correlation between the predicted and measured values. Again, however, the 3<sup>rd</sup> mode cannot be detected. The associated vibrational modes are shown in Figure 5.22. As stated earlier, the addition of the magnets stiffens the shaft and thereby increases the natural frequencies from those, which were predicted and measured for the shaft and laminations alone.

**Table 5.13 - Comparison of predicted and measured frequency spectrum**

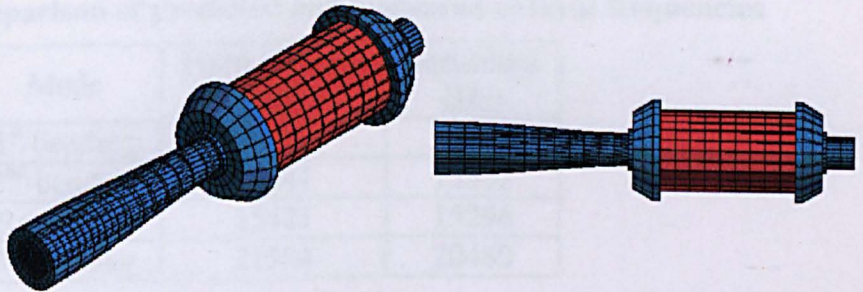
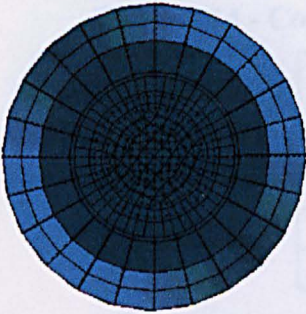
Mode	Finite element (Hz)	Measured (Hz)
1 <sup>st</sup> bending	3052	3008
2 <sup>nd</sup> bending	12609	12160
Rotational	15410	-
3 <sup>rd</sup> bending	21201	19904



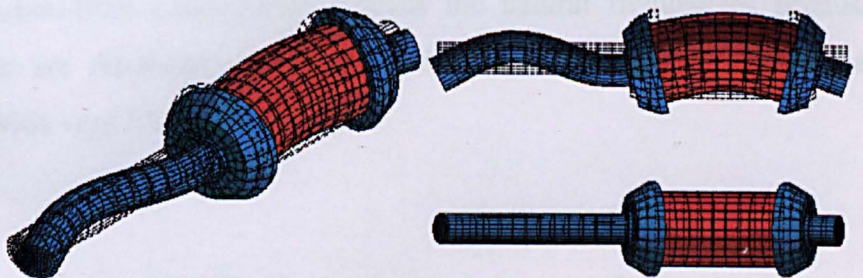
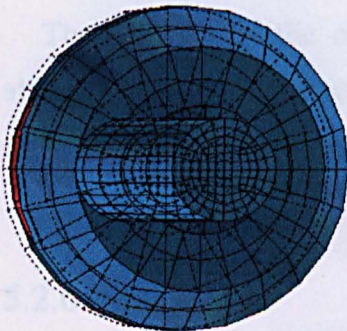
**1<sup>st</sup> bending mode – 3052 Hz**



**2<sup>nd</sup> bending mode – 12609 Hz**



**Rotational mode – 15410 Hz**



**3<sup>rd</sup> bending mode – 21201 Hz**

**Figure 5.22 - Vibrational modes for shaft with laminations and magnets**

### 5.2.5 Complete rotor

After the carbon fibre containment was added the natural frequencies were again measured prior to balancing. The measured frequency spectrum is shown in Figure 5.23. As can be seen from Table 5.14, there is a good correlation between the measured and predicted values. This

time, however, the rotational mode has been detected, although the reason for this is not known. Figure 5.24 shows the corresponding vibrational modes.

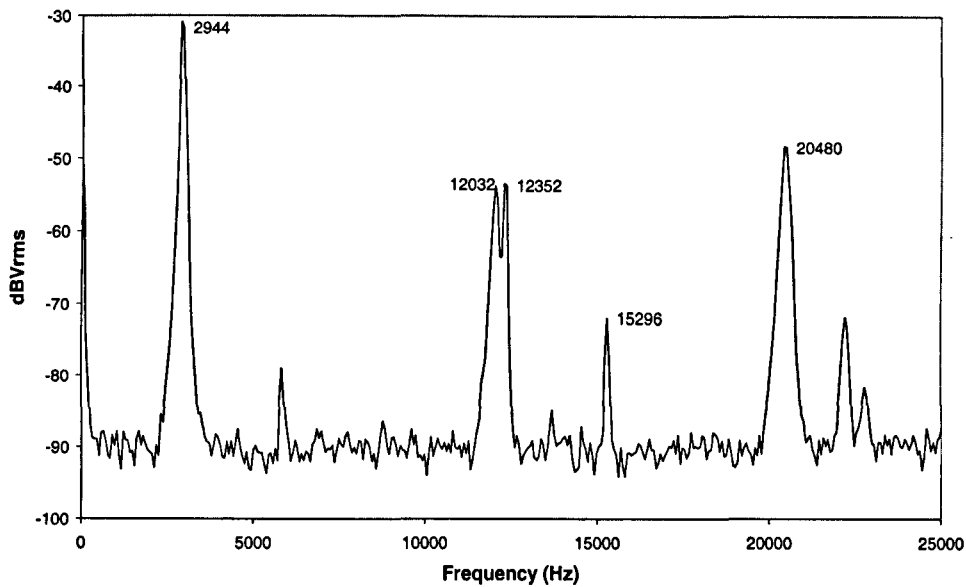


**Figure 5.23 - Measured frequency spectrum for complete rotor**

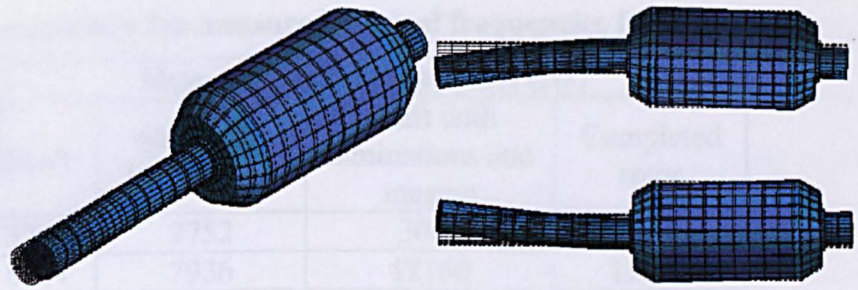
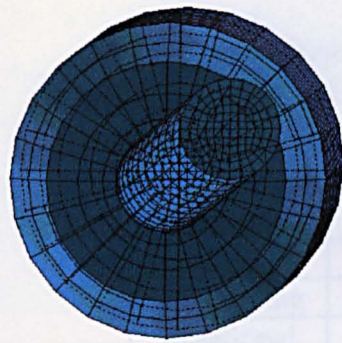
**Table 5.14 - Comparison of predicted and measured natural frequencies**

Mode	Finite element (Hz)	Measured (Hz)
1 <sup>st</sup> bending	3026	2944
2 <sup>nd</sup> bending	12641	12352
Rotational	15421	15296
3 <sup>rd</sup> bending	21504	20480

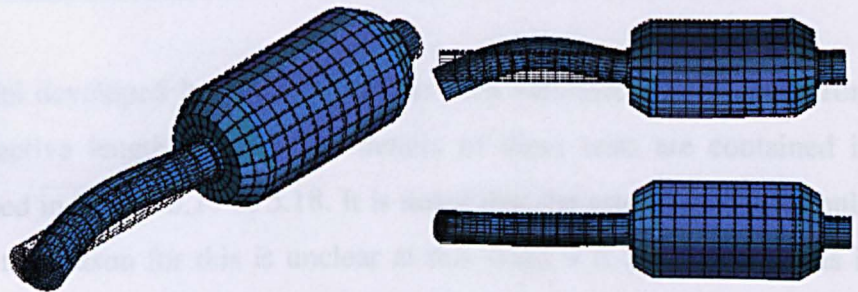
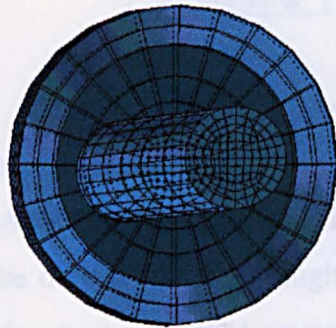
The addition of the carbon-fibre containment reduces the natural frequencies because although the carbon fibres are relatively strong along their direction of orientation, i.e. circumferentially, they provide very little axial stiffness.

## 5.2.6 Summary

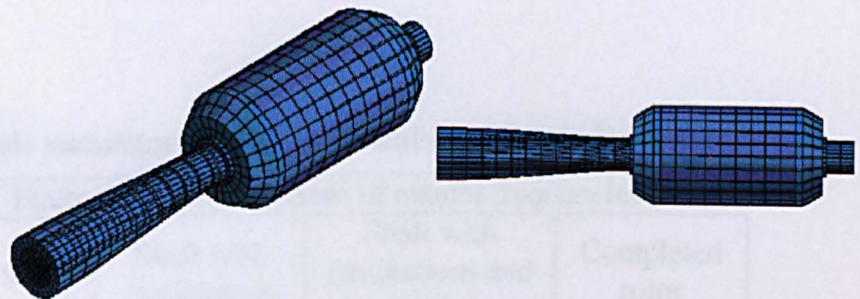
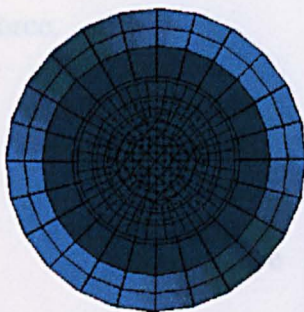
Good correlation has been observed between the finite element predictions and the measured natural frequencies, the main cause of any discrepancies being the fact that the finite element model assumes perfect contact between the surfaces, which in practice does not occur. Tables 5.15 & 5.16 summarise the natural frequencies and resonant modes at the various stages of construction of the rotor.



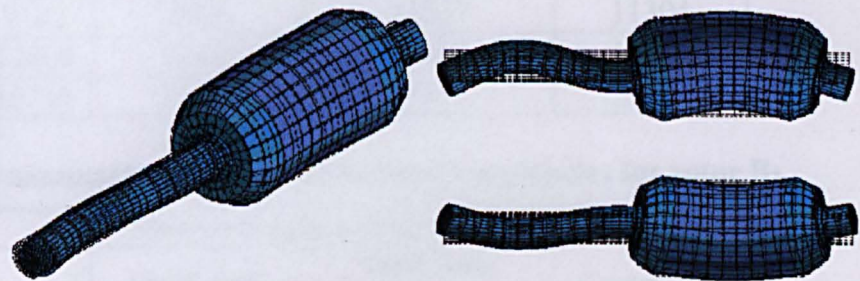
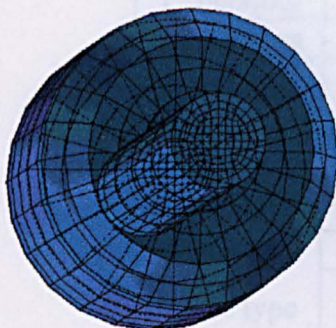
**1<sup>st</sup> bending mode – 3026 Hz**



**2<sup>nd</sup> bending mode – 12641 Hz**



**Rotational mode – 15421 Hz**



**3<sup>rd</sup> bending mode – 21504 Hz**

**Figure 5.24 - Vibration modes for complete rotor**

**Table 5.15 - Mode summary for finite element predictions for rotor A<sub>1</sub>**

Mode type	Finite element predictions of natural frequencies (Hz)			
	Shaft	Shaft with laminations	Shaft with laminations and magnet	Completed rotor
1 <sup>st</sup> bending	3138	2766	3052	3026
2 <sup>nd</sup> bending	8751	7941	12609	12641
Rotational	11710	8806	15410	15421
3 <sup>rd</sup> bending	15906	14082	21201	21504

**Table 5.16 - Mode summary for measured natural frequencies for rotor A<sub>1</sub>**

Mode type	Measured natural frequencies (Hz)			
	Shaft	Shaft with laminations	Shaft with laminations and magnet	Completed rotor
1 <sup>st</sup> bending	3200	2752	3008	2944
2 <sup>nd</sup> bending	8864	7936	12160	12352
Rotational	-	-	-	15296
3 <sup>rd</sup> bending	16320	13568	19904	20480

The finite element model developed in this section, was then validated on the rotor from motor B<sub>1</sub> with a shorter active length and the full details of these tests are contained in Appendix H and summarised in Tables 5.17 & 5.18. It is noted that the rotational mode could be detected, and although the reason for this is unclear at this stage it is thought that this is due to the modal hammer impacting the shaft at an angle and imparting a slight rotational force.

**Table 5.17 – Mode summary for finite element predictions for rotor B<sub>1</sub>**

Mode type	Finite element predictions of natural frequencies (Hz)			
	Shaft	Shaft with laminations	Shaft with laminations and magnet	Completed rotor
1 <sup>st</sup> bending	3373	3124	3273	3235
2 <sup>nd</sup> bending	9132	8936	11537	11304
Rotational	12804	12431	14680	14620
3 <sup>rd</sup> bending	16716	15252	19195	19182

**Table 5.18 - Mode summary for measured natural frequencies for rotor B<sub>1</sub>**

Mode type	Measured natural frequencies (Hz)			
	Shaft	Shaft with laminations	Shaft with laminations and magnet	Completed rotor
1 <sup>st</sup> bending	3392	2976	3328	3264
2 <sup>nd</sup> bending	9792	9216	11136	11200
Rotational	-	-	14592	14656
3 <sup>rd</sup> bending	17216	15776	18944	19200

### 5.3 Derivation of bearing stiffness

When the rotor is mounted in bearings, new resonant modes are introduced at critical speeds [Van88][Zhu89]. Each bearing can be considered as a spring whose spring constant (K) represents the stiffness of the bearing. When K is increased, the shape of the vibrational

mode at the critical speed changes. For example, Figure 5.25 illustrates the effect of changing the value of  $K$  for a uniform cylindrical shaft. The first 2 modes are referred to as the cylindrical and conical modes. For a symmetrical rotor the shape of these modes is as shown in Figure 5.26. Usually the third resonance mode encountered is the 1<sup>st</sup> bending mode of the shaft, which corresponds to the first mode detected on the resonance test for the unsupported rotor. For  $K=0$  it can be shown that this frequency should be the same as that for an unsupported (or a free-free) rotor, as shown in the previous section.

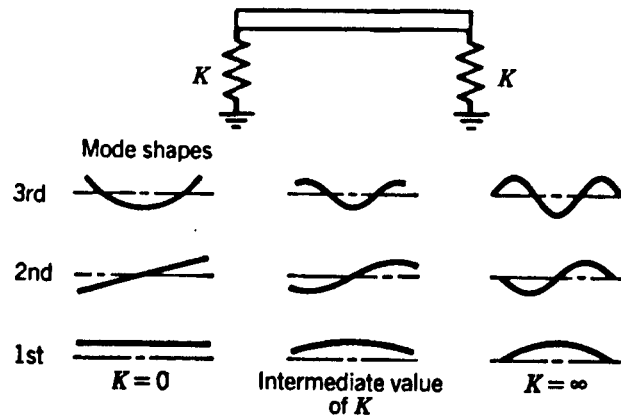


Figure 5.25 - Effect of bearing support stiffness on mode shapes [Van88]

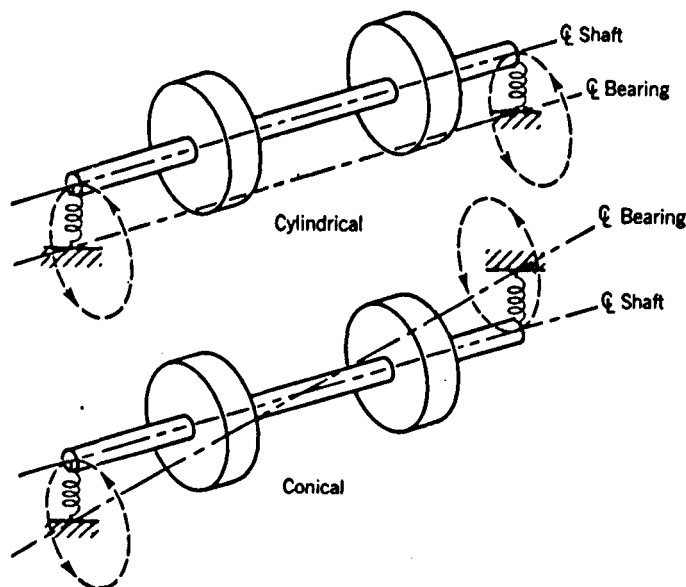


Figure 5.26 - Vibrational modes for  $K=0$  [Van88]

For a simple, symmetrical, rigid rotor supported by bearings as shown in Figure 5.27 a set of equations which describe the critical speeds for the cylindrical and conical modes can be derived [Van88] as shown in the matrix of Equation 5.2

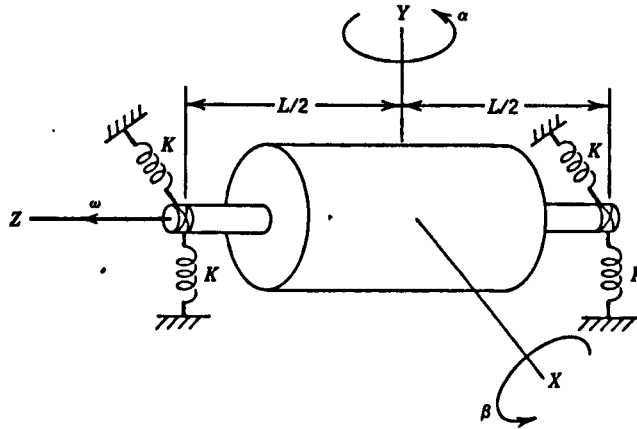


Figure 5.27 - Rigid rotor with bearings [Van88]

$$\begin{bmatrix} (ms^2 + 2K) & 0 & 0 & 0 \\ 0 & (ms^2 + 2K) & 0 & 0 \\ 0 & 0 & I_T s^2 + \frac{KL^2}{2} & I_P \omega s \\ 0 & 0 & -I_P \omega s & I_T s^2 + \frac{KL^2}{2} \end{bmatrix} \cdot \begin{Bmatrix} a_1 \\ a_2 \\ a_3 \\ a_4 \end{Bmatrix} = \begin{Bmatrix} 0 \\ 0 \\ 0 \\ 0 \end{Bmatrix} \quad (5.2)$$

The purely imaginary 'eigenvalues', or critical speeds of the system, are  $s_j = \pm i\omega_j$ , for  $j=1,2,3,4$ , where:

$$\omega_1 = \omega_2 = \sqrt{2K/m} \quad (5.3)$$

$$\omega_3 = \left[ \frac{I_P}{2I_T} \omega + \sqrt{\frac{KL^2}{2I_T} + \left( \frac{I_P}{2I_T} \omega \right)^2} \right] \quad (5.4)$$

$$\omega_4 = \left[ \frac{I_P}{2I_T} \omega - \sqrt{\frac{KL^2}{2I_T} + \left( \frac{I_P}{2I_T} \omega \right)^2} \right] \quad (5.5)$$

where  $I_P$ ,  $I_T$ ,  $K$  and  $m$  are, respectively, the polar moment of inertia, the transverse moment of inertia, the spring constant and the rotor mass. It can be seen that Equation 5.3 for the cylindrical mode is independent of the rotor speed, whereas the conical modes (Equations 5.4 & 5.5) are a function of the rotor speed. It can be shown that for a particular rotor there is a linear change in the critical speed of the conical mode. In practice however, equation 5.4 is not observed, as the mode tends to be negative or very small and is not excited. For a stationary rotor the analytical values for the conical modes reduce to give  $\omega = \sqrt{KL^2/2I_T}$ .

The system shown in Figure 5.27 assumes that the rotor is supported at 2 points by 2 springs, one on the x-axis, and one on the y-axis. In the finite element model, however, the springs are attached to each side of the rotor shaft, giving 4 fixing points. The reason for modelling the rotor in this way is so that the resonant modes lie along the axis rather than at

45° from the x and y-axes. The inclusion of 4 fixing points more accurately models the real situation, and the use of 2 springs in each of the x and y axis leads to the constant of each spring being half of the total constant on each axis. In the analytical model of Figure 5.27 the shaft is assumed to be rigid whereas in practice the shaft will flex. If the shaft can be assumed to be rigid then the analytical methods give very accurate values for the critical speeds. However, once the rotor shaft starts to flex, finite element analysis is required to find the 2 modal frequencies. By increasing the shaft stiffness to make it effectively rigid good agreement can still be obtained between finite element and analytical results. Despite the flexure of the rotor shaft, the bearing modes will still exhibit cylindrical and conical behaviour. It is suspected, and is normally the case, that the first 2 critical speeds for the cylindrical and conical modes will be within the operating speed range of the motor [Van88]. From the finite element predicted results shown in Figure 5.39, the cylindrical and conical mode can clearly be seen with a bearing stiffness of  $2 \times 10^4$  N/m.

In the finite element model each bearing is modelled using the finite element 'COMBIN14', which is a spring element connecting the shaft to the outside of the outer race of the bearing. The bearings are 'fixed' at the diameter of the outside race. This means that the outer end of the 'spring' element is fixed in the x, y & z planes, whilst still being free to rotate. The 'bearing' elements can be seen on the finite element meshes as radial lines from the shaft, the triangles at the ends representing the constraints in the x, y & z directions. It is also assumed that there are no axial vibrational modes.

### 5.3.1 Rotor from motor A<sub>1</sub>

In order to measure the rotor resonant modes and reduce the influence of the stator on the rotor resonant modes an empty aluminium frame was constructed. This frame had a hole cut in one side as can be seen in Figure 5.28 to enable the accelerometer to be placed on the active length of the rotor as shown in Figure 5.33.

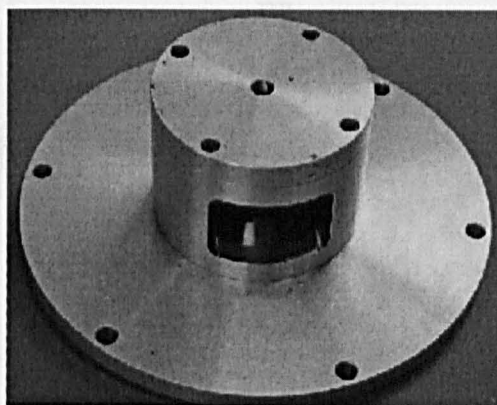


**Figure 5.28 - Empty stator frame for determination of bearing resonant modes**

Firstly, the resonant frequencies of the motor frame needed to be determined in order to account for them when determining the bearing natural frequencies. This involved making measurements on the frame without the rotor installed. The natural frequencies of the frame can be seen in Figure 5.29 whilst Figure 5.30 shows the frequency spectrum, which results with the rotor in place. By comparing the two spectra it can be assumed that the resonances shown in Figure 5.29 at 1632Hz, 2272Hz, 3040Hz, 6784Hz, 7360Hz, 12448Hz, 13376Hz and 14592Hz are due to the frame. These natural frequencies will change slightly when the rotor is in place as the dynamics of the system change slightly whilst the modes are also dependent on the siting of the accelerometer and, indeed on the magnitude of the applied impulse force. When the rotor is hit gently it is observed that the rotor modes tend to dominate the frequency spectrum, whilst when the rotor is hit harder the frame modes tend to dominate the frequency spectrum. This effect can be observed in Figures 5.31 & 5.32.

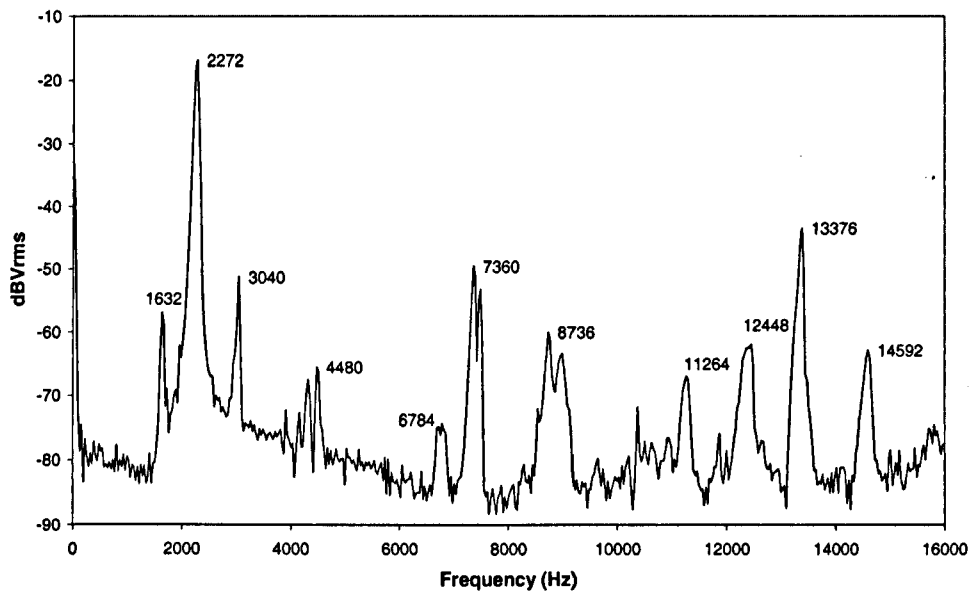


**Figure 5.29 - Frequency spectrum for frame without rotor**

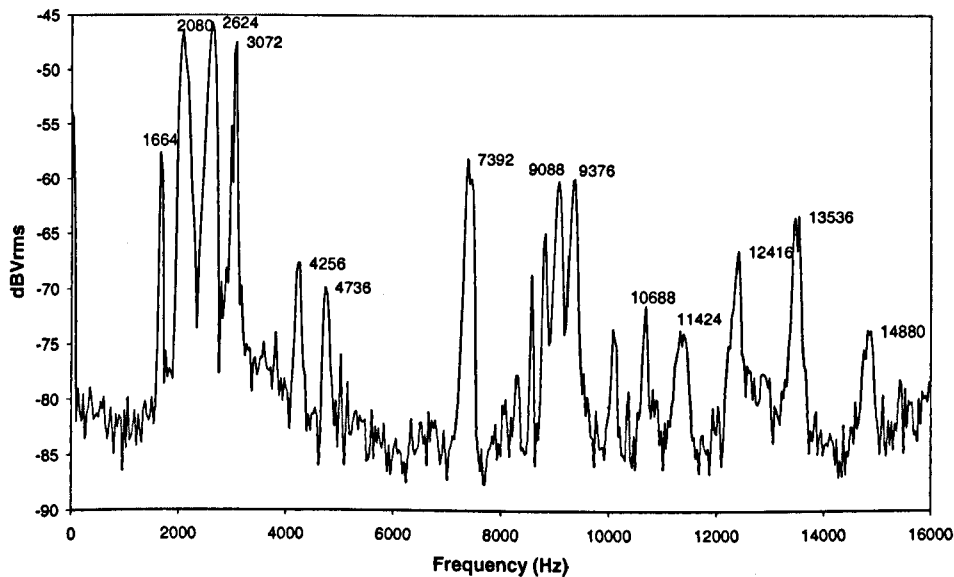


**Figure 5.30 - Frequency spectrum for frame with rotor**

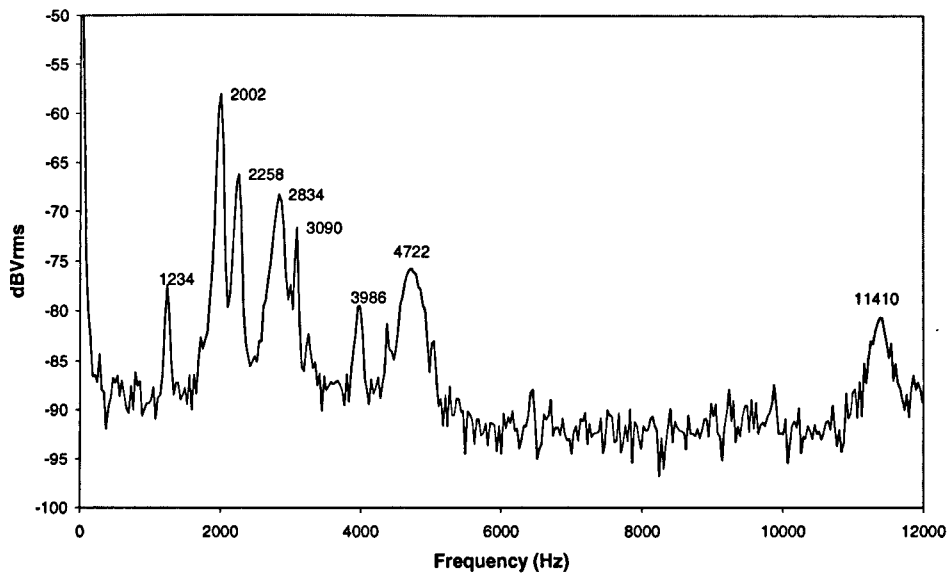


**Figure 5.31 - Frequency spectrum when hit gently**

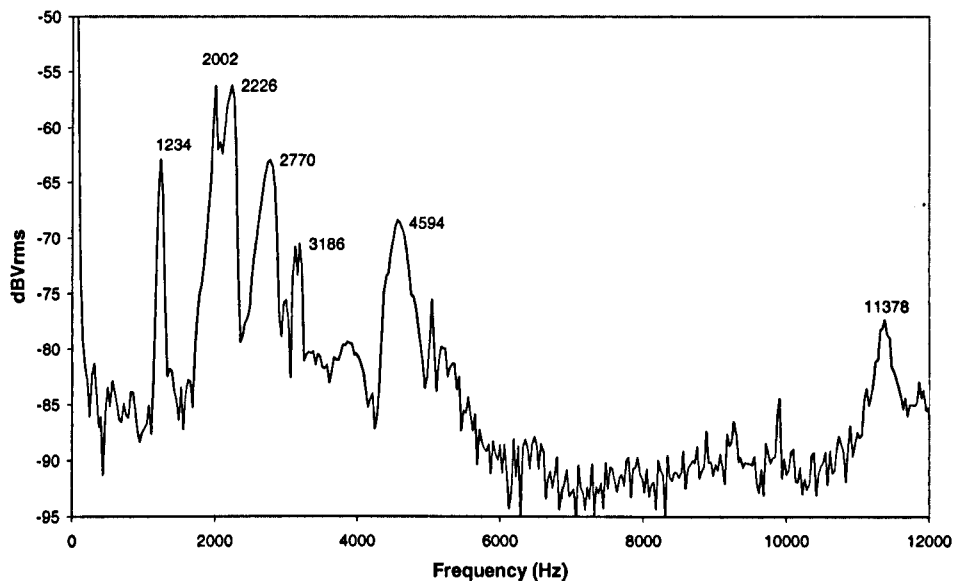


**Figure 5.32 - Frequency spectrum when hit harder**

From Figure 5.32, it can be seen that the peak amplitudes are generally larger than in Figure 5.31 indicating more force, and the modes due to the frame tend to dominate the spectrum. It is expected that there will be some interaction between the resonant modes with the mode peaks getting pulled together or masked by other resonant peaks. Here it is suspected that the frequencies at 1234 Hz are also due to the frame or frame fixings and are affected by assembling/reassembling the motor.

Once the resonant frequencies due to the frame had been determined, then an investigation was done to determine the bearing stiffness. It was expected that the measured bearing stiffness would be lower than the manufacturers quoted value of around  $5 \times 10^7$  N/m due to flexing of the aluminium end-caps and the fit of the bearings in the housings, which may allow some small movement of the bearing.

After testing the frame alone, the impulse response test was performed on the assembled motor (without the stator) in order to determine the bearing resonances. The accelerometer was located at various positions along the shaft extension, indicated by the arrows on the left of the figure, and on the active length of the rotor, as shown in Figure 5.33. The shaft was then tapped with the modal hammer at certain positions on the shaft extension to generate the frequency spectra shown in Figure 5.34.

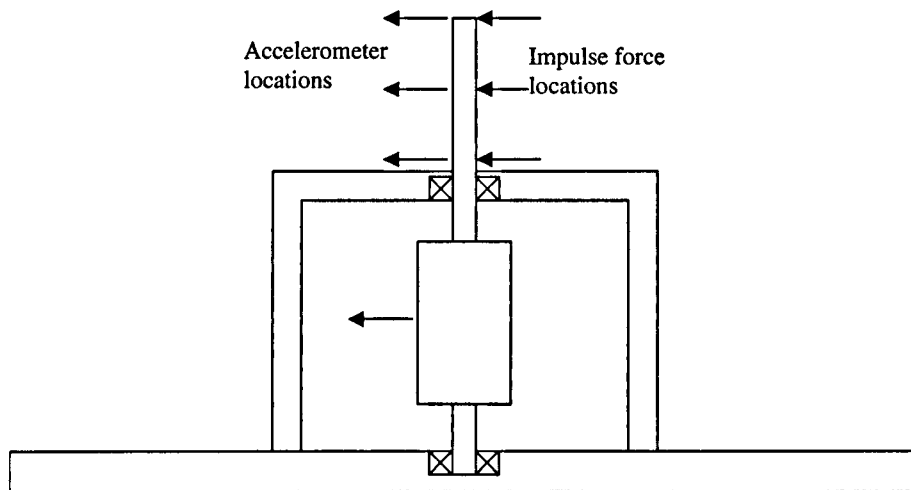


**Figure 5.33 - Location of accelerometer and impulse force locations**

In the frequency spectra of Figure 5.34, the frame resonant frequencies at around 2.2 kHz, are present where the accelerometer is located inside the frame even when the impulse force is very small. It is suspected that the resonance at 1234 Hz is the same as that which was detected at 1632 Hz in Figure 5.29, but which changed when the motor was disassembled and then reassembled between making the two sets of measurements. It should be noted that for these tests the rotor was hit gently in order to avoid exciting all of the frame resonances and crowding out the frequency spectra plot. Despite this, however, frame resonances were excited and detected when the accelerometer was located inside the frame.

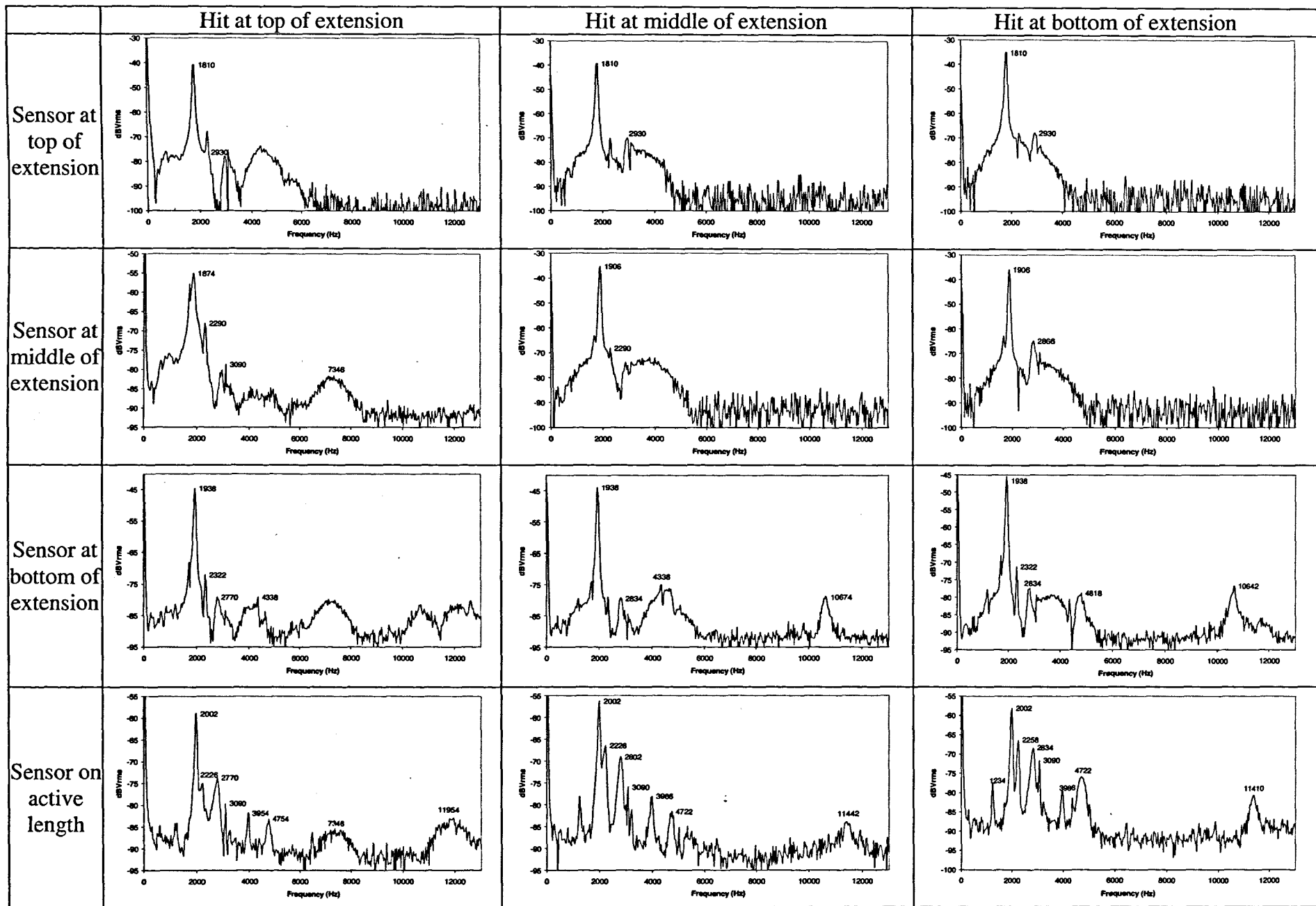
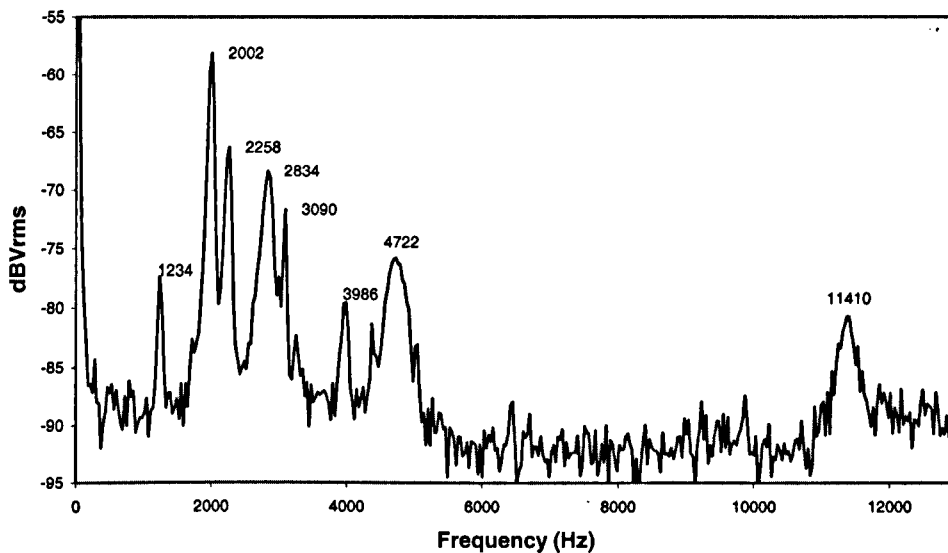


Figure 5.34 - Measured frequency spectra for complete motor A<sub>1</sub>

When the accelerometer was placed on the shaft outside the motor it was noted that the frequency of the first resonant mode decreased slightly as the accelerometer was moved further up the shaft away from the bearing. It is thought that this is due to the influence of the accelerometer in that it acts like a point mass and lowers the natural frequency of the shaft. The effect of the shaft extension on the rotor resonant frequencies is discussed in detail in section 5.4.1. With the accelerometer mounted on the shaft extension the first resonant mode, which is a combination of both the cylindrical bearing mode and a flexing of the shaft extension tends to dominate the frequency spectrum and masks the other modes. Since the positioning of the accelerometer influences the natural frequencies when placed on the shaft extension, the frequency spectra, which were measured when the accelerometer was placed on the rotor inside the frame, as shown in Figure 5.35, were used to determine the bearing resonances of the rotor since the influence of the accelerometer on the natural frequencies is then minimal, as its mass makes little difference to the mass distribution of the rotor.



**Figure 5.35 - Measured natural frequencies with accelerometer mounted on rotor inside frame**

From work done earlier in this section, some of the natural frequencies, which exist in the frequency spectrum of Figure 5.35 have been previously identified as frame resonant modes, and, consequently, can be ignored and these are listed in Table 5.19. However, it is appreciated that 'new' resonant modes could be introduced due to the mounting of the rotor in the frame. Therefore, whilst not being resonances associated with the frame modes they are not rotor modes, but result due to a combination of both the rotor and the frame.

**Table 5.19 - Natural frequencies and probable sources**

Frequency (Hz)	Frame or rotor mode
1234	Frame
<b>2002</b>	<b>Rotor</b>
2258	Frame
<b>2834</b>	<b>Rotor</b>
3090	Frame
<b>3986</b>	<b>Rotor</b>
<b>4722</b>	<b>Rotor</b>
<b>11410</b>	<b>Rotor</b>

Now that the rotor modes have been identified, a finite element analysis was performed to determine the mode shapes and the equivalent bearing stiffness. The finite element mesh and photograph of the rotor can be seen in Figure 5.36.

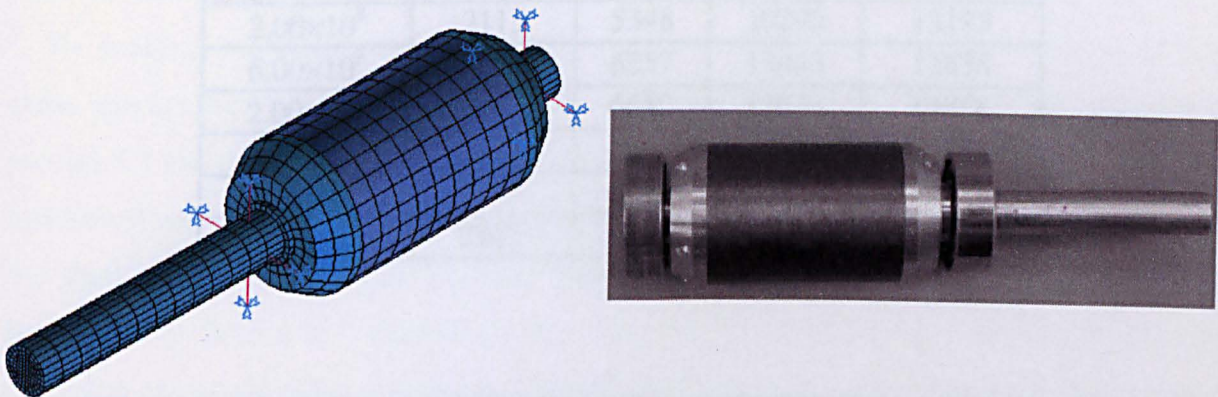


**Figure 5.36 - Finite element mesh and photograph of assembled rotor of motor A<sub>1</sub> including bearings**

The stiffness of the bearings was varied until the predicted modes converged to the measured modes. The variation of the natural frequencies with the bearing stiffness is shown in Table 5.20, and graphically in Figure 5.37. From the data, the most appropriate value of bearing stiffness is  $2.5 \times 10^7$  N/m.

As can be seen in Table 5.21 the predicted and the measured natural frequencies are not exactly the same. This could be due to the aluminium end-plate, which being thin in places which could lead to the measured apparent bearing stiffness being lower than expected as the outer race of the bearing would not be perfectly constrained as in the finite element model. Also one of the bearings has a spring washer, which applies the correct pre-load and this has been neglected in the finite element model.

**Table 5.20 - Variation of natural frequency with bearing stiffness for rotor from motor A<sub>1</sub>**

Bearing stiffness (N/m)	Mode frequencies (Hz)			
	Cylindrical	Conical	1 <sup>st</sup> bending	2 <sup>nd</sup> bending
2.00×10 <sup>4</sup>	76	105	3008	12533
2.00×10 <sup>5</sup>	242	331	3021	12534
4.00×10 <sup>6</sup>	1045	1361	3333	12556
1.00×10 <sup>7</sup>	1525	1936	3892	12589
1.20×10 <sup>7</sup>	1617	2071	4078	12599
1.60×10 <sup>7</sup>	1745	2309	4432	12620
2.00×10 <sup>7</sup>	1826	2517	4762	12640
<b>2.50×10<sup>7</sup></b>	<b>1892</b>	<b>2748</b>	<b>5140</b>	<b>12662</b>
3.00×10 <sup>7</sup>	1936	2951	5484	12685
3.50×10 <sup>7</sup>	1967	3133	5799	12707
4.00×10 <sup>7</sup>	1990	3296	6088	12729
5.00×10 <sup>7</sup>	2022	3579	6605	12770
6.00×10 <sup>7</sup>	2043	3819	7055	12810
2.00×10 <sup>8</sup>	2115	5348	10295	13175
6.00×10 <sup>8</sup>	2135	6257	12443	13838
2.00×10 <sup>9</sup>	2142	6689	13046	14888
1.60×10 <sup>10</sup>	2144	6871	13194	15371
2.00×10 <sup>11</sup>	2145	6896	13211	15371
1.60×10 <sup>12</sup>	2145	6898	13212	15371

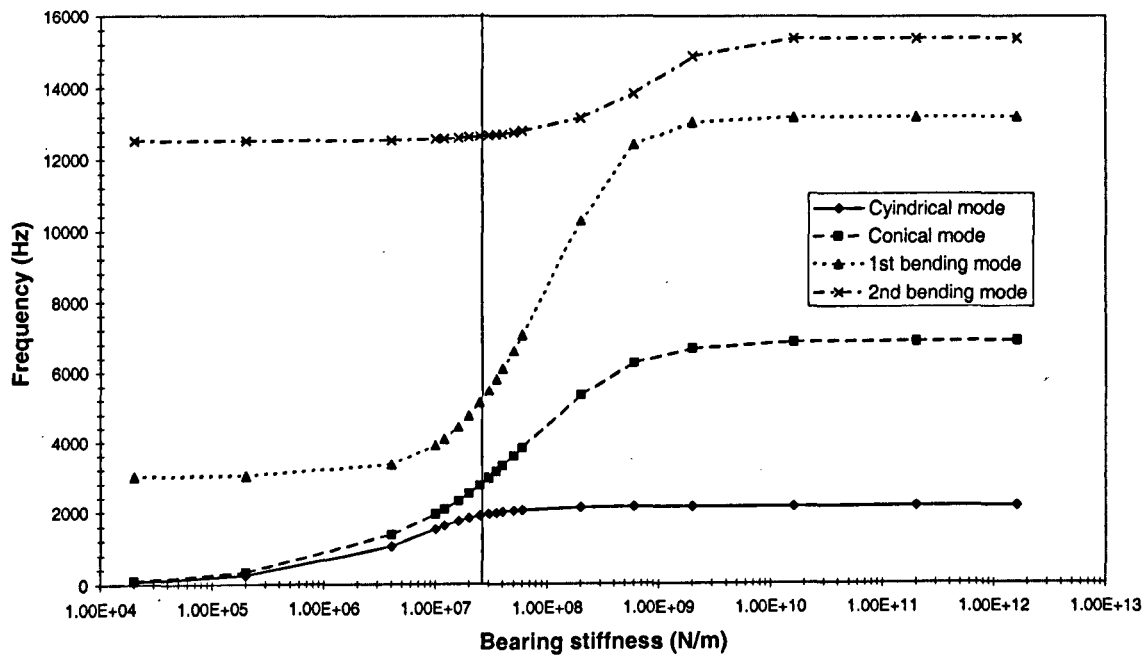


**Figure 5.37 - Variation of natural frequency with bearing stiffness**

**Table 5.21 - Comparison of predicted and measured values for a bearing stiffness of  $2.5 \times 10^7 \text{ N/m}$  for rotor with long active length**

Mode	Finite element (Hz)	Measured (Hz)
Cylindrical	1892	2002
Conical	2748	2834
1 <sup>st</sup> bending	5140	4722
2 <sup>nd</sup> bending	12662	11410

In order to display the resonant modes more clearly and to see the effect of the bearings on the rotor, the vibrational modes are presented as in Figure 5.39, which show the displacement in the y coordinate direction with the x-axis shown as a dotted line and the crosses representing the bearings. With a bearing stiffness of  $2 \times 10^4 \text{ N/m}$  the bending modes which are visible at 3008 Hz and 12538 Hz are almost identical to the free-free modes for the complete rotor, as shown in section 5.2.6.

By studying the mode shapes, some of which are shown in Figure 5.39, and performing some simple analytical calculations for the cylindrical bearing mode using equation 5.3 of section 5.3 the resonant modes can be identified. The first two modes are, respectively, the cylindrical and conical modes and the next two modes are the 1<sup>st</sup> and 2<sup>nd</sup> bending modes of the shaft the shapes of which are dominated by the shaft extension, as will be shown in section 5.4.1. With a low bearing stiffness the first 2 modes are very similar as the shaft extension causes the rotor to behave as shown in Figure 5.38. This distorts the mode shapes from what would normally be expected. In order to simplify the problem it is assumed that the shaft is rigid and weightless, and the oscillations are purely due to the mass  $m$ , which represents the laminations, the magnets, the carbon fibre, and the end-caps. In reality shaft flexing leads to 2 distinct modes, but this simplified model does not show this.

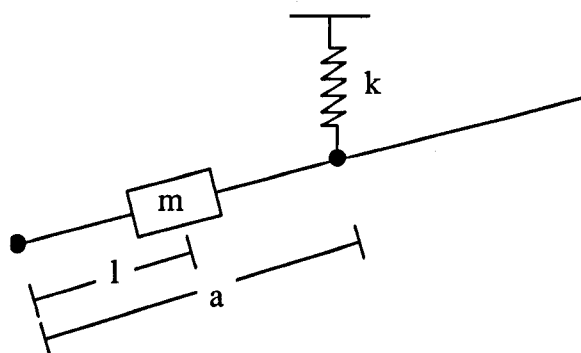


**Figure 5.38 - Analytical representation of finite element problem**

Using the representation of this system from [Har56], it can be shown that the resonant frequency is:

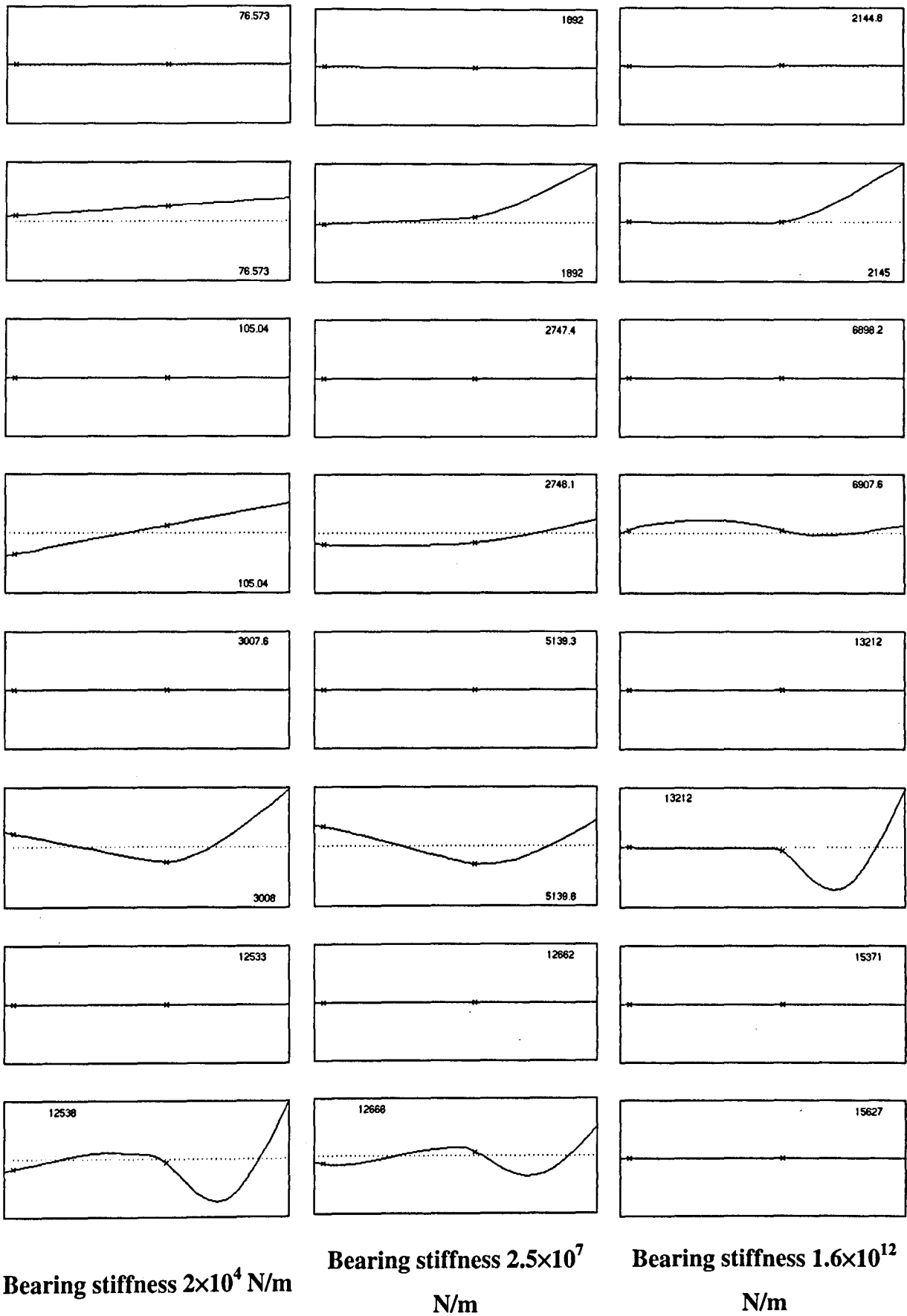


Figure 5.39 - Vibrational modes for various values of bearing stiffness (Motor A<sub>1</sub>)

$$\omega = \frac{a}{l} \sqrt{\frac{K}{m}} \quad (5.6)$$

where  $a$ ,  $l$  and  $m$  are defined in Figure 5.38. From the geometry of the rotor:  $m=0.10584$  kg,  $l=0.028$ m,  $a=0.056$ m,  $k = 1 \times 10^4$  N/m ( $K=2k$  or  $2 \times 10^4$ )

$$\therefore \omega = 614.7 \text{ rad/s}$$

$$f = 97.8 \text{ Hz}$$

Although this is somewhat higher than the 75.6 Hz, which is predicted from the finite element analysis, this method neglects the mass of the shaft, which would reduce the resonant frequency. The first bearing is not purely a pivot as assumed here, since it flexes slightly, which will also act to reduce the natural frequency.

Both the cylindrical and conical modes change quite significantly as the bearings stiffness is increased. The shaft extension flexes while the central part of the rotor is more rigid, and this flexure starts to dominate the mode frequency. At a bearing stiffness of  $2.5 \times 10^7$  N/m the bearings allow only a small movement, the majority being due to the flexure of the shaft. At this resonant frequency of 1897 Hz, or 113,820 rpm, this mode could cause problems by causing the shaft extension to become unbalanced and bend.

At the other extreme, where the bearing stiffness is  $2 \times 10^{11}$  N/m and are effectively rigid it can be seen from Figure 5.39 that the resonance modes are quite different. Now the flexing of the shaft extension clearly dominates the mode shapes.

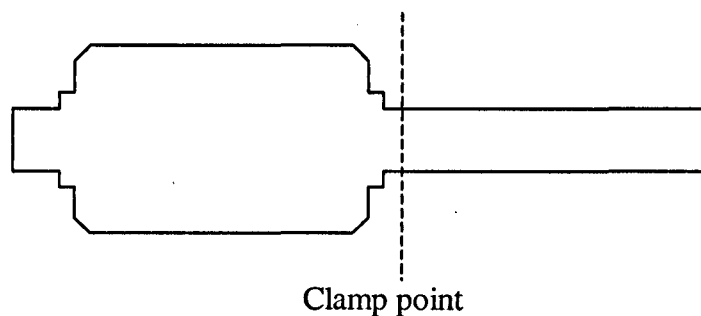


**Figure 5.40 - Diagram of rotor showing where bearing is assumed to be clamped**

When the bearings are stiff, the shaft extension can be considered to be clamped at the bearing, as shown in Figure 5.40, with the end free to vibrate. With this approximation, the natural frequency of the free shaft extension can be estimated using the equation 5.1 from section 5.2.1, viz.:

$$\omega_n = a_n \sqrt{\frac{EI_p}{\mu_1 l^4}} \quad (5.1)$$

In this case,  $a_1=3.52$ ,  $a_2=22.0$  from [Har56], and the remainder of the parameters are as defined previously. The shaft diameter is 8mm, and the shaft extension length is 43.5mm.

$$E=1.93 \times 10^{11} \text{ N/m}, I_p=2.01 \times 10^{-10} \text{ kg m}^2, \mu_l=0.4021 \text{ kg/m}$$

$$\omega_n=a_n \times 5191.4$$

$$\omega_1=18274 \text{ rad/s}$$

$$f_1=2908 \text{ Hz}$$

$$\& f_2=18177 \text{ Hz}$$

Whilst these values are somewhat higher than predicted by finite element analysis, it can be seen that the bearings restrict movement in the x and y directions. Whilst allowing rotor rotation, the bearing exhibits some qualities of a pivot, albeit quite heavily damped, during a resonance mode. In practice, however, the bearing behaviour will lie somewhere between the case assumed here and that of a free pivot at the bearing. For a free pivot, there is no first frequency, i.e.  $a_1=0$ , whilst the second frequency is predicted using equation 5.1, but with  $a_2 = 15.4$ . This predicts a resonant frequency of 12724Hz, which is closer to the value predicted by finite element analysis, viz. 12663 Hz.

It is generally accepted that it is the first bending mode that is the most destructive as it contains the most energy. Also due to its low frequency this mode often occurs with the operating speed range of a motor. The destructive power of the first bending mode was observed in the destruction of a rotor, shown previously in Figure 5.3.

### 5.3.2 Rotor from motor B<sub>1</sub>

The same test was performed for motor B<sub>1</sub> with the short active length. However, it should be noted that the bearing housing on this motor was slightly worn due to the bearing housing slipping at high speeds, and this may allow some slight movement and affect the resonance modes, and possibly introduce new modes. The measured frequency spectrum is shown in Figure 5.41

The bearing stiffness was deduced by the same method, which was employed for motor A<sub>1</sub>. In theory the bearing stiffness should be the same for both motors, but due to wear in the bearing housing its apparent value may be slightly different from that which was calculated earlier. The finite element mesh is shown in Figure 5.42.

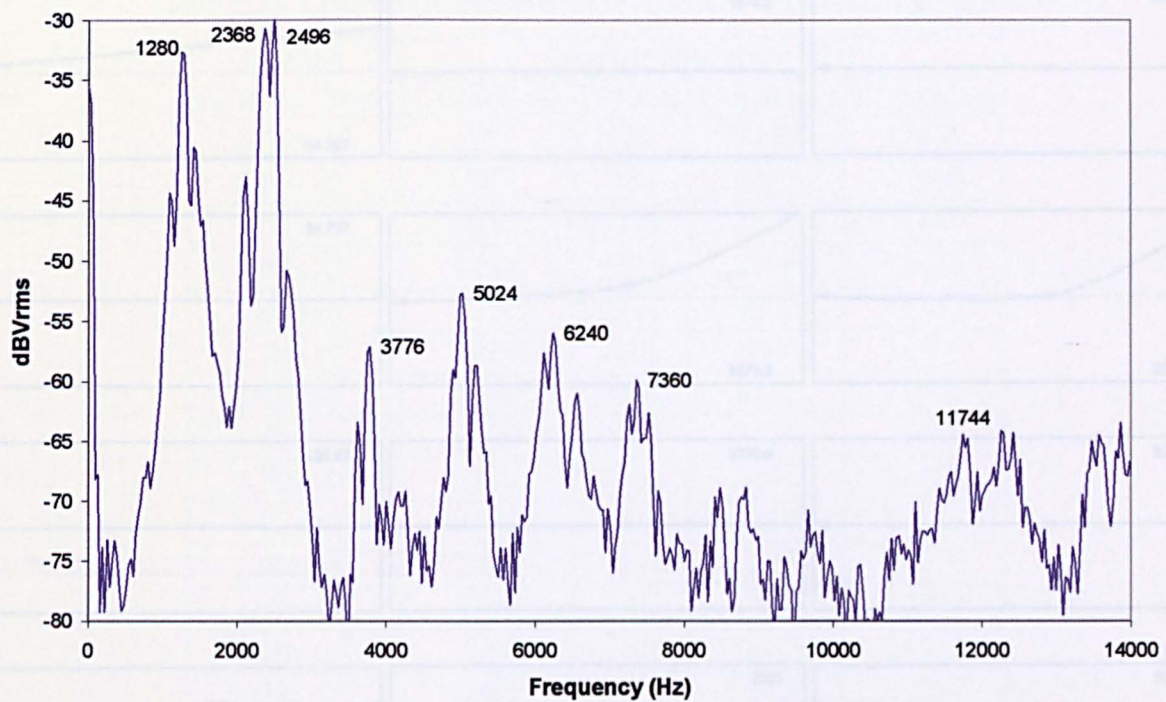


**Figure 5.41 - Measured frequency spectrum for complete motor B<sub>1</sub>**

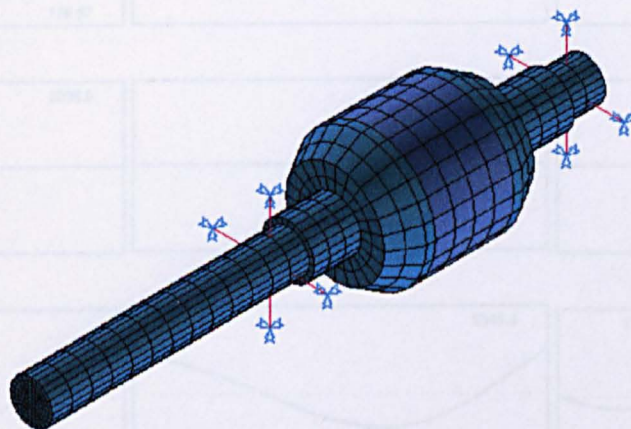
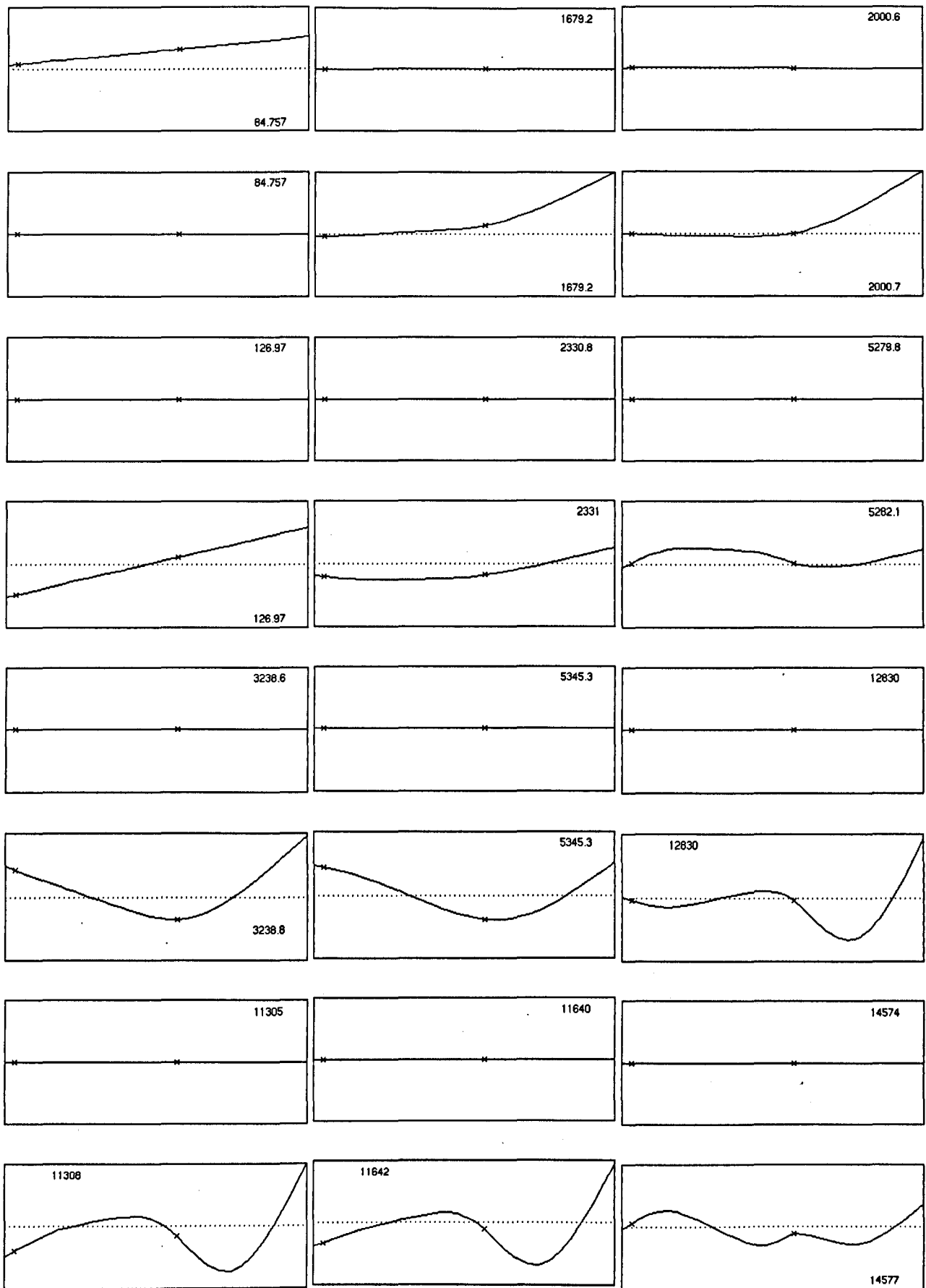


**Figure 5.42 - Finite element mesh for rotor from motor B<sub>1</sub>**

The predicted mode frequencies are given in Table 5.22, and shown graphically in Figure 5.43. As can be seen by comparing Figure 5.44 and Table 5.22 the best fit occurs when the bearing stiffness is  $1.4 \times 10^7$  N/m, for which finite element predicted natural frequencies are compared with measurements in Table 5.23.



Bearing stiffness  $2 \times 10^4$  N/m    Bearing stiffness  $1.4 \times 10^7$  N/m    Bearing stiffness  $2 \times 10^{12}$  N/m  
**Figure 5.43 - Vibrational modes for various values of bearing stiffness**

**Table 5.22 - Variation of natural frequency with bearing stiffness**

Bearing stiffness (N/m)	Mode Frequencies (Hz)			
	Cylindrical	Conical	1 <sup>st</sup> bending	2 <sup>nd</sup> bending
$2.00 \times 10^4$	85	127	3239	11305
$2.00 \times 10^5$	267	398	3267	11310
$2.00 \times 10^6$	824	1160	3566	11360
$4.00 \times 10^6$	1125	1514	3906	11414
$1.00 \times 10^7$	1557	2071	4832	11557
$1.20 \times 10^7$	1627	2207	5098	11599
<b><math>1.40 \times 10^7</math></b>	<b>1679</b>	<b>2331</b>	<b>5345</b>	<b>11640</b>
$1.60 \times 10^7$	1719	2445	5575	11680
$2.50 \times 10^7$	1821	2862	6442	11831
$4.00 \times 10^7$	1889	3334	7491	12024
$2.00 \times 10^8$	1979	4654	11290	12670
$1.60 \times 10^9$	1998	5191	12764	14052
$2.00 \times 10^9$	1998	5208	12778	14152
$2.00 \times 10^{10}$	2000	5273	12826	14532
$2.00 \times 10^{11}$	2000	5279	12830	14573
$2.00 \times 10^{12}$	2000	5280	12830	14577

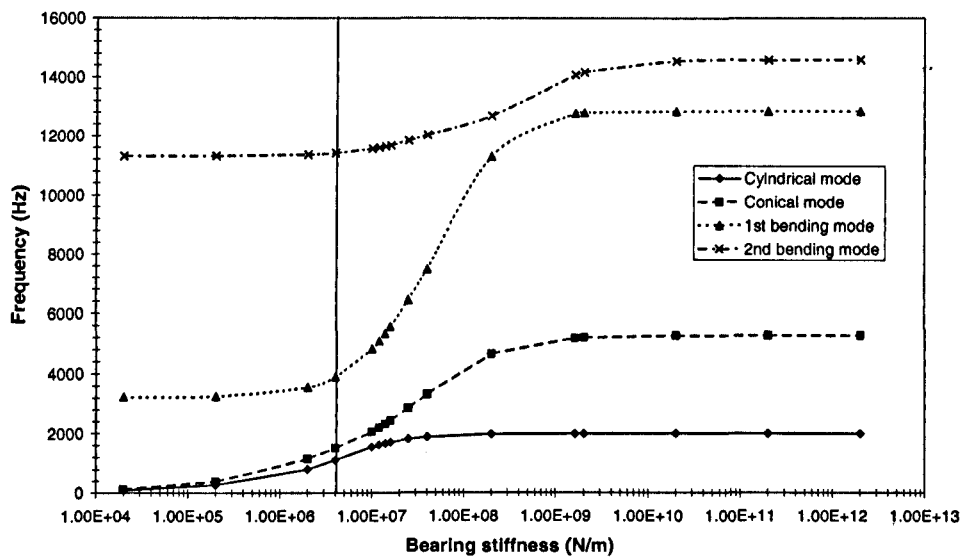


**Figure 5.44 - Variation of natural frequency with change in bearing stiffness for rotor with short active length**

At this stage it was not known for certain why such a large discrepancy existed between the predicted and measured resonant frequencies. However, it is suspected that it is partly due to the upper bearing moving slightly in its housing and therefore not clamping the bearing point as assumed in the finite element model. When the motor was run at high speed the acoustic noise increased and subsequent investigation indicated that the upper bearing had rotated in its housing, and there were signs of wear in the housing.

**Table 5.23 - Comparison of predicted and measured values for a bearing stiffness of  $1.4 \times 10^7 \text{N/mm}$**

Mode	Finite element (Hz)	Measured (Hz)
Cylindrical	1679	1248
Conical	2331	2368
1 <sup>st</sup> bending	5345	5024
2 <sup>nd</sup> bending	11640	11744

Figure 5.43 shows the vibrational modes, and again it can be seen that at higher values of bearing stiffness the mode shape is dominated by the shaft flexure.

## **5.4 Influence of leading design parameters**

As well as modelling the existing rotors, the influence of various design parameters on the rotor resonances was investigated viz.: the length of the shaft extension beyond the bearings, the influence of the shaft diameter and the spacing between the bearings.

### **5.4.1 Shaft extension**

Since the length of the shaft extension will have a major influence on the resonant modes. it was varied, the results being shown in Figure 5.45. As can be seen, if there is no extension beyond the bearing the frequency of the first bending mode is moved from 3kHz to 20kHz. The solid vertical line on the graph shows the shaft length of the prototype rotor with the long shaft extension. A reduction of the shaft extension length, from 42mm to 15mm indicated by a dashed line on the graph, moves the natural frequencies well above the operating speed range of the motor, viz. 120krpm (2kHz), and hence reduces the possibility that the modes will be excited.

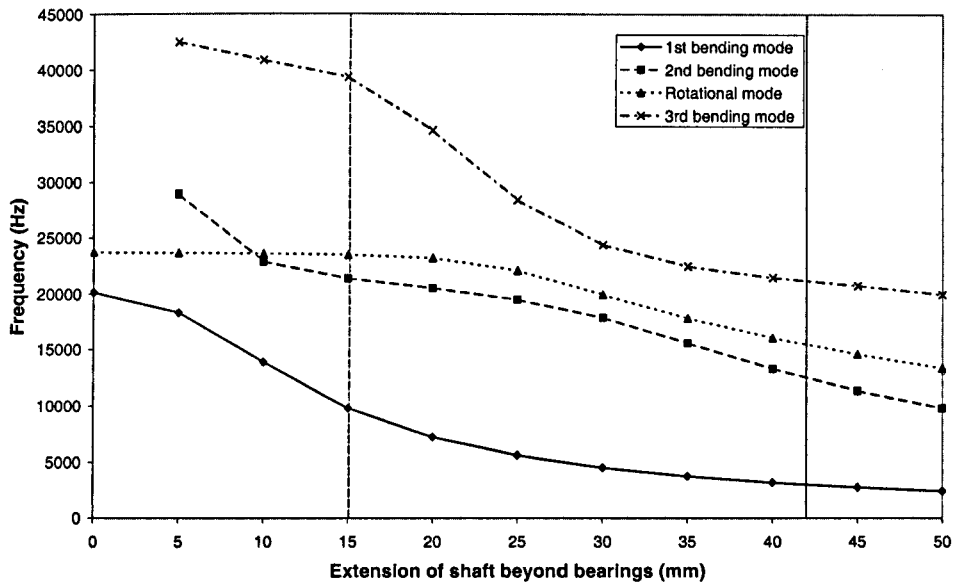


**Figure 5.45 - Variation in natural frequency with shaft extension, neglecting bearing modes**

The rotor was then re-modelled accounting for the bearing modes, which affect the bending modes slightly as the two bearings support the shaft in two places. As can be seen in Figure 5.46, the frequencies of the first two bending modes increase slightly. The first bending mode is now primarily determined by the vibration of the shaft extension as the bearings limit the flexing of the rotor shaft.

Shortening the rotor shaft such that it does not extend beyond the bearings moves all the rotor shaft bending modes well away from the operational speed range, but it also prevents the the rotor from being coupled to a load. A second rotor was manufactured with a shaft extension length of 15mm, as shown on Figures 5.45 & 5.46 by a dashed line. The first resonance mode due to bending of the shaft is predicted to occur at 9.8kHz for the free-free case and at just over 10kHz when the rotor is mounted in the bearings. It is, therefore, considerably higher than the maximum operating frequency of the motor. As can be seen from Figure 5.46 the introduction of the bearings introduces 2 extra modes at a comparatively low frequency, which are due to the rotor bouncing and pitching on the bearings.

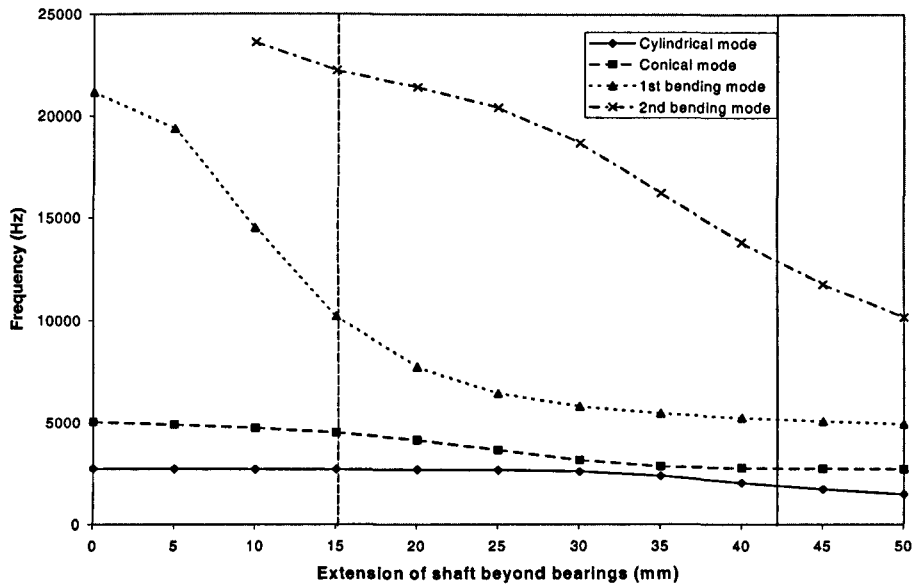


**Figure 5.46 – Variation in natural frequency with shaft extension, including bearing modes**

The first mode is due almost entirely to the vibration of the shaft extension. A simple analytical model based on a cantilever was employed to predict this mode. It assumes that the shaft is clamped as shown in Figure 5.47. A different clamping point from that which was used in section 5.3.1 is assumed, as the bearings are not included in this analytical model. The analytical formula is the same as the one, which was described in section 5.2.1, viz.:

$$\omega_n = a_n \sqrt{\frac{EI_p}{\mu_1 l^4}}$$

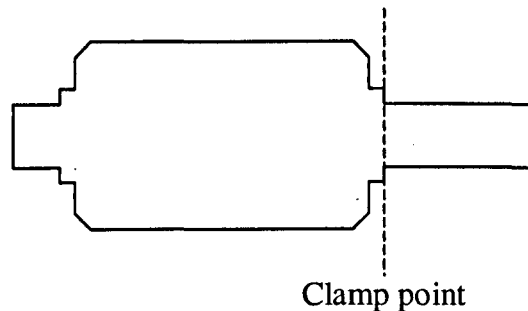


**Figure 5.47 - Rotor schematic showing clamping point**

In this case, only the value for  $a_1$ , which is 3.52 from [Har56], is required, as it is the first mode that is being investigated. In the model, the shaft length includes the 7mm, which is occupied by the bearing, and the diameter is 8mm.

Thus the equation gives:

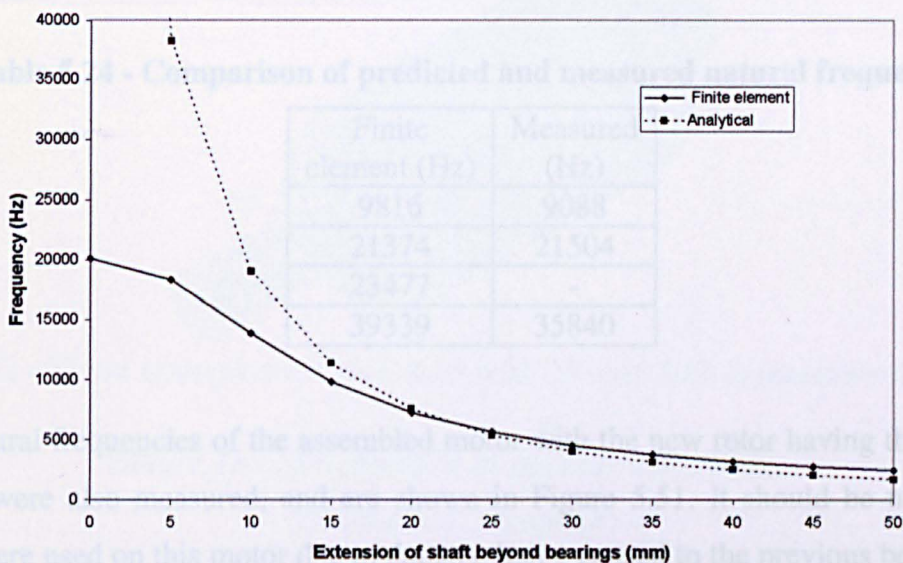
$$E = 1.93 \times 10^{11} \text{ N/m},$$

$$I_p = \pi d^4 / 64 = 2.01 \times 10^{10},$$

$$\mu_1 = \pi \rho d^2 / 4 = 0.4021 \text{ kg/m where } \rho = 8000 \text{ kg/m}^3, \quad l = \text{shaft extension} + 7 \text{ mm}$$

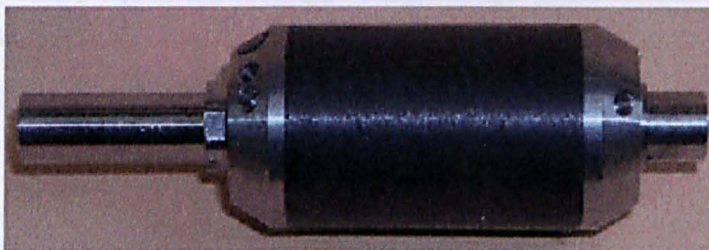
$$\omega = 3.52 \sqrt{\frac{96.476}{I^4}}$$

Figure 5.48 shows the influence of shaft extension on the natural frequency, as predicted by both the analytical model and finite element analysis. As can be seen, with a shaft extension above 15mm the analytical model yields results, which are comparable with those from the finite element analysis. For extensions below 15mm, however, the mode shape of the whole rotor shaft dominates the resonant mode, and the assumption that the shaft extension being equivalent to a cantilever clamped at one end is no longer valid.



**Figure 5.48 - Comparison between analytical and finite element predicted resonant frequencies for first rotor bending mode**

The second rotor with the shorter shaft extension of 15mm, shown in Figure 5.49, was then tested and its frequency spectrum is shown in Figure 5.50. As can be seen from Table 5.24 and Figure 5.45 the results are very close to those predicted by the finite element analysis. Again, the 3<sup>rd</sup> or rotational mode is not detected during the impulse response test.



**Figure 5.49 - Rotor with 15mm shaft extrusion**

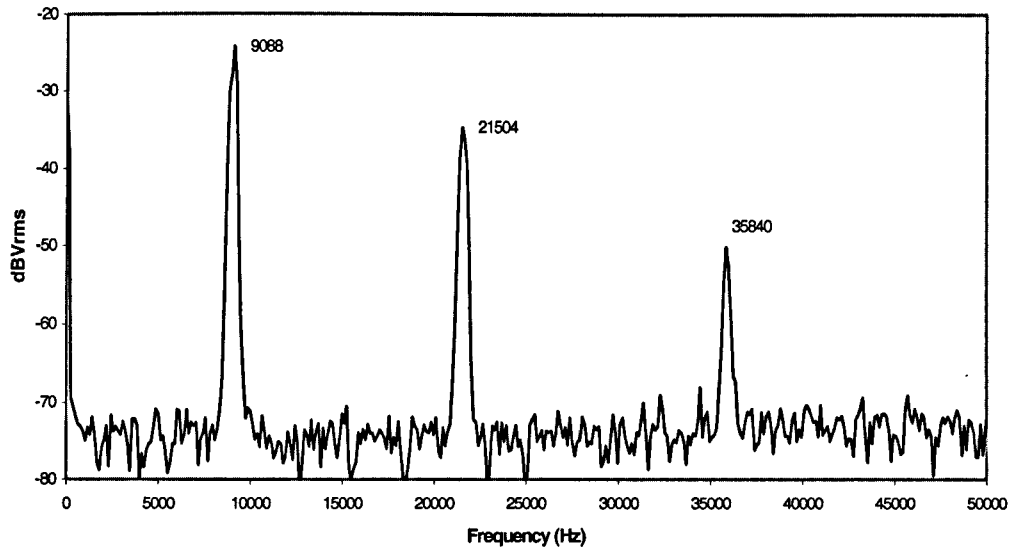


**Figure 5.50 - Frequency spectrum for rotor with 15mm shaft extension**

**Table 5.24 - Comparison of predicted and measured natural frequencies**

Finite element (Hz)	Measured (Hz)
9816	9088
21374	21504
23477	-
39339	35840

The natural frequencies of the assembled motor with the new rotor having the 15mm shaft extension were also measured, and are shown in Figure 5.51. It should be noted that new bearings were used on this motor due to damage being caused to the previous bearings at high speeds. Therefore, there may be a slight difference in the value of the stiffness constant.

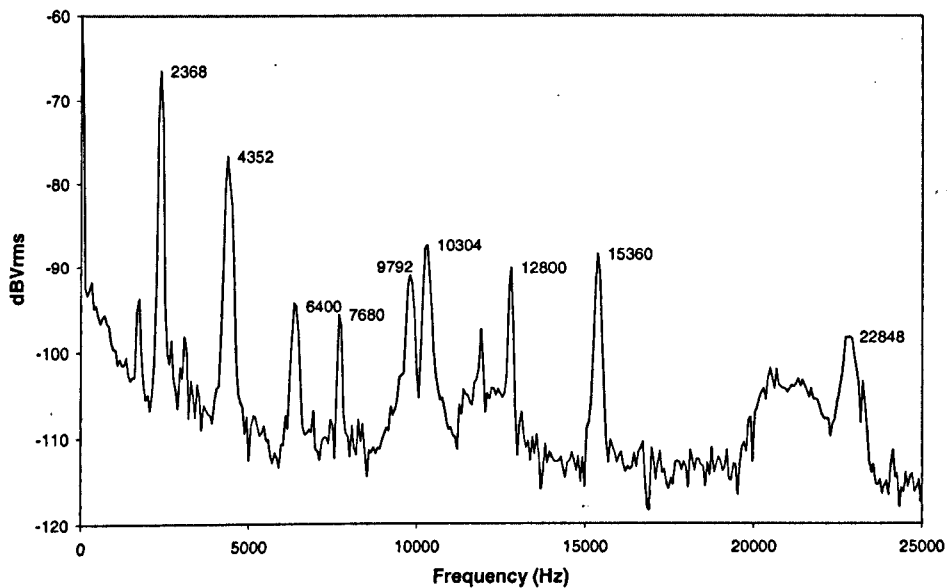


**Figure 5.51 - Frequency spectrum for motor with shaft extension of 15mm**

From the work, which is described previously in section 5.3.1 it can be assumed that several of these resonant modes are due to the motor frame rather than the rotor. The complete rotor was modelled using the finite element mesh shown in Figure 5.52. Table 5.25 indicates the modes that are likely to be due to the frame and rotor/bearing arrangement. However, it is appreciated that not all the modes, which are identified as rotor modes, will actually be due to the rotor, but will be caused by the interaction of the rotor with the frame. Also the natural frequencies of the frame will be increased due to the extra stiffening provided by the rotor, which depends to some extent on how rigidly the motor is assembled.

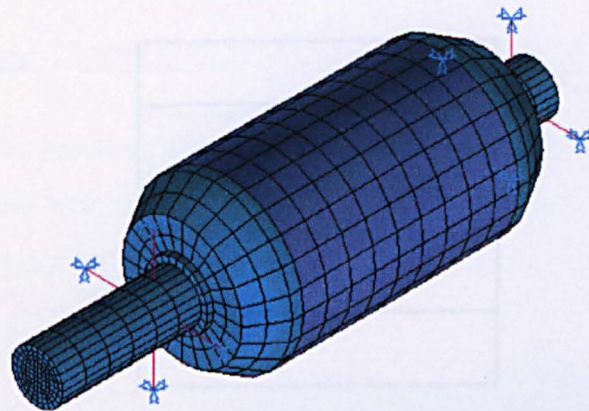


**Figure 5.52 - Finite element model for shaft with 15 mm shaft extension with bearings**

**Table 5.25 - Identification of possible mode sources**

Frequency (Hz)	Frame or rotor mode
<b>2368</b>	<b>Rotor</b>
<b>4352</b>	<b>Rotor</b>
6400	Frame
7680	Frame
9792	Frame
<b>10304</b>	<b>Rotor</b>
12800	Frame
15360	Frame
<b>22848</b>	<b>Rotor</b>

Using this data, the finite element analysis was repeated with the bearings represented. It was found that closer agreement between the measurements and the predictions was obtained at  $2.25 \times 10^7$  N/m, which while being slightly different from the value which calculated previously is probably due to the new bearings. The predicted natural frequencies are compared with the measured values in Table 5.26, and the mode shapes are shown in Figure 5.53. As can be seen there is a very good correlation between predictions and measurements, which validates the model for both the rotor and the bearings.

**Table 5.26 – Predicted and measured resonance modes for rotor with 15mm extension including bearings**

Mode	Finite element (Hz)	Measured (Hz)
Cylindrical	2598	2368
Conical	4301	4352
1 <sup>st</sup> bending	10184	10304
2 <sup>nd</sup> bending	22143	22848

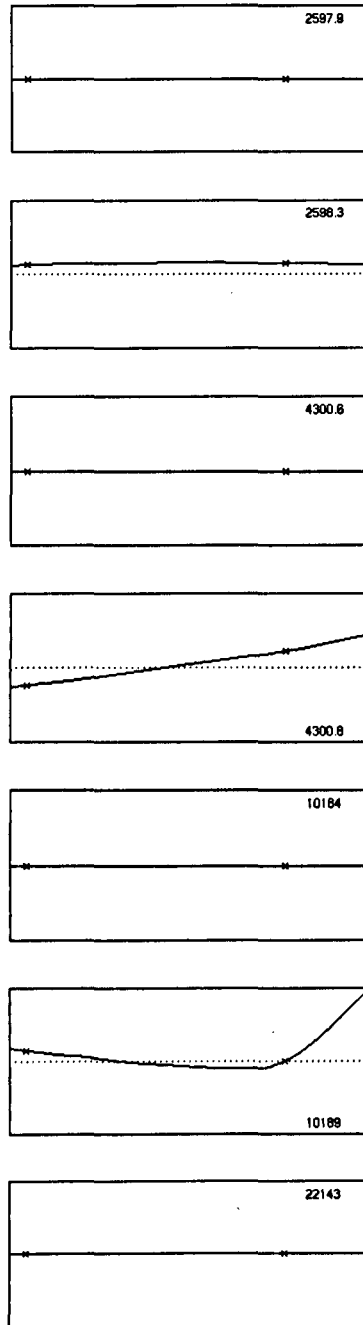


**Figure 5.53 - Resonant modes for rotor with 15 mm shaft extension including bearings**

## 5.4.2 Bearing spacing

Since each of the prototype motors,  $A_1$  &  $B_1$ , were designed to have the same space envelope, the rotors were designed such that the bearings were spaced the same distance apart. Therefore, on the rotor with the longer active length ( $A_1$ ) the bearings could not be brought any closer together. However, on the rotor with the shorter active length ( $B_1$ ) the bearings could be moved to investigate the effect this has on the resonant frequencies. Two investigations were performed, one with the shaft length maintained constant and the bearing spacing varied and the other with the shaft flush with the bearings, and the length being adjusted accordingly.

### a) Constant shaft length

This investigation was based on the finite element model shown in Figure 5.54. The shaft was assumed to be flush with the bearings as shown. The mesh shows the rotor with the bearings in the original position, i.e. the same as for the rotor with the longer active length.

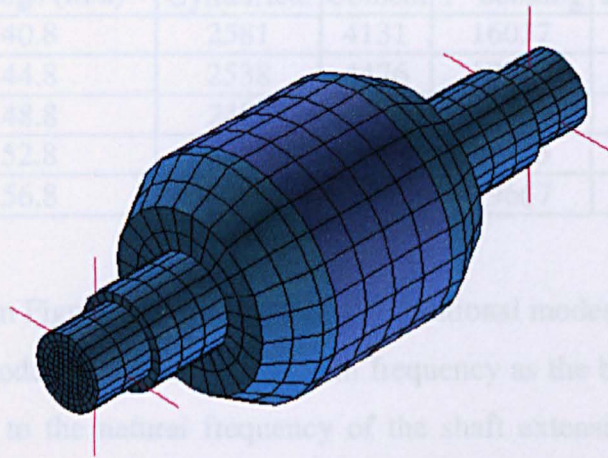


**Figure 5.54 - Finite element mesh showing bearing locations**

The bearings were gradually moved closer together in equal increments, the shaft length being kept constant to avoid any change in weight, which would affect the resonant frequencies. The results of the investigation are shown in Table 5.27 and in Figure 5.55.

### b) Variable shaft length

In this investigation, the shaft was again assumed to be flush with the bearings i.e. zero shaft extension. As the shaft length is changed which determines the bearing spacing, then a larger range of spacings can be investigated. As can be seen from Figure 5.57, the natural frequencies for the bearing modes increase dramatically as the bearings are brought closer together. This occurs as the shaft is effectively being clamped at shorter axial lengths with no

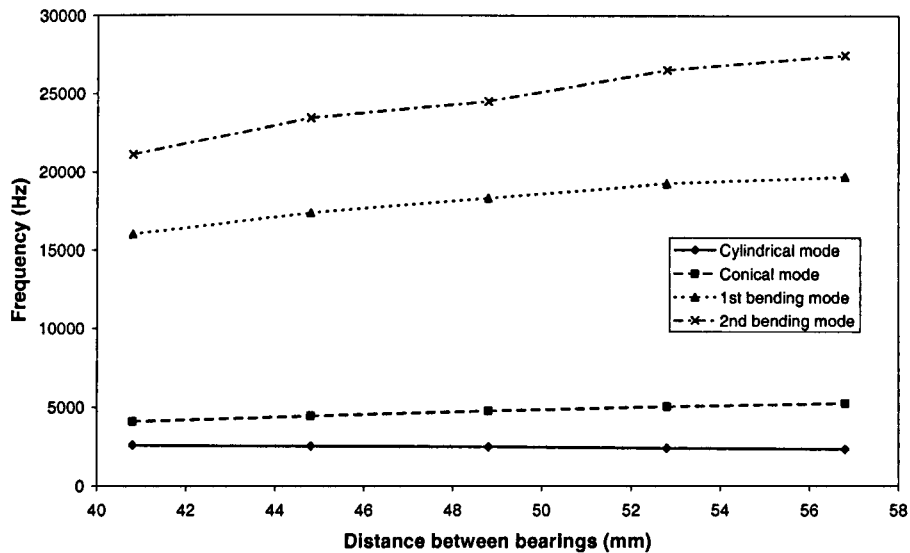


**Figure 5.55 - Variation of natural frequencies for change in bearing spacing, shaft length constant.**

**Table 5.27 - Variation in natural frequencies with change in bearing spacing**

Distance between bearings (mm)	Natural frequencies (Hz)			
	Cylindrical	Conical	1 <sup>st</sup> bending	2 <sup>nd</sup> bending
40.8	2581	4131	16037	21148
44.8	2538	4476	17350	23408
48.8	2482	4775	18305	24472
52.8	2413	5048	19245	26511
56.8	2335	5260	19667	27472

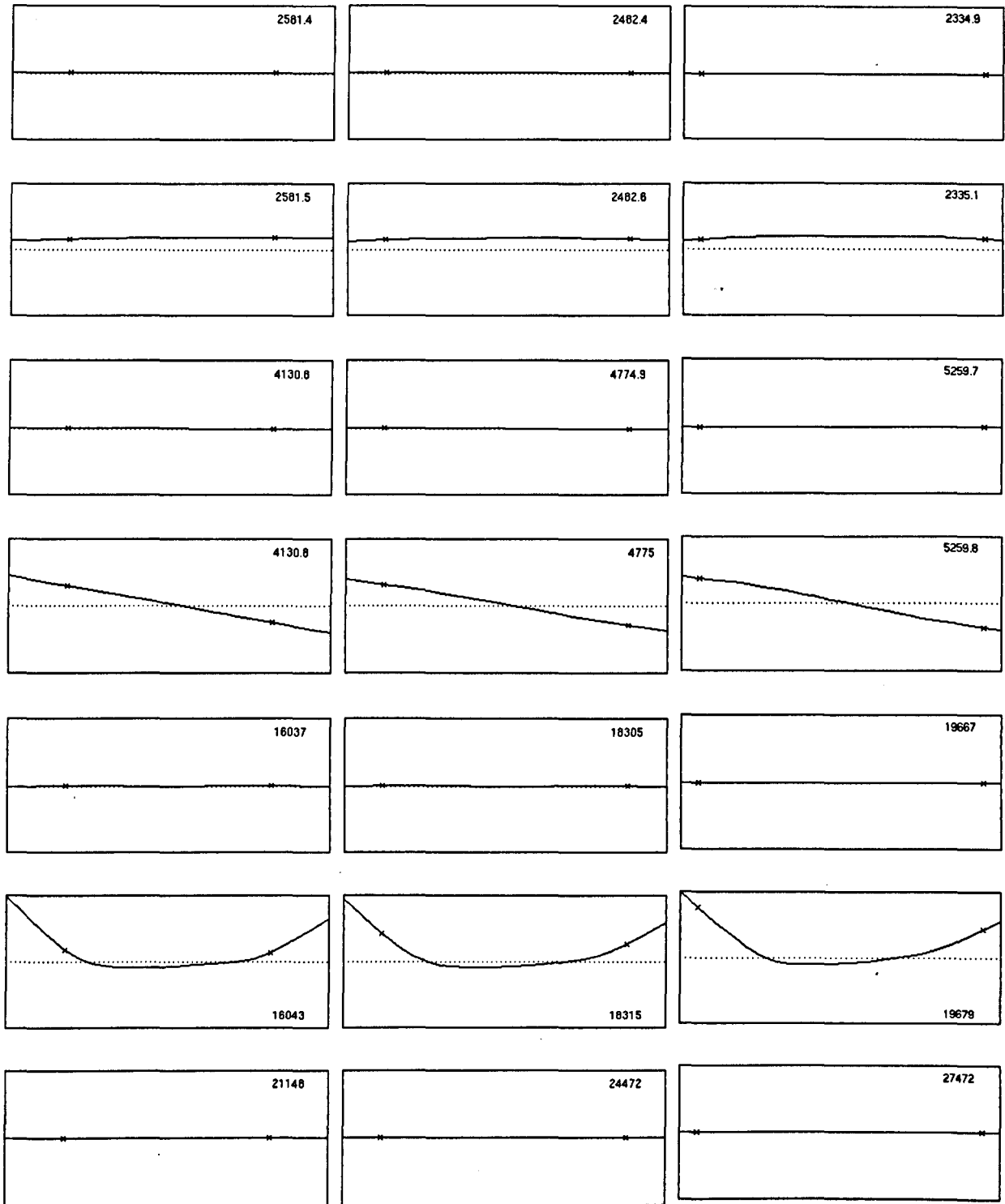
As can be seen from Figure 5.55, the 3<sup>rd</sup> and 4<sup>th</sup> vibrational modes, which correspond to the 1<sup>st</sup> and 2<sup>nd</sup> bending modes of the shaft, reduce in frequency as the bearings are moved closer together. This is due to the natural frequency of the shaft extension, which dominates the mode shapes as can be seen from the mode shapes in Figure 5.56.

There is very little change in the 1<sup>st</sup> resonant mode or the bearing cylindrical mode since these modes are dependent mainly on the stiffness of the bearings and the mass of the rotor. In this investigation the change in rotor mass is minimal, the only change in weight being the shoulder on the shaft which locks the bearings in place.

### b) Variable shaft length

In this investigation, the shaft was again assumed to be flush with the bearings i.e. zero shaft extension. As the shaft length is changed which determines the bearing spacing, then a larger range of spacings can be investigated. As can be seen from Figure 5.57, the natural frequencies for the bending modes increase dramatically as the bearings are brought closer together. This occurs as the shaft is effectively being clamped at shorter axial lengths with no

change in the stiffness of the shaft. Consequently, from the analytical work in section 5.4.1, as the length decreases the resonant frequencies rise. In addition there is a slight increase in the resonance modes as a result of the bearings due to the decreased rotor weight as the spacing is reduced.



**Bearings 40.8mm apart      Bearings 48.8mm apart      Bearings 56.8mm apart**  
**Figure 5.56 - Variation in natural frequency with change in bearing spacing with shaft length constant**

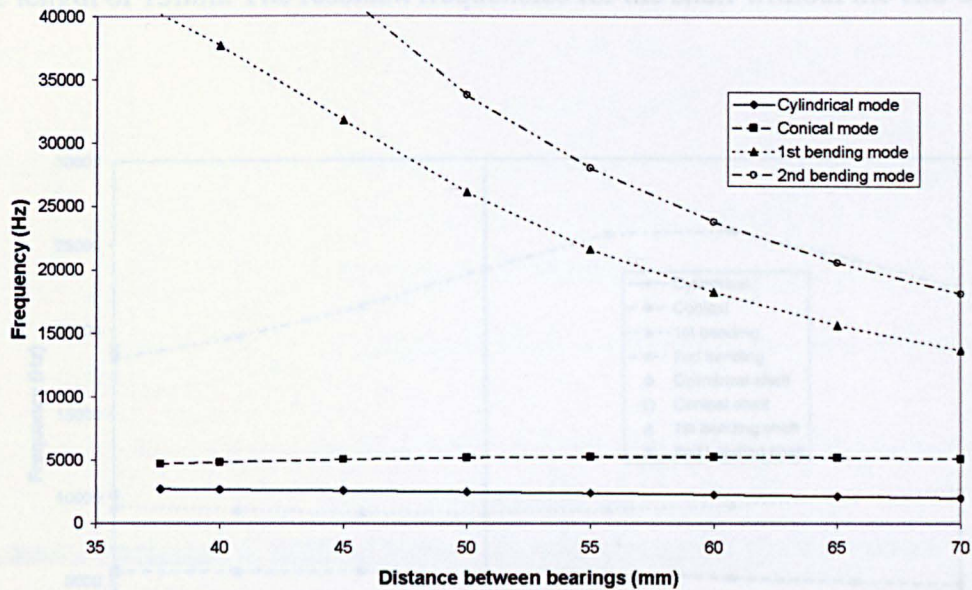
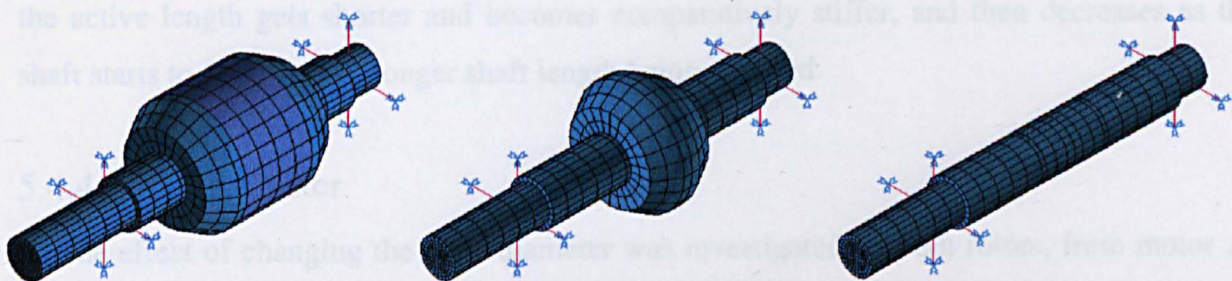


**Figure 5.57 - Variation of natural frequencies with change in bearing spacing, shaft length varying.**

### 5.4.3 Active length

For this investigation, the rotor that was modelled is the one, which was studied previously in section 5.4.1 with a 15mm shaft extension and the bearing stiffness was fixed at  $2.5 \times 10^7$  N/m. The active length was gradually reduced and changes in the resonant frequencies were calculated. There are two active lengths viz. 34.2mm and 15mm, which correspond to the 2 rotors which were built. Once the active length has been reduced to 0mm the end-caps on the shaft are completely removed and the resonant frequency of the shaft is obtained. Figure 5.58 shows the rotor mesh for a rotor with an active length of 15mm, zero active length, and with no end-caps.



**Rotor with 15mm active length   Rotor with zero active length   Rotor shaft with no end-caps**  
**Figure 5.58 - Rotor mesh during different stages of modelling**

The results of this investigation are shown in Figure 5.59. The solid vertical line indicates the rotor with an active length of 34.2mm and the dotted vertical line represents the rotor with

an active length of 15mm. The resonant frequencies for the shaft without the end-caps are also shown.

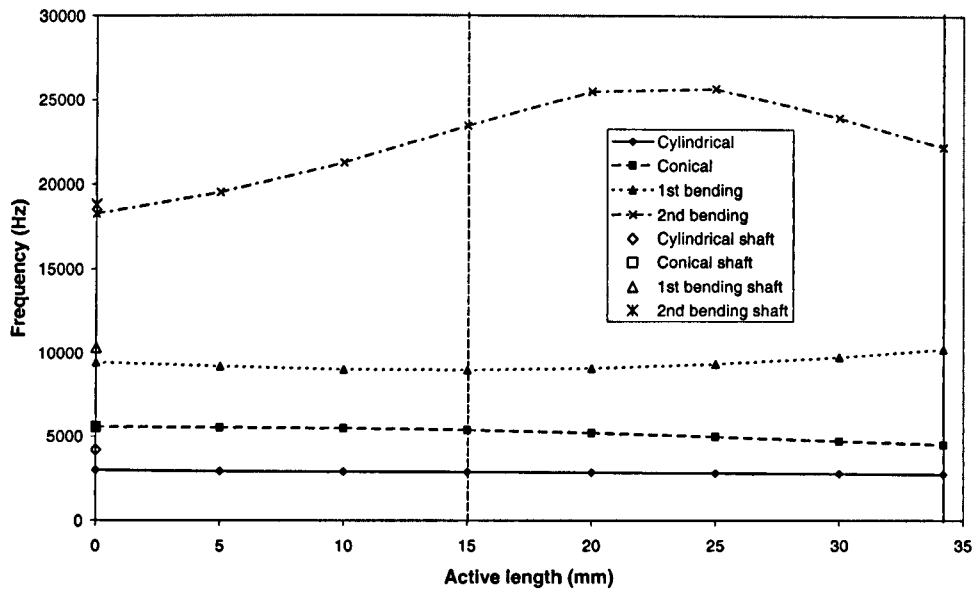


Figure 5.59 - Variation of natural frequency with active length

It can be seen that for the cylindrical bearing mode, the mode frequency increases as the active length is shortened. This is to be expected as the mass of the rotor is reducing and this resonance is proportional to the inverse of the rotor mass as can be seen from Equation 5.3. The frequency of the conical bearing increases slightly as the active length is reduced. This is due to the transverse inertia of the shaft decreasing as the rotor mass decreases, and can be anticipated from Equation 5.4.

The 1<sup>st</sup> bending mode decreases in frequency as the stiffness of the shaft decreases due to the reduction in active length, whilst the 2<sup>nd</sup> bending mode initially increases in frequency as the active length gets shorter and becomes comparatively stiffer, and then decreases as the shaft starts to flex due to a longer shaft length being exposed.

#### 5.4.4 Shaft diameter

The effect of changing the shaft diameter was investigated on both rotors, from motor A<sub>1</sub> and B<sub>1</sub>, but with the shorter shaft extension of 15mm.

##### a) Rotor with long active length

The bearing stiffness was fixed at  $2.5 \times 10^7$  N/m, as calculated previously in section 5.3.1. The shaft diameter was increased in increments from 2mm to 10mm, and the results are shown in Figure 5.60, whilst the corresponding vibrational modes are shown in Figure 5.62.

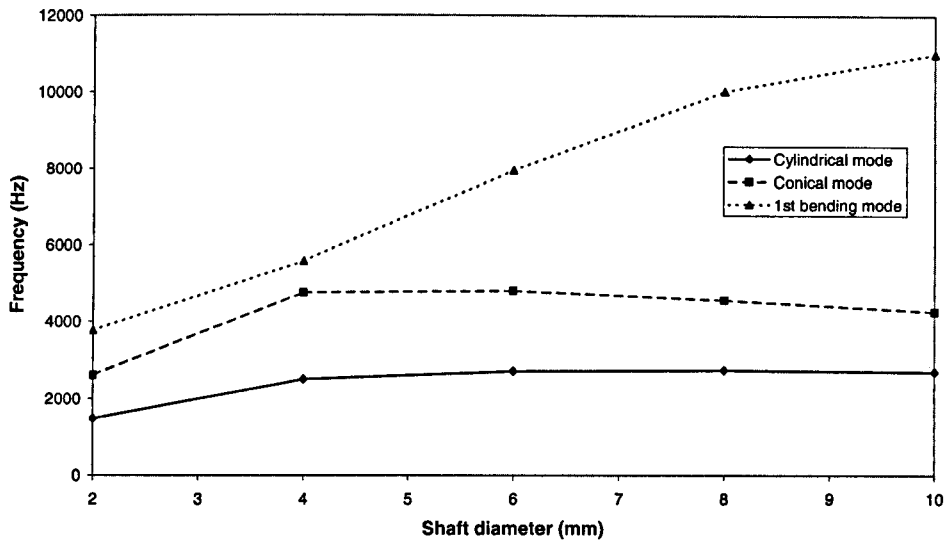


**Figure 5.60 - Variation in natural frequency with change in shaft diameter (longer rotor active length)**

### b) Rotor with short active length

The bearing stiffness was fixed at  $1.4 \times 10^7$  N/m, the value calculated previously in section 5.3.2, and the shaft diameter was increased in increments from 2mm to 10mm. The results are shown in Figure 5.61, whilst the corresponding vibration modes are shown in Figure 5.63.

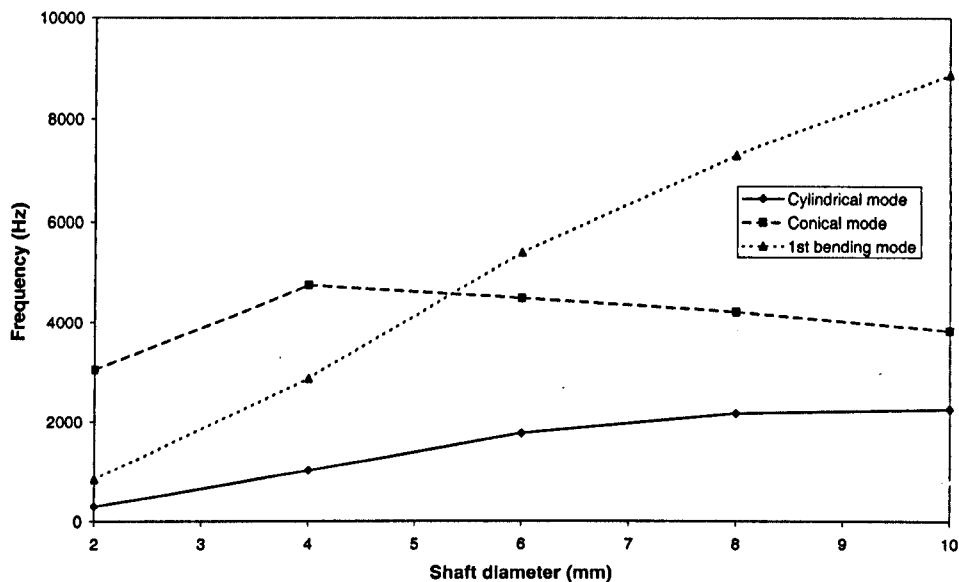
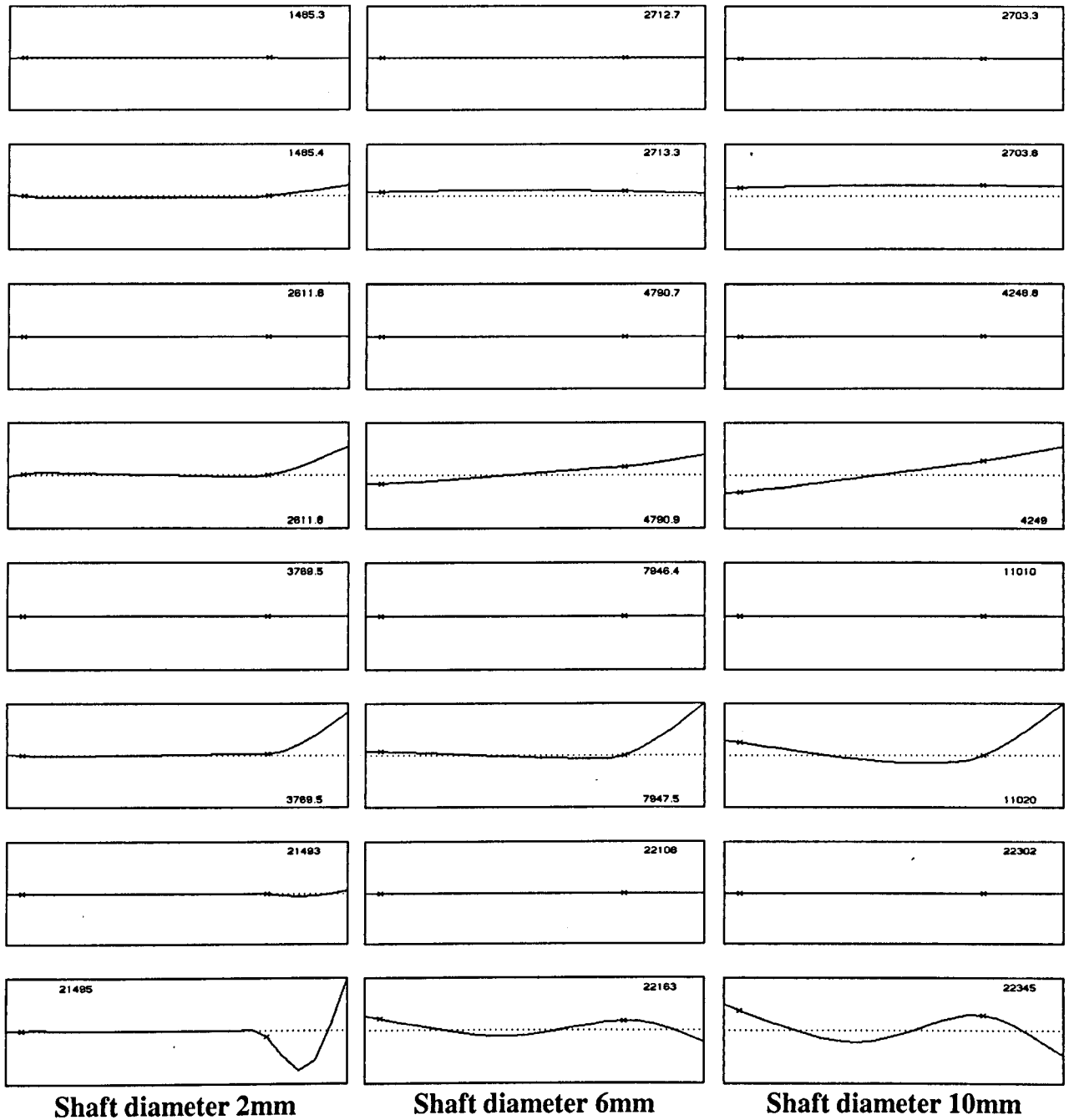


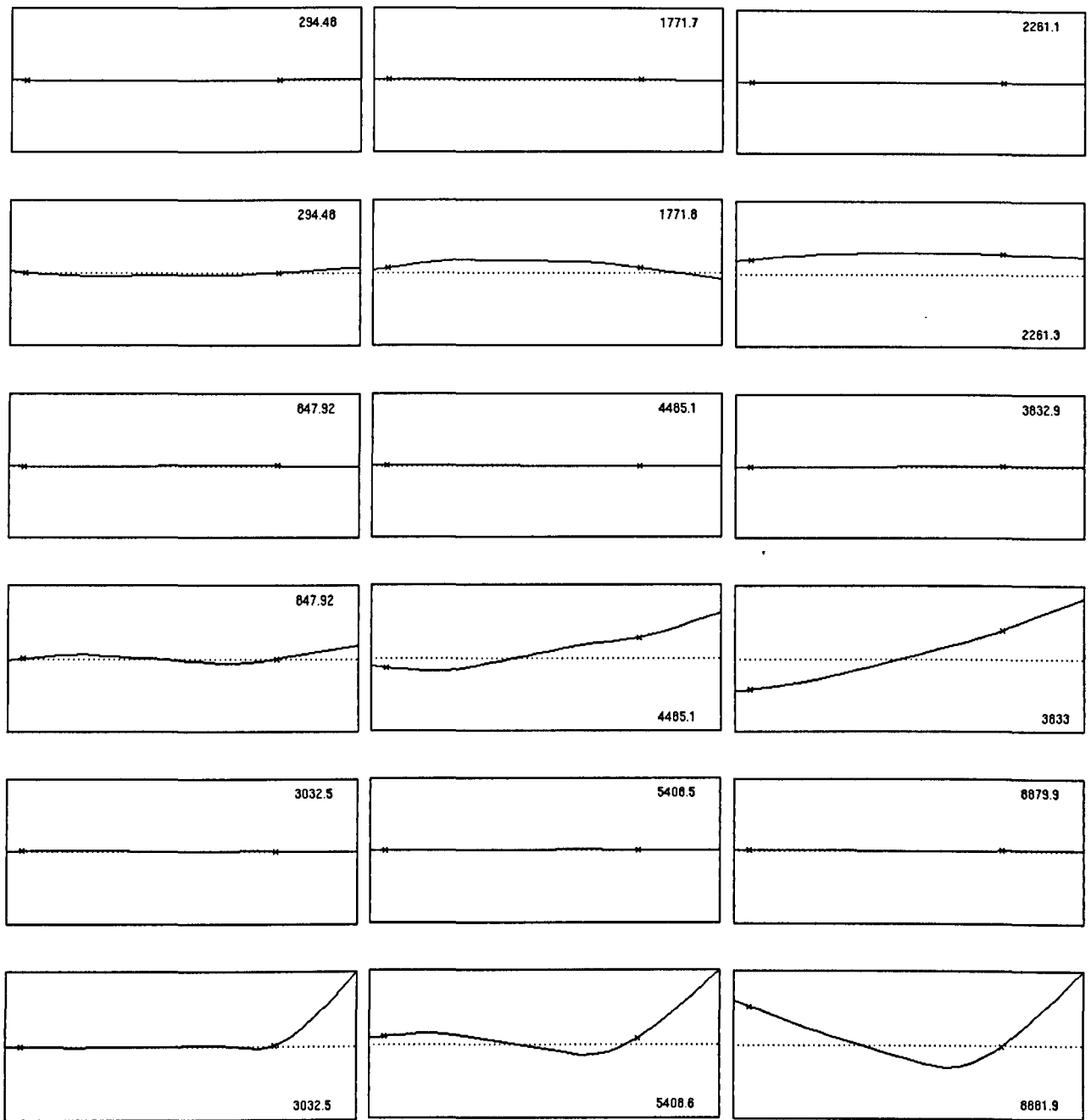
**Figure 5.61 - Variation in natural frequency with changes in shaft diameter (shorter rotor active length)**

From Figures 5.60 & 5.61, it can be seen that although there are slight differences in the frequencies of the first two modes due to the bearings there is a dramatic reduction in the natural frequency of the 1<sup>st</sup> bending mode as the shaft stiffness decreases. This is more pronounced on the rotor with the short active length, as the active section is comparatively stiff compared to the shaft, and therefore does not flex significantly.

From the theory in section 5.3, it can be seen that a reduction in the rotor mass should lead to an increase in the natural frequency of the bearing modes, and this can be seen in Figure 5.60 for a small shaft diameter. However, reduction of the shaft diameter makes the shaft more flexible and consequently the resonance mode is determined more by flexure of the shaft than by vibration of the bearings leading to a reduction in the bearing resonance modes at small shaft diameters. The changing nature of the resonance modes as the shaft diameter is reduced can clearly be seen in Figures 5.62 & 5.63.



Shaft diameter 2mm      Shaft diameter 6mm      Shaft diameter 10mm  
**Figure 5.62 - Variation in natural frequency with change in shaft diameter (longer active length)**



**Shaft diameter 2mm                      Shaft diameter 6mm                      Shaft diameter 10mm**  
**Figure 5.63 - Variation in natural frequency with changes in shaft diameter (shorter rotor active length)**

## 5.5 Summary

This chapter has described the construction of 2 rotors for a high-speed motor, and successfully employed finite element models to accurately predict the resonant modes. Results deduced from finite element analysis correlate well with the measured natural frequencies, and with the analytical methods, where these could be applied. From the work performed here the following observations could be made:

- The lamination material reduces the natural frequencies of the rotor. The laminations contribute extra mass to the rotor, but contribute little in the way of axial stiffness.

- The magnets whilst contributing significant mass to the rotor, being nearly as dense as the stainless steel, are comparatively stiff in the axial direction and therefore act to stiffen the rotor and increase the natural frequencies.

The carbon fibre magnet containment whilst being relatively strong along their direction of orientation, i.e. circumferentially are very weak axially and contribute only slightly to the rotor mass. Whilst the carbon fibre acts to reduce the natural frequencies of the rotor slightly the effect is minimal.

The models have successfully accounted for the bearing arrangements, and showed the effects of the introduction of the extra bearing modes on the natural frequencies. Again, good correlation with measured values for both rotors has been obtained. The influence of design parameters, such as the shaft extension, the bearing spacing and the active length on the resonant frequencies has been quantified as follows:

- The shaft extension beyond the bearings has a dramatic effect on the resonant modes of the motor. Once the shaft length starts to increase then the natural frequencies rapidly decrease and any significant length of shaft extension causes the 1<sup>st</sup> bending mode to occur inside the motor operating speed range. Conversely a very short shaft extension will not allow the motor to be coupled to a load. Based on the investigation into the effect of the shaft extension then two new rotors were manufactured such that the resonant frequencies of the shaft bending modes were moved well outside the operating speed range.
- Spacing of the bearings can significantly affect the resonance modes. This is of primary concern where the motor end windings are quite long, and there are a number of positions in which the bearings can be located. Moving the bearings closer to the motor can increase the motors natural frequencies, but only if the rotor shaft is shortened too and this could prevent the motor being coupled to a load. However, if the end-windings could be minimised or bent in such a way as to reduce their length, then a reduction of the distance between the bearings would be very beneficial in making sure the 1<sup>st</sup> and 2<sup>nd</sup> bending modes of the shaft occur well outside the motor operating speed range.
- A reduction of the shaft diameter directly affects the resonance modes as it significantly compromises the shaft stiffness. This effect is more pronounced when the active length is shorter, and on motor B<sub>1</sub> would lead to the first bending mode occurring inside the speed range of the motor for a shaft diameter of 3mm or less. Also a small shaft diameter could permit significant flexing of the shaft.

- Changing the active length does not significantly influence the resonant modes for the two rotors studied. The rotors first bending mode, however, is subject to the most change as that is heavily influenced by the stiffness of the active length. Once the active length starts to decrease the shaft bending starts to dominate reducing the natural frequency of this mode.

From the work described in this chapter some general conclusions can be drawn for general high-speed motor design. The shaft extension should be kept as short as possible and just long enough to allow coupling to a load. Extra bearings can be used to support the shaft, but high-speed bearings are comparatively quite expensive and require expensive lubrication strategies for continued operation. However, it is realised that the use of additional bearings can introduce new problems due to alignment and motor assembly. The shaft diameter should be of a reasonable diameter to limit the flexing caused by the resonance modes, but sufficiently small to allow cost effective bearings to be used as the cost of high-speed bearings starts to increase dramatically with the shaft diameter. Finally, for high-speed motors, analysis of the rotor resonant frequencies during the design stage is essential to ensure the shaft bending modes are well outside the motor speed range. This can be used to differentiate between motor designs of a similar electromagnetic performance to select the motor with the best resonant properties.

## Chapter 6 General conclusions

In this thesis, the influence of both electromagnetic and mechanical design parameters on the performance of high-speed (120krpm) permanent magnet brushless DC motors has been investigated. It has been shown that both aspects need to be considered at the design stage if a motor is to be designed and operate successfully at high speed.

### 6.1 Design of high-speed permanent magnet brushless DC motors for sensorless operation

In chapter 2, a 6-pole high-speed permanent magnet brushless DC motor with an external magnetically loaded composite rotor was designed to meet the specific application requirements of a company, and this motor highlighted issues which were addressed in the research that subsequently followed. The major issues were:

- The electromagnetic design considerations for high-speed motors so that they are suitable for sensorless operation. Previously, this had not been a design consideration.
- Optimisation of the rotor diameter to stator diameter (or split) ratio, which was not possible due to design constraints on the initial motor. Existing methodologies for determining the optimal split ratio does not account for the influence of iron loss, which is an increasingly important consideration at high speed.
- The mechanical design of the rotor, so as to avoid resonant modes in the operating speed range of a motor.

The prototype external rotor motor was not capable of being operated from a sensorless commutation scheme based on the detection of the zero-crossing of the back-emf waveform due to the phase current waveform being continuous. It was found that with the original external rotor motor design concept, such sensorless operation would not be achievable. Further, the motor would not have been capable of achieving its rated speed of 120krpm due to a resonance mode, which occurred at a speed of  $\approx 16$ krpm. In addition there may have been other critical speeds below 120krpm.

Chapter 3 investigated the design methodology for a high-speed motor for operation on a sensorless DC commutation strategy utilising the zero-crossing of the back-emf waveforms. In Chapter 1, it was shown that significant problems may exist with the use of discrete commutation sensors, in that they:

- They can be relatively bulky and, sometimes, fragile.
- They require additional components.

- They pose potential alignment problems, particularly in small motors.
- They may compromise reliability.
- They may exhibit hysteresis, which may cause a motor to operate away from optimum efficiency.

The above problems can be exacerbated at high rotor speeds, when, for mechanical reasons, the airgap needs to be comparatively large, compared with conventional low-speed motors. Eliminating the need for discrete rotor position sensors, and employing a sensorless commutation strategy would improve both the reliability and performance. However, in order to employ a brushless DC sensorless commutation strategy the motor phase currents need to be discontinuous and the diode conduction angle needs to be  $<30^\circ$  electrical so as to ensure that the zero-crossing of the back-emf is not obscured by the current free-wheeling through the diodes and clamping the phase voltage at the DC link voltage.

A prototype motor has been designed to specifically result in a low diode conduction angle, and it was compared with a motor, which was designed to have a more conventional geometry, in terms of the ratio of iron to copper. Both motors were designed to have the same space envelope and the same efficiency. It was shown that:

- Careful consideration needs to be paid to the diode conduction angle during the design stage if sensorless operation is to be realised. Neglecting this may result in a motor that cannot be operated as a sensorless machine using the relatively simple DC commutation strategies, which have been considered.
- The stator geometry of a motor, which results in a low diode conduction angle differs significantly from a conventional stator design, in that it contains considerably less copper and more lamination material, which results in a low winding inductance and a low flux density in the stator iron.
- The diode conduction angle is highly dependent on the load torque. Hence, designing a high torque motor specifically for a low diode conduction angle becomes more challenging if a sensorless control strategy is to be implemented.
- The motor which was designed to have a low diode conduction angle was successfully operated using a sensorless control strategy up to, and beyond, its rated operating speed of 120krpm whilst a motor with a high diode conduction angle required discrete commutation sensors as the zero-crossing of its back-emf waveform was obscured at high speed by the phase currents free-wheeling through the diodes.

- If a motor which is designed to result in a high diode conduction angle is operated with a considerably reduced load torque then sensorless operation is still possible at high-speed, but this ceases to become possible when load torque is applied. Clearly, this would not be commercially viable.

During the design stage of the prototype motors it was observed that the rotor diameter greatly affected the motor efficiency. The relationship of the rotor to stator diameter is referred to as the split ratio, and Chapter 4 investigated the influence of motor design parameters on the optimal split ratio for high-speed operation. Previous work [Cha93] had derived an optimal split ratio for a distributed (overlapping) winding motor topology accounting for the copper loss, and has been shown to contain mistakes. These have been corrected, and the analysis extended to cater for motors having another important winding topology, viz. a non-overlapping or concentrated winding. On investigating the influence of the winding design on the optimal split ratio, it was observed that motors with distributed windings have a higher optimal split ratio when compared with motors having concentrated windings and this is accentuated at high airgap flux densities. Comparisons of the results from the relatively simple analytical equations which were employed with those deduced from an extensive CAD system have shown that the simple model proposed in [Cha93] compares favourably in predicting the optimal split ratio, even though it neglects the end-windings, the form of the magnetisation, the airgap length and the winding inductance.

This simple model also neglected the stator iron loss and whilst this might be justified at low speeds, where the copper loss is usually the largest loss component, at high speeds the iron loss can become dominant. Consequently, derivation of the optimal split ratio needs to consider both the iron and copper loss. Whereas a simple formula can be derived for the optimal split ratio accounting purely for copper loss, it is not possible to derive an equivalent expression when iron loss is introduced, due to the added complexity. As the operating speed is increased, the iron loss increases significantly and it has clearly been shown that the optimal split ratio changes from one that is influenced mainly by the copper loss to one that is determined largely by the iron loss. The iron loss serves to significantly reduce the optimal split ratio compared with that when only the copper loss is accounted for. However, two methods were proposed which resulted in a reduced iron loss and a higher motor efficiency. These centred on reducing either the flux density in the iron by increasing the airgap length or by reducing the iron volume by reducing the active length of the motor. Whilst increasing the airgap length served to increase the copper loss, it was still possible to achieve an increase in overall efficiency by a reduction of the iron loss.

The use of a thinner lamination material or a higher grade material, such as cobalt steel, will undoubtedly reduce the iron loss significantly, but these materials are more expensive. Since, in many applications, the motor cost can be a major issue, it is envisaged that despite the availability of such alternative lamination materials, the iron loss could remain the major factor in determining the optimal split ratio. Irrespective of the stator lamination material the methods, which have been considered, would still be useful in reducing the total motor loss and maximising efficiency. In summary, it has been shown that the incorporation of the iron loss into the calculation of the optimal split ratio is essential for high-speed motors.

## **6.2 Mechanical resonance frequencies of high-speed brushless permanent magnet motor rotors**

Whilst the electromagnetic design aspects of high-speed, permanent magnet, brushless dc motors are clearly fundamental, the mechanical aspects of the design are of equal importance if a motor is not to exhibit destructive resonance modes. The consequences of overlooking critical mechanical aspects of motor design have been highlighted, when a resonance mode on a high-speed rotor was excited, resulting in the destruction of the rotor. Chapter 5 describes a detailed analysis of the rotor resonance and the contribution of the constituent rotor components to the natural frequencies of the rotor. A finite element model was constructed to facilitate accurate modelling of the rotor components and fine-tuning of the model parameters, where applicable, to ensure that the developed model accurately represents reality. The model was extended to cater for the addition of bearings and the influence of the bearings on the resonant modes of the rotor. From the investigation the following were observed:

- The lamination material serves to reduce the natural frequencies of the rotor, since whilst they contribute mass to the rotor, they contribute little to the axial stiffness. The resultant effect is to reduce the rotor natural frequencies.
- The permanent magnets whilst contributing significant mass to the rotor, being nearly as dense as the rotor back-iron, are comparatively stiff in the axial direction, and, consequently, act to stiffen the rotor and increase the natural frequencies.
- The carbon fibre magnet containment whilst being comparatively weak axially, despite being very strong circumferentially, adds very little mass to the rotor. Consequently, its effect on the natural frequencies of the rotor is minimal.

Once the finite element model had been validated, the influence of the rotor design parameters such as the shaft extension, the bearing spacing and the active length on the natural frequencies was then investigated. It was shown that a variation in these parameters

could have a significant effect on the natural frequencies, the most dramatic being the shaft extension beyond the bearings. This extension acts similar to a free beam, and if it is sufficiently long the first bending mode will be within the operational speed range of the motor. It is suspected that it was this mode, which was excited and caused the destruction of the rotor, which was described in Chapter 5. From the analyses, which were performed, it was possible to design rotors such that all the bending modes were outside the operational speed range of a motor, and, therefore, were unlikely to be excited. Whilst the shaft extension was an important consideration, other aspects, which also significantly influenced the rotor natural frequencies, were:

- The spacing of the bearings. Moving the bearings closer to the motor can increase the rotor natural frequencies, but only if the rotor shaft is shortened too. Clearly, however, this can prevent the motor from being coupled to a load. However, if the end-windings could be minimised or shaped in such a way as to reduce their length, then a reduction of the spacing between the bearings would be beneficial in taking the 1<sup>st</sup> and 2<sup>nd</sup> bending modes of the shaft outside the motor operating speed range.
- The shaft diameter directly affects the resonance modes as it significantly influences the shaft stiffness. This effect is more pronounced when the active length is short, and on motor B<sub>1</sub> with a shaft diameter of 3mm or less it led to the first bending mode occurring inside the speed range of the motor, since a small shaft diameter results in significant flexing of the shaft.

From the work, which has been described, it is, hopefully, evident that it is equally important to consider the mechanical aspects of high-speed motor design if resonance modes and their effects are to be avoided.

### **6.3 Overall conclusion**

Whilst each chapter has focussed on a particular issue related to high-speed permanent magnet brushless DC motors and each of these is important it is only by considering all the issues that a cohesive design methodology can be established. If a motor is to be mechanically robust, operated using a simple sensorless commutation scheme, and make efficient use of the available space envelope, the design process is an integrated process which considers all 3 research issues which have been investigated simultaneously, in order to identify the best possible motor design.

For example, when the investigation into the sensorless back-emf based commutation was carried out it was observed that motors with a low diode conduction angle tended to have a

relatively long active length and quite short end-windings whilst motors which resulted in a high diode conduction angle had a relatively short active length, and much longer end-windings. From the investigation into rotor resonance, this can clearly have repercussions in respect of the mechanical design of the motor. Motors with relatively short end-windings can have the bearings positioned relatively close to the active volume of the rotor, which, as seen, tends to be axially much stiffer than the shaft alone, which helps ensure that resonance modes are out of the operating speed range. Consequently, the shaft extension beyond the bearings, which is needed to couple a motor to its load, can be reduced, which could help move the resonance modes to speeds above the operating speed. The author is aware that the resonant frequencies will change when a load is coupled to the system, so consequently, attention to the overall mechanical system is critical. With a short active length and long end-windings, which the bearings are located further from the active volume of the rotor, which may cause the shaft between the active volume and the bearings to flex slightly thereby reducing the frequency of the resonant modes. One solution might be to inset the bearings closer to the motor, but this might require a comparatively long shaft extension.

During the investigation, it was seen that inclusion of the iron loss component in the analysis might significantly reduce the optimal split ratio. However, realising this, say by mounting the rotor magnets directly onto a stainless steel rotor shaft or making the shaft diameter very small to accommodate laminations, results in a reduction in the flux from the magnets, which would reduce the motor performance. However, a reduction of the rotor shaft may significantly reduce the frequency of the shaft bending modes.

From the work, which has been reported in this thesis, it is evident that both electromagnetic and mechanical design considerations and constraints are critical to the realisation of high-speed motors. An appreciation of the different aspects of machine design is vital for their reliable operation.

## References

- Ack92 Ackermann, B., Bolte, E., Howe, D., Jenkins, M.K., Zhu, Z.Q., "Frequency domain analysis of brushless dc motor performance", *European transactions on Electrical Power Engineering*, vol.2, pp.389-396, 1992.
- Ark92 Arkadan A.A., Vyas R., Vaidya J.G. and Shah M.J., "Effect of toothless stator design on core and stator conductors eddy current losses in permanent magnet generators", *IEEE Trans. on Energy Conversion*, Vol. 7, 1992, pp. 231-237.
- Ata00 Atallah K., Howe D., Mellor P.H., Stone D.A., "Rotor loss in permanent magnet brushless ac machines", *IEEE Transactions on Industry Applications*, Vol. 36 (6, 2000), pp. 1612-1617.
- Ata92 Atallah K., Zhu Z. Q., Howe D., "An improved method for predicting iron losses in brushless permanent magnet dc drives", *IEEE Transactions on magnetics*, Vol. 28 No. 5, pp. 3037-3039, Sept 1992.
- Ata93 Atallah K., "Iron losses in brushless permanent magnet DC machines", PhD Thesis, April 1993
- Ata97 Atallah K., Howe D., Mellor P.H., "Design and analysis of multi-pole Halbach (self-shielding) cylinder brushless permanent magnet machines", *Proc. of EMD'97*, Cambridge, pp. 376-380, 1997
- Bam99 Bamber N., "An introduction to composite aircraft structures", data sheet from Farnborough-aircraft.com Ltd, 1999
- Bec91 Becerra R.C., Jahns T.M., Ehsani M., "Four-quadrant sensorless brushless ECM drive", *IEEE Applied Power Electronics Conference and Exhibition - APEC*, pp. 202-209, 1991
- Bor94 Bornemann H. J., Ritter T., Urban C., Boegler P., Zaitsev O., Weber K., Rietschel H., "A flywheel for energy storage with frictionless high temperature superconductor bearings", *Fourth International Symposium on Magnetic Bearings*, Zurich, pp. 543 – 545, 1994
- Buc96 Buckley J.M., Atallah K., Bingham C.M, Howe D., "Magnetically loaded composite for roller drives", *IEE Colloquium on New magnetic materials*. London, UK, pp 5/1-6, 1998
- Cal00 Calverley S.D., Jewell G.W., Saunders, R.J., "Aerodynamic losses in switched reluctance machines", *Proc. IEE, Electr. Power Appli.*, vol.147, no.6, 2000, pp.443-448.
- Cal01 Calverley S.D., "Design of a high speed switched reluctance machine for automotive turbo-generator applications", PhD Thesis, 2001.
- Cal99 Calverley S.D., Jewell G.W., Saunders, R.J., "Design of a high-speed switched Reluctance machine for automotive turbo-generator applications", *Proc. of the SAE Conference on Future transportation Technology*, Costa Mesa, USA, 1999, SAE Technical Paper Series, 1999-01-2933.
- Cha00 Chaaban F.B. and El-Hajj A., "A cost effective design approach for permanent magnet brushless machines," *Electric machines and power systems*, Vol. 28, 2000, pp. 893-900.
- Cha93 Chabban F.B., "Determination of the optimum rotor/stator diameter ratio of permanent magnet machines", *Electrical Machines and Power Systems*, vol.22, 1993, pp.521-531.
- Che99 Chen Y.S., Zhu Z.Q., Howe D., "Slotless brushless permanent magnet machines: Influence of design parameters", *IEEE Trans, EC-14(3)*, 1999, pp. 686-691.
- Chi92 Chiba, A., and Fukao, T., "A closed-loop operation of super high-speed reluctance motor for quick torque response", *IEEE Trans. on Industry Applications*, vol.IA-28, no.3, 1992, pp.600-606.
- Coc99 Cochrane N.M., Pal S.K., "Direct drive high energy permanent magnet brushless dc

- motor with an integrated driver for a novel 30,000rpm atomiser”, Proc. IEE 9<sup>th</sup> Int. Conf. on Elec. Machines and Drives, 1999, pp.133-136.
- Con90 Consterdine E., Hesmondhalgh D.E., Reece, A.B. J., Tipping, D., “An assessment of the power available from a permanent magnet synchronous motor which rotates at 500,000rpm”, Proc. Int. Conf. on Elec. Machines, 1992, Manchester, pp.746-750.
- Ede00 Ede, J. D., Zhu, Z.Q., Howe, D., ‘A sensorless high-speed brushless DC motor’, Proc. 16th Int. Workshop on Rare-Earth Magnets and Their Application, Japan, September 2000, pp. 1049-1058.
- Ede01 Ede J.D., Zhu, Z.Q., Howe D., ‘Optimal split ratio for high-speed permanent magnet brushless DC motors’, Proc. International Conf. on Electrical Machines & Systems, 2001, China, pp 909-912
- Ede02a Ede J. D., Atallah K., Wang J. B., Howe D., “Effect of optimal torque control on rotor loss of fault tolerant permanent magnet brushless machines”, IEEE Trans. on Magnetics, Vol38 (5), 2002, pp.3291 - 3293
- Ede02b Ede, J. D., Zhu, Z.Q., Howe, D., ‘Rotor resonances of high-speed permanent magnet brushless motors’, IEEE Transactions on Industry Applications, Vol. 38, No. 6, December 2002, pp. 1542-1548.
- Eng97 Engstrom J., Magnussen F., Nee H-P, “Analytical calculation of winding losses of inverter-fed PM synchronous motors with air-gap windings and surface mounted magnet”, Proc. of EPE’97, pp. 399-404, 1997.
- Fuk00 Fukao T., “The evolution of motor drive technologies – development of bearingless motors”, Proc. IPEMC’2000, Beijing, pp.33-38.
- Fuk86 Fukao T., “Principles and output characteristics of super high-speed reluctance generator system”, IEEE Trans. Industry Applications, vol.IA-22, no.4, 1986, pp.702-707.
- Gav89 S.D. Gavey, “The vibrational behaviour of laminated components in electrical machines”, Proc. EMD89. IEE, pp. 226-231, 1989
- Gmb00 “Rare-earth permanent magnets”, Vacuumschmelze GmbH, data sheet PD-002, Hanau Germany, 2000
- Hal85 Halbach J., “Permanent magnets for production and use of high energy beams”, Proc. of the 8<sup>th</sup> International Workshop on Rare-Earth Magnets and their Application, pp. 123-136, 1985.
- Har56 Den Hartog, “Mechanical vibrations”, 4<sup>th</sup> edition, New York : McGraw-Hill, 1956.
- Har59 Harris C.O., “Introduction to stress analysis”, Macmillan Press, 1959
- Hes82 Hesmondhalgh D.E., Tipping D., “Slotless construction for small synchronous motors using samarium cobalt magnets”, IEE Proc.-B, Vol.129, no.5, 1982, pp.251-261.
- Hes83a Hesmondhalgh D.E., Tipping D., “Miniature sheet-rotor induction motors for extremely high speed”, Proc. IEE, B, vol.130, no.4, 1983, pp.265-277.
- Hes83b Hesmondhalgh D.E., Tipping D., “Effect of stator slotting on the performance of sheet-rotor induction motors”, Proc. IEE, B, vol.130, no.4, 1983, pp.381-391.
- Hes84 Hesmondhalgh D.E., Tipping D., “Some problems associated with designing motors for speeds of up to 150,000rpm”, Proc. Int. Conf. on Elec. Machines, Lausanne, Switzerland, Sept. 1984, pp.302-305.
- Hes85a Hesmondhalgh D.E., Tipping D., “A miniature transformer-coupled high-speed synchronous motor”, IEE Proc.-B, Vol.132, no.5, 1985, pp.319-326.
- Hes87 Hesmondhalgh D.E. Tipping, D., Armral M., “Design and construction of a high-speed high-performance direct-drive handpiece”, IEE Proc.-B, Vol.134, no.6, 1987, pp.286-296.
- Hof00 Hofmann H., Sanders S.R., “High-speed synchronous reluctance machine with minimised rotor losses”, IEEE trans. on Industry Applications, vol.36, no.2, 2000, pp.531-539

- Hon97 Honda Y., Yokote S., Higaki T., Takeda Y., "Using the Halbach magnet array to develop an ultrahigh-speed spindle motor for machine tools", Proc. IEEE IA annual meeting, 1997, pp.56-60.
- How94 Howe D., Mitchell J.K., Zhu Z.Q., Bolte E., Ackermann B., "An integrated CAD system coupling electromagnetic, thermal, and dynamic performance analyses of permanent magnet brushless motors", Proc. European Power Electronics Chapter Symposium on Electric Drive Design and Application, pp 221-226, 1994
- Iiz85 Iizuka K., Uzuhashi H., Kano M., Endo T., Mohri K., "Microcomputer control for sensorless brushless motor", IEEE Trans. Ind. Applications, Vol.IA-21, No.3, pp.595-601, 1985
- Ike90 Ikeda M., Sakabe S., and Higashi K., "Experimental study of high-speed induction motor varying rotor core construction", IEEE Trans. Energy Conversion, vol.5, no.1, 1990, pp.98-103.
- Jac88 Jack A.G., Acarnley P.P., Jowett, "Design of small high-speed brushless dc machines", Proc. ICEM, Pisa, Italy, 1988, pp225-229.
- Jac98 Jack A.G., "Electric machine cores from soft magnetic composites: Experience, possibilities and practicalities", PCIM '99, 1999, pp. 383-388
- Jam95 James B.P., and Al Zahawi B.A., "A high-speed alternator for a small scale gas turbine CHP unit", Proc. IEE Electrical Machines and Drives, 11-13 September 1995, pp.281-285,.
- Jay95 Jayawant B.V., Maynard M., Anbarasu R., "Design of high-speed permanent magnet machines in magnetic bearings", Proc. 7<sup>th</sup> IEE Int. Conf. on Electrical Machines and Drives, 1995, pp.418-422.
- Jok96 Jokinen T., and Arkkio A., "High-speed ac motors", Proc. Chinese Int. Conf. on Elec. Machines, August 29-31, 1999, pp.21-24. Also Proc. of Symposium on Power Electronics, Industrial Drives, Power Quality, Traction Systems (SPEEDAM), Capri, Italy, 5-7 June, 1996, ppB5-9-B5-14.
- Jok99
- Juf87 Jufer M., Osseni R., "Back-emf indirect detection for self-commutation of synchronous motors", 2nd EPE Conference, pp. 1125-1129, 1987
- Kas94 Kasarda M. E. F., Allaire P. E., Maslen E. H., Gillies G. T., "Design of a high speed rotating loss test rig for radial magnetic bearings", Fourth International Symposium on Magnetic Bearings, Zurich, pp. 577 – 582, 1994
- Lah00 Lahteenmaki J.K., Soitu V., "Comparison of solid steel rotors with a copper coating or with a copper cage for a 60kW 60,000rpm compressor", Proc. ICEM, 2000, 28-30 Aug. 2000, Finland, pp.623-626.
- Lar95 Larjola J., and Backman J.L.H., "Oil free bearings in high speed technology", Proc. IEEE/KTH Stockholm Power Tech Conference, Stockholm, Sweden, June 18-22, 1995, pp.63-68.
- Lee92 Lee P.W., Pollock C., "Rotor position detection techniques on brushless permanent magnet and reluctance motor drives", IEEE Ind. Applications Conference, pp. 448-455, 1992
- Liw61 Liwshitz-Garik M., Whipple C.C., "AC machines" D. Van Nostrand Company Inc. 1961
- Lon01 Long S.A. "Acoustic noise and vibration of switched reluctance machines", PhD thesis, November 2001
- Lon98 Long S.A., Zhu Z.Q., Howe D., "Vibrational behaviour of switched reluctance motors", Proc. ICEM '98, 1998, pp 2122-2127
- Mek99 Mekhiche M., Kirtley J.L., Tolikas M., "High speed motor drive development for industrial applications", Proc. IEMDC, IEEE, Seattle, 1999, pp.244-248.
- Miy80 Miyashita K., Yamashita S., Tanabe S., Shimosu T., Sento H., "Development of a high speed 2-pole permanent magnet synchronous motor", IEEE Trans. on PAS, vol.99, no.6, 1980, 2175-2181.

- Moh95 Mohan N., Undeland T.M., Robbins W.P., "Power electronics : Converters, Applications and design", 1995
- New90 Heinemann Newnes, "BS 070M20 (Mild Steel)", Engineering materials pocket book, 1990
- Ng98 Ng K., "Electromagnetic losses in brushless permanent magnet machines", PhD Thesis, 1998
- Oga90 Ogasawara S., Akagi H., "An approach to position sensorless drive for brushless DC motors", IAS Annual Meeting (IEEE Industry Applications Society), pp. 443-447, 1990
- Pal59 Palmgren A., "Ball and Roller Bearing Engineering", 3<sup>rd</sup> Edition, SKF press, 1959
- Pic96 Pickup I.E.D., Tipping D., Hesmondhaigh D.E., Al Zahawi B.A.T., "A 250,000rpm drilling spindle using a permanent magnet motor", Proc. Int. Conf. on Elec. Machines, 1996, Spain, pp.337-342.
- Pyr94 Pyrhonen J., Kurronen P., "Increasing the efficiency of high-speed solid-rotor induction machines", Proc. ICEM'94, vol.1, pp.47-52.
- Ram95 Rama J.C, Giececke A., "High speed electric drive applications, experience, potential and pitfalls – a global overview", IAS – PCIC '95, 1995, pp. 167-174
- Rei95 Reichert K., and Pasquarella G., "High-speed electric machines, status, trends and problems", Proc. IEEE/KTH Stockholm Power Tech Conference, Stockholm, Sweden, June 18-22, 1995, pp.41-49.
- Soo00 Soong W.L., Kliman G.B., Johnson R.N., White R.A., Miller J.E., "Novel high-speed induction motor for a commercial centrifugal compressor", IEEE Trans. on Industry Applications, vol.36, no.3, 2000, pp.706-713.
- Sta88 Staton D.A. "C.A.D. of permanent magnet D.C. motors for industrial drives", PhD Thesis, 1988.
- Tak91 Takahata R., Yotsuya T., "Rotational decay torques of superconducting magnetic bearings", IEEE Transactions on Magnetics, Vol 27 No. 2, pp. 2423 – 2426, 1991
- Tak94 Takahashi I., Koganezawa T., Su G., Ohyama K., "A super high speed PM motor drive system by a quasi-current source inverter", IEEE Trans., IA-30(3), 1994, pp.683-690.
- Tay40 H.D. Taylor, N.Y. Schenectady, "Critical speed behaviour of unsymmetrical shafts", Journal of Applied Mechanics, pp. A-71 – A-79, June, 1940
- Tim91 Timken, "Bearing selection and application data book", 1991
- Ure02 Urenco website, "[http://www.urenco.co.uk/uranium\\_enrichment\\_services.htm](http://www.urenco.co.uk/uranium_enrichment_services.htm)", Urenco, 2002
- Van88 Vance J. M., "Rotor dynamics of turbo machinery", John Wiley & Sons, 1988.
- Will89 K. Williams, R.K. Signal and S.P. Verna, "Vibrations of long and short laminated structures of electrical machines Part II – Results for long stators", Journal of Sound and Vibration, vol. 129, pp. 15-29, 1989
- Wu91 Wu R.S., Slemon G.R., "A permanent-magnet motor drive without a shaft sensor", IEEE Trans. Ind. Applications, Vol.27, No.5, pp.1005-1011, 1991
- Zhu01a Zhu Z.Q., Ng K., Schofield N., Howe D., "Analytical prediction of rotor eddy current loss in brushless machines equipped with surface-mounted permanent magnets, Part I: Magnetostatic Field Model", ICEMS 2001, 2001, pp. 806-809
- Zhu01b Zhu Z.Q., Ng K., Schofield N., Howe D., "Analytical prediction of rotor eddy current loss in brushless machines equipped with surface-mounted permanent magnets, Part II: Accounting for eddy current reaction field", ICEMS 2001, 2001, pp. 810-813
- Zhu01c Zhu Z.Q., Ng K., Howe D., "Analytical prediction of stator flux density waveforms and iron loss in brushless DC machines, accounting for load condition", ICEMS 2001, 2001, pp. 814-817
- Zhu01d Zhu Z.Q., Ede J. D., Howe D., "Design criteria for high-speed brushless dc motors

- for sensorless operation”, *International Journal of Applied Electromagnetics & Mechanics*, Vol. 15, 2002, pp. 79-87.
- Zhu02 Zhu Z.Q., Howe D., Chan C.C., “Improved analytical model for predicting the magnetic field distribution in brushless permanent magnet machines”, *IEEE Trans. on Magnetics*, Vol. 38 No.1, 2002, pp. 229-238.
- Zhu89 Zhu Z. Q., Howe D., “Effects of end-shields and rotor on natural frequencies and modes of stator of small electrical machines”, *Fourth International Conference on Electrical Machines and Drives*, 1989, pp 232-236
- Zhu92 Zhu, Z.Q., Howe, D., Ackermann B., “Analytical prediction of dynamic performance characteristics of brushless DC drives”, *Electric Machines and Power Systems*, Vol. 20 No. 6, 1992, pp. 661-678
- Zhu93a Zhu Z.Q., Howe D., Bolte E., Ackermann B., “Instantaneous magnetic field distribution in brushless permanent magnet dc motors, Part I: Open circuit field”, *IEEE Transactions on Magnetics*, Vol. 29 No. 1, pp 124-135, 1993
- Zhu93c Zhu Z.Q., Howe D., “Instantaneous magnetic field distribution in brushless permanent magnet dc motors, Part III: Effect of stator slotting”, *IEEE Transactions on Magnetics*, Vol. 29 No. 1, pp 143-151, 1993
- Zhu95 Zhu Z.Q., Howe D., Mitchell J.K., “Magnetic field analysis and inductances of brushless dc machines with surface-mounted magnets and non-overlapping stator windings,” *IEEE Transactions on magnetics*, vol.31, no.3, pp. 2115-2118, 1995.
- Zhu97 Zhu, Z.Q., Ng, K., Howe, D., “Design and analysis of a high-speed brushless permanent magnet motor for friction welding application”, *Proc.8th Int Conf. on Electrical Machines and Drives*, IEE, pp. 381-385,1997.

## List of publications

### Journal publications

1. Ede, J. D., Zhu, Z.Q., Howe, D., 'Rotor resonances of high-speed permanent magnet brushless motors', IEEE Transactions on Industry Applications, Vol. 38, No. 6, December 2002, pp. 1542-1548. Also presented at IEEE IEMDC 2001, Massachusetts Institute of Technology, U.S.A, pp. 967-972
2. Zhu Z.Q., Ede J. D., Howe D., "Design criteria for high-speed brushless dc motors for sensorless operation", International Journal of Applied Electromagnetics & Mechanics, Vol. 15, 2002, pp. 79-87. Also invited paper at 10<sup>th</sup> International Symp. on Applied Electromagnetics and Mechanics, Tokyo, May 2001, pp. 454-546

### Conference papers

1. Ede J.D., Zhu, Z.Q., Howe D., 'Optimal split ratio for high-speed permanent magnet brushless DC motors', Proc. International Conf. on Electrical Machines & Systems, 2001, China, pp 909-912
2. Ede, J. D., Zhu, Z.Q., Howe, D., 'A sensorless high-speed brushless DC motor', Proc. 16th Int. Workshop on Rare-Earth Magnets and Their Application, Japan, September 2000, pp. 1049-1058.

# Appendix A MLC motor designs

## EXTERNAL ROTOR SLOTLESS MACHINE

<b>Rated speed</b>	<b>120000 rpm</b>	<b>Output power</b>	<b>705.20 W</b>	<b>Number of pole pairs</b>	<b>3</b>
<b>Torque</b>	<b>56.12 mNm</b>	<b>DC link Voltage</b>	<b>500.00 V</b>	<b>Machine Type</b>	<b>DC</b>
<b>STATOR DIMENSIONS</b>		<b>ROTOR DIMENSIONS</b>		<b>WEIGHTS &amp; DENSITIES</b>	
Outer diameter of winding	119.0 mm	Motor outer diameter	126.8 mm	Magnet density	7700 kg/m <sup>3</sup>
Inner diameter of winding	99.0 mm	Yoke inner diameter	126.8 mm	Conductor density	8900 kg/m <sup>3</sup>
Winding thickness	10.0 mm	Yoke height	0.0 mm	Stator iron density	7650 kg/m <sup>3</sup>
Yoke outer diameter	99.0 mm	Magnet Inner diameter	124.8 mm	Rotor iron density	7650 kg/m <sup>3</sup>
Yoke inner diameter	70.0 mm	Magnet height	1.0 mm	Magnet weight	182.6 g
Yoke height	14.5 mm	Airgap length	2.9 mm	Conductor weight	1.04 kg
Core axial length	60.0 mm	Axial length	60.0 mm	Lamination weight	1.77 kg
Overall axial length	118.0 mm			Rotor iron weight	0.0 g
				Overall weight	2.99 kg
				Inertia	7.2e+02 gm <sup>2</sup>
<b>PERFORMANCE DETAILS</b>		<b>WINDING DETAILS</b>		<b>MAGNET DETAILS</b>	
Machine type	DC	Number of phases	3	Material	USER DEFINED
DC link voltage	500.00 V	Number of conductors	80	Remanence (20 °C)	0.11 T
Torque	56.12 mNm	Number of strands	2	Temp. coeff. Br	0.000
Speed	120000 rpm	Conductor diameter	0.59 mm	Est. magnet temp	20.0 °C
Output power	705.20 W	Mean length turn	295.9 mm	Remanence (Calc)	0.11 T
Input power	777.25 W	Winding pitch	180.0 *elec	Relative recoil permeability	1.05
Phase back emf (Pk)	114.57 V	Winding width	60.0 *elec	Magnetisation	HALBACH-AIR
Line back emf (Pk)	189.20 V	Packing factor	0.37	Magnet height	1.0 mm
Phase current (rms)	2.93 A	Conductivity	5.85e+07 S/m	Number of pole pairs	3
Motor current (ave)	1.55 A	Phase resistance	2.70 Ω	Pole arc/pole pitch	1.00
Current density (wire)	5.37 A/mm <sup>2</sup>	Phase self inductance	1.297 mH		
Current density (wdg)	1.23 A/mm <sup>2</sup>	(end component)	0.000 mH		
Efficiency	90.7 %	Phase mutual inductance	-0.489 mH		
Total loss	72.05 W	(end component)	0.000 mH		
Iron loss	0.56 W				
Resistive loss	69.76 W	<b>ROTOR IRON</b>			
Winding eddy loss	1.74 W	Material	Transil300_16T		
Drive ohmic loss	0.00 W	Yoke flux density	0.0 mT		
				<b>DRIVE CIRCUIT DETAILS</b>	
				Upper transistor resistance	0.00 Ω
				Lower transistor resistance	0.00 Ω
				Upper transistor voltage	0.00 V
				Lower transistor voltage	0.00 V
				Upper diode resistance	0.00 Ω
				Lower diode resistance	0.00 Ω
				Upper diode voltage	0.00 V
				Lower diode voltage	0.00 V
				Commutation angle	30.00 deg.
				Commutation width	0.0 deg.
				Diode conduction angle	60.0 deg.
<b>STATOR IRON</b>		<b>THERMAL DETAILS</b>			
Material	Transil300_16T	Ambient temperature	20 °C		
Yoke flux density	7.2 mT	Dissipation area	76.98 cm <sup>2</sup>		
Hysteresis loss factor K <sub>h</sub>	1.55e-02	Heat transfer coeff	100.00 W/m <sup>2</sup> °C		
Hysteresis loss factor α	2.45	Surface temperature	114 °C		
Eddy current loss factor K <sub>e</sub>	1.00e-04	Est. magnet temperature	20 °C		
Conductivity	1.33e+06 S/m				
Lamination thickness	0.35 mm				

Figure A.1 - Modified design with 80 turns per coil

## EXTERNAL ROTOR SLOTLESS MACHINE

Rated speed	120000 rpm	Output power	366.03 W	Number of pole pairs	3
Torque	29.13 mNm	DC link Voltage	500.00 V	Machine Type	DC
<b>STATOR DIMENSIONS</b>		<b>ROTOR DIMENSIONS</b>		<b>WEIGHTS &amp; DENSITIES</b>	
Outer diameter of winding	119.0 mm	Motor outer diameter	126.8 mm	Magnet density	7700 kg/m <sup>3</sup>
Inner diameter of winding	99.0 mm	Yoke inner diameter	126.8 mm	Conductor density	8900 kg/m <sup>3</sup>
Winding thickness	10.0 mm	Yoke height	0.0 mm	Stator iron density	7650 kg/m <sup>3</sup>
Yoke outer diameter	99.0 mm	Magnet Inner diameter	124.8 mm	Rotor iron density	7650 kg/m <sup>3</sup>
Yoke inner diameter	70.0 mm	Magnet height	1.0 mm	Magnet weight	182.6 g
Yoke height	14.5 mm	Airgap length	2.9 mm	Conductor weight	1.11 kg
Core axial length	60.0 mm	Axial length	60.0 mm	Lamination weight	1.77 kg
Overall axial length	128.0 mm			Rotor iron weight	0.0 g
				Overall weight	3.06 kg
				Inertia	7.2e+02 gm <sup>2</sup>
<b>PERFORMANCE DETAILS</b>		<b>WINDING DETAILS</b>		<b>MAGNET DETAILS</b>	
Machine type	DC	Number of phases	3	Material	USER DEFINED
DC link voltage	500.00 V	Number of conductors	80	Remanence (20 °C)	0.11 T
Torque	29.13 mNm	Number of strands	2	Temp. coeff. Br	0.000
Speed	120000 rpm	Conductor diameter	0.59 mm	Est. magnet temp	20.0 °C
Output power	366.03 W	Mean length turn	315.9 mm	Remanence (Calc)	0.11 T
Input power	388.60 W	Winding pitch	180.0 °elec	Relative recoil permeability	1.05
Phase back emf (Pk)	114.58 V	Winding width	60.0 °elec	Magnetisation	HALBACH-AIR
Line back emf (Pk)	189.20 V	Packing factor	0.37	Magnet height	1.0 mm
Phase current (rms)	1.53 A	Conductivity	5.85e+07 S/m	Number of pole pairs	3
Motor current (ave)	777.00 mA	Phase resistance	2.88 Ω	Pole arc/pole pitch	1.00
Current density (wire)	2.80 A/mm <sup>2</sup>	Phase self inductance	2.389 mH		
Current density (wdg)	0.64 A/mm <sup>2</sup>	(end component)	1.092 mH		
Efficiency	94.2 %	Phase mutual inductance	-1.036 mH		
Total loss	22.57 W	(end component)	-0.546 mH		
Iron loss	0.56 W				
Resistive loss	20.28 W	<b>ROTOR IRON</b>			
Winding eddy loss	1.74 W	Material	Transil300_16T		
Drive ohmic loss	0.00 W	Yoke flux density	0.0 mT		
<b>STATOR IRON</b>		<b>THERMAL DETAILS</b>		<b>DRIVE CIRCUIT DETAILS</b>	
Material	Transil300_16T	Ambient temperature	20 °C	Upper transistor resistance	0.00 Ω
Yoke flux density	7.2 mT	Dissipation area	76.98 cm <sup>2</sup>	Lower transistor resistance	0.00 Ω
Hysteresis loss factor K <sub>h</sub>	1.55e-02	Heat transfer coeff	100.00 W/m <sup>2</sup> ·°C	Upper transistor voltage	0.00 V
Hysteresis loss factor α	2.45	Surface temperature	49 °C	Lower transistor voltage	0.00 V
Eddy current loss factor K <sub>e</sub>	1.00e-04	Est. magnet temperature	20 °C	Upper diode resistance	0.00 Ω
Conductivity	1.33e+06 S/m			Lower diode resistance	0.00 Ω
Lamination thickness	0.35 mm			Upper diode voltage	0.00 V
				Lower diode voltage	0.00 V
				Commutation angle	30.00 deg.
				Commutation width	0.0 deg.
				Diode conduction angle	60.0 deg.

**Figure A.2 - Revised calculation for motor performance including end-winding calculation**

## EXTERNAL ROTOR SLOTLESS MACHINE

<b>Rated speed</b>	120000 rpm	<b>Output power</b>	682.67 W	<b>Number of pole pairs</b>	3
<b>Torque</b>	54.33 mNm	<b>DC link Voltage</b>	500.00 V	<b>Machine Type</b>	DC
<b>STATOR DIMENSIONS</b>		<b>ROTOR DIMENSIONS</b>		<b>WEIGHTS &amp; DENSITIES</b>	
Outer diameter of winding	119.0 mm	Motor outer diameter	126.8 mm	Magnet density	7700 kg/m <sup>3</sup>
Inner diameter of winding	99.0 mm	Yoke inner diameter	126.8 mm	Conductor density	8900 kg/m <sup>3</sup>
Winding thickness	10.0 mm	Yoke height	0.0 mm	Stator iron density	7650 kg/m <sup>3</sup>
Yoke outer diameter	99.0 mm	Magnet Inner diameter	124.8 mm	Rotor iron density	7650 kg/m <sup>3</sup>
Yoke inner diameter	70.0 mm	Magnet height	1.0 mm	Magnet weight	182.6 g
Yoke height	14.5 mm	Airgap length	2.9 mm	Conductor weight	1.13 kg
Core axial length	60.0 mm	Axial length	60.0 mm	Lamination weight	1.77 kg
Overall axial length	118.0 mm			Rotor iron weight	0.0 g
				Overall weight	3.08 kg
				Inertia	7.2e+02 gm <sup>2</sup>
<b>PERFORMANCE DETAILS</b>		<b>WINDING DETAILS</b>		<b>MAGNET DETAILS</b>	
Machine type	DC	Number of phases	3	Material	USER DEFINED
DC link voltage	500.00 V	Number of conductors	49	Remanence (20 °C)	0.11 T
Torque	54.33 mNm	Number of strands	2	Temp. coeff. Br	0.00
Speed	120000 rpm	Conductor diameter	0.79 mm	Est. magnet temp	20.0 °C
Output power	682.67 W	Mean length turn	295.9 mm	Remanence (Calc)	0.11 T
Input power	751.48 W	Winding pitch	180.0 °elec	Relative recoil permeability	1.05
Phase back emf (Pk)	70.18 V	Winding width	60.0 °elec	Magnetisation	HALBACH-AIR
Line back emf (Pk)	115.88 V	Packing factor	0.39	Magnet height	1.0 mm
Phase current (rms)	4.82 A	Conductivity	5.85e+07 S/m	Number of pole pairs	3
Motor current (ave)	1.50 A	Phase resistance	933.00 mΩ	Pole arc/pole pitch	1.00
Current density (wire)	4.97 A/mm <sup>2</sup>	Phase self inductance	0.793 mH		
Current density (wdg)	1.24 A/mm <sup>2</sup>	(end component)	0.306 mH		
Efficiency	90.8 %	Phase mutual inductance	-0.337 mH		
Total loss	68.82 W	(end component)	-0.153 mH		
Iron loss	0.56 W				
Resistive loss	64.91 W	<b>ROTOR IRON</b>			
Winding eddy loss	3.35 W	Material	Transil300_16T		
Drive ohmic loss	0.00 W	Yoke flux density	0.0 mT		
<b>STATOR IRON</b>		<b>THERMAL DETAILS</b>		<b>DRIVE CIRCUIT DETAILS</b>	
Material	Transil300_16T	Ambient temperature	20 °C	Upper transistor resistance	0.00 Ω
Yoke flux density	7.2 mT	Dissipation area	76.98 cm <sup>2</sup>	Lower transistor resistance	0.00 Ω
Hysteresis loss factor K <sub>h</sub>	1.55e-02	Heat transfer coeff	100.00 W/m <sup>2</sup> ·°C	Upper transistor voltage	0.00 V
Hysteresis loss factor α	2.45	Surface temperature	109 °C	Lower transistor voltage	0.00 V
Eddy current loss factor K <sub>e</sub>	1.00e-04	Est. magnet temperature	20 °C	Upper diode resistance	0.00 Ω
Conductivity	1.33e+06 S/m			Lower diode resistance	0.00 Ω
Lamination thickness	0.35 mm			Upper diode voltage	0.00 V
				Lower diode voltage	0.00 V
				Commutation angle	30.00 deg.
				Commutation width	0.0 deg.
				Diode conduction angle	60.0 deg.

**Figure A.3 - New stator design to operate at 50mNm**

## Appendix B MLC motor construction

A schematic of the stator assembly is shown in Figure B.1 the stator windings being potted in Stycast for mechanical strength.

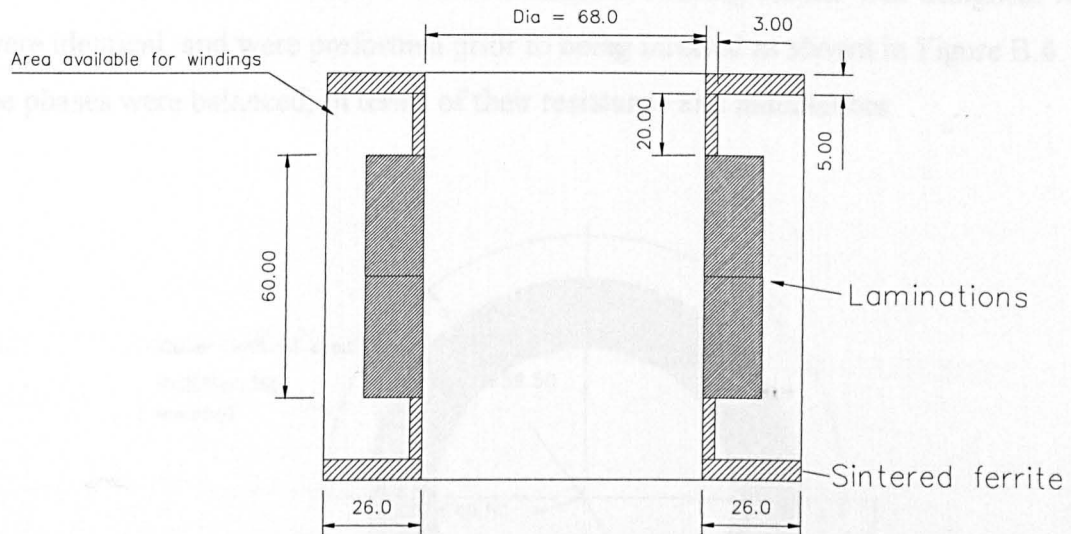


Figure B.1 - Schematic of stator assembly

### Stator laminations

Since the ferrite screening components could only be manufactured in limited sizes, the internal diameter of the stator was reduced from 70mm to 68mm so as to be consistent. A lamination from the prototype motor is shown Figure B.2, the slots being introduced to support strips of rigid insulation, which serve to locate and form the stator windings.

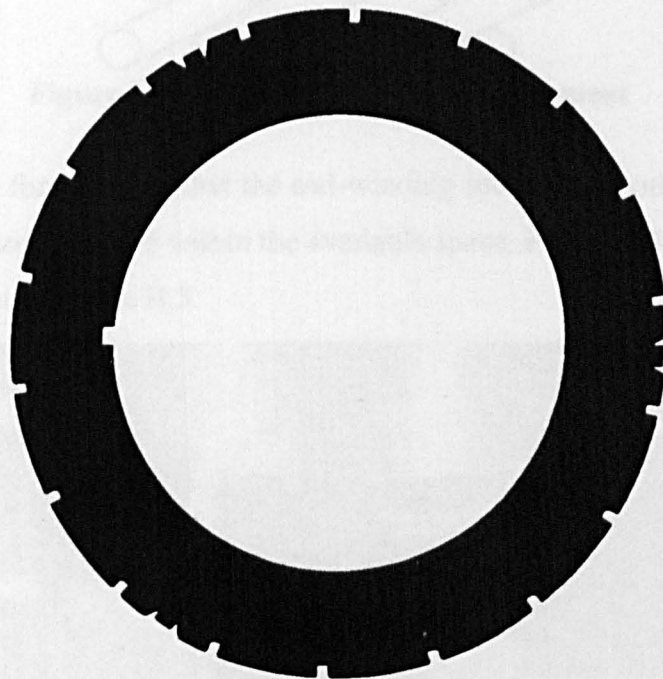


Figure B.2 - Stator lamination

### Stator winding

Due to the limited space envelope, the stator winding had to be very compact, an axial length of 20mm being available at each end to accommodate the end-windings.

Each coil spans  $60^\circ$  mechanical, which as can be seen from the lamination design shown in Figure B.3, embraces three slots, for which a suitable winding former was designed. All the coils were identical, and were preformed prior to being inserted as shown in Figure B.4. Thus, all three phases were balanced, in terms of their resistance and inductances.

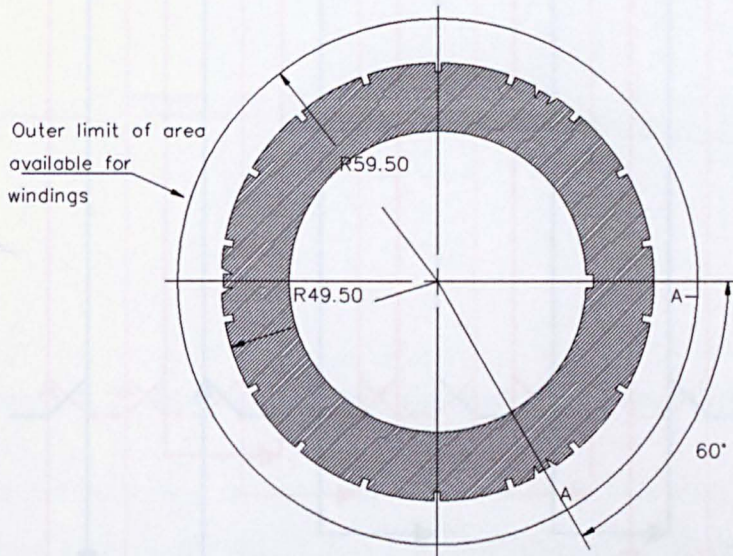


Figure B.3 - Schematic of stator cross-section

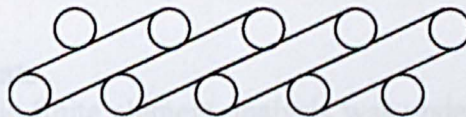


Figure B.4 - Schematic of coil arrangement

The windings were formed such that the end-winding sections of both the upper and lower coil sides could be accommodated within the available space, Figure B.1. A photograph of the end-windings is shown in Figure B.5.

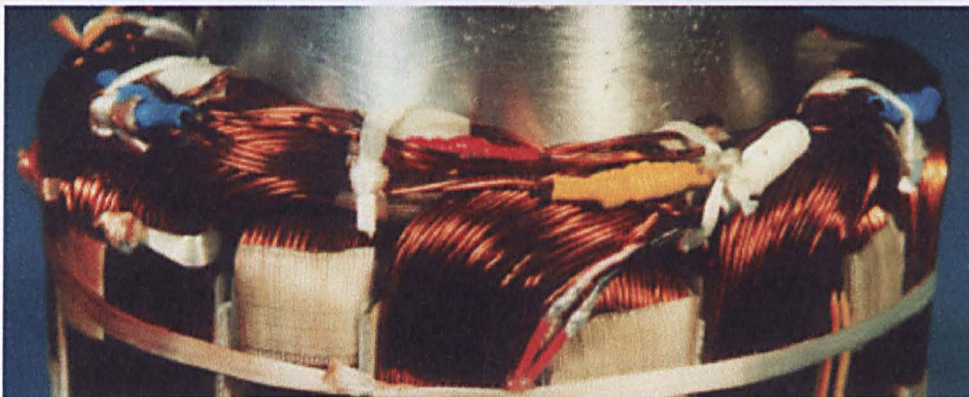
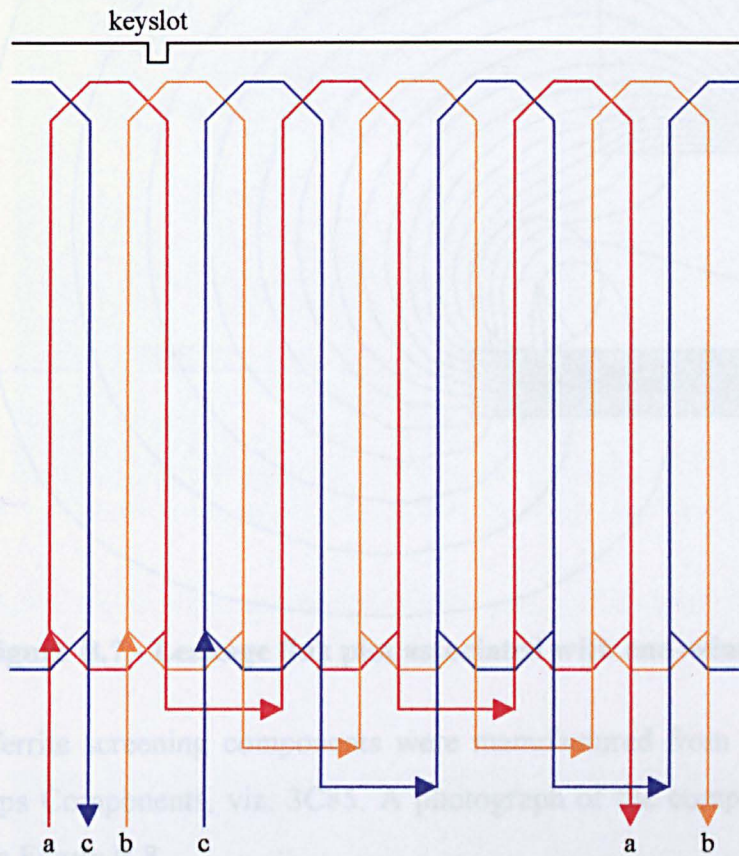


Figure B.5 - View of stator end-winding

The coils were connected in series to form the respective phases, as shown in Figure B.6, and the star point was brought out to enable easy measurement of the parameters of the assembled motor and allow the possibility of connecting a sensorless drive to the motor.



**Figure B.6 - Winding layout showing connection of phases**

### **Ferrite screening components**

A simplified magnetostatic finite element analysis was undertaken to determine the grade of sintered soft ferrite material which is required to contain the leakage flux. The flux plot shown in Figure B.7, which corresponds to current flowing down a single conductor which is equivalent in magnitude to the actual end-winding ampere-conductors at rated load.

*Figure B.5 - End-region winding arrangement prior to attachment to stator*

### *Assembly of stator*

*The prefabricated coils were attached to the stator, and some thermistors were mounted on the coils to allow for the possibility of temperature monitoring of the stator, as can be seen in Figure B.9.*

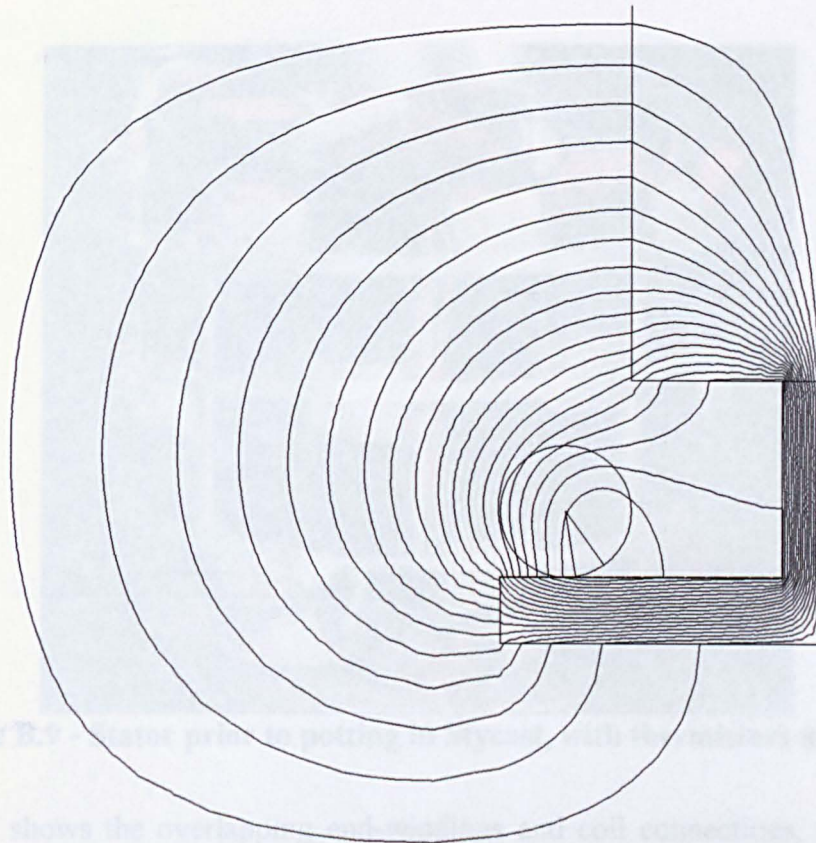


**Figure B.7 - Leakage flux plot associated with end-winding**

The sintered ferrite screening components were manufactured from a grade of material supplied by Philips Components, viz. 3C85. A photograph of the components for one end-region is shown in Figure B.8.



**Figure B.8 - End-region shielding arrangement prior to attachment to stator**

#### **Assembly of stator**

The preformed coils were attached to the stator, and some thermistors were mounted on the coils to allow for the possibility of temperature monitoring of the stator, as can be seen in Figure B.9.

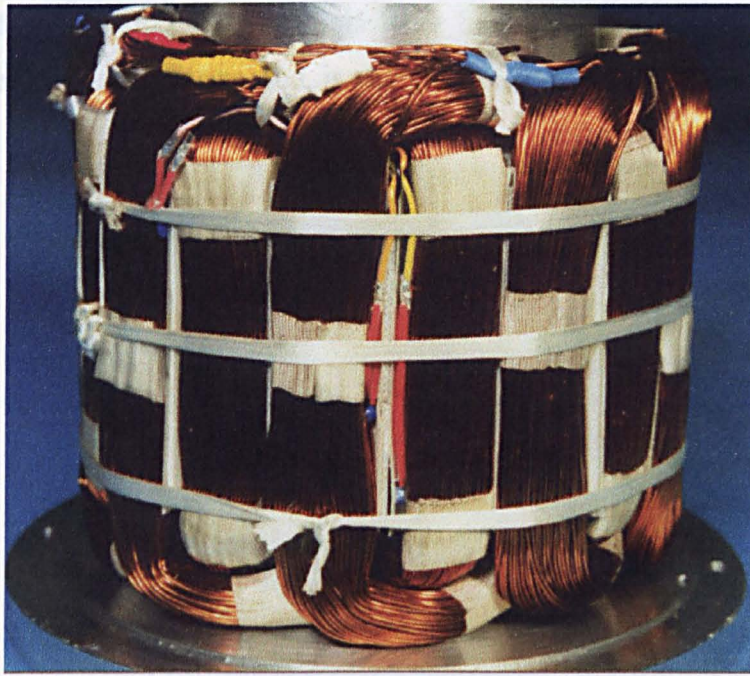


**Figure B.9 - Stator prior to potting in Stycast, with thermistors attached**

Figure B.10 shows the overlapping end-windings and coil connections, the three phases being identified by red, yellow and blue insulation.



**Figure B.10 - Stator windings showing Phase connections**

### Potting of stator in Stycast

The completed stator, after the windings have been potted in Stycast and the sintered ferrite and end-pieces have been attached, is shown in Figure B.11.



**Figure B.11 - Finished stator, with ferrite end-pieces**

### Impulse magnetising fixture

The possible designs of magnetising fixture are listed in Table B.1. The Four types of fixture investigated are as follows:

- Type I has 2 conductor positions per half pole-pitch
- Type II has 2 conductor positions per half pole-pitch and one in the centre of the pole
- Type III has 3 conductor positions per half pole-pitch
- Type IV has 3 conductor positions per half pole-pitch and one in the centre of the pole

It is obvious that the more positions of conductors per half pole-pitch, the higher the flux density in the magnet. However, the difficulty in fixture fabrication is proportional to the number of positions. As a compromise between the maximum flux density and degree of manufacture, type III, viz. 3 positions per half pole pitch and 2 layers of conductor has been chosen as a final magnetising fixture as shown in Figure B.12, and is used to magnetise the MLC rotor.

**Table B.1 – Comparison of Halbach magnetising fixture designs**

Type	Number of layers	Conductor Diameter (mm)	Resistance (mΩ)	Inductance (μH)	Peak Current (kA)	Max flux density (T)	Rise time (μs)	Max temperature (°C)
I	1	4.5	3.24	2.87	60	2.02	144	57
	2	4.5	6.26	10.11	37	2.18	241	45
	3	4.5	9.3	20.32	27.15	2.1	334	38.5
II	1	5	3.27	4.19	53.2	2.185	166	47
	2	5	6.35	14.84	31.7	2.25	289	37
III	1	4	6.12	6.19	44.6	2.48	193	59
	2	4	12	22.4	25.56	2.509	347	43
IV	1	4	7.13	8.14	39.9	2.61	217	55
	2	4	13.6	29.5	22.5	2.624	397	41

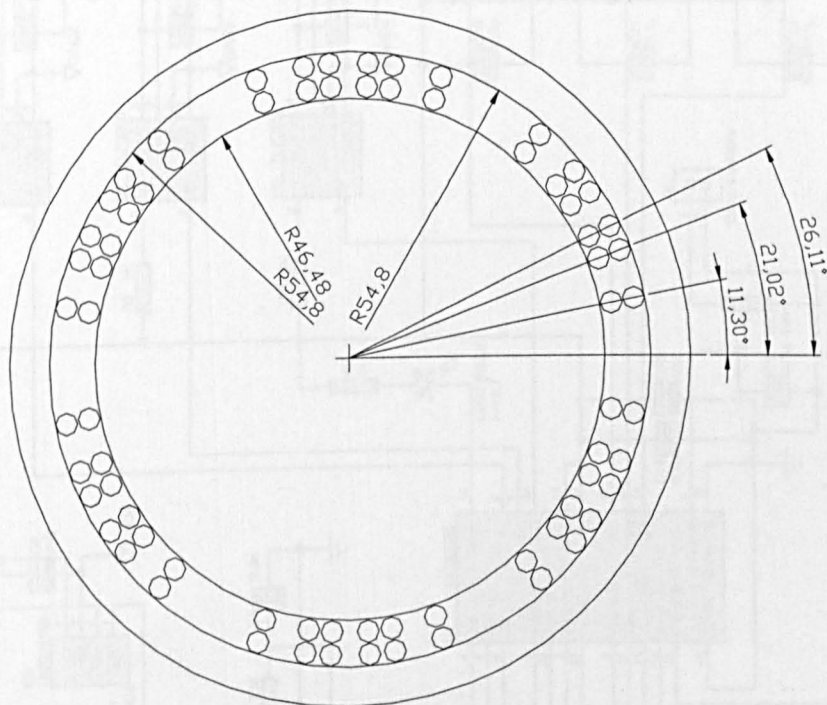


**Figure B.12 – 6-pole Halbach impulse magnetising fixture**

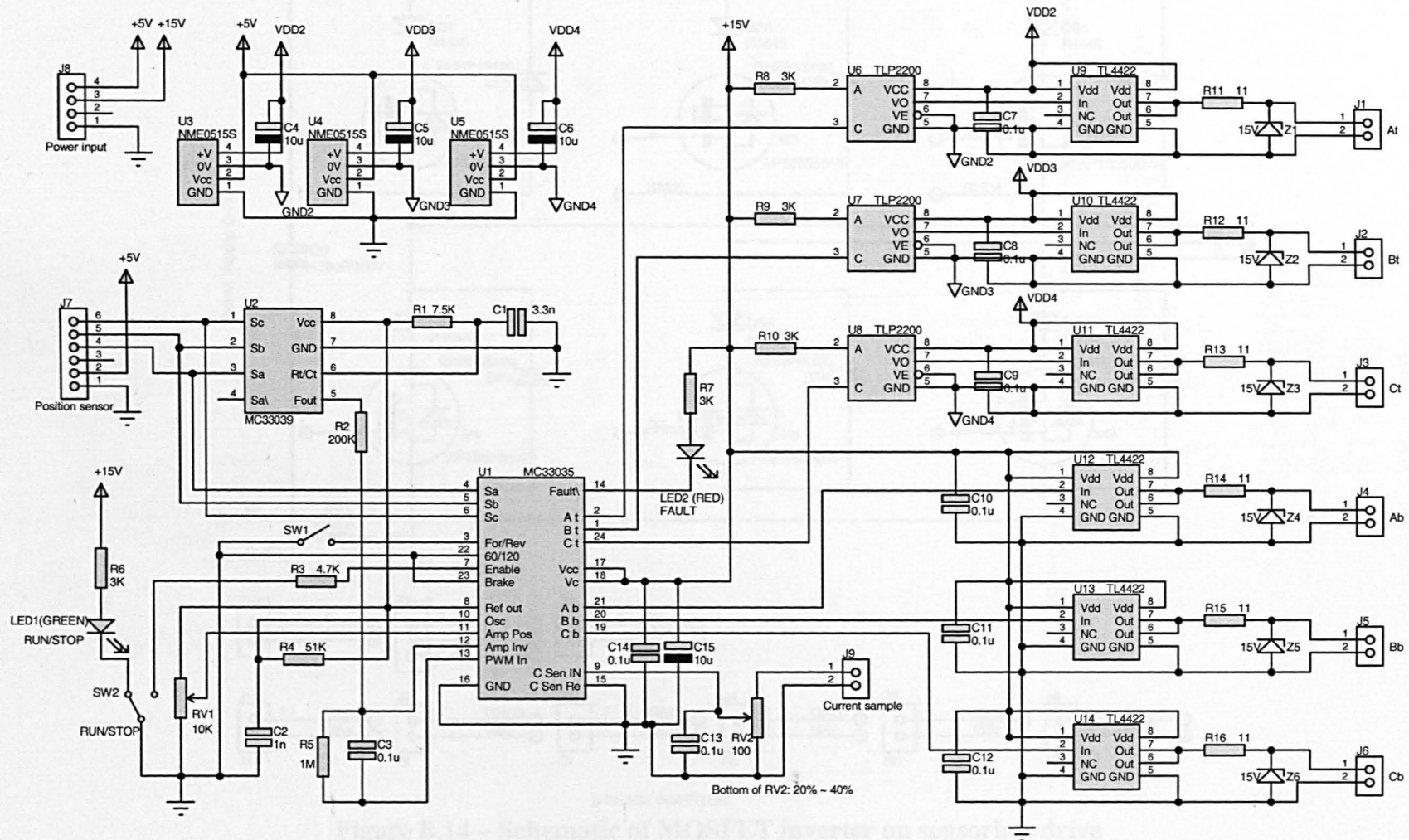


Figure B.13 – Schematic of control circuit for MOSFET drive

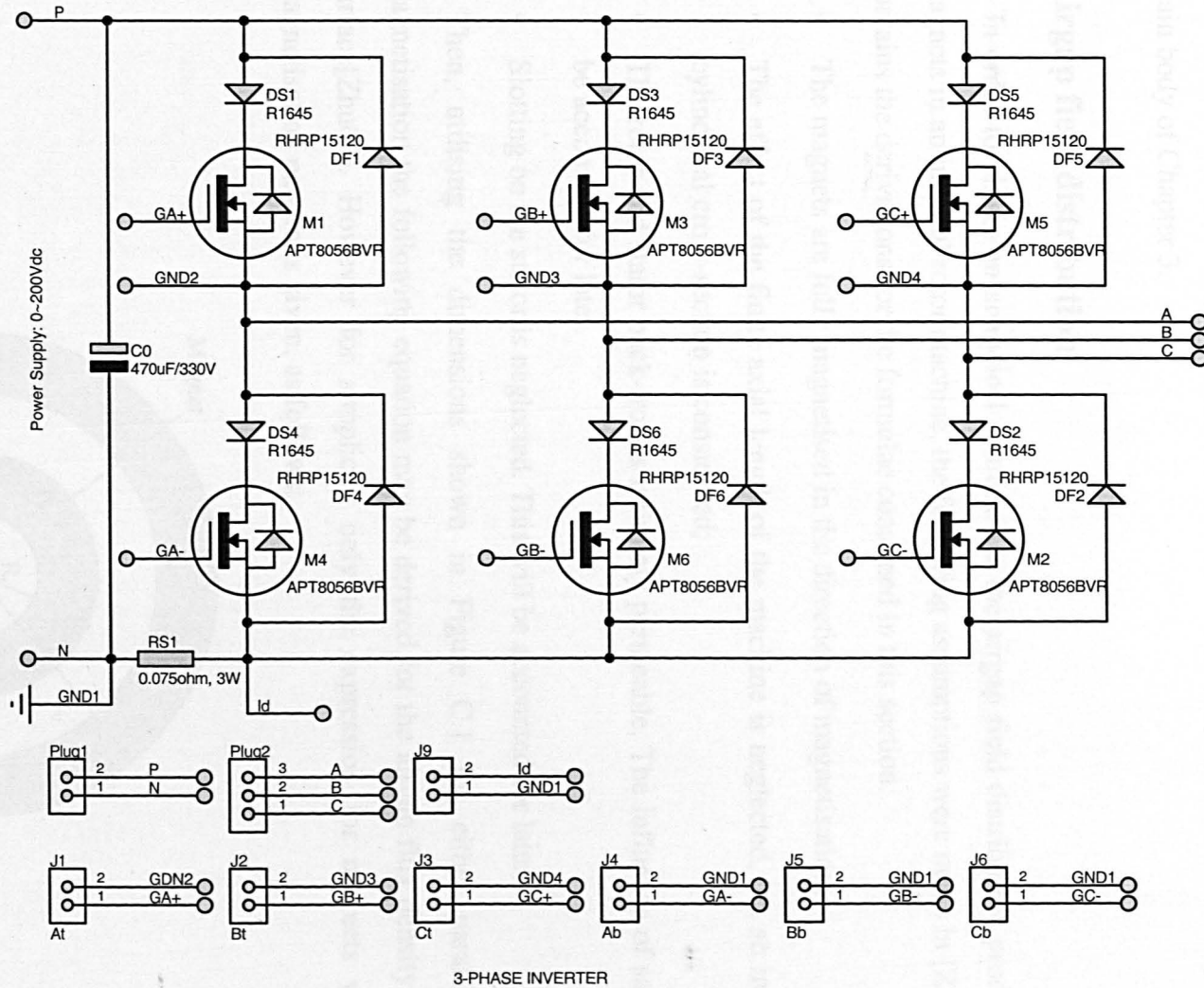


Figure B.14 – Schematic of MOSFET inverter on sensorless drive

## Appendix C Design equations for proprietary CAD software

The CAD software which is described here has been developed over a period of time in the Electrical Machines and Drive Group at the University of Sheffield. Recent modifications include the implementation of alternative magnetisation distributions, viz. parallel magnetisation. Some finite element validation is described in this appendix, whilst validation of routines for calculating the winding inductances and the back-emf are contained in the main body of Chapter 3.

### Airgap field distribution

In order to obtain an analytical solution for the airgap field distribution produced by the magnets in an internal rotor machine, the following assumptions were made in [Zhu02] which contains the derivations for the formulae contained in this section:

- The magnets are fully magnetised in the direction of magnetisation;
- The effect of the finite axial length of the machine is neglected, i.e. an infinitely long cylindrical cross-section is considered;
- The rotor and stator back-iron is infinitely permeable. The influence of saturation will be accounted for later.
- Slotting on the stator is neglected. This will be accounted for later.

Then, utilising the dimensions shown in Figure C.1 for either parallel or radial magnetisation the following equation may be derived for the airgap flux density at the stator surface[Zhu02]. However for simplicity only the expression for magnets with parallel magnetisation pattern is given, as follows:

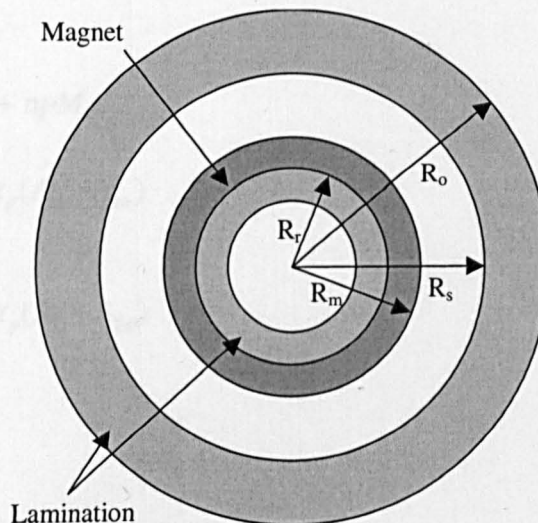


Figure C.1 - Model showing salient dimensions

For  $np=1$ ,

$$B_{rl}(\theta) = \frac{\mu_0 M_n}{\mu_r} \left\{ \frac{A_{3n} \left(\frac{R_m}{R_s}\right)^2 - A_{3n} \left(\frac{R_r}{R_s}\right)^2 + \left(\frac{R_r}{R_s}\right)^2 \ln \left(\frac{R_m}{R_r}\right)^2}{\left[ \frac{\mu_r + 1}{\mu_r} \left[ 1 - \left(\frac{R_r}{R_s}\right)^2 \right] \right] \left[ \frac{\mu_r - 1}{\mu_r} \left[ \left(\frac{R_m}{R_s}\right)^2 - \left(\frac{R_r}{R_m}\right)^2 \right] \right]} \right\} \cos \theta \quad (\text{C.1})$$

and for  $np \neq 1$ ,

$$B_{rl}(\theta) = \sum_{n=1,3,5,\dots}^{\infty} \frac{2\mu_0 M_n}{\mu_r} \frac{np}{(np)^2 - 1} \left(\frac{R_m}{R_s}\right)^{np+1} \left\{ \frac{(A_{3n} - 1) + 2 \left(\frac{R_r}{R_m}\right)^{np+1} - (A_{3n} + 1) \left(\frac{R_r}{R_m}\right)^{2np}}{\left[ \frac{\mu_r + 1}{\mu_r} \left[ 1 - \left(\frac{R_r}{R_s}\right)^{2np} \right] \right] \left[ \frac{\mu_r - 1}{\mu_r} \left[ \left(\frac{R_m}{R_s}\right)^{2np} - \left(\frac{R_r}{R_m}\right)^{2np} \right] \right]} \right\} \cos np\theta \quad (\text{C.2})$$

where :

$p$  = number of pole pairs

$B_r$  = remanence of permanent magnets

$\mu_0$  = permeability of free space

$\mu_r$  = relative recoil permeability of magnets

$$A_{3n} = \left( np - \frac{1}{np} \right) \frac{M_m}{M_n} + \frac{1}{np} \quad \text{for } np \neq 1 \quad (\text{C.3a})$$

$$A_{3n} = 2 \frac{M_{r1}}{M_1} - 1 \quad \text{for } np = 1 \quad (\text{C.3b})$$

where :

$$M_n = M_m + np M_{\theta n} \quad (\text{C.4})$$

$$M_m = \frac{B_r}{\mu_0} \alpha_p (A_{1n} + A_{2n}) \quad (\text{C.5})$$

$$M_{\theta n} = \frac{B_r}{\mu_0} \alpha_p (A_{1n} - A_{2n}) \quad (\text{C.6})$$

where :

$$A_{1n} = \frac{\sin \left[ (np + 1) \alpha_p \frac{\pi}{2p} \right]}{(np + 1) \alpha_p \frac{\pi}{2p}} \quad (\text{C.7})$$

$$A_{2n} = 1 \quad \text{for } np=1 \quad (\text{C.8a})$$

$$A_{2n} = \frac{\sin \left[ (np - 1) \alpha_p \frac{\pi}{2p} \right]}{(np - 1) \alpha_p \frac{\pi}{2p}} \quad \text{for } np \neq 1 \quad (\text{C.8b})$$

$\alpha_p$  = magnet pole-arc to pole-pitch ratio

However, a simplified version of equations C.1 & C.2 was developed for a motor with a parallel-magnetised 2-pole magnet in [Zhu97], and is given in equation C.9 for the airgap field at the stator surface. This is a special case as the resultant airgap field distribution is a sine wave, i.e. there are no harmonics present and are of particular interest as this was the magnetisation employed in the motors. 2-pole parallel magnetisation is preferable due to a sinusoidal airgap field distribution, a sinusoidal stator flux density leading to a reduced iron loss and a higher overall stator flux density. Also parallel magnetised magnets are easier to manufacture and only require a solenoid fixture to magnetise when compared with a pre-built fixture for radial magnets.

$$B_{r1}(\theta) = \frac{B_r \left( 1 - \frac{R_r^2}{R_m^2} \right)^2 \left( \frac{R_m^2}{R_s^2} \right) \sin \theta}{\left( 1 + \frac{R_m^2}{R_s^2} \right) \left( 1 - \frac{R_r^2}{R_m^2} \right) + \mu_r \left( 1 - \frac{R_m^2}{R_s^2} \right) \left( 1 + \frac{R_r^2}{R_m^2} \right)} \quad (\text{C.9})$$

Numerous finite element analyses have confirmed the validity of the foregoing equations, and with the model depicted in Figure C.1 and the dimensions shown below a good agreement was reached between the two methods, as can be seen in Figure C.2 where the dimensions are for the prototype motor A<sub>1</sub>.

Dimensions:  $R_r = 7\text{mm}$ ,  $R = 10\text{mm}$ ,  $R_s = 15\text{mm}$ ,  $R_o = 35\text{mm}$ ,  $B_r = 1.13\text{T}$ ,  $\alpha_p = 1$  and  $\mu_r = 1.05$

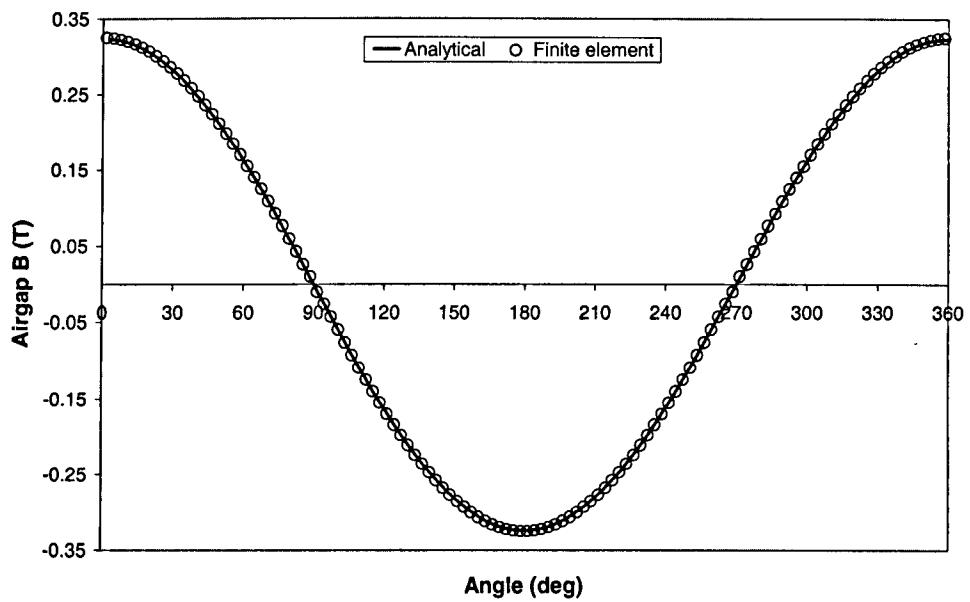


**Figure C.2 - Comparison between finite element and analytical calculation of flux density at stator surface**

### Slotting effects

So far it has been assumed that the motor has a slotless topology. However, by considering the permeance of the airgap due to stator slots, it is possible to account for the effect of stator slotting on the open-circuit field in order to calculate the resultant flux entering the stator iron [Zhu93c]. Figure C.3 shows the idealised model of the motor topology. For simplicity, the following assumption was made:

- The permeability of the stator and rotor back-iron is infinite, i.e.  $\mu = \infty$

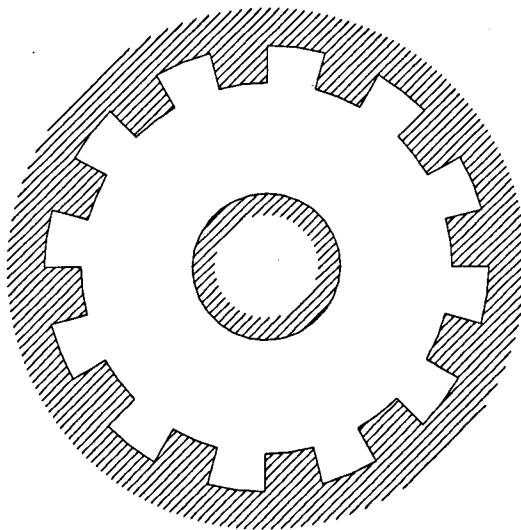


**Figure C.3 - Model used for calculating relative permeance of slotted airgap**

It has been shown in the previous section that the airgap flux density can be expressed as a Fourier series. However, this calculation neglected the effect of stator slotting, which can be accounted for by employing the relative permeance of the airgap region, viz.:

$$B_{open-circuit}(r, \alpha, \alpha_{ma}) = B_{magnet}(r, \alpha, \alpha_{ma}) \tilde{\lambda}(r, \alpha) \quad (C.10)$$

where  $r$ ,  $\alpha$ ,  $\alpha_{ma}$  and  $\tilde{\lambda}$  are the radius, circumferential co-ordinate, angle of rotation of the rotor and the relative permeance respectively.

The relative permeance,  $\tilde{\lambda}$ , is defined as having unity maximum value, and consequently is obtained by dividing  $\lambda$ , the airgap permeance, by a reference permeance,  $\Lambda_{ref}$ , equal to the one-dimensional permeance of an equivalent slotless stator motor, where:

$$\lambda_{ref} = \frac{\mu_0}{g + \frac{h_m}{\mu_r}} \quad (C.11)$$

where  $g$  and  $h_m$  are the airgap length and the magnet height, respectively. Therefore,

$$\tilde{\lambda}(r, \alpha) = \frac{\lambda(r, \alpha)}{\Lambda_{ref}} \quad (C.12)$$

where  $\lambda(r, \alpha)$  is equal to the airgap flux density distribution,  $B'(r, \alpha)$ , in the magnet/airgap region and is calculated as follows

$$\lambda(r, \alpha) = \begin{cases} \Lambda_0 \left[ 1 - \beta(r) - \beta(r) \cos \frac{\pi}{0.8\alpha_0} \alpha \right] & \text{for } 0 \leq \alpha \leq 0.8\alpha_0 \\ \Lambda_0 & \text{for } 0.8\alpha_0 \leq \alpha \leq \alpha_0/2 \end{cases} \quad (C.13)$$

where  $\Lambda_0 = \mu_0 / g'$ ,  $g' = g + h_m / \mu_r$ , and  $\beta(r)$  is determined by the conformal transformation method as:

$$\beta(r) = \frac{1}{2} \left[ 1 - \frac{1}{\sqrt{1 + \left( \frac{b_0}{2g'} \right) (1 + v^2)}} \right] \quad (C.14)$$

where  $b_0$  is the width of a stator slot openings and  $v$  is determined from :

$$y \frac{\pi}{b_0} = \frac{1}{2} \ln \left[ \frac{\sqrt{a^2 + v^2} + v}{\sqrt{a^2 + v^2} - v} \right] + \frac{2g'}{b_0} \arctan \frac{2g'}{b_0} \frac{v}{\sqrt{a^2 + v^2}} \quad (C.15)$$

$$\text{and } a^2 = 1 + \left( \frac{2g'}{b_0} \right)^2 \quad (C.16)$$

with  $y = r - R_s + g'$

To be consistent with the expression for the airgap flux density distribution expressed as a Fourier series, which simplifies computation, the permeance can also be expressed as :

$$\tilde{\lambda}(\alpha, r) = \sum_{\mu=0}^{\infty} \tilde{\Lambda}_{\mu}(r) \cos \mu Q_s (\alpha + \alpha_{sa}) \quad (\text{C.17})$$

where  $Q_s$  is the number of stator slots and  $\alpha_{sa}$  is a coefficient of the winding pitch, which in the motor topology under consideration is  $\pi/Q_s$  and  $\tilde{\Lambda}_{\mu}(r)$  can be deduced as:

$$\tilde{\Lambda}_0(r) = \frac{1}{K_c} \left( 1 - 1.6\beta \frac{b_0}{\tau_t} \right) \quad (\text{C.18})$$

and

$$\tilde{\Lambda}_{\mu}(r) = \frac{2}{\alpha_t} \int_{\alpha_t/2}^{\alpha_t/2} \tilde{\lambda}(r, \alpha) \cos \mu Q_s \alpha \, d\alpha \quad (\text{C.19})$$

$$= \frac{4}{\alpha_t} \left\{ \int_b^{0.8\alpha_0} \left( 1 - \beta(r) - \beta(r) \cos \frac{\pi}{0.8\alpha_0} \right) \cdot \cos \frac{2\pi}{\alpha_t} \mu \alpha \, d\alpha + \int_{b.8\alpha_0}^{0.5\alpha_t} \cos \frac{2\pi}{\alpha_d} \mu \alpha \, d\alpha \right\} \quad (\text{C.20})$$

$$= -\beta(r) \frac{4}{\pi\mu} \left\{ 0.5 + \frac{\left( \mu \frac{b_0}{\tau_t} \right)^2}{0.78125 - 2 \left( \mu \frac{b_0}{\tau_t} \right)^2} \right\} \cdot \sin \left( 1.6\pi\mu \frac{b_0}{\tau_t} \right) \quad (\text{C.21})$$

where  $K_c$  and  $\tau_t$  are the Carter coefficient and the stator tooth pitch, respectively.

Utilising the permeance expressions deduced above it is possible to calculate the tooth body flux using the Fourier coefficients of the airgap flux density and permeance and integrating over one slot-pitch.

### Back-emf waveform

Utilising the open-circuit field distribution and relative permeance expressions given in the previous sections, it is possible to calculate the back-emf waveform induced in a phase winding [Zhu93d]

The open-circuit flux density distribution at the stator bore is:

$$B_{open-circuit}(\alpha, t) = \tilde{\Lambda}_0 \sum_n B_n \cos np(\alpha - \alpha_{ma}) \quad (\text{C.22})$$

where  $\alpha_{ma} = \omega_r t + \theta_0$  and  $\theta_0$  is an initial angle.

From this, the flux linking a coil can be calculated as:

$$\Psi = \int_{-(\alpha_y/2)}^{\alpha_y/2} B_{open-circuit}(\alpha, t) R_s l_{eff} d\alpha \quad (C.23)$$

where  $\alpha_y$ ,  $R_s$ ,  $l_{eff}$  are the winding pitch angle, the stator bore radius and the effective axial length, respectively.

From this it can be shown that for both slotted and slotless motors:

$$\Psi = \tilde{\Lambda}_0 \sum_n \frac{\Phi_n}{np} K_{dn} \cos np\alpha_{ma} \quad (C.24)$$

where

$$\Phi_n = 2B_n R_s l_{eff} \tilde{\Lambda}_0 \quad (C.25)$$

and

$$K_{dn} = \sin np \frac{\alpha_y}{2} \quad (C.26)$$

where  $\tilde{\Lambda}_0$  and  $K_{dn}$  are the mean relative permeance and the winding pitch factor, respectively. Therefore, the emf induced in one turn of a coil is:

$$e = -\frac{d\Psi}{dt} = \tilde{\Lambda}_0 \sum_n 2B_n R_s l_{eff} \omega_r K_{dn} \cos np\alpha_{ma} \quad (C.27)$$

$$= \sum_n \omega_r \Phi_n K_{dn} \sin np\alpha_{ma} \quad (C.28)$$

which can be re-written to give the induced emf per phase for a distributed multi-pole winding as:

$$e = \sum_n E_n \sin np\alpha_{ma} \quad (C.29)$$

where

$$E_n = \omega_r \Phi_n N_p K_{dpn} \quad (C.30)$$

where  $N_p$  is the number of series turns per phase,  $K_{dpn} = K_{dn} K_{pn}$  is the winding factor, where  $K_{pn}$  and  $K_{dn}$  are, respectively, the winding distribution factor and the winding pitch factor.

## Inductance calculation

### A. Slot inductance

Previous work on inductance calculations usually utilises the 1-d analysis which is normally used for induction machines in which the airgap length is comparatively small and the airgap component of inductance tends to dominate. In permanent magnet machines the magnets have a low recoil permeability, (generally  $\leq 1.1$ ), and thus the effective airgap is

much larger and the slot component of inductance may be dominant. [Zhu95] presents a method for calculating the inductances of permanent magnet brushless machines having non-overlapping windings with 2 coils being present in the same slot, as illustrated in Figure C.4. For simplicity, however, the following assumptions are made:

- The slots are rectangular, and have the dimensions shown in Figure C.4.
- The stator teeth and back-iron are infinitely permeable.
- Slot leakage flux passes straight across the slot openings.

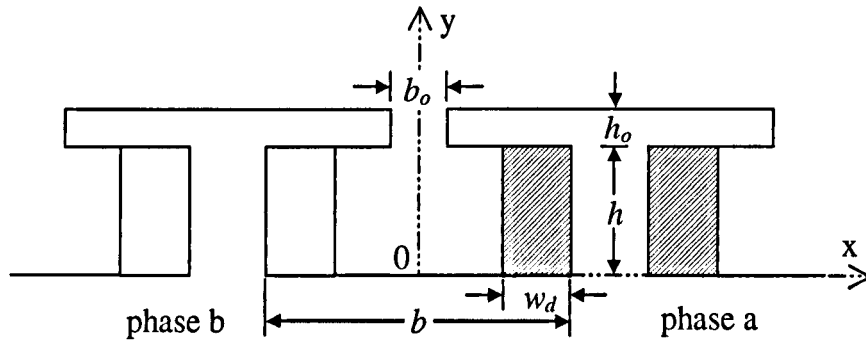


Figure C.4 - Simple slot structure neglecting curvature

The self-inductance can be derived analytically from the total energy, viz:

$$W = \frac{1}{2} L_{sa} I_a^2 \quad (C.31)$$

The total energy can be subdivided into 2 component parts, viz.  $W_I$  and  $W_{II}$ , where  $W_I$  is associated with the current carrying region  $v$  and  $W_{II}$  is associated with the boundary regions. Therefore,

$$W_I = \frac{1}{2} \int_v (A_a \cdot \delta_a) dv = \frac{l_{eff} \delta_a}{2} \int_{y=0}^h \int_{x=\frac{b}{2}-w_d}^{\frac{b}{2}} A dx dy \quad (C.32)$$

$$W_{II} = -\frac{1}{2} \oint_s (H_a \times A_a) ds = -\frac{l_{eff} I_a}{2b_0} \int_{\frac{b_0}{2}}^{\frac{b_0}{2}} A \Big|_{y=h} dx \quad (C.33)$$

where  $A_a$  and  $H_a$  are the vector potential and the magnetic field strength due to phase  $a$  winding current source,  $a_a$ , respectively:

By simple substitution the self-inductance ( $L_{sa}$ ) can be calculated as follows:

$$L_{sa} = 2\mu_0 l_{eff} \frac{n_t^2}{p} \lambda_{sa} \quad (C.34)$$

where  $l_{eff}$ ,  $n_t$  and  $p$  are defined, respectively, as the effective axial length, the number of series turns per phase and the number of pole pairs.  $\lambda_{sa}$  is the permeance coefficient, and is defined as:

$$\lambda_{sa} = \frac{h}{3b} + \frac{2}{w_d^2 hb} \sum_{n=1,2,3} \frac{1}{\left(\frac{n\pi}{b}\right)^4} \left(\sin \frac{n\pi d}{b}\right)^2 - \frac{8}{w_d hb_0 b} \sum_{n=2,4,6,\dots} \left(\frac{b}{n\pi}\right)^4 \cos \frac{n\pi}{2} \sin \frac{n\pi w_d}{b} \sin \frac{n\pi b_0}{2b} \\ + \frac{8}{b_0^2 b} \sum_{n=2,4,6,\dots} \left(\frac{b}{n\pi}\right)^3 \left(\frac{1+e^{-\frac{2nxh}{b}}}{1-e^{-\frac{2nxh}{b}}}\right) \left(\sin \frac{n\pi b_0}{2b}\right)^2 \quad (\text{C.35})$$

The mutual inductance is also be calculated from the energy relationship, but due to symmetry of the slot only half of the mutual energy is considered. Therefore,

$$W = 1/2 MI_a I_b \quad (\text{C.36})$$

The energy  $W$  consists of components  $W_I$  &  $W_{II}$  as previously, where

$$W_I = \frac{1}{2} \int_v (A_a \cdot \delta_b) dv = \frac{l_{eff} \delta_b}{2} \int_{y=0}^h \int_{x=-\frac{b}{2}}^{\frac{b}{2}+w_d} A dx dy \quad (\text{C.37a})$$

$$W_{II} = -\frac{1}{2} \oint_s (H_b \times A_a) ds = -\frac{l_{eff} I_b}{2b_0} \int_{\frac{b_0}{2}}^{\frac{b_0}{2}} A \Big|_{y=h} dx \quad (\text{C.37b})$$

where  $H_b$  is the magnetic field strength due to the phase b winding current source,  $\delta_b$ . The mutual inductance is then obtained from :

$$M_{sab} = -2\mu_0 l_{eff} \frac{n_t^2}{p} \lambda_{sab} \quad (\text{C.38})$$

where the permeance coefficient is given by :

$$\lambda_{sab} = \frac{1}{2} \left[ \frac{h}{3b} + \frac{2}{w_d^2 hb} \sum_{n=1,2,3} \frac{(-1)^n}{\left(\frac{n\pi}{b}\right)^4} \left(\sin \frac{n\pi w_d}{b}\right)^2 - \frac{8}{w_d hb_0 b} \sum_{n=2,4,6,\dots} \left(\frac{b}{n\pi}\right)^4 \cos \frac{n\pi}{2} \sin \frac{n\pi w_d}{b} \sin \frac{n\pi b_0}{2b} \right. \\ \left. + \frac{8}{b_0^2 b} \sum_{n=2,4,6,\dots} \left(\frac{b}{n\pi}\right)^3 \left(\frac{1+e^{-\frac{2nxh}{b}}}{1-e^{-\frac{2nxh}{b}}}\right) \left(\sin \frac{n\pi b_0}{2b}\right)^2 \right] \quad (\text{C.39})$$

However, when  $w_d=0.5b$ , i.e. the winding occupies the entire slot area, then the slot permeance coefficients become:

$$\lambda_{sa} = \frac{h_0}{b_0} + \frac{h}{3b} + \frac{b}{12h} + \sum_{n=2,4,6,\dots} \frac{2}{n\pi} \left(\frac{1+e^{-\frac{2nxh}{b}}}{1-e^{-\frac{2nxh}{b}}}\right) \left(\frac{\sin \frac{n\pi b_0}{2b}}{\frac{n\pi b_0}{2b}}\right)^2 \quad (\text{C.40})$$

&

$$\lambda_{sab} = \frac{1}{2} \left[ \frac{h_0}{b_0} + \frac{h}{3b} - \frac{b}{12h} + \sum_{n=2,4,6,\dots} \frac{2}{n\pi} \left( \frac{1+e^{-\frac{2nxh}{b}}}{1-e^{-\frac{2nxh}{b}}} \right) \left( \frac{\sin \frac{n\pi b_0}{2b}}{\frac{n\pi b_0}{2b}} \right)^2 \right] \quad (\text{C.41})$$

## B. Airgap inductance

The 'effective' airgap component of inductance is given by

$$L_\delta = 2\mu_0 l_{\text{eff}} \frac{n_t^2}{pq} \lambda_{L\delta} \quad (\text{C.42})$$

$$\& M_\delta = 2\mu_0 l_{\text{eff}} \frac{n_t^2}{pq} \lambda_{M\delta} \quad (\text{C.43})$$

where:

$$q = \frac{Q_s}{2pm} \quad (\text{C.44})$$

$$\lambda_{L\delta} = \frac{2}{\pi^2} \frac{q\tau}{g'} \sum_n \left( \frac{K_{dpn} K_{son}}{n/p} \right)^2 F_n(R_s) \quad (\text{C.45})$$

$$\lambda_{M\delta} = \frac{2}{\pi^2} \frac{q\tau}{g'} \sum_n \left( \frac{K_{dpn} K_{son}}{n/p} \right)^2 F_n(R_s) \cos \frac{n}{p} \frac{2\pi}{3} \quad (\text{C.46})$$

$$F_n(R_s) = g' \frac{n}{R_s} \frac{1 + \left( \frac{R_r}{R_s} \right)^{2n}}{1 - \left( \frac{R_r}{R_s} \right)^{2n}} \quad (\text{C.47})$$

The effective airgap length is given by  $g' = K_c K_s \left( g + \frac{h_m}{\mu_r} \right)$  where  $K_s$  is the magnetic saturation factor, the winding factor  $K_{dpn}$  is  $K_{dn} K_{pn}$  where  $K_{pn} = \sin n \frac{\alpha_y}{2}$  &

$$K_{dn} = \frac{\sin q \frac{n\pi}{Q_s}}{q \frac{n\pi}{Q_s}}, \text{ respectively, and } \alpha_y \text{ \& } K_{son} \text{ are the winding pitch or coil span and slot}$$

opening factor respectively.

## C. End winding inductance

The equations for end-winding inductance are described in Chapter 2, section 2.5.1.

### Copper loss

Slotless permanent magnet brushless machines generally have a relatively low airgap field due to the large effective airgap length. Therefore, they tend to have a higher electric loading and a lower magnetic loading than slotted machines. At low speeds, the predominant loss component is the copper loss, which can be expressed as

$$P_{cu} = m_{ph} I^2 R_{phase} \quad (C.48)$$

where,  $m_{ph}$ ,  $R_{phase}$ ,  $I$  are the phase number, the phase resistance and the phase current respectively.

In slotted motors, the majority of the airgap flux passes down the stator teeth, and flux leakage, which crosses the slots and winding conductors, is generally negligible. As a result, the parasitic eddy current loss is negligible and the dominant copper loss is the resistance loss.

### Iron loss

The stator iron loss tends to be dominant at high-speed, and whilst slotless motors tend to have a large mechanical airgap and consequently a lower flux density in the stator back-iron than for slotted motors. Once the airgap flux density waveform is known the total iron loss,  $P_i$ , calculated as the sum of a hysteresis loss component,  $P_h$ , and an eddy current or dynamic loss component,  $P_d$ , can be calculated [Ata90] i.e.

$$P_i = P_h + P_d \quad (C.49)$$

The hysteresis loss is caused by localised irreversible changes during the magnetisation process, which make it dependent only on the maximum flux density. When the flux waveform does not cause minor recoil loops, it can be expressed as:

$$P_h = k_h \cdot f \cdot B_m^\alpha \quad (C.50)$$

where  $f$  and  $B_m$  are the frequency and amplitude of the flux density, respectively, and  $k_h$  and  $\alpha$  are constants determined experimentally from either an Epstein ring test or a single-sheet test for the particular grade of lamination material. However, if the flux waveform causes minor loops, an empirical correction must be applied, viz.:

$$P_h = k_h \cdot f \cdot B_m^\alpha \cdot K(B_m) \quad (C.51)$$

where  $K(B_m) = 1 + \frac{0.65}{B_m} \sum \Delta B_i$ , and  $\Delta B_i$  is the change in flux density during the excursion around a minor loop.

The eddy current loss density can be expressed as:

$$P_d = P_c + P_{exc} \quad (C.52)$$

where  $P_c$  is the classical loss density, predicted on the assumption of a homogeneous lamination, and is given by:

$$P_c = \frac{\sigma d^2}{12\delta} \cdot \frac{1}{T} \int_T \left( \frac{dB(t)}{dt} \right)^2 dt \quad (C.53)$$

where,

$\sigma$  is the electrical conductivity of the lamination material,

$d$  is the thickness of the lamination, and

$\delta$  is the mass density of the lamination material.

For a sinusoidal time-varying flux density waveform, C.53 becomes:

$$P_c = \frac{\sigma d^2 \pi^2}{6\delta} f^2 B_m^2 \quad (C.54)$$

The excess loss  $P_{exc}$ , which is generated as a result of domain wall movements, and may exceed the classical eddy current loss, can be written as:

$$P_{exc} = \frac{k_e}{T} \int_T \left| \frac{dB(t)}{dt} \right|^{1.5} dt \quad (C.55)$$

For a sinusoidal time-varying flux density waveform, C.55 becomes

$$P_{exc} = 8.67 k_e f^{1.5} B_m^{1.5} \quad (C.56)$$

where,  $k_e$  is again determined experimentally for an Epstein ring or single sheet test.

The CAD software uses these equations and assuming the iron loss is constant in separate sections of the stator can make an estimate of the total loss. A diagram showing the various stator sections in which the iron loss was calculated is shown in Figure C.5, where the curvature of the motor is neglected for reasons of simplicity. In the area in which rotational flux exists, marked on the diagram, then these areas are counted in both the radial calculation of the tooth loss density and the tangential calculation of the back-iron and tooth tip loss density.

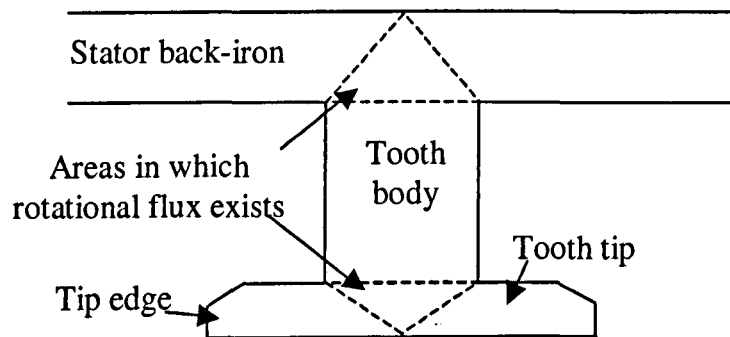


**Figure C.5 - Constituent sections in the stator iron loss calculation**

The iron loss calculation is validated by finite element analyses in chapter 3 where the rotational nature of the flux in the above sections of the stator core is clearly evident.

## Appendix D Data Acquisition

In order to accurately capture the motor performance parameters and ensure sufficient data is available to measure the motor torque using the run-down method a suitable data capture and logging system was required. For the data acquisition itself a suitable Data Acquisition card (or DAQ card) was selected. The PCI-MIO-16E1 is capable of capturing data at 1.25 Ms/s with appropriate software and depending on the computer specifications. This was used in conjunction with a SCXI 1120 for the actual scaling of the data prior to sampling by the DAQ card. This unit also provides isolation, which is required to protect against the high voltages that could be present should a fault occur. Labview 5.01 was selected as the software to control the card being made by the same company as the DAQ card and consequently providing the least trouble in connecting and compatibility.

Whilst the card was capable of sampling at 1.25Ms/s, if multiple channel capture is required then the actual sample rate is much lower as will be discussed later. However, despite this limitation it was still possible to capture the required data.

During a test the following data is required :

- Motor speed (measured using a hall sensor)
- DC link voltage
- DC link current
- Phase voltage & current waveforms to show the diode conduction angle
- A time reference for the run-down tests

However, as the phase current and voltage waveforms could not be adequately captured using the DAQ card they were captured using a Digital oscilloscope. The data logging method is discussed in some detail in the next section.

### Labview Data logging

A simplified schematic of the system is shown below in Figure D.1. The signal wires monitor the DC link voltage, the DC link current (via a current transducer), one of the motor phase currents (also via a current transducer), one motor phase voltage and the signal from one of the hall sensors. During motor operation these signal wires are sampled at a rate of 50,000 samples per second per channel for 10,000 samples. This is repeated every half second.

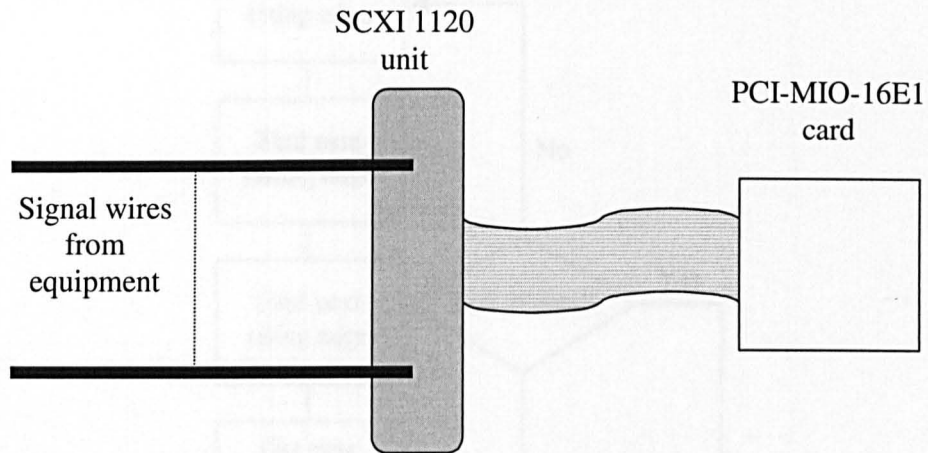


**Figure D.1 - Simplified schematic of data acquisition system**

Once the PCI-MIO-16E card has captured the data the following operations are then performed and written to a data file along with a time reference signal:

- The DC link current and DC link voltage are multiplied together and the mean taken for the DC input power.
- Using the hall sensor signal, the motor speed is calculated using the method shown below in Figure D.2. At each stage a check is performed to see if the sampled data is reached, but this check is not shown here for reasons of clarity.

Once steady state has been reached, then the phase current and voltage waveform are captured and the data acquisition switches to just monitoring the motor speed. This is monitored at intervals of  $1/10^{\text{th}}$  of a second to try and capture as much information as possible from the rundown test.

The Labview model used to acquire and process the data is shown in Figure D.3, whilst the speed measurement routine is expanded out in Figure D.4.

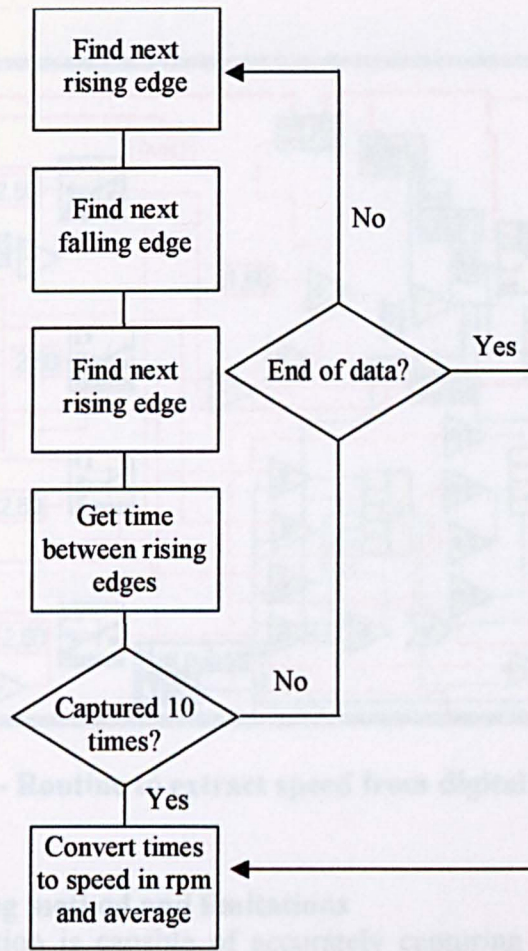


Figure D.2 - Flow diagram for speed measurement from hall sensor signal

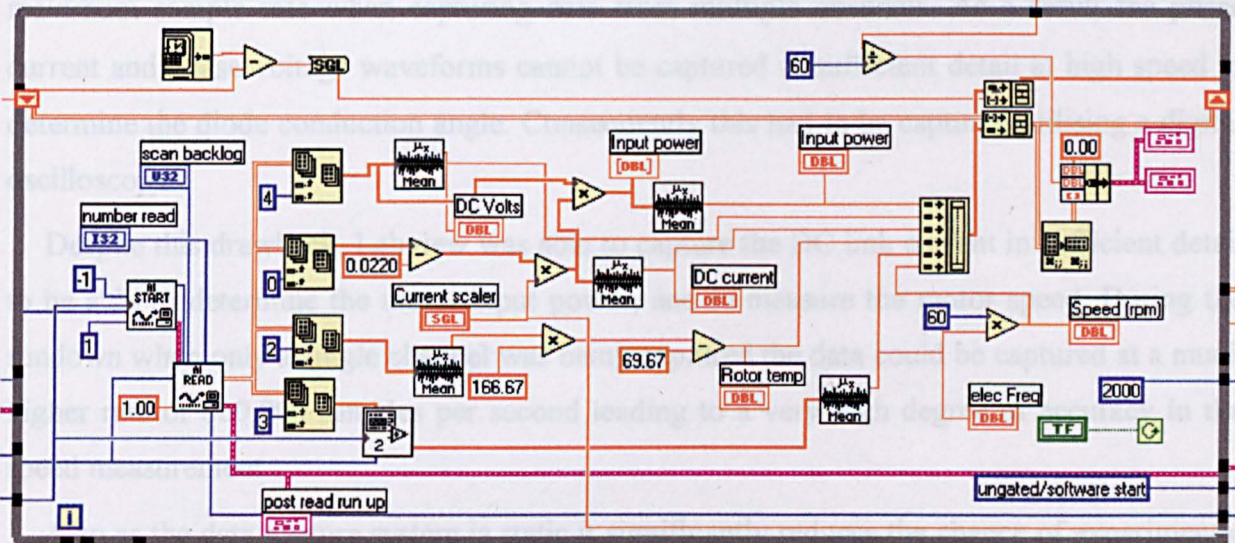


Figure D.3 - Main data logging routine

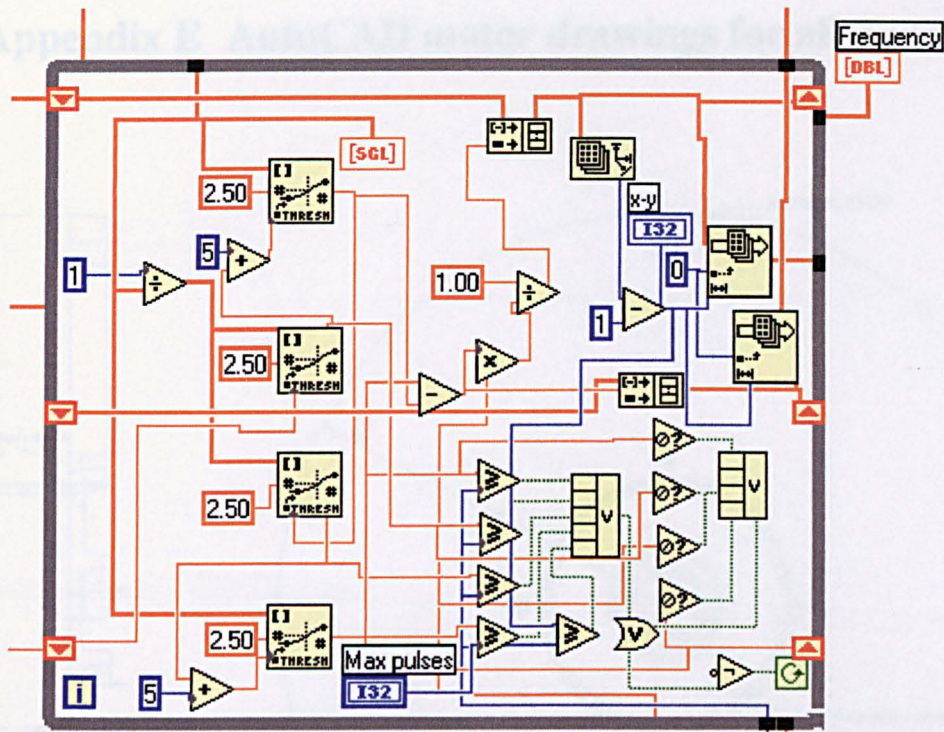


Figure D.4 - Routine to extract speed from digital waveform

#### Advantages of data logging method and limitations

Whilst the data acquisition is capable of accurately capturing the speed signal and the waveforms at a relatively low sample rate, once the sample rate is moved above 50,000 samples per second then aliasing was observed. This was caused by the bandwidth of the switch that changes between channels on the SCXI interface. This effectively limits the maximum sample rate when capturing data from multiple channels. As a result the phase current and phase voltage waveforms cannot be captured in sufficient detail at high speed to determine the diode conduction angle. Consequently this had to be captured utilising a digital oscilloscope.

Despite this drawback, Labview was able to capture the DC link current in sufficient detail to be able to determine the motor input power, and to measure the motor speed. During the rundown when only a single channel was being captured the data could be captured at a much higher rate of 800,000 samples per second leading to a very high degree of accuracy in the speed measurement.

Also as the data capture system is static it significantly reduces the chance of experimental error on data recording, and accurate measurement of the rundown speed would have been impossible using any other method.

## Appendix E AutoCAD motor drawings for all motors

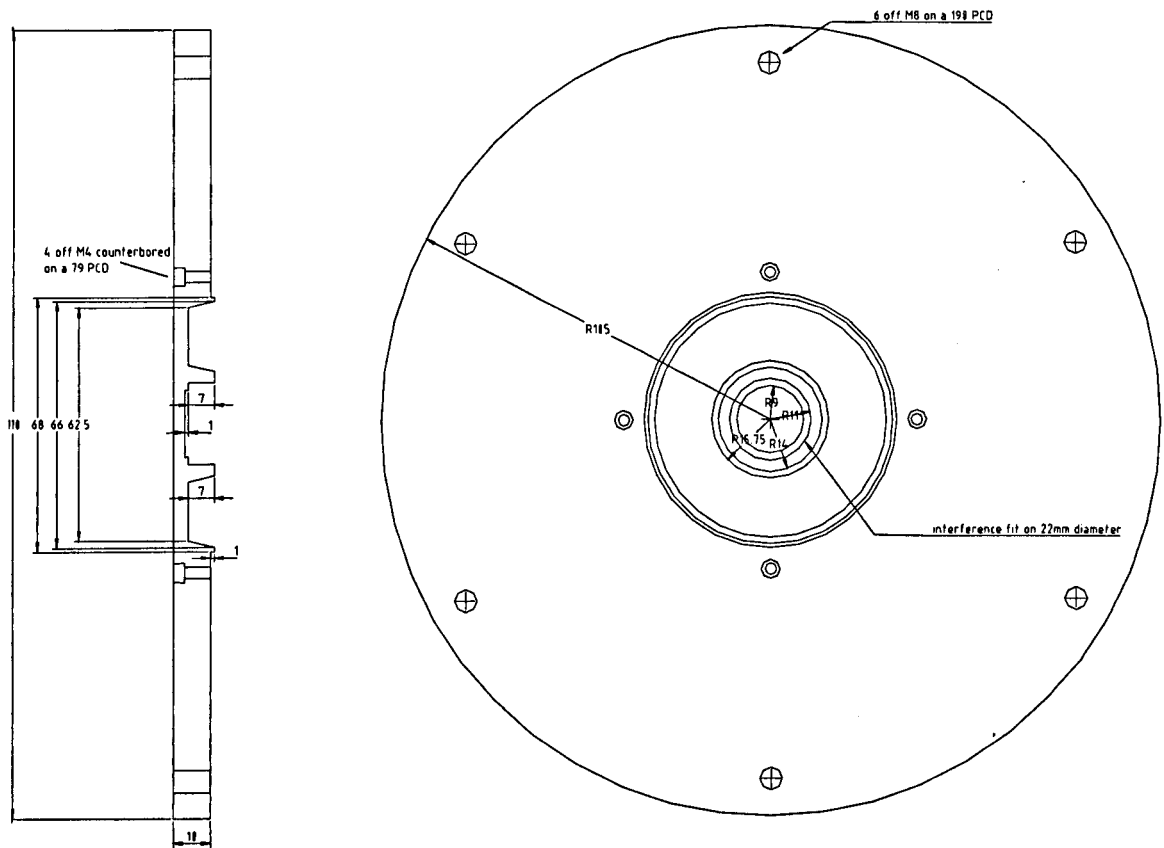


Figure E.1 – Base plate for 100mNm motors

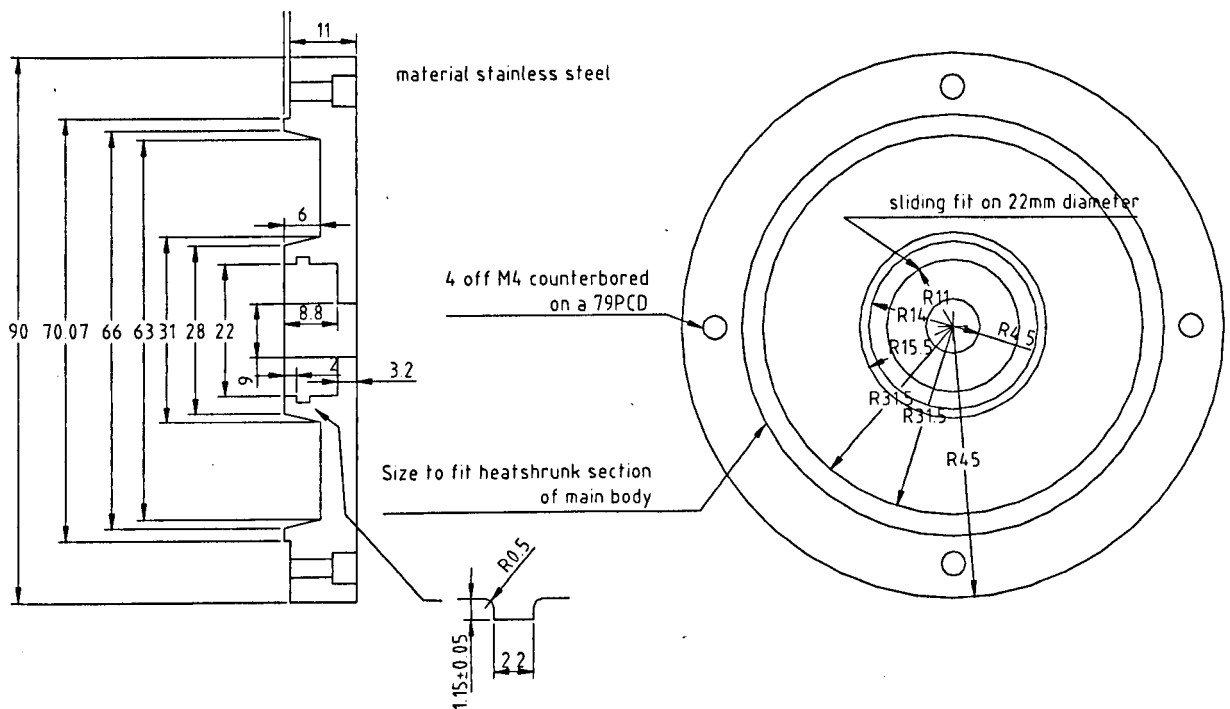
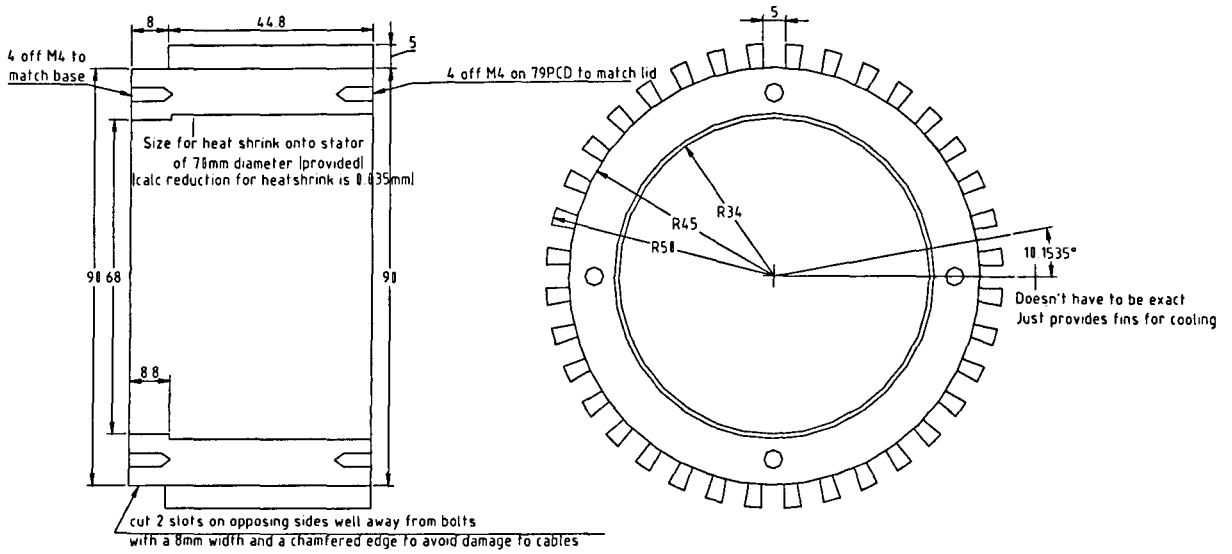
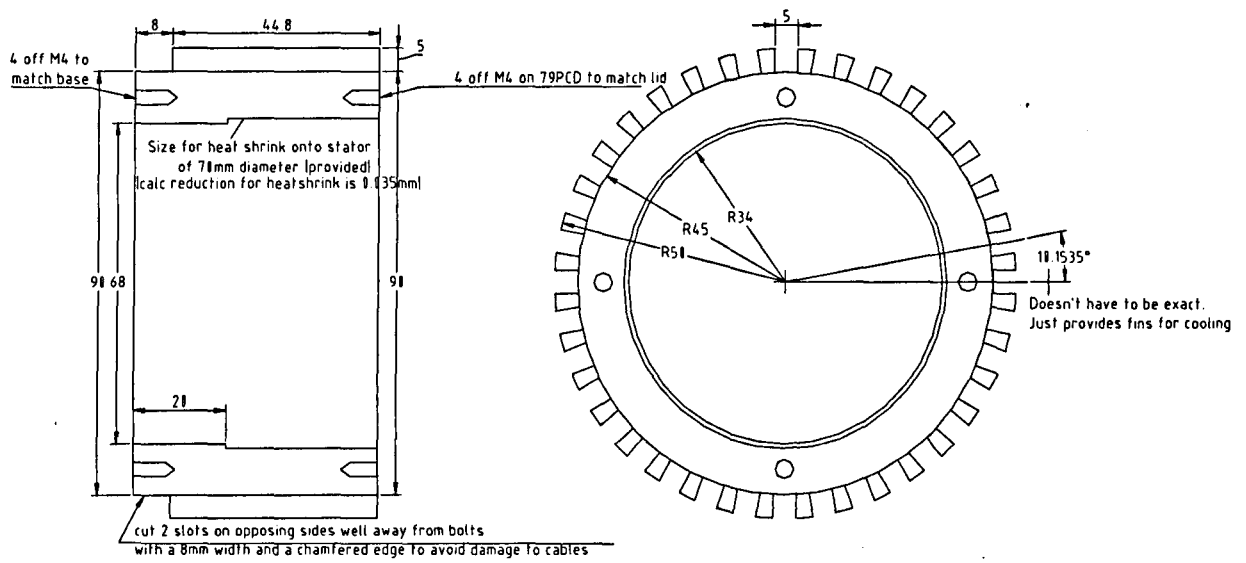


Figure E.2 – Lid plate for 100mNm motors



**Figure E.3 – Frame body for motor A<sub>1</sub>**



**Figure E.4 – Frame body for motor B<sub>1</sub>**

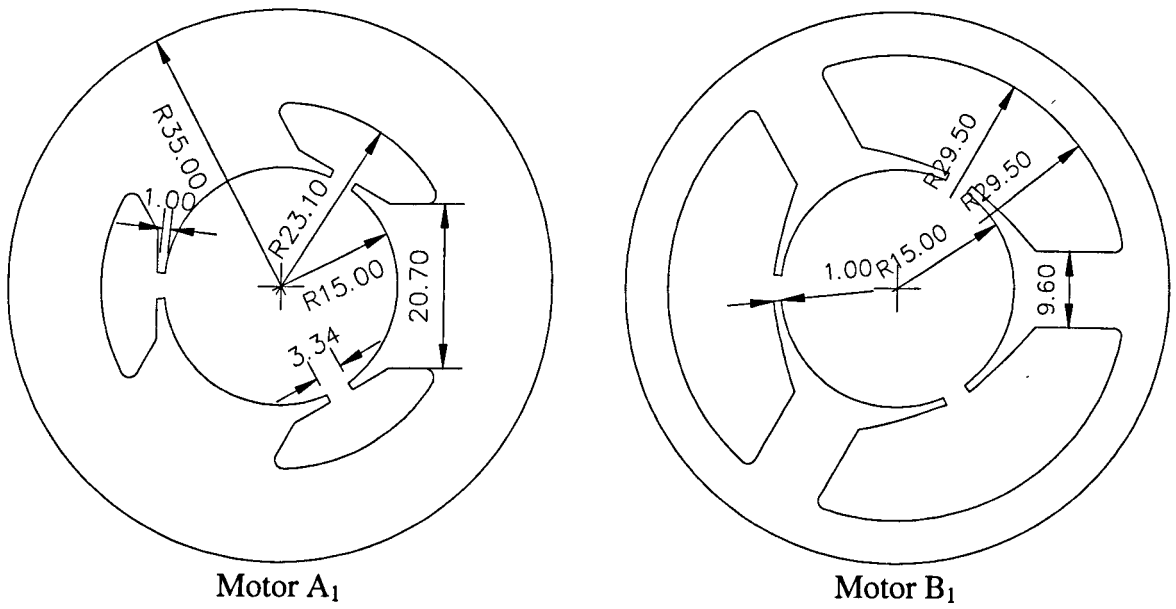


**Figure E.5 – 100mNm laminations**

Non magnetic steel

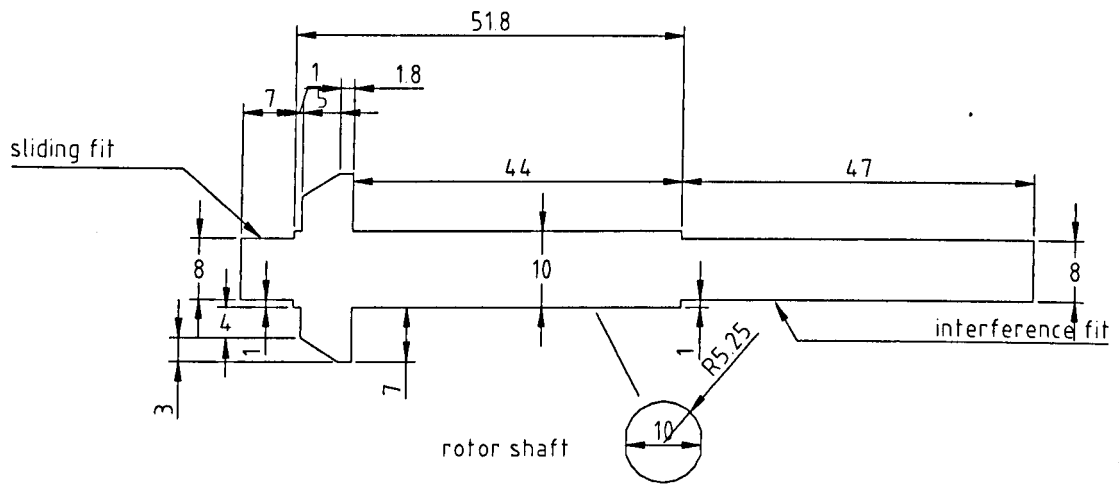


**Figure E.6 - Rotor schematic for motor A<sub>1</sub>**

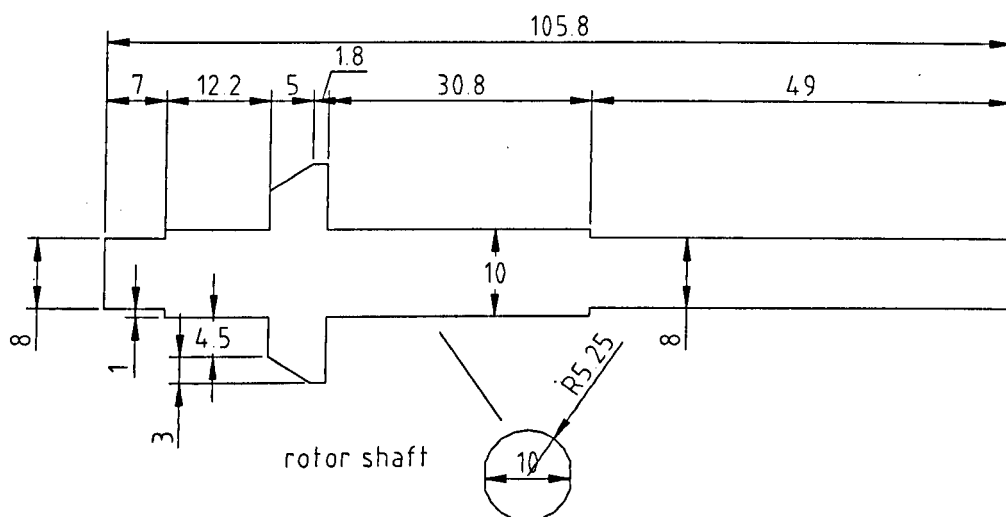


**Figure E.7 – Rotor schematic for motor B<sub>1</sub>**

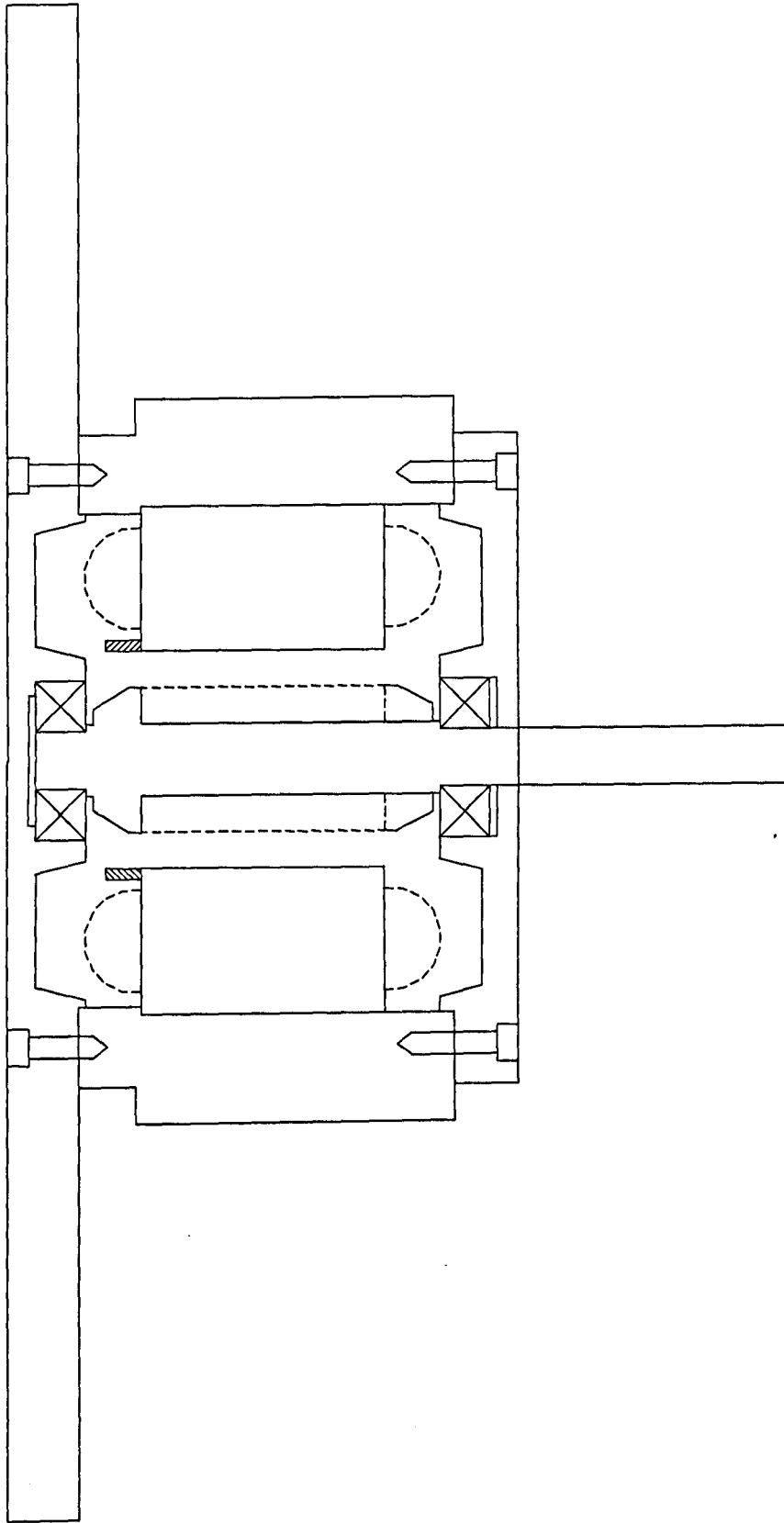


**Figure E.8 – Sample completed assembly for 100mNm motors**

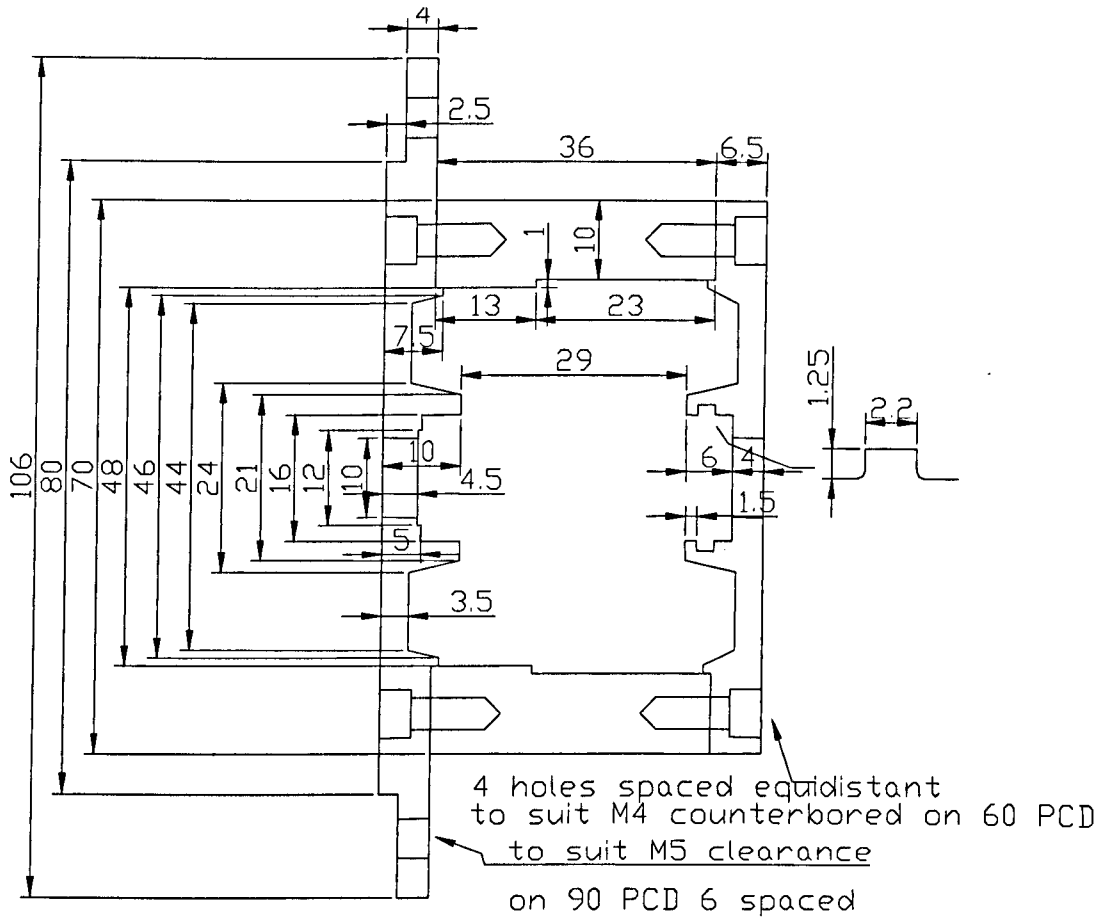


**Figure E.9 - Frame for motor A<sub>2</sub>**

material stainless steel

mirror endcap to make sliding endcap

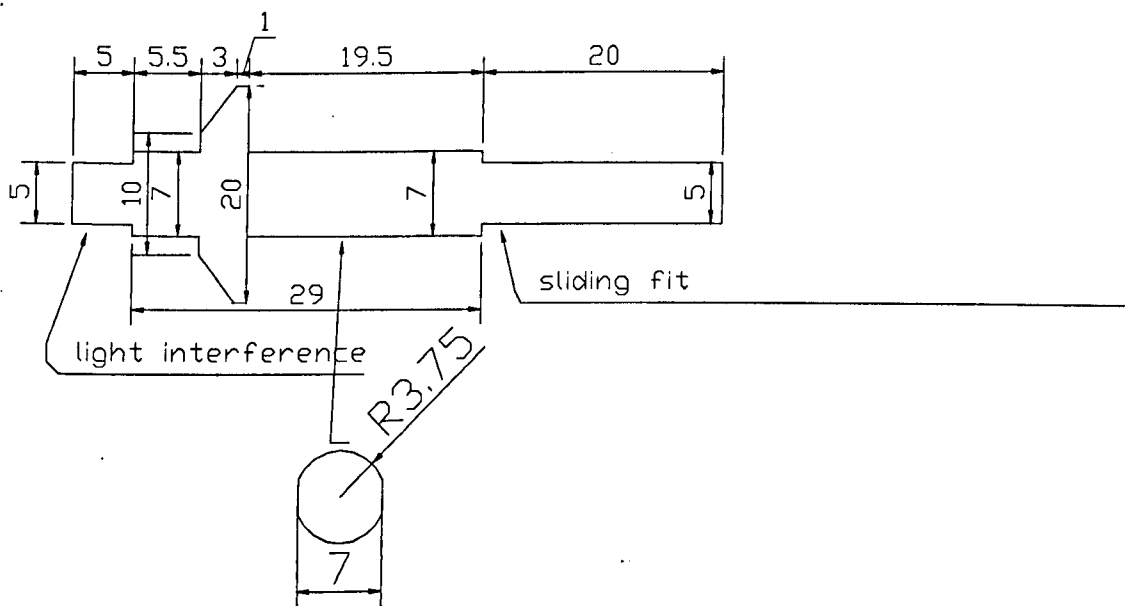


**Figure E.10 - Rotor for motor B<sub>2</sub>**

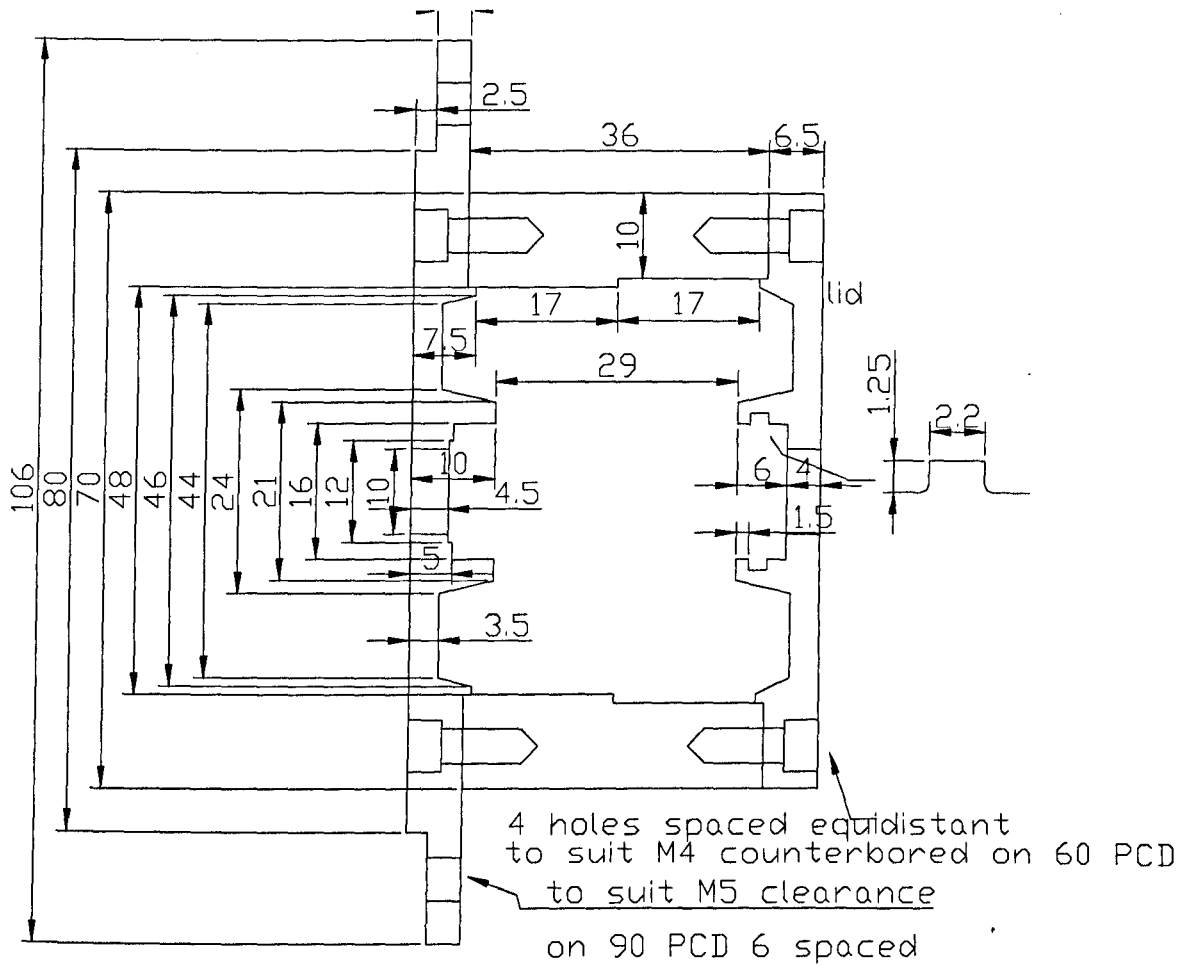


**Figure E.11 – Frame for motor B<sub>2</sub>**

material stainless steel

mirror endcap to make sliding endcap

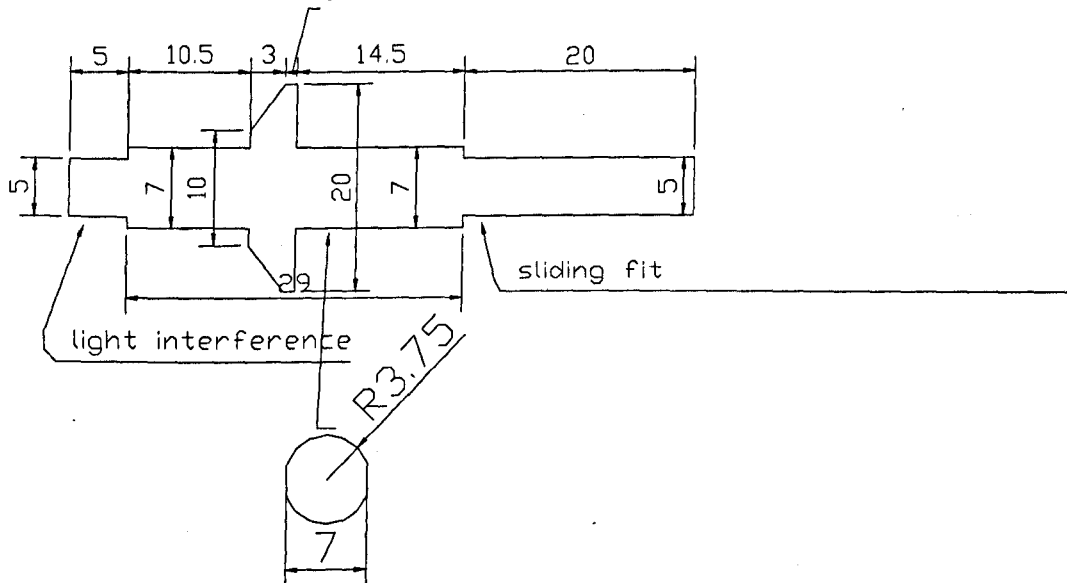


**Figure E.12 – Rotor for motor B<sub>2</sub>**

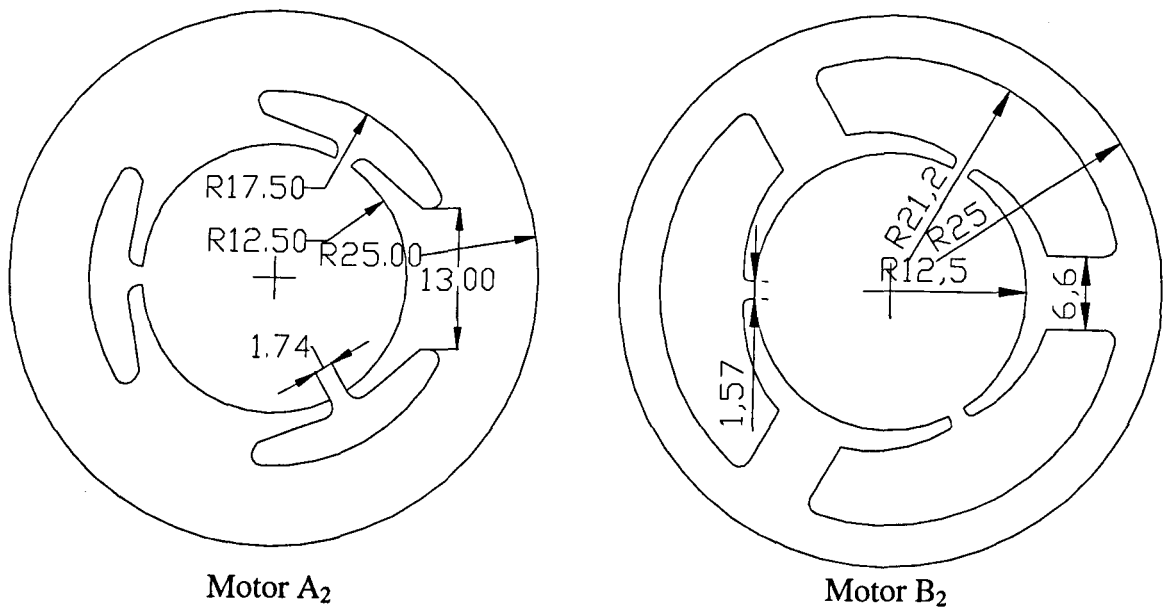


**Figure E.13 – 15mNm laminations**

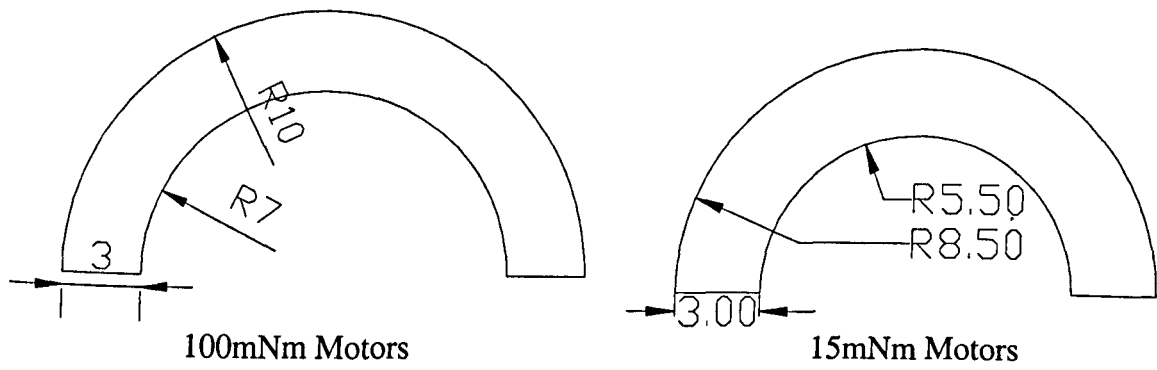


**Figure E.14 – Magnet arcs**

**Table E.1 – Motor materials**

Magnets	Ugimax 34B1 ( $B_r=1.22T$ $\mu_r=1.05$ )
Laminations	Transil 335
Rotor shaft	Stainless steel
Frame base and body	Aluminium
Frame lid	Stainless steel

## **Appendix F Further experimental investigations to determine load torque on 100mNm motors (A<sub>1</sub> & B<sub>1</sub>)**

### **(a) “Run-down” test for torque measurement accounting for stator iron loss**

The ‘run-down’ test, described and validated previously in Chapter 2, is again used to deduce the torque when running at high speed, since coupling a dynamometer to the rotor shaft would present several problems, not least in the coupling. All the couplings found so far have been for relatively low speeds and as the speed increases then the cost of the couplings seems to increase dramatically.

Previously, the ‘run-down’ test assumed that the stator iron loss was negligible. However, the iron loss is now significant, and indeed dominates the motor loss. The no-load iron loss can, however, be deduced using finite element analysis, and can be accounted for by subtracting it from the output power of the motor during the ‘run-down’ test. This assumption can safely be made as during the ‘run-down’ of the motor the windings do not carry any current and consequently the iron loss is the no-load iron loss.

During ‘no-load’ operation, the drive has to overcome the friction torque of the bearings and the windage loss, the iron loss and the copper loss, whilst the friction and windage torque is the torque being measured, since it is the load, which was imposed on the motor. The iron loss appears as an additional torque component during operation, and once the drive was disconnected it manifests itself as a braking torque on the motor. Consequently, the output torque at a particular speed can be calculated by subtracting the calculated iron loss at that speed from the output power measured from the ‘run-down’ test, since the copper loss can be ignored on run-down, as the windings are open-circuited.

### **(b) ‘Run-down’ test results for 100mNm motor with low diode conduction angle**

The motor was tested using the rundown test described previously. Measurements were taken for increments of ~20V in the DC link voltage. The speed, input current and power were recorded by the data logging software, and the torque was deduced from the ‘run-down’ method. The test results are given in Table F.1 whilst the phase current waveform, when running near the rated speed, is shown in Figure F.1.

**Table F.1 - Test results for motor with low diode conduction angle**

DC Link voltage (V)	Speed (rpm)	DC Link current (A)	Input power (W)	Calculated torque (mNm)	Iron loss (W)	Torque due to iron loss (mNm)	Corrected torque (mNm)	Output power (W)	Efficiency (%)
20.3	12876	0.253	5.12	3.74	1.0	0.73	3.01	4.1	79.4
40.1	26217	0.253	10.14	3.46	2.9	1.04	2.42	6.6	65.5
60.3	39600	0.317	19.13	4.8	5.5	1.32	3.48	14.4	75.5
80	52595	0.442	35.44	6.39	8.6	1.56	4.83	26.6	75.0
100	66116	0.468	46.84	7.76	12.5	1.81	5.95	41.2	88.0
120	79354	0.625	75.35	8.8	16.9	2.04	6.76	56.2	74.6
140	92402	0.826	116.1	11.78	21.9	2.26	9.52	92.1	79.4
160	105473	0.943	151.5	13.4	27.3	2.47	10.93	120.7	79.7
180	119343	0.964	174	13.9	33.7	2.70	11.20	140.0	80.5
190	126243	1.086	207	15.35	37.1	2.81	12.54	165.8	80.1

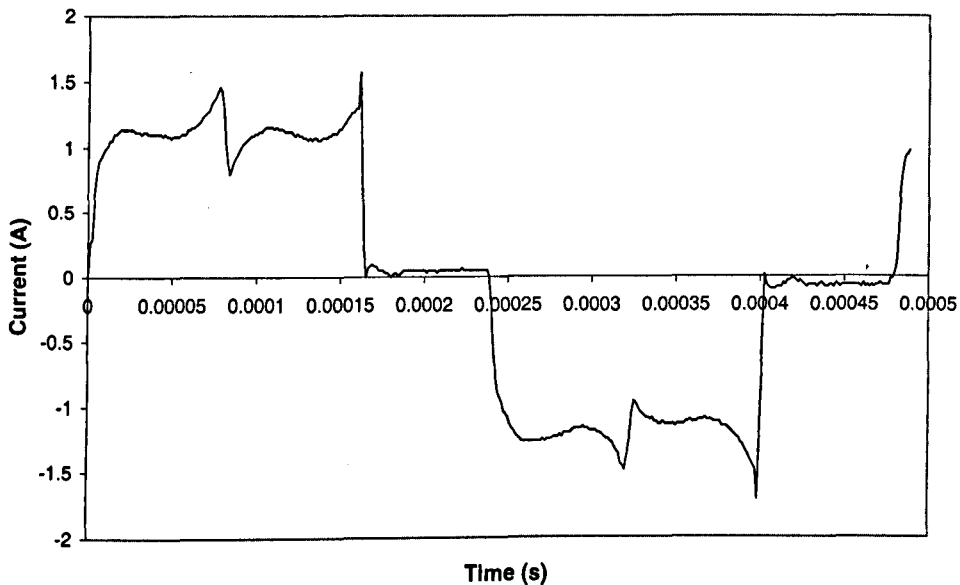


**Figure F.1 - Phase current waveform at ~126krpm**

As can be seen in Table F.1, with a DC link voltage of 100V there is a rather sudden and large increase in efficiency. However, it was suspected that this was associated with a resonance mode, which caused the motor to decelerate quickly from the original speed on the 'run-down' test. An increase in the level of the emitted acoustic noise was also observed at this voltage, which would also suggest a resonant mode, which is investigated in detail in Chapter 5.

It is appreciated that the torque on the motor is very small, and that the measurement accuracy could affect the results. Also, as this is effectively the bearing torque, then small changes such as the pre-load on the bearings and the fit of the bearings on the shaft, will affect the applied torque. Such variations, due to tolerances in component manufacture, are

impossible to predict and control. Consequently, some differences are expected between the two motors.

From the calculated torques shown in Table F.1, it can be seen that they are significantly less than the design torque of 100mNm. Thus, the phase current is significantly lower than the rated current, and the copper loss, therefore, is comparatively small. The iron loss, however, being speed dependent remains relatively high, which accounts for the comparatively low efficiency. A higher load torque would result in a higher efficiency, as the iron loss would not be so dominant.

**(c) Rundown test results for 100mNm motor with high diode conduction angle**

The test results are shown in Table F.2, and a typical phase current waveform is shown in Figure F.2.

**Table F.2 – Test results for motor with high diode conduction angle (B<sub>1</sub>)**

DC Link voltage (V)	Speed (rpm)	DC Link current (A)	Input power (W)	Calculated torque (mNm)	Iron loss (W)	Torque due to iron loss (mNm)	Corrected torque (mNm)	Output power (W)	Efficiency (%)
20	16870	0.293	5.86	3.15	1.66	0.94	2.21	3.9	66.6
40	34640	0.379	15.16	4.16	4.91	1.35	2.81	10.2	67.2
60	52060	0.475	28.5	5.21	9.36	1.72	3.49	19.0	66.8
80	69290	0.616	49.28	6.84	14.95	2.06	4.78	34.7	70.4
100	86210	0.749	74.9	8.46	21.52	2.38	6.08	54.9	73.2
120	102829	0.923	110.76	9.94	29.09	2.70	7.24	77.9	70.4
140	118546	1.15	161	11.3	37.01	2.98	8.32	103.3	64.1
160	133191	1.5	240	13.6	45.36	3.25	10.35	144.3	60.1

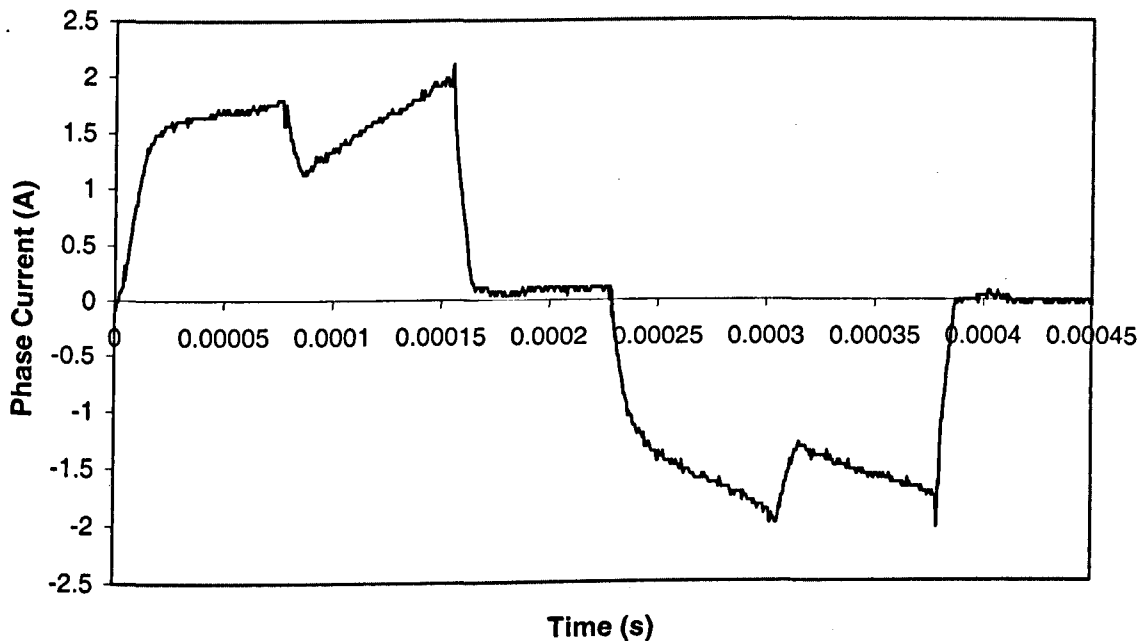


**Figure F.2 - Phase current waveform at ~133krpm**

From Table F.2, it can be seen that the developed torque is lower than for the other 100mNm motor. As discussed previously, this is probably due to tolerances in manufacture. Due to the low torque the diode conduction angle is correspondingly lower than was predicted at the motor design stage.

### Comparison of run-down test results for 100mNm motors

Figures F.3 – F.8 compare the performance characteristics of the two motors so that some differences become apparent.

In Figure F.3 it can be seen that motor B<sub>1</sub>, with the higher diode conduction angle, operates at a significantly higher speed for the same DC link voltage. However, as seen in Figure F.4 the phase current is generally higher than that for motor A<sub>1</sub> for the same speed, even though the input power is similar, as seen in Figure F.5. Despite having a higher DC link current, the torque is generally lower for motor B<sub>1</sub>, as can be seen in Figure F.6. This results in a higher output power and consequently a higher efficiency for motor A<sub>1</sub>.

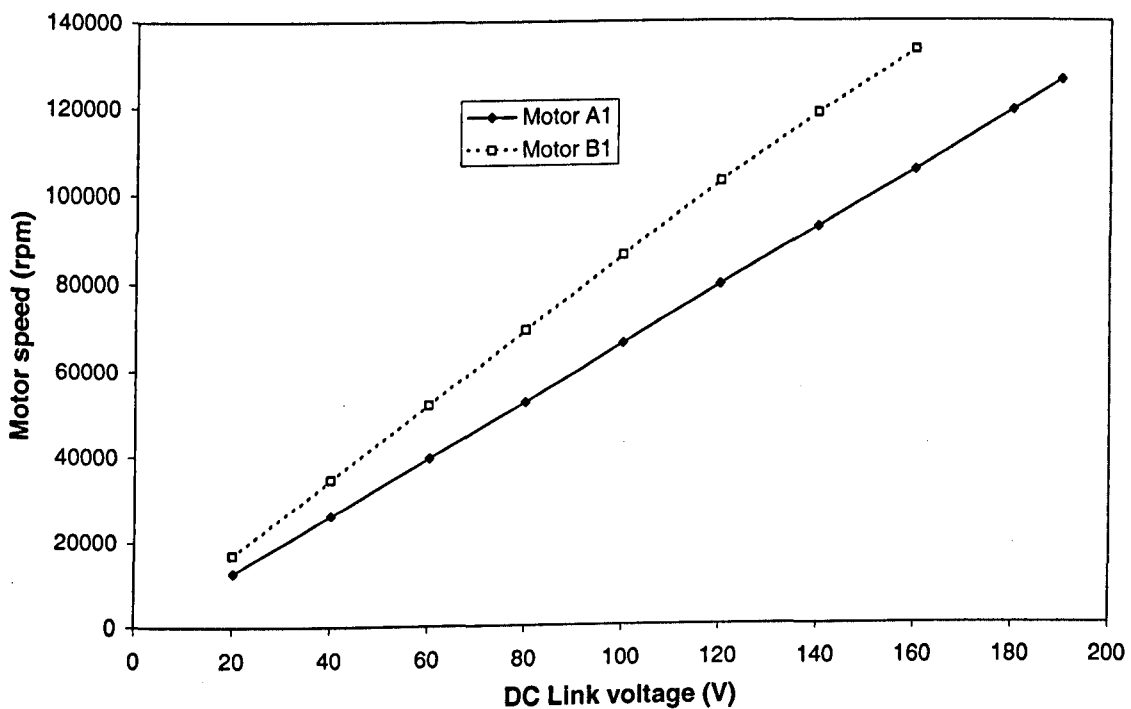


Figure F.3 - Comparison of speed against DC link voltage

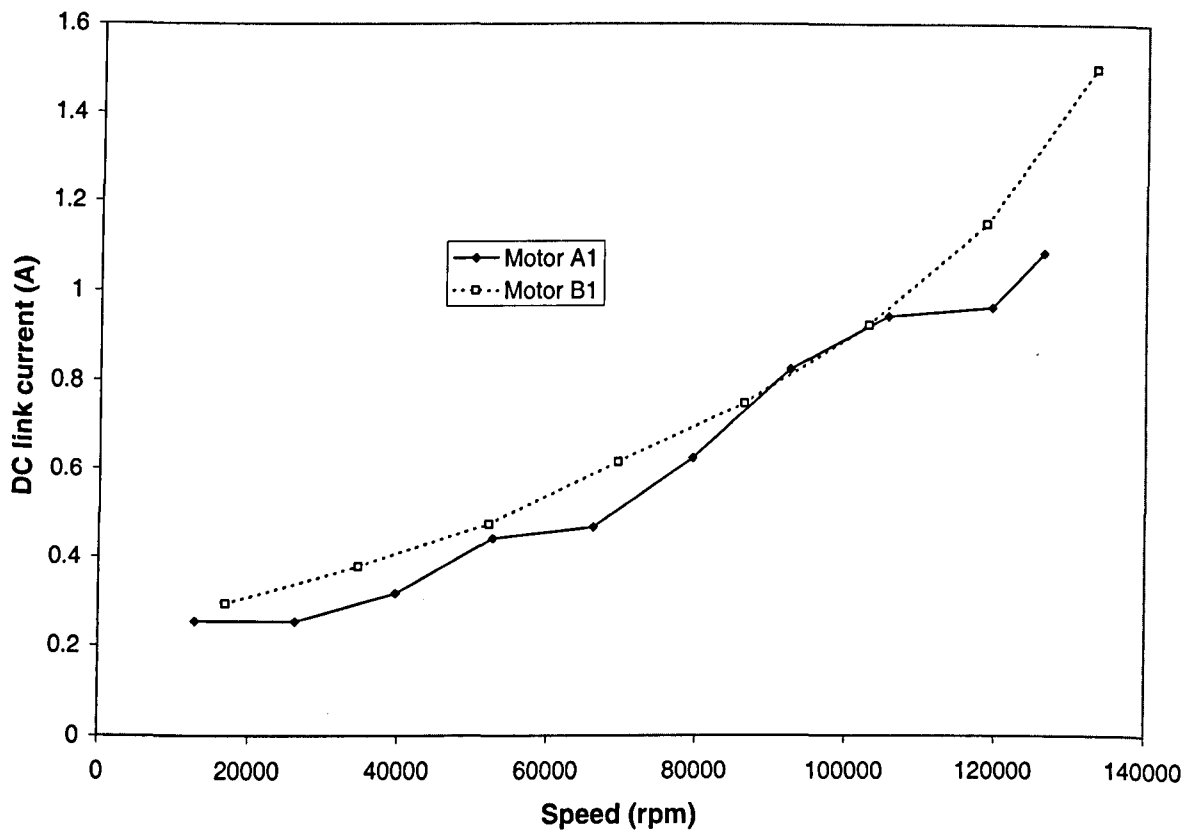


Figure F.4 - Comparison of DC link current against speed.

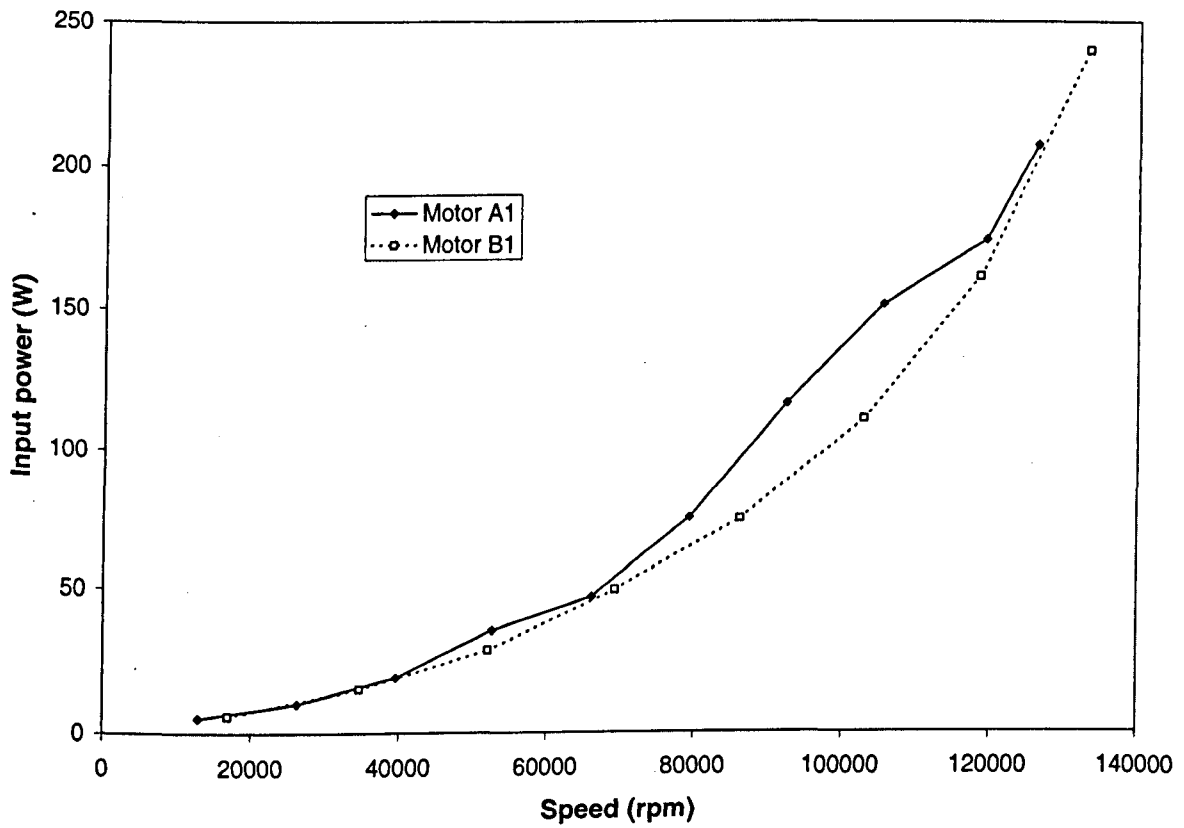


Figure F.5 - Comparison of Input power against speed

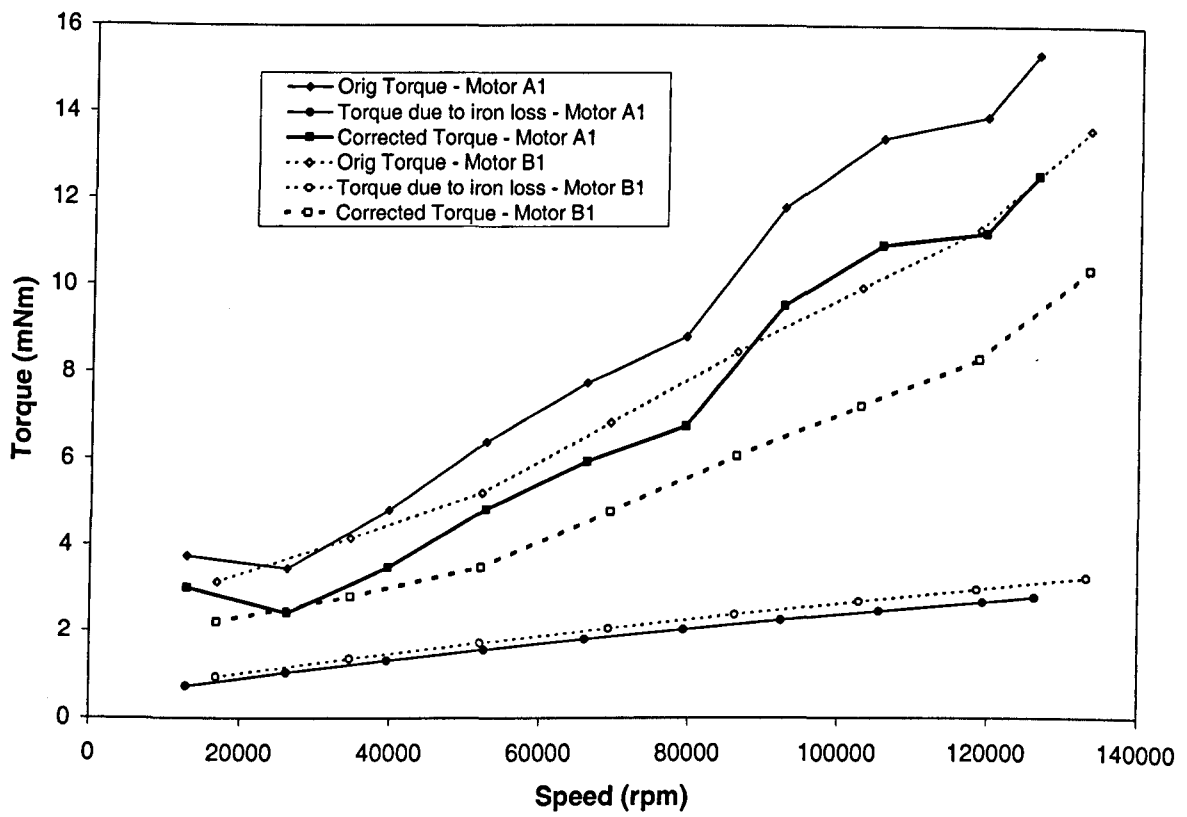


Figure F.6 - Comparison of torque against speed

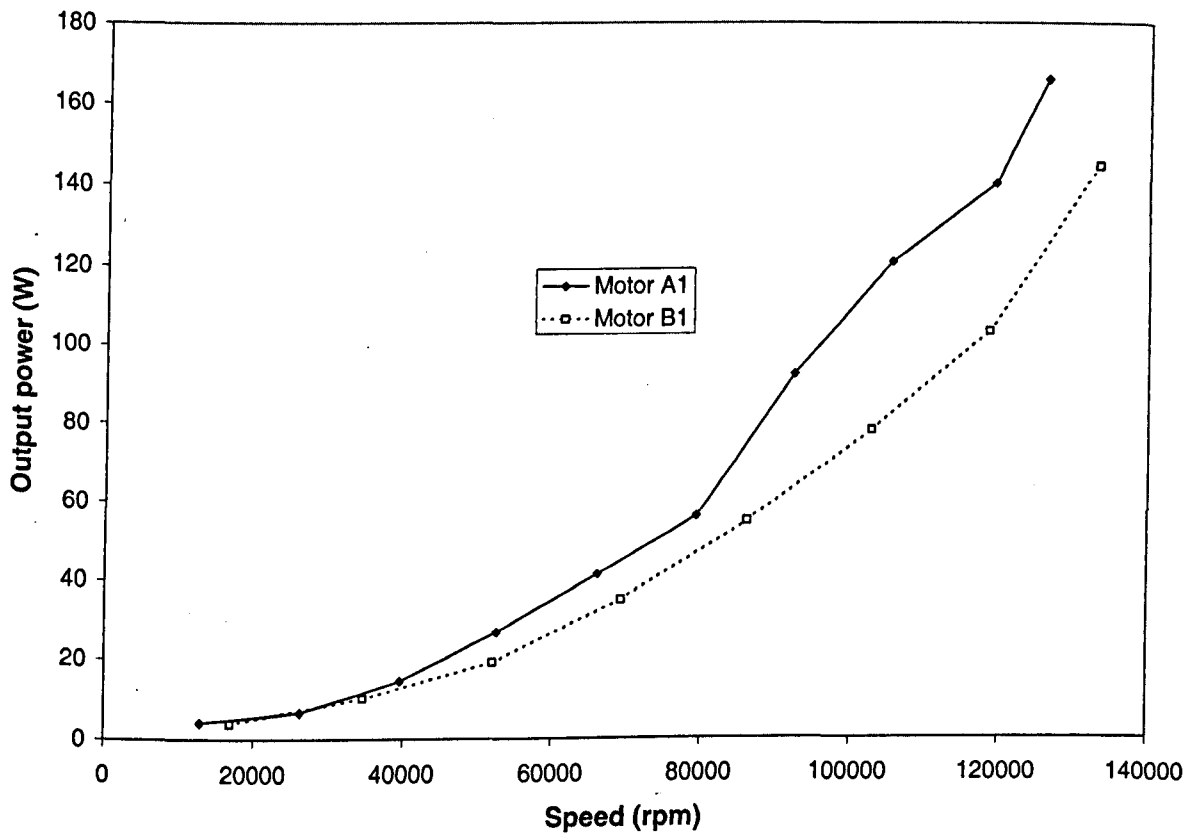
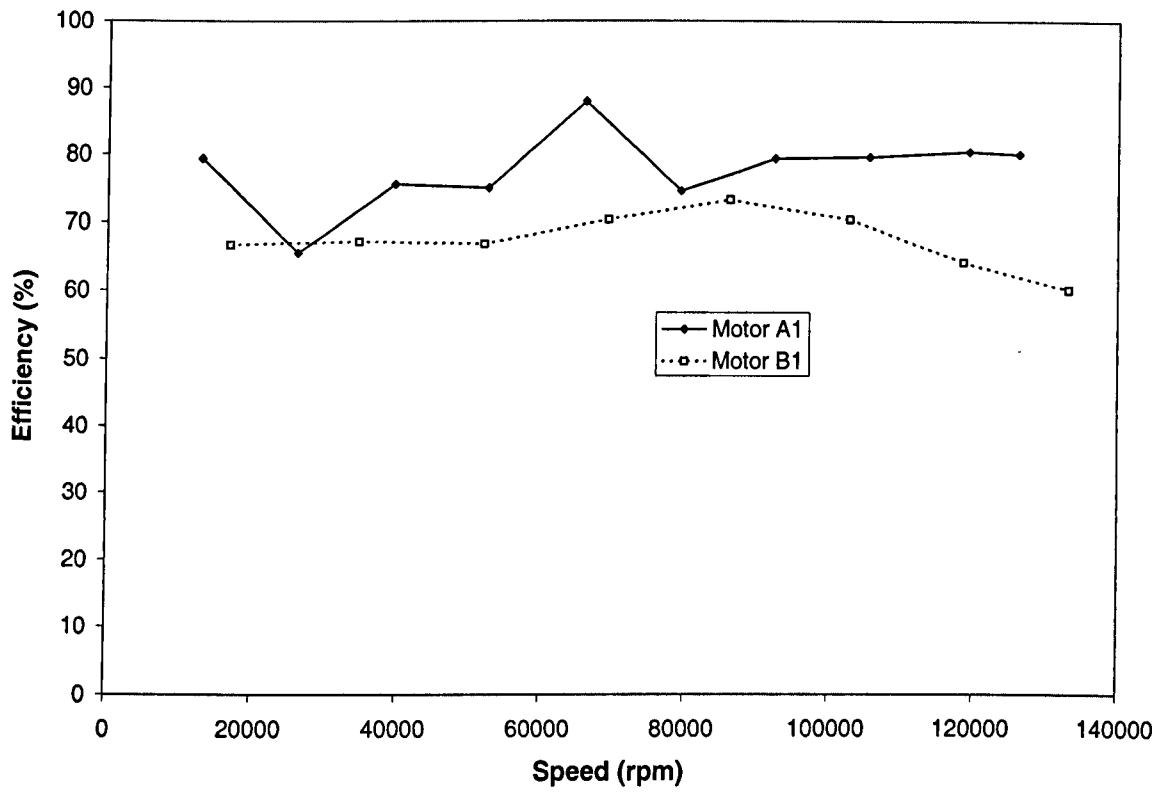


Figure F.7 - Comparison of output power against speed



**Figure F.8 - Comparison of efficiency against speed**

As mentioned previously in this appendix, generally the efficiency of the motors is much lower than predicted. This is due to the low torque, and it is predicted that as the torque is increased the efficiency will increase to the predicted efficiency of ~90%.

## Appendix G Winding design methodology

During the course of the investigation it was observed that the variation of the copper loss with the split ratio as predicted by the CAD software had a 'jagged' nature when the number of turns was low, and the developed torque also departed from the specified torque. This is investigated as follows.

### (a) Calculation of winding area and mean length turn

The magnetic circuit determines the tooth width ( $w_t$ ) and the radial thickness of the stator back-iron ( $d_b$ ), which, in turn, determine the slot geometry, as shown in Figure G.1.

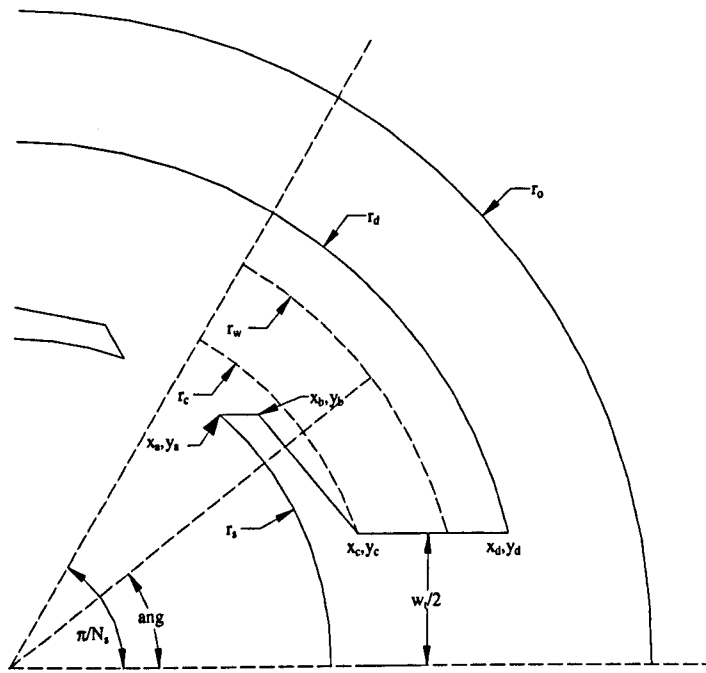


Figure G.1 - Calculation of winding dimensions

Initially the area available for the winding needs to be calculated, and certain dimensions need to be calculated, viz.:

$$x_a = r_s \cos\left(\alpha \frac{\pi}{Q_s}\right) \quad y_a = y_b = r_s \sin\left(\alpha \frac{\pi}{Q_s}\right)$$

where  $\alpha$  is the tooth tip to slot pitch ratio.

$$d_b = r_o - r_d$$

$$x_b = x_a + \text{tooth tip height (determined by tooth flux density)}$$

The distance between  $x_b$  and  $x_c$  is determined by the wedge angle ( $\gamma$ ), which is governed by the tooth flux density.

$$x_c = x_b + \left( y_b - \frac{w_t}{2} \right) \frac{\cos(\pi - \gamma)}{\sin(\pi - \gamma)} \text{ and } y_c = w_t/2$$

From  $x_c$  and  $y_c$  the radius  $r_c$ , and  $x_d$  can easily be obtained,  $r_w$  is then calculated by:

$$r_w = r_c + \frac{2}{3}(r_d - r_c)$$

It is then assumed that the end-winding forms an arc between the slots on either side of a tooth. Hence, the axial length of the end-winding is the dotted line along  $r_w$  shown in Figure G.1

$$b_w = r_w \sin\left(\frac{\pi}{Q_s}\right) - \frac{w_t}{2}$$

Using  $b_w$ , the overall length of the motor is calculated from the lamination axial length +  $2*b_w$ .

Using the slot geometry calculated previously, the area of the winding enclosed by the lines  $r_d$  and  $r_c$ , the edges of a tooth, and the middle of a slot can be shown to be :

$$a_w = \frac{\pi}{2} \frac{(r_d^2 - r_c^2)}{Q_s} - \left\{ \frac{(x_d - x_c)w_t}{2} + \frac{r_d^2 \theta_d}{2} - \frac{w_t x_d}{4} - \frac{r_c^2 \theta_c}{2} + \frac{w_t x_c}{4} \right\}$$

$$\text{where } \theta_c = a \sin\left(\frac{w_t}{2r_c}\right), \theta_d = a \sin\left(\frac{w_t}{2r_d}\right)$$

The mean turn is then assumed to occur on the dotted line  $r_w$  half way between the edge of the tooth and the middle of the slot. The angle between this point and the middle of the tooth, again using Figure G.1, is:

$$ang = \frac{1}{2} \left( \frac{\pi}{Q_s} - a \sin\left[\frac{w_t}{2r_w}\right] \right) + a \sin\left[\frac{w_t}{2r_w}\right]$$

The mean length per turn is calculated as

$$mlt = 2(l_a + \pi r_w \sin(ang))$$

where  $l_a$  is the lamination axial length

$$\text{The mean resistance per turn, } res_{turn} = 2 \frac{(l_a + \pi r_w \sin(ang))}{\sigma k_p a_w}$$

where  $\sigma$  and  $k_p$  are the conductivity and the slot packing factor, respectively.

### (b) Initial winding design

Using the data calculated in the previous section, it is possible to obtain an initial estimate of the number of turns and the rated motor current. Whilst it is possible to set the number of turns and current to arbitrary values and then deduce the number of turns from an iterative process, it is initially estimated by neglecting the winding inductance.

From the resistance per turn per coil calculated in the previous section, resistance per turn per phase is:

$$res_{phase} = res_{turn} \times \text{Coils per phase}$$

The initial back-emf per coil per turn is estimated from:

$$emf_{turn} = 4B_m w_t l_a p f$$

where  $B_m$  and  $p$  are the tooth (stator) flux density, number of pole-pairs.  $f = \frac{\omega}{2\pi}$  where  $\omega$  is mechanical angular speed.

The emf per turn per phase is given by:

$$emf_{phase} = emf_{turn} \times n_t K_w$$

where  $n_t$  &  $K_w$  are the number of series turns per phase and the winding factor respectively.

If the inductance is ignored, the steady-state voltage equation is simply:

$$V = E + IR$$

The input power of the motor is then

$$VI = EI + I^2 R$$

If  $P = P_o + P_{fe}$  (neglecting friction), where  $P_o$  and  $P_{fe}$  are the output power and iron loss, respectively, then  $P = EI$ , and, hence, the motor current is  $I = \frac{P}{E}$ , on a per phase basis.

However, since 2 phases are conducting at any instant then  $I = \frac{P}{2emf_{phase}}$ .

Thus, an estimate can be made for the number of turns, viz.:

$$N_p = \frac{u}{2(emf_{turn} + r_{turn} I)}$$

where  $u$  is the DC link voltage

The resistance per phase can then be calculated using

$$R = r_{turn} \times N_p^2$$

The induced back-emf and winding inductance can now be calculated from the number of turns.

### (c) Final winding design

Once the initial estimate of the winding design has been made, an iterative approach is used to determine the correct number of turns, using a dynamic simulation [Zhu92], to determine the motor torque, current, diode conduction angle, copper loss and back-emf. The method is summarised below.

The required number of turns is deduced in 3 stages, viz.:

- a) The motor design is simulated and the diode conduction angle is determined. The number of turns per coil is then reduced until the diode conduction angle is below  $60^\circ$  electrical.
- b) The number of turns is then increased or decreased by 10% until almost the required torque is obtained.
- c) Finally, an iterative routine is used to adjust the number of turns by progressively smaller increments until the developed torque matches the specified value.

However, at this point, the number of turns is likely to be a fractional number. For machines having a large number of turns, rounding off the number of turns to the nearest integer will make negligible difference to the performance. However, for machines with a low number of turns rounding can make a large difference to the performance. Hence, when the number of turns is rounded off to the nearest whole number then not only is the phase resistance and inductance recalculated, but a steady-state dynamic simulation is performed to determine the torque, diode conduction angle, current and back-emf voltage. Rounding the number of turns can change the torque significantly from the specified torque, particularly for motors with a small number of turns. This can best be seen by examining the influence of the number of turns on the torque in the graphs shown in Figure G.2. When the number of turns is relatively large the torque is relatively insensitive to the number of turns. However, above a split ratio of  $\sim 0.35$  when the number of turns drops below 20 the torque becomes much more sensitive to the number of turns.

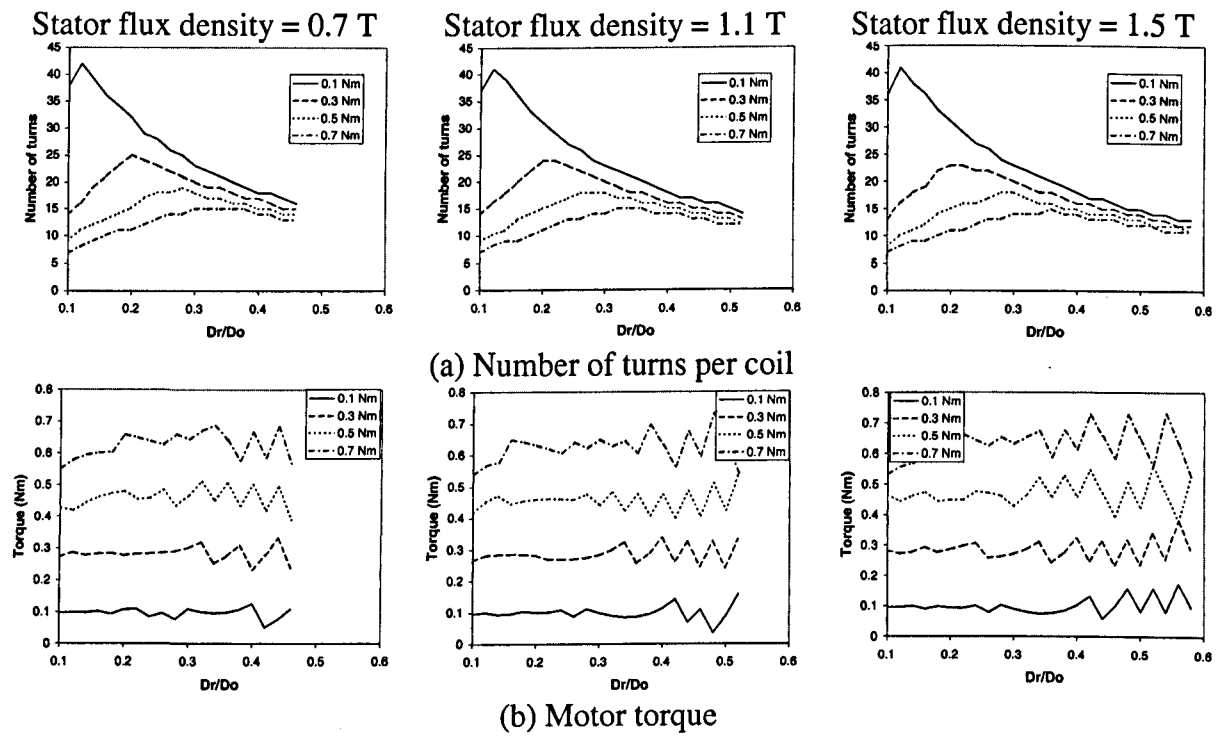


Figure G.2 - Influence of integer number of turns on torque for 2-pole motor

This effect is much more noticeable on a 4-pole motor, Figure G.3, for the same operating conditions as previously due to its higher frequency and lower number of turns per coil than those of the 2-pole motors. It can be seen that the torque variation is much more pronounced particularly at higher split ratios. Figure G.4 compares the motor performance when the number of turns is a “fractional” number and an integer.

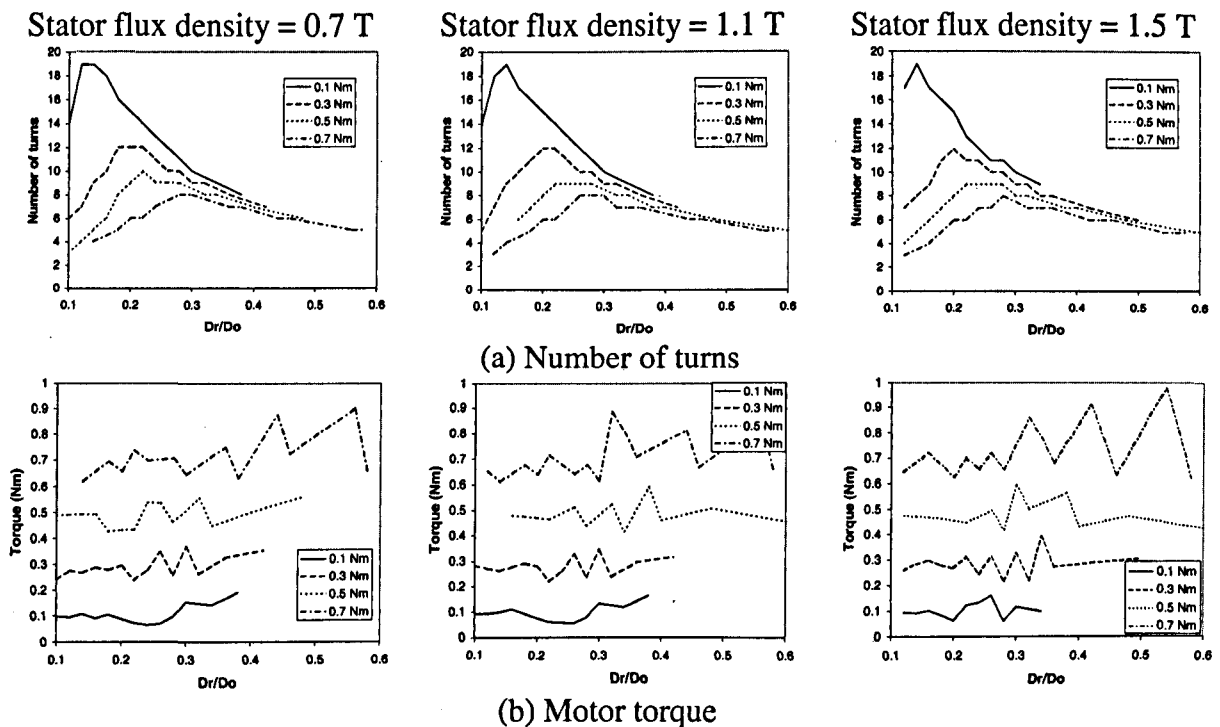


Figure G.3 - Influence of integer number of turns on torque for 4-pole motor

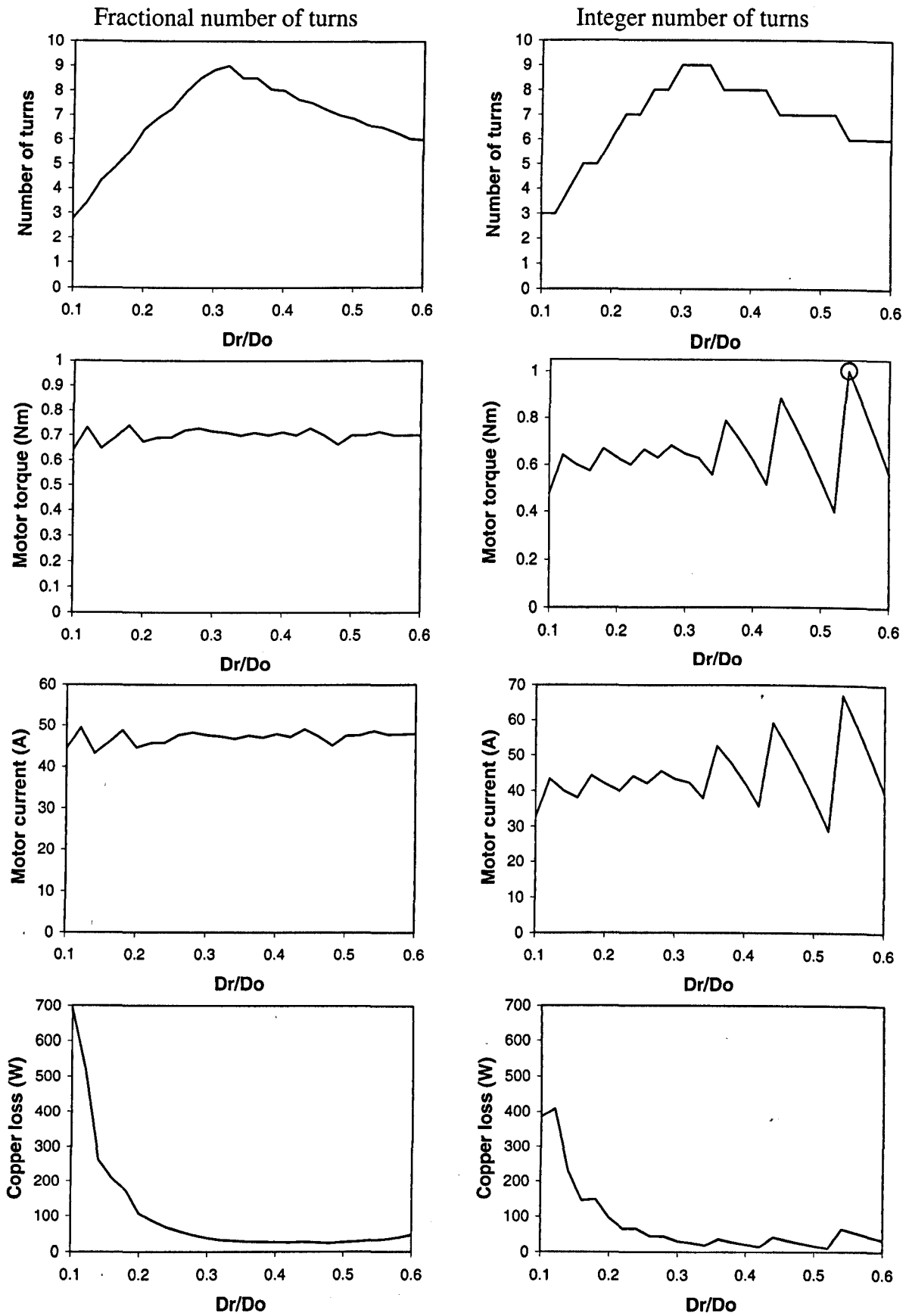


Figure G.4 - Comparison of number of turns, torque, rated current and copper loss

**(d) Improved winding design**

One method of correcting the developed torque is by adjusting the magnetic loading by modifying the airgap length. For the 4-pole motor, highlighted in Figure G.4, if the specified design torque is 0.7Nm and the original airgap length is 3mm then the “ideal” number of turns will be ~6.3 with a current of ~47A and a peak phase emf of 99.8V. However, the actual number of turns can only be chosen as the nearest integer i.e. 6, the corresponding peak phase emf is reduced to 93.6V and the current is increased to 67A, whilst the torque becomes 1Nm which is larger than the rated torque. If the airgap length is reduced slightly to 2.67mm, then the peak back emf is 98.6V and the current is 48A whilst the number of turns becomes exactly 6 and the torque is 0.7Nm.

## Appendix H Validation of finite element analysis on rotor B<sub>1</sub>

After analysing the rotor from motor A<sub>1</sub> the same tests were performed on the shorter rotor from motor B<sub>1</sub> and the results were compared with values obtained from finite element analysis.

### a) Shaft with one end-cap

The dimensions of the rotor are shown in Figure H.1, a schematic of the complete rotor being shown in section 5.2.1. The only significant difference between this rotor and the rotor of motor A<sub>1</sub> is that the axial length of the magnets and laminations is reduced. Therefore it is anticipated that the natural frequencies of this rotor will be similar to those for the longer rotor, although since its active length is shorter and the laminations and magnets are lighter the resonant frequencies will be slightly higher.

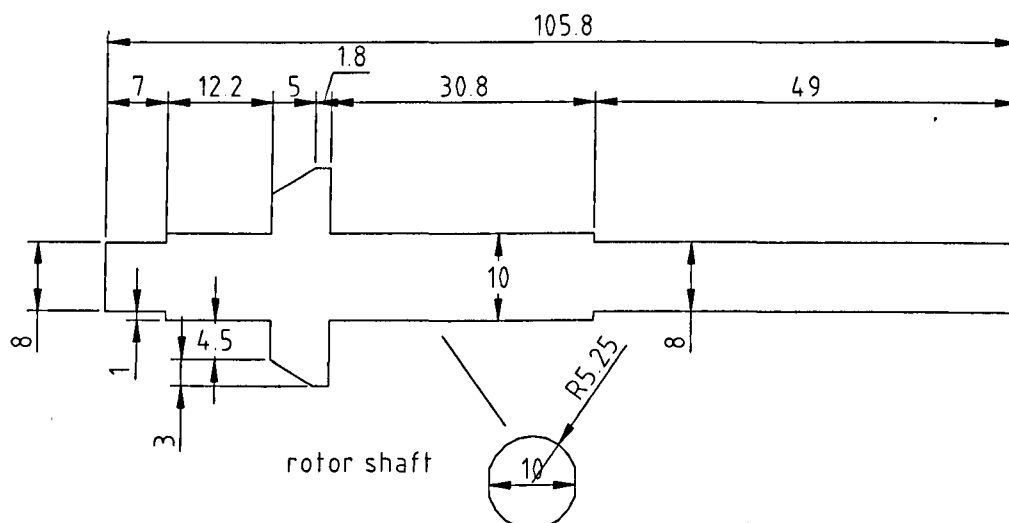


**Figure H.1 - Rotor shaft for short active length**

The measured frequency spectrum is shown in Figure H.3, and the observed resonant frequencies are compared with finite element predicted results in Table H.1, where it can be seen that there is good correlation. The vibrational modes are shown in Figure H.2.

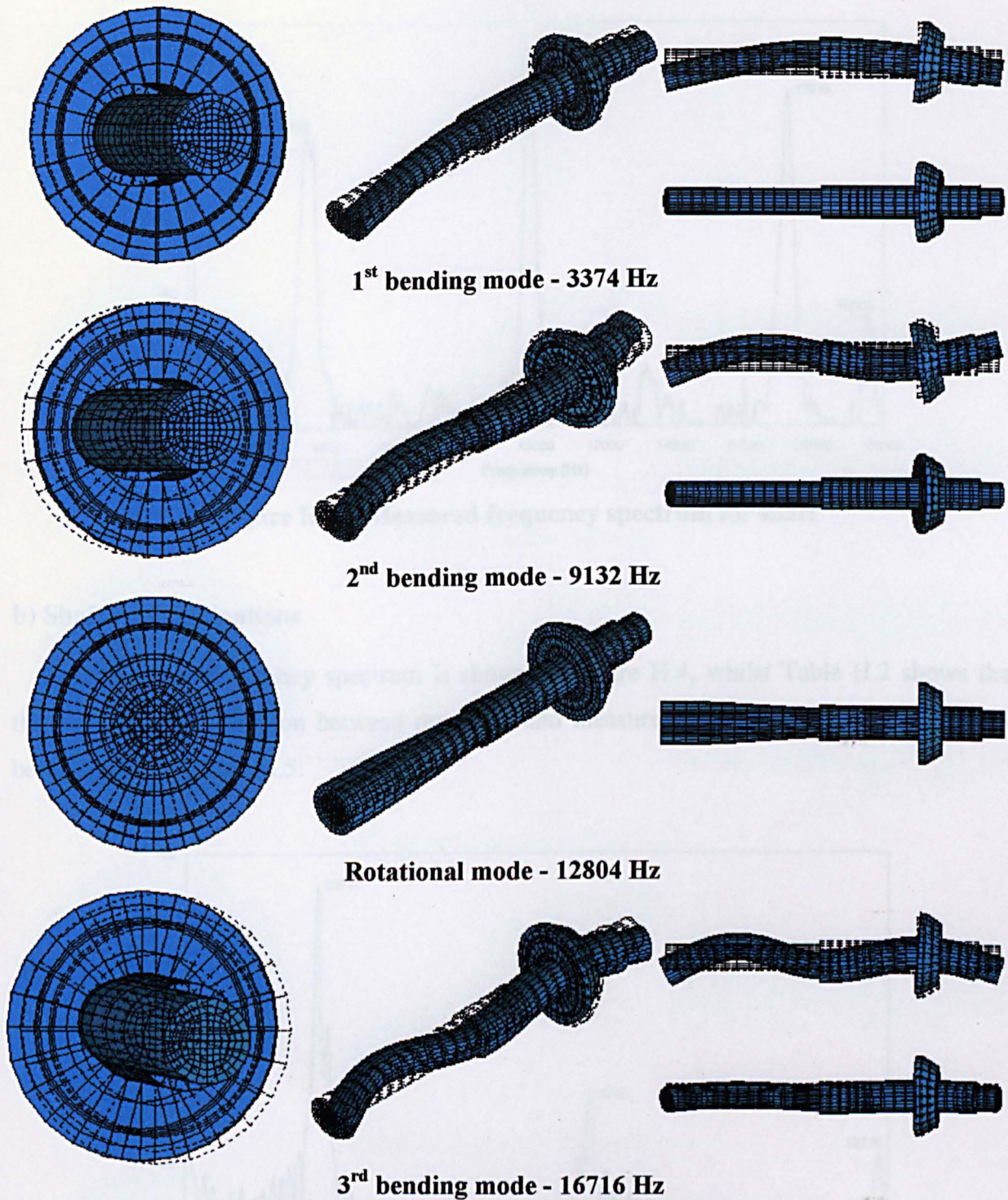
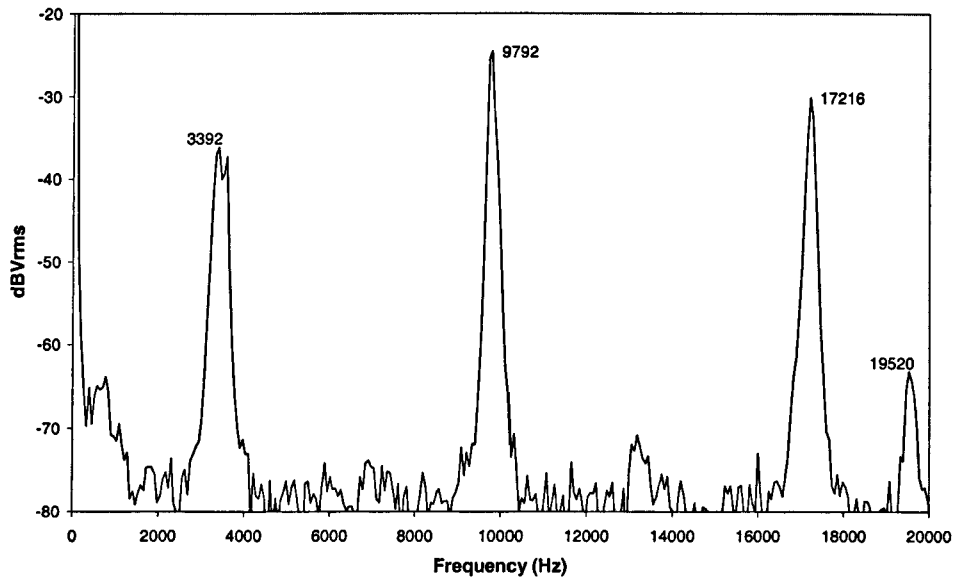


Figure H.2 - Vibrational modes for shaft

Table H.1 - Comparison of predicted and measured natural frequencies

Mode	Finite element (Hz)	Measured (Hz)
1 <sup>st</sup> bending	3374	3392
2 <sup>nd</sup> bending	9132	9792
Rotational	12804	-
3 <sup>rd</sup> bending	16716	17216



**Figure H.3 – Measured frequency spectrum for shaft**

**b) Shaft with laminations**

The measured frequency spectrum is shown in Figure H.4, whilst Table H.2 shows that there is a good correlation between predicted and measured results. The vibrational modes being shown in Figure H.5.

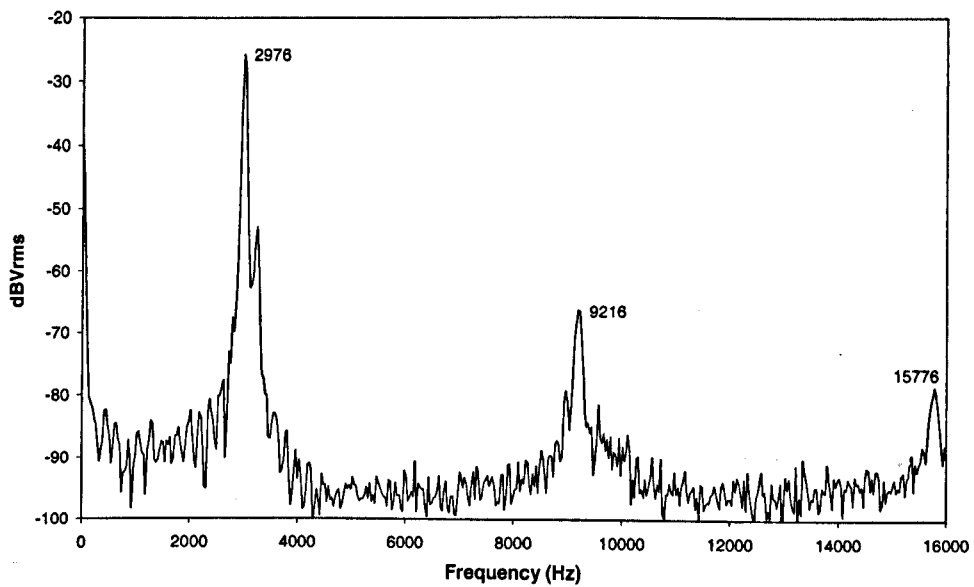
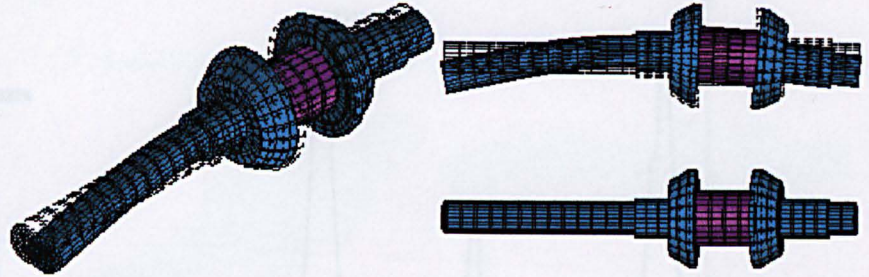
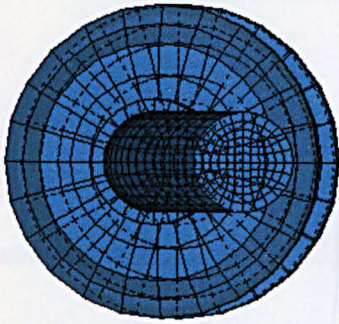


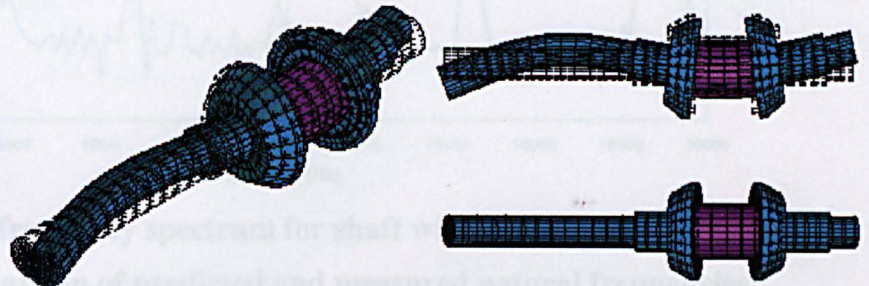
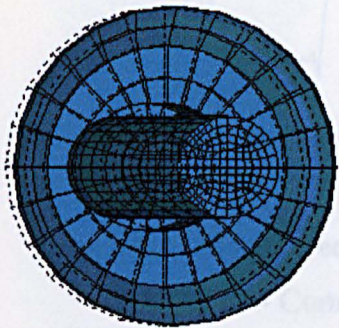
**Figure H.4 - Measured frequency spectrum for rotor shaft with laminations**

**Table H.2 - Comparison of predicted and measured natural frequencies**

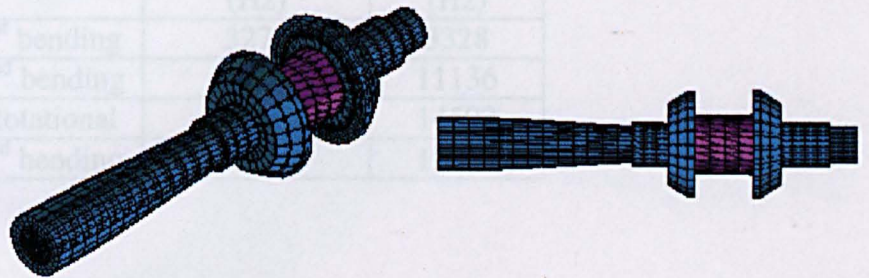
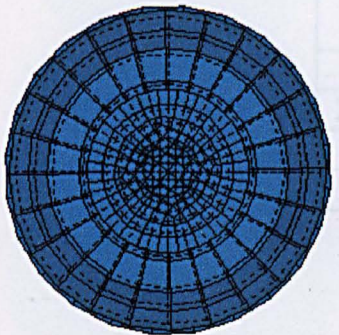
Mode	Finite element (Hz)	Measured (Hz)
1 <sup>st</sup> bending	3124	2976
2 <sup>nd</sup> bending	8936	9216
Rotational	12431	-
3 <sup>rd</sup> bending	15252	15776



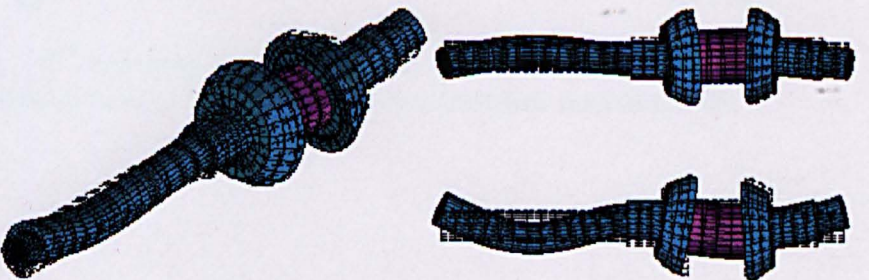
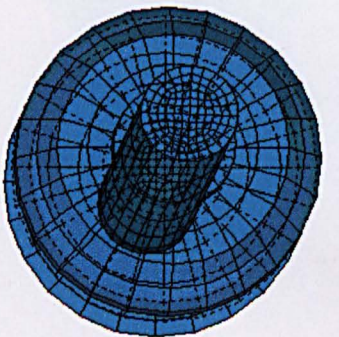
1<sup>st</sup> bending mode- 3124 Hz



2<sup>nd</sup> bending mode - 8936 Hz



Rotational mode - 12431 Hz



3<sup>rd</sup> bending mode - 15252 Hz

Figure H.5 - Vibrational modes for shaft with laminations

**c) Rotor shaft with laminations and magnets**

The measured frequency spectrum is shown in Figure H.6, and the predicted and measured natural frequencies are compared in Table H.3. The vibrational modes are shown in Figure H.7.

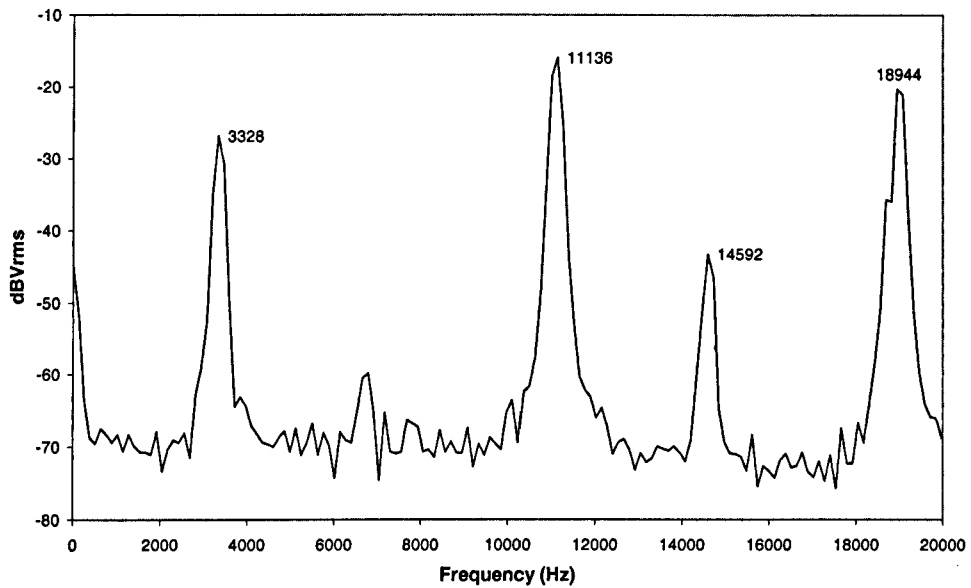
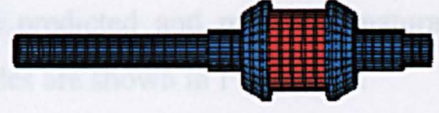
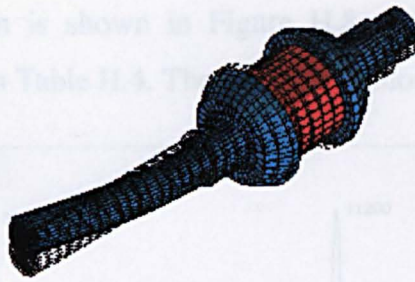
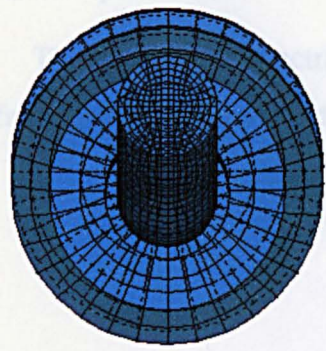


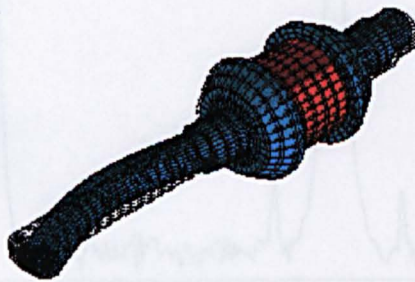
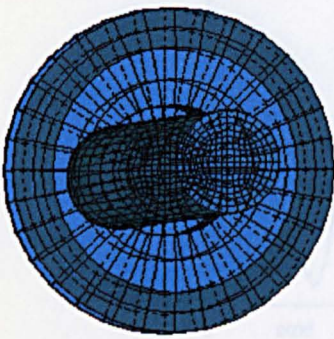
**Figure H.6 - Measured frequency spectrum for shaft with laminations and magnets**

**Table H.3 - Comparison of predicted and measured natural frequencies**

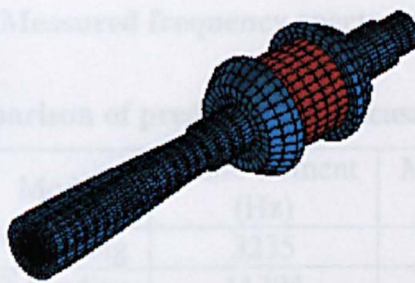
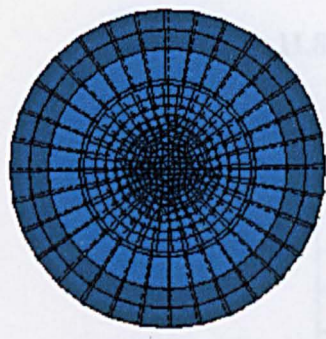
Mode	Finite element (Hz)	Measured (Hz)
1 <sup>st</sup> bending	3273	3328
2 <sup>nd</sup> bending	11357	11136
Rotational	14680	14592
3 <sup>rd</sup> bending	19195	18944



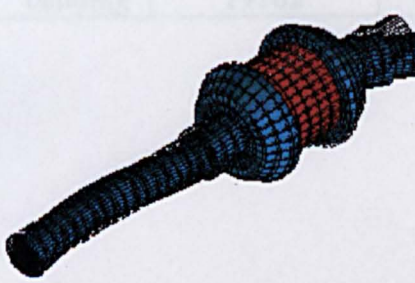
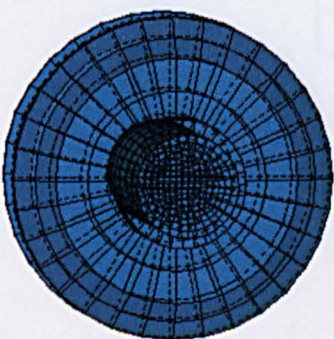
**1<sup>st</sup> bending mode - 3273 Hz**



**2<sup>nd</sup> bending mode - 11357 Hz**



**Rotational mode - 14680 Hz**



**3<sup>rd</sup> bending mode - 19195 Hz**

**Figure H.7 - Vibrational modes for shaft with laminations and magnets**

#### d) Complete rotor

The frequency spectrum is shown in Figure H.8, the predicted and measured natural frequencies are compared in Table H.4. The vibrational modes are shown in Figure H.9.

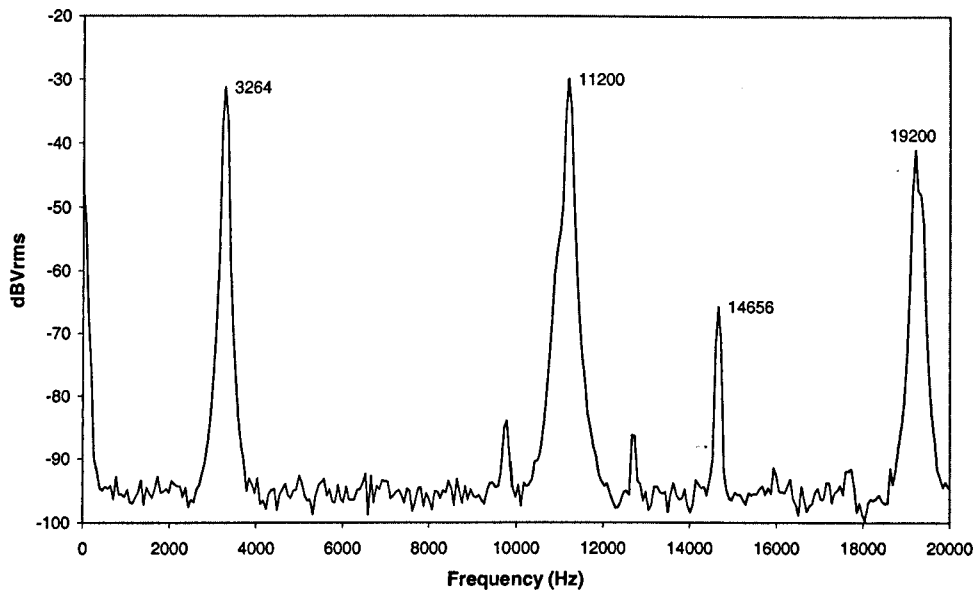
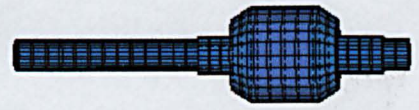
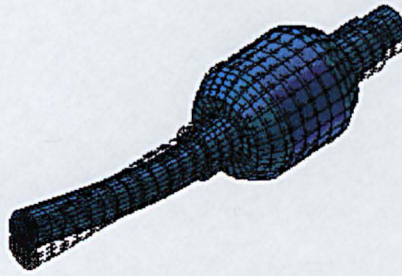
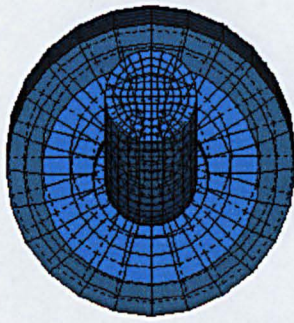


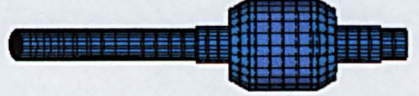
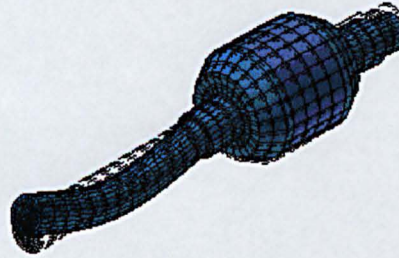
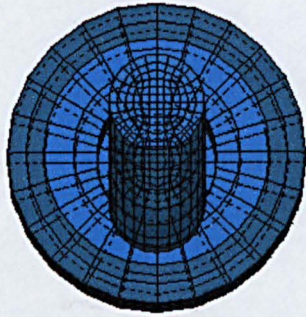
**Figure H.8 - Measured frequency spectrum for complete rotor**

**Table H.4 - Comparison of predicted and measured natural frequencies**

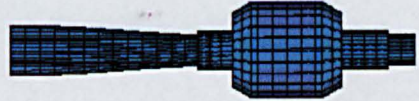
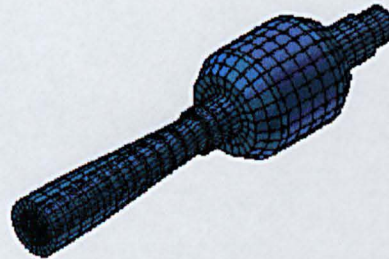
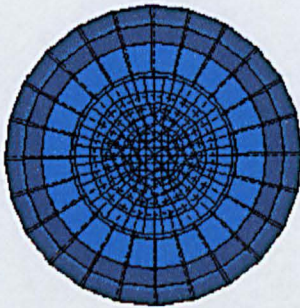
Mode	Finite element (Hz)	Measured (Hz)
1 <sup>st</sup> bending	3235	3264
2 <sup>nd</sup> bending	11304	11200
Rotational	14620	14656
3 <sup>rd</sup> bending	19182	19200



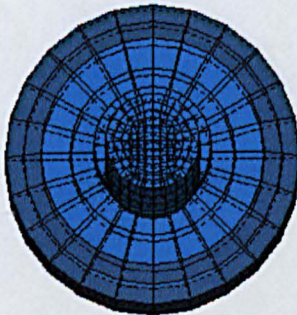
**1<sup>st</sup> bending mode- 3235 Hz**



**2<sup>nd</sup> bending mode - 11304 Hz**



**Rotational mode - 14620 Hz**



**3<sup>rd</sup> bending mode – 19182 Hz**

**Figure H.9 - Vibration modes for completed rotor**